NGU Report 2007.042

KONTIKI Final Report Continental Crust and Heat Generation In 3D

NGU
Norges geologiske undersøkelse
Geological Survey of Norway

Geological Survey of Norway
NO-7491 Trondheim, Norway
Tel.: 47 73 90 40 11
Telefax 47 73 92 16 20

REPORT

Report no.: 2007.042 | ISSN 0800-3416 | Grading: Confidential to 31.12.2012

Title:
KONTIKI Final Report, CONTInental Crust and Heat Generation In 3D

Authors:
Odleiv Olesen, Niels Balling, Cécile Barrère, Niels Breiner, Børre Davidsen, Jörg Ebbing, Harald Elvebakk, Laurent Gernigon, Janusz Koziel, Ole Lutro, Kirsti Midttømme, Øystein Nordgulen, Lars Olsen, Per Terje Osmundsen, Christophe Pascal, Randi K. Ramstad, Jan Steinar Rønning, Jan Reidar Skilbrei, Trond Slagstad and Bjørn Wissing

Client:
StatoilHydro ASA

County:
Østfold, Akershus, Oppland, Sogn & Fjordane, Møre & Romsdal, Sør-Trøndelag, Nord-Trøndelag, Nordland and Troms

Commune:

Map-sheet name (M=1:250.000)

Number of pages: 438 Price (NOK):
Map enclosures:

Fieldwork carried out: 2005-2007

Date of report: 31.12.2007

Project no.: 3066.00

Person responsible:
Øystein Nordgulen

Summary:
The KONTIKI Final Report summarises the results from the three-year KONTIKI Project (CONTInental Crust and Heat Generation In 3D) established by NGU and StatoilHydro to improve the understanding of heat flow along the Norwegian continental margin. A compilation of c. 4000 new and old geochemical data is used to produce the first map of radiogenic heat production in bedrock, covering large tracts of Norway. In general, granitic rocks have higher heat production than intermediate and mafic rocks. Sedimentary rocks display variation in heat production that can be ascribed to sedimentary processes. Age and metamorphic grade do not appear to affect heat production significantly, whereas tectonic setting appears to impart some effect in that extensional or within-plate rocks have higher heat production than similar rocks formed along plate margins. A total of 11 deep wells (c. 350-1000 m) have been established for temperature logging and heat flow calculations in mainland Norway. Calculated palaeoclimatic corrections range from +2 to +9 mW/m² (i.e. 5-20% of original heat flow values). The new heat flow map shows that heat flow values in Norway are much higher than previously proposed. The two most robust features on the map are the relatively high and low heat flows in the Oslo Region and Nordland respectively. New geochronological data from basement samples from the North Sea and Norwegian Sea show that the upper basement to a large degree consists of magmatic and metasedimentary rocks that can be correlated with rocks in tectonostratigraphically high (i.e., Upper and Uppermost Allochthons) nappes within the Scandinavian Caledonides. Both 3D crustal and thermal models have been produced from the Mid-Norwegain continental margin. Our 3D modelling suggests that substantial heat flow variations between 35 and 65 mW/m² occur at the base of the sedimentary basins in the inner parts of the mid-Norwegian Margin. We show that the structure and nature of the basement underlying these basins are the most likely factors influencing heat flow variations at typical wavelengths of 10s to 100s of km. One of the major outcomes of the modelling and the heat flow and heat production data collected on land, is that the Moho heat flow should range in between 30 to 40 mW/m^2, a value in the lower part of this range being the preferred one. The temperature of the outer Mid-Norwegian margin is lower than previously assumed and the petroleum potential of the area should be reconsidered.

Keywords: Geofysikk (Geophysics)	Kontinentalsokkel (Continental shelf)	Tolkning (Interpretation)
Berggrunnsgeologi (Bedrock geology)	Magnetometri (Magnetometry)	Varmestrøm (Heat flow)
Petrofysikk (Petrophysics)	Gravimetri (Gravimetry)	Fagrapport (Scientific report)

CONTENTS

1 INTRODUCTION

Understanding heat flow variation in sedimentary basins is of vital importance for the success of petroleum exploration campaigns. While the industry has invested much in understanding the thermal input related to lithospheric thinning, it appears that comparatively little has been done on the subject of heat flow from different types of basement. StatoilHydro and NGU established therefore the KONTIKI Project (Continental Crust and Heat Generation In 3D) to improve the knowledge on the varying heat flow on the Norwegian continental shelf. The age and thickness of the continental crust may also affect the surface heat flow. We have therefore studied how the heat flow is dependent on the age of basement provinces.

Petroleum reservoirs occur mainly within the Golden Zone (60-120^{o}C) (Bjørkum et al. 1998, Nadeau et al. 2005). The depth to this temperature interval depends to a large degree on the basement heat production which contribute to approximately 50% of the heat flow values offshore Norway (Ritter et al. 2004). Only 10% of the heat is produced within the sedimentary rocks of the basins. The heat production within the crystalline basement depends on the content of radioactive elements such as potassium, uranium and thorium. The content of these elements shows a wide variation within the mainland crystalline basement of Norway. Partly due to a lack of systematic data compilation, the knowledge of the basement rock composition below the Norwegian continental shelf is very poor or almost non-existing in large areas.

Relatively acidic rocks of the Precambrian gneisses and granites generate more heat than intermediate-mafic rocks within the Caledonian nappes and high-grade metamorphic units (e.g. the Lofoten gneiss complex). The latter rock units are representative for middle and lower crust. While mafic rocks within underplated bodies and other mafic igneous rocks provide an important transient heat pulse, they have a low radioactive heat production. The transient heat flow from these c. 50Ma old intrusives has returned to near-equilibrium today (Ritter et al. 2004). Assuming a constant heat production from the continental crust in basin modelling studies offshore Norway will lead to considerable errors in the calculation of the temperature regime in sedimentary basins. Analysis of offshore and onshore well data is a fundamental step to obtain detailed input for heat flow and thermal gradients.

The present project has aimed at compiling lithogeochemical information on basement rocks along the coast of Norway with emphasis on characterizing the U, Th and K content. Geophysical information such as seismic, aeromagnetic and gravity data, together with well penetrations of basement and age dating of the basement rocks, have provided a basis for extending this information below the offshore sedimentary basins. The Geological Survey of Norway (NGU) holds complete gravity and aeromagnetic databases from the whole of the Norwegian mainland and offshore areas in addition to detailed information on the mainland bedrock geology. The onshore-offshore geophysical interpretations have therefore been constrained by geochemical analysis and age-dating of basement core samples obtained from offshore exploration wells.

Seismic velocity and seismic reflection patterns from offshore basement rocks will help in distinguishing between Caledonian nappe complexes and more massive Precambrian granites

and gneisses. Hence, a first order distribution of basement-related heat flow has been mapped.

An additional element of relevance to the heat flow in sedimentary basins is the structural relief of the basement; basement highs most likely act as focussing points for fluid that are being driven out from the overlying sediments. The basement highs will also focus the heat flow since the thermal conductivity in basement rocks is usually higher than in sedimentary sequences. An element of the project has therefore been to map the basement structure and to combine this with the mapped rock type distribution.

Table 1.1. Petrophysical properties of the main basement provinces in central and northern Norway (adapted from Telford *et al.* 1976, Dobrin & Savit 1988, Mjelde *et al.* 1992, 1993, Olesen *et al.* 1990, 1991, 1997a,b, 2002, Osmundsen et al. 2003, Skilbrei 1988, Skilbrei *et al.* 1991, 2002).

Geological province	Density kg/m^3	Magnetic susceptibility (SI)	Magnetic remanence (Q-value)	Seismic velocity km/s	Seismic reflectivity	Heat production
Precambrian granites and acidic gneisses	2650-2710	0.00030-0.03000 frequently high magnetisation	low < 0.3	5.5-6.0	low	Intermediate - very high
Metamorphic core complexes (e.g. Lofoten and Vestranden)	2750-2850	0.00070-0.05000 frequently high magnetisation	intermediate 0.2-5	5.9-6.8	intermediate?	low - intermediate
Caledonian nappes	2800-3000	0.00090-0.05000 most frequently low magnetisation	low-intermediate 0.1-10	5.7-7.0	intermediate	low - intermediate

2 RADIOGENIC HEAT PRODUCTION OF ARCHAEAN TO PERMIAN GEOLOGICAL PROVINCES IN NORWAY

Trond Slagstad, NGU

2.1 Introduction

Radiogenic heat production in the continental crust is a major factor determining the thermal structure of continents. Investigations into this structure therefore depends on plentiful and geographically widespread sampling and geochemical analysis to gain insight into absolute values of heat production as well as likely variation, the latter providing constraints on the uncertainty of the models. In an effort to further our understanding of the thermal and geological structure of Scandinavia and the continent-ocean transition of the western Baltic shield, the Geological Survey of Norway (NGU), in collaboration with Statoil, have undertaken a project involving determination of radiogenic heat production rate, heat flow density and thermal conductivity in Norway. As part of this work, c. 2000 new chemical analyses and an equal number of previously published analyses have been compiled to produce the first heat production map covering a major part of Norway. Further sampling and analysis on a national scale is continuously being carried out, mainly through NGU's LITO-project (ngu.no/lito), and the purpose of this contribution is to present and make available this rather extensive dataset so that it may be employed by other workers in this or related fields. Additional data, both from analyses of new samples as well as compilation of existing data, will be presented continuously through NGU's planned bedrock geochemical database, available online in 2008.

2.2 Sources of heat production data

The heat production rate of individual samples is calculated following Rybach (1988), based on the samples' K, U and Th concentrations, and density. The chemical data used to calculate heat production come from various sources, summarised in Table 2.1. The majority of the samples have been analysed by XRF (K) and LA–ICP–MS (U, Th), thus a complete set of major and trace element data exists for each of these samples. The remaining samples have been analysed by γ-ray spectrometry, thus for these samples only the concentrations of heat producing elements are available. The analytical procedure, detection limits, accuracy and precision of the γ-ray spectrometry method are described by Raade (1973) and Killeen & Heier (1975). For several geological units, heat production data based on both XRF/LA–ICP–MS and γ-ray spectrometry exist. Average heat production rates for such units are similar regardless if they are based on the older γ-ray data or more modern XRF/LA–ICP–MS data, suggesting that the quality of the former are good.

Table 2.1. Sources of heat production data.

Source	No.	Analytical method
LITO-project	1613	XRF, LA–ICP–MS
Various NGU samples	623	XRF, LA–ICP–MS
Killeen & Heier (1975)	629	γ-ray spectrometry
Raade (1973)	967	γ-ray spectrometry
Ormaasen (1976)	102	γ-ray spectrometry

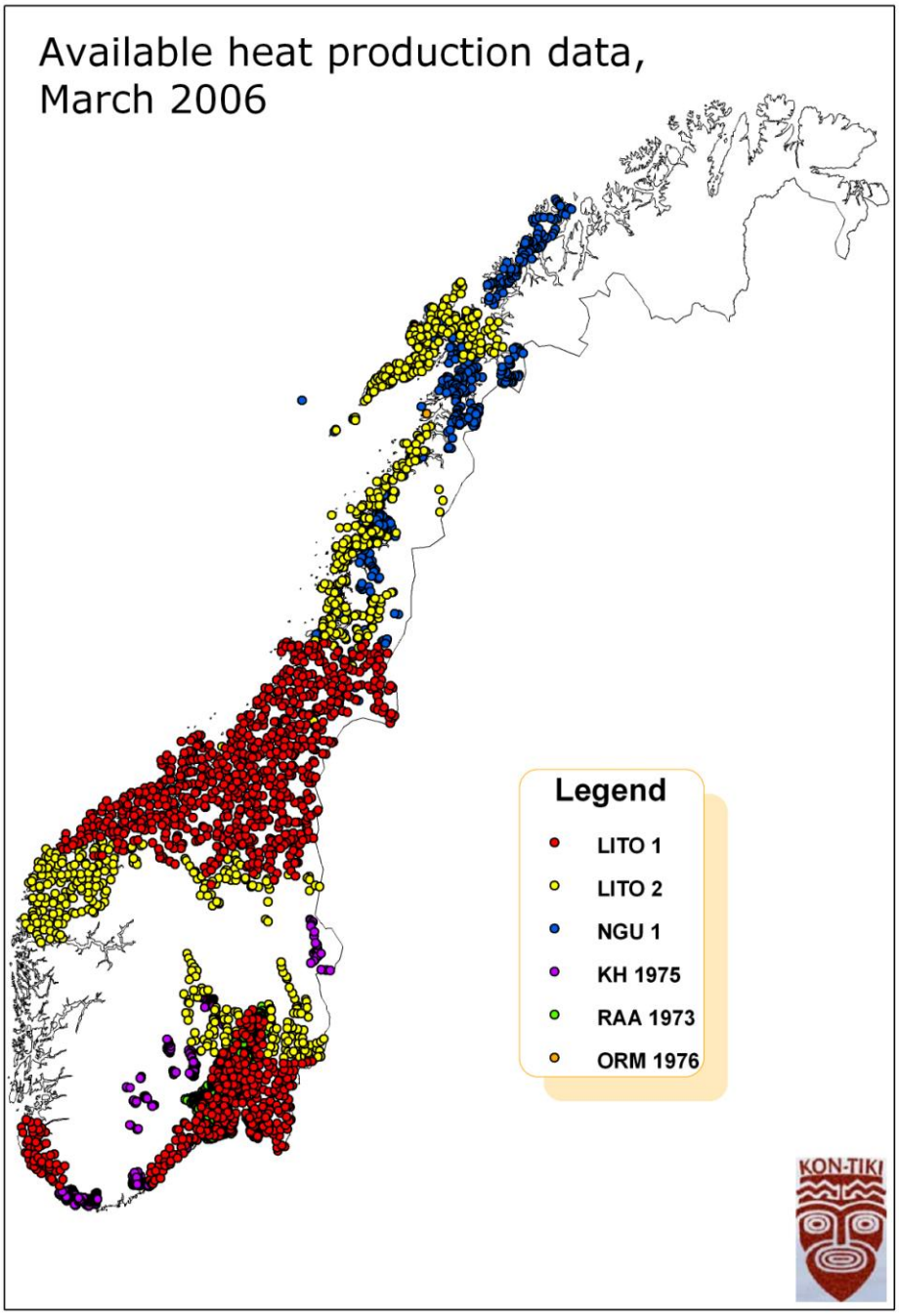

Figure 2.1. Map showing the distribution of available heat production data as of March 2006. See Table 2.1 for explanation of legend.

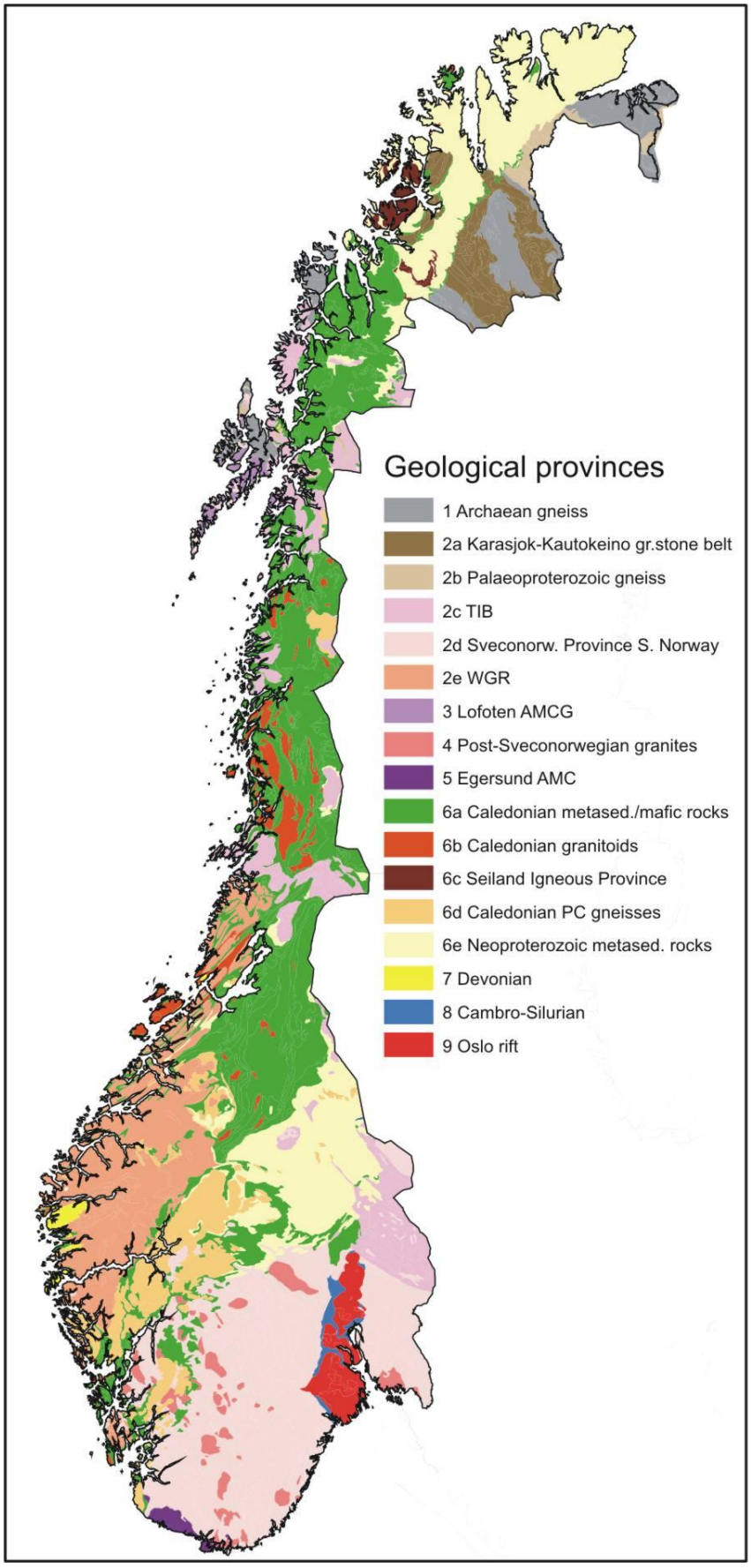

Figure 2.2. Simplified geological map, modified after Sigmond (1996).

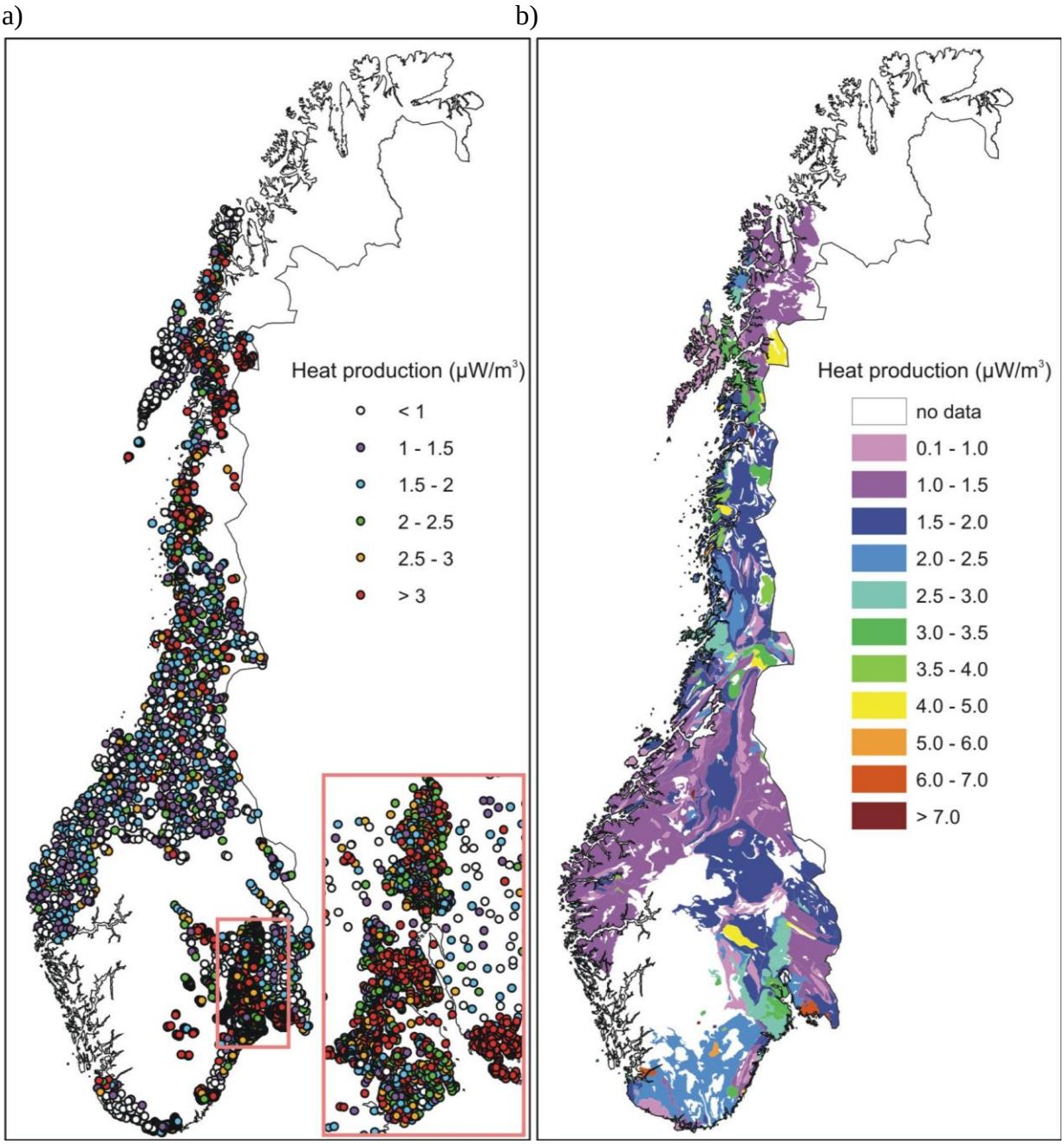

Figure 2.3. (a) Heat production data. (b) Average heat production rates for geological units where data are available.

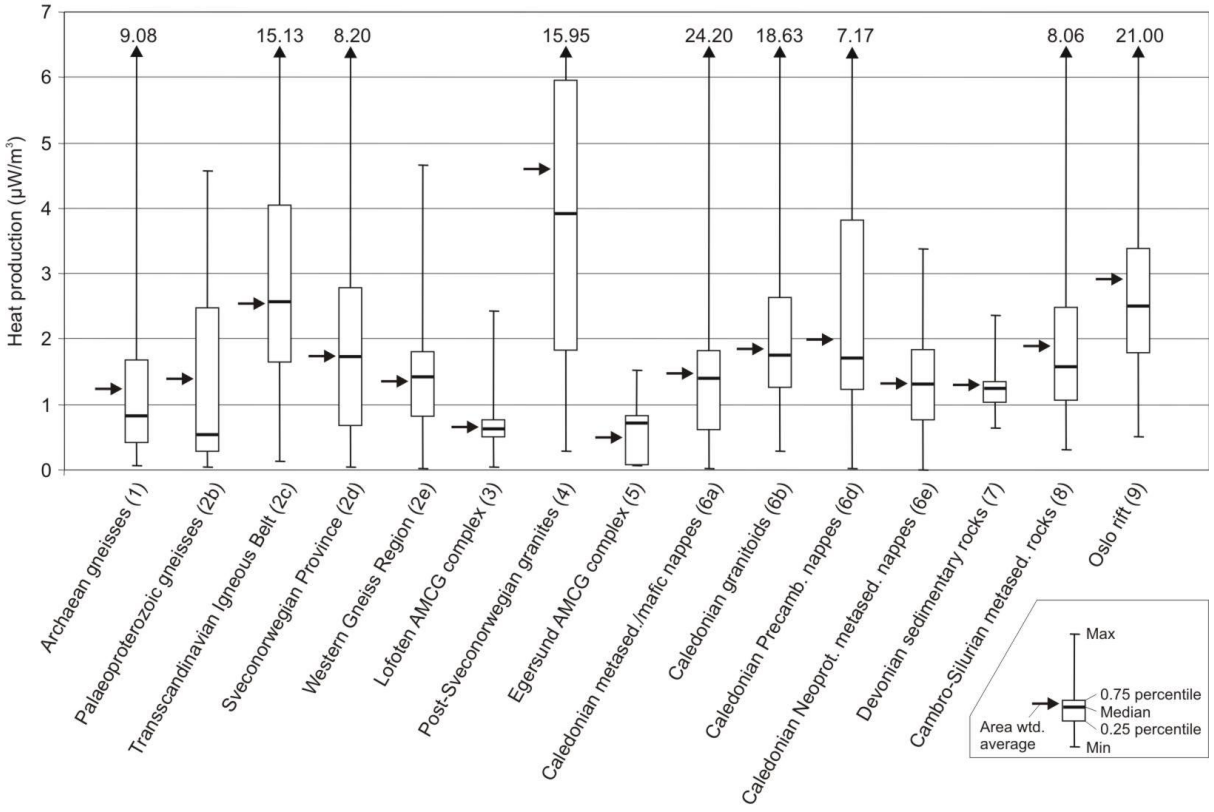

Figure 2.4. Heat production data from geological units presented in Table 2.2 and Fig. 2.2.

2.3 Geological evolution, heat production and heat flow of Archaean to Permian geological units in Norway

A number of factors of which lithology, tectonic setting, tectonometamorphic history and age are the most obvious, may influence the heat production and heat flow of a geologically distinct terrain. The work presented here is part of a larger effort to enhance our understanding of the geological and thermal structure of the continental margin of Norway (and the Baltic Shield). This means that heat production values must be assigned to geological units onshore that can be correlated offshore onto the continental margin using seismic or potential field data. With these objectives in mind, I will present and discuss the heat production data in reference to specific geological units, subdivided based on lithology, tectonic setting, tectonometamorphic history and age. The subdivision includes nine major and several minor provinces, ranging in age from Archaean to Permian; however, geochemical data are not presently available from all of these provinces. Table 2.2 presents a summary of geological and heat production information. The numbers in parentheses below refer to provinces on the simplified geological map (Fig. 2.2) and Table 2.2. The heat production data are presented graphically in Figs. 1b and 1c, and Fig. 2.4 shows calculated average heat production for units as defined by Sigmond (1996).

2.3.1 Archaean gneissic rocks (1)

Rocks of Archaean crystallisation or depositional age are found in several areas in northern Norway. The most intensely studied area is a chain of islands running from southern Lofoten to the island Vanna in West Troms (Fig. 2.2). This area is underlain by intermediate metavolcanic rocks, migmatised during the Late Archaean, tonalitic to granitic gneisses, and greenstone remnants (Griffin et al. 1978, Zwaan 1995, Corfu et al. 2003). Pb–Pb whole rock isochrons and Rb/Sr isotopic data from migmatite and granite on Langøya and Hinnøya yield ages of c. 2700 Ma and c. 2600 Ma, respectively (Griffin et al. 1978). Magmatic activity in this area between 2700 and 2600 Ma is corroborated by an interpreted U–Pb zircon crystallisation age of 2689±6 Ma for a granite on Kvaløya (Corfu et al. 2003). The rocks typically contain upper amphibolite- to granulite-facies assemblages, and the tectonometamorphic history includes a Late Archaean event responsible for migmatisation of the metavolcanic rocks (Griffin et al. 1978), as well as a Late Palaeoproterozoic (1870–1790 Ma) granulite-facies event related to emplacement of the Lofoten–Vesterålen anorthosite-mangerite-charnockite-granite (AMCG) suite (Corfu 2004a), discussed below.

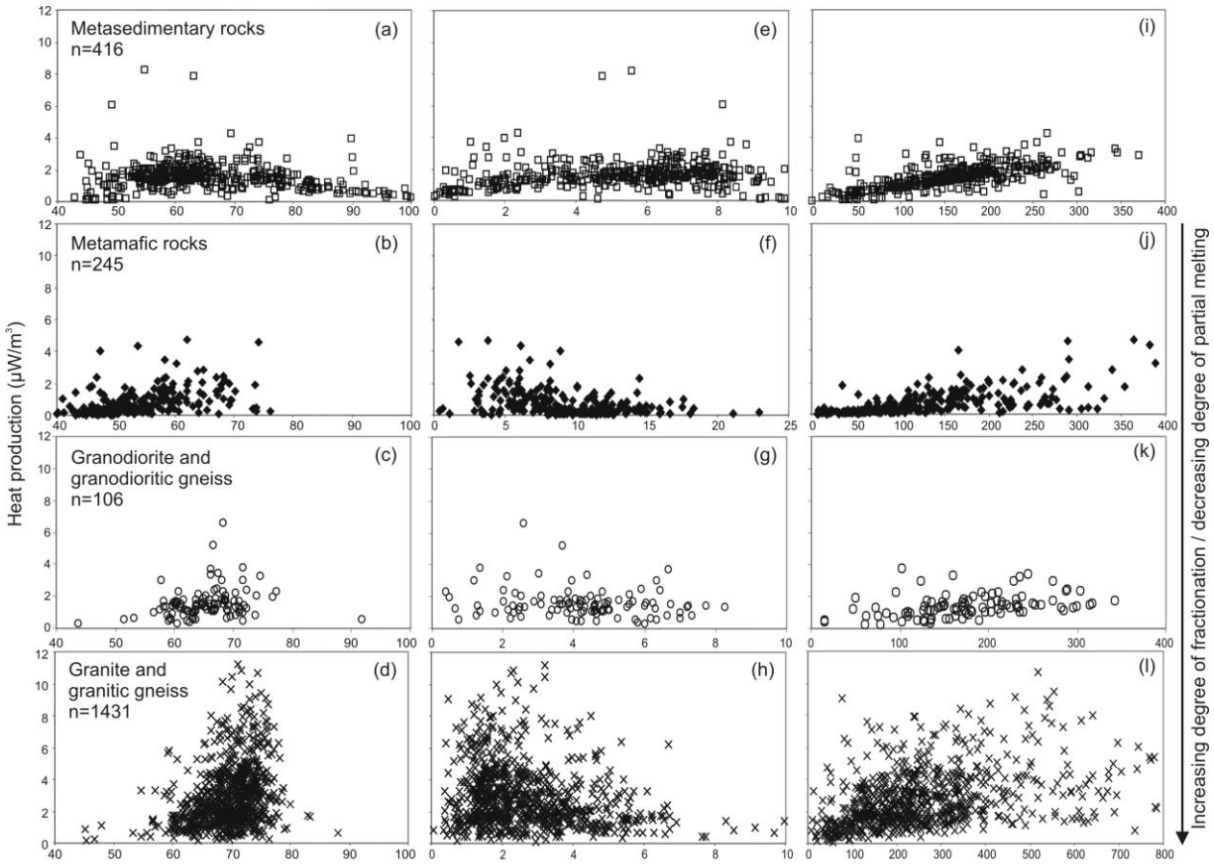

Figure 2.5. Heat production vs. chemical composition sorted by rock type.

Table 2.2. Simplified geological history and heat production rates of geological provinces in Norway.

	Geological province	n	Age (Ma)	Lithology	Tectonic setting	Tectonometamorphic history	Heat production rate ($\mu W/m^3$)		Heat flow (mW/m^2)	
							Area wtd. mean[1]	Median ±1σ	Mean ±1σ (n)	Median
1	Archaean gneisses	95	3000–2500	Dominantly tonalitic to granitic gneisses		Early Proterozoic (c. 2.0–1.8 Ga) amphibolite- to granulite-facies metamorphism.	1.25	0.81 ± 1.48	38 ± 8 (2)	38
2	Proterozoic gneissic rocks									
2a	Karasjok-Kautokeino greenstone belts, NE Norway	n.d.	2100-2000	Tholeiitic metabasalts, amphibolites and interlayered metasedimentary rocks	Continental rifting and oceanic subduction	Metamorphosed under greenschist- to amphibolite-facies conditions during obduction onto the Karelian craton at c. 1.9 Ga.	n.d.	n.d.	24 (1)	24
2b	Palaeoproterozoic gneisses	17	2000–1900	Garnet-quartz-feldspar paragneiss and hypersthene-plagioclase orthogneiss	Deposition in continental back-arc basin	High-grade metamorphism during continent-continent collision at c. 1900 Ma	1.42	0.54 ± 1.44	38 ± 3 (16)	38
2c	Transscandinavian Igneous Belt (TIB)	571	1810–1770	Alkali-calcic to calc-alkaline quartz monzonites to granites	Active continental margin, back-arc extension	Deformation and metamorphism at c. 1.46–1.42 and 1.0 Ga in SW Sweden. Variable Caledonian effects in NW Norway at c. 420 Ma.	2.57	2.57 ± 2.03	38 ± 8 (4)	38
2d	Sveconorwegian Province, S Norway	385	1500–1000	Tholeiitic to calc-alkaline, intermediate to felsic, metavolcanic and –plutonic suites	Active continental margin and continental back-arc.	Local crustal reworking at 1.26–1.16 Ga. Continent-continent collision and associated medium- to high-grade metamorphism at c. 1.0 Ga. Very low-grade Caledonian metamorphism at c. 400 Ma in western areas.	1.76	1.73 ± 1.45	43 ± 8 (25)	45
2e	Western Gneiss Region, W Norway	332	1750–1000	Dominantly tonalitic to granitic gneisses	Active continental margin	Sveconorwegian and Caledonian high-grade metamorphism at c. 1000 and 400 Ma, respectively.	1.36	1.41 ± 0.82	42 ± 9 (8)	41

	Geological province	n	Age (Ma)	Lithology	Tectonic setting	Tectonometamorphic history	Heat production rate ($\mu W/m^3$)		Heat flow (mW/m^2)	
							Area wtd. mean[1]	Median ±1σ	Mean ±1σ (n)	Median
3	Lofoten anorthosite-mangerite-charnockite-granite (AMCG) complex	130	1800–1790	Mangerite, smaller volumes of gabbro, anorthosite, charnockite and granite	Related to TIB 1 magmatism	Crystallised under low-P granulite-facies conditions. No significant later metamorphic events.	0.65	0.61 ± 0.32	n.d.	n.d.
4	Post-Sveconorwegian granites, S Norway	473	930–920	Dominantly granite, locally grading to diorite	Extensional, post-tectonic magmatism	Generally no significant metamorphic overprinting.	4.61	3.92 ± 2.54	58 ± 17 (12)	59
5	Egersund anorthosite-mangerite-charnockite (AMC) complex	47	930	Massive anorthosite, lesser volumes of leuconorite, mangerite and charnockite	Extensional, post-tectonic magmatism	Very low-grade Caledonian metamorphism at c. 400 Ma.	0.57	0.71 ± 0.42	21 (1)	21
6	Caledonian thrust-sheets									
6a	Late Proterozoic to Palaeozoic metasedimentary and metamafic rocks	561	500–450	Metagreywacke, phyllite, mica schist, lesser volumes of marble and greenstone.	Passive margin sequences. Greenstones formed in oceanic arc / back-arc.	Low- to high-grade metamorphism during the Caledonian orogeny at c. 450–400 Ma.	1.47	1.40 ± 1.39	48 ± 8 (12)	49
6b	Caledonian intrusive rocks	167	480–430	Dominantly calc-alkaline diorite, tonalite, granodiorite and granite. Minor trondhjemitic intrusions.	Active continental margin.	Variable overprinting during the Caledonian orogeny at c. 430–410 Ma.	1.85	1.74 ± 1.85	66	66
6c	Seiland igneous province	n.d.	570–560	Gabbro, lesser volumes of ultramafic rocks and intermediate granitoid rocks.	Intracontinental rift.	Variable overprinting during the Caledonian orogeny at c. 420 Ma.	n.d.	n.d.	n.d.	n.d.
6d	Precambrian gneissic rocks	35	1690–950	Syenitic to monzonitic gneisses, anorthosite-mangerite-charnockite-granite suites	Active continental margin. AMCG suite formed in intraplate setting (?)	Late Sveconorwegian, high-grade metamorphism at c. 930 Ma. Variable, but locally high-grade metamorphism at c. 450 Ma.	2.01	1.70 ± 1.78	41 ± 11 (4)	43

	Geological province	n	Age (Ma)	Lithology	Tectonic setting	Tectonometamorphic history	Heat production rate ($\mu W/m^3$)		Heat flow (mW/m^2)	
							Area wtd. mean[1]	Median ±1σ	Mean ±1σ (n)	Median
6e	Neoproterozoic metasedimentary rocks	48	1000–500	Quartzitic to arkosic sandstone, mica schist, pelite and volumetrically subordinate carbonate	Continental shelf	Variable high- to low-grade Scandian and pre-Scandian metamorphism in Finnmark. Low-grade overprinting in Lillehammer during the Scandian phase at c. 430-400 Ma.	1.35	1.31 ± 0.82	43 ± 6 (4)	42
7	Devonian sedimentary rocks	15	400–390	Fluvial sandstones, conglomerate, breccia	Post-orogenic extension	No metamorphic overprinting.	1.33	1.23 ± 0.47	n.d.	n.d.
8	Cambro–Silurian sedimentary rocks	37	540–420	Marine shales, carbonates, sandstones	Epicontinental basin, later foreland basin	Low-grade metamorphism and deformation during the Caledonian orogeny at c. 420 Ma; local contact metamorphism during formation of Oslo rift at c. 300–280 Ma.	1.89	1.56 ± 1.45	48 ± 8 (6)	51
9	Oslo Rift	1044	300–280	Tholeiitic basalts, monzonite, syenite and granite	Intracontinental rift.	No metamorphic overprinting.	2.93	2.50 ± 1.64	45 ± 8 (4)	46

See text for details and references.

[1]Area-weighted heat production of all map units classified within the particular geological province.

Other areas underlain by Archaean rocks include Finnmarksvidda, where rocks belonging to the Raiseatnu and Jergol Complexes are exposed, and large tracts of the Sørvaranger area. Lithologically, the Raiseatnu and Jergol Complexes are rather similar and composed dominantly of medium- to high-grade orthogneisses of tonalitic, granitic and dioritic composition (Siedlecka et al. 1985), whereas the Sørvaranger area is more varied and comprises mica schists and mica gneisses in addition to tonalitic to granitic orthogneisses (Levchenkov et al. 1993).

Ninety-five samples of Archaean gneisses from West Troms yield a median heat production of 0.81 ± 1.48 $\mu W/m^3$ and an area-weighted heat production of 1.25 $\mu W/m^3$ (Fig. 2.4). No heat production data from Finnmark are available.

2.3.2 Proterozoic gneissic rocks (2)

2.3.2.1 Karasjok–Kautokeino greenstone belts, NE Norway (2a)

The Karasjok and Kautokeino greenstone belts in E Finnmark (Fig. 2.2) consist of tholeiitic metabasalts, tuffaceous greenstones and amphibolites interlayered with metasedimentary rocks (Siedlecka et al. 1985). A Sm–Nd whole-rock age of c. 2100 Ma from komatiites of the Karasjok greenstone belt was interpreted by Krill et al. (1985) to date crystallisation of the komatiite. The greenstone belts are believed to have formed as a result of crustal extension and/or rifting at c. 2100 Ma, producing various mafic volcanic rocks, followed by subduction and formation of arc-related magmatic rocks at c. 2000 Ma (Krill et al., 1985; Marker, 1985). These oceanic provinces were thrust westwards onto the Archaean Karelian craton at c. 1.9 Ga (Krill et al. 1985, Braathen & Davidsen 2000). The rocks were mostly metamorphosed under low to medium conditions (sub-greenschist to amphibolite-facies) (Siedlecka et al. 1985) during this event.

Unfortunately, no heat production data are currently available from the Karasjok–Kautokeino greenstone belts; however, judging from the lithological make up of this province, relatively low heat production appears likely.

2.3.2.2 Levajok Granulite Complex (2b)

The Levajok Granulite Complex is sparsely exposed in Norway but widens towards the east and southeast into Finland and Russia and forms a unit of regional extent; it is therefore included here as a separate unit. The granulite complex consists of two main lithologies (Marker 1985, Siedlecka et al. 1985) of which the oldest is a garnet-quartz-feldspar paragneiss that most likely represents continental back-arc basin flysch deposits. Younger, hypersthene-plagioclase orthogneisses probably represent intrusions into the paragneiss at c. 2000–1900 Ma, possibly coeval with granulite-facies metamorphism during continent-continent collision (Bernard-Griffiths et al. 1984).

Seventeen samples of Palaeoproterozoic gneisses from a small area on Andøya, West Troms, yield a median heat production of 0.54 ± 1.44 μW/m^3 and an area-weighted heat production of 1.42 μW/m^3 (Fig. 2.4). Unfortunately, no heat production data are available from the Granulite Complex in Finnmark; the heat production of this province is therefore poorly constrained even though the available data yield reasonable values.

2.3.2.3 Transscandinavian Igneous Belt (TIB) (2c)

The Transscandinavian Igneous Belt (discussion limited to TIB 1 as defined by Åhäll & Larson 2000) forms a c. 1400 km long and up to 200 km wide belt of c. 1810–1770 Ma magmatic rocks from SE Sweden to NW Norway (Fig. 2.2). The belt is composed of alkali-calcic to calc-alkaline quartz monzonitic to granitic plutons and associated volcanic rocks, and subordinate mafic and hybrid rocks (Åhäll & Larson 2000), that include juvenile crustal components as well as a significant mantle contribution (Andersson, 1991). Most workers favour an active continental margin setting for the TIB, involving eastward subduction beneath the western margin of Baltica and back-arc extension (e.g., Wilson 1980, Andersson, 1991). In central Sweden, the TIB rocks are generally undeformed and unmetamorphosed, whereas in SW Sweden they have a polymetamorphic history involving deformation and amphibolite-facies metamorphism at c. 1.46–1.42 Ga, during the Hallandian orogey, and during the Sveconorwegian orogeny at c. 1.0 Ga (Christoffel et al. 1999, Söderlund et al. 2002, Möller et al. 2007). In NW parts of the TIB (i.e., in NW Norway) the TIB rocks display variable Caledonian effects, locally with migmatisation at c. 420 Ma (Skår 2002).
Five-hundred and seventy-one samples from the Transscandinavian Igneous Belt in South-east, Central and North-central Norway yield a median heat production of 2.57 ± 2.03 μW/m^3 and an area-weighted heat production of 2.57 μW/m^3 (Fig. 2.4).

2.3.2.4 Sveconorwegian Province, S Norway (2d)

The Sveconorwegian Province in S Norway and SW Sweden is generally divided into four Palaeoproterozoic to Mesoproterozoic domains (Fig. 2.2). The easternmost domain (aptly referred to as the Eastern Segment) consists mainly of reworked granitoid orthogneisses of TIB affinity and is included in the discussion above. The remaining part of the Sveconorwegian Province consists mainly of greenschist to amphibolite-facies (locally granulite-facies) tholeiitic and calc-alkaline, intermediate to felsic, metavolcanic and –plutonic suites that formed at around 1.5 Ga (Bingen et al. 2005 and references therein). Most of these rocks probably formed along an active continental margin at that time (Bingen et al. 2005, Slagstad & Marker, unpublished data). In addition, rhyolite-dominated, bimodal volcanic suites underlie large tracts of S Norway. These rocks formed at c. 1.26–1.16 Ga and attest to crustal reworking, possibly in a continental back-arc setting (Bingen et al. 2002, Brewer et al. 2004). The last event to affect the area was the Sveconorwegian orogeny, which is generally ascribed to continent-continent collision at c. 1.0 Ga. In addition, western areas were affected by very low-grade Caledonian overprinting at c. 400 Ma (Verschure et al., 1980).

Three-hundred and eighty-five samples from the Sveconorwegian Province in South Norway yield a median heat production of 1.73 ± 1.45 μW/m^3 and an area-weighted heat production of 1.76 μW/m^3 (Fig. 2.4).

2.3.2.5 Western Gneiss Region, W Norway (2e)

The Western Gneiss Region (Fig. 2.2) represents the westward continuation of the Sveconorwegian Province and Transscandinavian Igneous Belt, metamorphosed under low- to high-grade conditions, locally with formation of eclogite, during the Caledonian orogeny (Milnes et al. 1997). Lithologically, the Western Gneiss Region is dominated by tonalitic to granitic gneisses, locally migmatitic, and augen gneisses. Most of the rocks formed in the interval 1.75–1.5 Ma (Gaál & Gorbatschev 1987, Tucker et al. 1990, Skår & Pedersen 2003), probably along the active margin of Baltica. In addition, some granitic units formed during the Sveconorwegian orogeny (Skår & Pedersen 2003). The rocks record both Sveconorwegian and Caledonian high-grade metamorphism at c. 1000 and 400 Ma, respectively (Tucker et al. 1990, Skår & Pedersen 2003).

Three-hundred and thirty-two samples from the Western Gneiss Region yield a median heat production of 1.41 ± 0.82 μW/m^3 and an area-weighted heat production of 1.36 μW/m^3 (Fig. 2.4).

2.3.3 Lofoten AMCG complex (3)

More than half of the surface area in Lofoten–Vesterålen (Fig. 2.2) is underlain by a distinct suite of rocks dominated by mangerite and retrogressed equivalents that intruded Archaean gneisses and Early Palaeoproterozoic supracrustal rocks (Griffin et al. 1978). This suite of rocks is typically referred to as the Lofoten AMCG complex. Detailed U–Pb zircon geochronological work by Corfu (2004a) shows that the AMCG complex was emplaced during two distinct event. The first event at 1870–1860 Ma included emplacement of the composite Hopen pluton, consisting of gabbro, mangerite and charnockite, and the granitic Lødingen pluton. The second, main event at 1800–1790 Ma also included a variety of rock types, ranging from gabbro and anorthosite, through mangerite and charnockite, to granite. A subsequent period, lasting 30–40 million years, included intrusion of pegmatite dykes and local hydration of the dry AMCG rocks. Formation of the Lofoten AMCG complex was most likely linked to prolonged and widespread tectonic and magmatic activity along the Baltic margin related to the first and major phase of formation of the Transscandinavian Igneous Belt between c. 1810–1770 Ma (TIB 1 of Åhäll & Larson 2000), but the exact tectonic setting is poorly known. Petrogenetic models suggest that the suite formed by polybaric fractionation of tholeiitic basaltic magmas combined with assimilation of country rocks (Wade 1985, Markl & Höhndorf, 2003). Pressure estimates of c. 400 MPa (Markl et al. 1998) suggest emplacement at mid-crustal levels which begs the question of whether the granulite-facies metamorphism of the Archaean country rocks represent regional

metamorphism (cf., Griffin et al. 1978) or is a contact metamorphic effect. The Lofoten AMCG complex and the surrounding Archaean gneissic rocks were only weakly affected by the Caledonian orogeny, and evidence of Caledonian effects is limited to local resetting of titanite (Corfu 2004b) and mica (Steltenpohl et al. 2004). One-hundred and thirty samples from the Lofoten AMCG complex yield a median heat production of 0.61 ± 0.32 μW/m^3 and an area-weighted heat production of 0.65 μW/m^3 (Fig. 2.4).

2.3.4 Post-Sveconorwegian granites, S Norway (4)

A distinct geological feature of S Norway is Post-Sveconorwegian granites forming subcircular intrusions in older Mesoproterozoic crust (Fig. 2.2). Several of these granite are well known for having anomalously high heat production rates (Killeen & Heier 1975, Slagstad 2006), and include the Iddefjord and Flå granites. Although granite is the dominant lithology, some plutons grade into more intermediate to mafic (diorite) compositions (Pedersen & Maaloe 1990). U–Pb zircon dating of some of these granites yield ages around 920–930 Ma (Eliasson & Schöberg 1991, Nordgulen et al. 1997). The source characteristics, petrogenesis and tectonic setting in which these granites formed is uncertain, however, most studies suggest they may have formed in an extensional tectonic regime by partial melting of middle to lower crustal source rocks with some input of mantle-derived magmas (Eliasson 1992, Andersen et al. 2001).

Four-hundred and seventy-three samples of post-Sveconorwegian granites in South Norway yield a median heat production of 3.92 ± 2.54 μW/m^3 and an area-weighted heat production of 4.61 μW/m^3 (Fig. 2.4).

2.3.5 Egersund AMC complex (5)

The Egersund anorthosite-mangerite-charnockite (AMC) complex in SW Norway (Fig. 2.2) formed at c. 930 Ma (e.g., Schärer et al. 1996), succeeding Sveconorwegian metamorphism and deformation by c. 60 million years. Formation of the Egersund AMC complex was contemporaneous with widespread post-Sveconorwegian granitic magmatism elsewhere in S Norway. The Egersund AMC complex consists of massive anorthosite and lesser volumes of leuconorite, mangerite and charnockite (e.g., Bolle et al. 2003) and probably formed by partial melting of a lower crustal gabbronoritic source (Schiellerup et al. 2000, Vander Auwera et al. 2003). The rocks of the Egersund AMC complex are generally unmetamorphosed, possibly with the exception of local, very low-grade Caledonian overprinting at c. 400 Ma (Verschure et al. 1980).

Forty-seven samples from the Egersund AMCG complex yield a median heat production of 0.71 ± 0.42 μW/m^3 and an area-weighted heat production of 0.57 μW/m^3 (Fig. 2.4), i.e., similar to that of the Lofoten AMCG complex.

2.3.6 Caledonian thrust-sheets (6)

2.3.6.1 Late Proterozoic to Palaeozoic metasedimentary and metamafic rocks (6a)

This group is by far the largest and diverse of the Caledonian units discussed here and extends from Magerøya to the north to Bergen to the south (Fig. 2.2). Lithologically, the group is dominated by metagreywackes, phyllites and mica schists, but also encompasses marbles and ophiolitic greenstones (Sigmond et al. 1984). These metasedimentary and metavolcanic rocks constitute nappes and nappe complexes that also include a variety of Caledonian granitoid rocks; the latter are discussed separately below because they are lithologically distinct and are expected to have different heat production rates from the former. Most of the rocks included in this group were deposited in Cambro-Silurian time (c. 500–450 Ma) and metamorphosed under greenschist- to upper amphibolite-facies, and locally eclogite-facies conditions (Bryhni & Andréasson 1985) at c. 450–400 Ma during the Caledonian orogeny.

Five-hundred and sixty-one samples from a major portion of the Caledonian orogen yield a median heat production of 1.40 ± 1.39 $\mu W/m^3$ and an area-weighted heat production of 1.47 $\mu W/m^3$ (Fig. 2.4).

2.3.6.2 Caledonian intrusive rocks (6b)

Rocks of this group are found mainly in central and north-central Norway (Fig. 2.2) and are dominated volumetrically by the Smøla–Hitra and Bindal Batholiths (Gautneb & Roberts 1989, Nordgulen et al. 1993). Lithologically, the two batholiths encompass dominantly calc-alkaline diorite, tonalite, granodiorite and granite that probably formed in a magmatic arc setting at c. 480–430 Ma (Gautneb & Roberts 1989, Nordgulen et al. 1993, 2001). In addition, several smaller, dominantly trondhjemitic intrusions (Size 1985) dated at c. 490–435 Ma (Dunning & Grenne 2000, Roberts et al. 2002, Nilsen et al. 2003) are included in this group. The rocks display variable metamorphic and deformational overprinting related to the Caledonian orogeny at c. 430–410 Ma (Tucker et al. 2004).

One-hundred and sixty-seven samples of mainly granitoid intrusive rocks within the Caledonian orogen yield a median heat production of 1.74 ± 1.85 $\mu W/m^3$ and an area-weighted heat production of 1.85 $\mu W/m^3$ (Fig. 2.4).

2.3.6.3 Seiland Igneous Province (6c)

The Seiland Igneous Province in western Finnmark (Fig. 2.2) is dominated by tholeiitic, calc-alkaline and alkaline gabbros and rarer monzonitic, dioritic and ultramafic bodies (e.g., Robins & Often 1996). Recent dating of the voluminous gabbros shows that they formed in a comparatively short time interval, from c. 570–560 Ma (Roberts et al. 2006), most likely in an intracontinental rift setting (Krill & Zwaan 1987, Roberts et al. 2006). The province was

subjected to Scandian deformation and medium- to high-grade metamorphism at c. 420 Ma, and evidence of a preceding tectonic event is lacking (Krill & Zwaan 1987, Roberts et al. 2006, Slagstad et al. 2006).

Unfortunately, no heat production data are available from the Seiland Igneous Province; however, judging from the lithological make up of this province, relatively low heat production appears likely.

2.3.6.4 Precambrian gneissic rocks (6d)

The most prominent and well-studied units included in this group are the Jotun, Lindås and Dalsfjord nappes in south-central Norway (Fig. 2.2). These nappes are commonly regarded as erosional remnants of a once continuous nappe complex covering much of South Norway (Hossack 1984, Norton 1986). The nappes consist of syenitic to monzonitic gneisses that formed at c. 1690 Ma (Schärer 1980), synchronous with widespread magmatism along the Baltic continental margin (see above). These gneissic rocks were intruded by gabbroic magmas at c. 1450 Ma (Corfu & Emmet 1992) and anorthosite-charnockite-mangerite-granite suites at c. 1250 and 950 Ma (Bingen et al. 2001). The rocks underwent late Sveconorwegian amphibolite- to granulite-facies metamorphism at c. 930 Ma (Schärer 1980, Corfu & Emmet 1992, Bingen et al. 2001), and locally high-grade (up to eclogite-facies) metamorphism at c. 450 Ma (Bingen et al. 2001) during the Caledonian orogeny.

Thirty-five samples from small occurrences in South-east and North-central Norway yield a median heat production of 1.70 ± 1.78 $\mu W/m^2$ and an area-weighted heat production of 2.01 $\mu W/m^3$ (Fig. 2.4); however, no data are available from either the Jotun, Lindås or Dalsfjord nappe, and the heat production of these units can only be regarded as poorly constrained.

2.3.6.5 Late Mesoproterozoic to Neoproterozoic metasedimentary rocks (6e).

Rocks belonging to this unit are widespread in Finnmark, N. Norway and the Lillehammer area, SE Norway (e.g., Nystuen 1981, Roberts, 1985) (Fig. 2.2). Lithologically, the rocks range from quartzitic to arkosic sandstone, mica schist, and pelite to volumetrically subordinate carbonate. Deposition mainly took place at various times beginning in the Late Mesoproterozoic and continuing through the Neoproterozoic, and in most cases the rocks appear to represent continental or shelf deposits. The rocks were deformed and metamorphosed during the Scandian phase of the Caledonian orogeny at c. 430–420 Ma (Siedlecka et al. 1987, Kirkland et al. 2006a, Slagstad et al. 2006), and in Finnmark there is evidence of older Neoproterozoic deformation (Kirkland et al. 2006b). The grade of metamorphism varies from high to low in Finnmark, whereas it is generally low in the Lillehammer area.

Forty-eight samples of Neoproterozoic sedimentary rocks in South Norway yield a median heat production of 1.35 ± 0.82 $\mu W/m^3$ and an area-weighted heat production of 1.35 $\mu W/m^3$

(Fig. 2.4); however, considering the low number of samples and the lack of data from North Norway, I regard this province as poorly constrained in terms of heat production.

2.3.7 Devonian sedimentary rocks (7)

The Devonian basins along the west coast of Norway between Bergen and Trondheim (Fig. 2.2) consist dominantly of fluvial sandstones, conglomerates and breccias (Osmundsen & Andersen 2001). Most of the rocks were deposited during a short time interval between 400 and 390 Ma and rest on the underlying Western Gneiss Region basement with an extensional tectonic contact. The basement locally preserves evidence of Caledonian eclogite-facies metamorphism at c. 400–420 Ma (Griffin et al. 1985, Kullerud et al. 1986), i.e., just preceding deposition of the overlying rocks. No significant post-depositional metamorphic activity has affected the rocks.

Fifteen samples of Devonian sedimentary rocks yield a median heat production of 1.23 ± 0.47 $\mu W/m^3$ and an area-weighted heat production of 1.33 $\mu W/m^3$ (Fig. 2.4). The low number of samples makes this estimate highly uncertain.

2.3.8 Cambro–Silurian sedimentary rocks within the Oslo Rift (8)

Metasedimentary rocks of Cambro–Silurian age are preserved within the downfaulted Oslo rift (Fig. 2.2). The majority of the Cambro–Silurian rocks consist of marine shales, carbonates and sandstones. The rocks were deposited first in an epicontinental basin on the Baltic Shield (Cambrian through much of the Ordovician), later in the foreland basin to the Caledonian orogeny to the west (Late Ordovician to Late Silurian) (Bjørlykke 1974). The rocks were deformed and metamorphosed at low-grade during the Scandian phase of the Caledonian orogeny at c. 420 Ma, and underwent local contact metamorphism during formation of the Oslo Rift at c. 300–280 Ma (Goldschmidt 1911). Of particular interest here is the presence of relatively thick layers of black alum shale, well known for its high contents of U (Andersson et al. 1985, Samuelsson & Middleton 1998), near the base of the Cambro–Silurian sequence. The alum shales occur extensively in Scandinavia, from Finnmark in northernmost Norway to South Sweden and Denmark, and were deposited along the Baltoscandian margin in Mid Cambrian to earliest Ordovician time, possibly in response to early Caledonian subduction of the margin (Gee 1987).

Thirty-seven samples of Cambro–Silurian sedimentary rocks yield a median heat production of 1.65 ± 1.45 $\mu W/m^3$ and an area-weighted heat production of 1.89 $\mu W/m^3$ (Fig. 2.4). The low number of samples makes the estimate uncertain. Only one sample of alum shale is included in the database; however, since this rock type by no means dominates the Cambro–Silurian suite, this is unlikely to affect the value significantly.

2.3.9 Permian magmatic rocks of the Oslo Rift (9)

The Oslo Rift is an intracontinental rift that formed in the Late Carboniferous–Early Permian as a result of regional extensional strain in northern Europe at that time (Fig. 2.2). Peak magmatic activity was concentrated in a rather narrow time interval from c. 300 to 280 Ma (Neumann et al. 2004 and references therein). The rifting and associated magmatic activity took place in 5 stages, starting with widespread basaltic volcanism of tholeiitic and alkaline composition, intrusion of larvikite (monzonite) and extrusion of trachytic rhomb porphyry lavas. The latest stages of the rift evolution were dominated by intrusion of large batholiths of monzonitic, syenitic and granitic composition (Neumann et al. 2004 and references therein). No post-magmatic metamorphic activity has affected the rocks.

A large dataset consisting of 1044 analyses is available from the magmatic rocks of the Oslo Rift, yielding a median heat production of 2.50 ± 1.64 $\mu W/m^3$ and an area-weighted heat production of 2.93 $\mu W/m^3$ (Fig. 2.4).

2.4 Discussion

The already extensive, and growing, geochemical database from Norwegian bedrock allows for comprehensive investigations into the factors that control the distribution of the heat producing elements. Since the purpose of this paper is to characterise the heat production of the main geological provinces in Norway, a major part of this discussion focuses on average heat production rates obtained from a variety of rock types that in some cases formed at different times and in different tectonic settings. However, in general the geological provinces delineated here are dominated by a comparatively small number of lithologies that display rather modest geological variation (i.e., composition, age, metamorphic grade, tectonic setting) to make such a discussion meaningful. Because granite (*sensu lato*) is the main host for the heat producing elements, the heat production of Norwegian granites is discussed in particular, emphasising the relationship between the tectonic setting in which the granite formed and its heat production rate.

2.4.1 Heat production vs. lithology and chemical composition

Lithological variation is the primary factor controlling the distribution of heat production in the crust (Kukkonen & Lahtinen 2001). In general, granitic rocks have relatively high heat production whereas intermediate and mafic lithologies produce less heat, however, in reality heat production within the same lithology may vary by an order of magnitude or more. To facilitate the discussion of heat production and its dependence on lithology, I have subdivided the samples for which we have a complete geochemical data set (XRF and LA–ICP–MS) into 4 lithological groups. 'Metasedimentary rocks' encompass arkose, quartzite, mica schist, phyllite and greywacke; 'Metamafic rocks' include gabbro, amphibolite, diorite and

greenstone/-schist; 'Granite and granitic gneiss' and 'Granodiorite and granodioritic gneiss' are self-explanatory. As expected, the mafic rocks yield the lowest heat production with an average of 0.74 $\mu W/m^3$, and the granitic rocks the highest heat production with an average of 2.95 $\mu W/m^3$. The granodioritic and metasedimentary rocks yield similar, intermediate heat production with averages of 1.54 and 1.55 $\mu W/m^3$, respectively. These values are as expected, and the variation within each lithological group in relation to chemical composition is perhaps more interesting. Fig. 2.5 shows heat production vs. SiO_2, Fe_2O_3 and total rare earth element (REE) content for the different lithological groups. SiO_2 and Fe_2O_3 represent the samples' major element composition and reflect the mineralogical composition of the samples, whereas Total REE represents trace elements mainly hosted by accessory phases including zircon and monazite, which are also the main hosts of the heat producing elements (e.g., Bea 1996). The metasedimentary rocks show a small increase in heat production with increasing SiO_2 at low SiO_2, then a gentle decrease (Fig. 2.5a). The trend is opposite with respect to Fe_2O_3 (Fig. 2.5e). In contrast the other 3 groups, consisting of magmatic rocks and orthogneisses, display increasing heat production with increasing SiO_2 (Figs. 2.5b-d) and vice versa with respect to Fe_2O_3 (Figs. 2.5f-h). These variations reflect different mechanisms controlling the mineralogical and major element composition of sedimentary and magmatic rocks (Kukkonen & Lahtinen 2001). The composition of sedimentary rocks partly reflects their source, resulting in correlations that are similar to those observed in magmatic rocks, and partly sedimentary sorting due to variation in the size and density of different minerals. Mica-rich rocks such as schist and phyllite represent low degrees of sedimentary sorting whereas quartz-rich rocks such as arkose and quartzite represent high degrees of sorting. Since U- and Th-bearing minerals are commonly hosted by micas, sedimentary sorting results in an inverse correlation between heat production and degree of sorting. The variation in heat production with SiO_2 and Fe_2O_3 in the metasedimentary rocks reflects both these processes. Between 45 and 60 wt.% SiO_2, heat production increases with increasing SiO_2. The rocks in this range include mica schist and phyllite, representatives of poorly sorted sediments, and the variation in heat production most likely reflects that of the source. Rocks with >60 wt.% SiO_2 consist of mica schist and phyllite at low SiO_2 and arkose and quartzite at higher SiO_2, representing increasing degrees of sorting, resulting in an inverse correlation between SiO_2 and heat production. The other lithological groups represent magmatic rocks of mafic to intermediate ('Metamafic rocks'), intermediate to felsic ('Granodioritic rocks'), and felsic ('Granitic rocks') composition. The increase in heat production with SiO_2 and opposite for Fe_2O_3 is consistent with magmatic processes where low degrees of partial melting and/or high degrees of fractionation result in high SiO_2/low Fe_2O_3 melts with high incompatible element (including U, Th) contents. At very high SiO_2 and low Fe_2O_3, the relationship breaks down due to crystallisation of accessory phases that deplete the residual melt in incompatible elements; thus, further fractionation and concomitant increase and decrease in SiO_2 and Fe_2O_3, respectively, does not lead to increased levels of elements which were incompatible earlier in the fractionation process.

Figures 2.5i-l show how heat production varies with total REE content. In most rocks, REE are hosted by accessory phases and REE content may therefore be used as a proxy for the amount of accessory phases in a rock. All rock types show a relatively well-defined positive correlation between total REE content and heat production, supporting the general consensus that the heat producing elements are hosted dominantly by accessory phases (e.g., Fountain, 1986, Kukkonen & Lahtinen 2001).

2.4.2 Heat production vs. tectonic setting

Differences in chemical composition have long been used to discriminate between different tectonic settings (e.g., Pearce & Cann 1973). From the above discussion on heat production and chemical composition, one may therefore expect similarly consistent differences in heat production. Since the purpose of this contribution is to characterise the heat production of different geological units or provinces, there is a certain lumping of different lithologies formed in different tectonic settings. I therefore base this discussion on three provinces that display rather narrow lithological variation and where the tectonic setting is relatively well defined.The Palaeoproterozoic Transscandinavian Igneous Belt consists of granitic rocks formed along the active margin of Baltica in a subduction setting, and yields a median heat production of 2.57 $\mu W/m^3$. The Post-Sveconorwegian granites formed during the Early Neoproterozoic, following the Sveconorwegian orogeny. Although the process(es) leading to their formation is uncertain, it is clear that they formed in an intracontinental setting. The Post-Sveconorwegian granites yield a median heat production of 3.92 $\mu W/m^3$. The Permian Oslo Rift represents magmatic rocks formed in an intracontinental rift and yields a median heat production of 2.50 $\mu W/m^3$. However, the Oslo Rift consists of a variety of rock types including syenites and other intermediate rocks, as well as basalts. Including only Permian granites in the calculation yields a median heat production of 3.23 $\mu W/m^3$. These results compare well with numerous investigations showing that rocks formed in continental, extensional settings, be it continental back-arcs, continental rifts, or post-orogenic extension, are enriched in incompatible elements (Frost et al. 1999, Slagstad et al. 2004, Anderson & Morrison 2005). There are probably a number of reasons for the difference in composition between rocks formed in intraplate and plate margin settings. The most obvious difference is that most plate margin magmas form by partial melting in the mantle wedge overlying a subduction zone, whereas intraplate magmas commonly form in areas where upwelling of hot asthenospheric melts induces partial melting of lower crustal rocks. Lower crustal rocks, although generally depleted relative to upper crustal rocks, are significantly more enriched in heat producing elements than the mantle wedge, thus providing a source for relatively enriched magmas. Tectonic setting can therefore be used as a rough guide to a province's heat production.

2.4.3 Heat production vs. age

Radiogenic heat production is sometimes considered to decrease with increasing age, although some studies fail to find such a correlation (e.g., Kukkonen and Lahtinen, 2001). Fig. 2.4 shows the heat production rates of the various geological provinces considered here, broadly arranged in chronological order. Fig. 2.4 shows that there is no clear-cut relationship between geological age and heat production, despite the fact that the Archaean gneisses display relatively low heat production rates, with a median of 0.81 ± 1.48 μW/m^3. This is similar to that of Archaean gneisses in Finland (0.79 ± 1.33 μW/m3, Kukkonen and Lahtinen, 2001). However, both the Palaeoproterozoic Lofoten and the Early Neoproterozoic Egersund AMCG complexes display significantly lower heat production rates. Notably, the two AMCG complexes display similar heat production rates despite an age difference of c. 900 million years. This shows that lithological variation exerts a first-order control on heat production. It is therefore more relevant to compare the Archaean gneisses with younger provinces with a similar lithological make up, in particular the Sveconorwegian province in South Norway and the Western Gneiss Region. These provinces consist mainly of Mesoproterozoic intermediate to felsic gneisses, not unlike the Archaean gneisses, but have heat production rates that are somewhat higher (Table 2.2, Fig. 2.4). The available data indicate that a correlation between heat production and geological age may exist, but that this correlation is weak and in most cases obscured by lithological variation. This conclusion is further supported by data from the Palaeoproterozoic Transscandinavian Igneous Belt and the Permian Oslo Rift, which both consist largely of granitoid rocks and display virtually identical heat production despite an age difference of nearly 1.5 billion years. Thus, predicting heat production rates based on geological age clearly is not feasible, a conclusion which is in line with that proposed by Kukkonen and Lathinen (2001).

2.4.4 Heat production vs. metamorphic grade

Many workers assume that heat production decreases with increasing metamorphic grade or crustal depth because during orogenesis, partial melting at lower to middle crustal levels commonly forms melts rich in incompatible elements, including the heat producing elements, that may migrate to higher structural levels (Heier, 1965) (see Slagstad et al., 2005 for a discussion of this process). This should lead to a depletion of high producing elements at low crustal levels, and concomitant enrichment at higher crustal levels where the melts are emplaced as plutons (e.g., Sandiford and McLaren, 2002; Sandiford et al., 2002). However, exceptions to this "rule" have also been found. For example, Andreoli et al. (2006) reported that radiogenic heat production in the Western Namaqualand Belt, South Africa, increases with increasing metamorphic grade and suggested that the introduction of CO_2-rich fluids (cf., Frost and Frost, 1987), rather than removal of H_2O-rich melts, was the cause of granulite-facies metamorphism and possibly enrichment in heat producing elements. Thus, granulite-facies metamorphism may be brought about in different ways that may have widely different impacts on the composition and thus heat production of the affected rocks.

Although the concept of a rather homogeneous, low-heat producing lower crust is clearly oversimplified (cf., Flowers et al. 2006), it has long been recognised that the middle and lower crust must be depleted in heat producing elements relative to the upper crust to avoid impossibly high temperatures at depth within the crust (e.g., Morgan & Sass 1984). Unfortunately, true lower crustal rocks are exposed in only a few locations in the world, but several studies investigating the variation in heat production in vertical cross sections through the middle to upper crust have been undertaken. Ashwal et al. (1987) investigated a c. 25 km thick vertical section through amphibolite- to granulite-facies Archaean rocks in the Kapuskasing area, Superior Province, Ontario. Their work showed no relationship between vertical depth/metamorphic grade and heat production, which they suggested could be a typical feature of rather "mafic" geological provinces, whereas more "granitic" provinces are more likely to display such a relationship. Brady et al. (2006) presented heat production data from the Sierra Nevada Batholith, California, and showed that it increased from c. 2 to 3 $\mu W/m^3$ in the uppermost 5 km, then dropped to 0.5–1 $\mu W/m^3$ at 15 km depth and remained constant at that level to the Moho. These studies show that heat production does not vary continuously or predictably with crustal depth, but that abrupt changes related to lithological variation is the norm.

The Lofoten–Vesterålen area in north Norway, including the Lofoten AMCG complex, is sometimes cited as an example of lower crustal rocks having undergone depletion in incompatible elements due to regional metamorphism (Heier and Adams, 1965). However, more recent work suggests that the amphibolite- to granulite-facies transition in this area, interpreted by Heier (1960) to be a gradual metamorphic transition, could be a contact metamorphic effect (Corfu 2004a). It is notable that the Lofoten AMCG complex has a heat production that is nearly identical to the unmetamorphosed Egersund AMCG complex, suggesting that the low heat production of the former is lithologically/tectonically controlled rather than determined by metamorphic grade.

The above discussion shows that considerations of the impact of metamorphic grade on heat production are hampered by the strong effect of lithological variation. This means that not only is comparing lithologically different high- and low-grade rocks useless, even comparing lithologically similar high- and low-grade rocks may be meaningless due to the large variation observed among similar rock types. These complexities imply that meaningful investigations into the distribution of heat producing elements and the controlling processes can only be undertaken in areas where the geological setting is particularly favourable. One such area is the Sognefjorden transect, where Caledonian folding and thrusting has resulted in the exposure of a c. 30 km vertical cross section (Milnes et al. 1997) through Sveconorwegian crust. The cross section includes Sveconorwegian granulites (source?), migmatites (melt transfer zone?) and granites (shallow crustal "deposits" of heat producing elements) (Skår & Pedersen 2003), that may reflect processes related to crustal differentiation. Syn-orogenic granites are also found elsewhere in SW Norway (Slagstad & Marker, unpub. data 2006), suggesting that the middle to lower crust underwent relatively

widespread melting during Sveconorwegian orogenesis. This evolution would have had a major impact on the distribution of heat producing elements and thus the thermal structure of the Sveconorwegian crust, which in turn may have affected its behaviour during subsequent Caledonian orogenesis. The Sognefjorden transect is therefore an obvious candidate for further investigations into the 'hows', 'whys' and 'so whats' regarding distribution of heat producing elements on a crustal scale.

2.5 Conclusions

Radiogenic heat production varies significantly within different geological provinces; a variation that can generally be ascribed to lithology - provinces dominated by granitic rocks tend to have higher heat production than provinces dominated by more intermediate and mafic rocks. No clear relationship between heat production and metamorphic grade could be observed. Other studies suggest that such a general relationship is unlikely, and typically overridden by lithological variation. Tectonic setting appears to have some bearing on radiogenic heat production, and in general rocks formed in extensional continental settings have somewhat higher heat production than rocks formed along plate margins. This is not surprising considering that similar lithologies formed in different tectonic settings tend to be differently enriched in many trace elements, including the heat producing elements.

3 PETROPHYSICAL AND THERMAL PROPERTIES OF PRE-DEVONIAN BASEMENT ROCKS ON THE NORWEGIAN CONTINENTAL MARGIN

Trond Slagstad, Cécile Barrère, Børre Davidsen & Randi K. Ramstad, NGU

3.1 Introduction

Gravimetric and magnetic surveys along the Norwegian continental margin has significantly improved our understanding of the margin's crustal architecture and has allowed correlations between the onshore and offshore realms (e.g., Doré et al. 1997, Olesen et al. 1997, 2002, 2004a, Skilbrei et al. 2002, Lyngsie et al. 2006), in addition to yielding important information to the petroleum industry. In addition, the location of hydrocarbon accumulations is strongly dependent on the temperature structure of the subsurface (e.g., Bjørkum & Nadeau 1998), which in turn depends strongly on variations in thermal conductivity and radiogenic heat production. However, models employing data from offshore gravimetric, magnetic and thermal surveys are hampered by a lack of ground-truth petrophysical data, and at present, the petrophysical properties along the Norwegian continental margin have to be inferred from onshore datasets and educated estimates. In an ongoing project at NGU, we aim to characterise the basement along the Norwegian continental margin (defined here as the dominantly pre-Devonian crystalline rocks underlying the ubiquitous Mesozoic cover) in terms of mineralogical and chemical composition, petrophysical properties and tectonometamorphic history. The work is based on samples from 23 wells that have penetrated basement rocks, made available by the Norwegian Petroleum Directorate and Statoil. The purpose of this brief communication is to present petrophysical data from 12 wells (15 samples) in the North Sea, 5 wells (6 samples) in the Norwegian Sea and 6 wells (12 samples) in the Barents Sea (Fig. 1). The analyses include determination of density, magnetic remanence, magnetic susceptibility, thermal conductivity and radiogenic heat production. The samples are described in Appendix A and a discussion on the geological significance of a subset of the samples is presented by Slagstad and Davidsen (this report).

3.2 Analytical methods

3.2.1 Petrophysical properties

Measurements of density, remanence and magnetic susceptibility are conducted following procedures described by Torsvik & Olesen (1988) and Olesen (1988).

3.2.2 Thermal conductivity

Measurements of thermal conductivity are conducted on 2 cm thick circular disks. A constant heat flow is induced to the top of the sample by placing a heat source with a constant temperature approximately 10 mm above the top surface of the sample. The heat is transferred as radiation. The sample is insulated on all other surfaces and the temperature is measured at the base of the sample. The thermal conductivity (K) is calculated from Equation

1 based on measured thermal diffusivity (α) and density (ρ), and assumed specific heat (Cp) of the sample. The specific heat capacity is assumed to be 850 J/(kg*K) for all rock types.

$$K = \rho C_p \alpha \qquad \textbf{(1)}$$

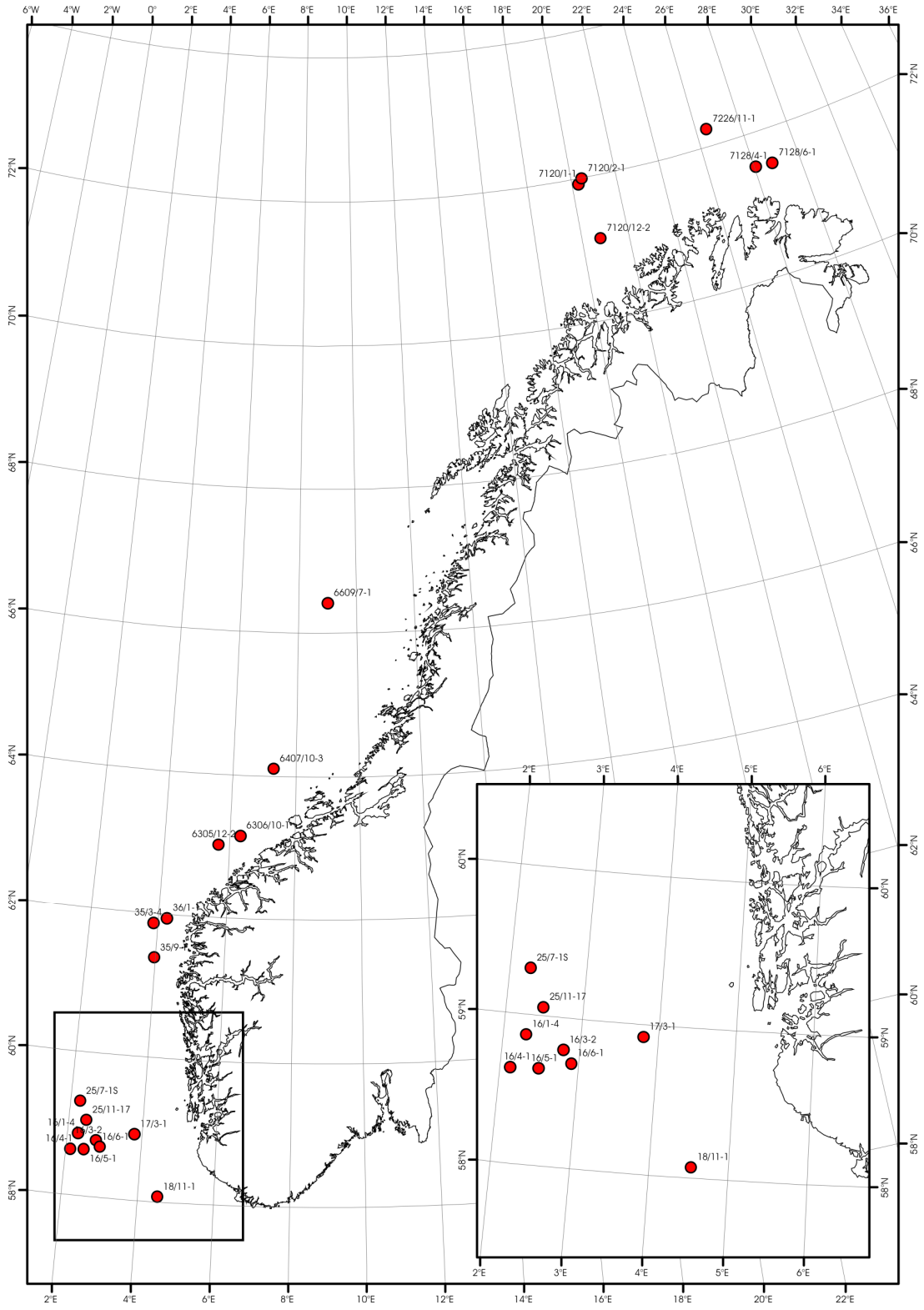

Figure 3.1. Map showing the locations and names of wells from which basement samples have been obtained.

3.2.3 Radiogenic heat production

Radiogenic heat production is calculated from U, Th and K concentrations determined by standard XRF and LA–ICP–MS techniques at NGU and measured densities (δ) using Equation 2 (Rybach 1988).

$$A = \delta*(9.52C_U + 2.56C_{Th} + 3.48C_K)*10^{-5}$$

where C_U and C_{Th} represent U and Th concentrations in ppm, respectively, and C_K represents K concentration in wt.%.

3.3 Petrophysical and thermal properties

The petrophysical and thermal data are presented in Table 1a and 1b, respectively. Compilations of onshore petrophysical data show that most geological units display highly varied magnetic properties, typically ranging between 2 and 3 orders of magnitude (Skilbrei 1989), greatly limiting the value of a small dataset with poor geological control (due to pinprick offshore sampling). However, despite the difficulties in extending these very localised measurements to a larger rock volume, they represent additional information to the onshore petrophysical database at NGU. The main purpose of this contribution is therefore to disseminate the available data so that they are available to other researchers who may find them useful. For the same reason, we limit ourselves to a very brief and general discussion.

Most of the offshore samples are relatively low-magnetic, which is compatible with the geological information (Slagstad and Davidsen, this report) suggesting that the shallow basement along much of the continental margin consists of rocks that may be correlated with the Caledonian Uppermost Allochthon on land (cf., Olesen et al. 2002). In particular, the granites encountered in wells# 16/3–2, 16/4–1, 16/5–1 and 6407/10–3 yield Caledonian ages and may be correlated with the low-magnetic Bindal batholith (Olesen et al. 2002). The diabase from well# 7120/2–1 confirms the presence of thick mafic dykes within the basement of the Loppa High This is in agreement with the joint interpretation of potential field modelling (Barrére et al. 2007) that proposes a tongue of basement affected by mafic dykes all along the fault complexes boarding the west of the Loppa High.

Table 3.1a Petrophysical data from offshore basement samples.

Well name	Depth (m)	Area	UTM N 33	UTM E 33	North	East	Lithology	Density (kg/m^3)	Magnetic suscept. (10^{-6} SI)	Magnetic remanence (10-3 A/m)	Electrical resistivity (ohm*m)
16/1-4	1937.0	North Sea	-229828.85	6594677.75	58° 51` 55.20`` N	2° 17` 56.12`` E	Leucogabbro	2765	448.4	32.1	130
16/3-2	2017.7	North Sea	-203251.98	6580710.13	58° 47` 12.80`` N	2° 47` 34.70`` E	Granite	2680	949.7	48.8	39845
16/4-1	2907.4	North Sea	-244161.22	6571492.48	58° 38` 18.33`` N	2° 8` 17.03`` E	Altern. qtzite/siltstone	2778	221.3	2.8	3829
16/4-1	2908.6	North Sea	-244161.22	6571492.48	58° 38` 18.33`` N	2° 8` 17.03`` E	Granite	2646	88	6.9	11075
16/5-1	1929.3	North Sea	-223218.48	6568643.35	58° 38` 53.66`` N	2° 29` 39.69`` E	Granite	2662	179.8	11.3	403
16/6-1	2059.7	North Sea	-198150.46	6570064.43	58° 42` 06.00`` N	2° 54` 44.00`` E	Porph. volcanic rock	2591	181.1	9.5	768
17/3-1	2849.5	North Sea	-142831.77	6584837.28	58° 55` 02.50`` N	3° 48` 21.33`` E	Breccia	2750	553.3	10.3	1100
17/3-1	2850.7	North Sea	-142831.77	6584837.28	58° 55` 02.50`` N	3° 48` 21.33`` E	Breccia	2661	58.3	0	14854
18/11-1	2082.3	North Sea	-115993.06	6484691.74	58° 4` 21.30`` N	4° 32` 00.10`` E	Porph. volcanic rock	2639	207.4	22	1465
25/7-1S	3548.2	North Sea	-222102.79	6643919.64	59° 18` 35.23`` N	2° 16` 05.37`` E	Brecciated siltstone	2883	1406.8	68.7	110
25/7-1S	3554.3	North Sea	-222102.79	6643919.64	59° 18` 35.23`` N	2° 16` 05.37`` E	Qtz-rich sandstone	2722	48.8	9.2	553
25/11-17	2259.5	North Sea	-215189.08	6613788.79	59° 3` 26.66`` N	2° 29` 06.59`` E	Siltstone	2656	291.6	0	415
35/3-4	4088.3	North Sea	-83357.16	6909289.80	61° 51` 54.54`` N	3° 52` 26.99`` E	Qtz-rich mica schist	2773	234.1	0	2288
35/9-1	2313.6	North Sea	-86677.17	6855419.47	61° 23` 07.95`` N	3° 59` 03.72`` E	Breccia	2619	286.4	0	38
36/1-1	5212.3	North Sea	-61687.96	6914606.22	61° 56` 40.36`` N	4° 15` 43.86`` E	Granitic gneiss	2676	104.3	5.2	835
6305/12-2	3158.3	Norwegian Sea	28797.72	7022065.95	63° 1` 11.39`` N	5° 40` 06.44`` E	Brecciated siltstone	2740	456.8	9.6	198
6306/10-1	3158.5	Norwegian Sea	64013.84	7032601.60	63° 9` 26.32`` N	6° 19` 41.45`` E	Leucogabbro	2767	2836.2	58.6	363
6306/10-1	3159.2	Norwegian Sea	64013.84	7032601.60	63° 9` 26.32`` N	6° 19` 41.45`` E	Leucogabbro	2732	1001.7	20	1403
6407/10-3	2972.1	Norwegian Sea	125535.18	7131162.42	64° 6` 11.66`` N	7° 18` 11.43`` E	Granite	2631	1186.7	108.9	11622
6609/7-1	1944.7	Norwegian Sea	233299.23	7378996.84	66° 24` 56.49`` N	9° 1` 14.91`` E	Brecciated silt-/ sandstone	2622	14.7	0	958

Well name	Depth (m)	Area	UTM N 33	UTM E 33	North	East	Lithology	Density (kg/m^3)	Magnetic suscept. (10^{-6} SI)	Magnetic remanence (10-3 A/m)	Electrical resistivity (ohm*m)
6609/7-1	1945.8	Norwegian Sea	233299.23	7378996.84	66° 24` 56.49`` N	9° 1` 14.91`` E	Altern. silt-/ sandstone	2580	24.6	11	1121
7120/1-1	4002.2	Barents Sea	683414.57	7987752.07	71° 55` 00.83`` N	20° 18` 07.13`` E	Amphibolite	3085	777.1	27.2	n.a.
7120/12-2	4675.8	Barents Sea	708967.97	7901370.91	71° 7` 30.30`` N	20° 48` 19.00`` E	Qtz-rich augen gneiss[§]	2676	177.8	5	15060
7120/12-2	4678.2	Barents Sea	708967.97	7901370.91	71° 7` 30.30`` N	20° 48` 19.00`` E	Qtz-rich augen gneiss	2656	181.3	10.1	37368
7128/4-1	2527.2	Barents Sea	959034.83	7987711.91	71° 32` 27.33`` N	28° 4` 54.08`` E	Altern. silt-/ sandstone	2638	242.8	28.6	95
7128/4-1	2528.1	Barents Sea	959034.83	7987711.91	71° 32` 27.33`` N	28° 4` 54.08`` E	Altern. silt-/ sandstone[§]	2617	260.4	46.1	177
7128/6-1	2540.5	Barents Sea	985048.93	7990989.58	71° 31` 04.99`` N	28° 49` 03.41`` E	Sandstone	2689	124.8	11	1722
7226/11-1	5198.8	Barents Sea	888671.33	8052767.94	72° 14` 18.16`` N	26° 28` 44.78`` E	Biotite-rich schist/gneiss	2794	337.9	6.5	2295
7120/2-1	3478.0	Barents Sea	688803	7995815	71° 58` 57.94`` N	20° 28` 35.09`` E	Diabase[§]	2762	42281	475.4	n.a.
7120/2-1	3479.0	Barents Sea	688803	7995815	71° 58` 57.94`` N	20° 28` 35.09`` E	Diabase[§]	2727	34025.5	291.6	n.a.
7128/4-1	2527.0	Barents Sea	959034.83	7987711.91	71° 32` 27.33`` N	28° 4` 54.08`` E	Altern. silt-/ sandstone[§]	2640	207	0	n.a.
7128/6-1	2541.73	Barents Sea	985048.93	7990989.58	71° 31` 04.99`` N	28° 49` 03.41`` E	Sandstone[§]	2622	125.8	0	n.a.
7226/11-1	5198.3	Barents Sea	888671.33	8052767.94	72° 14` 18.16`` N	26° 28` 44.78`` E	Biotite-rich schist/gneiss[§]	2783	315.8	5	n.a.

Table 3.1b. Thermal data from offshore basement samples.

Well name	Depth (m)	Area	UTM N 33	UTM E 33	North	East	Lithology	Thermal conductivity (W/mK)	n	K (wt.%)	Th (ppm)	U (ppm)	Heat production (µW/m3)
16/1-4	1937.0	North Sea	-229829	6594678	58° 51` 55.20`` N	2° 17` 56.12`` E	Leucogabbro	2.38	1	2.80	2.83	8.37	2.7
16/3-2	2017.7	North Sea	-203252	6580710	58° 47` 12.80`` N	2° 47` 34.70`` E	Granite	3.12	1	2.25	8.70	2.62	1.5
16/4-1	2907.4	North Sea	-244161	6571492	58° 38` 18.33`` N	2° 8` 17.03`` E	Altern. qtzite/siltstone	2.51 (2.17-2.94)	4	3.82	10.8	3.64	2.1
16/4-1	2908.6	North Sea	-244161	6571492	58° 38` 18.33`` N	2° 8` 17.03`` E	Granite	3.18	1	3.11	11.5	1.11	1.3
16/5-1	1929.3	North Sea	-223218	6568643	58° 38` 53.66`` N	2° 29` 39.69`` E	Granite	3.23	1	2.89	10.7	2.89	1.7
16/6-1	2059.7	North Sea	-198150	6570064	58° 42` 06.00`` N	2° 54` 44.00`` E	Porph. volcanic rock	2.89	1	2.26	0.34	0.96	0.5
17/3-1	2849.5	North Sea	-142832	6584837	58° 55` 02.50`` N	3° 48` 21.33`` E	Breccia	2.69	1	0.04	1.81	0.60	0.3
17/3-1	2850.7	North Sea	-142832	6584837	58° 55` 02.50`` N	3° 48` 21.33`` E	Breccia	3.93	1	0.05	1.59	0.55	0.3
18/11-1	2082.3	North Sea	-115993	6484692	58° 4` 21.30`` N	4° 32` 00.10`` E	Porph. volcanic rock	3.25	1	0.11	7.14	2.12	1.0
25/7-1S	3548.2	North Sea	-222103	6643920	59° 18` 35.23`` N	2° 16` 05.37`` E	Brecciated siltstone	2.42	1	0.11	2.96	0.91	0.5
25/7-1S	3554.3	North Sea	-222103	6643920	59° 18` 35.23`` N	2° 16` 05.37`` E	Qtz-rich sandstone	4.69	1	2.67	3.65	0.96	0.8
25/11-17	2259.5	North Sea	-215189	6613789	59° 3` 26.66`` N	2° 29` 06.59`` E	Siltstone	2.04	1	4.81	9.00	1.56	1.5
35/3-4	4088.3	North Sea	-83357	6909290	61° 51` 54.54`` N	3° 52` 26.99`` E	Qtz-rich mica schist	2.00	1	3.16	9.13	2.22	1.5
35/9-1	2313.6	North Sea	-86677	6855419	61° 23` 07.95`` N	3° 59` 03.72`` E	Breccia	2.34 (2.25-2.47)	3	1.27	3.31	1.19	0.6
36/1-1	5212.3	North Sea	-61688	6914606	61° 56` 40.36`` N	4° 15` 43.86`` E	Granitic gneiss	2.70 (2.54-2.80)	3	3.89	11.9	1.75	1.6
6305/12-2	3158.3	Norwegian Sea	28798	7022066	63° 1` 11.39`` N	5° 40` 06.44`` E	Brecciated siltstone	2.85	1	0.72	0.11	0.29	0.2
6306/10-1	3158.5	Norwegian Sea	64014	7032602	63° 9` 26.32`` N	6° 19` 41.45`` E	Leucogabbro	2.76	1	1.29	4.66	2.68	1.2
6306/10-1	3159.2	Norwegian Sea	64014	7032602	63° 9` 26.32`` N	6° 19` 41.45`` E	Leucogabbro	2.94	1	1.60	7.08	1.96	1.2
6407/10-3	2972.1	Norwegian Sea	125535	7131162	64° 6` 11.66`` N	7° 18` 11.43`` E	Granite	3.56	1	4.41	58.3	2.65	5.0
6609/7-1	1944.7	Norwegian Sea	233299	7378997	66° 24` 56.49`` N	9° 1` 14.91`` E	Brecciated silt-/sandstone	5.15 (4.95-5.44)	3	1.66	3.25	0.92	0.6

Well name	Depth (m)	Area	UTM N 33	UTM E 33	North	East	Lithology	Thermal conductivity (W/mK)	n	K (wt.%)	Th (ppm)	U (ppm)	Heat production (µW/m3)
6609/7-1	1945.8	Norwegian Sea	233299	7378997	66° 24` 56.49`` N	9° 1` 14.91`` E	Altern. silt-/ sandstone	3.58	1	2.76	7.84	2.34	1.3
7120/1-1	4002.2	Barents Sea	683415	7987752	71° 55` 00.83`` N	20° 18` 07.13`` E	Amphibolite	2.69	1	0.93	3.42	1.07	0.7
7120/12-2	4675.8	Barents Sea	708968	7901371	71° 7` 30.30`` N	20° 48` 19.00`` E	Qtz-rich augen gneiss[§]	2.72 (2.60-2.82)	3	1.69	16.2	4.85	2.5
7120/12-2	4678.2	Barents Sea	708968	7901371	71° 7` 30.30`` N	20° 48` 19.00`` E	Qtz-rich augen gneiss	2.94	1	2.90	4.29	0.40	0.7
7128/4-1	2527.2	Barents Sea	959035	7987712	71° 32` 27.33`` N	28° 4` 54.08`` E	Altern. silt-/ sandstone	n.a.	0	4.18	21.2	5.51	3.2
7128/4-1	2528.1	Barents Sea	959035	7987712	71° 32` 27.33`` N	28° 4` 54.08`` E	Altern. silt-/ sandstone[§]	n.a.	0	3.68	19.3	4.62	2.8
7128/6-1	2540.5	Barents Sea	985048.93	7990989.58	71° 31` 04.99`` N	28° 49` 03.41`` E	Sandstone	4.90	1	1.47	2.58	0.87	0.5
7226/11-1	5198.8	Barents Sea	888671	8052768	72° 14` 18.16`` N	26° 28` 44.78`` E	Biotite-rich schist/gneiss	3.75 (3.70-3.81)	3	2.43	12.6	2.55	1.8
7120/2-1	3478.0	Barents Sea	688803	7995815	71° 58` 57.94`` N	20° 28` 35.09`` E	Diabase[§]	n.a.	0	n.a.	n.a.	n.a.	n.a.
7120/2-1	3479.0	Barents Sea	688803	7995815	71° 58` 57.94`` N	20° 28` 35.09`` E	Diabase[§]	n.a.	0	n.a.	n.a.	n.a.	n.a.
7128/4-1	2527.0	Barents Sea	959035	7987712	71° 32` 27.33`` N	28° 4` 54.08`` E	Altern. silt-/ sandstone[§]	n.a.	0	n.a.	n.a.	n.a.	n.a.
7128/6-1	2541.73	Barents Sea	985048.93	7990989.58	71° 31` 04.99`` N	28° 49` 03.41`` E	Sandstone[§]	n.a.	0	n.a.	n.a.	n.a.	n.a.
7226/11-1	5198.3	Barents Sea	888671	8052768	72° 14` 18.16`` N	26° 28` 44.78`` E	Biotite-rich schist/gneiss[§]	n.a.	0	n.a.	n.a.	n.a.	n.a.

4 NGU WELL LOGGING 2006-2007

Harald Elvebakk, NGU

4.1 Introduction

Temperature logging was carried out in 11 boreholes in Norway during 2006 (the Fredrikstad hole was logged in 2007). Overview map in Fig. 4.1 shows the locations of the boreholes. NGU acquired a new water quality sonde (Robertson Geologging Ltd.) including a high-resolution temperature sensor, which was used in most of the boreholes. The new sonde could not be used in old 46 mm boreholes in the mining areas of Bleikvassli and Sulitjelma. Borehole data information is shown in Table 4.1.

The mining company Crew Minerals drilled the boreholes in Hurdal, and the Kontiki Project got access to these boreholes for temperature logging. The Fredrikstad well was reopened late 2006 and logged in March 2007.

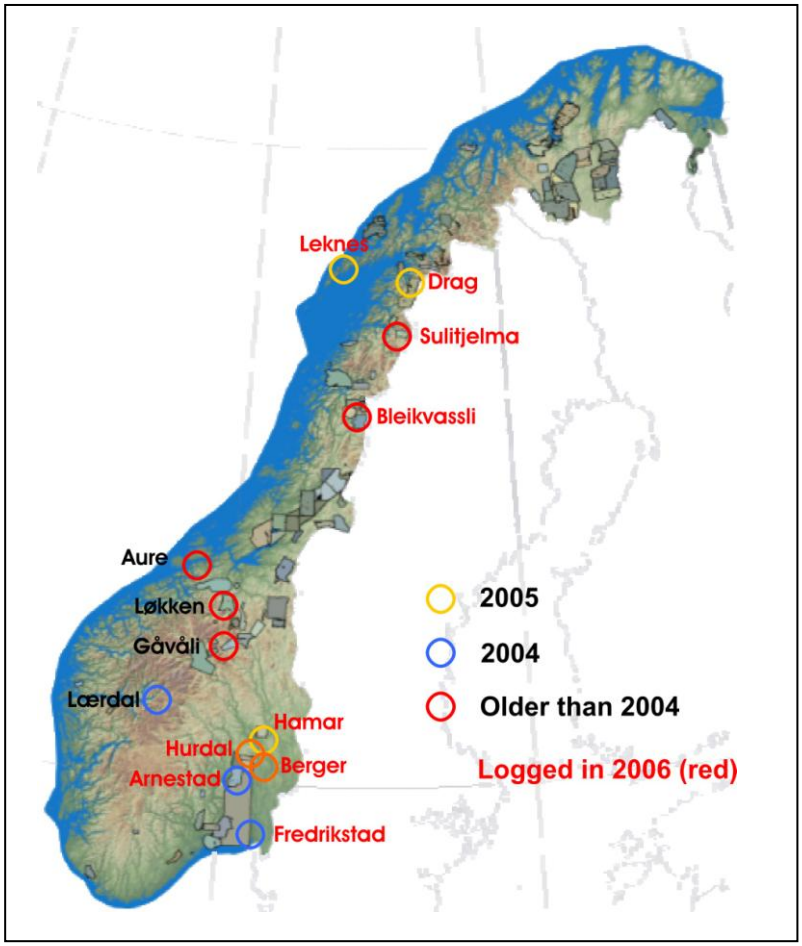

Figure 4.1. Overview map and locations of logged boreholes in 2006/07. Colours of the circles indicate year of drilling while colur of location names indicate year of logging: black – 2005 (Aarhus Unversity), red – 2006 (NGU).

Table 4.1. Borehole data information.

Locality	North (wgs 84)	East (wgs 84)	Zone	Altitude (m.a.s.l.)	Date of logging	Dip (deg)	Depth (m)	Drilling
Arnestad	6630237	583546	32V	11	25.11.06	vertical	672	Mar. 2004
Berger	6654660	615271	32V	152	24.11.06	vertical	705	2002/2003
Bleikvassli	7312764	448397	33W	421	15.08.06	68	640	1998
Drag	7547296	542688	33W	24	19.08.06	vertical	780	2005
Fredrikstad	6563857	610104	32V	32	20.03.07	vertical	800	2005/2006
Hamar	6744216	612597	32V	221	28.11.06	vertical	816	2005
Hurdal 2	6707593	610379	32V	321	06.10.06	59	905	2005
Hurdal 3	6707483	610565	32V	307	07.10.06	59	915	2005
Hurdal 5	6707118	610273	32V	270	05.10.06	84	585	2005
Leknes	7562103	443663	33W	27	23.08.06	vertical	800	2005
Sulitjelma	7443493	540599	33W	805	17.08.06	70	1024	1980

4.2 Temperature sondes

The water quality sonde has seven sensors, which can measure simultaneously.
The sensors are listed below. Logging speed is 3 m/min. Readings are taken every cm.

- **Temperature, - Resolution 0.001, Accuracy 0.02 °C, Range –1 to 49 °C**
- Water conductivity - Accuracy 0.02 µS/cm, Range 0 to 62 mS/cm
- Dissolved oxygen - Accuracy 0.1 ppm, Range 0 to 50 ppm
- pH - Accuracy 0.01 pH, Range 0 to 14 pH
- Redox -Accuracy 10 mV, Range -1000 to 1000 mV
- Nitrate - Range 0 to 100 mg/l
- Pressure, - Accuracy 0.25 % of full scale, Range 0 to 1500 dbar

Water quality sonde (right)
RG 1100 m winch (left)

The old NGU temperature sonde (with fluid conductivity and natural total gamma) has an accuracy of +/- 0.5 °C. The sonde has shown repeatable data and in fact the accuracy is better than +/- 0.5 °C. The third sonde used in the Kontiki project is the sonde constructed by the Geophysics group of Aarhus University. This sonde was used for temperature logging in 2005 (Balling 2006).

A comparison between the three sondes was done by logging the Løkken 1020 m borehole. The new NGU sonde and the Aarhus sonde came up with the same gradient. The result is shown below. Fig. 4.2 shows the temperature logs from all three sondes in a part of the Løkken borehole.

Calculated maximum 100m gradients (175 – 275 m):
•Aarhus: 1.38 °C /100m
•NGUnew: 1.38 °C /100m
•NGUold: 1.34 °C /100m

Maximum deviation
NGU old: +/- 3%

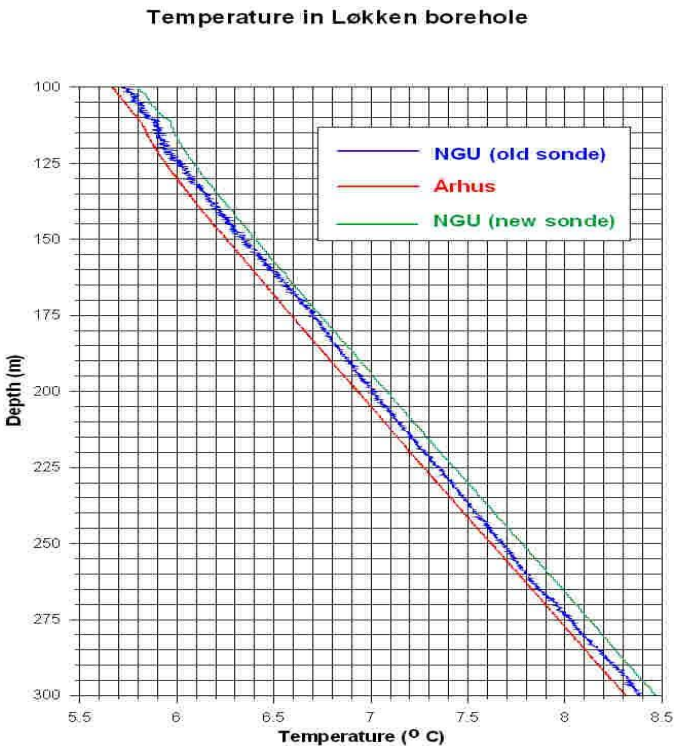

Figure 4.2. Temperature logs from a part of the Løkken borehole.

Regression calculations using the Løkken borehole data from the three sondes were done and the result is shown below.

In average: $T_{NGU\ New} = T_{NGU\ Old} + 0.059 = T_{Aarhus} + 0.166$

NGU Old
–unstable readings
–more noise
–but still aceptable gradients

NGU new, same gradient as *Aarhus* sensor, but higher values Both with accuracy in the order of 0.02 °C.

4.3 Results 2006

All the boreholes were logged at least one year after drilling, except the Fredrikstad well, which was reopened (4 – 5 months). For such long time (one year) the disturbance from the drilling process should not influence the temperature and the calculated gradients.

The temperature gradients are calculated using running least-squares gradients of a straight line with depth intervals of 20 m and 100 m. For each borehole the temperature log and the 20 m and 100 m interval gradients are presented. Fig. 4.3 shows temperature logs from all the boreholes with average gradients. Bottom temperatures and average temperature gradients are shown in table 2.

Local disturbances like water inflow can influence the temperature in a borehole. This can be observed as a change (up or down) in the temperature and is caused by water bearing open

fractures in the borehole. The water conductivity will in most cases also change at the same site in the borehole.

The vertical depths of the boreholes are calculated using the water pressure measured by the water quality sonde or by the borehole deviation sonde measuring the dip angle and azimuth. The temperature gradients are calculated using the vertical depth.

Table 4.2. Average temperature gradient in the 2006 boreholes.

Locality	Average gradient [^{O}C/km]	Bottom temperature [^{O}C]	Vertical depth [m]
Arnestad	26.5 (upper) 12.1 (lower)	20.8	625
Berger	15.9	14.8	703
Bleikvassli	18.1	13.3	603
Drag	17.0	16.7	779
Fredrikstad	17.9	19.6	733
Hamar	24.6	24.0	817
Hurdal 2	21.2	20.9	783
Hurdal 3	21.4	23.4	903
Hurdal 5	21.6	18.1	572
Leknes	19.0	19.5	800
Sulitjelma	21.3	21.2	960

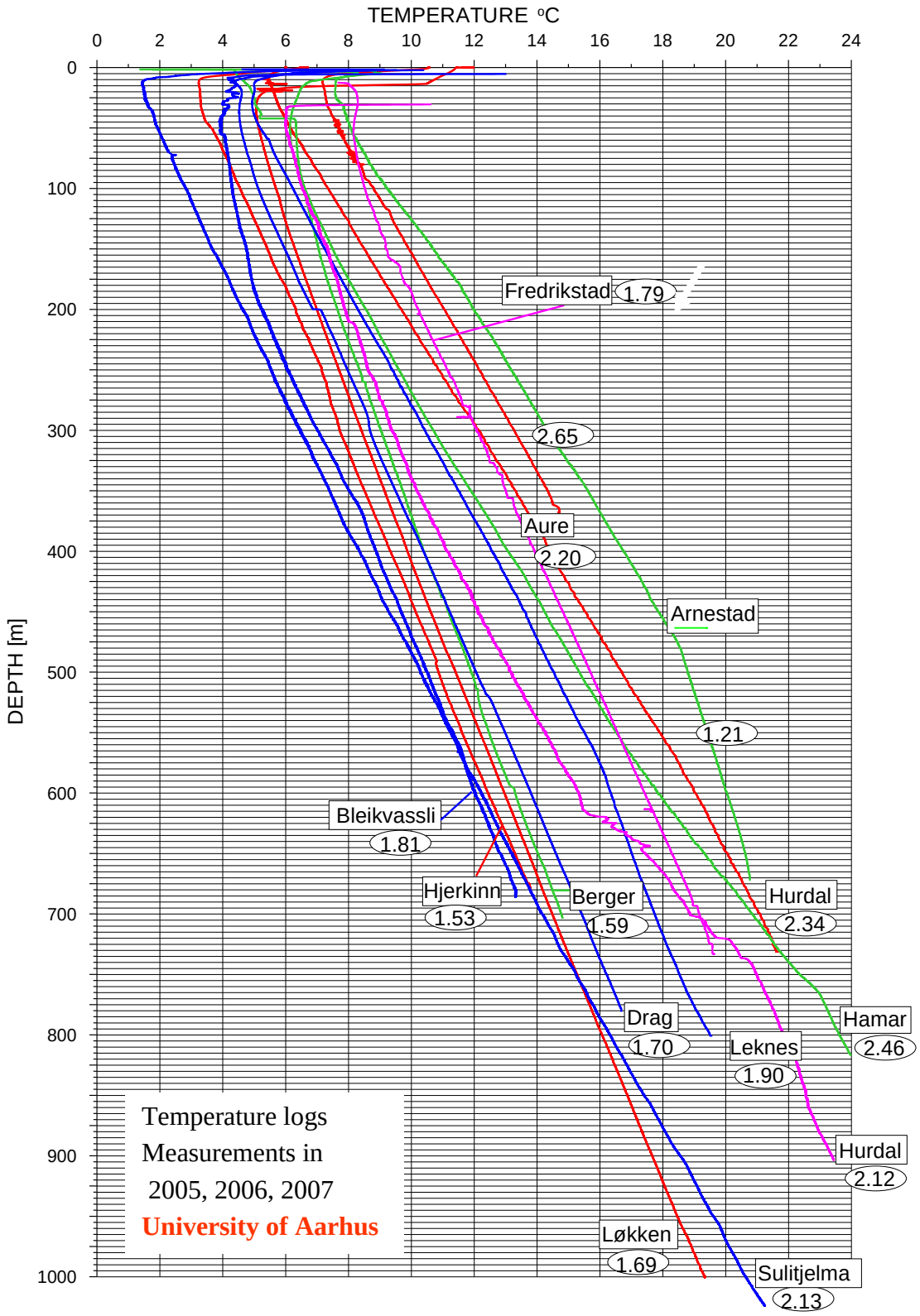

Figure 4.3. Overview of all temperature logs in 2005, 2006 and 2007.

4.3.1 Arnestad

Fig. 4.4 shows the logs from Arnestad. It should be remarked that the upper 450 m consists of the Cambrosilurian sedimentary rocks in the Oslo area. The underlying granite with a higher thermal conductivity, results in a decreasing temperature gradient from 450 m. The average gradient in the upper part is 26.5 °C/km and 12.1 °C/km in granite.

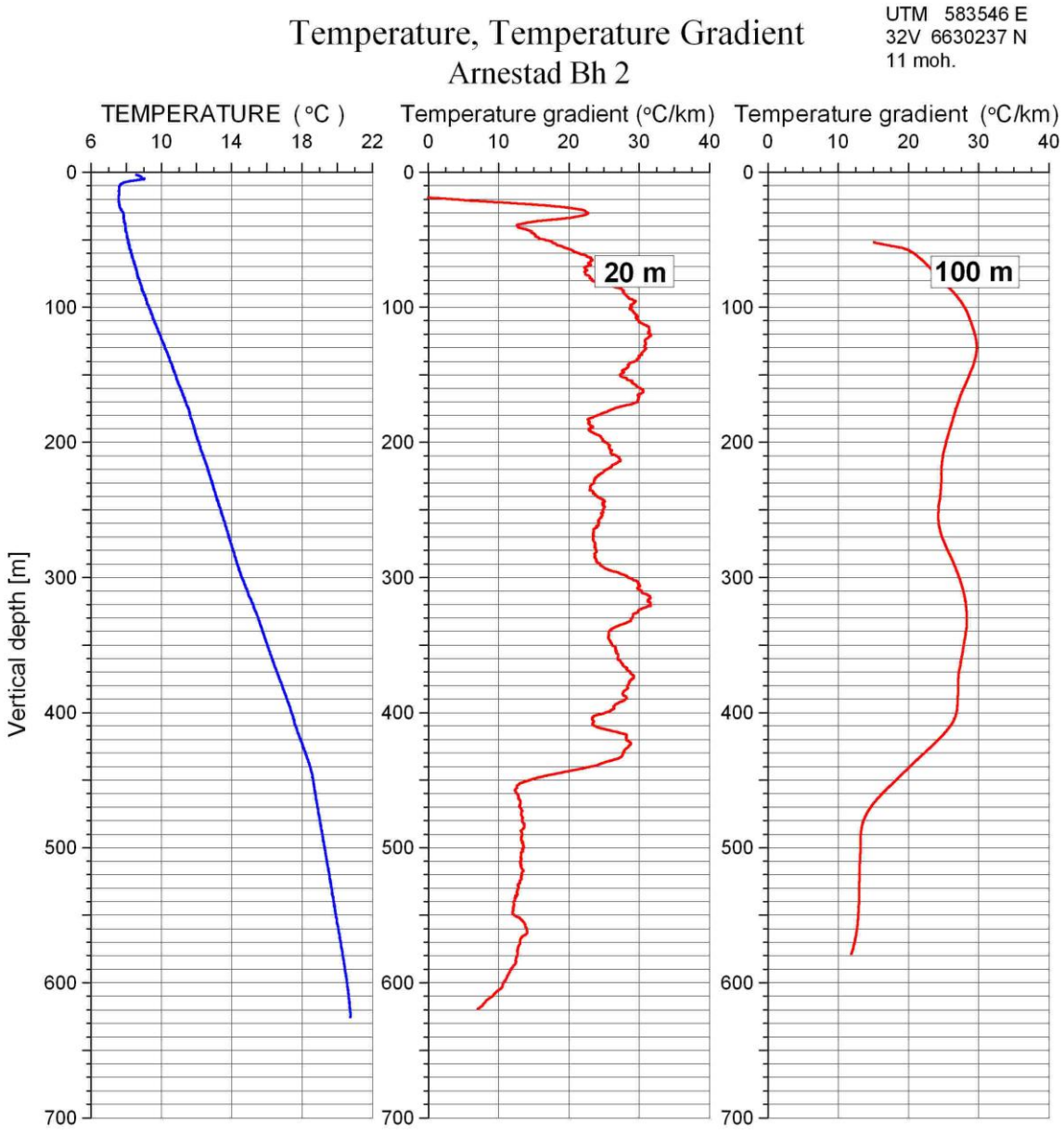

Figure 4.4. Temperature and temperature gradient in the Arnestad borehole.

4.3.2 Berger

Fig. 4.5 shows the logs from Berger borehole. Both Arnestad and Berger were measured by Aarhus University (Balling 2006). NGU wanted to measure the same boreholes with the new water quality sonde because the Aarhus data were some noisy. The average temperature gradient in the Berger borehole is 15.9 °C/km. During the drilling operation mud (bentonite) was used. The lower part of the borehole was still filled up with the mud, and the sonde was stuck at 705 m depth. Big efforts were made to loosen the sonde and bring it to the surface. The temperature doesn't seem to be influenced by this problem.

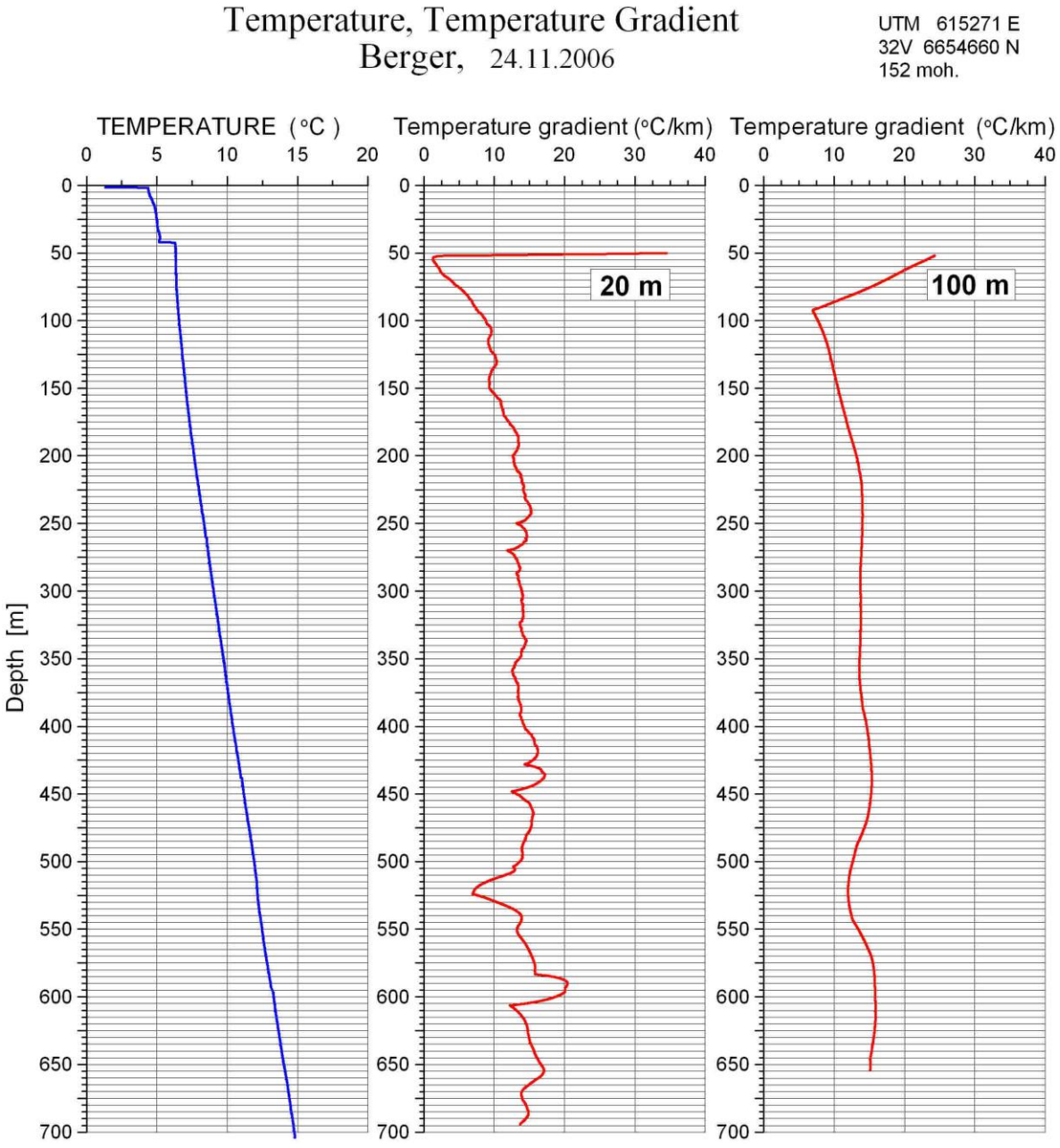

Figure 4.5. Temperature and temperature gradient in the Berger borehole.

4.3.3 Bleikvassli

The Bleikvassli borehole, Fig. 4.6, was drilled for mining prospecting in 1998. The cores from the borehole was lost, but samples from another borehole, 250 m to the south-east in the same geological settings, were used for thermal conductivity measurements. The average temperature gradient is 18.1 °C km.

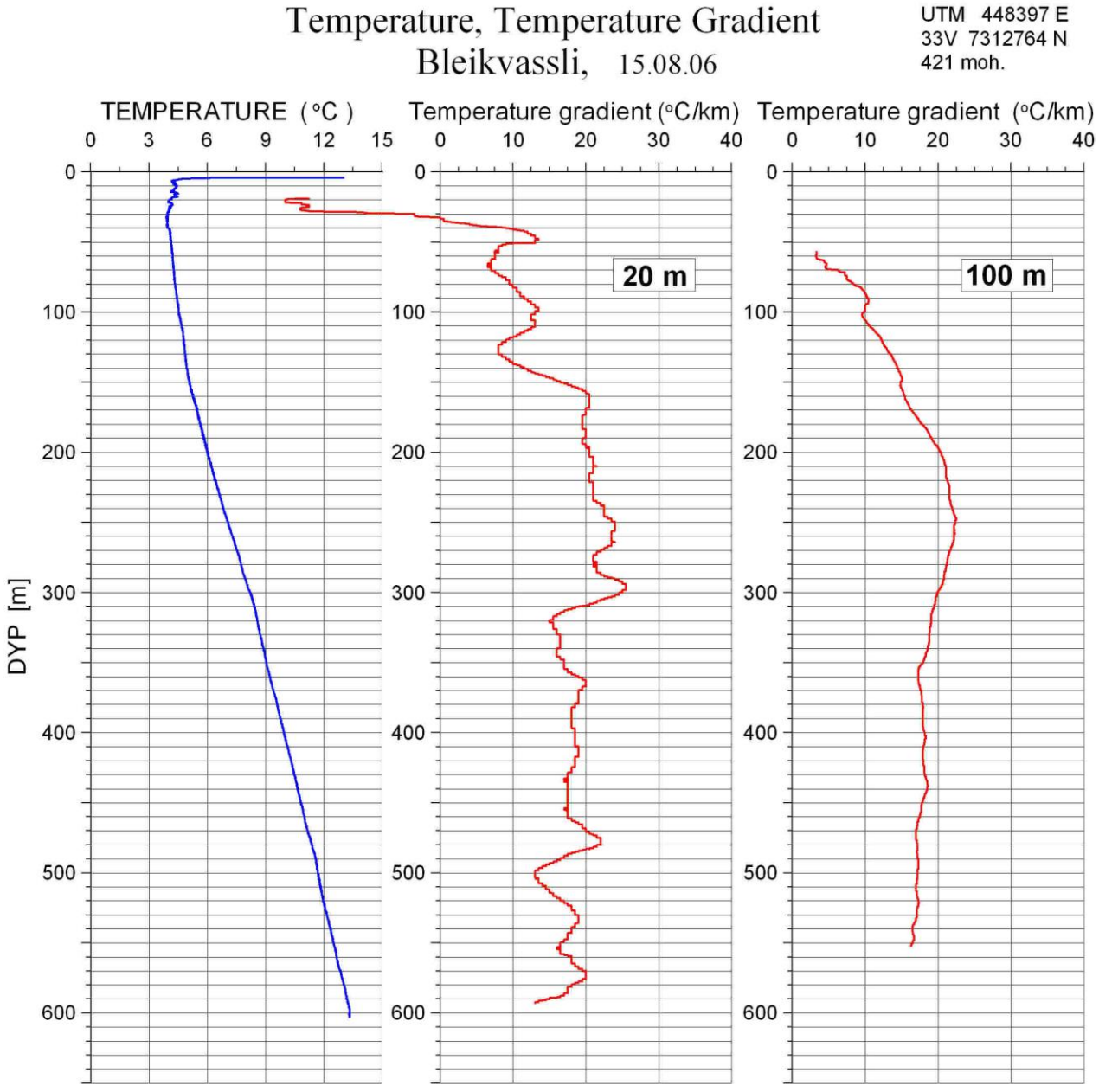

Figure 4.6. Temperature and temperature gradient in the Bleikvassli borehole.

4.3.4 Drag

The Drag borehole was drilled in the Tysfjord granite in Nordland. Temperature log and gradients are shown in Fig. 4.7. A local very high gradient can be observed at 200 m depth caused by an increase in the temperature at the same depth. The water quality also increase (not reported). This indicates an open fracture with inflow of water. The average temperature gradient is 17.0 °C/km.

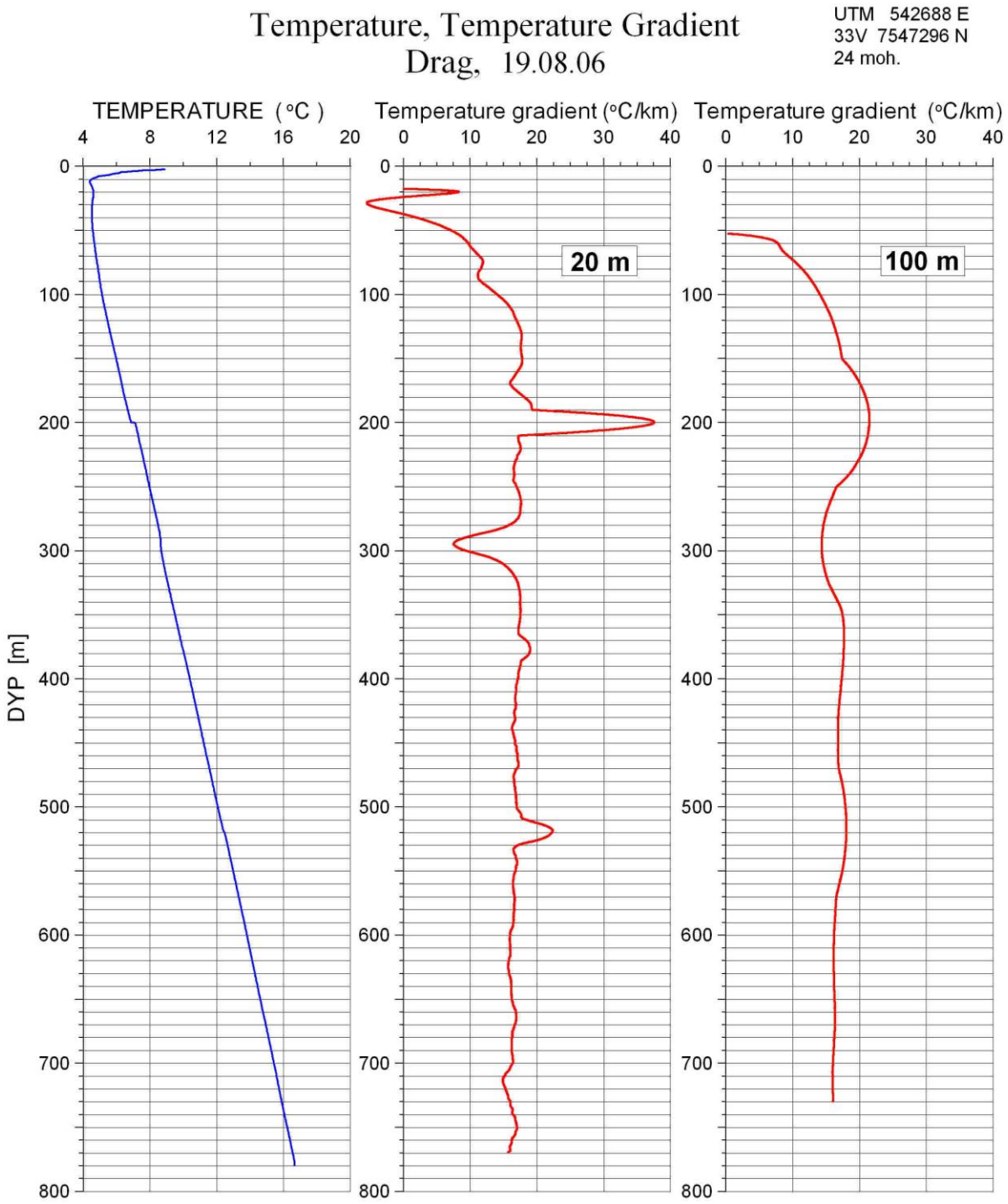

Figure 4.7. Temperature and temperature gradient in the Bleikvassli borehole.

4.3.5 Fredrikstad

The Fredrikstad borehole, Rødsmyra skole, is a 140 mm well with no core sampling. Logging was first performed in 2005 (Balling 2006), but the well was blocked at 150 m. The well was filled up with clay from a fracture zone at 150 m. The well was reopened in November 2006 and cased down to 180 m, and logging was performed in March 2007. Fig. 4.8 shows the temperature log and gradients. Big local variations in the 20 m interval gradient are observed at 150 –170 m and 280 – 360 m. Below 400 m the gradient is stable and the average value is 17.9 °C/km.

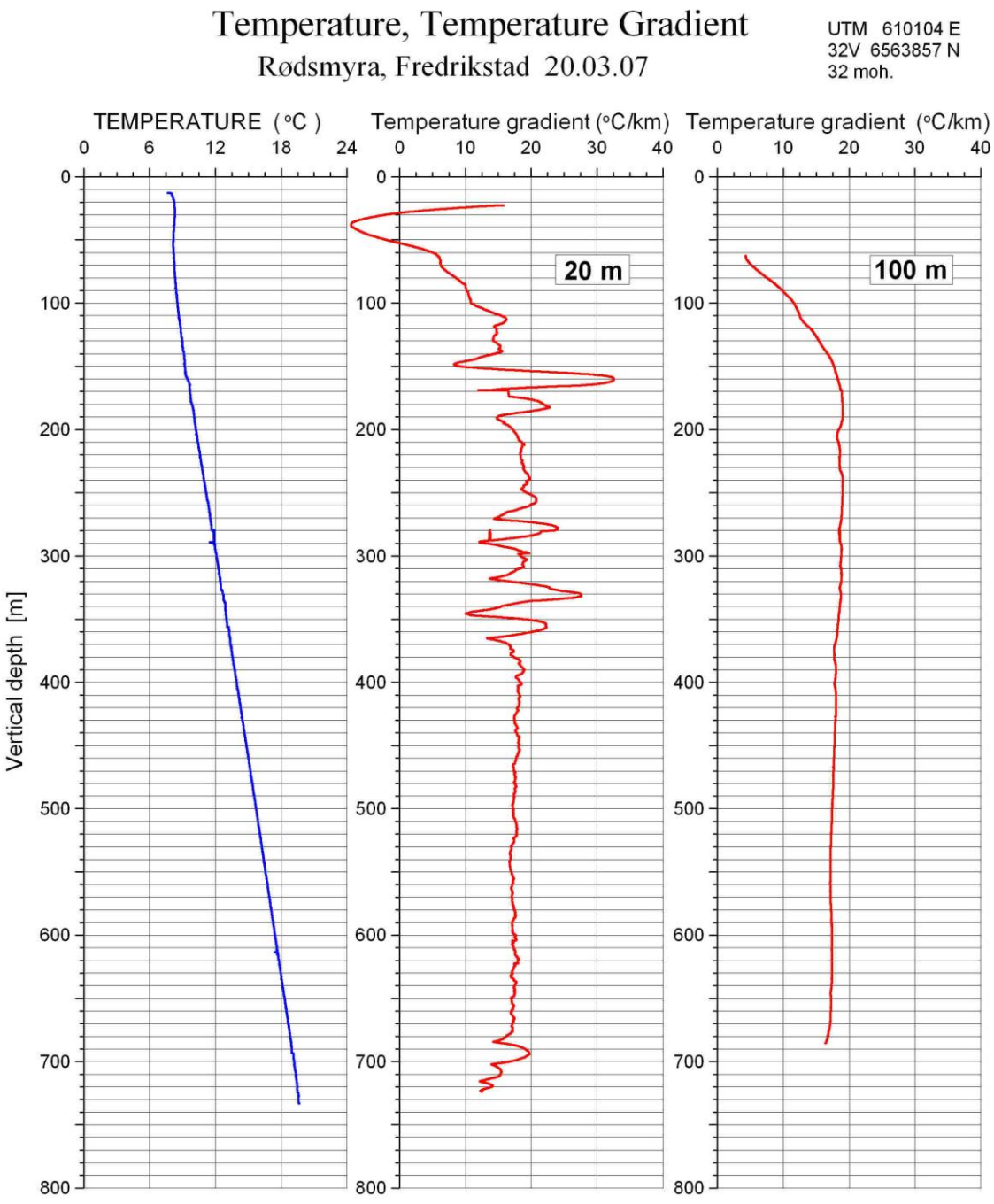

Figure 4.8. Temperature and temperature gradient in the Fredrikstad borehole.

The complete hole was supposed to be drilled in Idefjord granite. The well was inspected by optical televiewer, but the image was bad below the casing. The upper 150 m was logged by OPTV before reopening. In this case the recorded image was good, showing granite. Logs of water conductivity, natural gamma, resistivity and P-wave velocity confirm that there are no big variations in the rock. These logs are shown in Fig. 4.9. The gamma values are quite high (200 – 400 cps) indicating granite. The resistivity log is quite constant and high (5000 – 6000 ohmm) except several low resistivity zones at 190 – 270 m, 412 m and 640 m. The P-velocity is close to 5000 m/s (granite). The water conductivity is quite high below 170 m. This could be inflow of saline water, the well starts at 32 m.a.s.l., and it is not far from the shore. The water conductivity changes several times from 170 – 390 m, and the 20 m interval temperature gradient changes seem coincide with these changes.

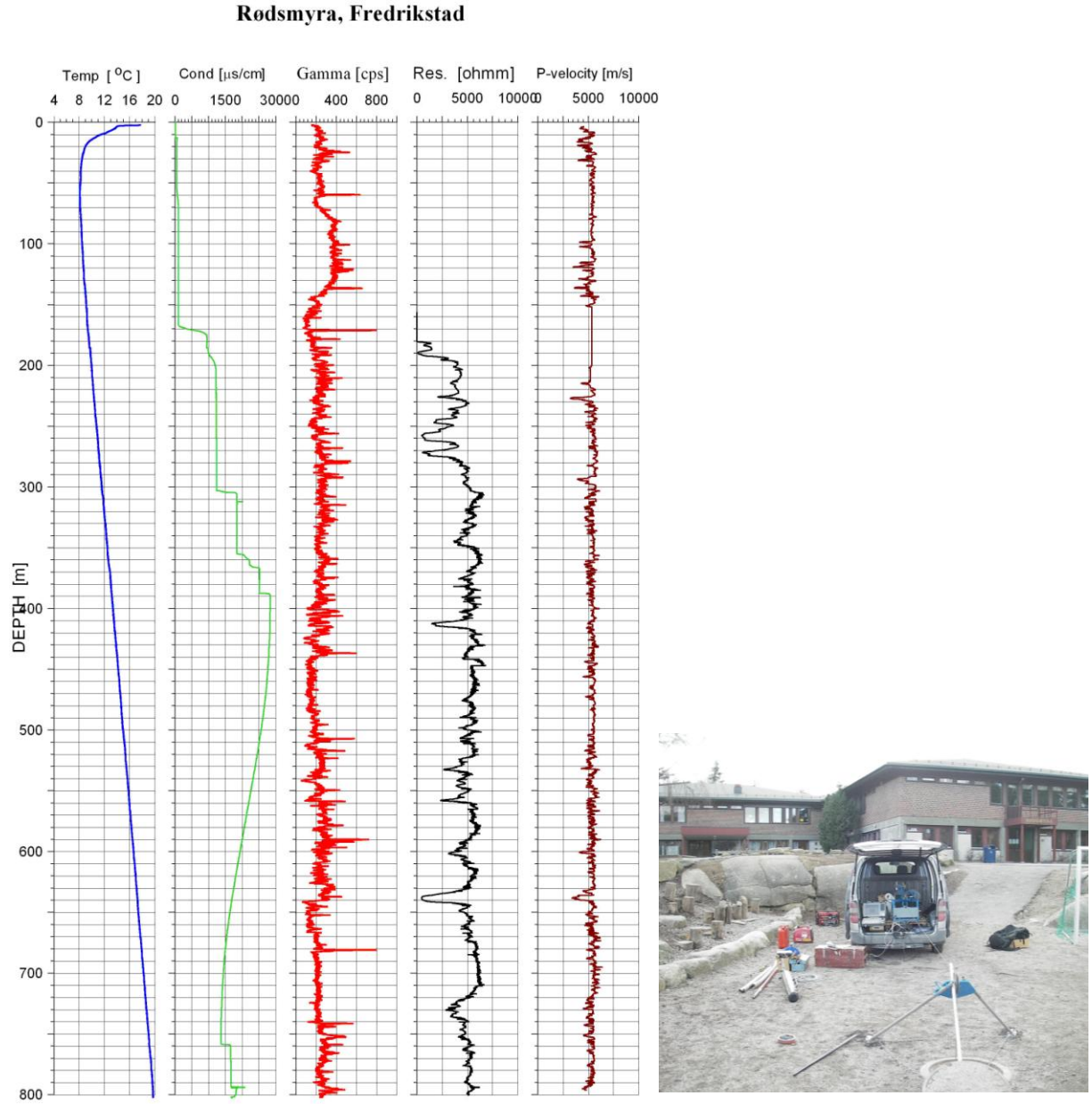

Figure 4.9. Temperature, water conductivity, natural gamma, resistivity, and P-wave velocity, Fredrikstad borehole.

4.3.6 Hamar

Fig. 4.10 shows temperature log and gradients from the Hamar borehole. The gamma log has been added. The average temperature gradient is 24.6 °C/km, but it can be seen that the gradient is decreasing from about 760 m. Down to this depth the rock consists of sedimentary rocks (sandstone, limestone and alum shale). Under the sedimentary rocks granite with higher thermal conductivity leads to a decreasing thermal gradient. The alum shale is clearly indicated by the gamma log.

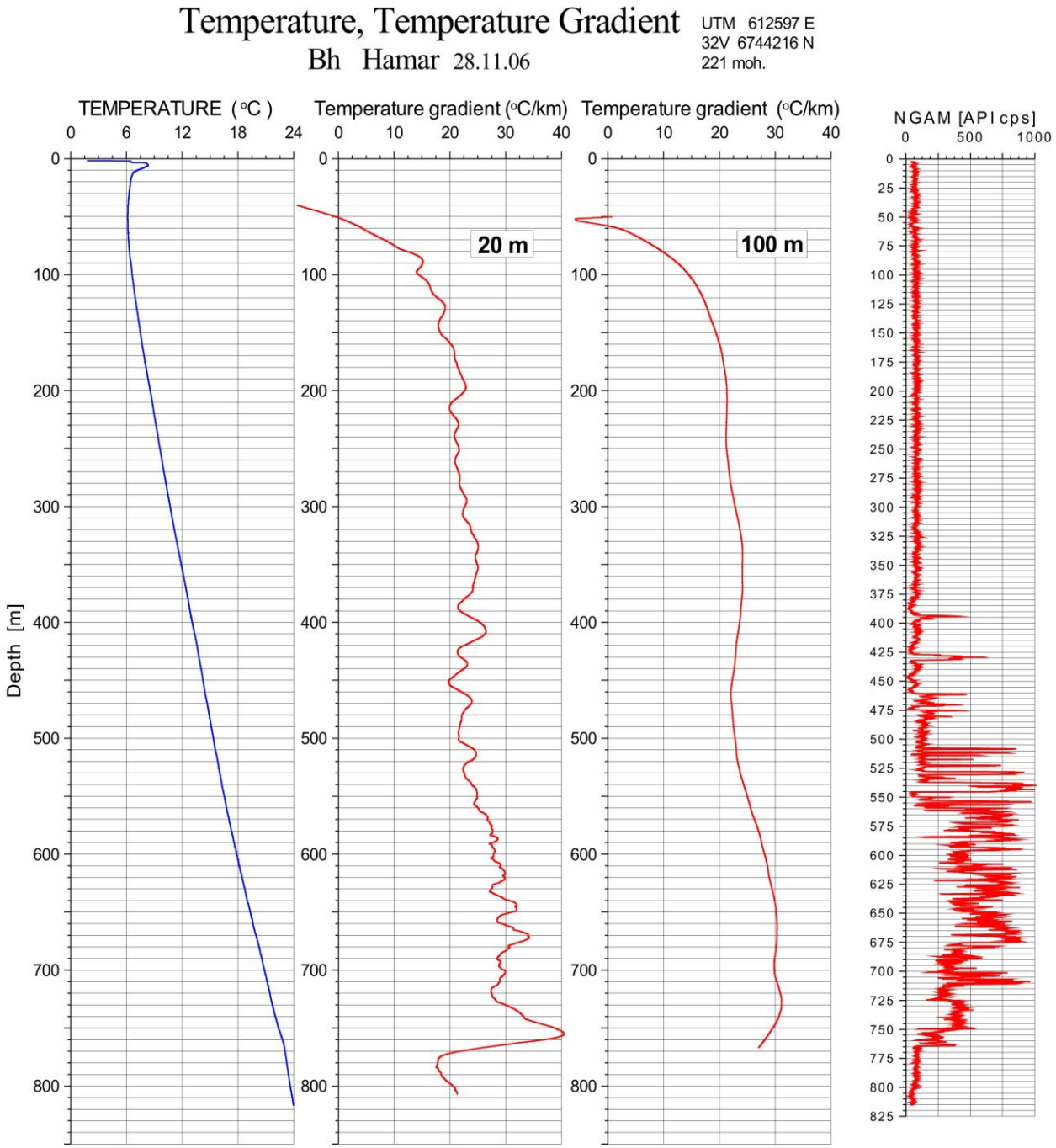

Figure 4.10. Temperature, temperature gradient and natural gamma in the Hamar borehole.

4.3.7 Hurdal 2

Fig. 4.11 shows the temperature gradients from Hurdal Bh 2005-02. The average temperature gradient is 21.2 °C/km. The gradient is disturbed by some local temperature variations between 640 and 680 m depth. This can be inflow of water. The water conductivity shows no changes at the same depth.

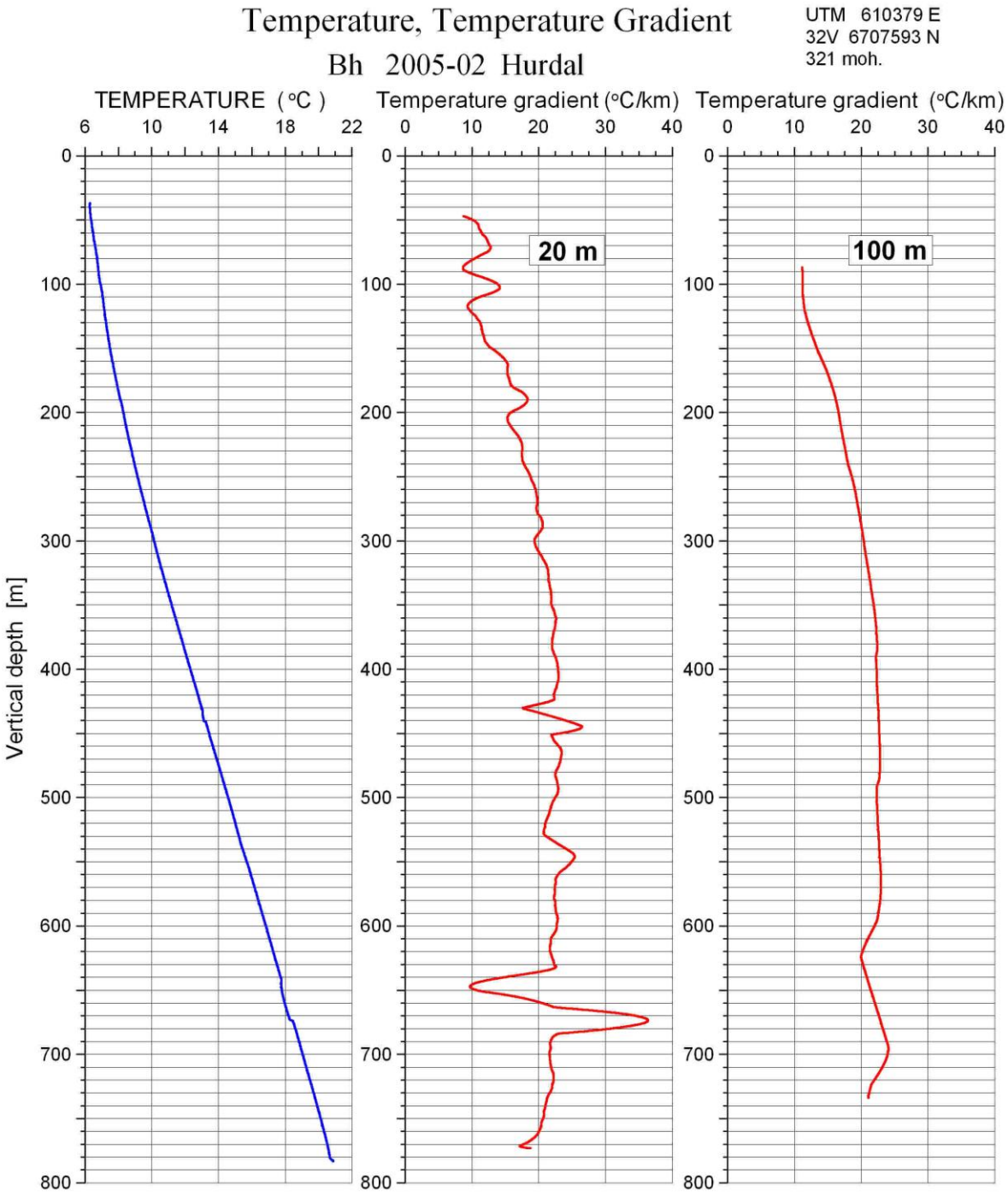

Figure 4.11. Temperature and temperature gradient in Bh 2005-02 Hurdal.

4.3.8 Hurdal 3

Fig. 4.12 shows temperature, temperature gradient and water conductivity in Bh 2005-03 in Hurdal. Big local variations in the gradient between 610 and 750 m are probably caused by water inflow. The temperature gradient increases rapidly from 610 m depth to a peak value of 75 °C/km at 625 m depth and 53 °C/km at 720 m. There is a big increase in the water conductivity at 720 m, which might confirm the water inflow.

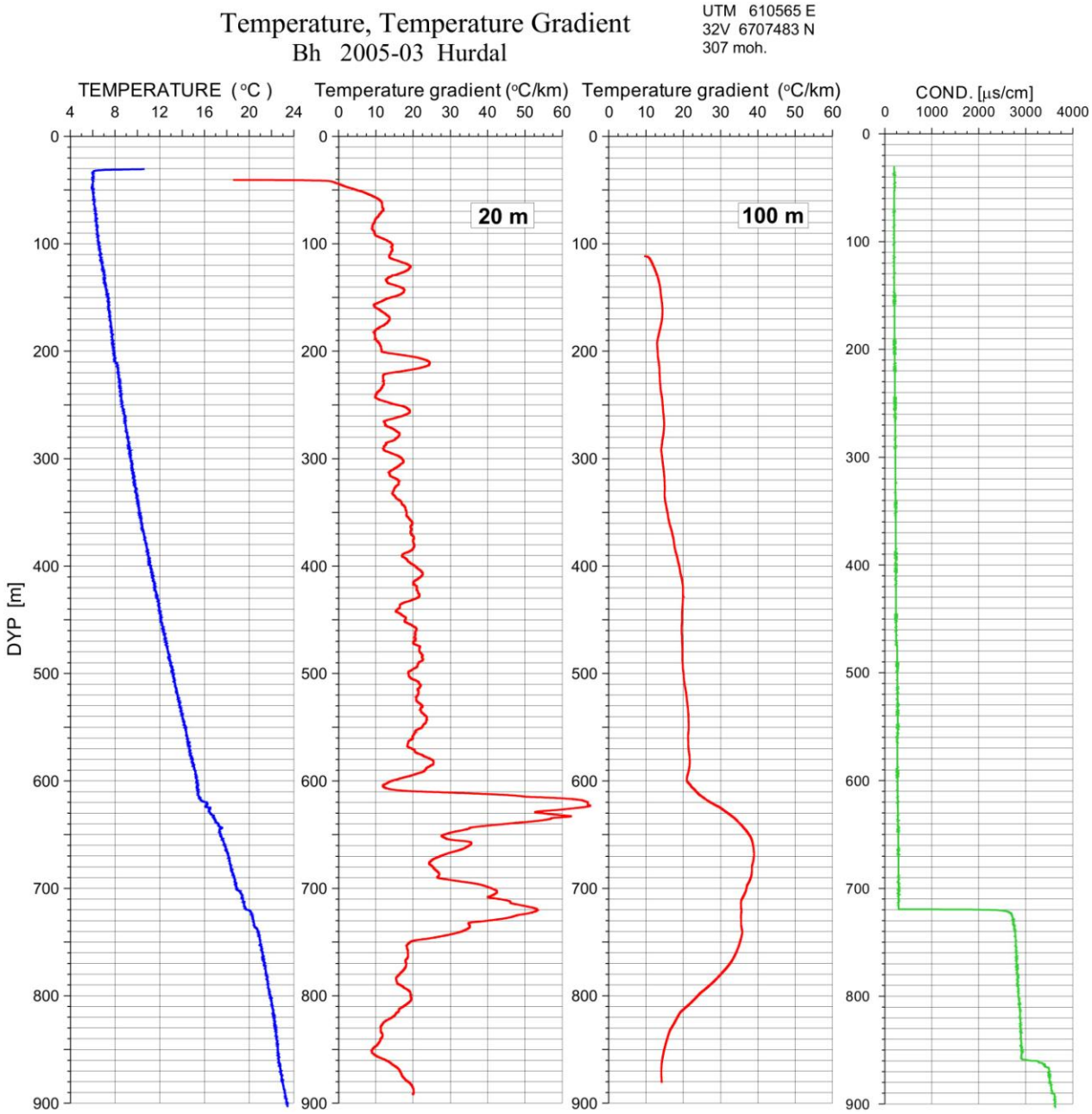

Figure 4.12. Temperature, temperature gradient and water conductivity in Bh 2005-03 Hurdal.

4.3.9 Hurdal 5

Bh 2005-05 was drilled to 750 m depth, but when the logging took place it was blocked at 585 m. The temperature log and gradients are shown in Fig. 4.13. Average temperature gradient is 21.6 °C/km.

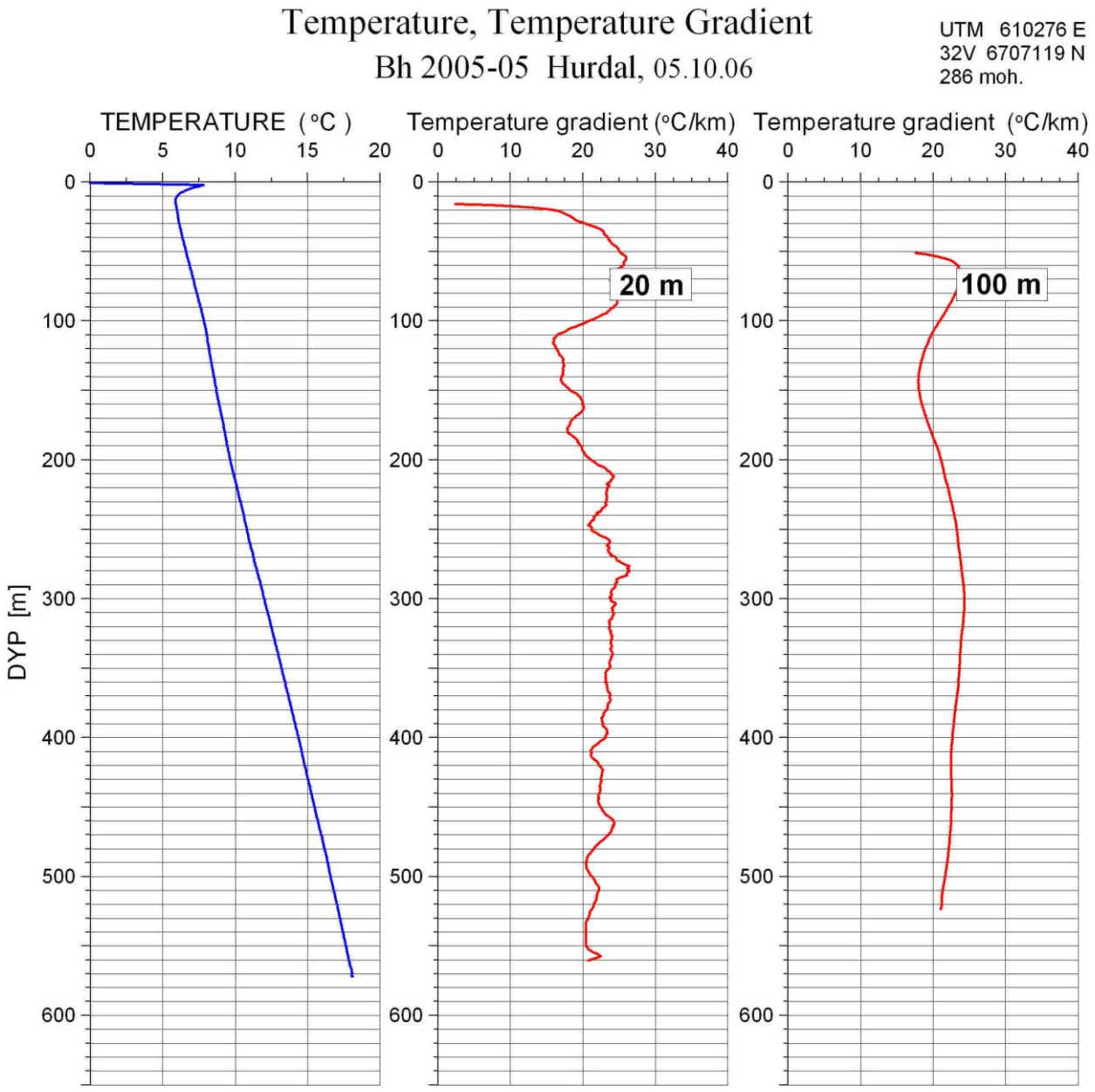

Figure 4.13. Temperature and temperature gradient in Bh 2005-05 Hurdal.

4.3.10 Leknes

Fig. 4.14 shows the temperature log, gradients and gamma for the Leknes borehole. The gradient is close to constant down to 550 m depth, about 20 °C/km. From this depth the gradient decrease, probably due to a change in the thermal conductivity. The gamma log indicates a change in the rock type at 570 m. The geological log confirms this change. The upper part of the borehole consists of granitic orthogneiss. From 540 - 590 there are alternating layers of diabas and gneiss. From 592 m to the bottom there is light greyish granite.

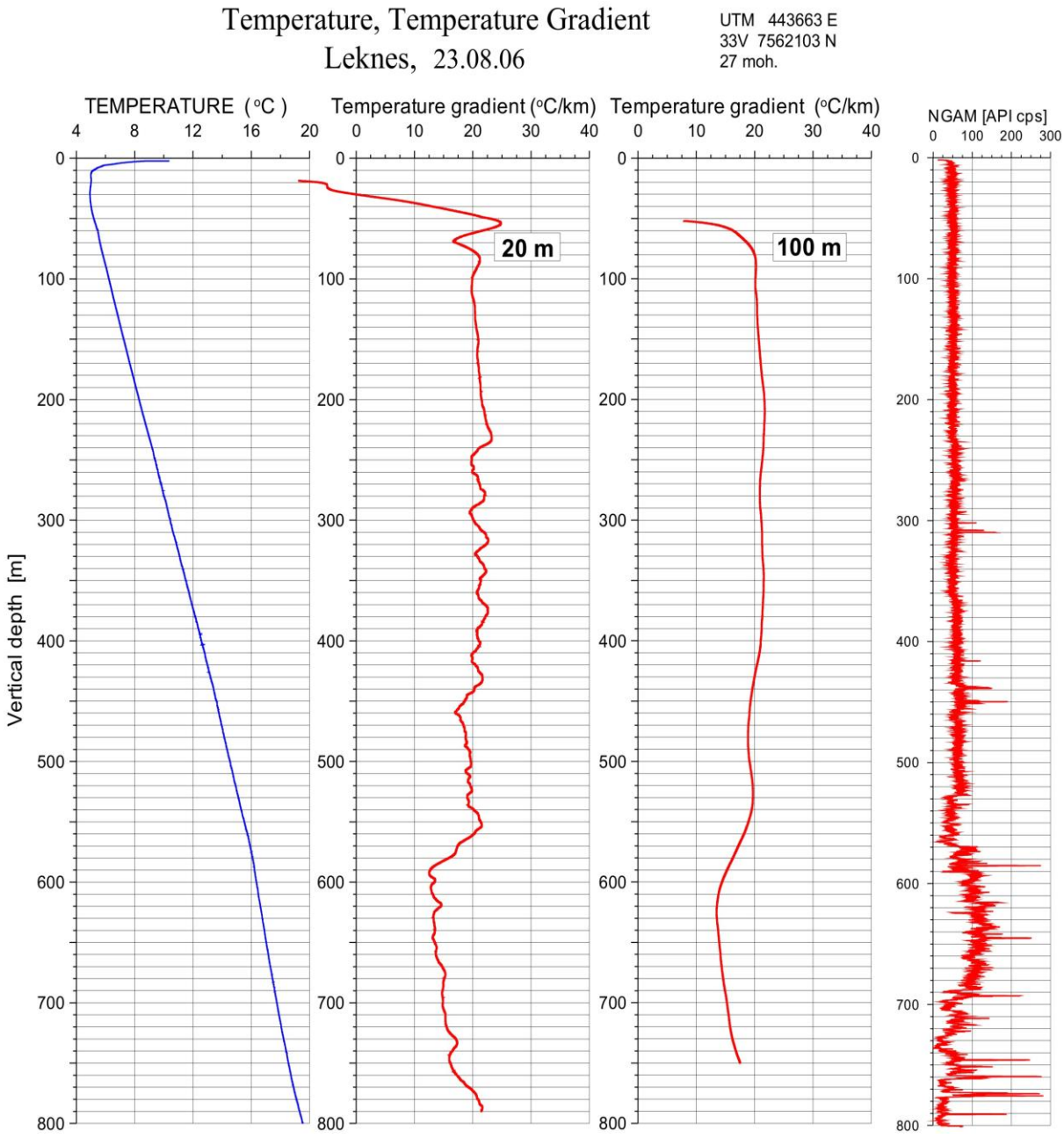

Figure 4.14. Temperature, temperature gradient and gamma in the Leknes borehole.

4.3.11 Sulitjelma

Fig. 4.15 shows the temperature log and gradients from the Sulitjelma borehole. The average gradient is 21.3 °C/km. Because of the slim diameter (46 mm) the old NGU temperature sonde was used. The borehole was located 5 km to the southwest of Jakobsbakken old mining area in Sulitjelma. Helicopter was used to transport the logging equipment to the borehole site, see Fig. 4.16.

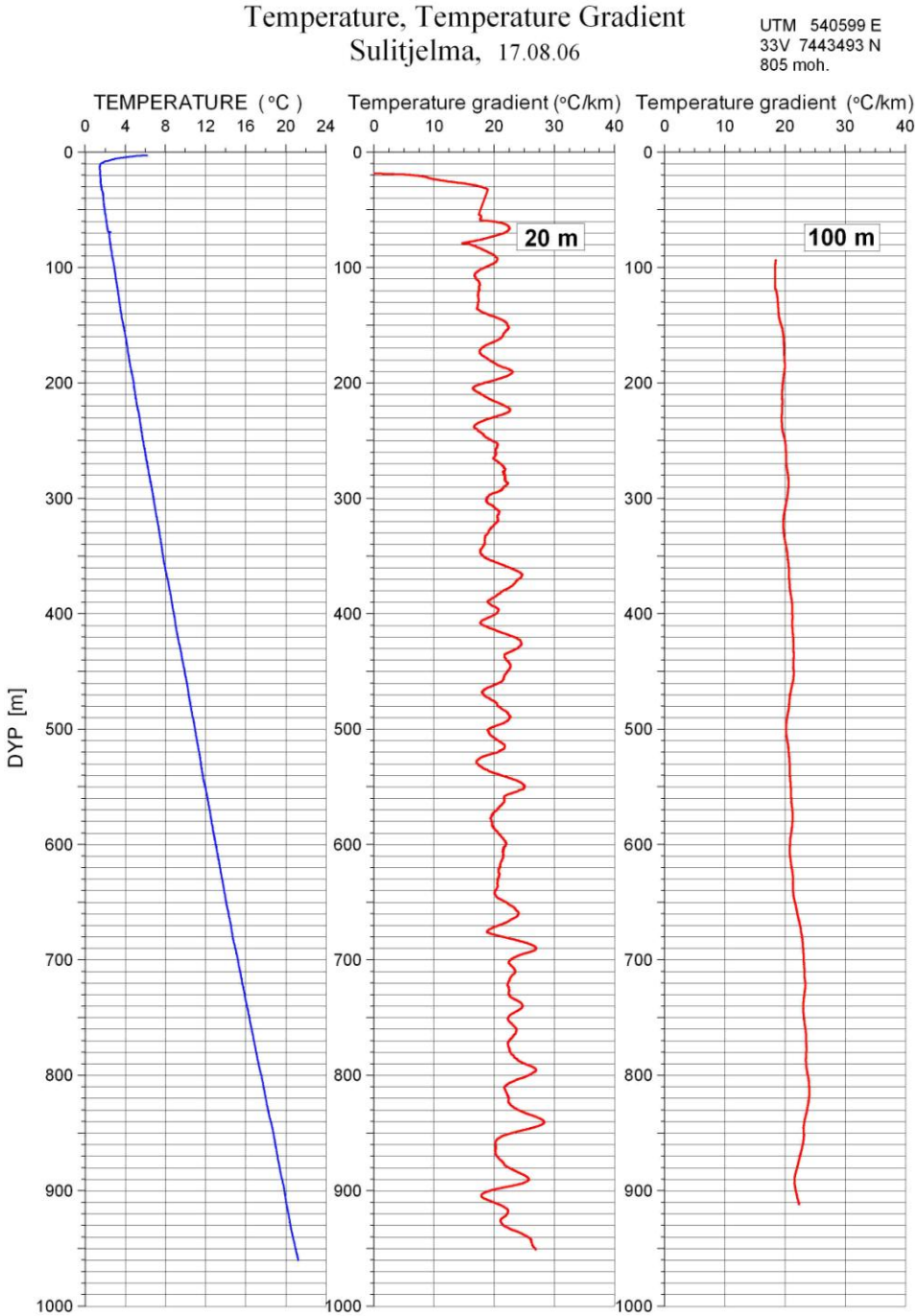

Figure 4.15. Temperature and temperature gradient in the Sulitjelma borehole.

Figure 4.16. Helicopter transport of the winch (left). Logging the Sulitjelma borehole (right).

5 TEMPERATURE LOGGING BY UNIVERSITY OF AARHUS 2005

Niels Balling & Niels Breiner, Department of Earth Sciences, University of Aarhus, Denmark

5.1 Introduction

In August 2005 temperature logging was carried out in a total of 10 boreholes in southern Norway. Seven boreholes with accessible (vertical) depths ranging from 154 to 982 m and three shallow holes, about 50 m deep, were measured. Two of the shallow holes were drilled in the Lærdal tunnel (Lærdal 1 and 2) and one at the surface above the tunnel (Lærdal surface). Basic borehole information including location, depth range covered by temperature measurements and time of drilling is summarized in Tables 5.1 and 5.2. Map locations are shown in Fig. 5.1.

The temperature data have been applied together with new measurements of thermal conductivity in the determination of terrestrial heat flow at the sites of measurements (Chapter 4 in the present report). This chapter describes the Århus equipment and measuring techniques used for the borehole temperature measurements, the data processing and results of measurements in terms of temperatures and temperature gradients. The logs from Berger and Arnestad were affected by high-frequency noise because og high-voltage electricity in the neighbourhood and were remeasured by NGU with their new logging instruments (see previous chapter). The Berger and Arnestad data obtained by University of Aarhus have therefore been removed from the present chapter but can be found I nthe Kontiki 2006 Report. Because the Rødsmyra drill hole in Fredrikstad was blocked at a depth of c.a 150 m we have also removed this

The temperature measurements were part of cooperation between the Geological Survey of Norway, Trondheim and the Department of Earth Sciences, University of Aarhus in relation to the Kontiki Project.

5.2 Equipment and measuring techniques

The applied temperature logging equipment has been developed and constructed by the geophysics group at the University of Aarhus. It consists of a traditional logging winch carrying the logging cable (here 1500 m), a temperature-sensing probe, an electronic recording unit as well as a depth counter, cable weight unit, a tripod and an electrical power generator. The whole system for boreholes down to 1500 m is usually transported in an ordinary department car (Figs 5.2-5.5). (Equipment for deeper boreholes, up to 5000-7000 m, is available with the winch built on a four-wheel trailer).

The temperature measurement technique is based on the high-precision quartz oscillator principle. A specially cut quartz crystal forms an integral part of an electrical oscillator, the frequency of which is almost linearly related to the ambient temperature. The temperature sensitive quartz crystal is placed in the front tip of the temperature-logging probe together with the associated oscillator electronics. Electrical power for the oscillator and the return oscillator

temperature signal are sent between the surface equipment and the down-hole probe through the logging cable.

The system is operated in two-conductor transmission, with one proper conductor, here a single conductor cable (type Rochester, outer diameter 3.16 mm) with amour/borehole water forming the second conducting unit. To avoid unacceptable signal damping, the temperature signal is transmitted at a rather low frequency of about 2 kHz, as compared to the basic frequency of the quartz oscillator of about 9 MHz. The current consumption of the temperature probe is below 10 mA, which ensures signal transmission also under high resistivity conditions ("one proper conductor"). In the surface recording unit the temperature bearing frequency signal is filtered and multiplied (in phase lock loops) up to about 28 MHz. Here 1 Hz corresponds to a temperature resolution of 0.001 °C. The basic construction principles are described in detail by Balling *et al.* (1981).

Figure 5.1. The locations of boreholes logged by the University of Aarhus in 2005 are indicated by red dots. The boreholes in Arnestad, Berger and Fredikstad have been relogged by NGU because of technical problems (noise from of high-voltage installations in the neighboorhood of the drill locations) and blocking of borehole at a shallow depth (Rødsmyra in Fredrikstad).

Table 5.1. Basic information for seven borehole localities, (UTM coordinates, zone 32) – including time of logging, dip (average degrees deviation from vertical) and total vertical depth of logged intervals. Locations marked with a star (*) have been relogged because of high-frequency noise and are also presented in the previous chapter.

Locality	Northing (m)	Easting (m)	Altitude (m)	Date of logging	Dip	Depth (m)	Time og drilling
1 Rødsmyra, Fredrikstad *	6563857	610104	28	24.08.05	vertical	154	Dec. 2004
2 Arnestad, Asker *	6630237	583546	11	23.08.05	vertical	681	Mar. 2004
3 Berger; Skedsmo *	6654660	615271	152	25.08.05	5.8	647	2002/2003
4 Nordli, Hurdal	6707213	610093	276	26.08.05	vertical	750	ca. 1979
5 Gåvålivatnet, Hjerkinn	6904727	532846	ca. 960	17.08.05	20.7	648	ca. 1986
6 Løkken, Meldal	7001453	530797	ca. 310	18.08.05	16.5	985	July 1981
7 Kjøsnesbogen, Aure	7031460	486454	ca. 25	19.08.05	17.1	355	ca. 1990

Table 5.2. Basis information on time of logging, borehole depth and bottom temperature for the three shallow Lærdal boreholes (one at the surface and two in the Lærdal tunnel).

Locality	Northing (m)	Easting (m)	Altitude (m)	Date of logging	Depth (m)	Bottom temp (°C)	Time og drilling
Lærdal surface	6761624	410507	1261	31.08.05	49	2.4	Sept. 2004
Lærdal tunnel 1			c. 245	22.08.05	52	17.1	Sept. 2004
Lærdal tunnel 2			c. 245	21.08.05	44	17.0	Sept. 2004

The oscillator frequency signal is calibrated to temperature using a commercial laboratory quartz thermometer as temperature standard. For each logging probe, a fifth-degrees least-squares polynomium is applied to define the relation between frequency and temperature. Under normally good field and local electrical noise conditions, the system has a temperature resolution of 0.001-0.003 °C and an absolute accuracy between 0.01 and 0.05 °C.

The length of cable running into the borehole (depth of probe), is measured by an electronic depth counter. The cable runs over a system of stabilizing wheels including a measuring wheel (Fig. 5.5), the angular rotation of which is recorded. The depth counter is calibrated by direct measurement of length of sections of cable run into a borehole. By experience, the reproducibility as well as accuracy of the depth measurement is normally around 0.1 % (+/- 1 m per 1000 m).

The running of the logging system is controlled by a microprocessor, which also transfers data directly to an ordinary PC (via an RS 232 communication port) where they are processed,

displayed and recorded to disc files. During logging the following parameters are recorded and stored: time, oscillator frequency and associated temperature, depth of probe, logging speed, weight of probe system and cable in borehole (measured at top tripod). These data are currently visible on screen where also a temperature-depth plot is shown. Thus, recordings are followed in real time during logging (Fig 5.5). The stop of depth penetration of the probe at borehole bottom, or at an unexpected local borehole blocking, is easily recognized by observing a combined drop in cable weight and stop in increase of temperature.

Under the special electrical measuring conditions on several present sites in Norway, where the national power system is without a proper electrical zero conductor, our present measuring system with one proper conductor is sensitive to ambient electrical ground currents. This may, as we shall see, induce significant noise in temperature signals, which needs special filtering.

5.3 Borehole logging procedure

The temperature logging is carried out running down-hole in continuous mode at constant speed. Temperature measurements at probe tip running down-hole ensure recordings at undisturbed borehole conditions. The borehole water temperature is measured, which, if no flow of water inside the hole is present, accurately represents the adjacent formation temperature. No attempts were made to accurately measure the temperature within the uppermost few metres of the air-filled part of boreholes above the water table. For most of the present boreholes a nominal logging speed of 10 cm/s was applied and a sample rate of 1 s resulting in a sample density of 10 cm. For the shallow Lærdal-boreholes a logging speed of 5 cm/s was used with a sample density of 5 cm. The procedure of borehole temperature logging is in agreement with international standard procedures (Beck & Balling 1988).

5.4 Data processing

The temperature information is to be presented in terms of temperature versus depth and temperature gradient versus depth. For some borehole sites, as mentioned above, ground electrical noise is induced into the borehole cable transmission systems, which results in equivalent significant temperature noise superimposed on the unperturbed temperature-depth signal. The temperature noise has a character which makes efficient noise filtering possible. Filtered data plots for all sites of measurements except Rødsmyra, Arnestad and Berger are shown in Figs. 5.6-5.12 and unfiltered versions of the same data are shown in Figs. C1- C10 in Appendix C of the Kontiki 2006 Report (Balling & Breiner 2006). The induced noise has the character of either rather local noise spikes (e.g. at Lærdal, Figs. C1 in Appendix C of the Kontiki 2006 Report (Balling & Breiner 2006)) or regular almost harmonic perturbations (e.g. at Arnestad

and Berger, Figs. C2 and C3 in the same appendix). Amplitudes of noise vary from 0.01 to 0.1 °C up to locally around 0.5 °C. Little or no significant noise is observed at Gåvålivatnet and Løkken.

The true temperature-depth function around a local depth point may be approximated by a constant temperature-gradient function. This means that filtering using a linear least-squares relation is appropriate. Filtering thus results in removing local temperature deviations (noise) from a local constant-gradient relation. For each borehole, a running constant depth-interval gradient has been applied. For all sites, except the high-noise sites of Arnestad and Berger, a running 5 m interval gradient filter was used. For Arnestad and Berger, a 30 m interval gradient was used.

For boreholes with little or some noise, the 5 m filtering generally results in temperature-depth relation with close to normal local high-precision temperature resolution. The 30 m filter is also very efficient in removing noise, but local potential real gradient variability over depth intervals below the length of filter is, of course, highly smoothed. At shallow depth (around 0-20 m), filtering may have the negative side effect of significantly perturbing local temperature variations such as those associated with the annual temperature wave (e.g. Figs. 5.10-5.12). For the interpretation of data, in particular from the uppermost parts of boreholes, unfiltered and filtered data need to be mutually compared and analysed.

Figure 5.2. The temperature logging system in the field, here at Gåvålivatnet, Hjerkinn.

Figure 5.3. The logging winch is installed inside the logging car together with the electronic steering and recording unit.

Figure 5.4. The electronic depth counter. An additional mechanical counter is also used (on top of the unit with the small white wheel.

Figure 5.5. The electronic unit. Measured temperatures together with other recorded parameters (depth, weight of probe and cable and logging speed) can be followed in real time on the screen.

5.5 Results of measurements and a preliminary analysis

Temperature and interval temperature gradients are shown for each borehole. For the deeper and intermediate deep boreholes, running least-squares gradients over depth intervals of 20 m and 100 m are calculated both for the filtered (Figs. 5.6-5.12) and unfiltered data sets (Figs. C1-C7 in Appendix C of the Kontiki 2006 Report (Balling & Breiner 2006)). For the shallow Lærdal boreholes, interval gradients for 10 and 20 m are calculated. Temperature data sampled at all depth points are applied in the gradient calculations. The gradient plots are based on gradients calculated at depth increments of 1 m.

Borehole temperatures and temperature gradients undisturbed by the process of drilling a borehole and associated (or subsequent) circulation of bore-fluid or other effects related to drilling a hole are referred to as equilibrium temperatures and equilibrium temperature gradients. Such values accurately represent the undisturbed formation temperatures and are used together with the associated values of rock thermal conductivity to calculate heat flow, basically from the product of temperature gradient and thermal conductivity (e.g. Powel et al. 1988). The determination of heat flow should, as far as possible, be based on accurate values of equilibrium temperatures. Disturbing effects other than those directly related to the drilling process include ground water circulation inside the hole induced by the presence of the borehole.

The time needed for a borehole to reach temperature equilibrium depends on several factors including the time used for drilling, type of drilling and the accuracy of temperatures needed. It may be relatively long as compared to the time of drilling in particular if high-precision local temperature gradients are required (Bullard 1947, Beck & Balling 1988). Boreholes drilled before 2002 are unlikely to have any significant disturbances from the drilling. Temperature data from those drilled in 2004 (Tables 5.1 & 5.2) need analysis for potential minor disturbances. Temperature disturbances due to flow of groundwater inside the hole may be present independent of the time since drilling. Such disturbances are typically seen as local significant temperature gradient anomalies at the depths of in- and/or outflow of water.

Local temperature and temperature gradient anomalies may also be due to natural flow of water in cracks, fractures or porous units. Longer wavelength temperature and temperature gradient anomalies may be associated with local topography or transient effects related to short-term as well as long-term surface climatic temperature variations (e.g. Powel et al.1988). Such effects need to be corrected for, as far as possible, before background terrestrial heat flow is calculated.

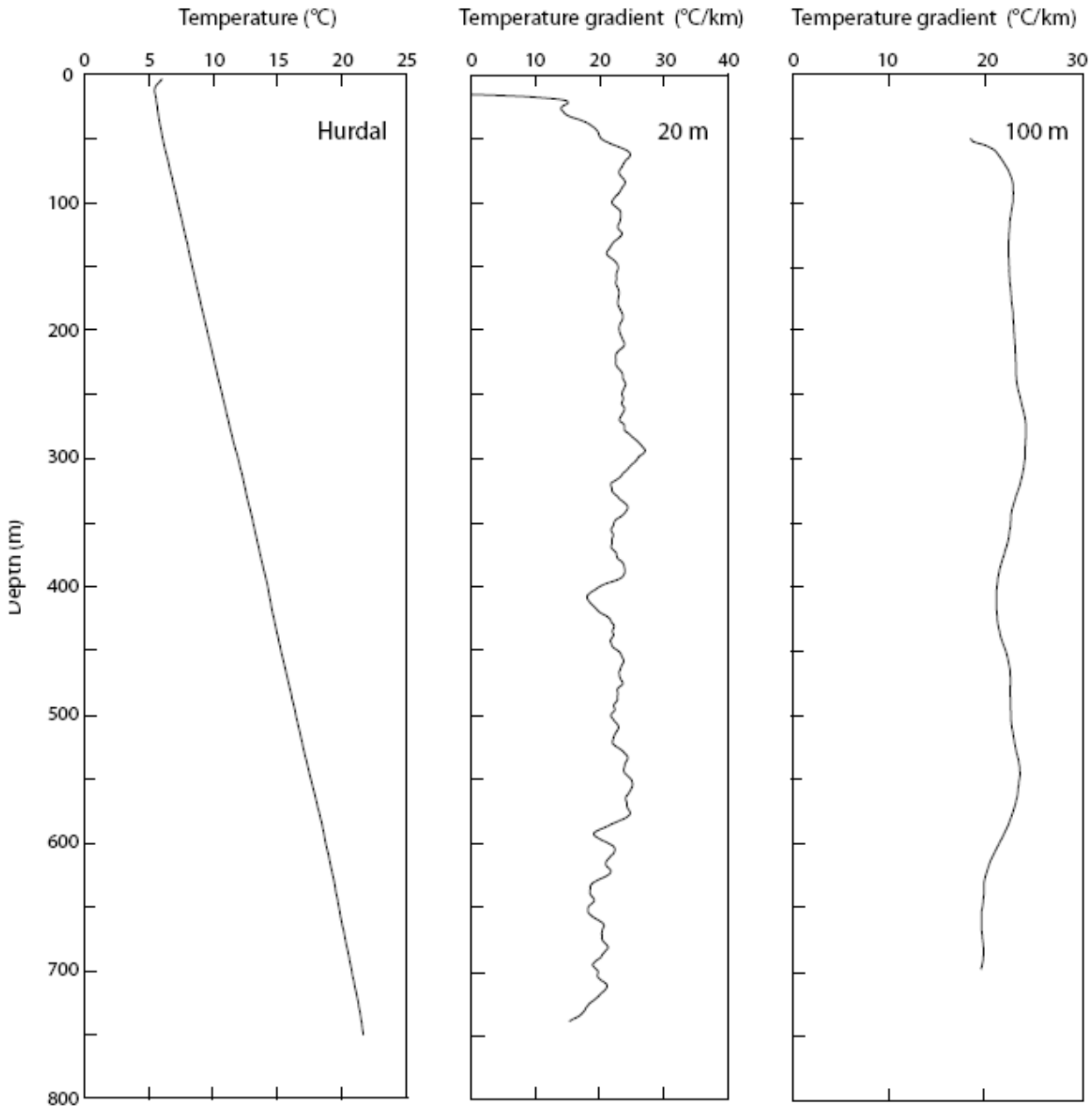

Figure 5.6. Temperature and mean interval temperature gradients as indicated for borehole Nordli, Hurdal.

The present analysis and comments are preliminary. A more detailed analysis needs to be carried out integrated with an analysis of relations between temperature gradients, rock thermal conductivity and lithology. For several reasons, temperatures in the upper parts of boreholes may include some disturbances (topography, groundwater, palaeoclimate). Therefore, in addition to temperature gradients shown in Figs. 5.6-5.12, average temperature gradients are calculated for the depth intervals below 300 m for the deeper holes (Table 5.3).

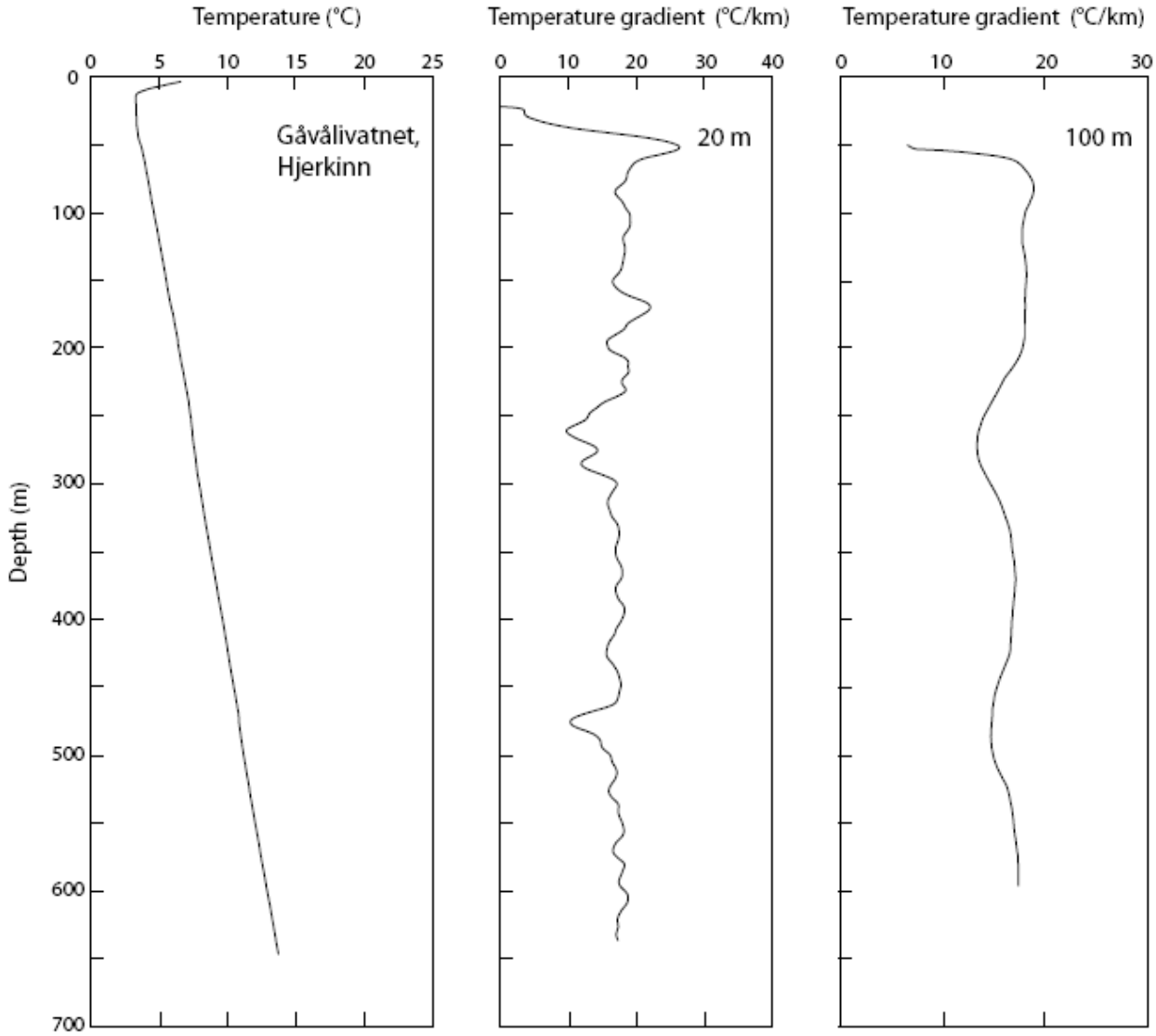

Figure 5.7. Temperature and mean interval temperature gradients as indicated for borehole Gåvålivatnet, Hjerkinn.

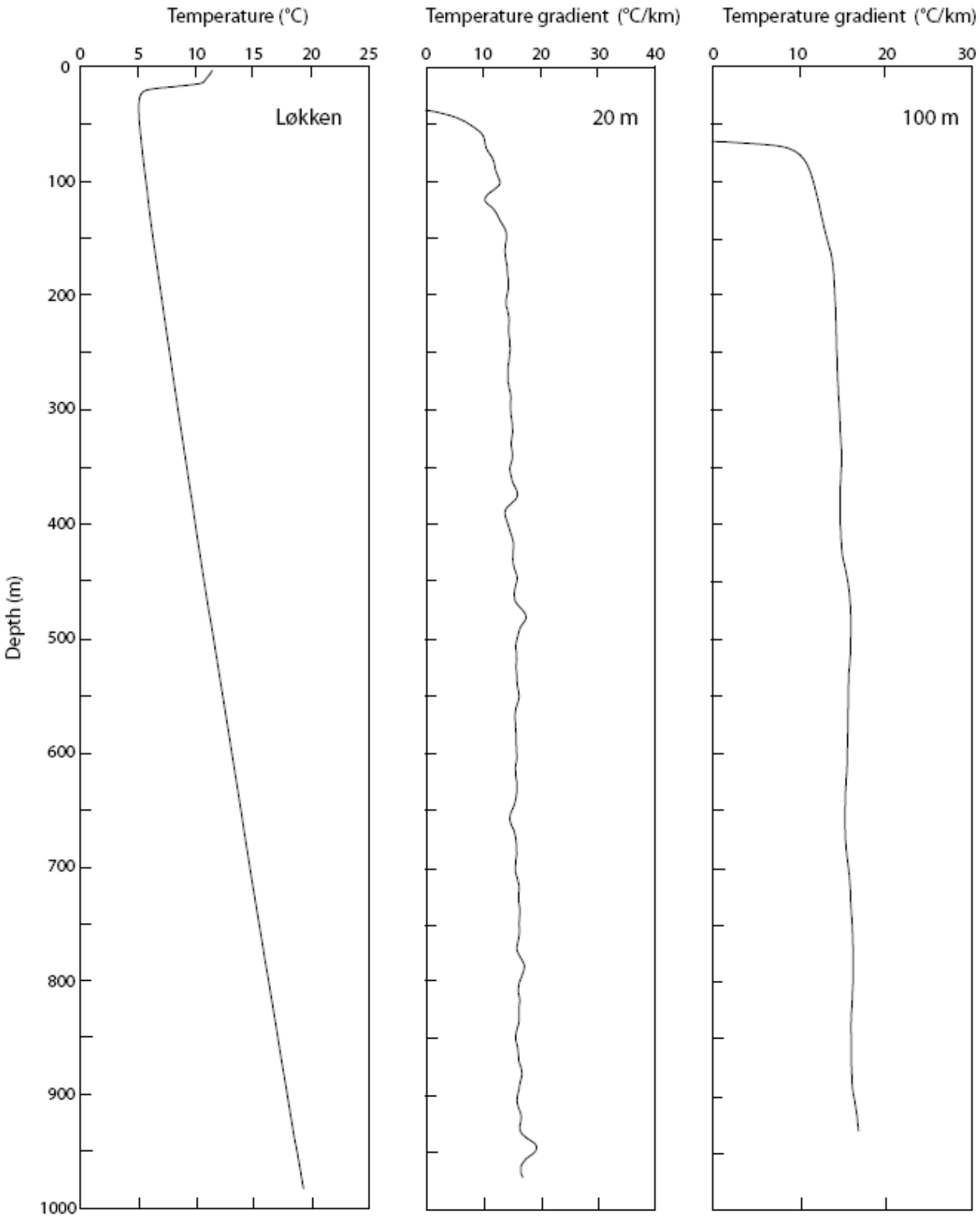

Figure 5.8. Temperature and mean interval temperature gradients as indicated for borehole Løkken.

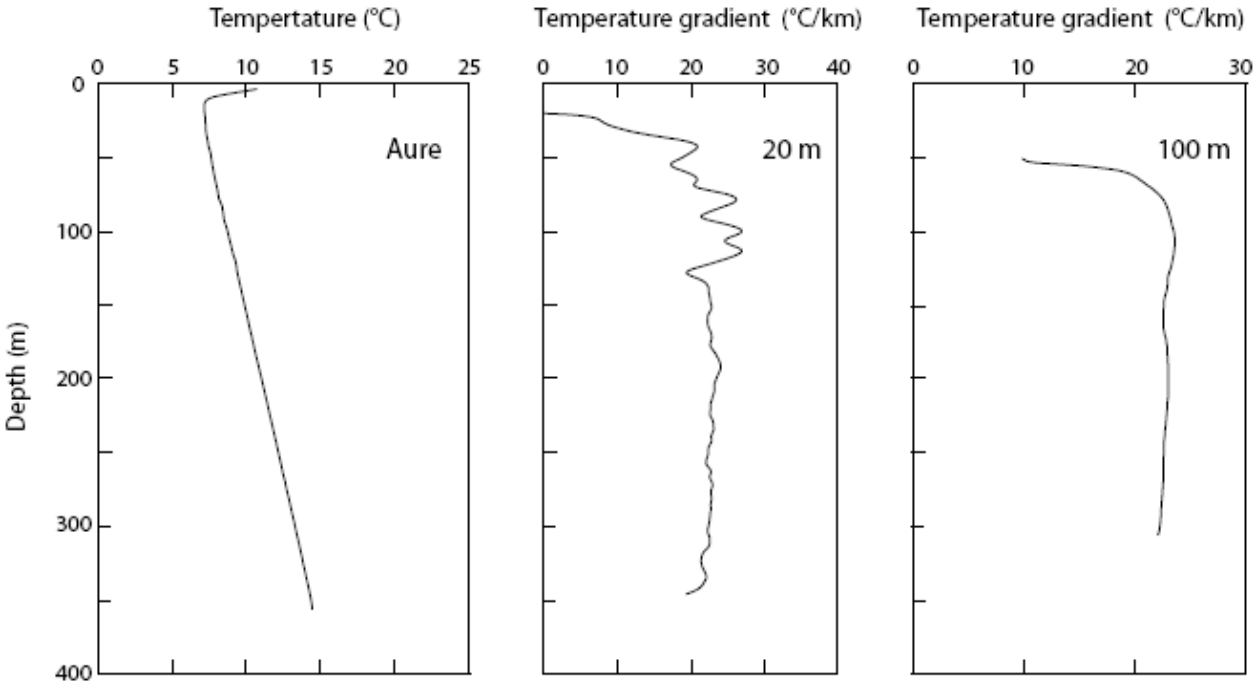

Figure 5.9. Temperature and mean interval temperature gradients as indicated for borehole Kjøsnesbogen, Aure.

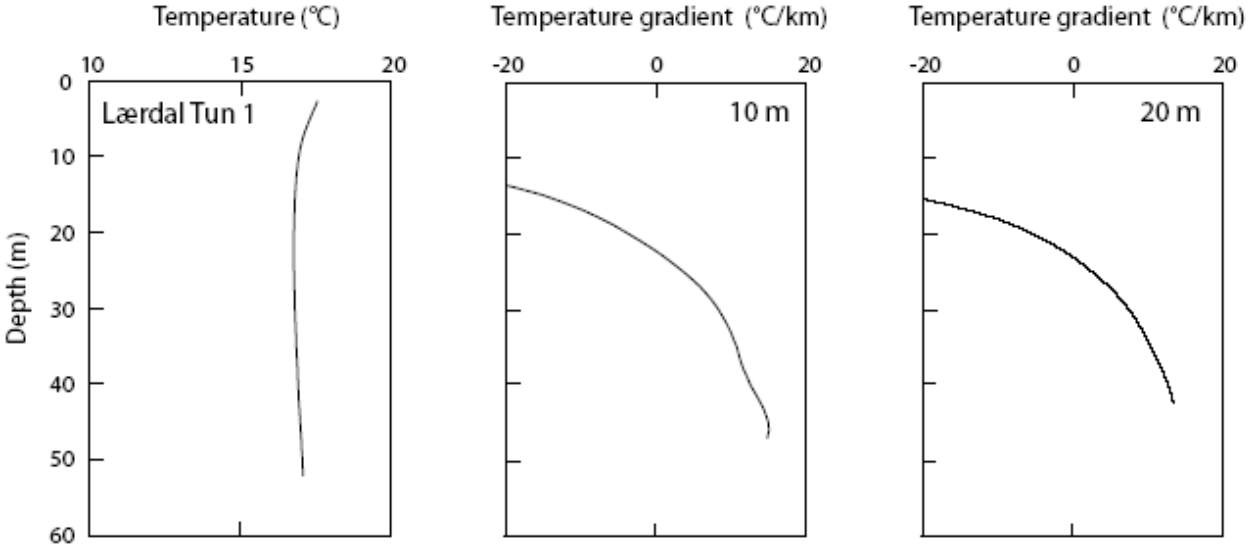

Figure 5.10. Temperature and mean interval temperature gradients as indicated for borehole Lærdal tunnel 1.

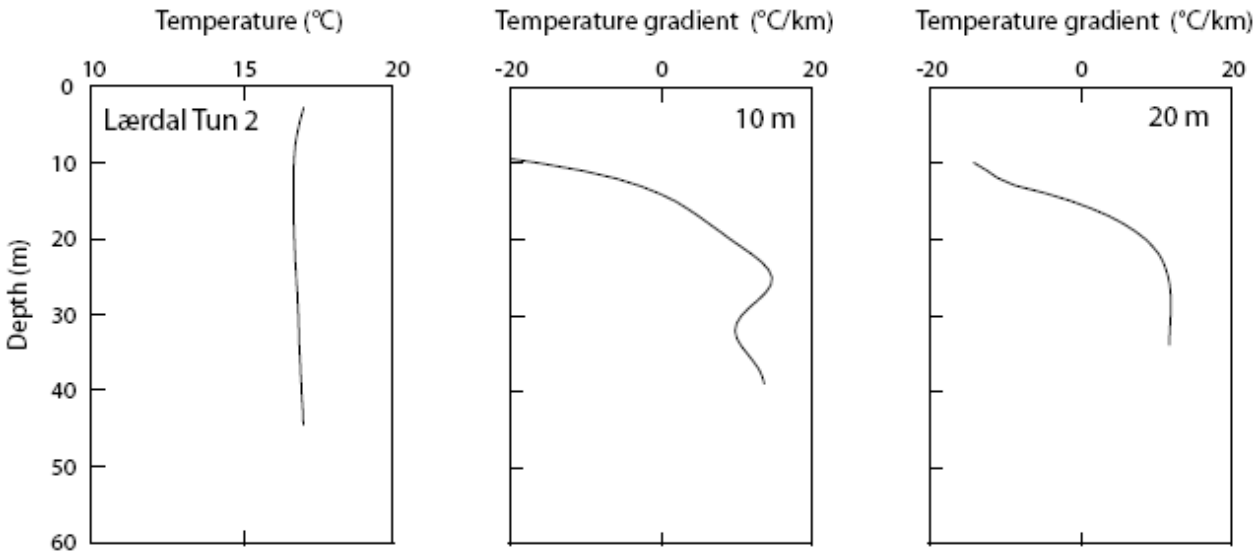

Figure 5.11. Temperature and mean interval temperature gradients as indicated for borehole Lærdal tunnel 2.

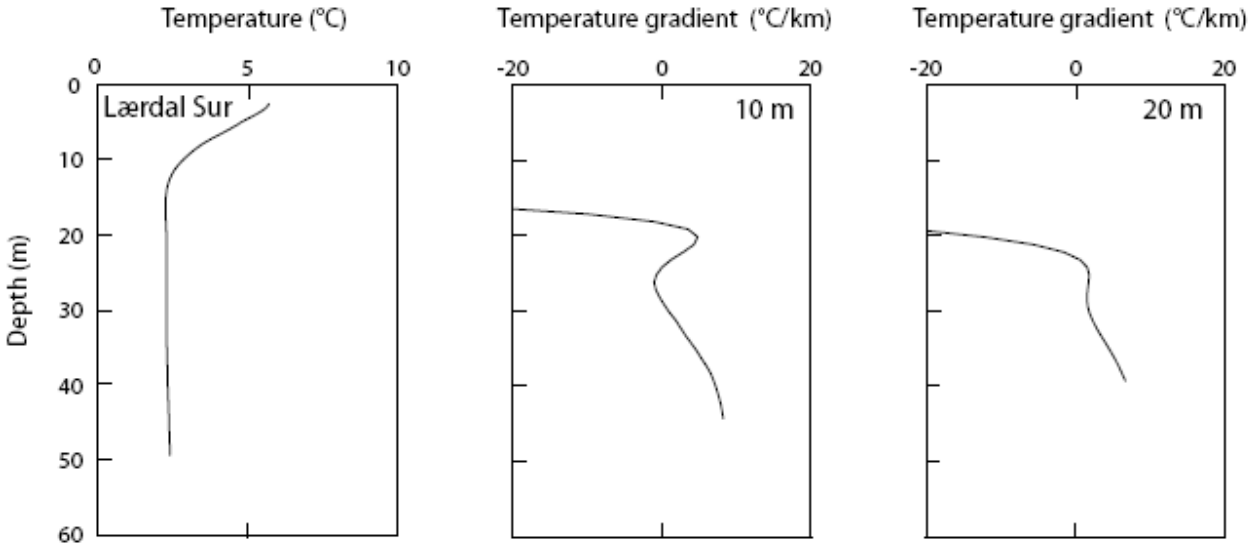

Figure 5.12. Temperature and mean interval temperature gradients as indicated for borehole Lærdal surface.

Table 5.3. Average least-squares temperature gradient from 300 m to bottom, temperatures measured at bottom and the surface intercept temperature using linear extrapolation from the depth interval indicated. Locations marked with a star (*) have been relogged because of highfequency noise and the new results were presented in the previous chapter.

Locality	Depth Interval (m)	Average temp. gradient (°C/km)	Temp. at bottom (°C)	Surface intercept temp. (°C)
2 Arnestad *	300 - 681	17.0	20.9	11.0
3 Berger *	300 - 647	15.2	14.3	4.4
4 Hurdal	300- 750	21.9	21.6	5.4
5 Gåvålivatnet, Hjerkinn	300 - 648	16.5	13.7	3.0
6 Løkken	300 - 982	15.9	19.3	3.6

Most deep mean gradients are around 15-17 °C/km. The mean gradient for Hurdal is significantly higher, 21.9 °C/km. Most boreholes are characterised by having rather constant gradients over large depth sections, sometimes almost the whole measured depth interval. Hurdal has an almost constant gradient around 22 °C/km below 60 m and with some local variability (Fig. 5.6), Løkken has a well defined gradient around 16 °C/km below 150 m with a slightly systematic increase with depth and some local variability, which may be related to local water movements (Fig.5.8).

At Gåvålivatnet we observe some gradient variability around a mean value of about 17 °C/km, locally down to 10 °C/km at about 260 and 480 m (Fig. 5.7), which needs further analysis in relation to variations in thermal conductivity and potential water movements. At Kjøsnesbogen we observe a rather well-defined high gradient, 22-23 °C/km between 140 and 350 m (Fig. 5.9).

In the shallow Lærdal tunnel boreholes negative gradients are seen in the upper 15-20 m (Figs. 5.10 and 5.11). This may be related to a minor boundary temperature increase associated with the tunnel. Temperatures in the deeper parts of the holes seem unaffected by the existence of the tunnel. Also the shallow Lærdal surface hole has a negative or near zero gradient above 30 m (Fig. 5.12), which may be related to surface temperature variations (annual and longer term).

The average temperature gradient between the Lærdal surface location and the tunnel boreholes using the data in Table 5.2 is 14.4 °C/km. The size of temperature gradient variations is in good agreement with those previously observed in Norway (e.g. Grønlie 1977) and in the Fennoscandian region in general (Balling 1995).

As an integrated part of the determination of terrestrial heat flow, temperature gradients are to be analysed in relation to thermal conductivity, which is beyond the scope of this report.

6 THERMAL CONDUCTIVITY MEASUREMENTS

Kirsti Midttømme, Randi K. Ramstad, Harald Elvebakk, Janusz Koziel, Ole Lutro, Øystein Nordgulen, Odleiv Olesen, Trond Slagstad & Bjørn Wissing, NGU

Thermal conductivity of rock samples is measured with a transient method. Comparable measurements have been carried out at the laboratories of the University of Aarhus and the Geological Survey of Finland. Thermal conductivities are measured on core samples from the boreholes or on rock samples that are representative for the rocks in the borehole (Table 6.1)

Table 6.1. Thermal conductivity samples.

Location	**Number of th. cond samples**	**Type of sample**	**NGU report**
Drag	69	Core samles	2006.0392 Lab. rep
Leknes	146	Core samples	2006.0503 Lab. rep
Sulitjelma	103	Core samples	2006.0525 Lab. rep
Bleikvassli	117	Core samples from a neighbouring borehole	2006.0530 Lab. rep
Aure	5	Rock samples	2005.0380 Lab. rep
Løkken	83	Core samples	2006.0056 Lab. rep
Hjerkinn	120	Core samples	2006.0056 Lab. rep
Lærdal 1, Lærdal tunnel	69	Core samples	2005.0311 Lab. rep
Lærdal 2, Lærdal tunnel	75	Core samples	2005.0297 Lab. rep
Aurland	25	Core samples	2006.0009 Lab. rep
Hamar	98	Core samples	2006.0260 Lab. rep
Hurdal Dh 02	74	Core samples	2007.0004 Lab. rep
Hurdal Dh 03	80	Core samples	2007.0004 Lab. rep
Hurdal Dh 05	45	Core samples	2007.0040 Lab. rep
Berger	61	Rock + Litho samples	2005.0176 Lab. rep + NGU Rep 2000.073
Arnestad	152	Rock samples	NGU rep 2004.013
Fredrikstad	31	Rock + Litho samples	2005.0176 Lab. rep 2006.0005

6.1 Method

Thermal conductivity of rock samples is measured with a transient method. A constant heat flow is induced to the top of the samples. The heat mechanism is radiation and the heat source, with a constant temperature of 300ºC ±2K, is placed 10 mm above the top surface of the sample. The sample is insulated on all other surfaces. The temperature is measured at the base of the sample. Thermal diffusivity (a) is estimated from the temperature – time plot, and the thermal conductivity (k) is calculated from thermal diffusivity, (a) measured density (r) and expected specific heat capacity (cp) of the sample using equation 1:

$$k = rcpa \qquad (1)$$

The theory of this method is described in Carslaw & Jaeger (1959) and Middleton (1993). Quality controls are carried out by measurements on the standard material Pyroceram 9606. The apparatus at NGU was improved in December 2005 and the error of the thermal diffusivity measurements is now within ± 5%.

6.2 Comparable thermal conductivity measurements at the University of Aarhus and the Geological Survey of Finland, fall 2005

To ensure the validity of the thermal conductivities measured at NGU, samples were sent to the University of Aarhus and the Geological Survey of Finland for comparable measurements.

A total of 14 identical samples was measured with the needle probe method at the University of Aarhus and 8 of the samples of length 20 mm measured at NGU were cut in two samples of length 9 mm and measured with the divided bar apparatus at Geological Survey of Finland (GTK). The results are shown in Fig. 6.1.

A general trend is that NGU measures the lowest thermal conductivity values and University of Aarhus measures the highest values. The deviations between the values measured at University of Aarhus and NGU are within the range of –16.0 % to + 14.8 %. The deviation between GTK and NGU's values are in the range –6.6 % to +8.6 %.

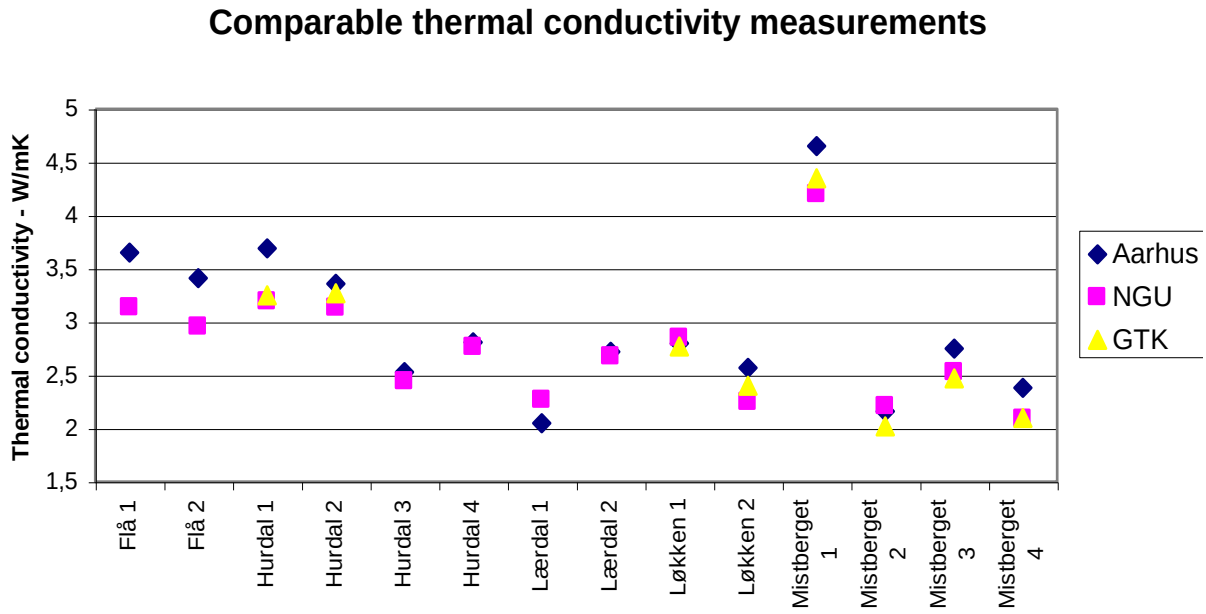

Figure 6.1. Comparable thermal conductivity measurements at the University of Aarhus, NGU and the Geological Survey of Finland (GTK).

6.3 Results from thermal conductivity measurements of rock samples

Thermal conductivities were measured on 69 core samples from the borehole in Drag. All samples, except of two pegmatite samples, consist of granitic gneiss.

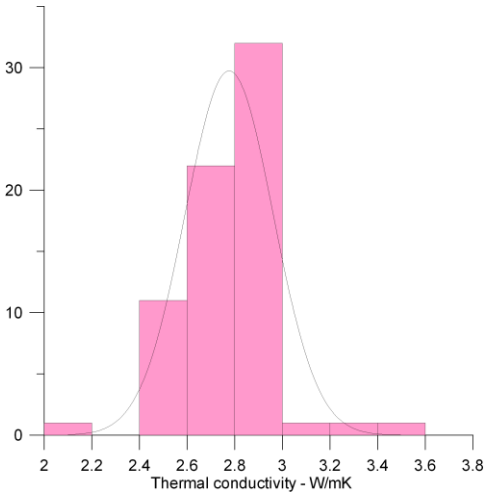

Drag

69 core samles

Median value: 2.8 W/m·K
Mean value : 2.8 W/m·K
Minimum value: 2.1 W/m·K
Maximum value: 3.5 W/mK

Figure 6.2. Thermal conductivities measured on core samples from Drag. The normal distribution line is shown.

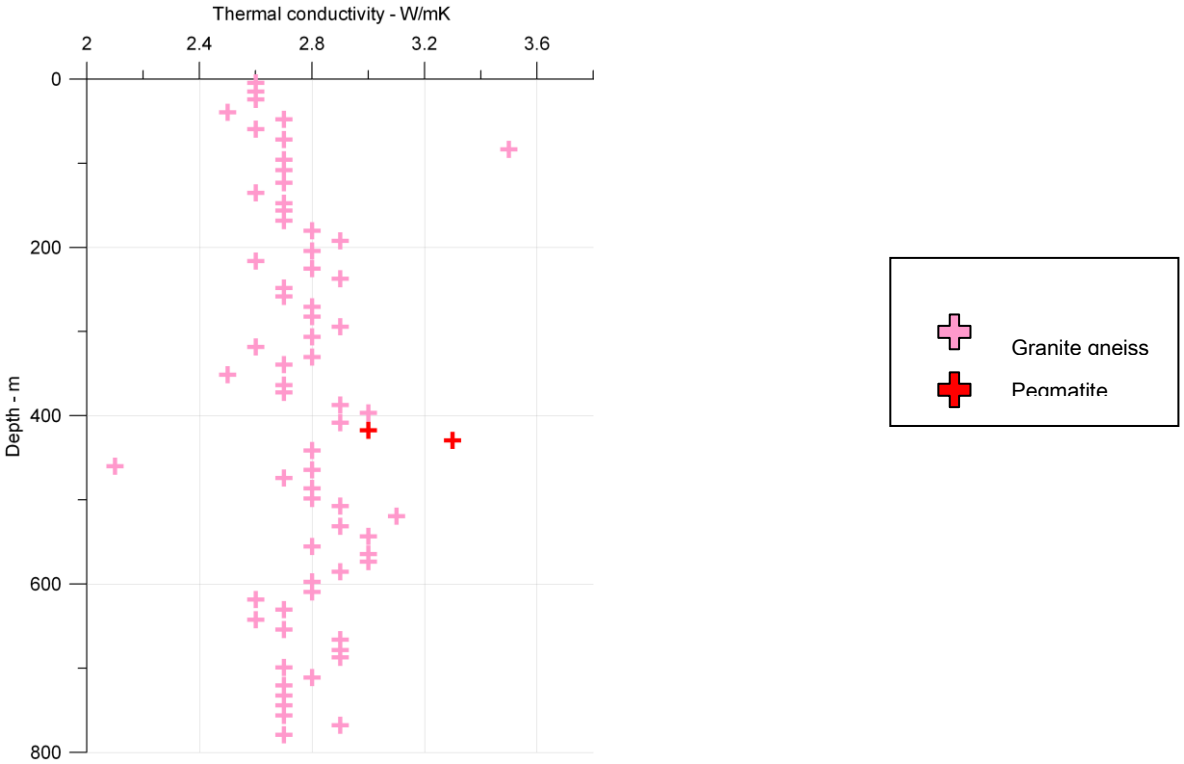

Figure 6.3. Thermal conductivities of the Drag borehole plotted with depth. The colour of the dots shows the rock.

Thermal conductivity is constant in the range 2.6 to 3.0 W/mK and with few outliers in the 800 m deep borehole at Drag. The variation in thermal conductivities is mainly due to mineralogical variations. Structural variations in grain size, foliation and texture seem to have minor effect on the thermal conductivities for these samples.

Leknes

Leknes

146 core samples
Minimum value: 1,9 W/m·K
Maximum value: 4.9 W/mK

Median value: 2.2 W/m·K
Mean value : 2.4 W/m·K

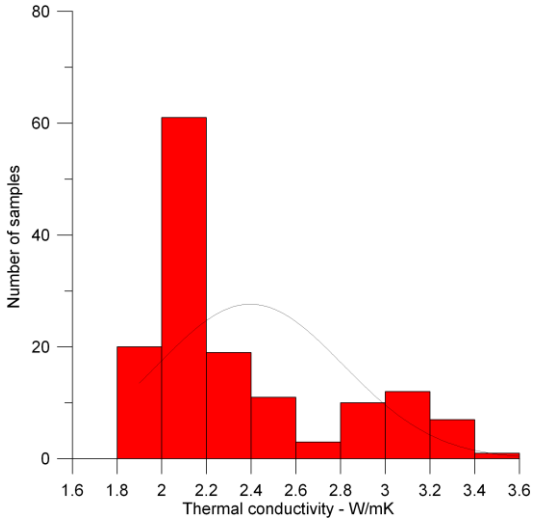

Figure 6.4. Thermal conductivities measured on core samples from Leknes borehole. The normal distribution line is shown.

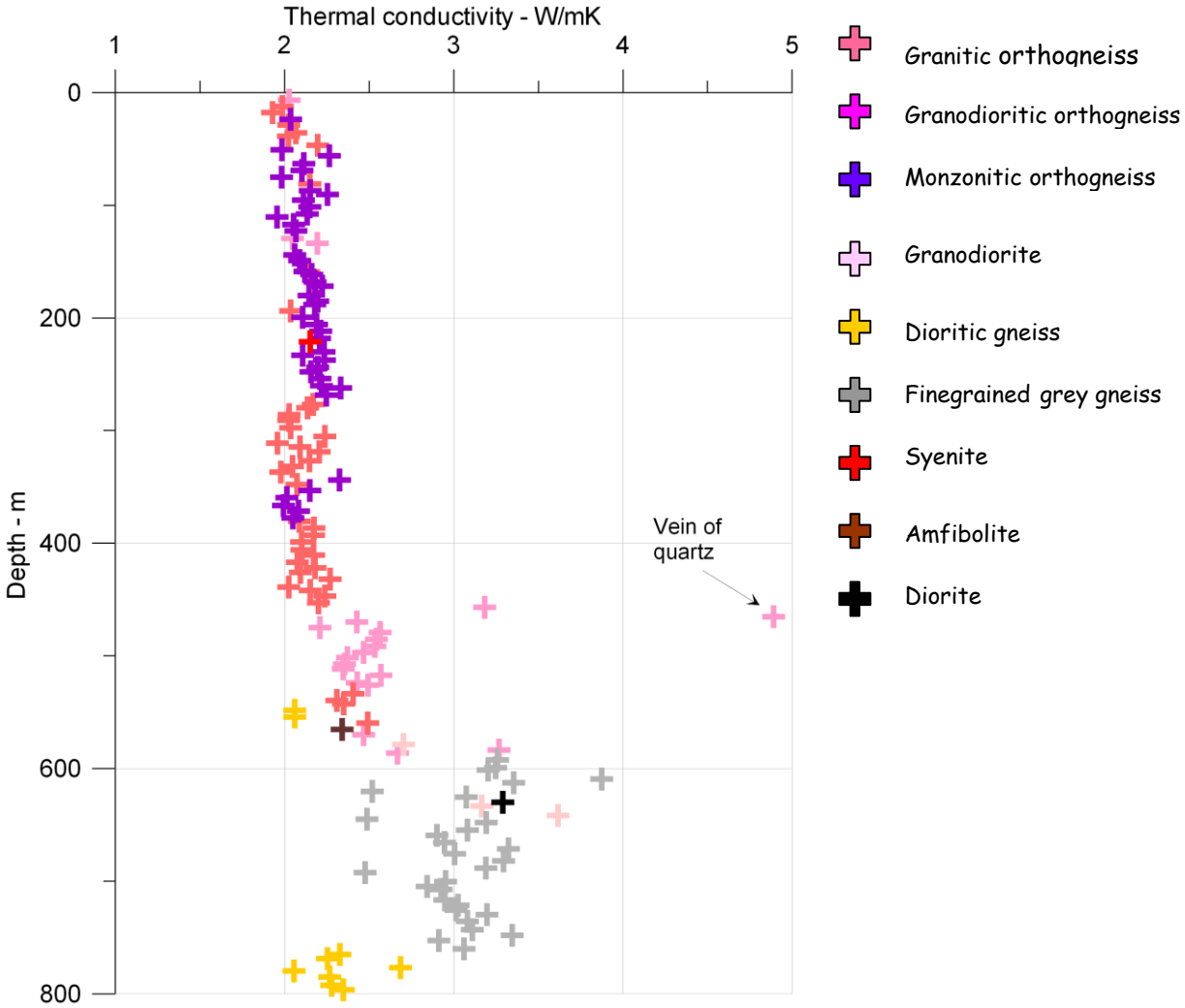

Figure 6.5. Thermal conductivities of the Leknes borehole plotted with depth. The colour of the dots denotes the lithology.

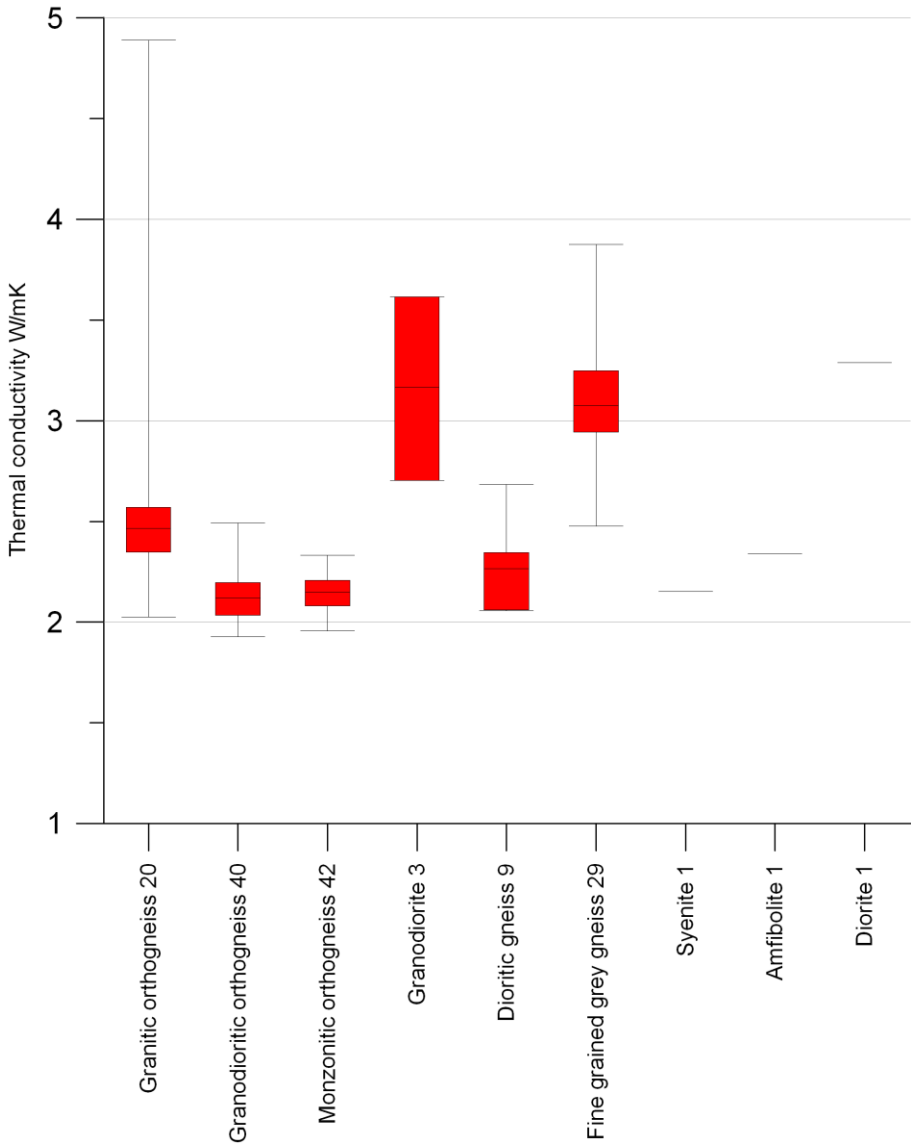

Figure 6.6. Boxplots of thermal conductivities of the rocks from the borehole at Leknes The red box contains the mid 50% of data while the median value is marked with a line inside the box. The brackets above and below the line denote 95 % confidence interval. The digits after the rock name denote the number of thermal conductivity samples.

Thermal conductivities in the Leknes borehole are in general low with a median value of 2.2 W/mK. The conductivities are higher in the interval 570 –760 m.

Thermal conductivities of the orthogneiss and dioritic gneiss samples are below 2,6 W/mK. Many of these samples are coarse-grained and a higher thermal conductivity was therefore expected. Thermal conductivities of the four lower metamorphic granodiorite and diorite samples are higher. The increased thermal conductivity can be explained by the fact that the mica flakes are more disorientated in these samples.

Thermal conductivities of the 29 samples of fine grained grey gneiss are in the range 2.5 –3.9 W/mK. Though the samples are fine-grained, these samples seem to have a high content of ore minerals which increase thermal conductivities of the samples.

The variations in thermal conductivity with depth are inversely correlating with the variation of the temperature gradient (Fig. 6.14)

Sulitjelma

Sulitjelma

103 core samles

Median value: 2.3 W/m·K
Mean value: 2.4 W/m·K
Minimum value: 1.9 W/m·K
Maximum value: 3.6 W/m·K

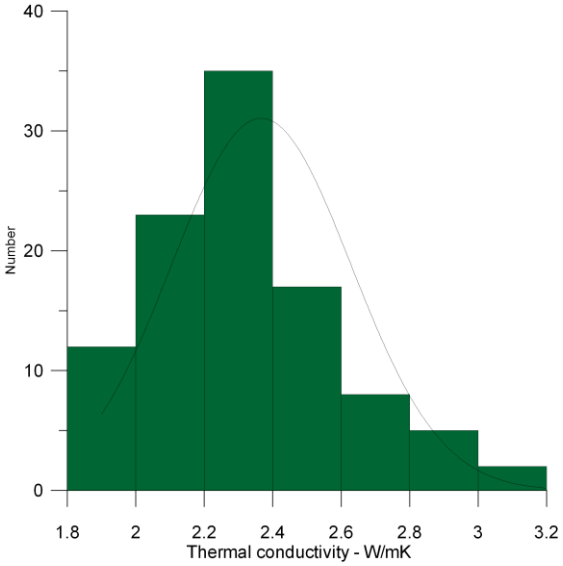

Figure 6.7. Thermal conductivities measured on core samples from the Sulitjelma borehole. The normal distribution line is shown.

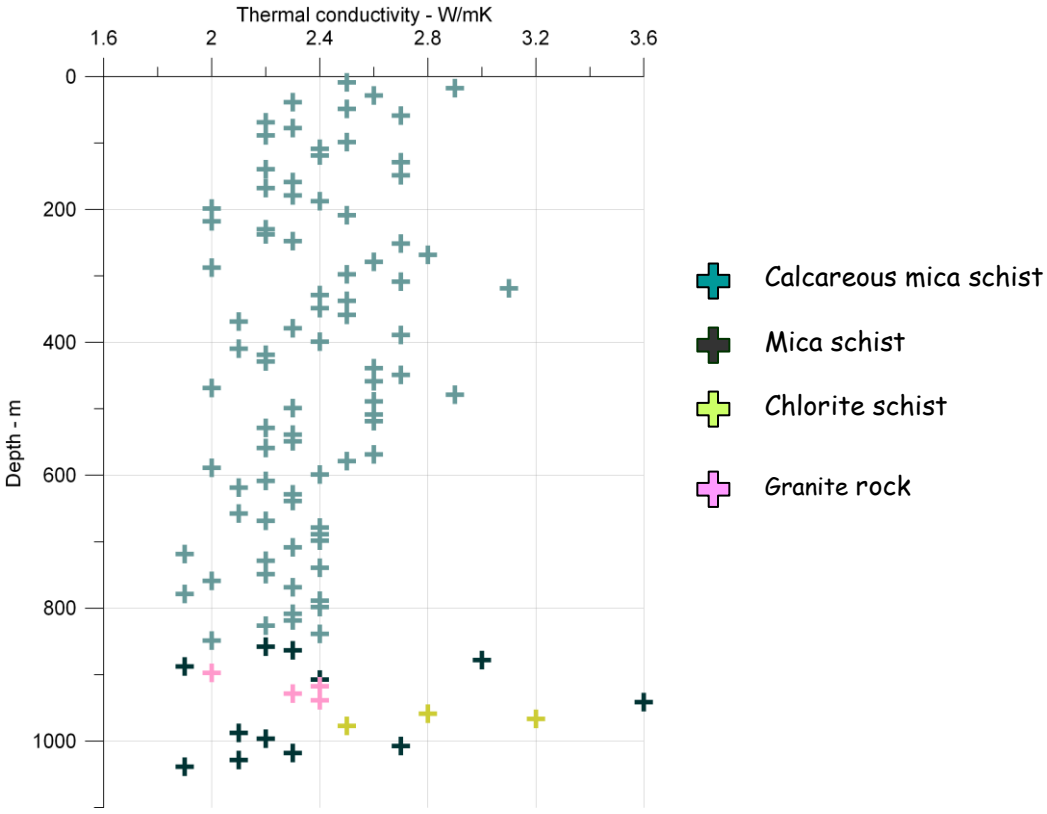

Figure 6.8. Thermal conductivities of the Sulitjelma borehole plotted with depth. The colour of the dots shows the lithology.

Thermal conductivities were measured on 103 core samples from the borehole in Sulitjelma. The samples consist of mainly mica schist. The conductivity was measured perpendicular or tilted to the layering. Thermal conductivities vary from 1.9 to 3.6 W/mK. Thermal conductivity of mica schists is anisotropic, where the conductivity parallel to the layering is higher than that perpendicular to the layering. The degree of tilting due to the layering of the thermal conductivity samples will affect the measured value.

The thermal conductivities are lower in the interval 590 – 870 m. The temperature gradient plot (Fig. 6.15) shows that the temperature gradient is highest in these intervals. The temperature was logged to 950 m depth.

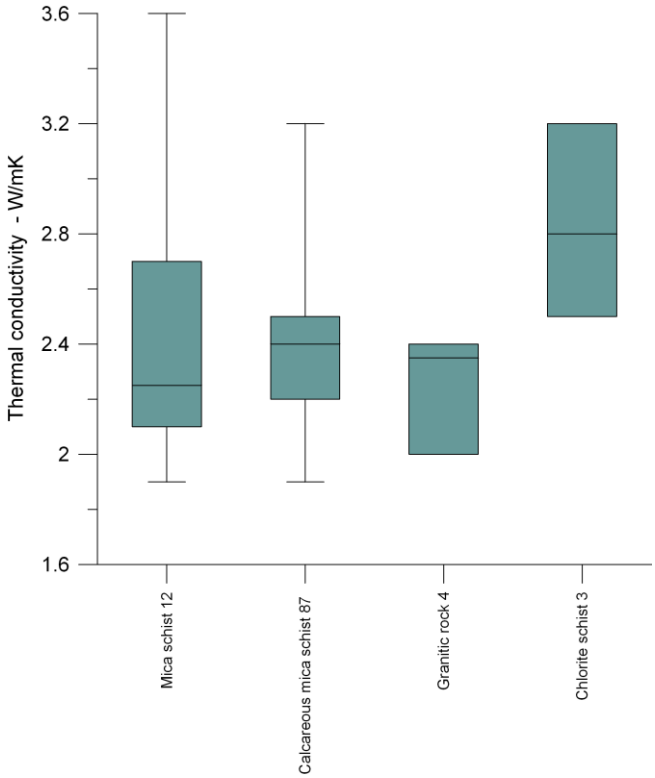

Figure 6.9. Boxplots of thermal conductivities of the rocks from the borehole at Sulitjelma The grey box contains the mid 50% of data while the median value is marked with a line inside the box. The brackets above and below the line denote 95 % confidence interval. The digits after the rock name denote the number of thermal conductivity samples.

Bleikvassli

117 core samles

Median value: 2.5 W/m·K
Mean value: 2.7 W/m·K
Minimum value: 1.6 W/m·K
Maximum value: 6.7 W/mK

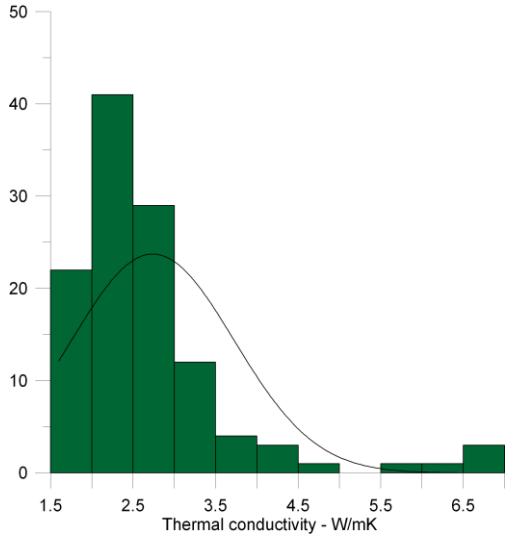

Figure 6.10. Thermal conductivities measured on core samples from Bleikvassli borehole. The normal distribution line is shown.

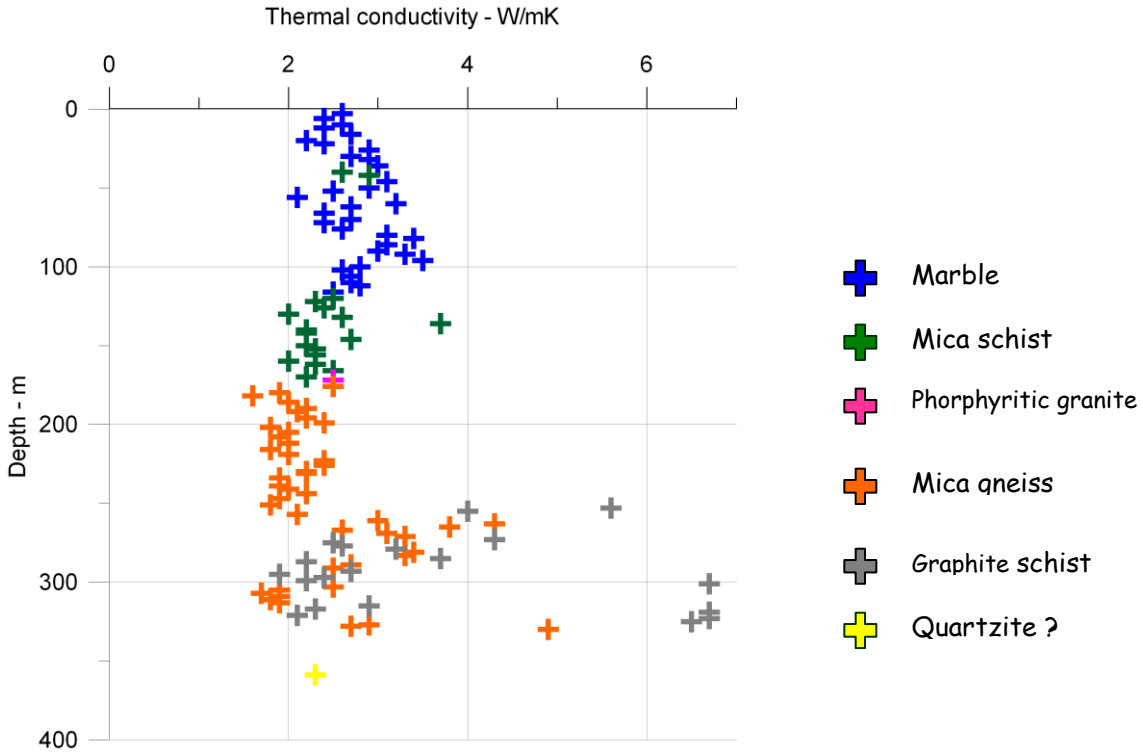

Figure 6.11. Thermal conductivities of samples from the Bleikvassli borehole plotted with depth. The colour of the dots represents the lithology.

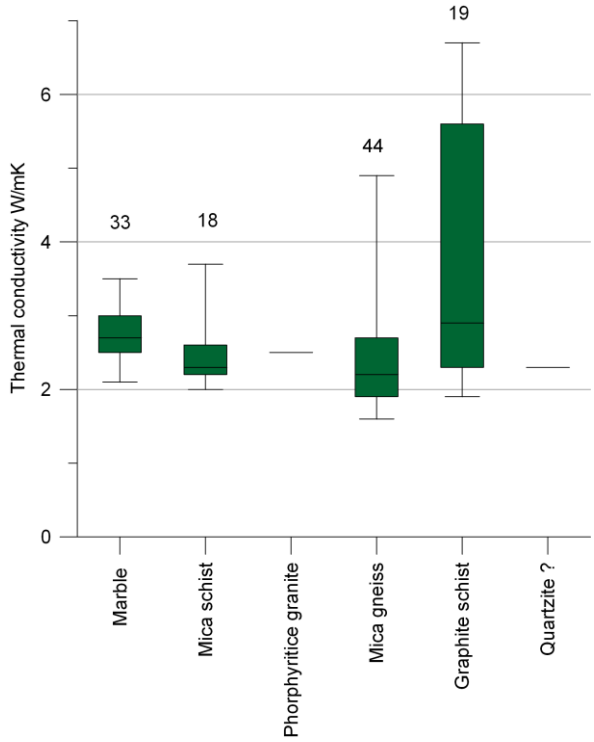

Figure 6.12. Boxplots of thermal conductivities of the rocks from the borehole at Bleikvassli. The green box contains the mid 50% of data while the median value is marked with a line inside the box. The brackets above and below the line denote 95 % confidence interval. The number above the boxes shows the number of thermal conductivity samples.

Thermal conductivities from the Bleikvassli borehole vary from 1.6 W/mK to 6.7 W/mK. In particular varies the thermal conductivities of the samples from the last 100 m of the borehole. These samples are classified as graphite schist and different types of mica gneiss. Abounding of ore might be the explanation for the very high thermal conductivities (above 5.5 W/mK) of five of the graphite schist samples. The samples have different angel of inclination to the layering. Thernal conductivities particular for mica rich samples and schist samples are anisotropic. The large variation of thermal conductivities for these rock samples might be due to the effect of anisotropy.

Thermal conductivities are not correlated with the temperature log since the core samples are from at different boreholes then the temperature measurements.

Hjerkinn

Thermal conductivity was measured on 120 core samples from the Hjerkinn borehole.

Hjerkinn

120 core samles

Median value: 2.5 W/m·K
Mean value : 2.6 W/m·K
Minimum value: 2.0 W/m·K
Maximum value: 6.4 W/mK

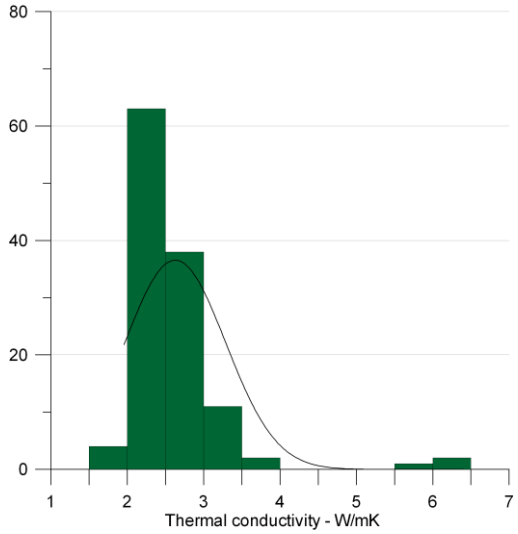

Figure 6.13 Thermal conductivities measured on core samples from the borehole at Hjerkinn The black line shows the normal distribution line.

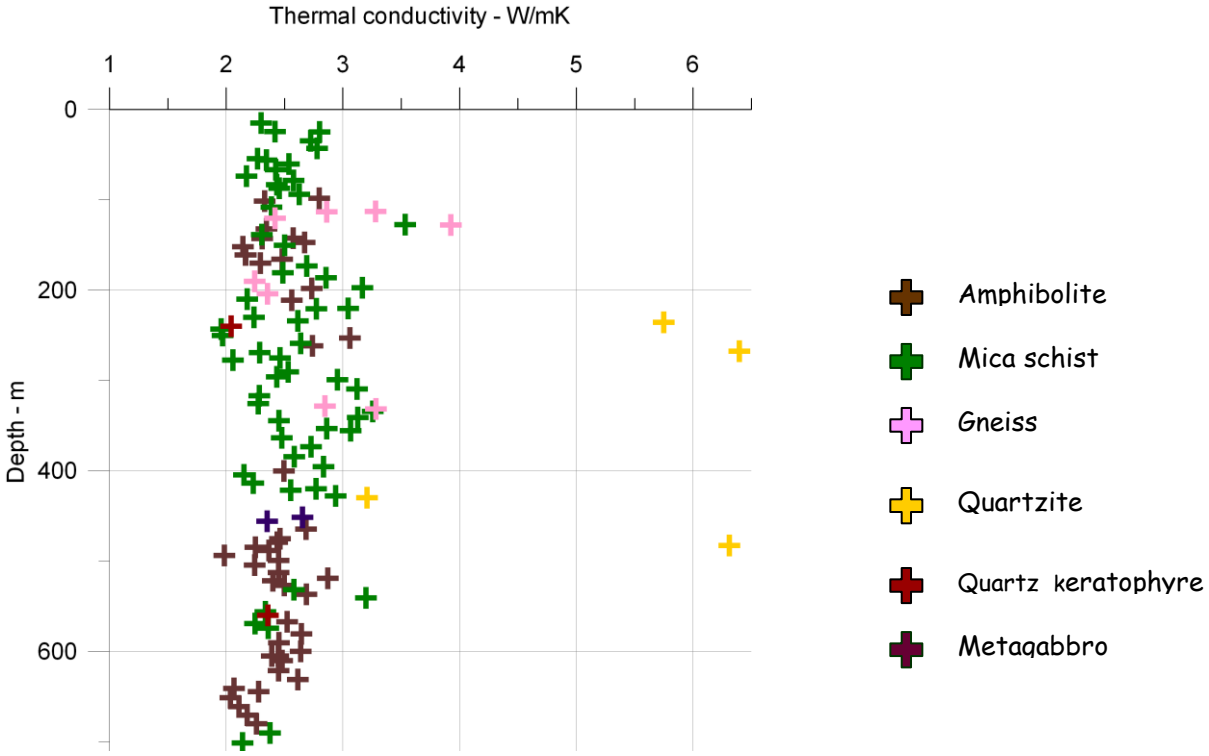

Figure 6.14. Thermal conductivities of the Hjerkinn borehole plotted with depth. The colour of the dots represents the lithology.

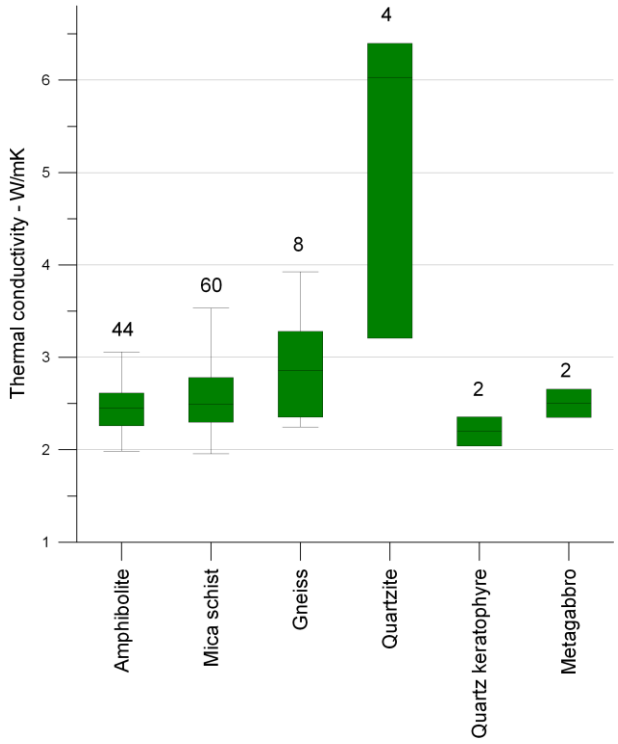

Figure 6.15. Boxplots of thermal conductivities of the different rocks from the borehole at Hjerkinn. The green box contains the mid 50% of data while the median value is marked with a line inside the box. The brackets above and below the line denote 95 % confidence interval. The numbers above the boxes denote the number of thermal conductivity samples.

Thermal conductivities of the 121 samples vary from 2.0 W/mK to 6.4 W/mK with a median value of 2.5 W/mK. The measured thermal conductivities of the different rock types are plotted in Fig. 6.15. Most of the amphibole and mica schist samples are in the range 2.3 – 2.8 W/mk. The variation in measured thermal conductivities of these samples is due to mineralogical and textural variation. The samples are measured with the layering perpendicular or with some angle to the layering. The thermal conductivities, particular for the mica schist samples are expected to be anisotropic.

Three of the four quartzite samples have much higher thermal conductivities. The two major decreases in the temperature gradient plot (Balling & Breiner 2006, Fig. 5.7) correlates with two of quartzite and gneiss zones in the borehole (Folldal Verk 1985).

Løkken

Løkken

83 core samles

Median value: 3.1 W/m·K
Mean value : 3.1 W/m·K
Minimum value: 2.6 W/m·K
Maximum value: 3.6 W/mK

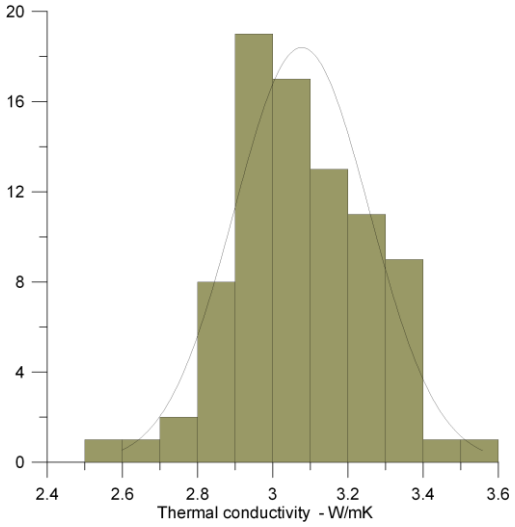

Figure 6.16 Thermal conductivities measured on core samples from the borehole at Løkken The black line show the normal distribution line.

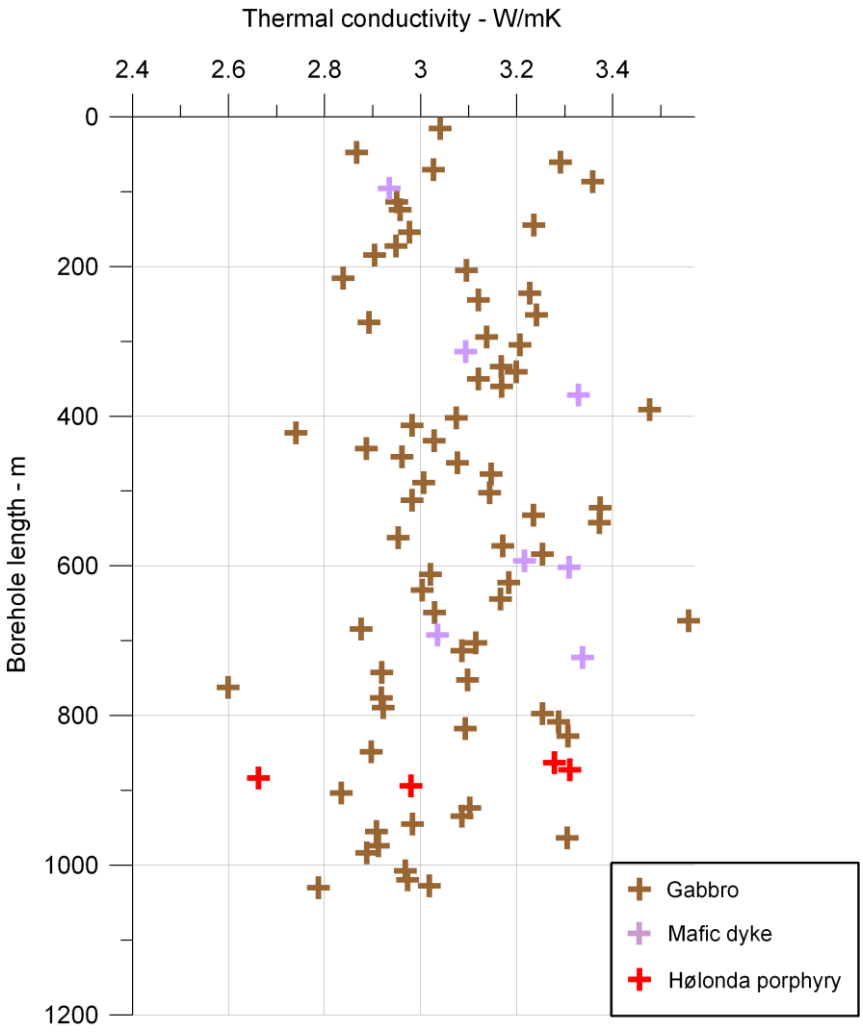

Figure 6.17. Thermal conductivities of the borehole at Løkken plotted against borehole length. The colour of the dots denotes the rock type.

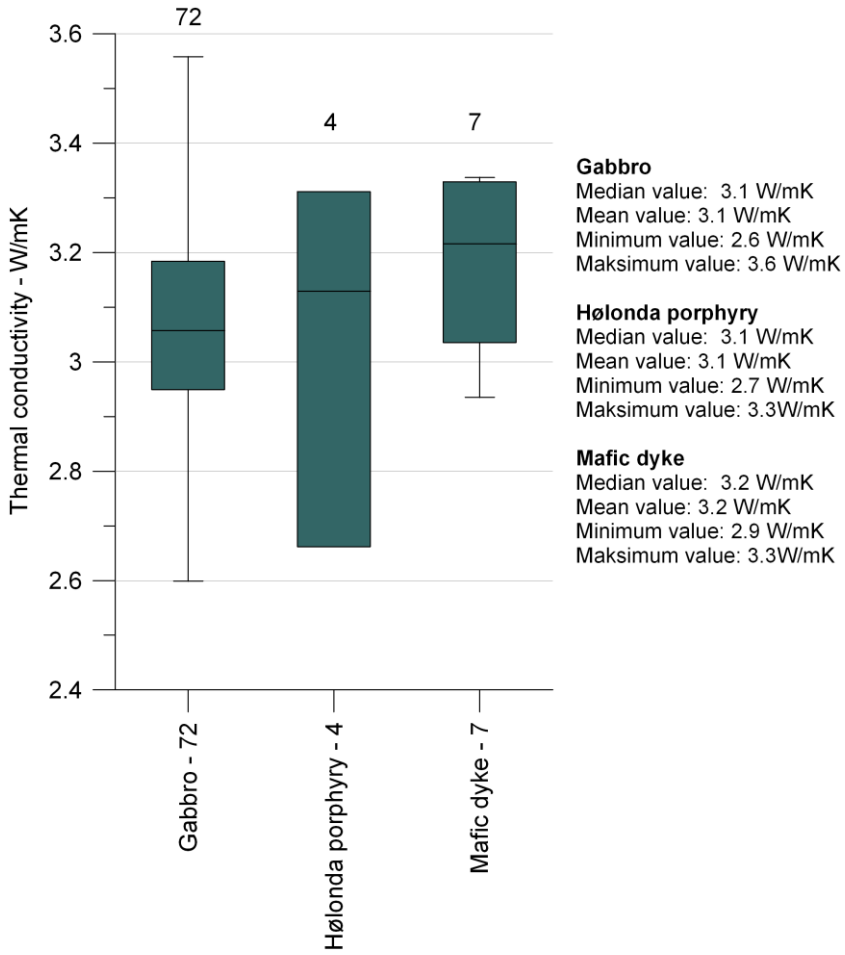

Figure 6.18. Boxplots of thermal conductivities of the rocks from the borehole at Løkken The grey box contains the mid 50% of data while the median value is marked with a line inside the box. The brackets above and below the line denote 95 % confidence interval. The digits after the rock name denote the number of thermal conductivity samples.

Thermal conductivities were measured on 83 samples from the 1030 long (985 m deep) borehole at Løkken. The lithology of the borehole is described in a report from Orkla Industrier. Thermal conductivities are in general high with a variation from 2.6 W/mK to 3.6 W/mK.

The lithology of the samples is classified as gabbro, Hølonda porphyry and mafic dyke. Thermal conductivities of the different rocks are shown as boxplot in Fig. 6.18. The grey box contains the mid 50% of data. 87 % of the samples are gabbro. All rock types have high thermal conductivities. But the mafic dyke samples seem to have somewhat higher thermal conductivity than the gabbro and the Hølonda porphyry samples.

There is no clear correlation between the textural and structural parameters i.e. grain size and the measured thermal conductivities. 87 % of the samples are gabbro and for these samples there is an effect of mineralogy where the samples with high content of pyroxen and magnetite have the highest thermal conductivities. There seems also to be a trend where saussurite samples and samples with higher content of epidote have lower thermal conductivity.

The temperature logged in the Løkken borehole (Fig. 5.7 in Balling & Breiner 2006) shows a nearly linear trend and the temperature gradient log is low and nearly constant at 15 K/km with the depth. The temperature gradient log fits with the thermal conductivity measurements, since the thermal conductivity is high and relative constant with depth.

Aure

Thermal conductivities were measured on two rock samples taken close to the borehole at Aure. The samples are dioritic gneiss. Sample 1 is coarse-grained and Sample 2 is fine-grained. Measured thermal conductivities are plotted in Fig. 6.19

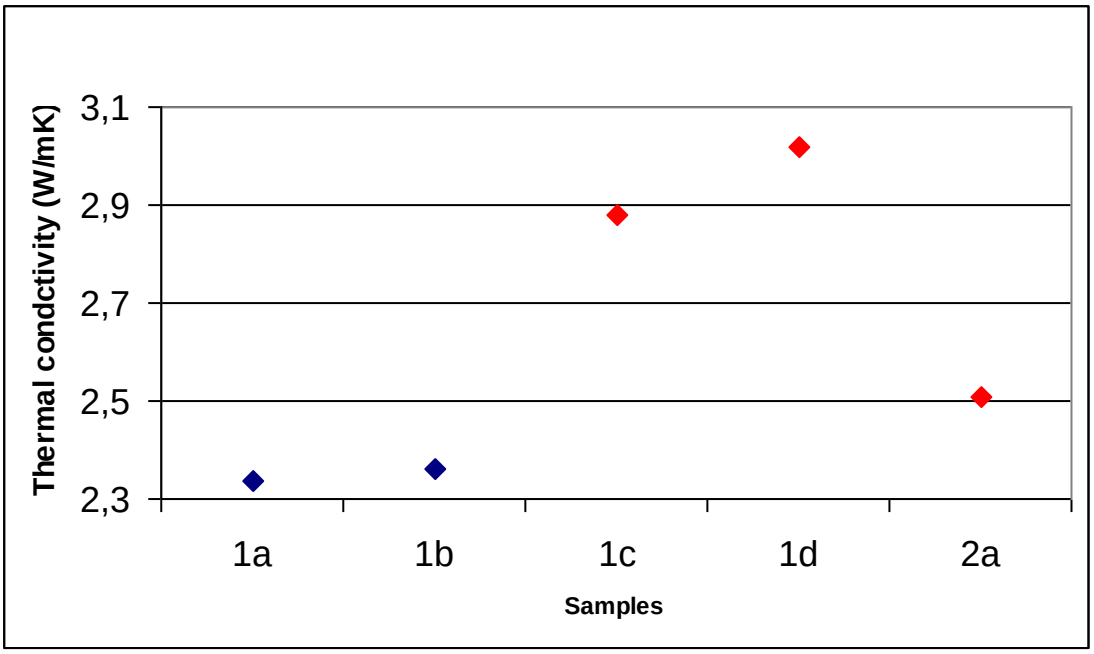

Figure 6.19 Thermal conductivities measured on rock samples from Aure. Red dots are measured parallel and blue dots are measured perpendicular to the layering.

The anisotropy effect of the thermal conductivity ($a=k_{\parallel} / k_{\perp}$) measured for sample 1 is 1.25. Lower thermal conductivity of sample 2 may be explained by a fine-grained texture and a higher content of dark minerals than in sample 1.

The temperature gradient log (Fig. 5.9) shows variation in the temperature gradient in the upper 130 m of the borehole. The variation is assumed to be an effect of changes in the lithology.

Lærdal

Two boreholes of about 50 m depth, Lærdal 1 and 2, were drilled in the Lærdal tunnel and located 9.7 km and 11.24 km, respectively, from the Lærdal entrance to the tunnel. Aurland borehole was drilled on the mountain above the Lærdal tunnel. All 3 boreholes are located in gneiss.

Lærdal 1

69 core samples

Median value: 2.9 W/m·K
Mean value: 2.9 W/m·K
Minimum value: 2.4 W/m·K
Maximum value: 5.7 W/mK

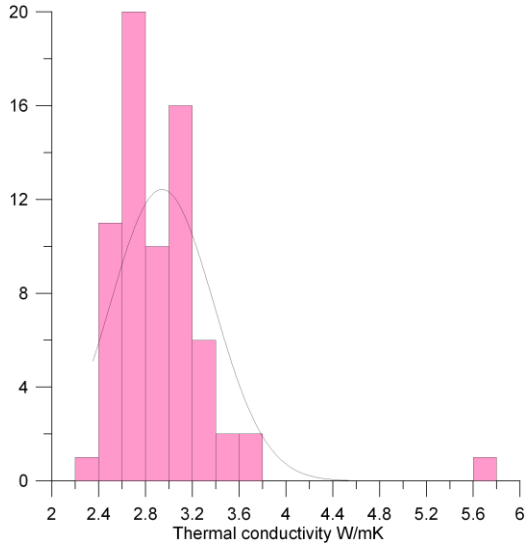

Figure 6.20. Thermal conductivities measured on core samples from the Lærdal 1 borehole at The black line show the normal distribution line.

Lærdal 2

75 core samples

Median value: 3.3 W/m·K
Mean value : 3.1 W/m·K
Minimum value: 2.1 W/m·K
Maximum value: 4.0 W/mK

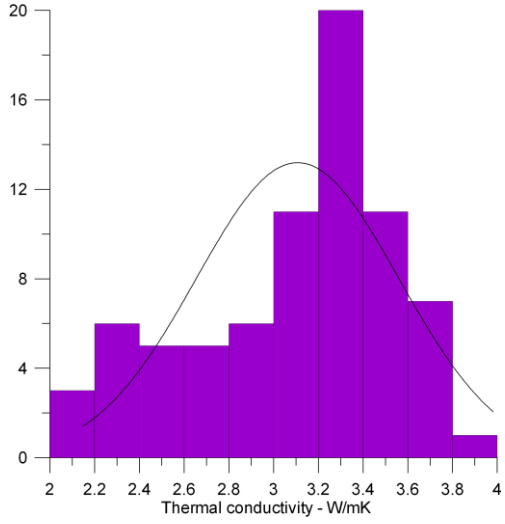

Figure 6.21. Thermal conductivities measured on core samples from the Lærdal 2 borehole. The black line show the normal distribution line.

Aurland

25 core samples

Median value: 2.6 W/m·K
Mean value : 2.8 W/m·K
Minimum value: 2.1 W/m·K
Maximum value: 3.9 W/mK

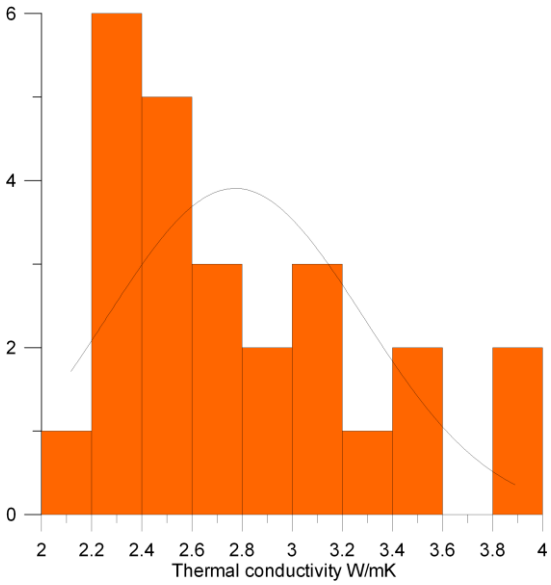

Figure 6.22. Thermal conductivities measured on core samples from the Aurland borehole. The black line shows the normal distribution line.

All samples Lærdal + Aurland

169 core samples

Median value: 3.0 W/m·K
Mean value : 3.0 W/m·K
Minimum value 2.1 W/m·K
Maximum value 5.7 W/mK

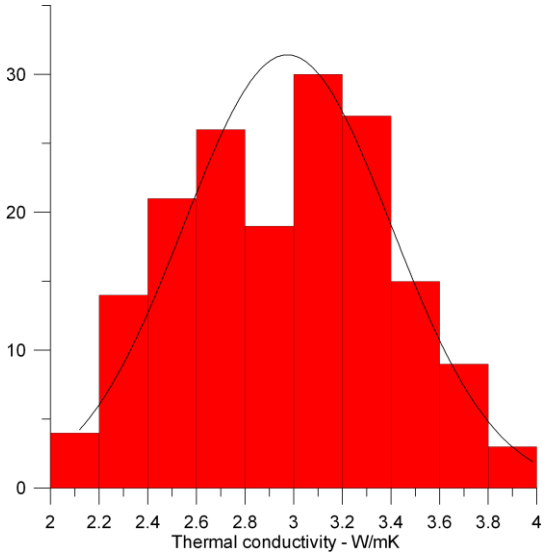

Figure 6.23. Thermal conductivities measured on core samples from the Aurland and Lærdal boreholes. The black line shows the normal distribution line.

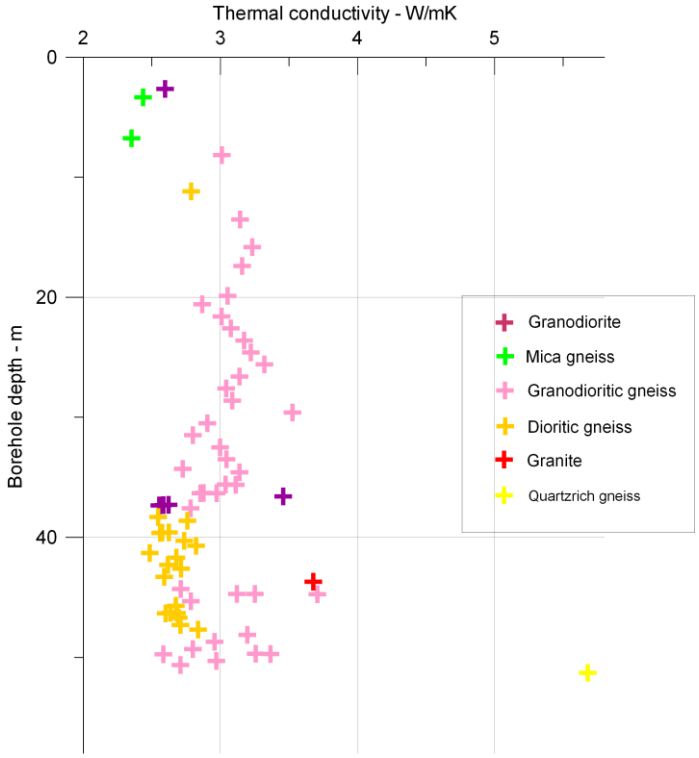

Figure 6.24. Thermal conductivities of the Lærdal 1 borehole in the Lærdal tunnel plotted with the borehole depth. The colour of the dots shows the rock type.

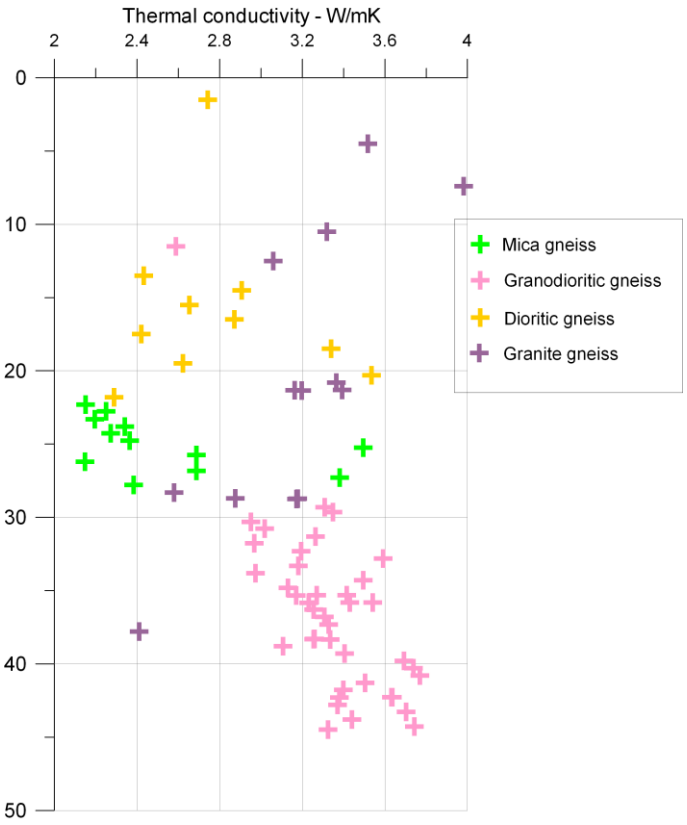

Figure 6.25. Thermal conductivities of the Lærdal 2 borehole in the Lærdal tunnel plotted with the borehole depth. The colour of the dots shows the rock type.

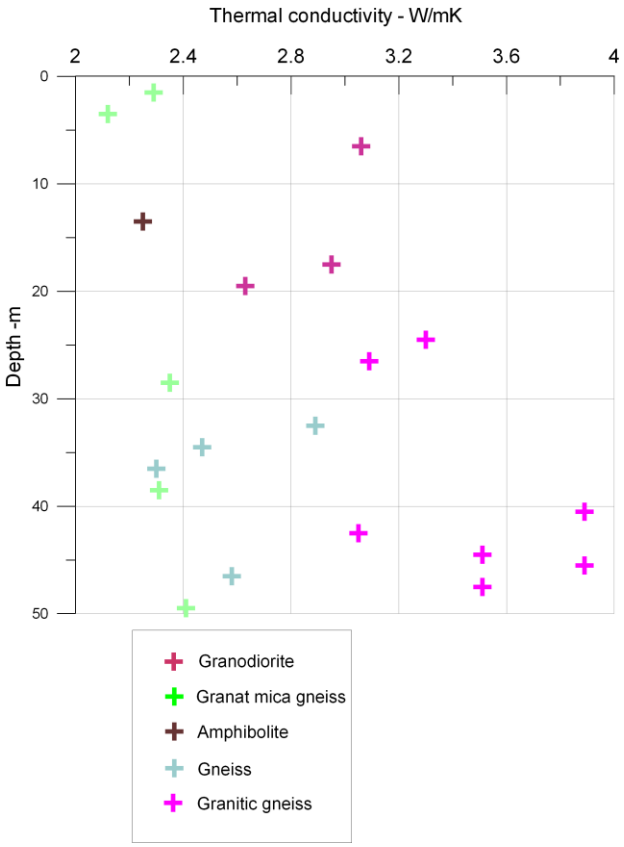

Figure 6.26. Thermal conductivities of the Aurland borehole plotted with the borehole depth. The colour of the dots shows the rock type.

The mean thermal conductivity of all samples is 3.0 W/mK. Thermal conductivities from the Aurland borehole is in general lower than for the two Lærdal boreholes.

There is a trend with increasing thermal conductivities with depth for Lærdal borehole. A similar but not so clear trend is shown for the Aurland borehole. There is a correlation between rock type and thermal conductivities.

The temperature measurements in these boreholes are more uncertain than for the deeper boreholes since these boreholes is only 50 m deep and the temperature logged in these holes is effected by the surface temperature and the last centuries climate change.

The temperature gradient log for Lærdal borehole 2 (Fig. 5.11) is inversely correlated to the thermal conductivities. The temperature gradient is highest at a depth of 25-30 m where the bedrock consists of mica gneiss with a low thermal conductivity.

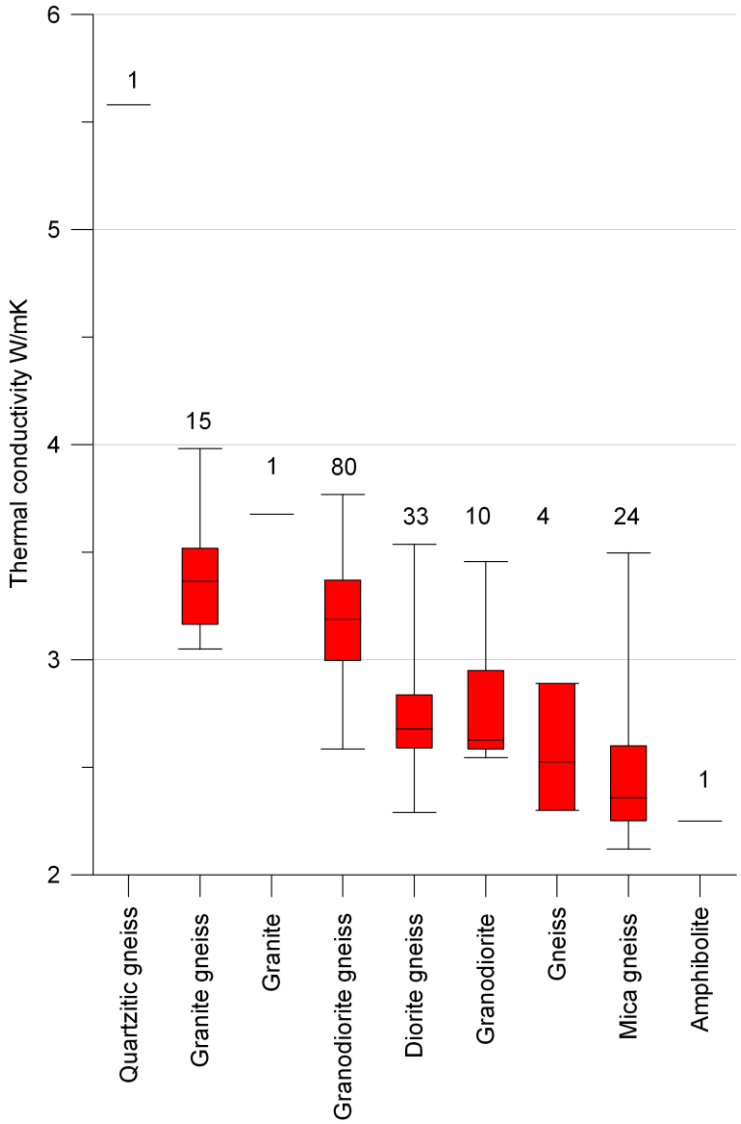

Figure 6.27. Boxplots of thermal conductivities of the rocks from the Aurland and Lærdal 1 & 2 boreholes. The red boxes contain the mid 50% of data while the median value is marked with a line inside the box. The brackets above and below the line denote 95 % confidence interval. The brackets above and below the line denote the 95 % confidence interval. The numbers above the boxes denote the number of thermal conductivity samples.

Thermal conductivity varies with rock type. The sample of quartzrich gneiss has very high thermal conductivity. Also granite gneiss and granodiorite gneiss have higher thermal conductivities than the other samples.

Hamar

Hamar

98 core samples

Median value: 2.2 W/m·K
Mean value : 2.2 W/m·K
Minimum value: 1.4 W/m·K
Maximum value: 4.5 W/mK

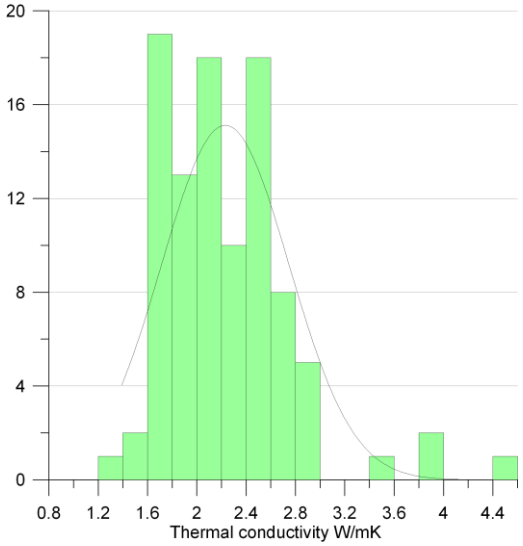

Figure 6.28. Thermal conductivities measured on core samples from the Hamar borehole. The black line shows the normal distribution line.

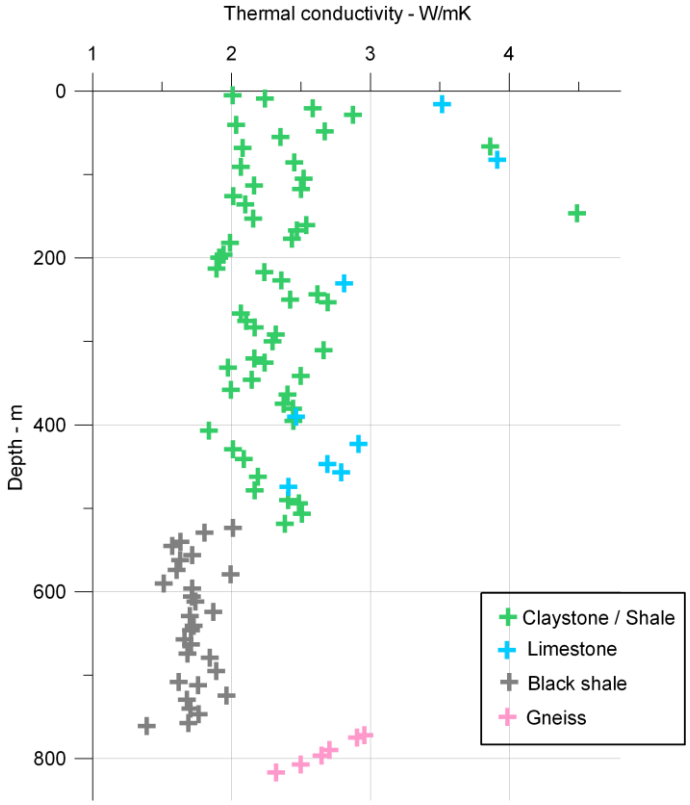

Figure 6.29. Thermal conductivities of the Hamar borehole plotted with the borehole depth. The colour of the dots shows the rock type.

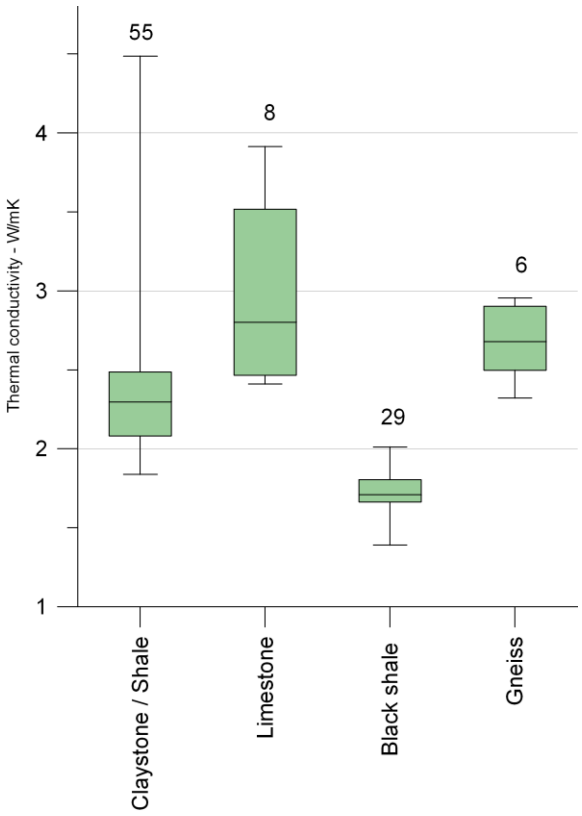

Figure 6.30. Boxplots of thermal conductivities of the rocks from Hamar boreholes. The green boxes contain the mid 50% of data while the median value is marked with a line inside the box. The brackets above and below the line denote 95 % confidence interval. The brackets above and below the line denote the 95 % confidence interval. The numbers above the boxes denote the number of thermal conductivity samples.

Thermal conductivities were measured on 98 core samples from the Hamar borehole. In general the thermal conductivities are low with a mean value of 2.2 W/mK In particular the thermal conductivity of the 29 black shale samples is very low 1.4 –2.0 W/mK. All of the four shale and limestone samples with thermal conductivities above 3.0 W/mK have veins of quartz parallel to the heat flow direction.

The thermal conductivity-depth plot (Figure 6.29) is inversely correlated with the temperature plot (Figure)

Hurdal.

Hurdal borehole Dh02

74 core samples

Median value: 2.9 W/m·K
Mean value: 3.2 W/m·K
Minimum value 2.5 W/m·K
Maximum valu:e 5.4 W/mK

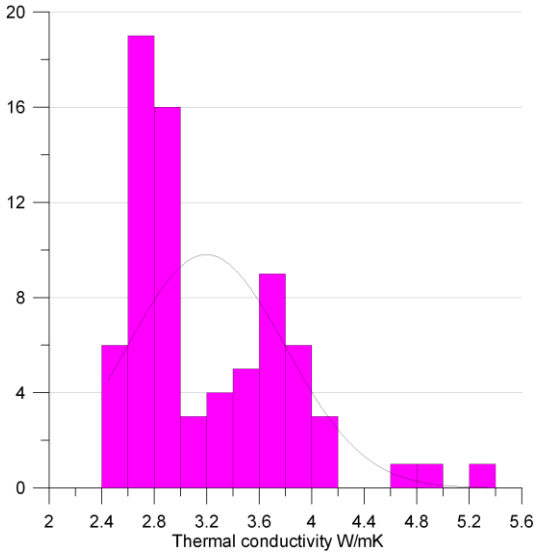

Figure 6.31. Thermal conductivities measured on core samples from the Hurdal borehole Dh02 borehole. The black line shows the normal distribution line.

Hurdal borehole Dh03

80 core samples

Median value: 3.0 W/m·K
Mean value : 3.0 W/m·K
Minimum value: 2.6 W/m·K
Maximum value: 3.7 W/m·K

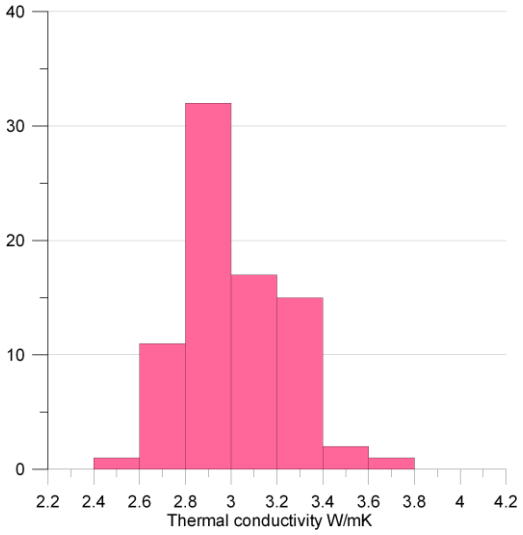

Figure 6.32. Thermal conductivities measured on core samples from the Hurdal borehole Dh03 borehole. The black line shows the normal distribution line.

Hurdal borehole Dh05

45 core samples

Median value: 3.2 W/m·K
Mean value : 3.2 W/m·K
Minimum value 2.7 W/m·K
Maximum value 4.1 W/mK

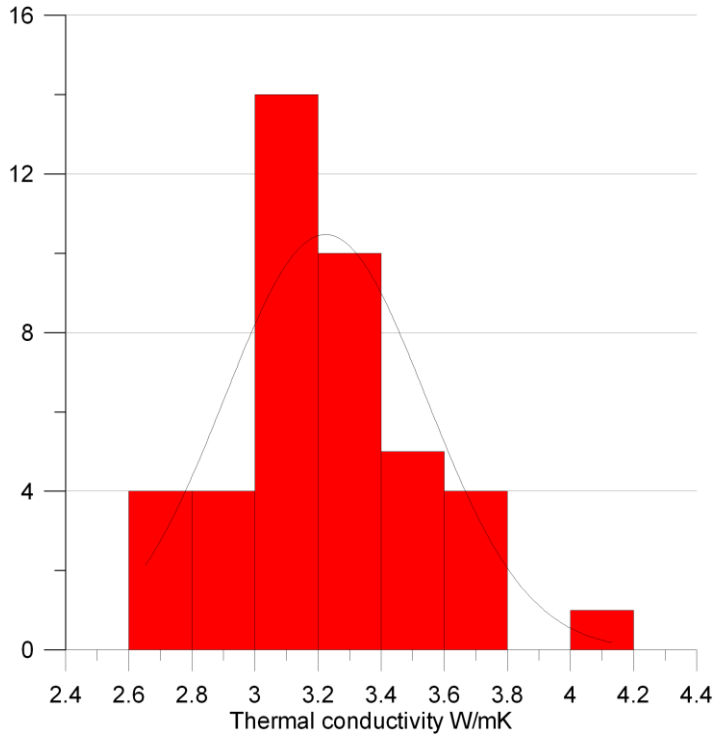

Figure 6.33. Thermal conductivities measured on core samples from the Hurdal borehole Dh05 borehole. The black line shows the normal distribution line.

All Hurdal boreholes
Dh02, Dh03 and Dh05

198 core samples

Median value: 3.0 W/m·K
Mean value: 3.1 W/m·K
Minimum value: 2.5 W/m·K
Maximum value: 5.4 W/m·K

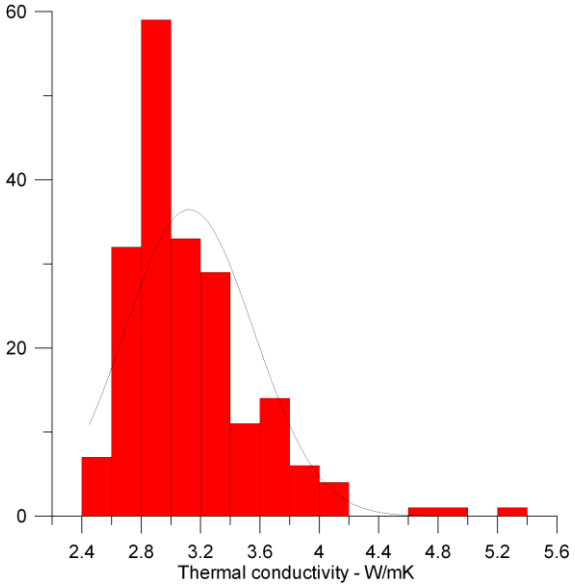

Figure 6.34. Thermal conductivities measured on core samples from all three Hurdal boreholes. The black line shows the normal distribution line.

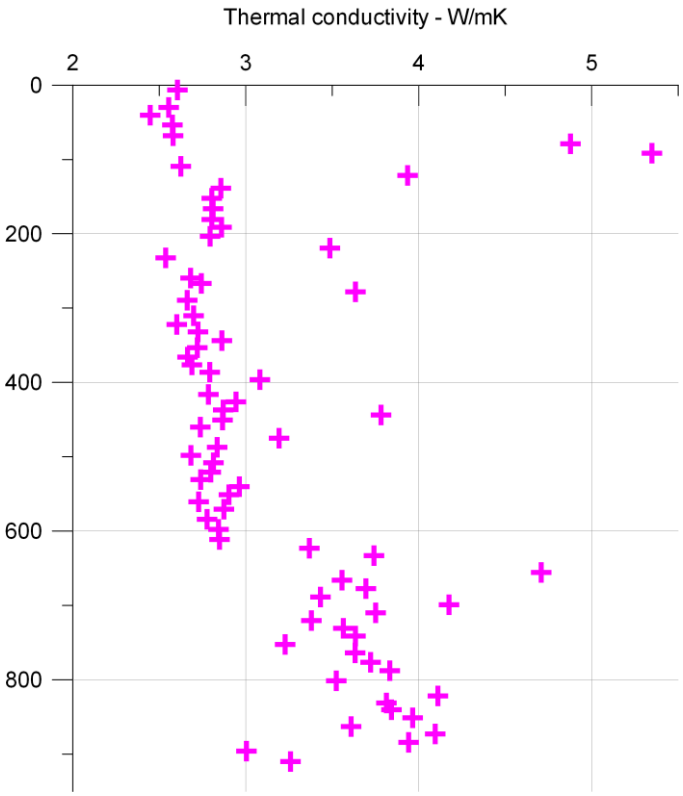

Figure 6.35. Thermal conductivities of the Hurdal Dh02 borehole plotted with the borehole length.

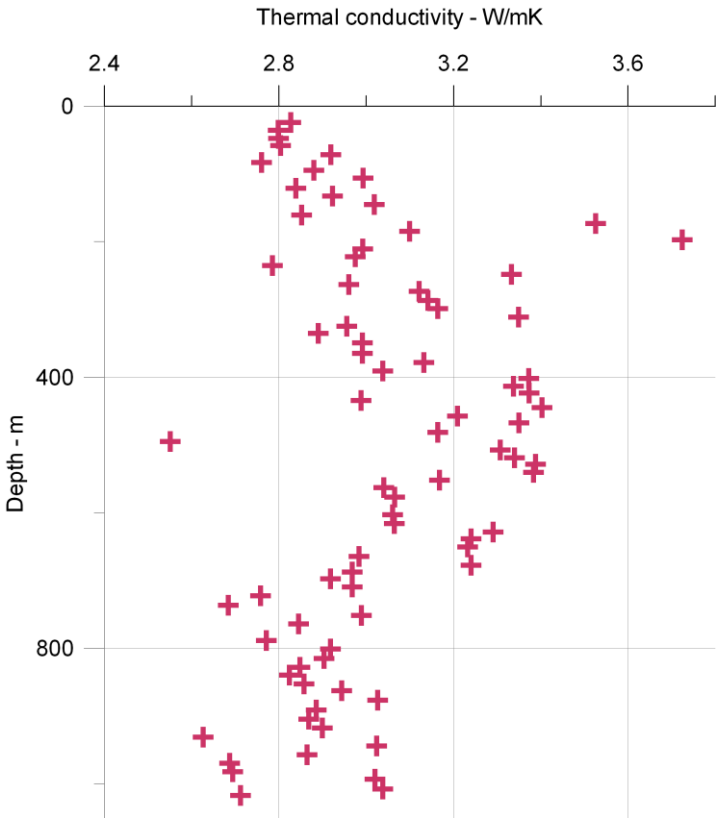

Figure 6.36. Thermal conductivities of the Hurdal Dh03 borehole plotted with the borehole length.

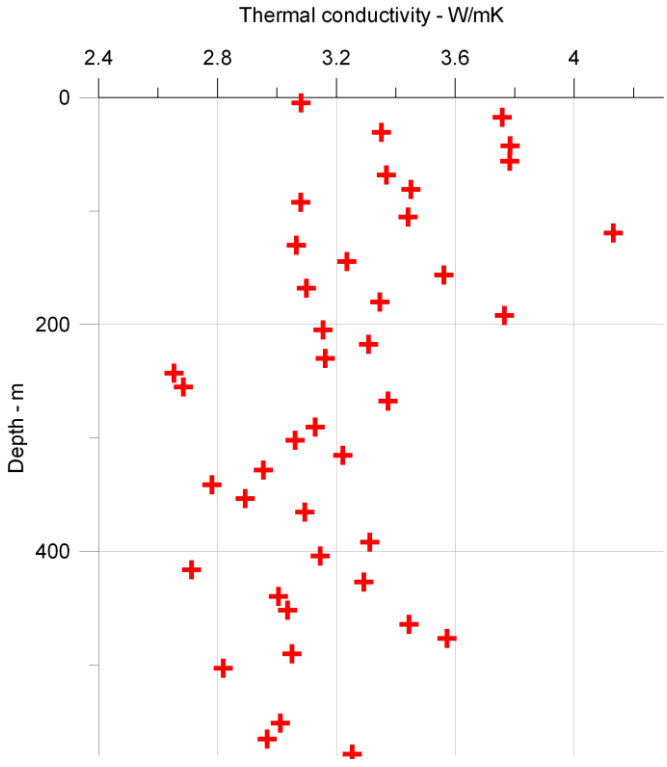

Figure 6.37. Thermal conductivities of the Hurdal Dh05 borehole plotted with the borehole length.

Thermal conductivities were measured on 198 core samples from three of the boreholes in Hurdal. Ale samples are syenite. Thermal conductivities vary from 2.5 to 5.4 W/mK with a mean value of 3.1 W/mK. Thermal conductivities varies with depth in all three boreholes (Figures 6.35-37). These variations are assumed to be related to mineralogical variations. Sulfide is detected in three of the samples with thermal conductivities above 4.0 W/mK for borehole Dh02.

Berger

The 650 m deep borehole at Berger is drilled in diorite. There are no thermal conductivity samples from the Berger area. Previous thermal conductivity measurements of diorite samples from Oslo area is shown in Fig. 6.38.

Measurement on twenty thermal conductiviy samples from Lørenskog, 15 km from Berger is shown in Fig. 6.39 These samples were prepared either parallel or perpendicular to the layering. The median value of these thermal conductivities is 2.8 W/mK.

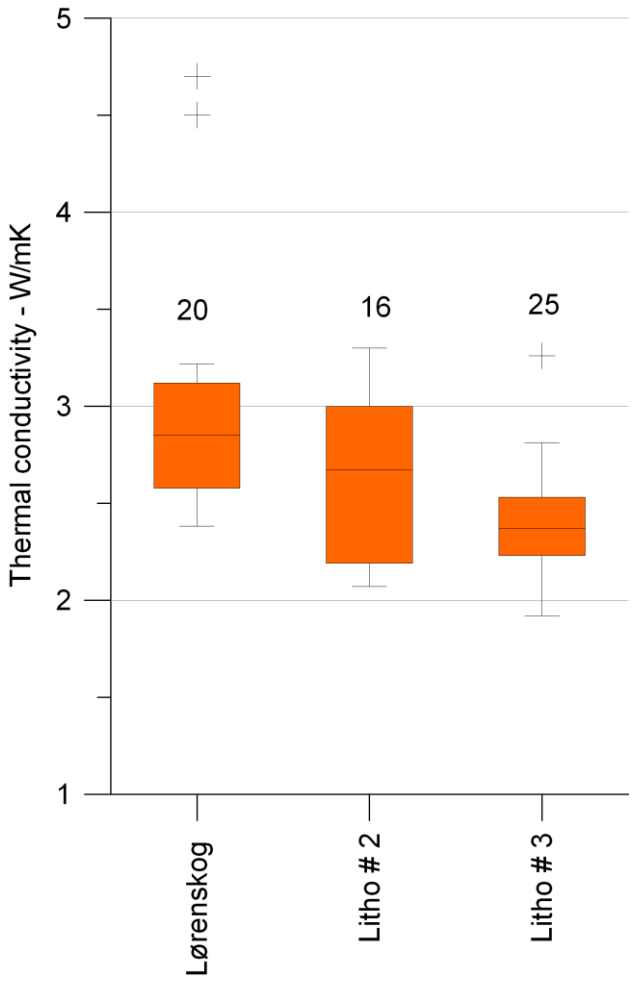

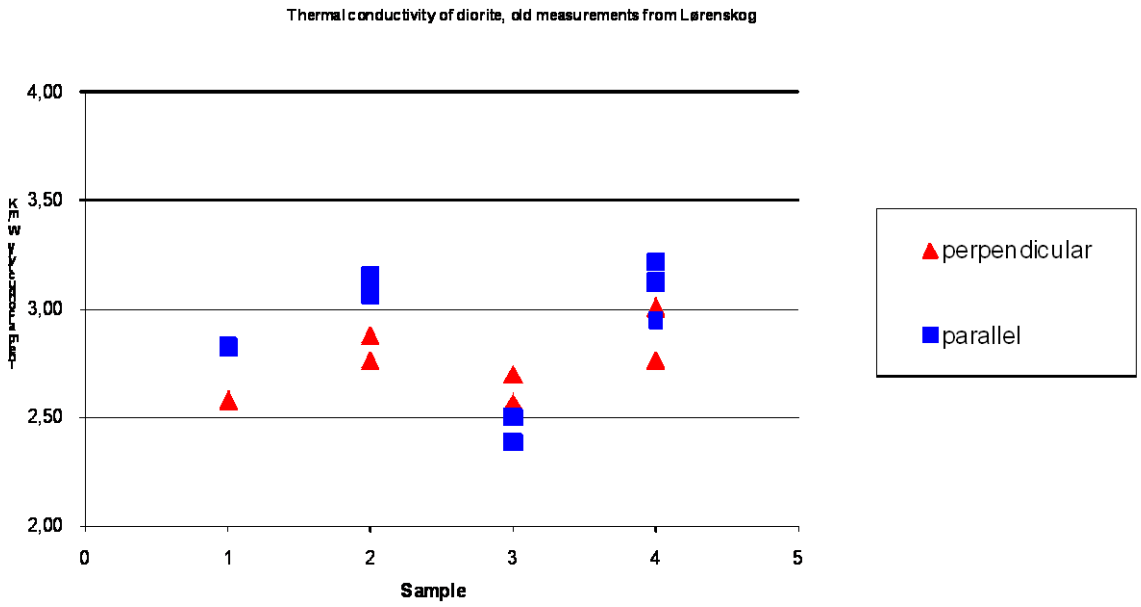

Figure 6.38. Thermal conductivities measured on diorite samples from Lørenskog.

Arnestad

A 685 m deep borehole was drilled at Arnestad school, Asker, in 2004. The lithology interpreted from optical televiewer and drilling log is shown in Fig. 6.39. The lithology of a 500 m deep borehole located 40 m away from the present Arnestad borehole, is described by Midttømme et al. (2004).

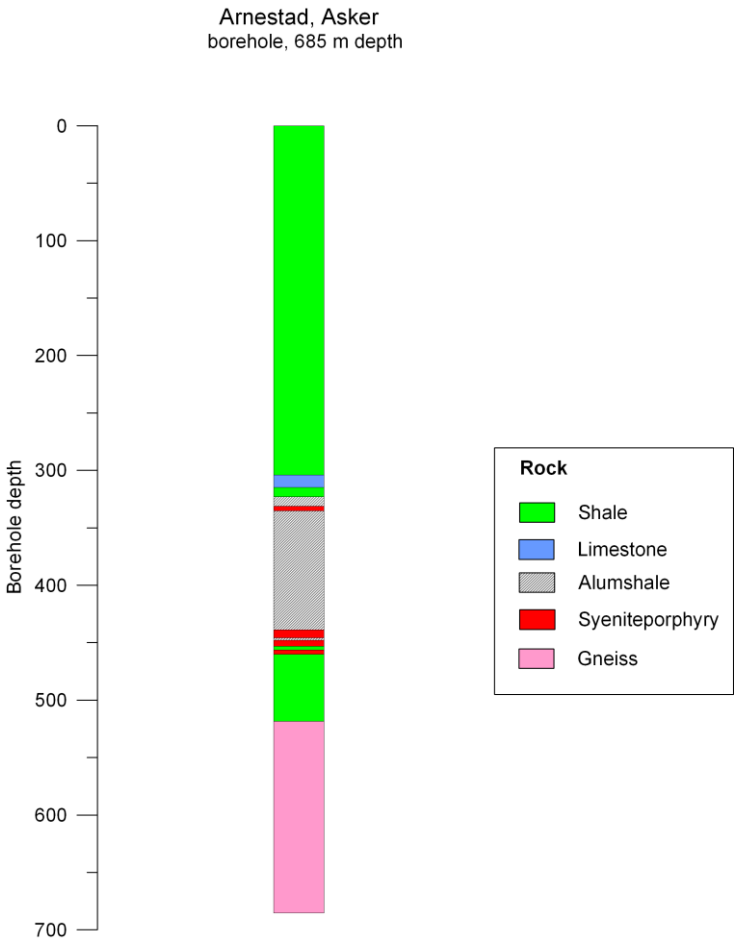

Figure 6.39. Lithology of the 684m deep borehole at Arnestad school, Asker.

Thermal conductivities have been measured on samples from Asker and Bærum and reported by Midttømme et al. (2000b, 2004). Boxplots of thermal conductivities measured on gneiss, syenite porphyry, claystone and limestone is shown in Fig. 6.40. Thermal conductivities of 29 core samples of Alumshale (Black shale) from Hamar borehole is measured. Fig. 6.29 and 6.30 shows the results of these measurements.

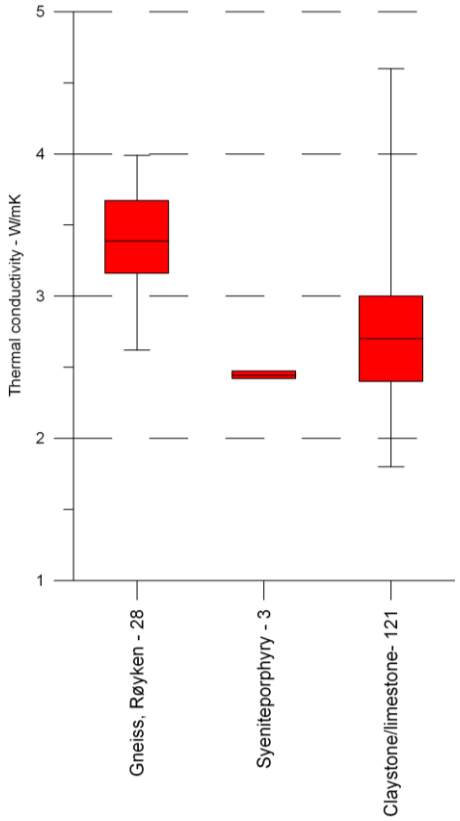

Figure. 6.40. Boxplots of old thermal conductivity measurements of gneiss from the Røyken area, syenite porphyry and claystone /limestone from Asker - Bærum area. The red box contains the mid 50% of data while the median value is marked with a line inside the box. The brackets above and below the line denote 95 % confidence interval. The digits listed after the rocktype represent the number of thermal conductivity samples.

Fredrikstad

A 800 m long borehole was drilled at Rødsmyra in Fredrikstad. The rock is Iddefjord granite. No core samples exist from the borehole and thermal conductivities is measured on rock samples from neighbouring area. (Fig. 6.41) Also litho samples measured on cores samples of Iddefjord granite si shown in Fig. 6.41

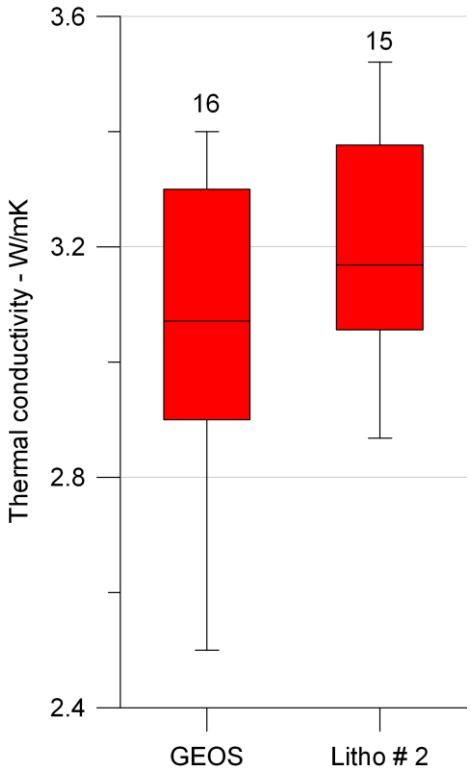

Figure 6.41. Boxplots of thermal conductivity measurements of Iddefjordsgranite Geos samples is rock samples from Rødsmyra Fredrikstad area and Litho #2 is core samples of Iddefjordsgranite. The red box contains the mid 50% of data while the median value is marked with a line inside the box. The brackets above and below the line denote 95 % confidence interval. The number above the boxes is the number of thermal conductivity samples.

7 HEAT FLOW OF EARLY MESOPROTEROZOIC TO PERMIAN GEOLOGICAL PROVINCES IN SOUTHERN NORWAY AND THE NORWEGIAN-GREENLAND SEA

Trond Slagstad, Niels Balling, Harald Elvebakk, Kirsti Midttømme & Lars Olsen.

7.1 Introduction

The geographical position of Norway is unusual as it encompasses a transition from stable cratonic lithosphere to the east (the Fennoscandian or Baltic Shield) through stretched continental lithosphere to oceanic lithosphere to the west and northwest (Fig. 7.1). The geological evolution contained within this area spans roughly 3 billion years, ranging from Late Archaean to Mesozoic, and includes numerous phases of orogenic and rift-drift activity concluding with crustal extension, rifting and formation of the Norwegian–Greenland Sea at c. 60 Ma. Slagstad (in prep.). This long-lasting history is discussed in greater detail with reference to heat flow and heat production. All geological processes are ultimately driven by heat from the Earth's interior; however, some recent studies have also suggested that variation in thermal properties within the crust may have had a direct influence on the geological evolution in certain areas (Bingen et al. 2006, Slagstad 2006). This variation in thermal properties, be it differences in radiogenic heat production or thermal conductivity, is as significant now as it was in earlier times. Thus, insight into the present-day variation is integral for understanding the nature of earlier geological processes, both in Norway and elsewhere, and has direct practical implications including utilisation of geothermal energy and locating hydrocarbon accumulations (e.g., Bjørkum & Nadeau 1998).

Along with data on radiogenic heat production, surface heat flow data are key in constraining thermal, rheological and compositional models of the lithosphere (Rudnick et al. 1998, Jaupart & Mareschal 2003, Afonso & Ranalli 2004). Unfortunately, a lack of high-quality heat flow and heat production data have hampered studies into how thermal properties have affected the geological evolution of Norway; thus, claims of a connection between thermal structure and geological evolution, although seemingly reasonable, are difficult to substantiate (Slagstad 2006).

The purpose of this paper is to present and discuss new heat flow determinations based on recent measurements of thermal gradients at thirteen sites in Norway (Fig. 7.2a). The sites consist of a total of 13 wells that are between 400 and 1000 m deep (Table 7.1), and thermal conductivity and heat production have been measured on core samples where possible. In contrast to earlier heat flow data from Norway (Fig. 7.2b), that were generally obtained from shallow (typically <200 m) boreholes and lake bottom measurements, the new data are from significantly deeper boreholes and have been corrected for both palaeoclimatic and topographic effects. The next chapter presents in addition new heat flow data from additional four wells in northern Norway. A comprehensive dataset of heat production of Norwegian bedrock is presented and discussed in relation to heat flow in Chapter 2.

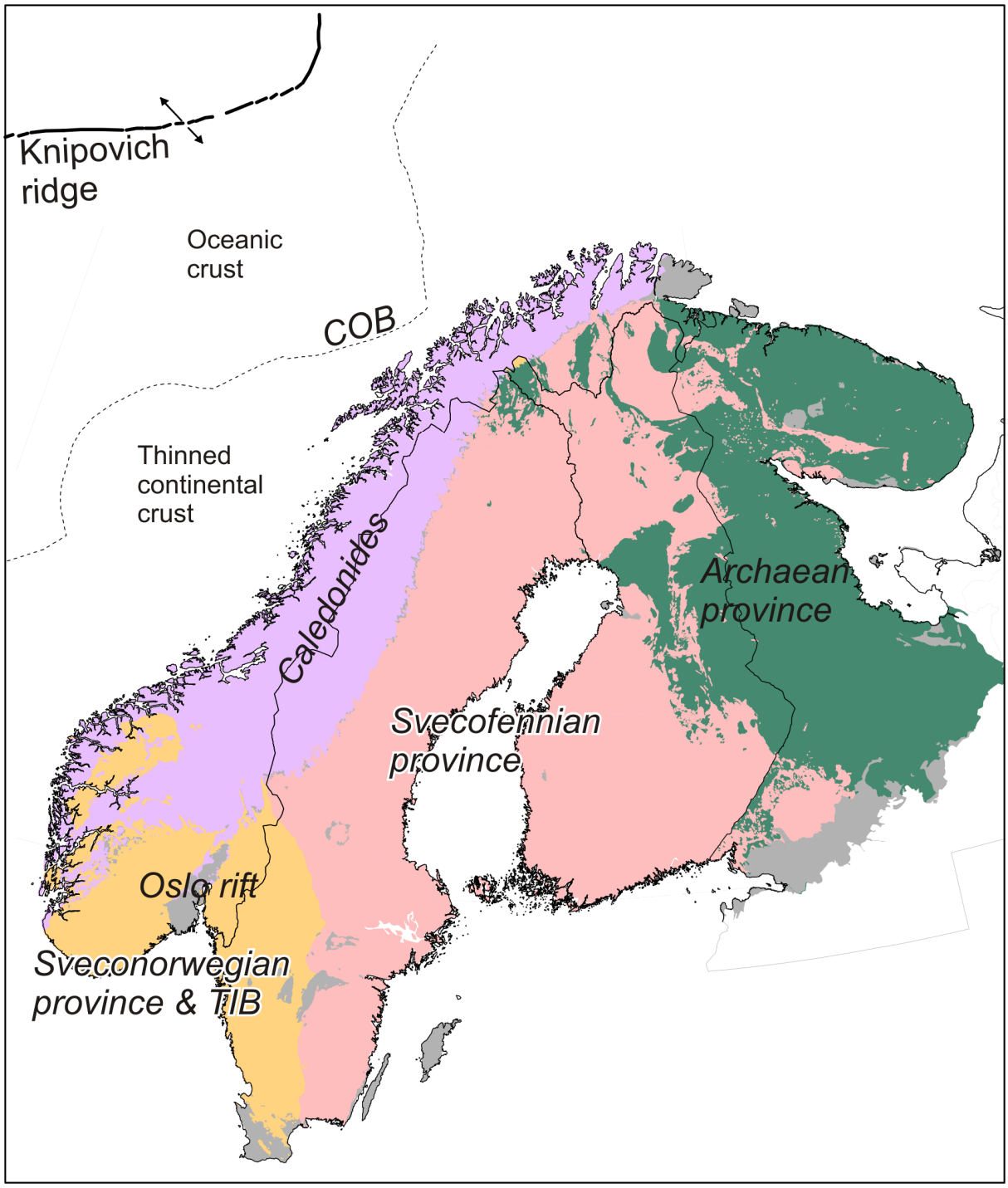

Figure 7.1. Simplified geological map of the Fennoscandian Shield and the Norwegian Sea. Modified after Koistinen et al. (2001) and Sigmond (1996). Abbreviations: COB = continent-ocean boundary; TIB = Transscandinavian Igneous Belt.

7.2 Methods

7.2.1 Temperature logging

Downhole temperatures were measured using a high-precision quartz oscillator, which under normally good field and local electrical noise conditions has a temperature resolution of 0.001–0.003°C and accuracy between 0.01 and 0.05°C. In general, a logging speed of 10 cm/s was applied with temperature measurements every 1 s. For the shallow boreholes in the Lærdal tunnel we used a logging speed of 5 cm/s. The procedures of borehole temperature logging is in agreement with international standard procedures (Beck & Balling 1988) and are described in detail in Olesen et al. (2006a).

The temperature data are presented below as plots of temperature vs. depth and thermal gradient vs. depth. The true temperature-depth function around a local depth point may be approximated by a constant temperature-gradient function, thus filtering using a linear least-squares relation is appropriate. We have used a running 5 m interval gradient for all sites except at Arnestad and Berger, where high noise warranted a larger, 30 m interval filter. The latter filter causes significant smoothing and may mask some local, real deviations from the steady-state gradient, such as the annual temperature wave.

7.2.2 Thermal conductivity measurements

Thermal conductivities were measured on 2cm-thick and 3–5 cm wide disks. Measurements were carried out on core samples where available and rock samples from the vicinity of the heat flow site where cores are missing. The thermal conductivity data are presented graphically along with temperature data from each heat flow site. The conductivity of each sample was determined using a transient method in which a constant heat flow is induced at the top of the sample.

The heat source maintains a constant temperature of 300 ± 2°C and is placed 1 cm above the sample with air between. The sample is insulated on the sides and the temperature at the base of the sample is monitored constantly. The thermal diffusivity (α) is estimated from the resulting temperature-time plot, and the thermal conductivity (K) is calculated from Equation 1 using measured density (ρ) and assumed specific heat capacity (C_p):

$$K = \rho C_p \alpha \qquad \text{Equation 1}$$

The specific heat capacity is assumed to be 850 J/(kg*K) for all samples. The theory of this method is described in Carslaw & Jaeger (1959) and Middleton (1993). The quality of the measurements is ensured by simultaneous measurement of the standard material Pyroceram 9606 (Assael et al. 2004), and the precision in the thermal diffusivity measurements better than ±5%.

Midttømme et al. (Chapter 6) describe the results of the thermal conductivity measurements for each heat flow site in detail. Thermal conductivities at depth points with 1 meter increment are calculated as running mean averages with depth intervals corresponding to those used in the least-squares calculation of the thermal gradient, typically 20 and 100 m.

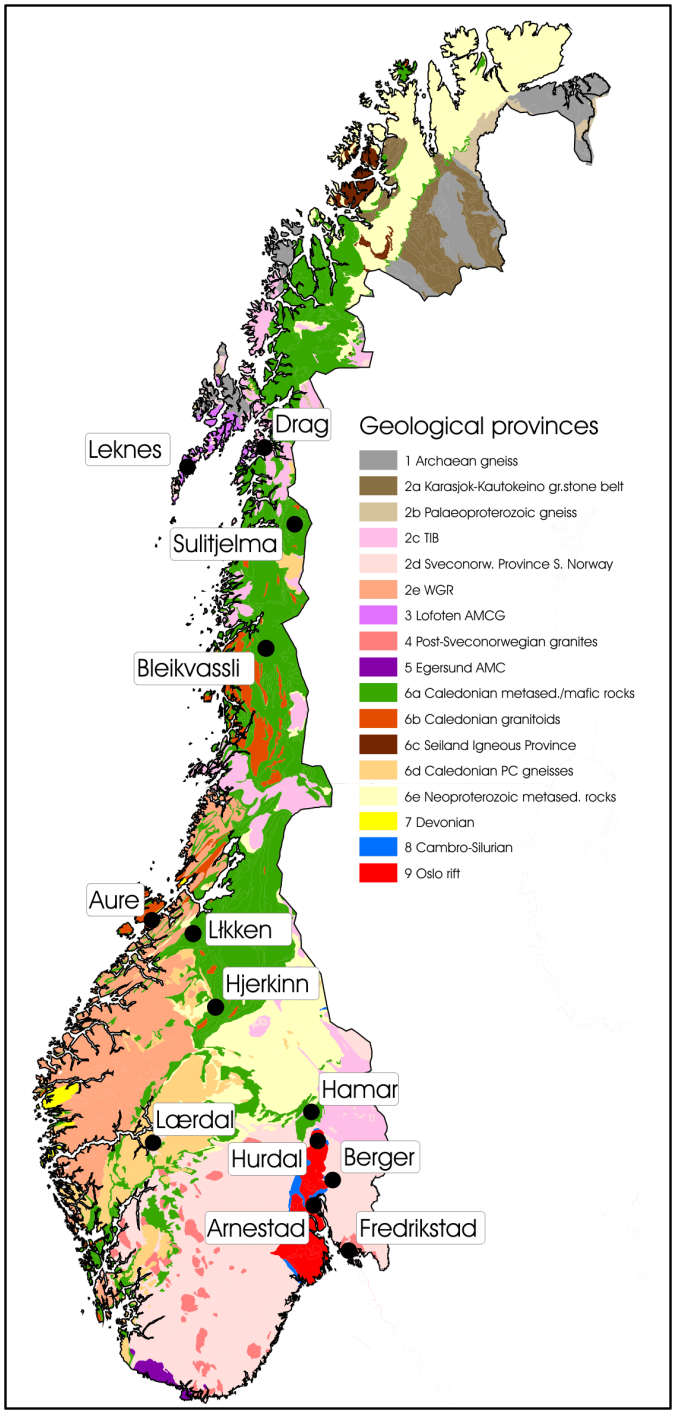

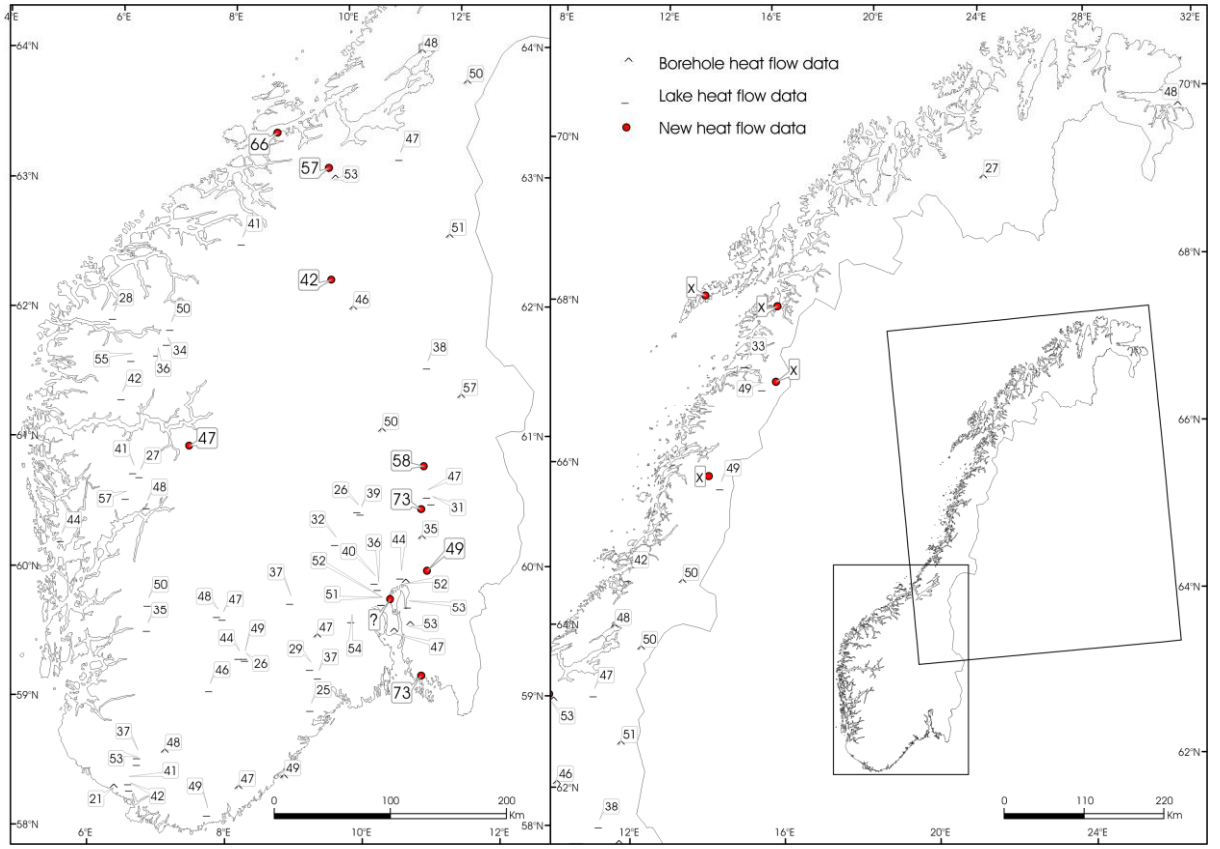

Figure 7.2 (a) Simplified geological map of Norway with new heat flow sites. Geology modified after Sigmond (2002). (b) All available heat flow data from the Norwegian mainland. New heat flow data from Nordland are presented in Chapter 8.

7.2.3 Corrections to measured thermal gradients

7.2.3.1 Topographic corrections

Topographic features may significantly influence subsurface temperatures and temperature gradient/heat flow (e.g., Blackwell et al. 1980). Generally speaking, isotherms are compressed beneath topographic lows (e.g., valleys) and extended beneath topographic highs (e.g., peaks), resulting in increased and decreased thermal gradients, respectively. This is shown schematically in Fig. 7.3.

The topographic corrections were made using a finite element method on topographic models based on digital elevation data with a horizontal resolution of 100 m and a vertical resolution of 1 m. The topographic relief forms the upper surface of a 10*10 km block with a thickness

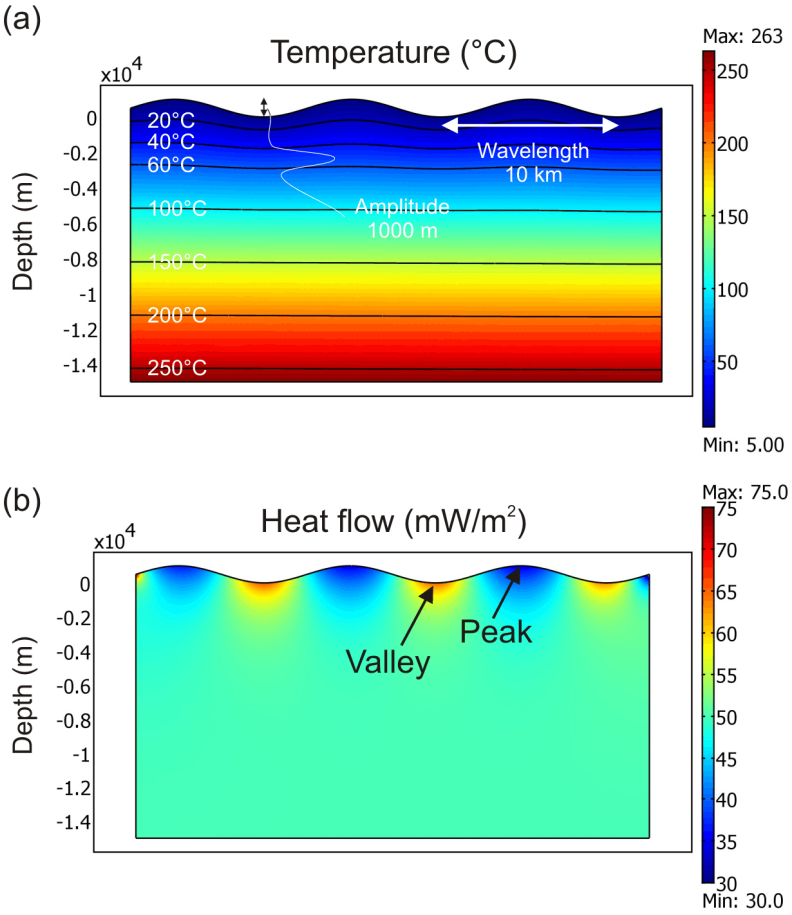

Figure 7.3. Thermal model illustrating how temperature (a) and heat flow (b) are affected by topography. The thermal parameters are: 5°C surface temperature, 50 mW/m^2 basal heat flow, a conductivity of 3 W/mK, and no internal heat production.

of 5 km plus topography. The heat flow site is located at the centre of the model. The topographic models for each heat flow site are shown in Fig. 7.4. The temperature at the upper surface decreases as a function of elevation by 6.5°C/km, which is similar to the atmosphere's lapse rate; the absolute temperature, on the other hand, does not affect the topographic correction and is set here at 5°C at sea level. The models assume constant and

homogeneous thermal conductivities, calculated as averages of the measured conductivities from the individual sites. The errors inherent in this assumption are small: on the order of <1 mW/m^2 at depths >200m for thermal conductivities between 2 and 4 W/mK. The heat flow into the model across the basal boundary is set close to the calculated, uncorrected heat flow. Again, the errors imposed by this assumption are small: on the order of <2 mW/m^2 at depths >200 m for a 20 mW/m^2 variation in heat flow.

7.2.3.2 Palaeoclimatic corrections

The effects of palaeoclimatic changes on subsurface temperature, and the need to correct for such effects to obtain reliable equilibrium heat flow densities were recognised a long time ago (Anderson 1934, Benfield 1939). Each temperature disturbance at the surface propagates into the subsurface at a rate determined by the diffusivity of the rock, and the depth of penetration of a measurable disturbance depends on both the amplitude and duration of the disturbance at the surface. Roughly speaking, the effects of Pleistocene ice ages, which lasted several hundred thousand years, extend to depths of several kilometres, climate

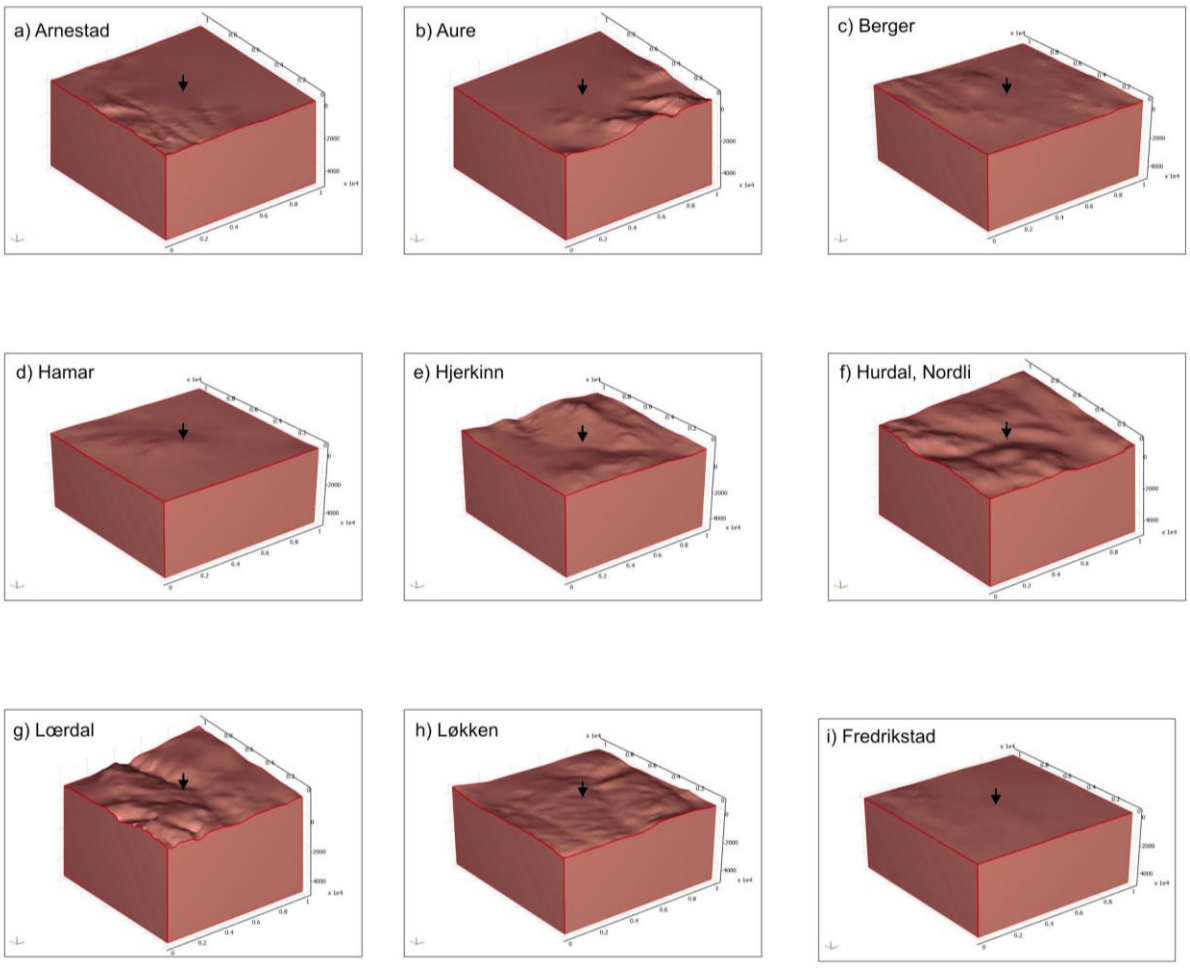

Figure 7.4. Topographic models used in calculating topographic corrections. The models are based on a digital elevation model with a horizontal resolution of 100 m and a vertical resolution of 1 m. The arrows denote the heat flow locations (situated in the centre of the model).

changes during the Holocene extend to depths of several hundred metres to a few kilometres, and seasonal changes extend to depths of a few tens of metres. The amplitude of the disturbance varies inversely with the elapsed time since the disturbance, which means that the amplitude of a Holocene disturbance will be greater than the amplitude of a similar Pleistocene disturbance.

The palaeoclimatic effects were calculated using the finite element method on models with constant and homogenous thermal conductivity and basal heat flow, and a surface temperature that varies according to the interpreted palaeoclimatic history at each heat flow site. In order to carry out the palaeoclimatic corrections, we have devised palaeoclimatic histories for the last 220,000 years at each heat flow site. The palaeoclimatic histories are based on the Weichselian glacial (~110–10 ka) and Holocene interglacial (10 ka to present) evolution, which are rather well known compared to preceding glacial/interglacial periods. The same palaeoclimatic history is repeated for the Saalian glacial/Eemian interglacial period (220–110 ka), because, although detailed data are more scant than for succeeding events, we know that conditions were comparable during the two glacial/interglacial periods (Andersen & Borns Jr 1994, p. 43). The palaeoclimatic evolution during the Weichselian glacial period

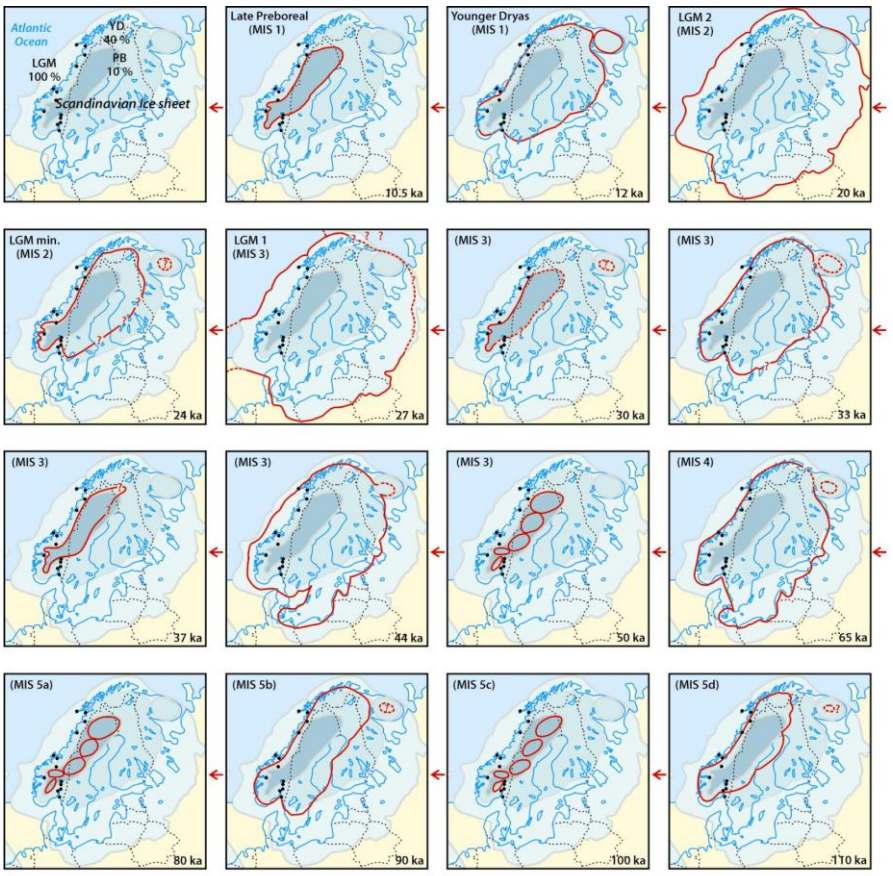

Figure 7.5. Map showing the locations of the new heat flow sites relative to ice cover during the Weichselian glaciation. MIS = marine isotope stage.

is based on a recent model of temporal ice cover variations in Scandinavia during this period (Olsen 2006). Fig. 7.5 shows a map of the investigated heat flow sites and temporal ice cover variations during the Weichselian glaciation. At times when the sites were glaciated (for most sites corresponding to Weichselian stadials), a temperature of –1°C is assumed at that site (cf., Jessop 1971). At times when the sites were ice-free (for most sites corresponding to Weichselian interstadials), a temperature 5°C below present-day temperatures at each site was assumed. This is based on observations suggesting that the Weichselian interstadials were significantly colder that at present (Andersen & Borns Jr 1994, p. 50). During the Holocene, temperatures are assumed to have increased to present-day temperatures by 8 ka and remained at that temperature since. Present-day temperatures are taken from data made available by the Norwegian Meteorological Institute (DNMI). The palaeoclimatic data (i.e., time-temperature) that form the basis for this correction are presented in Table 7.2. A piecewise cubic interpolation method is used to build up a continuous palaeoclimatic history from the individual data points.

7.3 Geological description and topographically and palaeoclimatically corrected heat flow measurements from 13 sites in Norway

7.3.1 Berger, Precambrian gneissic rocks

The heat flow site at Berger (Fig. 7.2a) is situated in dioritic gneisses that form part of the Romerike complex, comprising granitic to tonalitic and dioritic gneisses of Late Palaeoproterozoic to Early Mesoproterozoic age (Nordgulen 1999). The site is located approximately 5 km to the east of the nearest exposure of Permian magmatic rocks related to the formation of the Oslo Rift, and a Permian thermal overprinting at this site is inevitable.

The site consists of one borehole drilled to c. 650 m depth with an angle of 5.8° from the vertical. The thermal gradient at Berger is rather low at c. 13°C/km between 200 and 400 m depth, increasing to c. 16°C/km between 400 and 600 m depth (Fig. 7.6). Unfortunately, no core is available from the Berger borehole and the only lithological control is based on surface observations and interpretation of a televiewer recording to 480 m depth. These observations suggest that the dominant rock type down to c. 420 m depth is a medium-grained diorite, whereas from 420 to 480 m amphibolite appears to dominate. For the dioritic upper part we assume a thermal conductivity of 2.8 W/(m*K) (cf., Midttømme et al. 2000b), whereas the amphibolitic lower part is given a thermal conductivity of 2.6 W/(m*K). We assume the amphibolite is the dominant lithology to the bottom of the borehole. The uncorrected heat flow is rather constant at c. 40 mW/m^2 below 250 m depth. Above this depth, the heat flow drops off quite rapidly, most likely as a result of recent warming over the last 100–200 years. A similar effect is seen in most of the other boreholes investigated here, but correcting for such effects is considered outside the scope of this study and does not affect the estimates of terrestrial heat flow, which are based on data from the deeper parts of

the boreholes. The topographic correction is close to 0 mW/m^2 whereas the palaeoclimatic effect is c. 10 mW/m^2 in the upper 300 m of the borehole gradually dropping to c. 7 mW/m^2 at the bottom. The corrected heat flow below 250 m varies between 45 and 50 mW/m^2, with an average of 49 mW/m^2 for both the 20 and 100 m interval calculations. We take 49 mW/m^2 to be the best estimate of the heat flow at Berger. No heat production data are available from the borehole.

7.3.2 Lærdal, Precambrian gneisses within a Caledonian nappe

The heat flow site in Lærdal (Fig. 7.2a) consists of rather heterogeneous, variably migmatitic orthogneisses of dioritic to granodioritic composition. The rocks form part of a basement window beneath the Caledonian Jotun nappes, at the transition between the Sveconorwegian Province to the south and the Western Gneiss Region to the northwest. The rocks are undated but are most likely of Early Mesoproterozoic age.

This site consists of three boreholes; two within the 25 km long Lærdal tunnel (referred to as Lærdal 1 and Lærdal 2) and one at the surface c. 1 km above the tunnel (referred to as Aurland). The holes are shallow, only c. 50 m deep, and the purpose of drilling within the tunnel was to see if a relatively undisturbed thermal gradient representing the gradient at c. 1 km depth could be measured. This was, unfortunately, not the case. The temperature profiles from Lærdal 1 and Lærdal 2 show similar patterns: a negative gradient in the uppermost 15–25 m and a gradually increasing gradient at greater depth, reaching c. 15°C/km at the bottom of the holes (Figs. 7a,b). Thermal conductivities vary between 2.5 and 3.5 W/mK, with an average of 3 W/(m*K). The calculated (uncorrected) heat flow in both boreholes increases gradually to a value of 40–45 mW/m^2 at the bottom. However, equilibrium, steady-state heat flow does not appear to have been reached. The temperatures in the boreholes are most likely affected by the presence of the tunnel, and applying a topographic or palaeoclimatic correction to these values would be in vain. A similar temperature pattern is observed in the Aurland borehole (Fig. 7.7c), at the surface above the tunnel, and is most likely related to variations in surface temperatures. Thus, none of the boreholes yield useful heat flow data on their own. The average thermal gradient between the Aurland borehole and the tunnel boreholes is 14.4°C/km. Multiplying this value with the average thermal conductivity (3 W/(m*K)) yields an uncorrected heat flow of 43 mW/m^2. The topographic correction at the Lærdal site is negligible whereas the palaeoclimatic correction amounts to c. 5 mW/m^2 near the surface, dropping to c. 2 mW/m^2 at 1000 m depth. The best estimate of the heat flow at the Lærdal site is therefore taken to be 47 mW/m^2. Heat production from the three wells range from 0.5 to 2.5 μW/m^3 with an average of 1.7 μW/m^3 (Table 7.3).

7.3.3 Løkken, ophiolitic gabbro within a Caledonian nappe

The heat flow site at Løkken (Fig. 7.2a) is situated in ophiolitic gabbroic rocks and greenstones of Late Cambrian to Early Ordovician age that form part of the Caledonian Støren nappe (Grenne 1989, Roberts et al. 2002). The rocks were most likely obducted in the

Middle Ordovician and thrust into their present location during the Late Silurian Scandian event at c. 420 Ma.

The thermal gradient at Løkken is well defined at c. 16°C/km below 150 m with a small but systematic increase with depth (Fig. 7.8). The thermal conductivity is fairly constant, reflecting the relatively homogeneous lithology, mostly ranging between 3 and 3.2 W/(m*K). The uncorrected heat flow is nearly constant at 50 mW/m^2 below 500 m depth, and decreases gradually with decreasing depth. The topographic correction is <1 mW/m^2 whereas the palaeoclimatic correction is c. 10 mW/m^2 at depths <200 m, decreasing gradually to c. 4 mW/m^2 at the bottom of the borehole. The resulting corrected heat flow profile shows a rather consistent value at c. 55 mW/m^2 below 300 m depth. The average corrected heat flow is 57 mW/m^2 for both the 20 and 100 m interval calculations. We take 57 mW/m^2 to be the best estimate of the heat flow at Løkken.

The dominant lithology at Løkken is medium-grained gabbro with very low heat production rates between 0.01 and 0.09 μW/m^3. Between 860 and 900 m depth, the gabbros are intruded by the Early to Mid-Ordovician Hølonda porphyrite (Grenne & Roberts 1998), which yields higher heat production rates between 1.85 and 2.24 μW/m^3 (Table 7.3). This unit is, however, relatively subordinate, constituting a mere 4% of the borehole.

7.3.4 Hjerkinn, Early Palaeozoic metasediments within a Caledonian nappe

The heat flow site at Hjerkinn (Fig. 7.2a) consists of rather heterogeneous mica schist and amphibolite that form part of the Caledonian Blåhø nappe of inferred Cambrian to Ordovician age (Terry et al. 2000).

At Hjerkinn we observe some gradient variability around a mean value of about 17 °C/km, dropping to 10 °C/km at about 260 and 480 m (Fig. 7.9). The heterogeneous lithology is clearly expressed as highly variable thermal conductivities, ranging from c. 2 to 3.5 W/(m*K) over rather short depth intervals. The thermal conductivity shows a broad decrease with increasing depth. The 20 m-interval heat flow profile displays very large variation caused by individual samples with anomalous thermal conductivities. We therefore base our discussion of heat flow on the 100 m-interval calculations. The uncorrected heat flow is rather constant at 45–50 mW/m^2 between 80 and 180 m depth, and drops off to 35–45 mW/m^2 at greater depths. The Hjerkinn borehole is located within a small valley (Fig. 7.4e), and the elevated heat flow at shallow depths is probably (partly) a result of topographic effects. Applying a topographic correction removes the difference in thermal gradient between the shallow and deeper parts of the borehole; the heat flow is nevertheless slightly higher in the uppermost part due to the somewhat higher thermal conductivity. The palaeoclimatic correction is small at around 2 mW/m^2 for the entire depth of the borehole. The shallow part of the borehole displays large variation in corrected heat flow, ranging from 35 to 50 mW/m^2 between 100 and 300 m depth. Below 300 m depth, the variation is smaller, ranging from 36 to 46

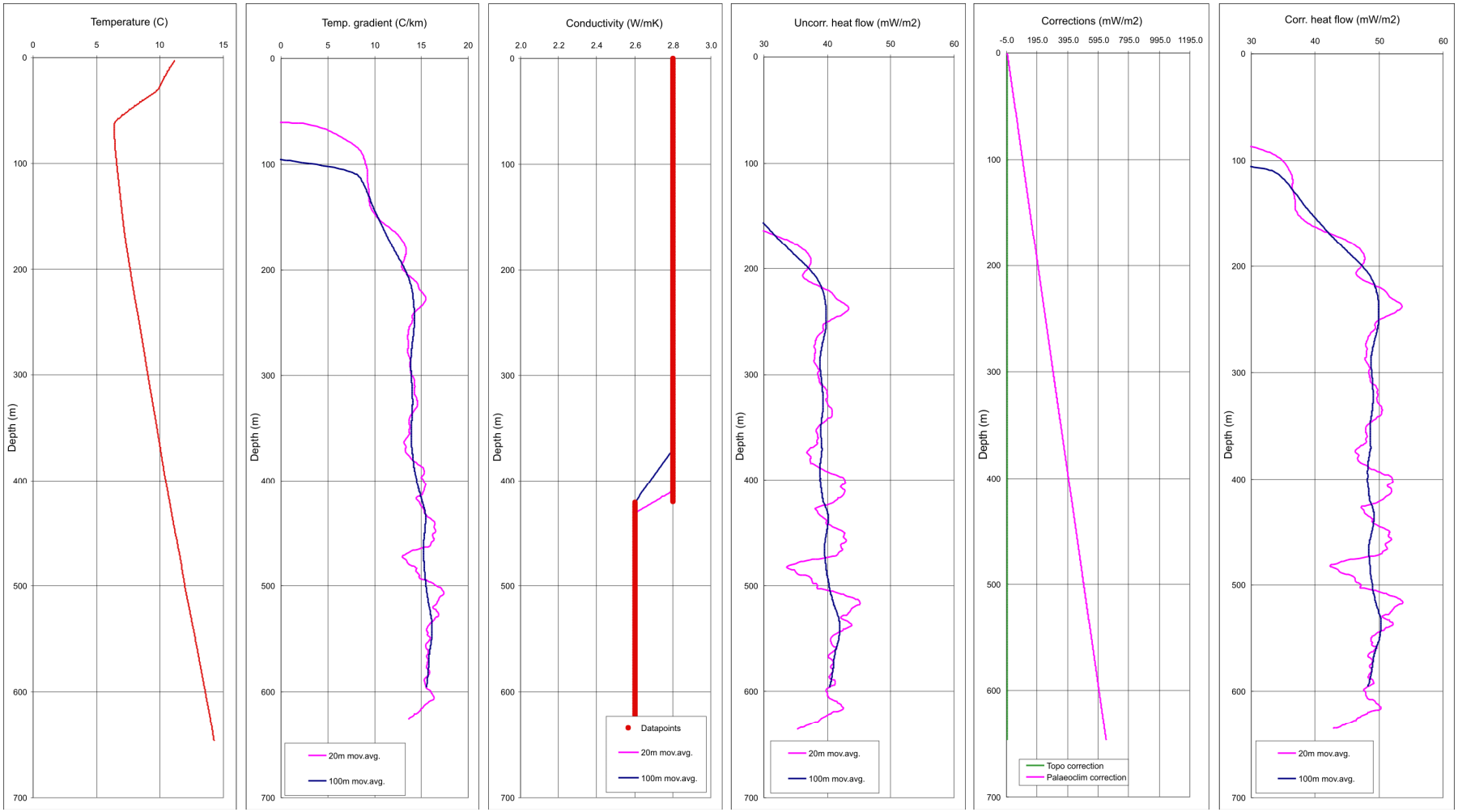

Figure 7.6. Plots showing temperature, thermal gradient, thermal conductivity, uncorrected and corrected heat flow, and topographic and palaeoclimatic corrections at the heat flow site at Berger.

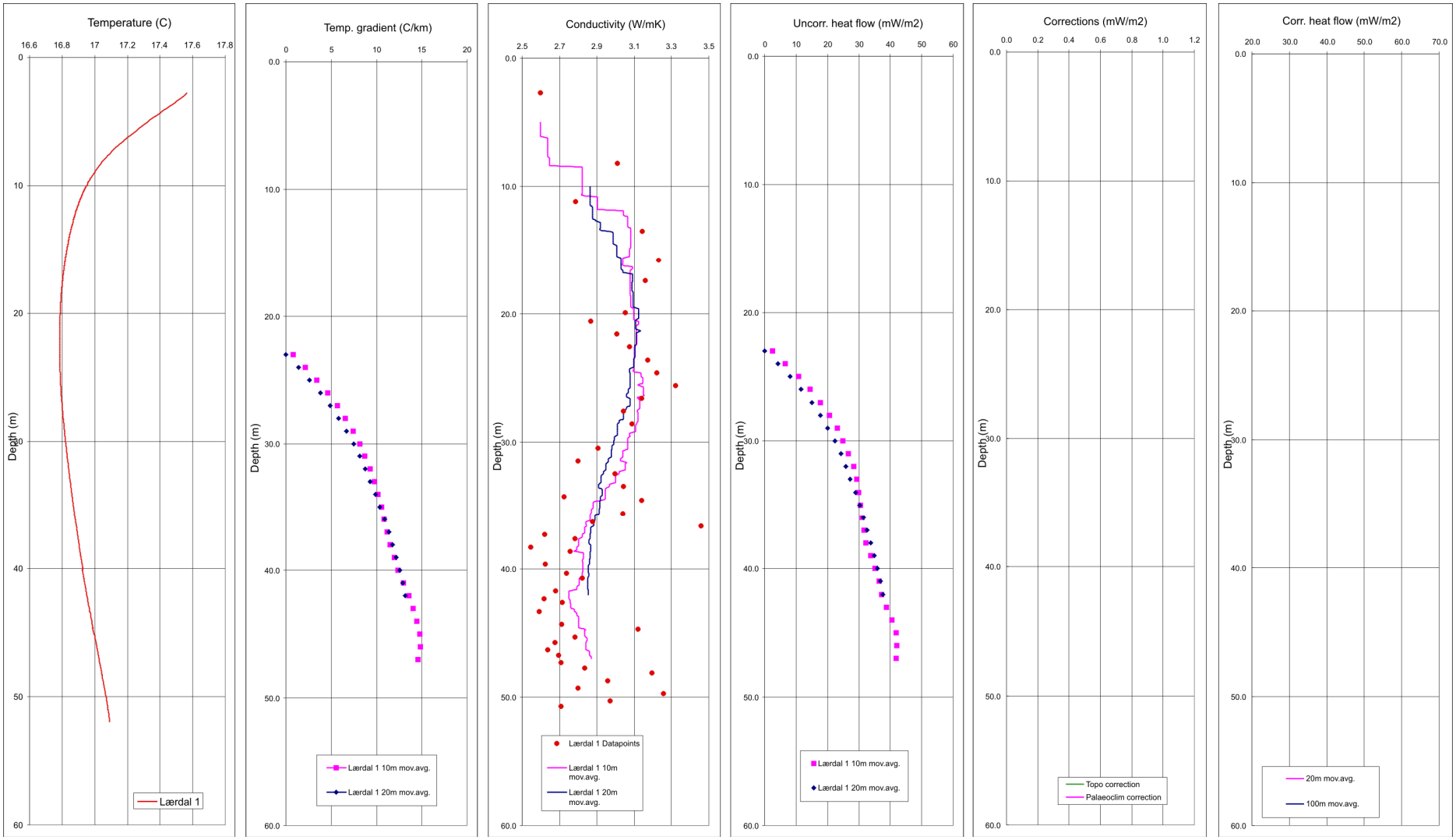

Figure 7.7a. Plots showing temperature, thermal gradient, thermal conductivity, uncorrected and corrected heat flow, and topographic and palaeoclimatic corrections at the heat flow site at Lærdal 1.

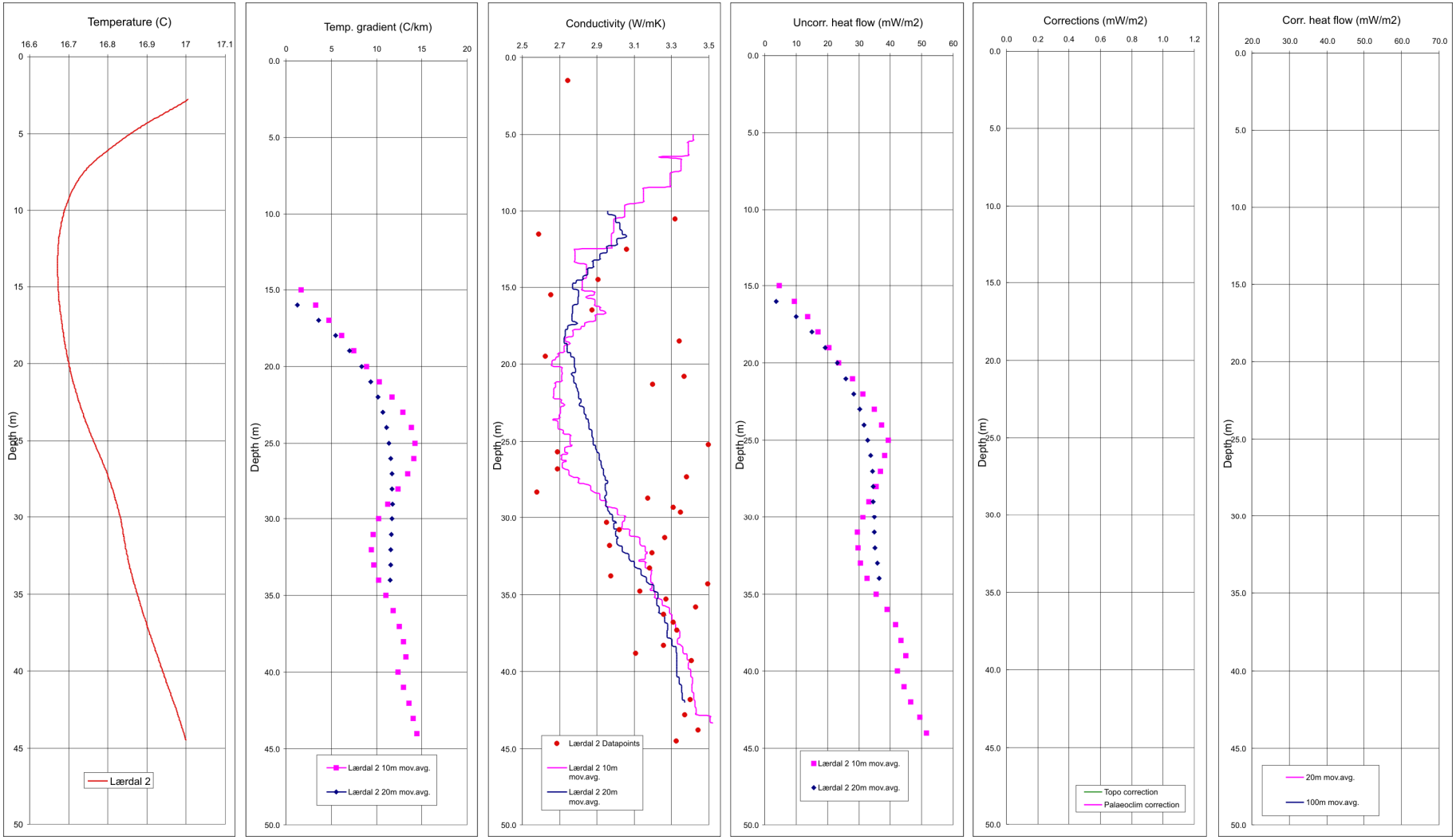

Figure 7.7b. Plots showing temperature, thermal gradient, thermal conductivity, uncorrected and corrected heat flow, and topographic and palaeoclimatic corrections at the heat flow site at Lærdal 2.

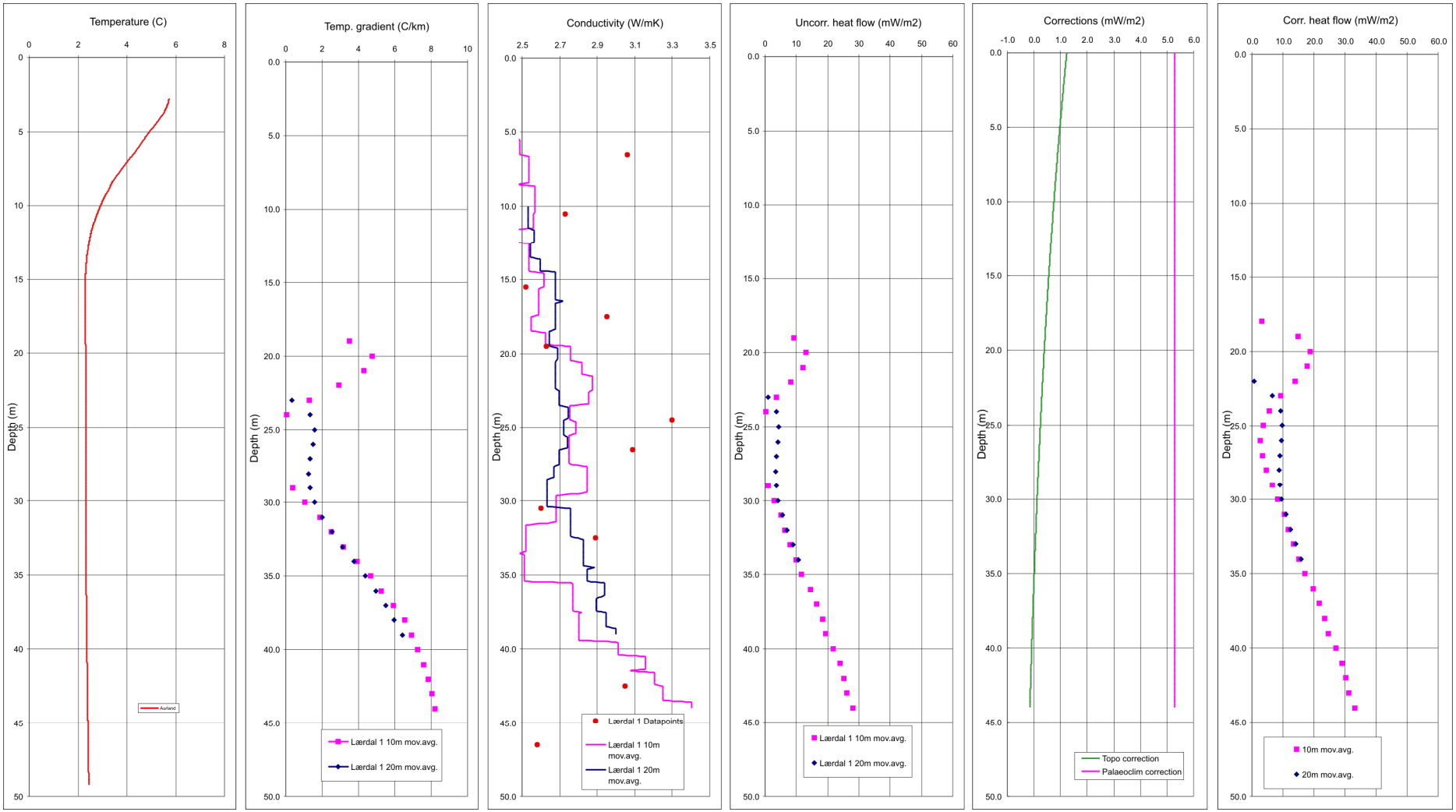

Figure 7.7c. Plots showing temperature, thermal gradient, thermal conductivity, uncorrected and corrected heat flow, and topographic and palaeoclimatic corrections at the heat flow site at Aurland.

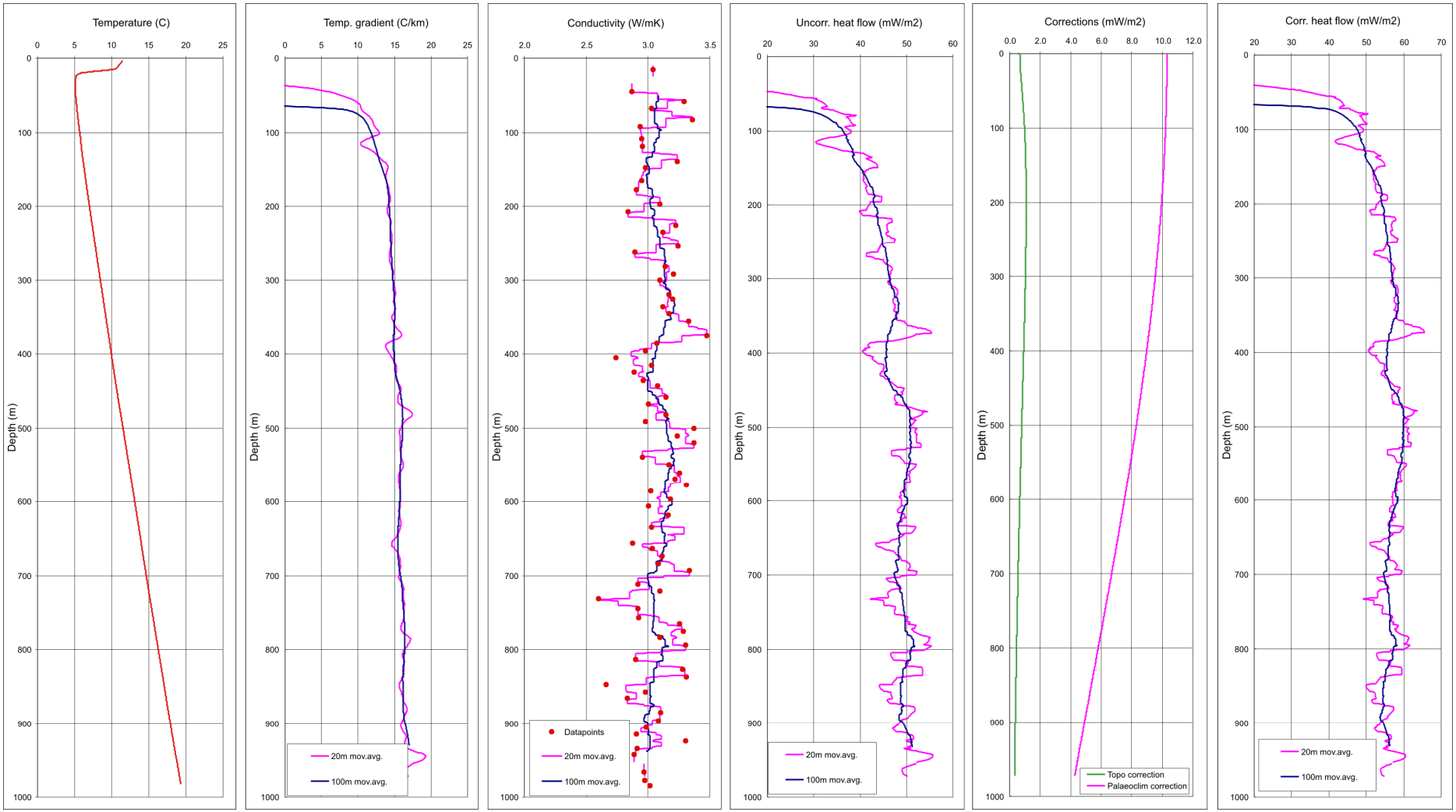

Figure 7.8. Plots showing temperature, thermal gradient, thermal conductivity, uncorrected and corrected heat flow, and topographic and palaeoclimatic corrections at the heat flow site at Løkken.

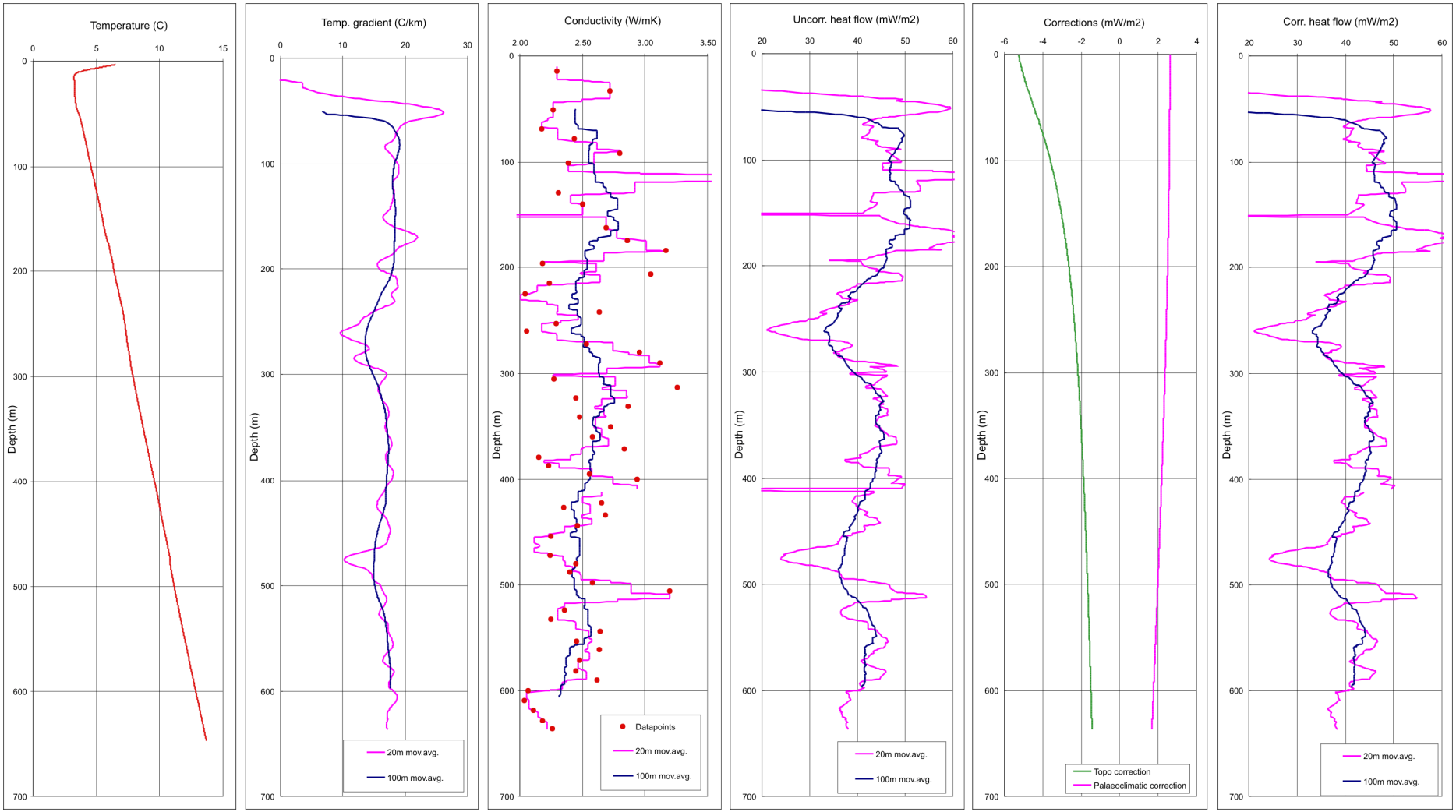

Figure 7.9. Plots showing temperature, thermal gradient, thermal conductivity, uncorrected and corrected heat flow, and topographic and palaeoclimatic corrections at the heat flow site at Hjerkinn.

mW/m^2, with and average heat flow of 42 mW/m^2. We take 42 mW/m^2 to be the best estimate of the heat flow at Hjerkinn.

The heterogeneous lithology at the Hjerkinn site and consequent large variation in thermal conductivity is obviously not ideal for carrying out heat flow determinations, and despite having sampled quite densely for conductivity measurements even denser sampling may be necessary to arrive at a better defined heat flow value. Heat production rates from Hjerkinn are low, ranging from 0.04 to 1.3 μW/m^3 with an average of 0.6 μW/m^3 (Table 7.3).

7.3.5 Aure, Caledonian intrusive rocks

The heat flow site at Aure (Fig. 7.2a) is situated within the quartz dioritic to dioritic Kjørsvika diorite gneiss, dated by Tucker et al. (2004) at c. 461 Ma. The diorite gneiss forms part of a large suite of Mid to Late Ordovician intrusion in the Caledonian Upper Allochthon, including the Smøla–Hitra Batholith.

The thermal gradient at Aure is rather well defined at c. 22–23°C/km below 150 m depth (Fig. 7.10). No core is available from this site and the only information about thermal conductivity comes from two hand samples of dioritic gneiss collected close to the borehole. The measurements show that the thermal conductivity parallel to the foliation in the rocks is approximately 1.25 times higher than perpendicular to the foliation, i.e., c. 2.9 W/(m*K) parallel vs. 2.3–2.4 W/(m*K) perpendicular to the foliation. A televiewer recording of the borehole shows that the rocks are fairly homogeneous, and a thermal conductivity of 2.5 W/(m*K) is used for the entire length of the borehole. This gives in an uncorrected heat flow around 56–57 mW/m^2 below 150 m depth. The topographic correction is slightly negative (-2 mW/m^2) whereas the palaeoclimatic correction is c. 12 mW/m^2 near the surface, decreasing to c. 10 mW/m^2 at the bottom of the borehole. The corrected heat flow below 150 m depth is nearly constant with an average of 66 mW/m^2 for both the 20 and 100 m interval calculations. We take 66 mW/m^2 to be the best estimate of the heat flow at Aure. Heat production data are available from two surface samples from the heat flow site yielding values of 1.2 and 1.4 μW/m^3 (Table 7.3).

7.3.6 Arnestad, Cambro–Silurian metasediments within the Oslo Rift

The heat flow site at Arnestad (Fig. 7.2a) is situated within Cambro–Silurian low-grade brownish shale with layers of limestone nodules that form part of the Arnestad Formation. The rocks were downfaulted into and preserved within the Oslo Rift in the Early Permian.

A low gradient at 12–13 °C/km is observed in the deepest parts (below 500 m) of the Arnestad borehole, whereas the upper part (200–460 m) shows a high gradient between 20 and 30 °C/km (Fig. 7. 11). At first hand, this difference would appear likely to be related to variation in thermal conductivity — the lower part of the borehole consists of high-conductivity granite (or granitic gneiss), whereas the upper part (above 500 m) consists of

low-conductivity shales. Unfortunately, a core is not available from this borehole and thermal conductivities have to be assumed from relevant measurements of surface samples. Midttømme (this report) presents a comprehensive discussion of relevant thermal conductivity measurements. The corrected heat flow values range between 50 and 90 mW/m^2, clearly showing that variation in thermal conductivity does not explain the observed variation in thermal gradient. The most likely explanation is either that the estimated conductivities are wrong, or that other effects, such as hydrogeological activity, affect the temperature in the borehole. At this stage we are at a loss explaining the observed temperatures at Arnestad.

Chemical data from 11 samples of borehole cuttings from the Arnestad borehole are available for heat production calculations. Shale is the dominant lithology, and 6 samples yield a range of heat production rate between 1.1 and 11.4 $\mu W/m^3$ with an average of 5.2 $\mu W/m^3$ (Table 7.3). Two samples of alum shale yield heat production rates of 29.5 and 31.2 $\mu W/m^3$, and 3 samples of basement granitic gneiss yield values between 2.8 and 3.5 $\mu W/m^3$.

7.3.7 Hamar, Cambro–Silurian metasediments within a Caledonian nappe

The heat flow site at Hamar (Fig. 7.2a) is situated within Cambro–Silurian low-grade shale and carbonate that were deposited in a shallow sea covering much of Scandinavia at that time. The rocks were thrust southeastwards during the Late Silurian Scandian event and today constitute part of the Os–Rø Nappe Complex. The rocks were downfaulted into and preserved within the Oslo Rift in the Early Permian.

The thermal gradient at Hamar is stable at 22–23°C/km between 200 and 500 m; it then increases to c. 30°C/km at 620 m depth and remains stable to 700 m depth where it starts to drop in the bottom 30–40 m of the borehole (Fig. 7.12). The increase in gradient at c. 500 m depth corresponds to the appearance of a zone dominated by black, low-conductivity alum shale. The transition from typically, 'high'-conductivity greenish shale and carbonate in the upper part of the borehole to low-conductivity black shale in the deeper part is transitional (i.e., alternating lithologies) and it is likely that the density of conductivity measurements is too low to adequately reflect this transition. At 770 m depth, the basement underlying the Cambro–Silurian shales is encountered. The basement rocks consist of granitoid augen gneiss and intermediate fine-grained gneiss with thermal conductivities ranging from 2.3 to 3 W/(m*K). This slight increase in thermal conductivity corresponds to a drop in the thermal gradient. The topographic and palaeoclimatic corrections range from c. 5 mW/m^2 near the surface to 1–2 mW/m^2 at the bottom of the borehole. The average corrected heat flow from 200 m depth to the bottom of the borehole is 56 mW/m^2 for both 20 and 100 m interval calculations. Excluding the depth interval between 500 and 620 m where the thermal gradient gradually increases, possibly due to inadequate conductivity measurements, the average corrected heat flow is 57 and 58 mW/m^2 for the 20 and 100 m interval calculations, respectively. <u>We take 58 mW/m^2 to be the best estimate of the heat flow at Hamar.</u>
No heat production data are available from the borehole.

7.3.8 Hurdal, Permian intrusive rocks within the Oslo Rift

The heat flow site in Hurdal (Fig. 7.2a) is situated within Permian syenitic rocks that form part of the Oslo Rift, and represents the youngest geological province considered in this study.The site consists of four boreholes that are between 600 and 900 m deep (Table 7.1). Core samples were made available by Crew Development from three of the holes (Dh02, Dh03, Dh05/05B), whereas no core is available from the older 'Nordli' hole. The boreholes are located within a distance of 500 m from each other, but nevertheless show rather varied temperature gradients and thermal conductivities (Figs. 13a, b, c, d).

Boreholes Dh02 and Dh03 are located c. 500 m (30–50 m vertical) uphill of boreholes Dh05/05B and Nordli. Dh02 and Dh03 have comparable thermal gradients which increase gradually from c. 11°C/km at 100m depth to c. 20–22°C/km at 400 m depth (Figs. 13a, b). Between 400 and 600 m depth, the thermal gradients are relatively stable at 20–22°C/km to c. 600 m depth, below which significant scatter, particularly in Dh03, is observed. The very large variation in thermal gradient is most likely related to ground-water flow. Thermal conductivities are relatively constant at c. 2.8 W/m*K in Dh02, before increasing to c. 3.7 W/m*K below c. 530 m depth. Thermal conductivities are slightly higher in Dh03 at c. 3.2 W/m*K, but decrease to c. 2.8 W/m*K below 600 m depth. The depth intervals 370–500 m and 420–600 m in Dh02 and Dh03, respectively, yield fairly constant heat flow with averages of 70 and 69 mW/m^2, respectively.

Boreholes Dh05/05B and Nordli are located near the axis of the Hurdal valley; the topographic correction is therefore slightly higher (c. 2 mW/m^2) than at Dh02 and Dh03. The thermal gradients from Dh05/05B and Nordli are comparable in magnitude, but are differently shaped (Figs. 13c, d). In Dh05/05B, the thermal gradient is highly variable in the uppermost 200 m, before stabilising at 21–24°C/km at greater depths with a maximum at c. 300 m depth. In Nordli, the thermal gradient is relatively stable at 21–24°C/km at 100 to 550 m depth, before dropping to c. 20°C/km at greater depth. Thermal conductivities in Dh05/05B decrease from c. 3.5 W/m*K in the uppermost 100 m to c. 3 W/m*K at c. 300 m depth, before increasing to c. 3.2 W/m*K. This variation is roughly inversely correlated with the thermal gradient, suggesting that at least some of the variation in the latter can be ascribed to conductivity variations. No data on thermal conductivity is available from Nordli; we therefore assume a value of 3.2 W/m*K for the entire borehole. The depth intervals 200–500 m and 100–550 m in Dh05/05B and Nordli, respectively, yield fairly constant heat flow with averages of 75 and 77 mW/m^2, respectively. The average heat flow from the four boreholes is 73 mW/m^2, taken here as the best estimate of the heat flow in Hurdal.

No heat production data are available from the borehole, however, 42 samples within 10 km of the heat flow site yield a moderately high average heat production of 2.5 $\mu W/m^3$ (Slagstad, this report). Along with the relatively young age of the Oslo Rift, the heat production data suggest that the average heat flow value of 73 mW/m^2 from the four boreholes is reasonable;

however, it is also possible that elevated heat production at depth is responsible for the high heat flow (cf., Slagstad 2006). However, the scattered temperature data show that other processes besides conductive heat transfer affects the temperature in this area, making the calculated value uncertain.

7.3.9 Fredrikstad, post-Sveconorwegian granite

The heat flow site in Fredrikstad (Fig. 7.2a) is located within the Iddefjord granite. The granite is part of a suite of post-Sveconorwegian granites that were emplaced at c. 920–930 Ma, following Sveconorwegian orogenesis in South Norway and Sweden (e.g., Pedersen & Maaloe 1990, Eliasson & Schöberg 1991). These post-Sveconorwegian granites, and the Iddefjord granite in particular, are well known for the high radiogenic heat production rates, locally exceeding 6 $\mu W/m^3$ (Killeen & Heier 1975, Slagstad 2006).

The thermal gradient at Fredrikstad is stable at 18–19°C/km between 180 and 330 m depth and then drops gradually before stabilising at c. 17°C/km at 530 m depth (Fig. 7.14). Unfortunately, no core is available from this borehole, which makes it impossible to relate this variation in thermal gradient to variations in thermal conductivity. Thermal conductivity was determined on 31 samples of Iddefjord granite, 11 of which came from the vicinity of the borehole site. Most samples yield thermal conductivities slightly above 3 W/m*K, ranging from 2.5 to 3.5 W/m*K with a mean and median of 3.1 W/m*K. Thus, the relatively moderate variation in gradient observed at the Fredrikstad site could be related to similarly moderate variations in conductivity. Here, we take a thermal conductivity of 3.1 W/m*K to apply to the entire borehole. The palaeoclimatic correction is c. 14 mW/m^2 at 200 m depth and drops gradually to 10 mW/m^2 at the bottom of the hole. The heat flow site is situated on a topographic high, resulting in a small topographic correction of <2 mW/m^2 at depths greater than about 200 m. The average corrected heat flow from 180 m depth to the bottom of the borehole is 70 mW/m^2 for both 20 and 100 m interval calculations. If only the most stable interval between 180 and 330 m depth is included, the average heat flow is slightly higher at 73 mW/m^2. <u>We take 73 mW/m^2 to be the best estimate of the heat flow at Fredrikstad.</u>

No heat production data are available from the borehole, however, 60 samples within 10 km of the borehole yield an average heat production of 6.3 $\mu W/m^3$ (Chapter 2), which helps to explain the large heat flow.

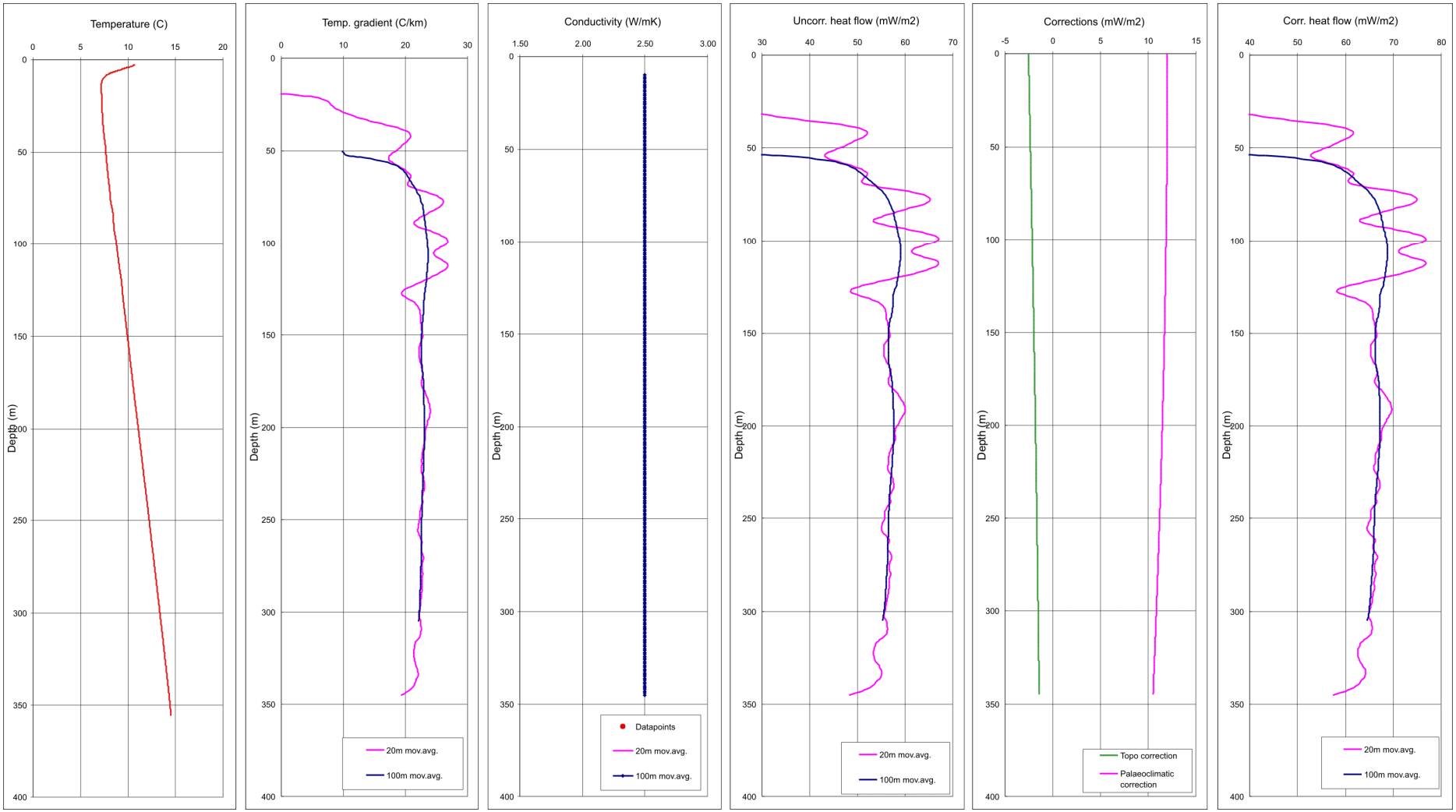

Figure 7.10. Plots showing temperature, thermal gradient, thermal conductivity, uncorrected and corrected heat flow, and topographic and palaeoclimatic corrections at the heat flow site at Aure.

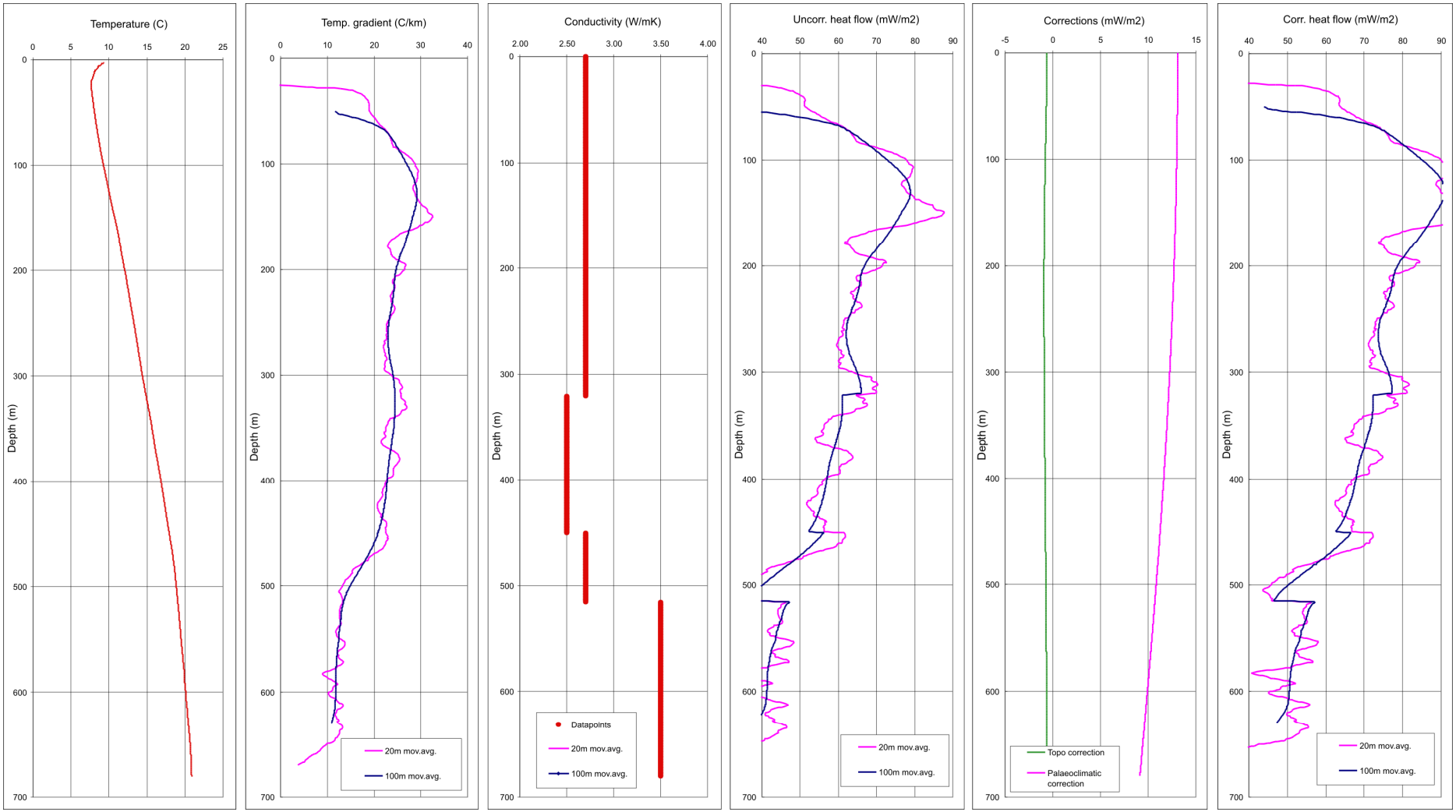

Figure 7.11. Plots showing temperature, thermal gradient, thermal conductivity, uncorrected and corrected heat flow, and topographic and palaeoclimatic corrections at the heat flow site at Arnestad.

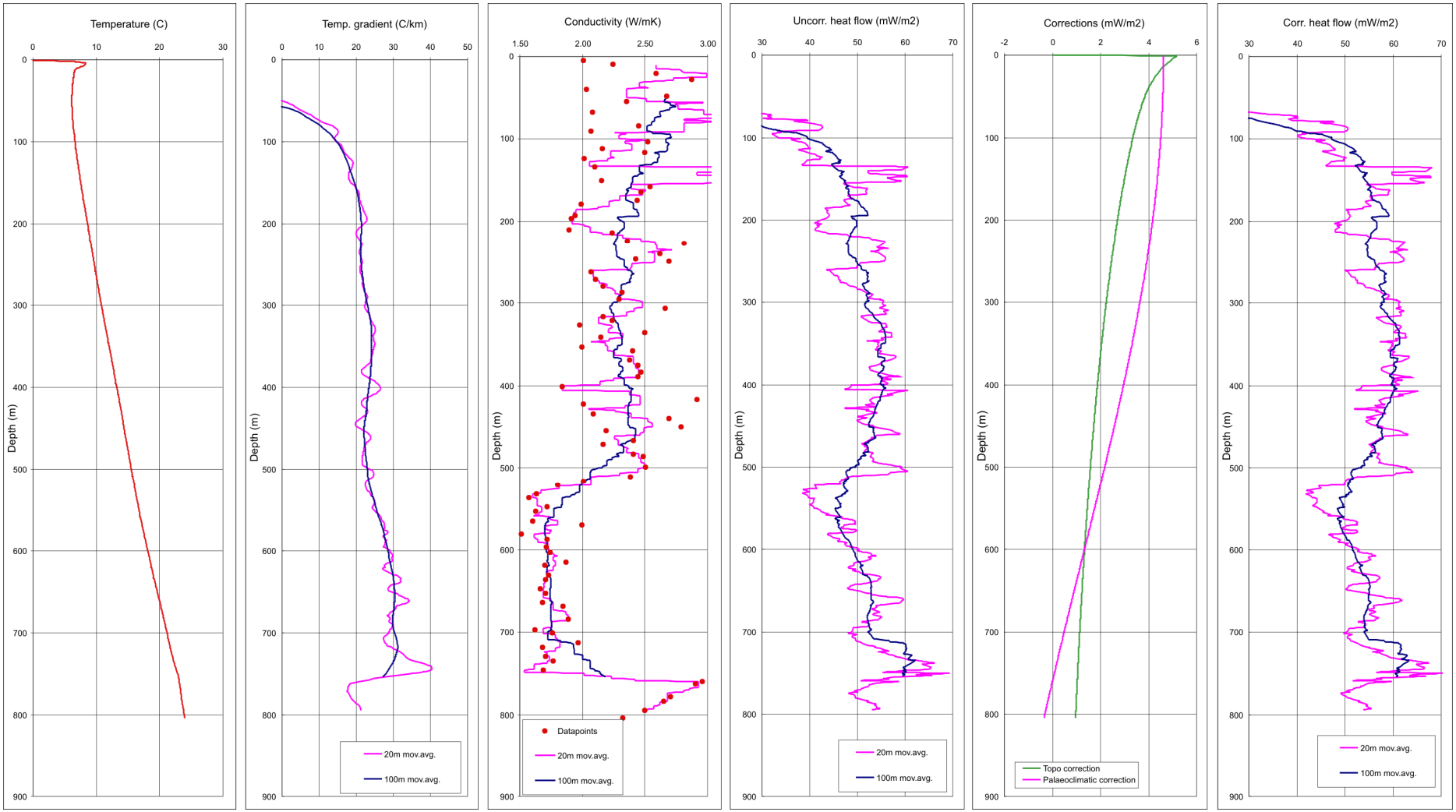

Figure 7.12. Plots showing temperature, thermal gradient, thermal conductivity, uncorrected and corrected heat flow, and topographic and palaeoclimatic corrections at the heat flow site at Hamar.

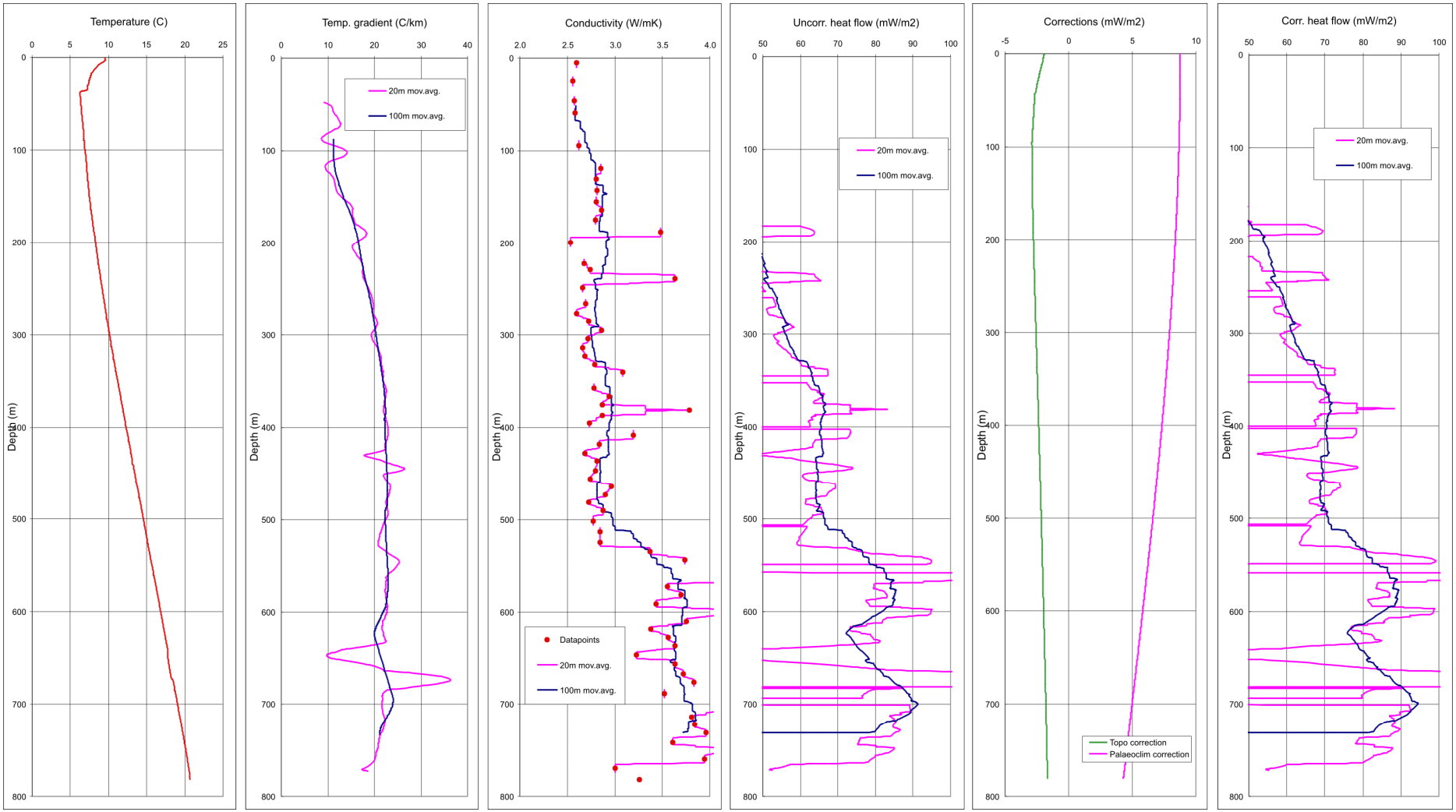

Figure 7.13a. Plots showing temperature, thermal gradient, thermal conductivity, uncorrected and corrected heat flow, and topographic and palaeoclimatic corrections at the heat flow site at Hurdal, borehole Dh02.

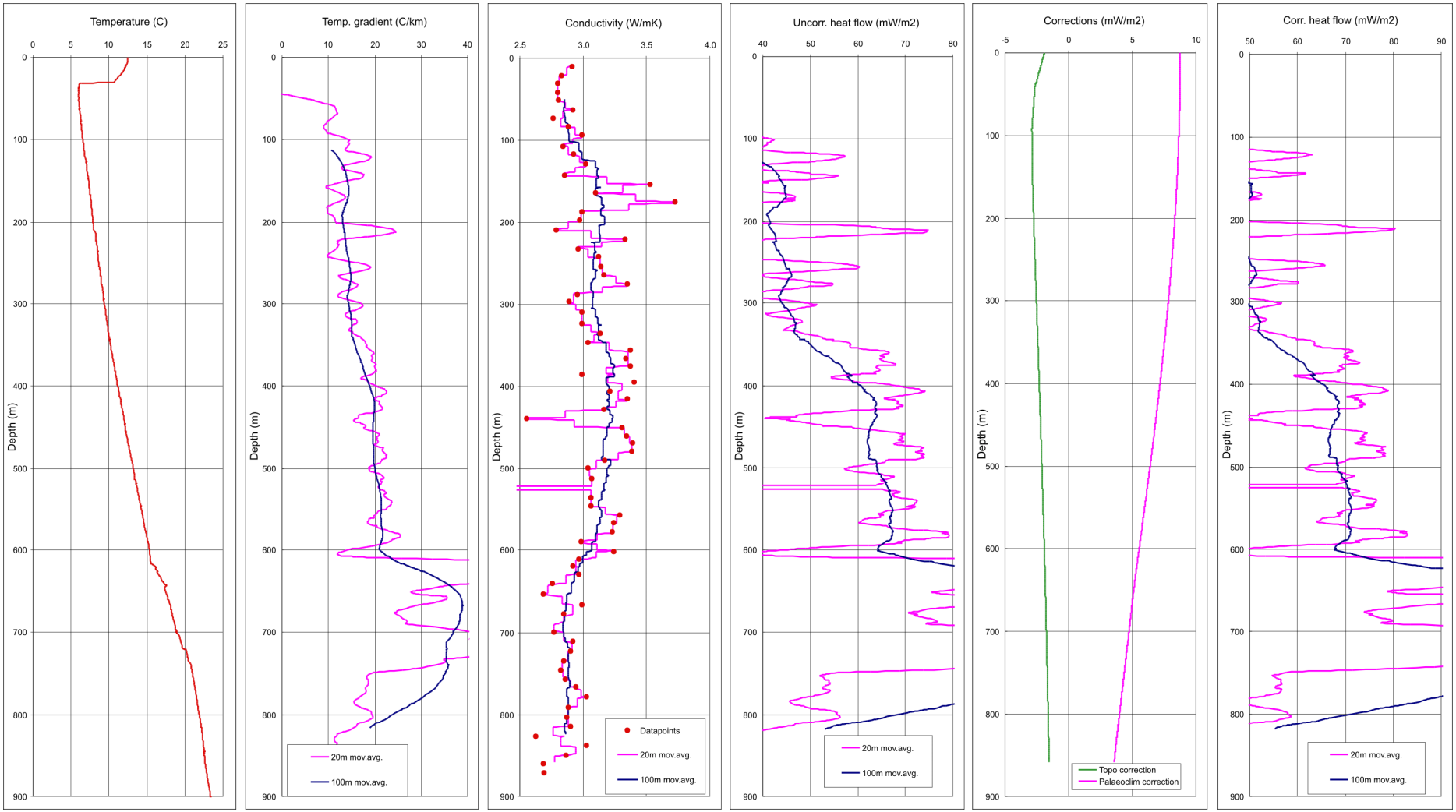

Figure 7.13b. Plots showing temperature, thermal gradient, thermal conductivity, uncorrected and corrected heat flow, and topographic and palaeoclimatic corrections at the heat flow site at Hurdal, borehole Dh03.

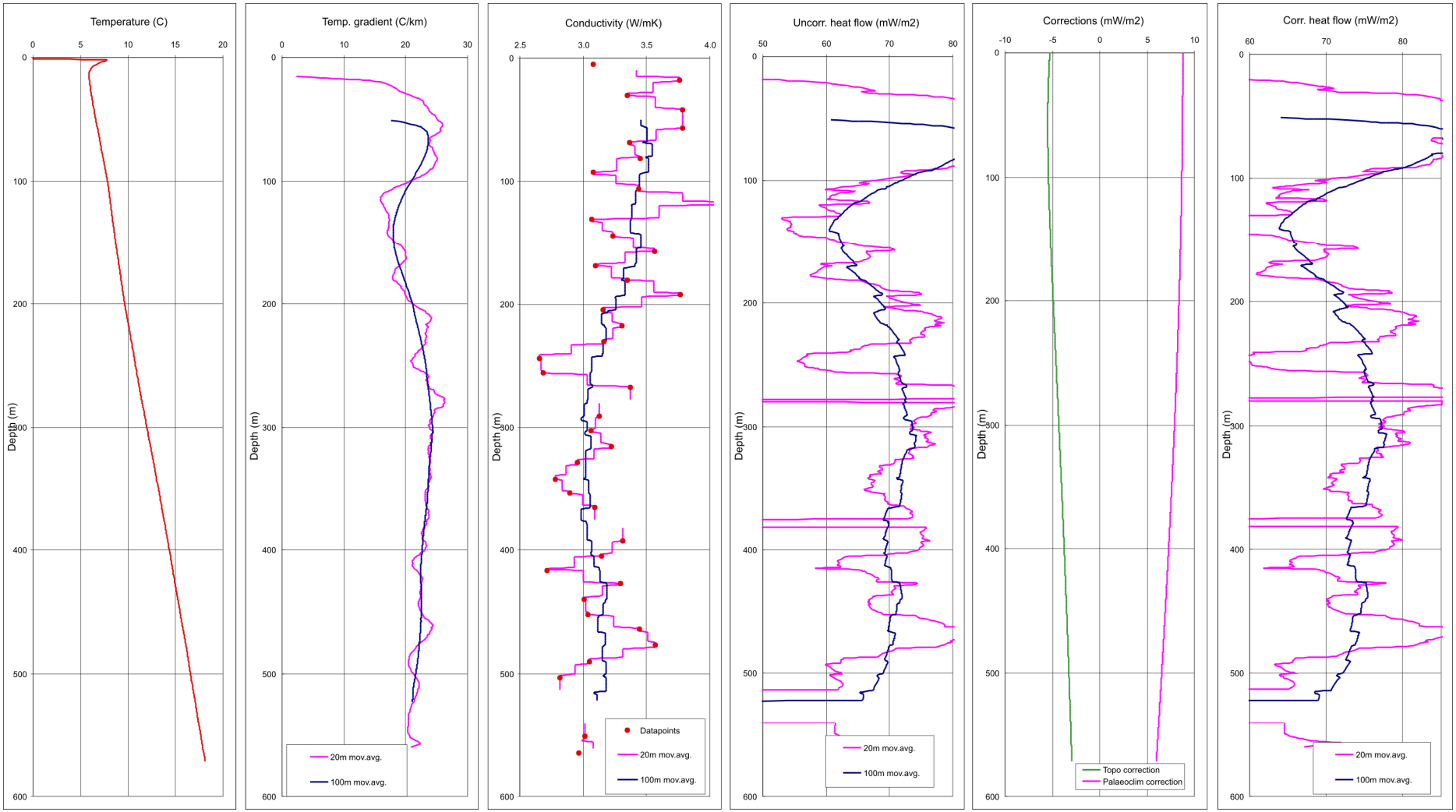

Figure 7.13c. Plots showing temperature, thermal gradient, thermal conductivity, uncorrected and corrected heat flow, and topographic and palaeoclimatic corrections at the heat flow site at Hurdal, borehole Dh05.

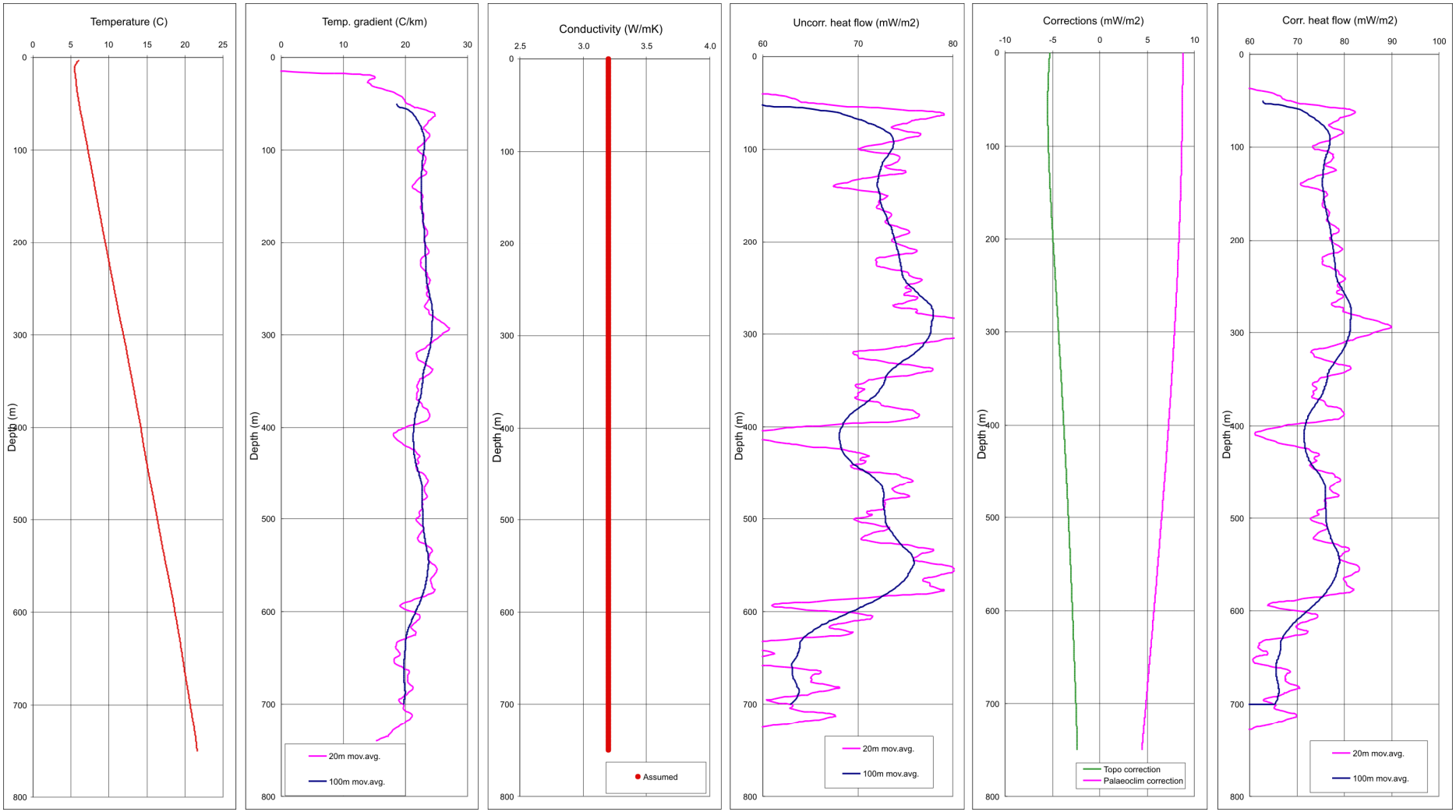

Figure 7.13d. Plots showing temperature, thermal gradient, thermal conductivity, uncorrected and corrected heat flow, and topographic and palaeoclimatic corrections at the heat flow site at Hurdal, borehole Nordli.

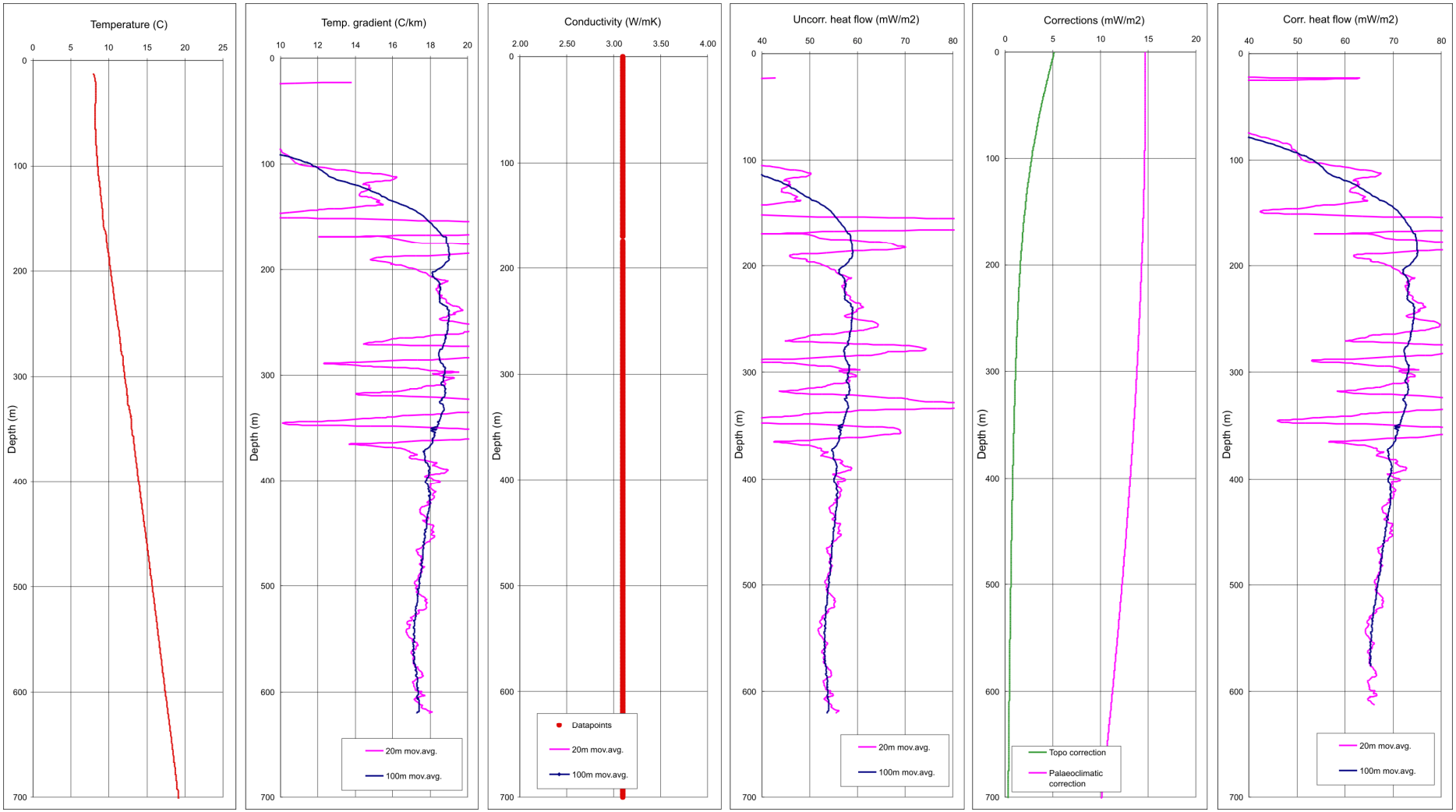

Figure 7.14. Plots showing temperature, thermal gradient, thermal conductivity, uncorrected and corrected heat flow, and topographic and palaeoclimatic corrections at the heat flow site at Fredrikstad.

Table 7.1 Details of the heat flow sites.

Site	Coordinates	UTM Zone[1]	Elevation (m)	Vertical depth (m)	Interval[2] (m)	Dip[3]	Heat flow[4] (mW/m^2)	
							Average	Range
Berger	615271 6654660	32	152	647	250–647	5.8	**49**	42–54
Lærdal tunnel							**47**	n.a.
Lærdal1	In tunnel		245	52	n.a.	0	n.a.	n.a.
Lærdal2	In tunnel		245	44	n.a.	0	n.a.	n.a.
Aurland	410507 6761624	32	1261	49	n.a.	0	n.a.	n.a.
Løkken	530797 7001453	32	310	985	300–985	16.5	**57**	49–66
Hjerkinn	532846 6904727	32	960	648	300–648	20.7	**42**	24–54
Aure	486454 7031460	32	25	355	150–355	17.1	**66**	57–70
Arnestad	583546 6630237	32	11	625		24.8		
Hamar	612597 6744216	32	221	816	200–500 620–816	0	**58**	48–70
Hurdal							**73**	
Hurdal Dh 02	610379 6707593	32	321	783	370–500	32.1	70	69–72
Hurdal Dh 03	610565 6707483	32	307	903	420–600	27.3	69	66–71
Hurdal Dh05/05B	610273 6707118	32	270	572	200–500	11.6	75	71–78
Hurdal Nordli	610093 6707213	32	276	750	100–550	0	77	72–82
Fredrikstad	610109 6563857	32	28	733	180–330	0	**73**	72–75

[1]WGS84.

[2]Vertical depth interval used in heat flow calculation.

[3]Deviation (°) from vertical.

[4]Corrected for topographic and palaeoclimatic effects. See text and figures for details re. thermal conductivity, gradients and magnitude of corrections. The range of calculated heat flow values relates to the 20 m interval calculations; the range of values from the 100 m interval calculations is obviously smaller.

Table 7.2 Palaeoclimatic histories used to correct the heat flow data.

Time (ka)	Berger	Lærdal	Løkken	Hjerkinn	Aure	Arnestad	Hamar	Hurdal	Fredrikstad
>220e3	3.9	0.2	2.8	-1.4	5.6	5.6	3.3	2.7	6.8
-220e3	-1	-1	-2.2	-1	0.6	-1	-1	-1	1.8
-210e3	-1.1	-4.8	-2.2	-6.4	0.6	0.6	-1.7	-2.3	1.8
-200e3	-1	-1	-2.2	-1	0.6	-1	-1	-1	-1
-190e3	-1.1	-4.8	-2.2	-6.4	0.6	0.6	-1.7	-2.3	1.8
-165e3	-1	-1	-1	-1	-1	-1	-1	-1	-1
-160e3	-1.1	-4.8	-2.2	-6.4	0.6	0.6	-1.7	-2.3	1.8
-154e3	-1	-1	-1	-1	-1	-1	-1	-1	-1
-147e3	-1.1	-4.8	-2.2	-6.4	0.6	0.6	-1.7	-2.3	1.8
-143e3	-1	-1	-1	-1	-1	-1	-1	-1	-1
-140e3	-1	-1	-1	-1	-1	-1	-1	-1	-1
-137e3	-1	-1	-1	-1	-1	-1	-1	-1	-1
-134e3	-1.1	-1	-2.2	-1	0.6	0.6	-1	-1	1.8
-130e3	-1	-1	-1	-1	-1	-1	-1	-1	-1
-122e3	-1	-1	-2.2	-1	0.6	-1	-1	-1	-1
-120.5e3	-1.1	-4.8	-2.2	-6.4	0.6	0.6	-1	-2.3	1.8
-118e3	3.9	0.2	2.8	-1.4	5.6	5.6	3.3	2.7	6.8
-110e3	-1	-1	-2.2	-1	0.6	-1	-1	-1	1.8
-100e3	-1.1	-4.8	-2.2	-6.4	0.6	0.6	-1.7	-2.3	1.8
-90e3	-1	-1	-2.2	-1	0.6	-1	-1	-1	-1
-80e3	-1.1	-4.8	-2.2	-6.4	0.6	0.6	-1.7	-2.3	1.8
-65e3	-1	-1	-1	-1	-1	-1	-1	-1	-1
-50e3	-1.1	-4.8	-2.2	-6.4	0.6	0.6	-1.7	-2.3	1.8
-44e3	-1	-1	-1	-1	-1	-1	-1	-1	-1
-37e3	-1.1	-4.8	-2.2	-6.4	0.6	0.6	-1.7	-2.3	1.8
-33e3	-1	-1	-1	-1	-1	-1	-1	-1	-1
-30e3	-1	-1	-1	-1	-1	-1	-1	-1	-1
-27e3	-1	-1	-1	-1	-1	-1	-1	-1	-1

Time (ka)	Berger	Lærdal	Løkken	Hjerkinn	Aure	Arnestad	Hamar	Hurdal	Fredrikstad
-24e3	-1.1	-1	-2.2	-1	0.6	0.6	-1	-1	1.8
-20e3	-1	-1	-1	-1	-1	-1	-1	-1	-1
-12e3	-1	-1	-2.2	-1	0.6	-1	-1	-1	-1
-10.5e3	-1.1	-4.8	-2.2	-6.4	0.6	0.6	-1	-2.3	1.8
-8e3	3.9	0.2	1.8	-1.4	5.6	5.6	3.3	2.7	6.8
0	3.9	0.2	2.8	-1.4	5.6	5.6	3.3	2.7	6.8

Initial conditon (i.e. >220 ka) is a steady-state condition with a surface temperature equal to present-day-temp.
Temperatures during stadials are set at -1C (i.e., temp at base of ice).
Temperatures during interstadials are set at 5C below present-day temperature.

Table 7.3 U, Th and K data and heat production from some of the wells where heat flow has been measured.

Sample	Depth (m)	Rock type	Density (kg/m^3)	U (ppm)	Th (ppm)	K (wt.%)	Heat production (μW/m^3)
Arnestad, chemical data from borehole cuttings.							
34101	36	Shale	2700	2.31	7.44	2.27	1.3
34102	102	Shale	2700	2.25	4.82	1.52	1.1
34103	174	Shale	2700	20.0	14.3	3.79	6.5
034104A	246	Shale	2700	8.41	14.1	2.17	3.3
034105A	306	Shale	2700	24.4	17.9	4.12	7.9
034106A	348	Alunskifer	2700	109	14.9	4.29	29.5
034107A	408	Alunskifer	2700	116	16.0	3.50	31.2
034108A	468	Shale	2700	39.5	13.2	3.08	11.4
034109A	558	Granite	2650	5.06	15.6	4.57	2.8
034110A	606	Granite	2650	6.89	15.4	4.47	3.3
034111A	684	Granite	2650	6.64	19.5	4.63	3.5
Hjerkinn							
G98.2	98.2	Amphibolite	2800	0.24	0.66	0.20	0.1
G191.2	191.2	Mica schist	2850	0.65	0.96	1.28	0.4
G270.5	270.5	Mica schist	2800	1.9	5.14	1.14	1.0
G390.3	390.3	Mica schist	2850	1.18	3.83	0.93	0.7
G550	550	Intermediate gneiss	2800	2.12	6.68	2.30	1.3
G649.2	649.2	Amphibolite	2900	0.06	0.06	0.17	0.0
G700.3	700.3	Mica schist	2750	1.45	4.82	1.39	0.9
Aure							
AURE1		Granodioritic gneiss	2750	1.10	9.69	2.76	1.2
AURE2		Dioritic gneiss	2800	2.56	7.45	1.54	1.4
Lærdal tunnel							
Lærdal 1							
L1-2.8	2.8	Granodioritic gneiss	2750	0.60	2.28	1.80	0.5
L1-35.3	35.3	Granodioritic gneiss	2750	1.87	25.3	2.17	2.5
L1-46.8	46.8	Dioritic gneiss	2850	0.74	7.01	3.10	1.0
Lærdal 2							
L2-14.5	14.5	Dioritic gneiss	2700	1.41	4.61	1.78	0.8
L2-37.8	37.8	Dioritic gneiss	2690	1.47	9.21	5.79	1.6
L2-42.3	42.3	Granitic gneiss	2600	2.05	18.0	3.99	2.1
Aurland							
Au3	3	Mica schist	2800	1.71	7.84	3.97	1.4
Au24.6	24.6	Granitic gneiss	2650	1.86	8.50	4.98	1.5
Au48	48	Granitic gneiss	2620	4.71	8.67	4.21	2.1
Løkken							
Lø193.3	193.3	Gabbro	2900	0.07	0.07	0.22	0.05
Lø278.3	278.3	Gabbro	3000	0.05	0.07	0.07	0.03
Lø607.6	607.6	Gabbro	3000	0.02	0.03	0.23	0.03
Lø718.8	718.8	Gabbro	3000	0.02	0.02	0.04	0.01
Lø864.1	864.1	Hølonda porphyry	2880	3.86	14.0	0.35	2.13
Lø877.8	877.8	Hølonda porphyry	2880	4.20	14.4	0.24	2.24
Lø899	899	Hølonda porphyry	2900	3.41	11.7	0.39	1.85
Lø929.1	929.1	Gabbro	3020	0.07	0.12	0.17	0.05
Lø997.8	997.8	Gabbro	2980	0.08	0.11	0.61	0.09
Lø1030.1	1030.1	Gabbro	2890	0.02	0.05	0.39	0.05

8 HEAT FLOW DATA FROM NORTHERN NORWAY

Christophe Pascal, Harald Elvebakk, Odleiv Olesen & Bjørn Wissing, NGU

8.1 Introduction

The present chapter presents in detail complementary heat flow data from northern Norway (Nordland). Previous data from that area were merely scarce and very poor in quality. Four lake measurements and four measurements in drilholes resulted in an average heat flow of 45.3 mW/m^2 (Hänel et al. 1979). Because lake measurements are extremely sensitive to near lake-bottom temperature changes, amongst other factors (Hänel 1979), and because drillhole measurements were made at shallow depths and not corrected from paleoclimatic disturbances, it was of prime importance to acquire more reliable heat flow data before attempting any modelling effort offshore.

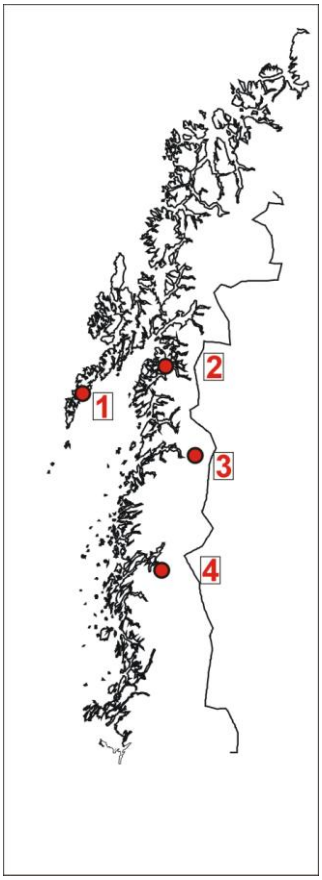

Figure 8.1. Location map of the Nordland wells: 1-Leknes, 2-Drag, 3-Sulitjelma, 4-Bleikvassli.

8.2 Data acquisition

Thermal logging was made during summer 2006 in Bleikvassli, Sulitjelma, Leknes and Drag (Fig. 8.1, Table 8.1). The two former wells were pre-existing mining wells whereas the two later were drilled for the project by the Finnish company Suomen Malmi Oy in 2005. Core material was available for sampling and for thermal conductivity measurements for all wells except for the Bleikvassli one, where conductivities have been tentatively extrapolated from a neighbouring well. The procedures related to thermal logging and measurement of thermal conductivities are extensively described in the Chapters 4 & 6 of the present report. An overview of the well coordinates and depths is given in Table 8.1.

8.3 Heat flow determinations

8.3.1 Analysis of temperature logs

The temperature logs together with measured thermal conductivities are shown in Fig. 8.2 (data corrected from deviation). A first analysis of the temperature logs reveals that for the first three wells (i.e. Leknes, Drag and Sulitjelma) their respective thermal gradients are almost constant for various hundreds of meters. In detail, the temperature gradient as well as the thermal conductivity at Leknes remains stable from ~50 m down to ~680 m depth. An abrupt decrease in thermal gradient occurs below ~680 m associated with a sharp increase in thermal conductivity (Fig. 8.2). Near the bottom of the well the gradient increases again while the conductivity returns to values similar to the ones measured in the upper parts. At Drag, both the thermal gradient and the thermal conductivity remain stable from ~50 m depth down to the bottom of the well. A sharp offset of the temperature plot is, however, seen at ~200 m depth, the plot being offset back but less sharply at ~300 m depth. There is no apparent correlation between changes in thermal conductivity and the observed offsets. The offsets could be related to water inflow/outflow in the drillhole although no clear signal of it has been detected on the water electrical conductivity log. For the Sulitjelma drillhole, the temperature log seems to gradually bend upwards when moving from ~25 m depth down to ~960 m (well bottom). It is interesting to note that this upward bending (i.e. increase of the thermal gradient) appears at first view to be correlated with the observed gradual decrease in thermal conductivity (Fig. 8.2). Frequent changes in the thermal gradient are seen in the Bleikvassli borehole. Those seem to be correlated to changes in thermal conductivity at depth but also to climatic or eventually hydrologic disturbances near the surface (i.e. note the near constant temperature from the surface down to ~100 m.

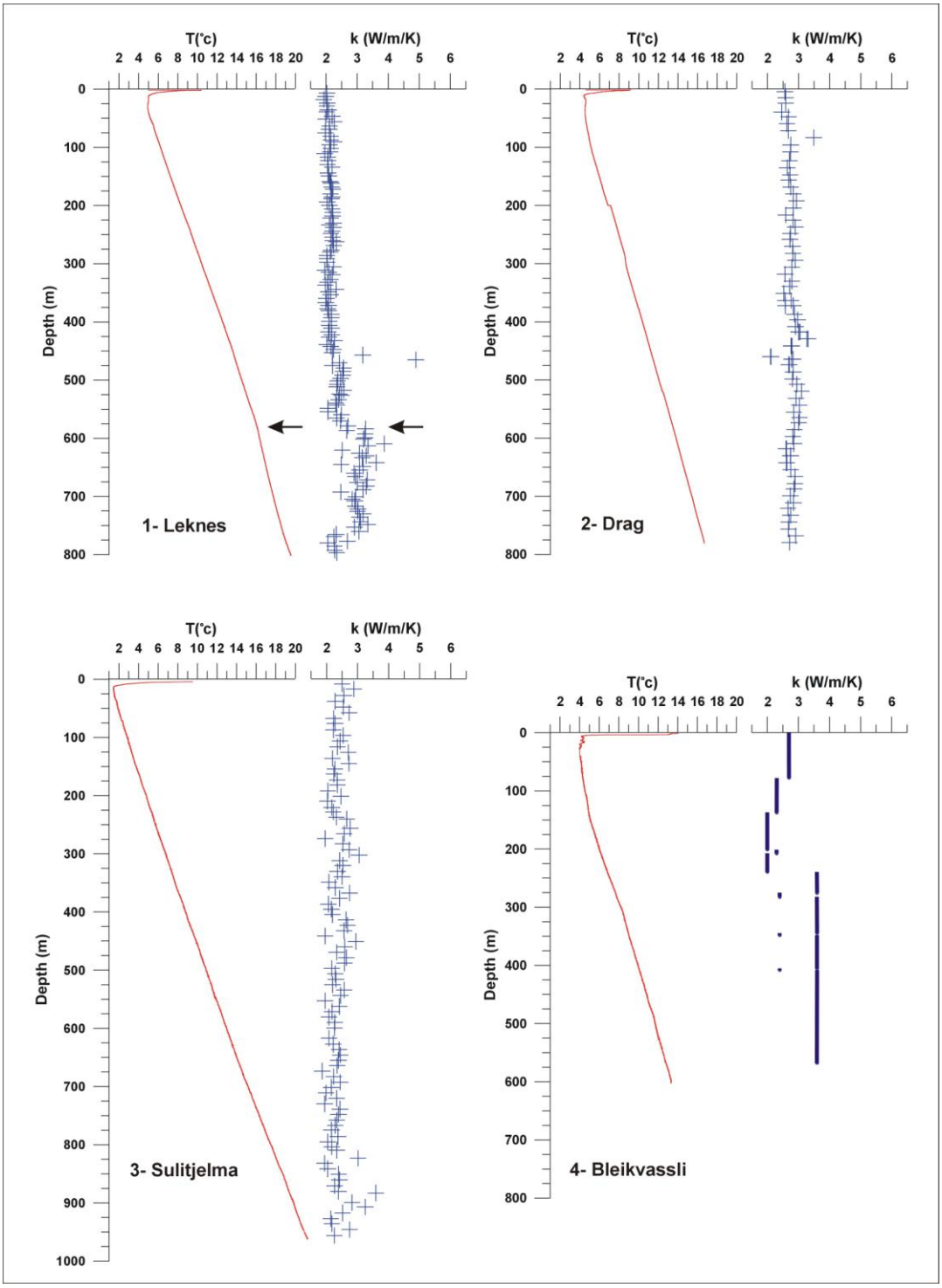

Figure 8.2. Temperature logs and measured thermal conductivities. Note the very good correlation between the decrease in gradient and the increase in conductivity at Leknes.

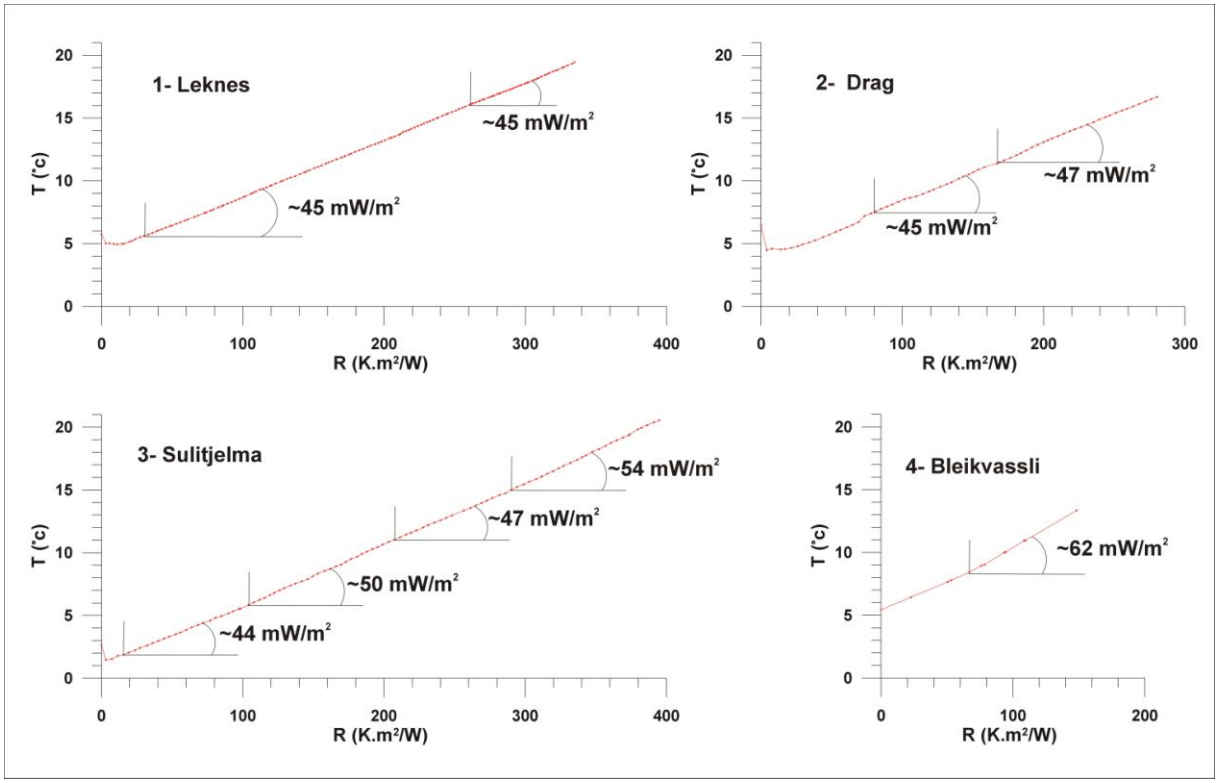

Figure 8.3. Bullard plots and estimated heat flow (uncorrected) in the four wells.

In order to detect eventual departures from steady-state thermal conditions in the wells, we used the "Bullard Method" (Bullard 1939). The Bullard Method is based on the concept of thermal resistance expressed as:

$$R(z_i) = \Delta z_i / k_i \qquad (8.1)$$

where k_i is the thermal conductivity of the rocks located in the depth interval Δz_i.
Temperature at depth z can be written as a function of heat flow and thermal resistance (for a detailed description of the method see e.g. Beardsmore & Cull 2001):

$$T(z) = T_0 + \sum_{i=1}^{N} q(\Delta z_i).R(z_i) \qquad (8.2)$$

where $q(\Delta z_i)$ is the heat flowing through the depth interval Δz_i, N the number of depth intervals in between the surface and depth z and T_0 mean temperature at the surface.
Temperature versus thermal resistance plots are consequently called Bullard plots. From equation (8.2) it is implicit that if the heat flow is constant through the whole depth section

sampled by the well (i.e. steady-state thermal conditions apply), the corresponding Bullard plot should be a line and the slope of the line should give the value of this constant heat flow. However, if heat flow variations occur in the well (i.e. the thermal field is not in equilibrium whatever the reasons are) the corresponding Bullard plot should be non-linear.

Fig. 8.3 shows the Bullard plots constructed from the temperature and conductivity data shown in Fig. 8.2. As expected the plots are concave upwards for low thermal resistance values (i.e. heat flow decreases close to the surface) and reflect the bending of the respective thermal logs when approaching the surface (Fig. 8.3). This pattern, that we attribute to recent climate amelioration in Scandinavia (e.g. Paranis 1975), is particularly pronounced in Drag but surprisingly restricted to the lowermost resistance values in Leknes and Sulitjelma. The Bullard plot of the data from the Bleikvassli well also suggests a concave upward shape, in agreement with the bending of its corresponding temperature log. However as a consequence of the scarcity of the used conductivity data (i.e. extrapolated from measurements on cores from a neighbouring well) the gradual nature of the bending of the Bullard plot disappears.

At first glance, all our Bullard plots quickly depict very regular lines when increasing thermal resistance (i.e. when moving downwards into the corresponding wells). In order to estimate eventual heat flow variations inside each well, we calculated series of regression lines fitting the linear trends seen on the Bullard plots. Noteworthy in doing so we selected exclusively data below the depth levels that are obviously affected by near-surface disturbances (i.e. short-term temperature variations at the surface and water circulation). All regression lines showed an excellent fit with the data and were characterised by regression coefficients higher than 0.99. The most spectacular result is obtained for the Leknes well where the heat flow is remarkably stable from ~70 m depth down to the bottom of the well at ~800 m depth and equals 45 mW/m^2 (Fig. 8.4). Heat flow values in the Drag well can also be considered as stable as long as they only vary by 2 mW/m^2 (i.e. from 45 to 47 mW/m^2) in between the two selected sections of the drillhole (respectively from 225 m to 440 m depth and from 440 m to 780 m depth). Furthermore, the 45 mW/m^2 value is merely contaminated by local fluid circulations in fractures as suggested by the two sharp changes in thermal gradient at ~200 and ~300 m depth (Fig. 8.3). The situation is totally different for the Sulitjelma drillhole, for which heat flow values seem to increase gradually from 44 mW/m^2 (at the 30 to 240 m depth range) to 54 mW/m^2 in the deepest parts of the well (i.e. ~700 to 960 m depth range), passing by 50 mW/m^2 and 47 mW/m^2 in the central parts of the well (from 250 to 500 m depth and

500 to 700 m depth respectively). Note that the slight decrease in heat flow from 50 to 47 mW/m^2 is not considered to be significant. The observed increase in heat flow with depth strongly suggests that the geothermal gradient, at the site of the Sulitjelma well, is disturbed by paleoclimate and/or topographic effects. The single heat flow value obtained for Bleikvassli (i.e. 62 mW/m^2) is significantly higher than for the other wells but this latter value remains uncertain. Because of the poorly constrained conductivity model that is used here, a fine analysis of its corresponding Bullard plot is not possible. Furthermore, the sharp break in slope seen in the corresponding Bullard plot could result from overestimation of the thermal conductivity in the deepest parts of the well.

8.3.2 Topographic and paleoclimatic corrections

In order to carry out topographic corrections, we used 3D finite-element numerical models (Fig. 8.4). The top surfaces of the models were built according to their respective digital elevation models in the four studied areas. The resolution of the input surface topographies was set to 200 m. Both the horizontal dimensions of the models (i.e. typically 10 to 20 km) and the selected resolution in topography were adopted after a qualitative check of the corresponding topographic maps and in agreement with the wavelength of the expected heat flow perturbation from the major topographic features, that were detected on the maps, and the penetration depth of the wells. In order to avoid any edge effect the well locations were placed at the centre of their respective FE models. After different modelling tests, we set up the base of the models at five km depth. The models aimed to simulate thermal steady-state situations and an average thermal conductivity for the whole modelled volume at each studied site was inferred from the measurements shown in Fig. 8.3. Boundary conditions consist in elevation-dependent temperatures at the surface and constant heat flow at the bottom of the models.

A lapse rate of 6.5 °C/km (i.e. decrease of air temperature with elevation) was applied (Powell et al. 1988). For each studied site, we used the estimated mean ground temperature from extrapolation of the corresponding "Bullard line" to the surface (Fig. 8.3, Table 8.2), and the elevation of the site as reference temperature and reference altitude respectively. After different tests the basal heat flow for each site was adjusted to the its most reasonable value. Noteworthy, the estimated topographic corrections are not sensitive to the applied basal heat flow values, provided that the latter remain in a reasonable range of values (i.e. in

between 40 and 70 mW/m^2) with respect to our uncorrected heat flow estimations (Fig. 8.3, Table 8.1).

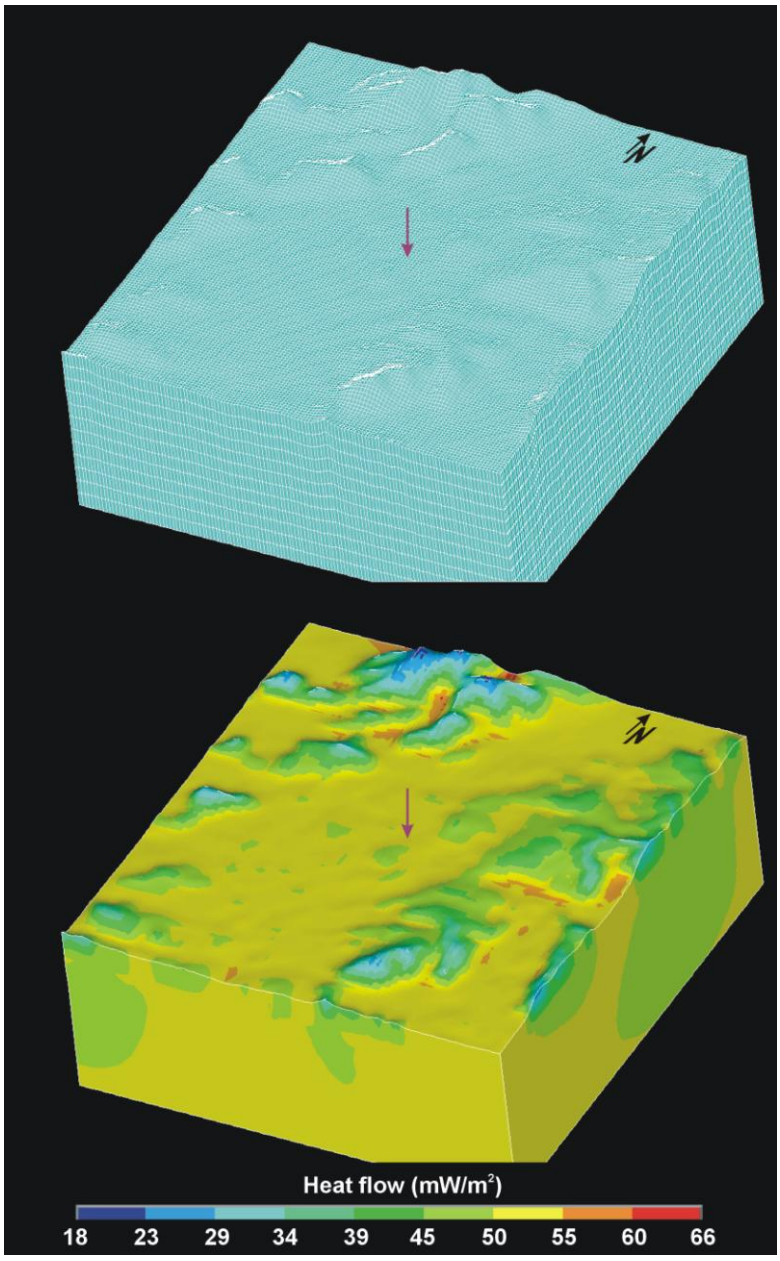

Figure 8.4. Example of 3D topographic corrections using finite-element methods (Leknes). Upper panel: numerical mesh, lower panel: computed heat flow. Purple arrows depict the location of the well.

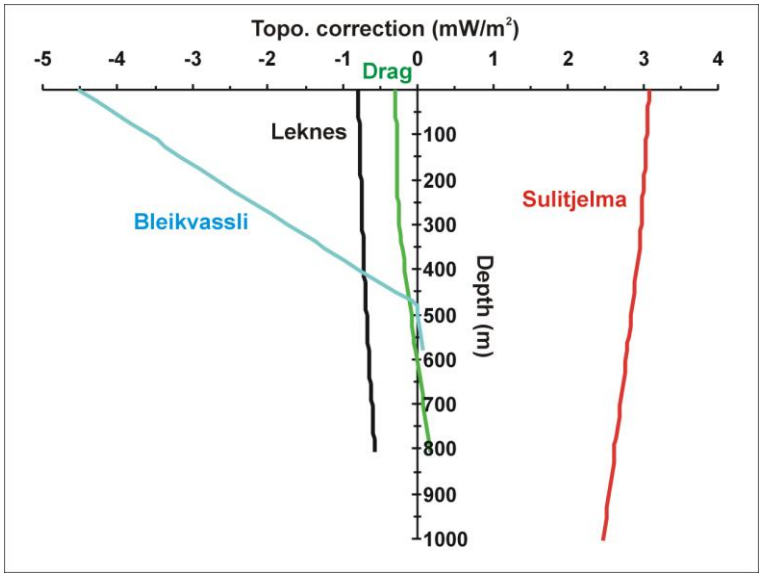

Figure 8.5. Topographic corrections applied to heat flow data for the four studied drillholes.

The results of the different models are 3D heat flow distributions (Fig. 8.4) from which we extracted the calculated topographic heat flow perturbation as a function of depth and for each studied well (Fig. 8.5). As expected the correction to be applied is positive when the drillhole is located on mountains (i.e. Sulitjelma) and negative when located in valleys (i.e. Leknes, Drag, and Bleikvassli). Also intuitively expected are the modest corrections to be applied at Leknes and Drag (i.e. less than 1 mW/m^2). A crude estimate on the systematic error attached to our heat flow values based solely on the accuracy of measured diffusivities (i.e. ±5%, Midttømme et al., Chapter 6 in the present report) is ±2 mW/m^2 and convinces us that topographic corrections at Leknes and Drag can simply be ignored. In contrast, the respective corrections to be applied at Sulitjelma and Bleikvassli are more significant. It is interesting to note that the topographic disturbance at Sulitjelma is relatively constant from the top to the bottom of the well (i.e. less than 0.6 mW/m^2 of variation) and cannot explain by itself the gradual heat flow increase detected on the Bullard plot (Fig. 8.3). The variation of the topographic perturbation in the Bleikvassli drillhole is much more dramatic and could eventually explain the sharp break in slope seen on its corresponding Bullard plot, but it is difficult to reach a firm conclusion here.

Because subsurface temperatures are mostly affected by local and microclimatic factors, paleoclimatic corrections cannot be carried out using a standardised procedure and a fine analysis of the available temperature logs, where paleoclimatic signals can eventually be detected, is a prerequisite to any attempt aiming at correcting estimated heat flow values (e.g.

Powell et al. 1988). In full agreement with this statement we firstly estimated the present-day mean ground temperatures (usually higher than mean air temperatures), from our Bullard plots (Table 8.2) in order to reconstruct back in time the temperature history. Heat flow disturbances due to varying temperatures through time were calculated using the semi-analytical formula (derived from e.g. Powell et al. 1988):

$$\Delta q(z) = \sum_{i=1}^{N} \Delta q(t_i, z) = \sum_{i=1}^{N} k\Delta T_i \frac{\exp(\frac{-z^2}{4\kappa t_i})}{\sqrt{\pi \kappa t_i}} \qquad (3)$$

where k and κ are respectively thermal conductivity and diffusivity as determined from laboratory measurements (Midttømme et al. Chapter 6 in the present report) and ΔT_i is instantaneous temperature change at time t_i BP.

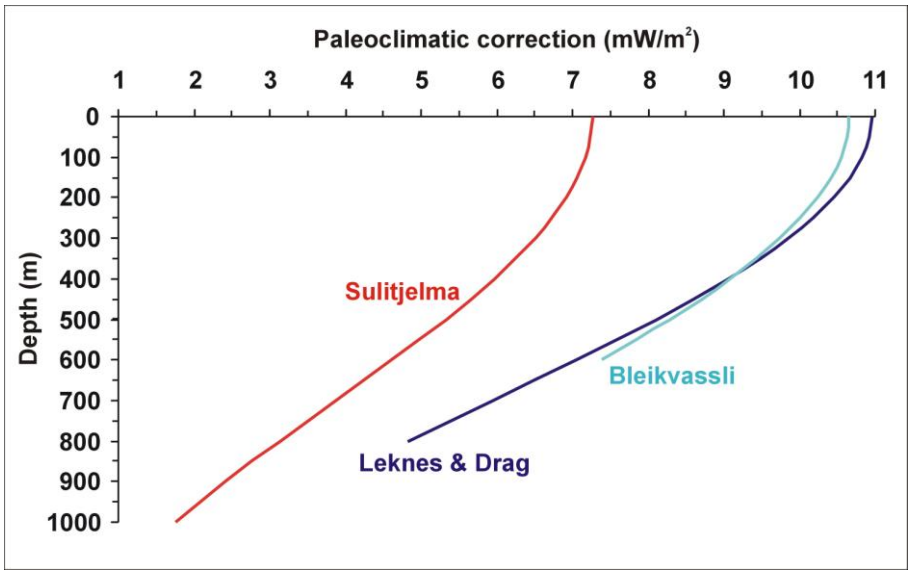

Figure 8.6. Tentative paleoclimatic corrections for the four studied drillholes.

As a starting point we tentatively adopted the scheme proposed by Slagstad et al. (Chapter 7 in the present report). The results suggest that, in Leknes, Drag and Sulitjelma, we should observe a variation in heat flow values by 5 mW/m^2 from 200 m depth down to the respective bottoms of the wells (Fig. 8.6). Therefore and comparing these estimates with the actual heat flow variations in these three wells (i.e. no variation for Leknes and Drag and 4 to 7 mW/m^2 for Sulitjelma, Fig. 8.3), it appears that the paleoclimatic corrections are clearly overestimated in the case of the Leknes and Drag drillholes but represent acceptable estimates in the case of the Sulitjelma one. It is difficult to judge of the validity of the corrections at Bleikvassli, but, based on the existing geographical affinities with Sulitjelma,

we can reasonably assume that the paleoclimatic scheme adopted previously is also valid here. In brief and taking results from the deepest parts of the wells, corrected heat flow values from both paleoclimatic and topographic effects are ~59 and ~69 mW/m^2 in Sulitjelma and Bleikvassli, respectively.

Concerning Leknes and Drag it is obvious that our first paleoclimatic model leads to erroneous corrections, if applied those corrections would result in non steady-state heat flow in the two wells. Bearing in mind that heat flow variations that can be observed in wells above ~1 km depth are mainly related to the latest major climatic change (i.e. final glacier retreat at ~8 ka), we calculated a set of eventual corrections testing different values for this last temperature increase but keeping unchanged the rest of the temperature history (Fig. 8.7). The results suggest that in order to explain the very constant heat flow values derived, in particular, from the Leknes well, the temperature increase had to be less than $\Delta T = 2°C$ and, therefore, the paleoclimatic correction is negligible. The case $\Delta T = 0°C$ leads to a negative correction (due to the remaining effects of the previous cooling) but, in absence of other constrains, we prefer to exclude this latter solution that would suggest that there has not been any climatic amelioration in Nordland at the Pleistocene-Holocene transition. In conclusion, both topographic and paleoclimatic corrections seem to be negligible at Leknes and Drag.

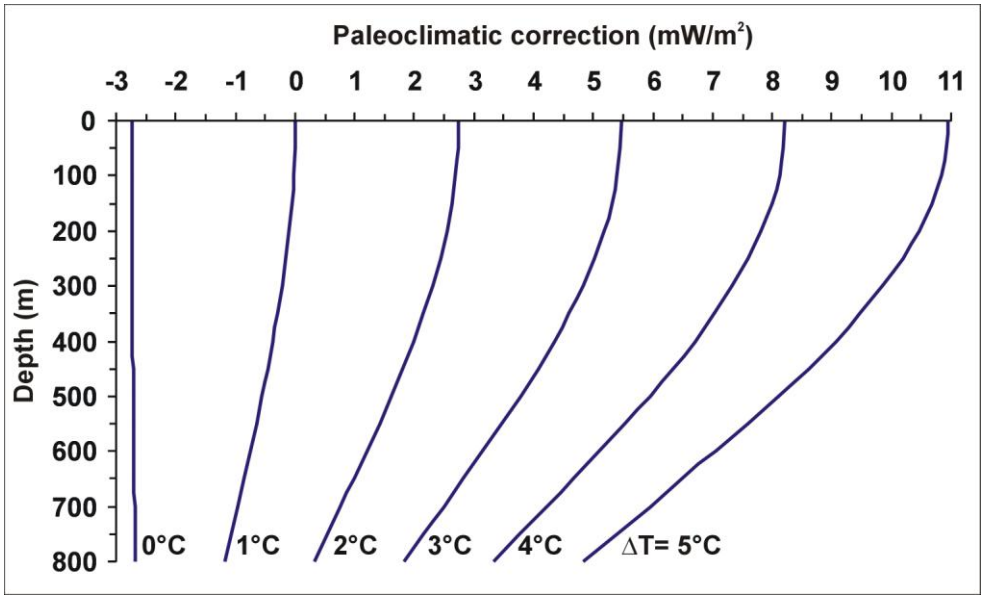

Figure 8.7. Computed paleoclimatic corrections at Leknes and Drag in function of temperature increase at t = 8 ka other parameters of the paleoclimatic history remaining constant (Table 8.2).

8.4 Conclusions

Heat flow calculations have been carried out on four wells located respectively in Leknes, Drag, Sulitjelma and Bleikvassli and with penetration depths ranging from ~600 m to ~960 m. Core material was available for the three first wells and has been densely sampled for thermal conductivity measurements resulting in highly accurate heat flow determinations.

Fine analysis of the thermal logs together with modelling of topographic and paleoclimatic perturbations showed that heat flow values are stable and relatively low in Leknes and Drag (i.e. 45 to 47 mW/m^2) but in the range of average continental heat flow values in Sulitjelma (i.e. 59 mW/m^2). Because of the lack of core material in Bleikvassli the corresponding heat flow value (i.e. 69 mW/m^2) is regarded as highly uncertain.

The low heat flow at Leknes is in agreement with the very depleted in heat producing elements crust of the Lofoten Archipelago (Fig. 8.1 and Slagstad et al., Chapter 2 in the present report). Conversely the "normal" heat flow value found in Sulitjelma goes along with the standard crustal heat generation values determined there. In brief, the significant heat flow reduction observed between Leknes and Sulitjelma (and possibly Bleikvassli as well) is very well correlated with the observed reduction from ~0.1 $\mu W/m^3$ to more than 1.5 $\mu W/m^3$ in crustal heat generation (Slagstad et al., Chapter 2 in the present report), supporting the idea that the most significant heat flow variations are indeed related to changes in basement composition. However, no significant increase of heat flow is observed between Leknes and Drag, whereas a tremendous increase in heat generation seems to take place between the two places (Slagstad et al., Chapter 2 in the present report). The very high heat generation values at Drag are related to the Tysfjord granite of TIB affinity. Our heat flow data together with results from potential field modelling (Olesen et al. 2002) suggest that only a thin layer of the granite might be present at Drag, the remaining crust being similar to the rocks found in Leknes but also in the vicinity of Drag.

Table 8.1 Drillhole data and estimated heat flow values.

Site	Coordinates[1]	Elevation (m)	Vertical depth (m)	Interval[2] (m)	Dip[3]	Heat flow (mW/m^2)	
						Uncorrected	Corrected
Leknes	7561940 443695	27	800	70-800	0	45	45
Drag	7547350 542680	24	780	440-780	0	47	47
Sulitjelma	540599 7443493	805	960	700-960	7-18	54	59
Bleikvassli (Bh 13-98)	7312764 448397	421	602	400-602	46-23	62?	69?

[1]UTM zone 33, WGS84.

[2]Vertical depth interval used in heat flow calculation.

[3]Deviation (°) from vertical (from top to bottom of the well).

Table 8.2 Tentative paleoclimatic model (see details in Slagstad et al., Chapter 7 in the present report).

Time (ka)	ΔT (°C) at Leknes and Drag	ΔT (°C) at Sulitjelma	ΔT (°C) at Bleikvassli
8	+5	+5	+5
10.5	0	-3	-1
12	0	0	0
20	0	+3	+1
24	0	-3	-1
27	0	3	+1
30	0	-3	-1
33	0	+3	+1
37	0	-3	-1
44	0	+3	+1
50	0	-3	-1
65	0	+3	+1
80	0	-3	-1
90	0	+3	+1
100	0	-3	-1
110	-5	-2	-4
118	+5	+5	+5
121	0	-3	-1
122	0	0	0
130	0	+3	+1
134	0	-3	-1
137	0	+3	+1
140	0	-3	-1
143	0	+3	+1
147	0	-3	-1
154	0	+3	+1
160	0	-3	-1
165	0	+3	+1
190	0	-3	-1
200	0	+3	+1
210	0	-3	-1
220	-5	-2	-4

Present-day temperatures (i.e. starting temperatures from 8ka back in time) from analysis of the borehole data are ~4°C at Leknes and Drag, ~1°C at Sulitjelma and ~3°C at Bleikvassli.

9 DEPTH TO CRYSTALLINE BASEMENT ON THE NORWEGIAN CONTINENTAL SHELF

Odleiv Olesen, Jörg Ebbing & Jan Reidar Skilbrei, NGU

9.1 Introduction

The basement depth surface constitutes an important horizon in a complete 3D crustal model. Ebbing & Lundin (2005), Olesen (2005) and Skilbrei (2005) compiled depth to crystalline basement maps from the North Sea, Norwgian Sea and the Barents Sea, respectively, in the 2005 Kontiki Report (Olesen et al. 2005). A depth to Precambrian basement map for northern Norway was reported by Ebbing et al. (2006c) in the 2006 Kontiki Report (Olesen et al. 2006a).

9.2 Potential field data

Aeromagnetic data from Norway and the adjacent continental margin have been compiled earlier (Skilbrei et al. 1991a, Olesen et al. 1997b, 2006b). The pre-1996 surveys were reprocessed during the periods of 1999-2001 and 2003-2004 using the median levelling and loop closure methods (Mauring et al. 2002, 2003) and these new versions of the NGU-69/-70/-73/-74/-75, Fairey-71, TAMS-84, BAMS-85, Hunting-86, BSA-87, SPA-88, LAS-89, Viking-93 and NAS-94, have been included in the present compilation. Statoil financed parts of this reprocessing within the Dragon database project (DiRect Access to Geophysics On the Net) in 1999/2000. Reprocessed data from the mid-Norwegian continental margin have been published by Olesen et al. (2002, 2004b) and Skilbrei et al. (2002, 2005) while the North Sea and Barents Sea data-sets remain unpublished. The more recent surveys SAS-96, VGVB-94, MBAM-97, VAS-97, VBE-AM-00, RAS-03, JAS-05, BAS-06 and NB-07 are also included in the new data compilation (Figs 9.1& 9.2).

A total of 10 additional offshore aeromagnetic surveys (Fig. 9.1) have been gridded to 500 x 500 m cells and added to the regional data compilation (Figs. 9.2). Specifications for these surveys are shown in Table 9.1. The CGG-76 survey (Compagnie Générale de Géophysique 1977) from the Jan Mayen Ridge was provided by the Norwegian Petroleum Directorate to the JAS-05 Project. The nine other surveys have been provided by the Atlantic Geoscience Centre, which is part of the Canadian Geological Survey in Halifax (Gordon Oakey, pers. comm. 2004). All these surveys were reprocessed for the Gammaa5 grid of the Arctic and North Atlantic area by Verhoef et al. (1996).

Table 9.1. Offshore aeromagnetic surveys compiled for the present study (*Figs. 9.1 & 9.2*). CGG - Compagnie Générale de Géophysique; GEUS – Geological Survey of Denmark and Greenland; NOO - Naval Oceanographic Office; NGU – Geological Survey of Norway; NPD – Norwegian Petroleum Directorate; NRL - Naval Research Laboratory

Year	Area	Operator	Survey name	Sensor elevation m	Line spacing km	Length km
1969	SW Barents Sea	NGU	NGU-69	200	4	26.200 .
1970	SE Barents Sea	NGU	NGU-70	200	4-8	22.800
1971	Viking Graben	Fairey	Fairey-71	300	2	11.100
1973	Vøring Basin	NGU	NGU-73	500	5	35.000
1972	North Norwegian-Greenland Sea	NRL (Vogt et al. 1979)	NRL-72	300	7.5	38.500
1973	South Norwegian-Greenland Sea	NRL (Vogt et al. 1979)	NRL-73	300	10 (20)	50.600
1973	Denmark Strait	NOO (Vogt et al. 1980)	NOO-73	160	5.5	60.400
1974	Norwegian Sea, east of Iceland	NOO	NOO-74a	160	10	5.500
1974	Norwegian Sea, SE of Iceland	NOO	NOO-74b	160	10	2.000
1974	NE Atlantic, south of Iceland	NOO	NOO-74c	160	5	22.200
1974	Norwegian North Sea	NGU	NGU-74	300	2-7	23.000
1975	Norwegian North Sea	NGU	NGU-75	300	1-6	19.000
1976	Jan Mayen Ridge	CGG/NPD	CGG-76	700	5	11.600
1979	East Greenland shelf	GEUS	GEUS-79	600	8	63.500
1983	Greenland Sea	NRL	NRL-83	300	20	13.000
1984	SW Barents Sea	CGG	TAMS-84	200	2	11.800
1985	SW Barents Sea	CGG	BAMS-85	200	4	16.900
1985	S of Faroe Islands	NOO	NOO-85	230	3	18.100
1986	Trøndelag Platform	Hunting	Hunting-86	200	2	57.000
1987	Vøring Plateau	NOO	NOO-87	230	5	16.900
1987	NW Barents Sea	NGU	BSA-87	250	4-8	34.000
1988	Spitsbergen	NGU	SPA-88	1550	5.5	13.300
1989	Lofoten	NGU	LAS-89	250	2	30.000
1991	Svalbard	Amarok/TGS-Nopec	SVA-91	900	7.5	27.800
1993	N. Viking Graben	NGU	Viking-93	150	0.5-2	28.000
1993	Hel Graben- Nyk High	World Geoscience	SPT-93	80	0.75	19.000
1994	Vøring Basin	Amarok/TGS-Nopec	VGVB-94	140	1-3	31.800
1994	Nordland Ridge-Helgeland Basin	NGU	NAS-94	150	2	36.000
1994	S. Viking Graben	Amarok/TGS-Nopec	VGVG-94	160	0.2	44.800
1996	Skagerrak	NGU	SAS-96	150	2	42.000
1997	Møre Basin	Amarok/TGS-Nopec	MBAM-97	220	1-2	46.600
1998	Vestfjorden	NGU	VAS-98	150	2	6.000
2000	Vøring Basin	TGS-Nopec	VBE-AM-00	130	1-4	17.300
2003	Røst Basin	NGU	RAS-03	230	2	30.000
2005	Jan Mayen FZ	NGU	JAS-05	230	5	32.600
2006	Barents Sea	NGU	BAS-06	230	2	30.000
2007	Norwegian Basin	NGU	NB-07	230	5	38.900
Total						1033.200

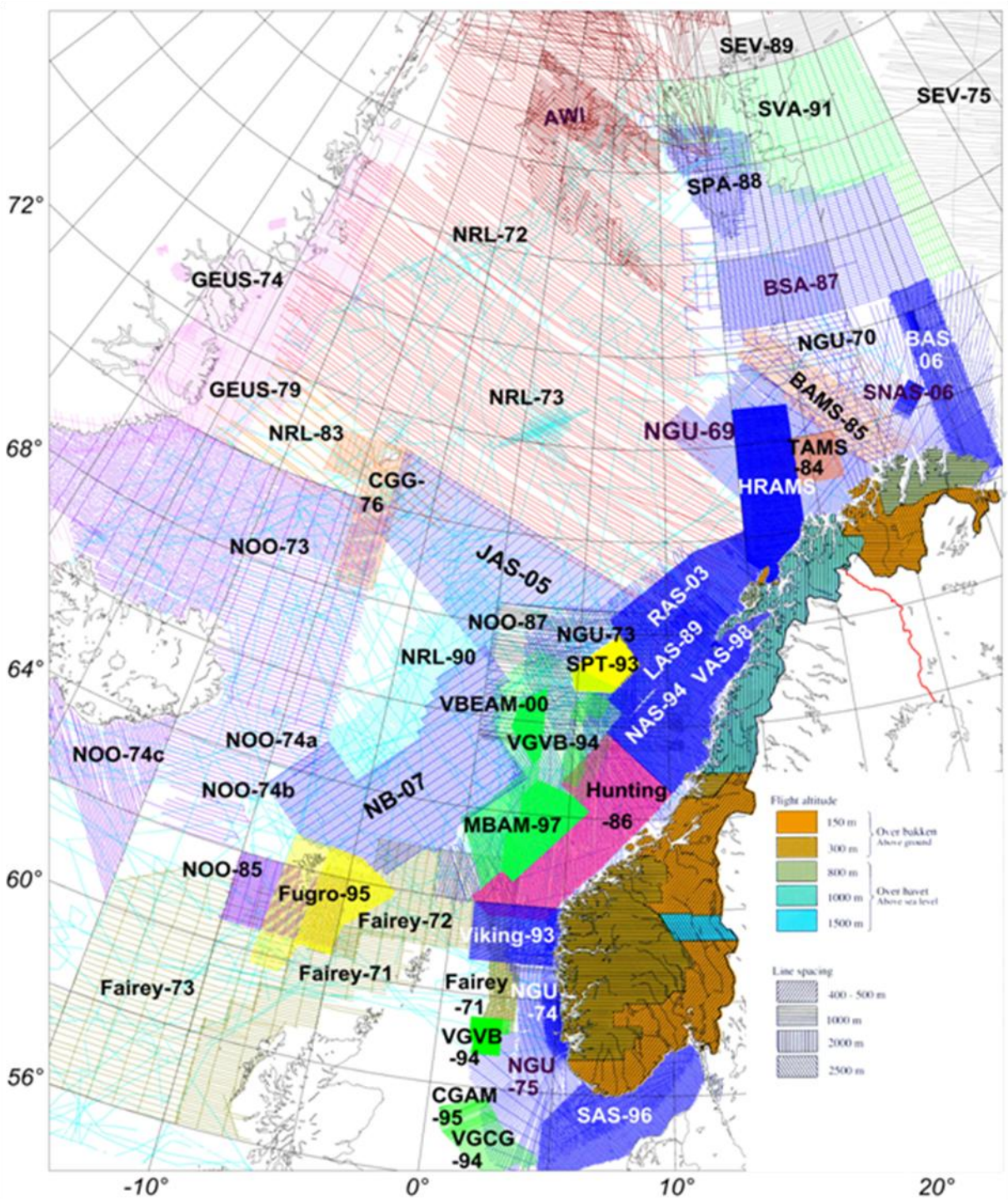

Figure 9.1 Compilation of magnetic surveys in the NE Atlantic area. The sub-grids from the 37 aeromagnetic surveys listed in Table 9.1 are produced from original profile data. The marine magnetic survey (pale blue), Fairey surveys to the west of Shetland (olive green lines) and the GEUS-survey on mainland Greenland (GEUS-74) are adapted from the Verhoef et al. (1996) Gammaa5 compilation and added to the regional data-set.

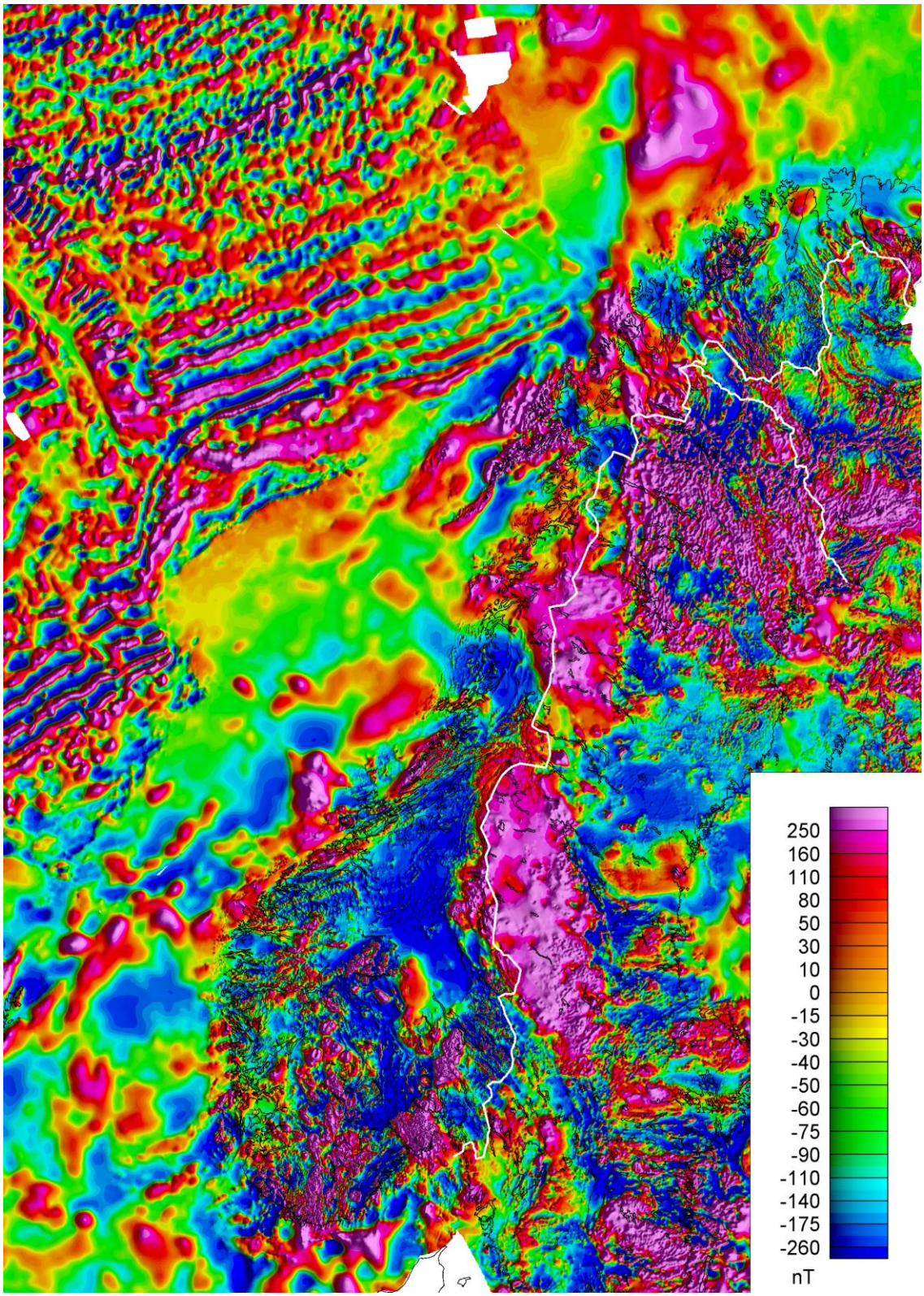

Figure 9.2. Aeromagnetic anomaly map from western Scandinavia – modified from Verhoef et al. (1996), Olesen et al. (1997) and Korhonen et al. (2002b). Technical specifications and locations of the individual surveys are shown in Table 9.1 and Fig. 9.1, respectively.

The mainland of Norway grid has previously been digitised into a 500x500 m matrix from manually drawn contour maps and the Definite Geomagnetic Reference Field (DGRF) has been subtracted (Nor. geol. unders. 1992). The mainland area was flown at different flight altitudes and line spacing dependent on the topography (Fig. 9.1).

We have also included Verhoef et al. (1996) grid-versions (5 x5 km) of the ship-magnetic data, including the Aegir Ridge NRL-90 data-set (Jung & Vogt 1997) and the aeromagnetic GEUS-74 and Fairey-71/72/73 (west of Shetland) surveys. These three datasets represent 25.000, 10.400 and 64.000 line-km, respectively, and are adding to the survey-list in Table. 9.1. Fig. 9.2 is also including the aeromagnetic data from Great Britain incorporated in Verhoef et al. (1996) 5x5 km grid.

The 5 x 5 km grids were regridded to 500 x 500 m cells before merging with the regional compilation. The new grid merging has been produced using the minimum curvature GRIDKNIT software from Geosoft (2005).

The gravity grid was compiled by Skilbrei et al. (2000) from gravity stations on mainland Norway in addition to marine gravity data from the Geological Survey of Norway, the Norwegian Mapping Authority, the Norwegian Petroleum Directorate and Norwegian and foreign universities and commercial companies (Fig. 9.3). The compiled grid was merged with gravity data from satellite altimetry in the deep-water areas of the Norwegian-Greenland Sea (Andersen & Knudsen 1998, Laxon & McAdoo 1994). The compiled free-air dataset has been interpolated to a square grid of 2 km x 2 km using the minimum curvature method (Geosoft 2005). The simple Bouguer correction at sea (Mathisen 1976) was carried out using the bathymetry data compiled by Dehls et al. (2000) and a density of 2200 kg/m^3. The International Standardization Net 1971 (I.G.S.N. 71) and the Gravity Formula 1980 for normal gravity have been used to level the surveys. The location of the gravity stations and the marine profiles are shown in Fig. 9.3.

An Airy-Heiskanen 'root' (Heiskanen & Moritz 1967) was calculated from a compiled topographic and bathymetric data-set (Dehls et al. 2000). The gravitational attraction from the 'root' was calculated using the AIRYROOT algorithm (Simpson et al. 1983). The isostatic residual (Fig. 9.4) was achieved by subtracting the gravity response of the Airy-Heiskanen 'root' from the observed Bouguer gravity data. Shaded relief versions (in grey tones) of the 100 km high-pass filtered grid is superimposed on the map.

Petrophysical data from numerous bedrock mapping projects, geophysical interpretation projects and the recent Lito Project are compiled in NGUs national petrophysical database (Fig. 9.5). Data from these density, susceptibility and remanence measurements have been systematically applied in the various forward modeling studies of the depth to basement studies on both mainland Norway and on the continental margin.

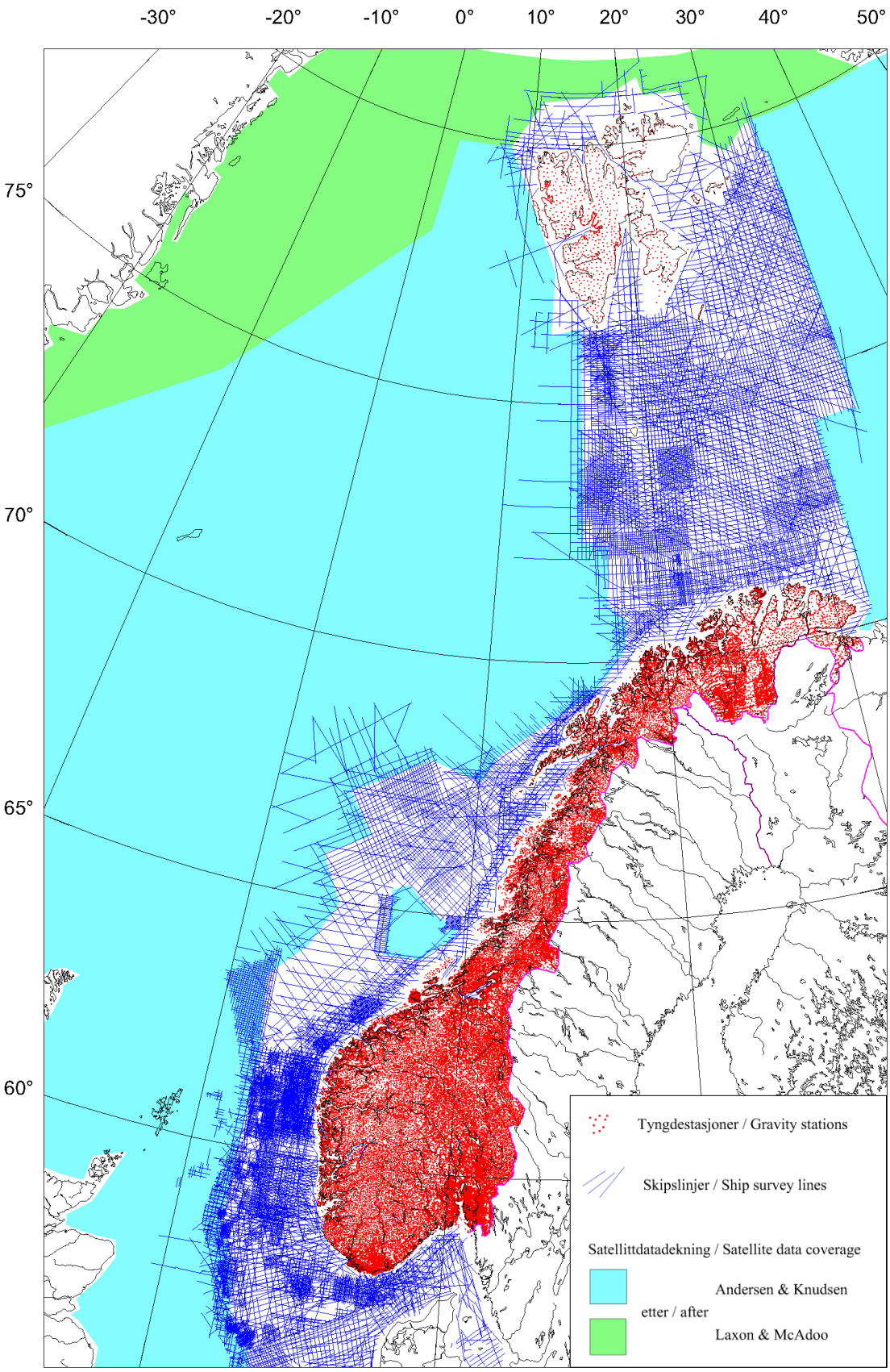

Figure 9.3. Compilation of gravity surveys in the NE Atlantic (Skilbrei et al. 2000).

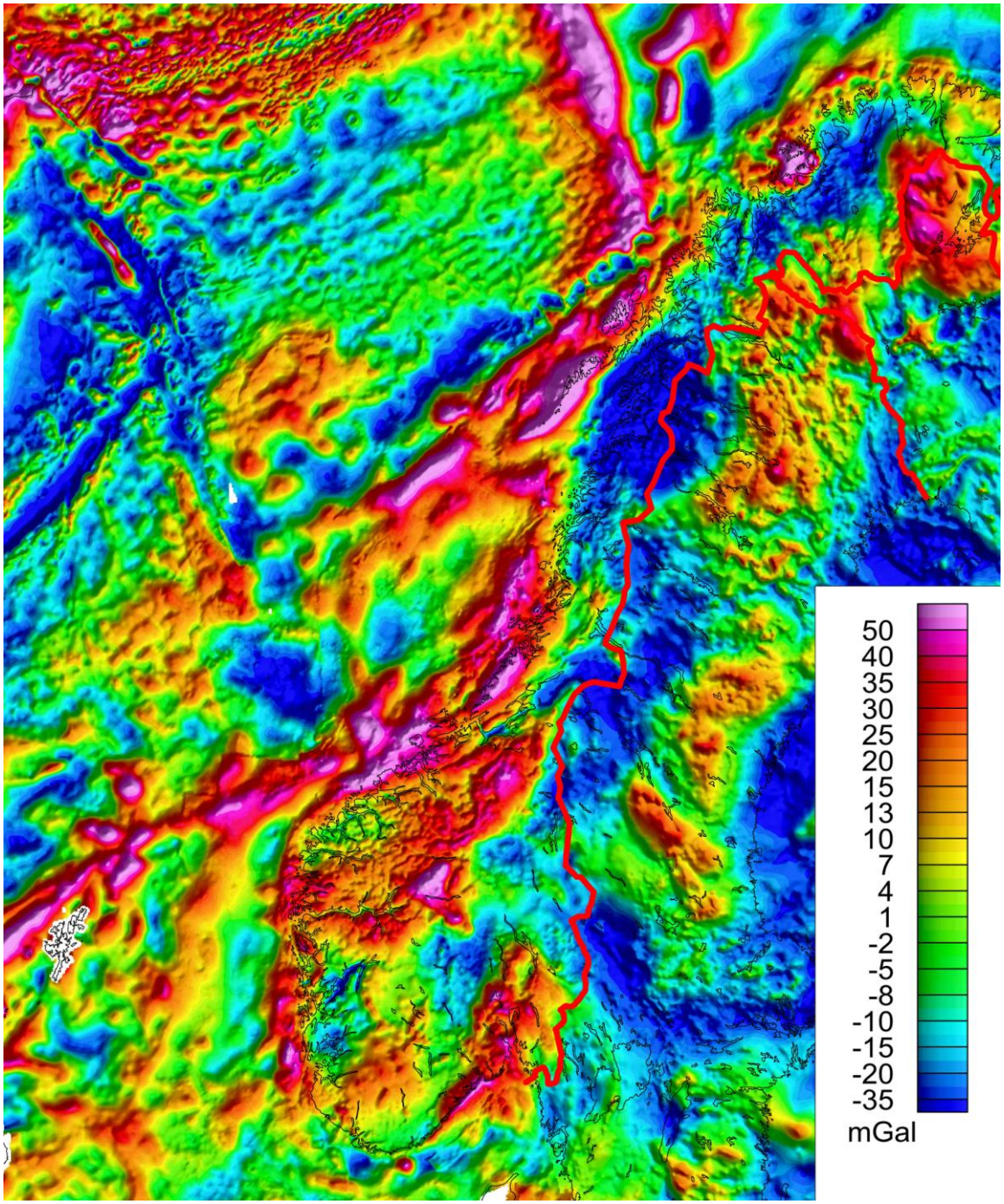

Figure 9.4. Isostatic residual of Bouguer gravity from western Scandinavia - based on gravity compilation by Skilbrei et al. (2000) and Korhonen et al. (2002a).

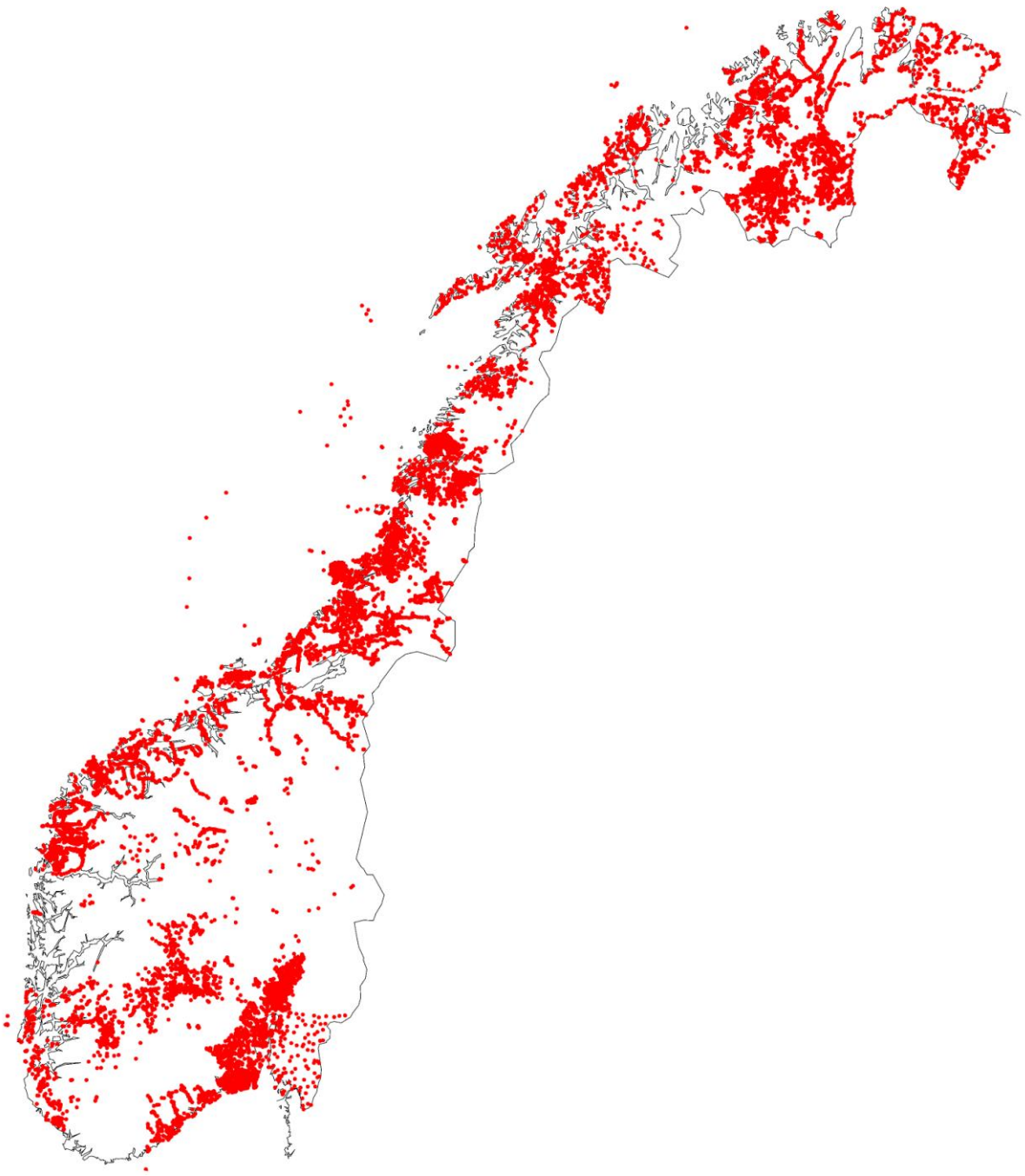

Figure 9.5. Petrophysical data, mainlad Norway from more than 30,000 bedrock samples (density, magnetic susceptibility and remanence) and offshore from 9.400 susceptibility measurements.

9.3 Basement structure map

Negative and positive anomalies on the continental shelf reflect to a large extent sedimentary basins and structural highs, respectively. The structural highs on the mid-Norwegian shelf contain high-density and highly magnetised rocks of assumed lower crustal origin and have been interpreted to represent reactivated core complexes (Osmundsen et al. 2002, Olesen et al. 2002, Skilbrei et al. 2002). Fig. 9.6 shows the spatial relationship between core complexes, low-angle detachments and the Transscandinavian Igneous Belt (TIB). The lower crustal rocks were exhumed along the low-angle detachments during a late phase of the Caledonian orogeny (Osmundsen et al. 2002). It is important to realise that similar core complexes of Proterozoic age exist in northern Fennoscandia (Fig. 9.6). They are usually referred to as gneiss domes (e.g. Lindroos & Henkel 1978, Midtun 1988, Henkel 1991, Olesen & Sandstad 1993) and are characterized by positive gravity and aeromagnetic anomalies similar to the younger core complexes in mid-Norway. The gneiss domes in northern Fennoscandia were most likely formed during a gravity collapse of the Proterozoic orogen that formed subsequent to continent-continent collision along the Levajok Granulite Belt (Fig. 9.6).

Of particular interest is the recognition of the structurally denuded basement culminations onshore Norway, and their bounding detachments. These major detachments formed during orogen-parallel extension, i.e. at a high angle to the orogenic front (Fig. 9.6). Similar age and style detachments are mapped in East Greenland: the Fjord Region and Ardencaple Detachments (Hartz et al. 2002).

Mapping onshore Norway and East Greenland has revealed the presence of NW-trending Late Caledonian extensional detachments (Braathen et al. 2000, Hartz et al. 2002, Schmidt-Aursch & Jokat 2005a, b), and it is reasonable to assume that the intervening area, now represented by the offshore parts of the continental margins, was similarly structured (Olesen et al. 2002). Precise correlation between the shear zones in E Greenland and Norway is speculative, however, since the degree of lateral relative motion between the continents during Devonian time remains uncertain. Extrapolating the onshore structures to the offshore realm, it can be deduced that the area outboard Nordland experienced NE-SE trending (i.e. orogen-parallel) late Caledonian gravity collapse. The Kollstraumen Detachment and Nesna and Sagfjord shear zones extend northwestwards below the Helgeland, Vestfjorden and Ribban basins. Downfaulted low-magnetic Caledonian nappes are interpreted to constitute the "basement" southwest of the Bivrost Lineament. Undulations of the offshore extension of the Sagfjord shear zone may have governed the location of the large-scale Mesozoic normal fault zones that bound the sides of the Lofoten and Utrøst Ridges (Olesen et al. 2002).

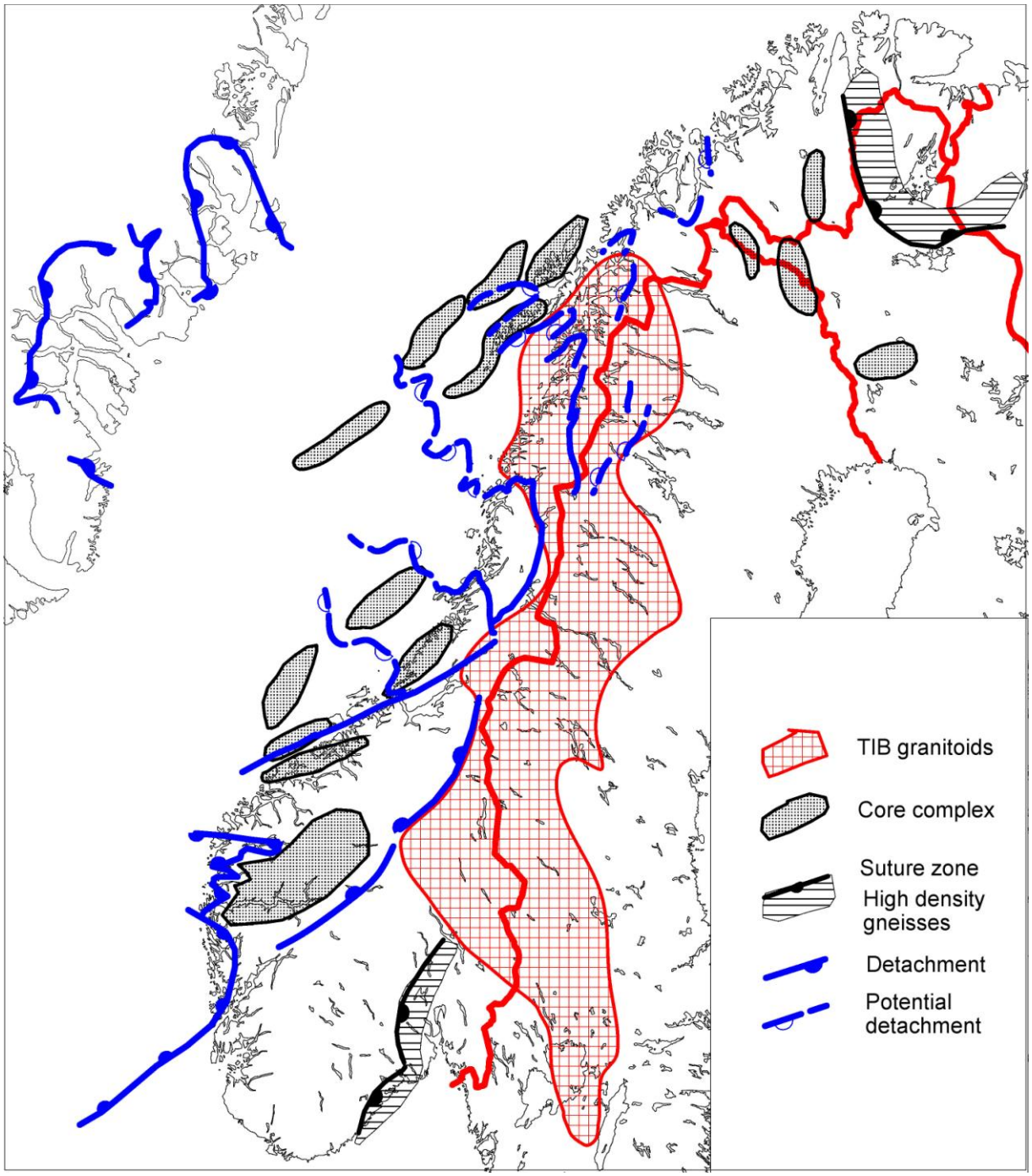

Figure 9.6. Regional structures compiled from interpretations of potential field data and bedrock mapping (Lindroos & Henkel 1978, Midtun 1988, Henkel 1991, Olesen & Sandstad 1993, Hartz et al. 2002, Olesen et al. 2002, 2006a, Osmundsen et al. 2002 and Skilbrei et al. 2002). Greenland is rotated back to pre-opening of the Atlantic in the Eocene.

9.4 Depth to Precambrian basement in northern Norway

We have for the Kontiki project compiled a basement structure map of northern Norway (Fig. 9.7) based on published maps by Henkel (1991), Olesen et al. (1990, 2002) and Osmundsen *et al.* (2002). The basement consists partly of Precambrian rocks, such as granites, gneisses and amphibolites, and partly of Caledonian nappes. The basement depths offshore Finnmark represent mostly depth to Precambrian basement, since the Caledonian nappes on the mainland of Finnmark constitute mostly low-magnetic metasediments. The basement depths in the Norwegian Sea (Nordland area) are on the other hand based on a combined interpretation of magnetic and gravity data and will mostly represent depths to crystalline basement, that is composed of both Precambrian and Caledonian rocks. There are, however, difficulties in distinguishing depths to crystalline basement from depth to Precambrian basement in parts of the offshore areas.

9.5 Basement depths, South Norway.

We have constructed a depth to the bottom of the 'Caledonian nappes' or a depth to autochthonous Precambrian basement in southern Norway (Fig. 9.8). The depths are generalized and simplified. In the Sparagmite region in the southeast it is based primarily on magnetic depth estimates. In Trøndelag, Jotunheimen and Vestlandet, it is constructed from gravity models and geological maps. The depth surface has more pronounced relief in the Sparagmite region than in the other areas. This is partly due to the calculated depth to magnetic basement estimates. Rather flat lying low-magnetic nappes are situated on top of a shallow magnetic basement.

9.5.1 Sparagmite region, Southern Norway.

In this region the sedimentary rocks are non-magnetic, while some of the rock units inside the 'Jotun Nappe Complex' and the 'Trondheim Nappe Complex', are highly magnetic. Within the Sparagmite region, the map is a reproduction of a published contour map of depth to magnetic basement in the Sparagmite region (by Knut Åm in Nystuen 1981). It is considered to reflect undulations of the crystalline basement-cover interface. As pointed out by Nystuen (1981), the high and the lows, with depths exceeding 4000 m below sea level, are continuous with basement windows that occur in the northern part of this map (e.g. Sigmond et al. 1984). The windows that form axial culminations of an anticlinal ridge can be followed from Aurland and Valdres in the southwest to the Norwegian-Swedish border. The depth map and its topography can represent culminations and depressions arranged *en echelon* and parallel to the anticlinal ridge along the southeast margin of the Trondheim Nappe Complex, and a common origin for the basement undulations is likely (Nystuen 1981). In fact, the

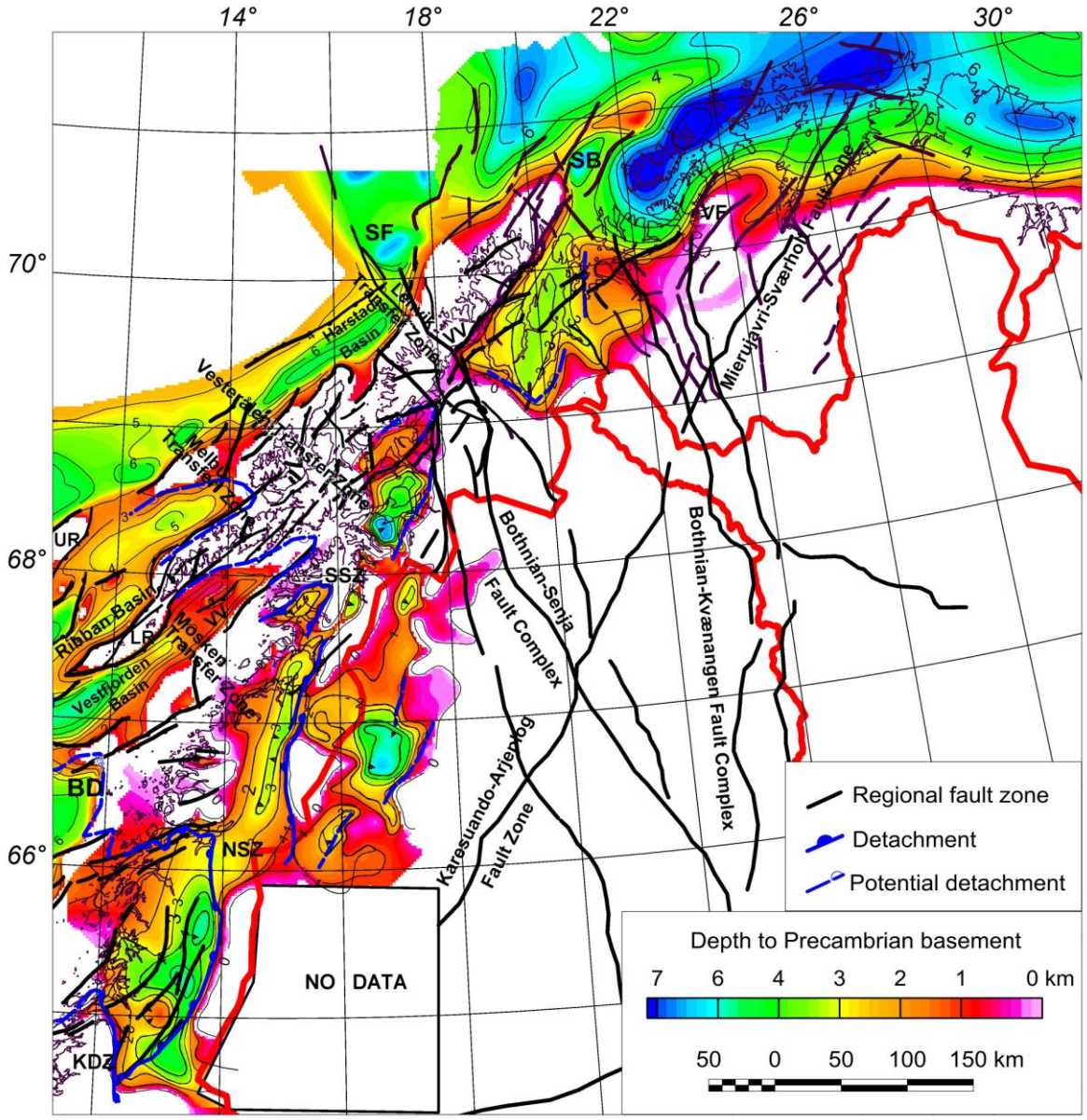

Figure 9.7. Basement structure map from northern Norway compiled from Henkel (1991), Olesen et al. (1990, 2002) and Osmundsen et al. (2002). BD – Bivrost Detachment, KDZ – Kollstraumen Detachment, LR – Lofoten Ridge, NSZ – Nesna Shear Zone, SB – Sørvær Basin, SF – Senja Fracture Zone, SS – Sagfjord Shear Zone; UR – Utrøst Ridge, VF – Vargsund Fault, VV – Vestfjorden-Vanna Fault Compex.

observation that "the sedimentological boundaries, thrust planes and basement domes bend parallel in the windows and the basement flexures in the Sparagmite region, suggest late- and/or post-Caledonian age for these structures" (Nystuen, 1981). Post-Caledonian faults also affect the structures strongly, including faults related to the Oslo rift, and many fault zones may represent reactivated Precambrian fault-/weakness zones. Over large areas, the affected surface is the so-called 'sub-Cambrian peneplain' (Nystuen 1981), on which the erosionally truncated magnetic bodies occur (some bodies may also occur beneath this surface).

9.5.2 Central and South Norwegian Caledonides.

The area includes the Trondheim Nappe Complex, Jotun Nappe Complex and Caledonian rocks in the greater Hardangerfjorden- and Bergen Arcs areas. In the area encompassing Trøndelag, Dovrefjell and Jotunheimen, the depths are based on gravity models. In a transect from Trondheim to Storlien, the gravity models were constructed by Skilbrei and Sindre (1991) and by Skilbrei et al. (2002). Elsewhere in Trøndelag and to Jotunheimen, it was constructed by Mekonnen (2004). In the Sunnfjord area (Devonian basins), it is based also on geological maps and a gravity profile by Skilbrei and Kihle (1998). The surface is highly speculative because only six different $2^1/_2$D density models have been used in the construction of the depth surface. In addition, only inaccurate models of Moho depths exist (Kinck et al. 1993). The latter degrades the precision of the gravity models. An estimate of the uncertainty is that the maximum depth of the Caledonian Complex is in the interval 8 km to 12 km in the Trondheim Nappe Complex. Beneath the Jotun Nappe Complex, it is 6-10 km (Skilbrei, 1989). A three dimensional model is needed in order to improve the estimate. South and southwest of Jotunheimen (Vestlandet), the depths are based on the dip of units measured on geological sections that appear in geological maps at a scale of 1:250.000 published by Jorde et al. (1995), Lutro & Tveten (1996), Nilsen & Wolff (1989), Ragnhildstveit & Hellingsen (1997), Ragnhildstveit et al. (1998), Siedlecka et al. (1987), Sigmond et al. (1984) and Sigmond (1998). The depicted surface is smoothed and simplified, and attempts to represent the bottom of the supracrustal units of Cambro-Silurian age, or the bottom of the Caledonian allochton.

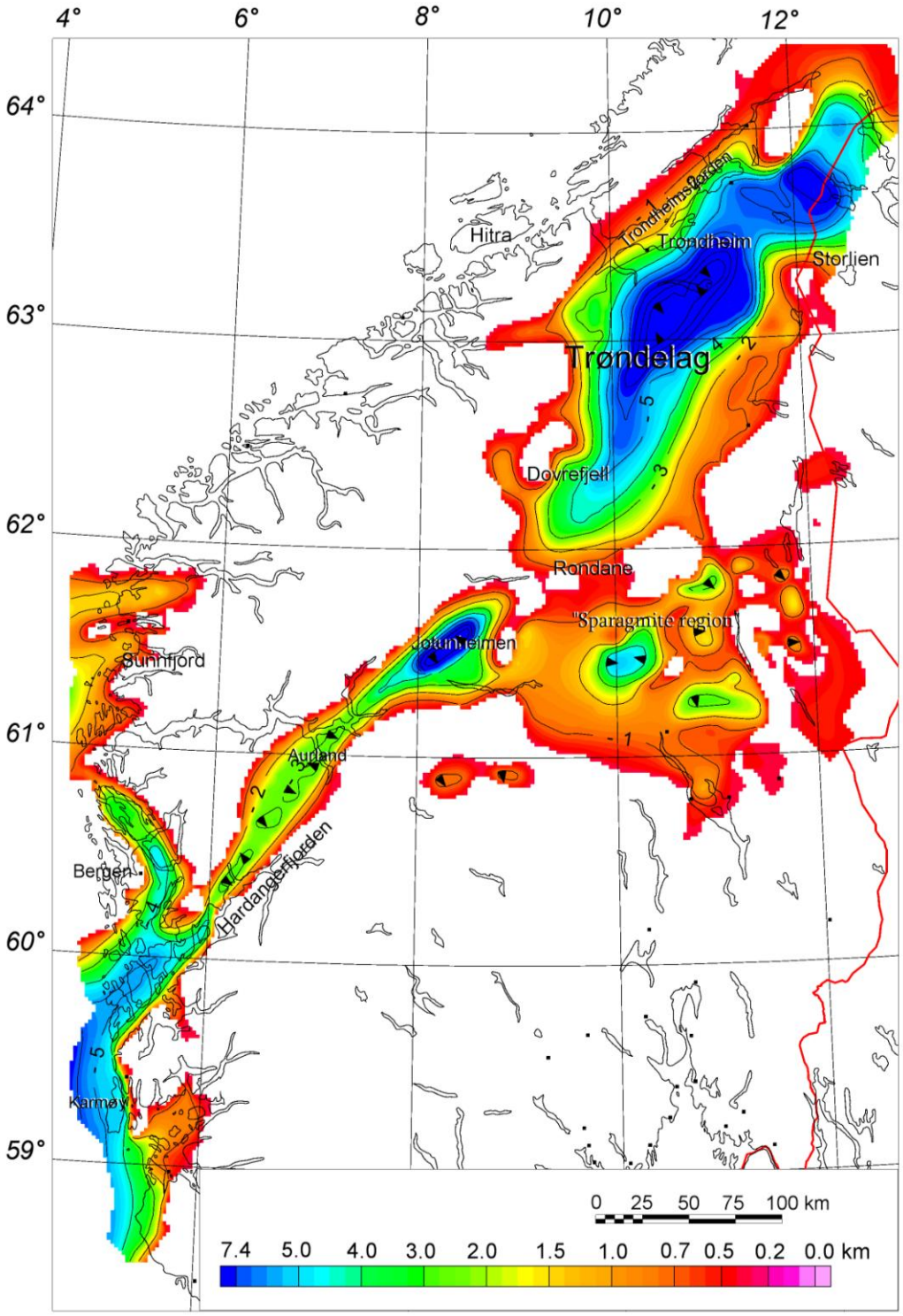

Figure 9.8. Estimated depths to the bottom of Caledonian rocks/nappes from sea level, South- and Central Norwegian Caledonides. Because the tectonic position of rocks of Precambrian age is uncertain in some areas (para-autochtonous/allochtonous), the surface is kept close to rock of Cambro-Silurian age, where possible. Note deep 'synclinoriums' in western Norway, Jotunheimen and in Trøndelag and a more detailed basement topography in eastern Norway (Sparagmite region). The latter is constrained by depth to magnetic basement estimates and geological maps (Nystuen 1981). In this area, strong gradients represent major basement faults and/or major basement flexures.

9.6 Basement depth map, northeastern North Sea

The depth to crystalline basement of the northeastern North Sea region (Fig. 9.9) has been compiled from five different sources (Fig. 9.10): a) Smethurst 2000, b) Hospers & Ediriweera 1991, c) Hospers et al. 1986, d) Olesen et al. 1997b, d) Sindre 1993. The Moho depth varies between 18 and 32 km and the thickness of the crystalline crust is consequently within the range of 30 to 10 km. The large variation of basement thickness implies a substantial variation in basement heat generation.

The Viking Graben and the Norwegian-Danish Basin constitute the main structural elements within our study area of the 'North Sea Rift Zone'. The basement depth ranges from (a) 1-6 km on platforms and structural highs, (b) 7-9 km on terraces and basins and more than 10 km below the grabens.

A the N-S trending belt of postorogenic granites (Smithson 1963, Smithson & Barth 1967, Balling & Falkum 1975, Falkum 1987) with high content of U-Th occur along the Mandal-Ustaoset Fault Zone (Sigmond 1985). The rock suite is magnetic and appears to be continuous below the Farsund Basin to the south (Fig. 9.2). The Sveconorwegian (c. 930 Ma) Rogaland Igneous Complex (Smithson & Ramberg 1979, Duchesne et al. 1987, Bingen & van Breemen 1996) to the northwest constitutes another major igneous province. The content of heat generating elemens of the norites and anorthosites of this province is, however, low. The latter complex stretches from southern Rogaland and offshore into the Egersund and Farsund Basins (Olesen et al. 2004a). A high-velocity body (eclogite) below the Horda Platform (Christiansson et al. 2000) will contribute to a reduced heat flow in this region.

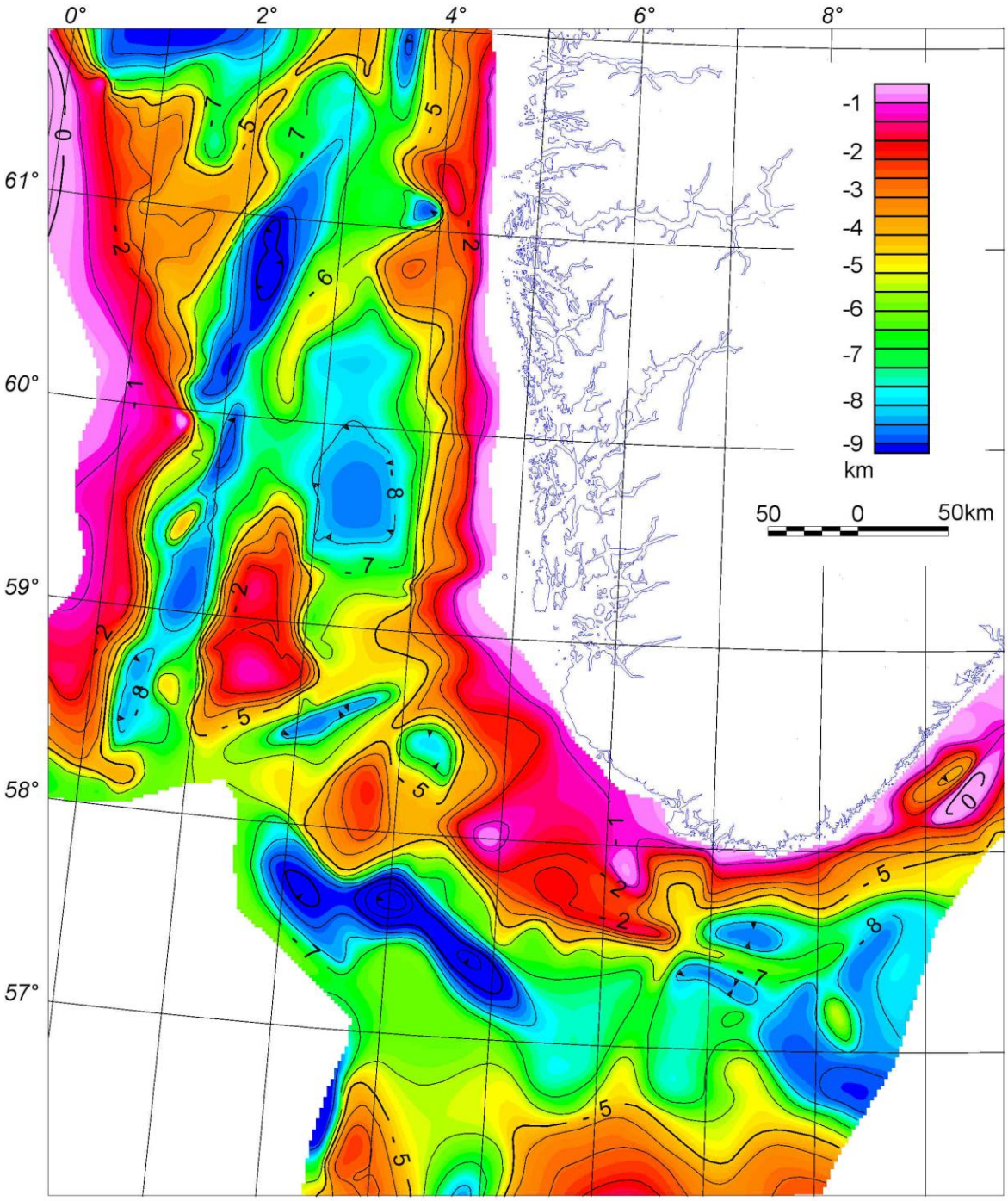

Figure 9.9. Compilation of the depth to crystalline basement from five different sources: a) Smethurst 2000, b) Hospers & Ediriweera 1991, c) Hospers et al. 1986, d) Olesen et al. 1997b, d) Sindre 1993. The northern Viking Graben will constitute one of the test areas of the Kontiki Project.

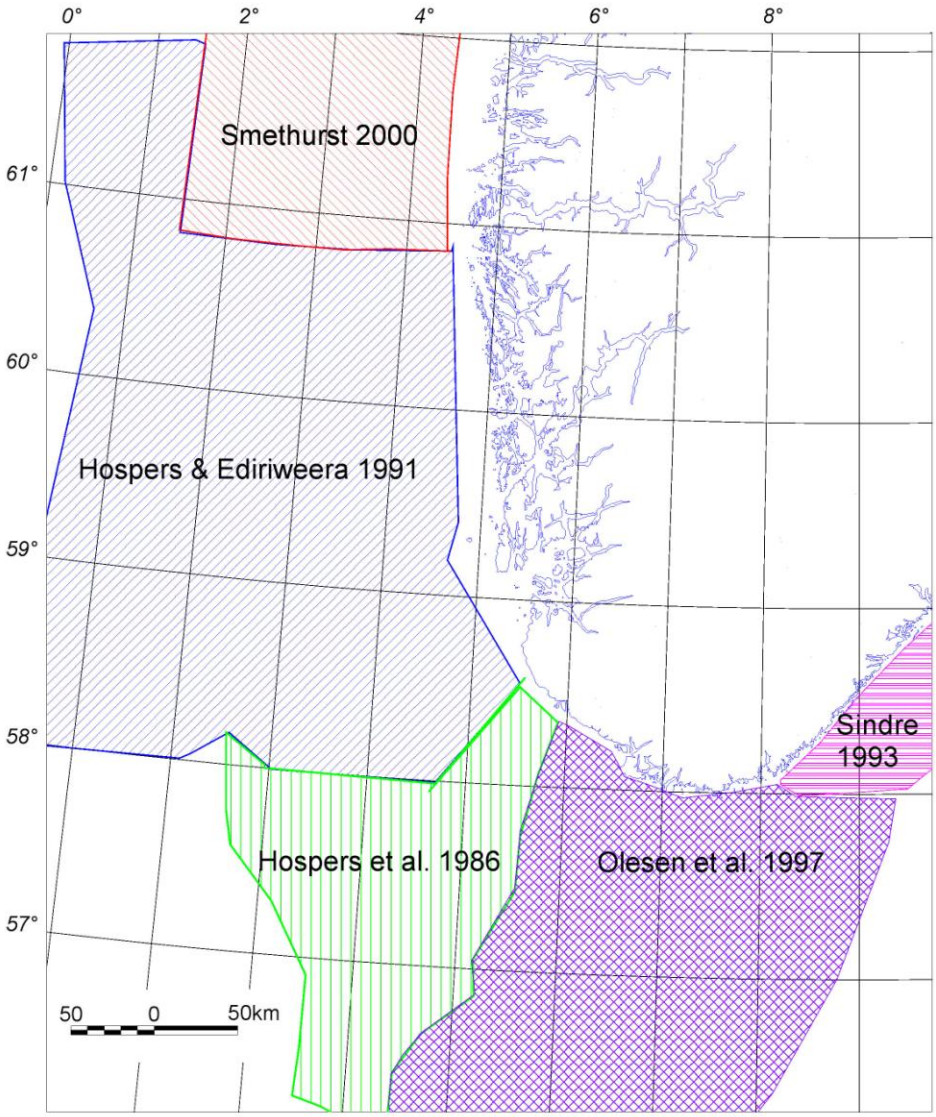

Figure 9.10. Sources of depth to crystalline basement compilation (Hospers et al. 1986, Hospers & Ediriweera 1991, Sindre 1993, Olesen et al. 1997b, Smethurst 2000).

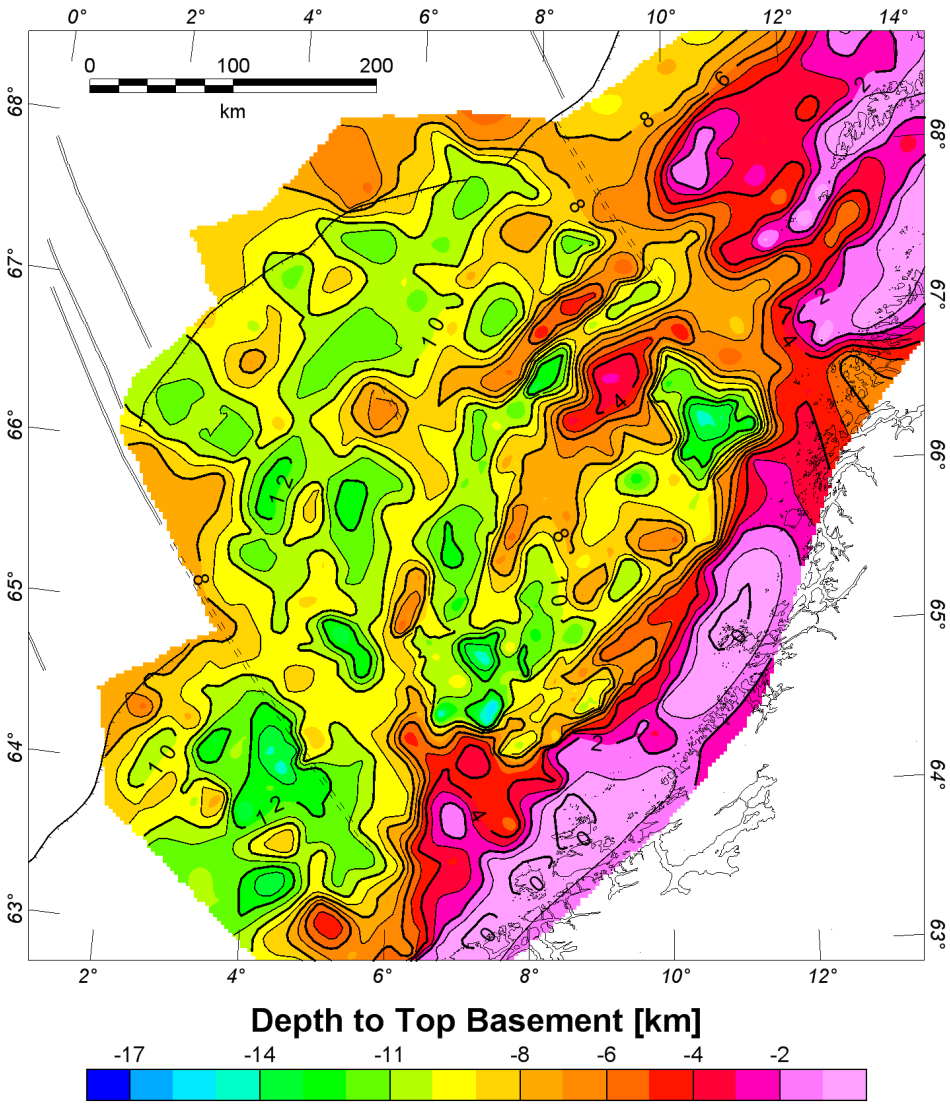

Figure 9.11. Depth to upper basement on the Mid-Norwegian continental margin (modified from Ebbing et al. 2006c). The depth to top basement is associated with the depth to the top of the Caledonian nappes with densities around 2.7 Mg/m3 and relatively low susceptibilities compared to the underlying Precambrian basement.

9.7 Upper basement map of the Mid-Norwegian continental margin

The map of the top upper basement (Fig. 9.11) is also described in paragraph 10.4.2.1 but is included in the present chapter to complete the description of the depth to basement data for Norway. The map reveals a deepening from the coastal area towards the continental margin. The Trøndelag Platform features shallow depths (<9 km), while top basement in the Vøring Basin generally is encountered between 11 and 15 km. The top basement map shows a variety of local features, such as basement highs correlating with the Nyk and Utgard Highs. These structural highs reveal positive gravity anomalies. The depth to the crystalline basement is affected by the basin depth and sediment thickness and the Tertiary domes, especially in the northern Vøring Basin (e.g. Naglfar Dome and Vema Dome). In the

southern Vøring Basin the depth to the top basement is similar, but this area lacks prominent basement highs.

The Møre margin to the south also reveals a deep top basement (12-15 km) but the top basement map shows less local features. The East Jan Mayen Fracture Zone marks an approximately 100 km lateral step in the margin. However, the Jan Mayen Lineament is not a well-expressed tectonic feature. Structurally, the transition between the Vøring and Lofoten margins is much more pronounced. Northeast of the Bivrost Lineament the top of the crystalline basement is located at a depth less than 10 km, and obviously reaches the surface on the Lofoten Ridge and at the northern terminations of the Vestfjorden and Ribban Basins. The Bivrost Lineament is a major tectonic boundary marked by both a vertical and apparent horizontal offset. The Utgard and Nyk Highs are suggested to be the southern continuations of the Lofoten Ridge and Røst High, respectively.

On the Trøndelag Platform the depth of the top basement is interpreted with hindsight to the structural interpretation provided by Statoil. The deepest seismic horizon was the Top Perm (Fig. 10.6), which locally exceeded 12 km in depth. At such a depth the density of the sedimentary rocks is not distinguishable from the underlying basement due to compaction (e.g. Ebbing et al. 2006a). Therefore, the depth to the basement was chosen to be deeper than the Permian horizon (except over the Frøya High, as explained below), but a depth estimate of the Permian succession from the density field model has a large degree of uncertainty.

9.8 Basement depth map from the Barents Sea and Svalbard

NGU has covered large parts of the Barents Sea and Svalbard with aeromagnetic measurements. The data sets have been described earlier (Åm 1975, Olesen et al. 1990, Skilbrei 1990). The magnetic studies carried out in this region include the mapping of volcanic rocks on Svalbard and in the northern Barents Sea, and the mapping of major basement faults and estimation of the depth to the magnetic basement. The basement map presented here is a compilation of depths published earlier.

Depth estimates were made on the original aeromagnetic profiles (the straight slope and Peters methods were used). The methods have been describes in Skilbrei (1991). In the southwestern Barents Sea, seismic data, well data and gravity data were also used to obtain tentative depths in the deep basins, using image analysis systems to correlate the faults with the potential field data. The exploration wells are unevenly distributed and only three of them have reached the basement. The other wells provide only minimum depths to the basement surface, mainly in the Hammerfest Basin.

Fig. 9.12 shows the map of depths to the crystalline basement from the Southwestern Barents Sea, which is derived from several available sources. It is important to note that only in some of the areas were the depth contours drawn solely from the magnetic depth estimates, and that

the map is a smoothed, generalised map. Locally (along the deep-seated fault zones that form some of the margins of the structural highs), the basement surface may be much steeper. Before contouring, the magnetic depth estimates were compared, where possible, with seismic data and well data. In this manner, an attempt was made to differentiate between intrasedimentary volcanic sources and basement sources. In the eastern part of the study area, only a few magnetic depth estimates were obtained. Neither the point distributions of these nor the seismic data would allow contouring. Using the gravity data combined with major faults interpreted from seismic data to have affected the basement (Gabrielsen et al. 1990, Gudlaugsson et al. 1998), we tentatively gridded the basement also in the eastern area.

A large portion of the study area is occupied by basins, some of which are extremely deep rift basins. As can be seen in Fig. 9.2, the continental crust in the southwestern Barents Sea is fragmented and divided into blocks by several highs and basins that are the result of different rifting events (e.g. Faleide et al. 1988, 1991, 1993). In the structural highs, the depths shown in Fig. 9.2 are similar to the depths that appear in a magnetic basement map that was published by Åm (1975). However, from the deep basins, there is a marked difference. This difference arises because of the lack of magnetic anomalies from the deep basins (and thereby no magnetic depth estimates), and because seismic and gravity data are now available. From the deep basins, gravity and reflection seismic data were used to obtain tentative depths to the crystalline basement. From the southern parts of the map, the depths are very similar to the depths that appear in a magnetic basement map published by Olesen et al. (1990) that covers Finnmark and the adjacent sea areas.

Also of interest are relatively small areas where the shallow estimates may indicate either basement blocks at relatively shallow depths, or the presence of igneous rocks within the sedimentary rocks overlying the crystalline basement (Fig. 9.2). The high area on the map southwest of Bjørnøya represents Tertiary volcanic rocks within the Vestbakken Volcanic Province (Faleide et al. 1988). Low-amplitude aeromagnetic anomalies occur over the Senja Ridge (SR). The magnetic depth estimates beneath the SR range from 2 km (in the north) to 3 km (in the south). The magnetic sources may represent crystalline basement rocks. On the Loppa High, on the landward side of the Harstad Basin, on the SR, and north of Varangerhalvøya, it is likely that the basement is relatively shallow. In the other cases shown, intrasedimentary volcanic rocks may be present (see discussion below). In the case of the area to the west of the deepest part of the Bjørnøya Basin, these sources occur relatively deep within the sedimentary basin (c. 8 km). However, this is still within the sediments, according to published interpretations of the seismic data (Gabrielsen et al. 1990, Faleide et al. 1991, 1993, Gudlaugsson et al. 1998).

Along the eastern margin of the Harstad Basin, magnetic sources occur at a depth of 4-4.5 km. This is within the Cretaceous sedimentary sequence. The magnetic sources probably represent volcanic rocks (basalts?).

Magnetic depth determinations performed on the analogue profiles showed some conspicuously shallow values on the Loppa High. Carboniferous ignimbrites occur in a borehole on the Loppa High (Gjelberg pers. comm. 2004). Shallow values occur also to the east of Bjørnøya. The estimated depths were compared with published reflection seismic profiles (Gabrielsen et al. 1990). Apparently, magnetic sources exist within both the Carboniferous-Permian and the Mesozoic sequences. The shallow estimates are located to the north of the wells that have been drilled in the southern Barents Sea. On Spitsbergen (Svalbard) and in Storfjorden, there are high-frequency magnetic anomalies that are probably due to dolerites occurring at a shallow level in the sedimentary section, far above the basement surface. (All the shallow estimates were removed from the maps before the contouring of the basement surface).

The Carboniferous period is associated with rifting throughout the entire region (Ziegler 1988), and this may well have involved some volcanic activity. On Magerøy (North Finnmark), a dolerite dyke of a Late Carboniferous age has been reported (Roberts et al. 1991), and on Varangerhalvøya, similar ages were obtained from fresh dolerites (Rice et al. 2004). On the Russian Barents Sea shelf, the Triassic strata are associated with lava units that give rise to magnetic anomalies northeast of Hopen (Grogan et al. 1998). Also, Permian strata in the Timan-Pechora and South Barents Basins, northwestern Russia, are known to contain volcanic rocks. On the basis of the above discussion, magnetic sources within the sedimentary rocks may be due to volcanic activity associated with the Late Palaeozoic rifting that affected the whole region. The shallowest sources probably represent dolerites of Late Jurassic/Early Cretaceous age and Triassic basalt. In the east Barents shelf, Triassic lava rocks and/or Triassic rocks. (In addition, Tertiary volcanic rocks occur along the western margin).

The range of depths is from 1.5 km to >10 km within the northern Barents Sea and Svalbard region. The map is valuable in mapping the structural highs as well as the sedimentary basins of the area. Comparison with seismic profiles demonstrates that, in some areas, the lower-middle part of the sedimentary column is probably Palaeozoic (Devonian-Permian, Skilbrei 1993, p. 3). It was found that it is generally impossible to trace the crystalline basement from the reflection seismic data in the easternmost areas, because the signal to noise ratio is poor beneath 3 seconds two way travel time (twt). Also, there is no way to know if the magnetic anomalies are due to sources within the crystalline basement only, or if some are due to volcanic rocks found at great depths within the sedimentary section. Therefore, in the eastern part, 'the magnetic basement surface' may be above the crystalline basement in some locations (Skilbrei 1993, p. 5). These depth estimates should be checked utilising modern seismic data.

In the western part of the study area (north of Bjørnøya), where the basement surface is depicted from the seismic data, there is generally good correlation between estimates made from magnetic anomalies and the depth to the acoustic basement.

The basement structures trend in the northwestern Barents Sea links up with the main tectonic trends on Spitsbergen. The basement rocks on Spitsbergen (Hecla Hoek rocks) also constitute the basement underlying the sedimentary rocks in the sea areas to the south of the island. The southwards continuation (into the sea areas) of the so-called West-Spitsbergen Fold and Thrust Belt, is indicated to end somewhere between Bjørnøya and Sørkapp (this is seen in unpublished residual gravity data). Major basement faults mapped on Spitsbergen are tentatively followed in a N-S direction southwards far into the Barents Sea (steep slopes in the basement surface).

The structure of the basement trend N-S and NNW-SSE on Spitsbergen. The prevailing trend of the basement surface suggests that later tectonic events may have occurred along (Precambrian or Caledonian) zones of weakness present in the basement. This suggests that the main fault zones present in the crystalline basement have imposed some control on the evolution of the Svalbard area and the adjacent Barents Sea.

A pattern of basement highs/horsts and sedimentary basins emerges from the map of the basement depths. The deepest part of the Devonian Graben is more than 8 km deep and trend N-S. The deep basin is bordered to the east by a southerly extension of the Billefjorden Fault Zone, which is the border fault to the Devonian graben in central-northern Spitsbergen. In general, interpretation of the depth to the magnetic basement confirms the existence of structures deduced from surface geology. The continuation of the BFZ to the south of Spitsbergen is indicated by the basement surface.

In the southwestern Barents Sea, Åm (1975a) attempted to map two different basement surfaces from the aeromagnetic data. A relatively "shallow refraction seismic and shallow magnetic basement" surface was interpreted to represent the 'Palaeozoic basement', and a deeper "magnetic basement surface" was interpreted to be the 'Precambrian surface'. Caledonian nappes occur on top of the Precambrian in Finnmark, north Norway, giving rise to aeromagnetic anomalies whose sources generally occur from beneath the nappes, although some of the Caledonian basic and mafic units give rise to anomalies (Åm 1975, Olesen et al. 1990).

The Loppa High is associated with pronounced magnetic anomalies. The basement may represent mafic or basic units (the Seiland Igenous Province in western Finnmark may be an analogue (Olesen et al. 2000), granites or high-grade felsic gneisses. A combined study of gravity, magnetic and seismic data is necessary in order to draw conclusions on the different possibilities.

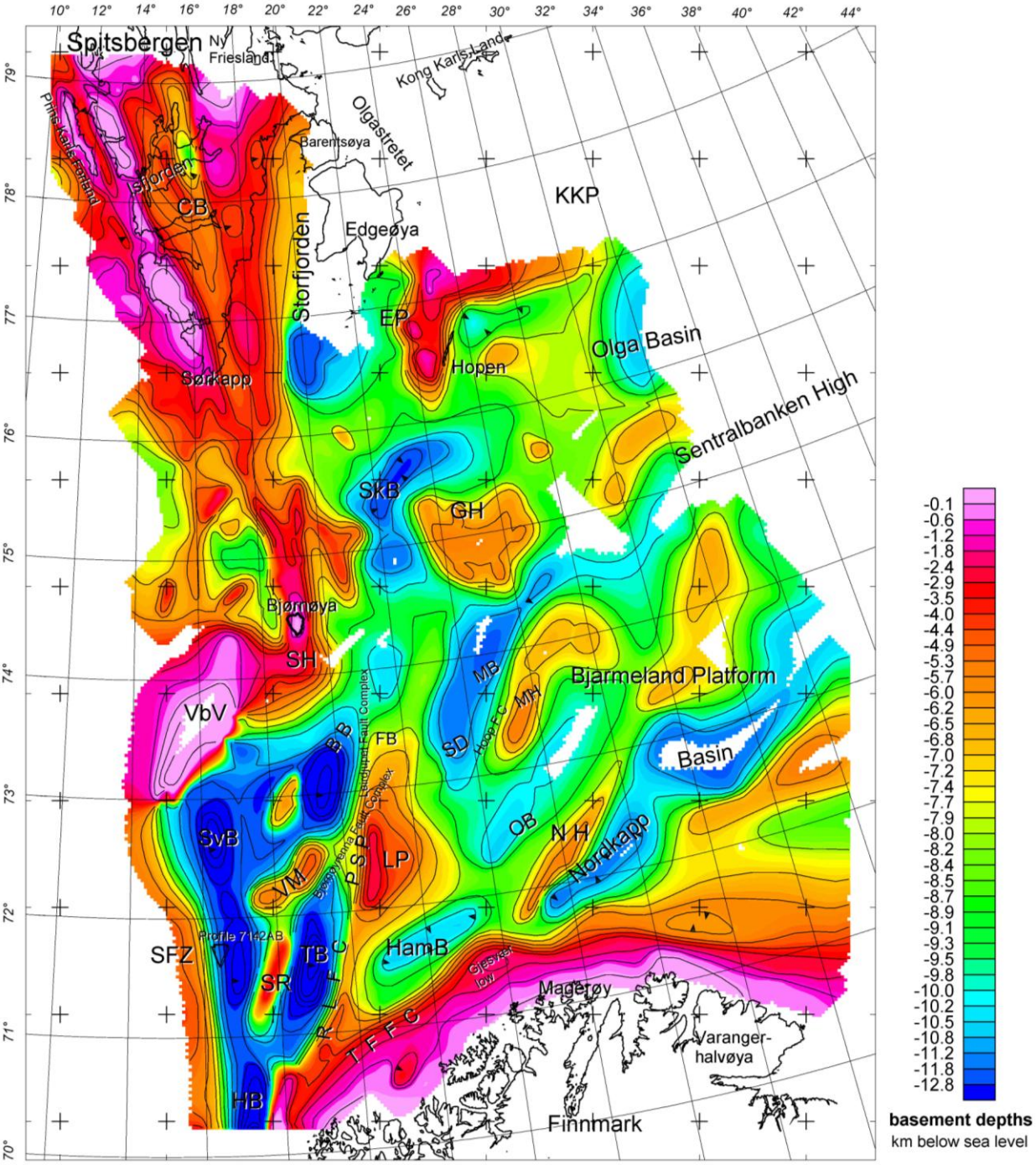

Figure 9.12. Depth to basement map, western Barents Sea area (Skilbrei 2005). The map has been generalised. It is a tentative map based on seismic-, well- and potential field data as well as earlier studies (Åm 1975, Gabrielsen et al. 1990, Olesen et al. 1990, Skilbrei et al. 1993). BB = Bjørnøya Basin, GH = Gardarbanken High, HB = Harstad Basin, HamB = Hammerfest Basin, LP = Loppa High, OB = Ottar Basin, MH = Mercurius High, PSP = Polhem Subplatform, SH = Norsel High, SkB = Sørkapp Basin, SvB = Sørvestsnaget Basin, RLFC = Ringvassøy Loppa Fault Complex, SD = Svalis Dome, SH = Stappen High, SFZ = Senja Fracture Zone, TFFC = Troms Finnmark Fault Complex, TB = Tromsø Basin, VbV = Vestbakken Volcanic Province.

10 AGE AND COMPOSITION OF BASEMENT ROCKS IN THE NORTH SEA AND NORWEGIAN SEA AND IMPLICATIONS FOR THE CONTINUITY OF THE CALEDONIAN–APPALACHIAN OROGENIC BELT

Trond Slagstad & Børre Davidsen, NGU

10.1 Introduction

It is generally believed that pre-Devonian crystalline basement rocks from the Norwegian mainland extend westwards beneath the Mesozoic sedimentary cover in the North Sea and Norwegian Sea, providing a link between the Norwegian and Scottish Caledonides. Evidence of such a link comes both from previous geochronological work (Frost et al. 1981) as well as from geophysical data (Abramovitz & Thybo 2000). Here, we present new U–Pb zircon age and geochemical data from basement samples in the North Sea and Norwegian Sea that provide much tighter constraints on the nature of the basement rocks in these areas and their geological evolution. The new data allow detailed correlations with onshore geology and provides significant new knowledge about the link between the Caledonian belts on either side of the North Sea and Norwegian Sea. Geochemical and petrophysical data have also been obtained from samples in the Barents Sea; however, here we focus on the samples from which we also have geochronological data.

Work on the Norwegian mainland shows that heat production varies by more than an order of magnitude and is closely linked to geological variation; a similar variation can be expected on the continental margin, with obvious effects on its thermal structure. The work presented here will help constrain the geological variation in the continental margin basement and play an integral role in constraining ongoing 3D thermal modelling of the Norwegian margin.

10.2 Analytical methods

Thirty samples of basement rocks from 22 wells in the North Sea, Norwegian Sea and Barents Sea (Fig. 10.1a) were obtained from the Norwegian Petroleum Directorate. Photos and brief descriptions of the samples are provided in Appendix A.

Zircon was separated from 11 samples from the North Sea and Norwegian Sea (Fig. 10.1b), using standard techniques including heavy liquids, magnetic separation and final hand picking under a binocular microscope. Zircons from 10 samples were analysed at by laser ablation–inductively coupled plasma–mass spectrometry (LA–ICP–MS) at the Geological Survey of Norway and 8 samples were analysed by secondary ion mass spectrometry (SIMS) at the Nordsim laboratory in Stockholm. Seven of the samples have been analysed using both techniques.

10.2.1 SIMS

Prior to SIMS analysis, the grains were mounted in epoxy and polished to approximately half thickness. CL images were obtained using a scanning electron microscope prior to analysis. Eighth samples were analysed using the Cameca IMS 1270 SIMS at the Nordsim laboratory,

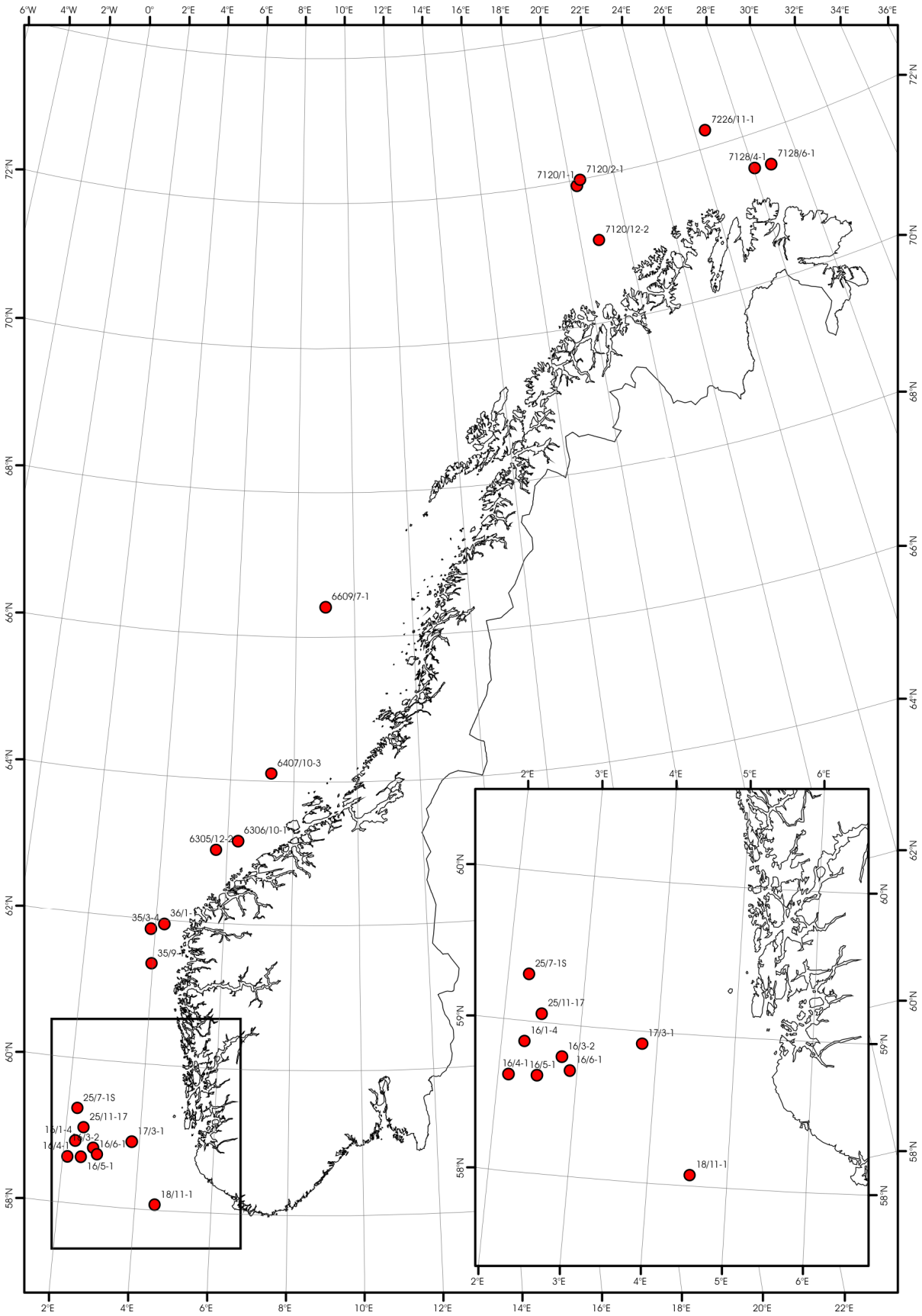

Figure 10.1a. Map showing the locations and names of wells from which basement samples have been obtained.

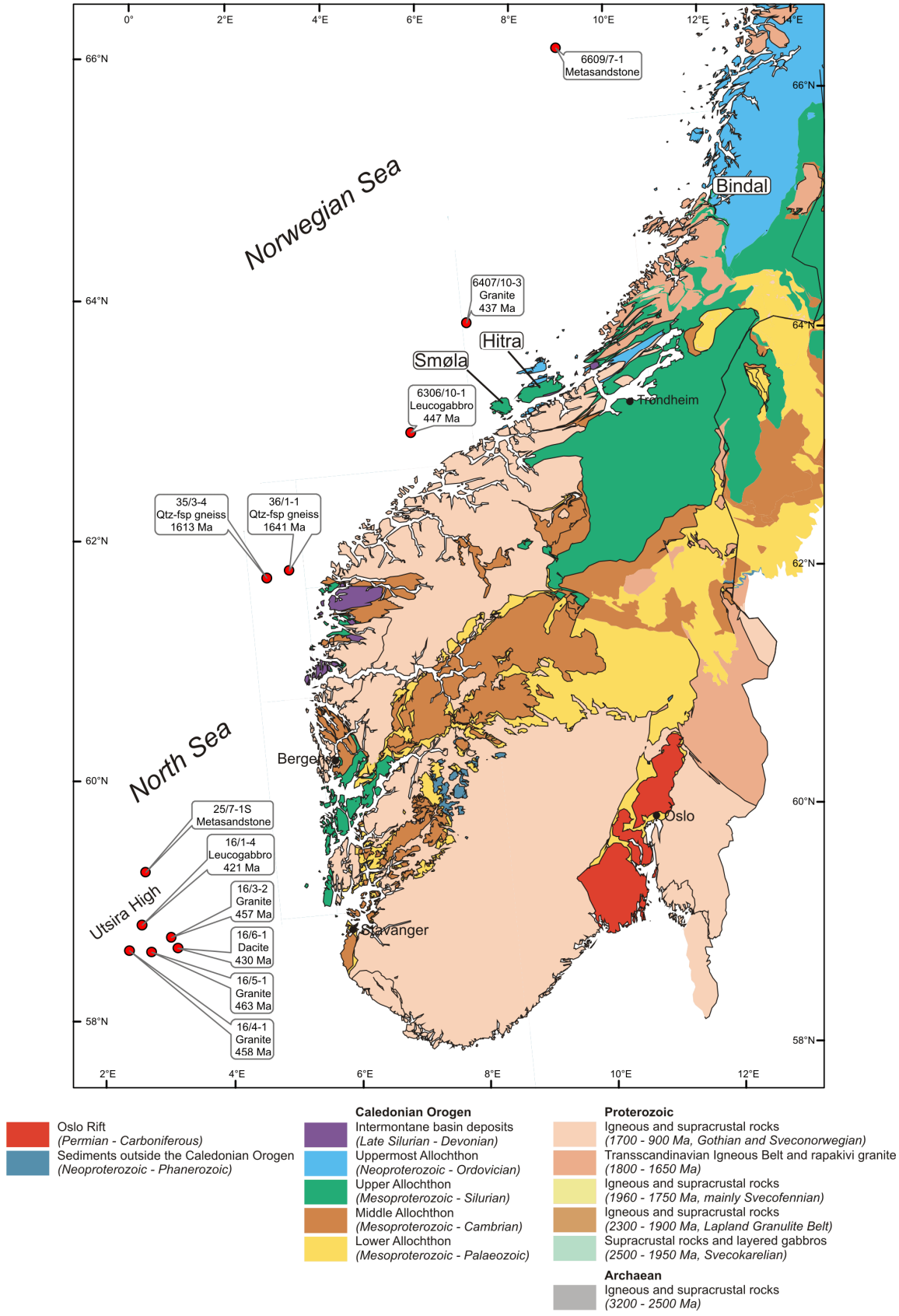

Figure 10.1b. Simplified geological map of South and Central Norway (modified after Solli and Nordgulen (2006) with locations and ages of samples selected for geochronological analysis.

Swedish Museum of Natural History, Stockholm. The analytical method, data reduction, error propagation, and assessment of the results are outlined in Whitehouse et al. (1997, 1999). The analyses were conducted with an O_2-beam of 4 nA and a spot size of 10–30 μm, calibrated to the Geostandard 91500 reference zircon with an age of 1065 Ma (Wiedenbeck et al. 1995). The error on the U/Pb ratio includes propagation of the error on the day-to-day calibration curve obtained by regular analysis of the reference zircon. A common Pb correction was applied using the ^{204}Pb concentration and present-day isotopic composition (Stacey & Kramers 1975).

10.2.2 LA–ICP–MS

The instrumentation used at NGU consists of a Finnigan MAT Element 1 single collector high-resolution sector ICP-MS, in this case alimented by a Finnigan MAT 266 nm (Nd:YAG) UV-laser.

During analysis the laser is operated in Q-mode, at a frequency of 10 Hz. Depending on the sample, the energy used on samples typically varies from about 0.01 mJ to 1.0 mJ, tuned to give the optimum counting statistics. To minimize elemental fractionation, the zircon crystals are ablated in a raster area mode, typically 80x60 μm. The sample aerosol is transported from the sample chamber in He gas, and introduced in the ICP-MS instrument as a mixture of He and Ar gas. The data are acquired in a time-resolved counting scanning mode for 60 sec. Masses ^{202}Hg, ^{204}(Hg+Pb), ^{206}Pb, ^{207}Pb, ^{208}Pb, ^{232}Th and ^{238}U are measured. Monitoring ^{202}Hg and assuming a ^{202}Hg/^{204}Hg ratio of 4.36 corrects the interference of ^{204}Hg on ^{204}Pb. A 60 sec delay is performed after each zircon analysis, and a 60 sec gas blanks acquired at regular intervals. The measured isotope ratios are corrected for element- and mass-bias effects using the Geostandard 91500 reference zircon (Wiedenbeck et al., 1995), normally based on 15 to 30 analyses during one analytical session. The data reduction is performed using MS Excel spreadsheets with Visual Basic macros developed in-house.

The LA–ICP–MS analyses were conducted in two stages. In stage 1, zircons were mounted directly on tape on transparent polycarbon slices and analysed at gradually higher laser energy. This procedure allows thin rims to be analysed first, before interior parts of the grains are exposed. In stage 2, the zircons were rotated 90° around the horizontal axes, mounted in epoxy and polished to c. half thickness. Cathodoluminescence (CL) images were obtained with a scanning electron microscope to reveal internal structures such as growth zoning and core-rim relationships, and in many cases showed the penetration depth of the previous LA–ICP–MS analyses. For data from the tape mount a common Pb correction was applied, using the ^{204}Pb concentration and present-day isotopic composition (Stacey & Kramers 1975).

Appendix B includes a more detailed account of the analytical procedure and discussion of potential pitfalls and limitations of the method.

The Isoplot program (Ludwig 2003) was used to regress and present the U–Pb isotope data. For concordant to near-concordant data sets, the age calculations are based on $^{206}Pb/^{238}U$ – $^{207}Pb/^{235}U$ -ratios. Slightly differing results may be obtained using alternative calculation models (e.g., averages based on $^{207}Pb/^{206}Pb$ ratios).

10.3 Petrographic and geochronological data

10.3.1 North Sea

10.3.1.1 16/1–4 (1937 m), leucogabbro

Sample 16/1–4 (1937 m) is a medium-grained leucogabbro (Fig. 10.2a), mainly consisting of strongly saussuritised plagioclase, amphibole and biotite, with accessory, secondary calcite in thin veins or as small crystal aggregates. The only evidence of deformation is a slight kinking observed in many biotite laths.

The zircons from sample 16/1–4 vary from stubby to elongate biprismatic, 100–300μm, with well-developed crystal faces. They display internal oscillatory zoning, often combined with sector zoning (Figs. 2b, c), typical of magmatic zircons (cf. Corfu & al. 2003). Some grains display a narrow CL-bright rim (0-5 μm), and occasionally CL-bright patches may occur within the grains. The zircons are colourless to skin coloured / faint brownish, and clear. Inclusions and fractures are common.

Nine SIMS analyses from 9 grains yield a concordia age of 420.8 ± 2.9 Ma (2σ; MSWD = 1.7), and 9 LA–ICP–MS analyses from 9 grains yield a concordia age of 427.4 ± 2.9 Ma (2σ; MSWD = 1.03). The combined SIMS and LA–ICP–MS analyses yield a concordia age of 423.2 ± 2.3 Ma (2σ; MSWD = 1.7), taken here to represent the crystallisation age of the leucogabbroic magma (Fig. 10.2d).

16/3–2 (2017.7 m), granite

Sample 16/3–2 (2017.7 m) is a medium-grained, unfoliated granite (Fig. 10.3a) consisting of plagioclase, K-feldspar and quartz, locally with development of myrmekite. Irregular, small grains of biotite and amphibole are the only mafic minerals, and the granite also contains some muscovite and minor epidote.

The zircons from sample 16/3–2 are stubby biprismatic, 100–300 μm, with well-developed crystal faces (Fig. 10.3b). They are skin coloured to brownish, and may have an iron oxide stained surface. Some inclusions and fractures occur. Internally, the zircons typically contain large, CL-bright, rounded cores with (sometimes truncated) oscillatory or irregular zoning, surrounded by thick, oscillatory-zoned rims (Fig. 10.3c). Given the high abundance of cores in the zircon, we consider the cores most likely to be inherited from the source of the granitic magma, whereas the rims represent zircon crystallised from the magma as it cooled.

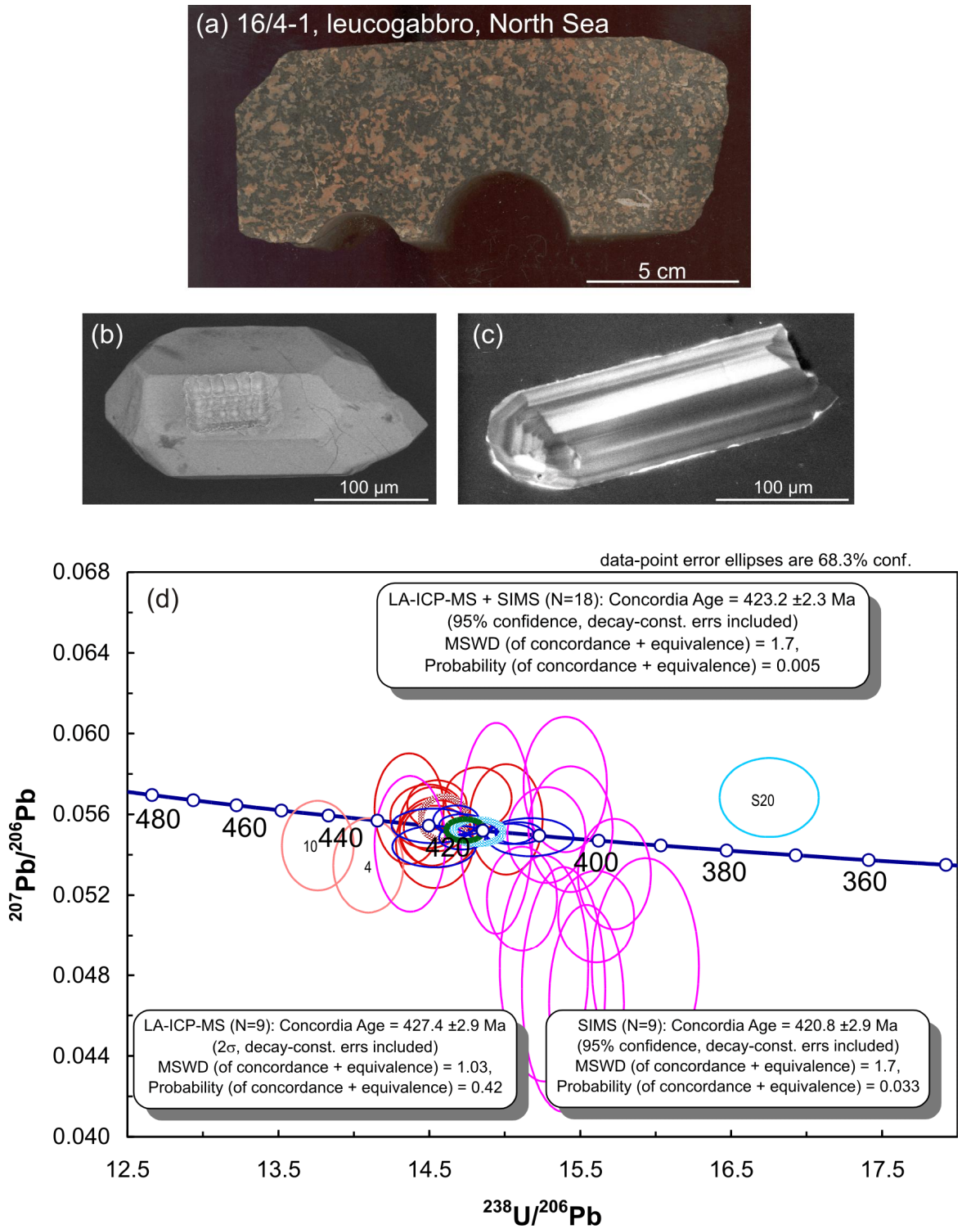

Figure 10.2. (a) Sample photo of leucogabbro from well 16/1–4 in the North Sea. (b) Backscatter image of tape mounted zircon; notice ablation pit after LA–ICP–MS analysis in this and other images. (c) CL image of zircon mounted in epoxy. (d) Terra-Wasserburg concordia diagram showing U–Pb SIMS data obtained from magmatic zircons similar to those shown in (b) and (c).

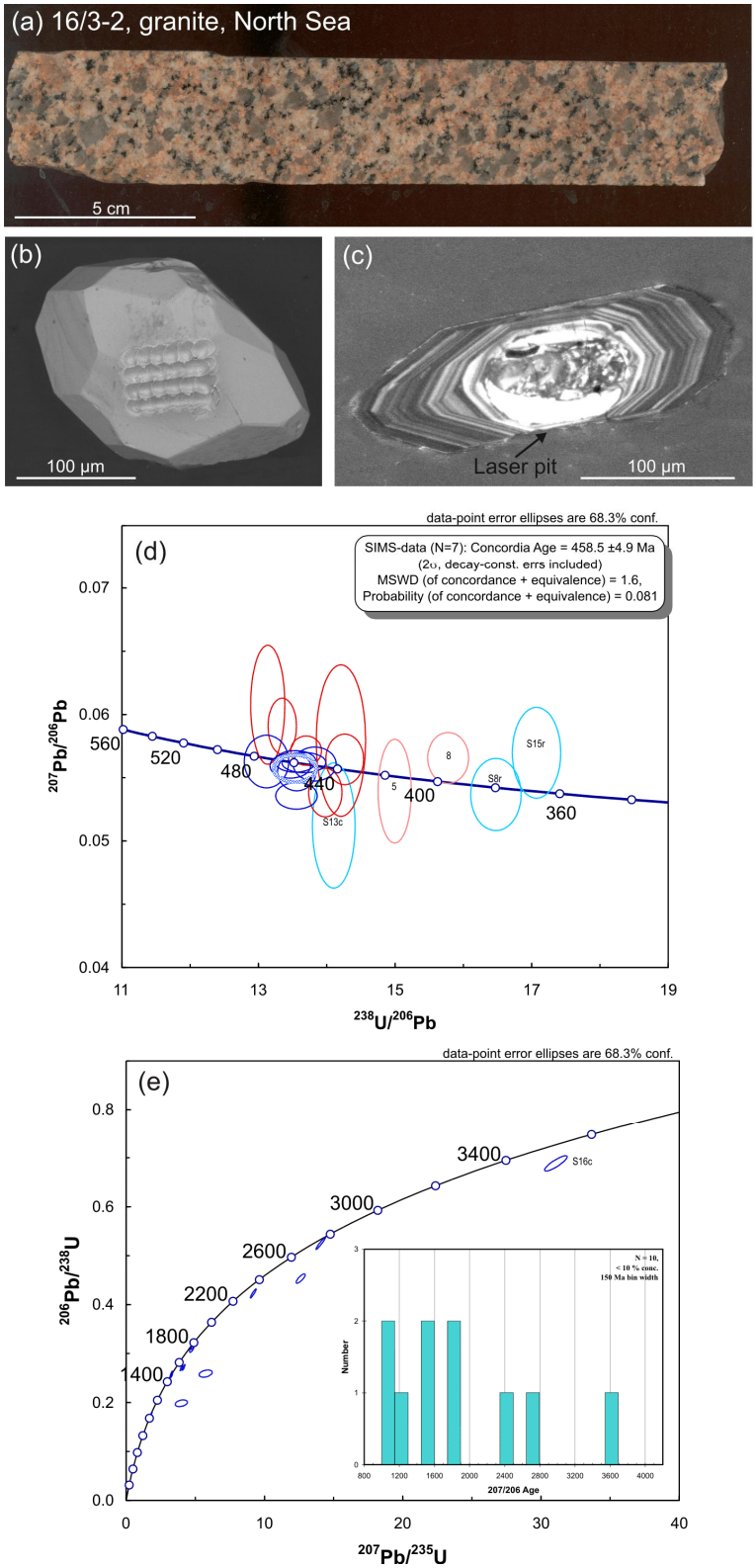

Figure 10.3. (a) Sample photo of granite from well 16/3–2 in the North Sea. (b) Backscatter image of tape mounted zircon. (c) CL image of zircon mounted in epoxy with a rounded inherited core and oscillatory-zoned rim. (d) and (e) Terra-Wasserburg concordia diagrams showing U–Pb SIMS data from oscillatory-zoned rims and inherited cores, respectively. Analysis 16c yielded a 4% discordant (2σ) 207Pb/206Pb age of 3605 ± 13 Ma, which is one of the oldest reported from Norway.

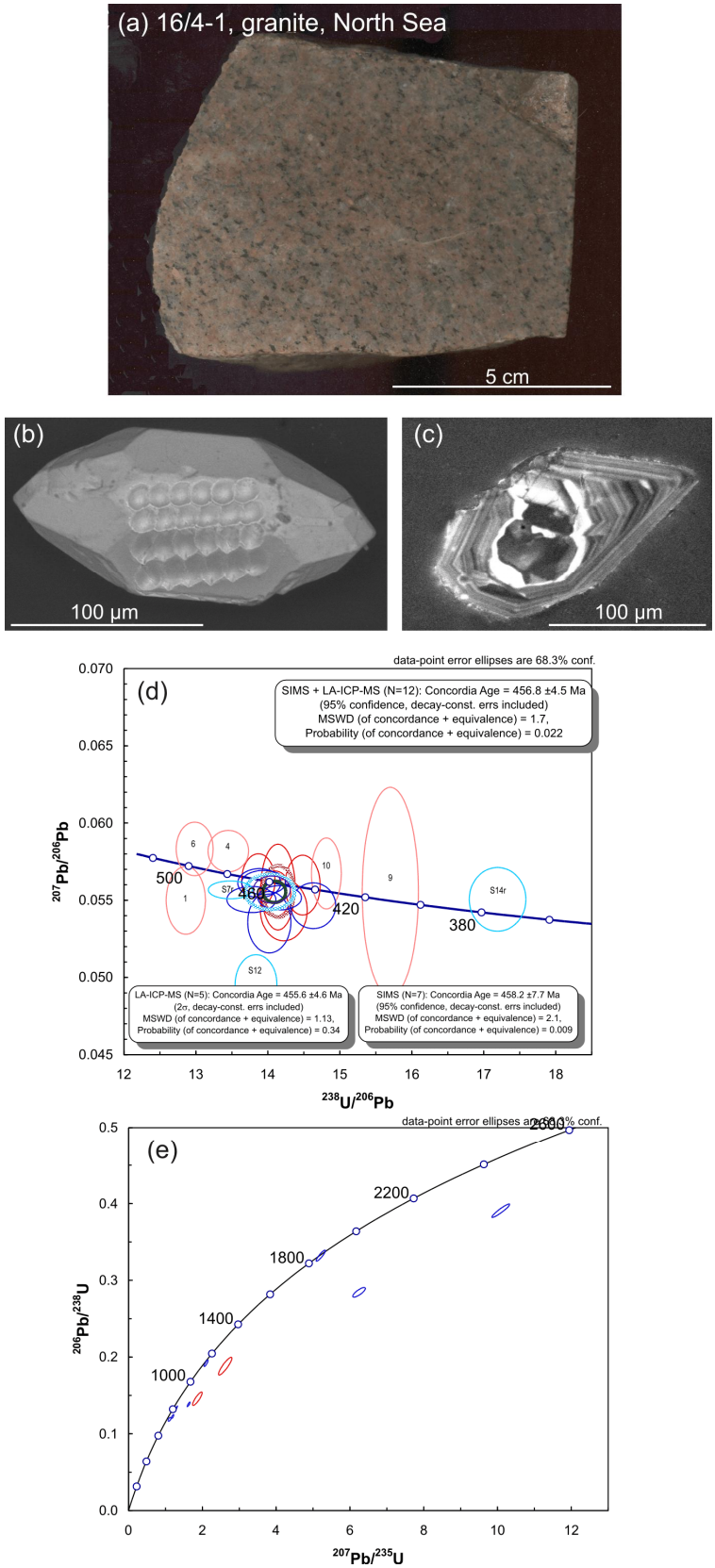

Figure 10.4. (a) Sample photo of granite from well 16/4–1 in the North Sea. (b) Backscatter image of tape mounted zircon. (c) CL image of zircon mounted in epoxy with an irregular inherited core and oscillatory-zoned rim. (d) and (e) Terra-Wasserburg concordia diagrams showing U–Pb SIMS data from oscillatory-zoned rims and inherited cores, respectively.

Seven SIMS analyses of oscillatory-zoned rims yield a concordia age of 458.5 ± 4.9 Ma (2σ; MSWD = 1.6), interpreted to date the crystallisation age of the granitic magma (Fig. 10.3d). Although giving comparable results, the LA–ICP–MS data are too scattered to be treated as concordant in the age calculation, and therefore omitted. Fifteen analyses of zircon cores yield $^{207}Pb/^{206}Pb$ ages ranging from 1044 to 3605 Ma (Fig. 10.3e). The large spread of the core ages strongly suggests that the granite was formed by anatexis of a sedimentary precursor, and that the core ages can be considered provenance ages for this (former) sediment.

10.3.1.2 16/4–1 (2908.6 m), granite

Sample 16/4–1 (2908.6 m) is a fine-grained granite (Fig. 10.4a), consisting mainly of K-feldspar, plagioclase and quartz. Biotite is the only mafic mineral and the rock also contains minor amounts of muscovite. The granite is undeformed except for moderately undulating extinction in quartz. Overlying the granite is a fine-grained sedimentary rock consisting of alternating layers of immature quartzite and dark grey siltstone. The granite clearly cuts the foliation in the overlying sedimentary rock. Like the granite, the sedimentary rock appears undeformed except for moderately undulating extinction in quartz.

The zircons from sample 16/4–1 are rather similar to those found in sample 16/3–2; they are skin coloured to brownish, stubby biprismatic, 100–300 μm, with well-developed crystal faces (Fig. 10.4b), and typically contain large (often CL-bright) cores surrounded by thick, oscillatory-zoned rims (Fig. 10.4c). Some of the cores themselves have oscillatory zoning that often becomes truncated, sometimes by a CL-brighter layer. As above, the rims most likely represent zircon crystallised from the magma, whereas the cores could be inherited from the source of the granitic magma or represent assimilated zircons during ascent and/or emplacement.

Seven SIMS analyses of 7 oscillatory-zoned rims yield a concordia age of 458.2 ± 7.7 Ma (2σ; MSWD = 2.1) and 5 LA–ICP–MS analyses of 5 tape-mounted grains yield a concordia age of 455.6 ± 4.6 Ma (2σ; MSWD = 1.13). The combined SIMS and LA–ICP–MS analyses yield a concordia age of 456.8 ± 4.5 Ma (2σ; MSWD = 1.7), interpreted to date the crystallisation age of the granitic magma (Fig. 10.4d).

Seven SIMS and 2 LA–ICP–MS analyses of zircon cores yield $^{207}Pb/^{206}Pb$ ages ranging from 942 to 2719 Ma (Fig. 10.4e); however, apart from two analyses at 1181 (S1) and 1861 (S2c) Ma, the cores yield strongly discordant ages.

10.3.1.3 16/5–1 (1929.3 m), granite

Sample 16/5–1 (1929.3 m) is a fine-grained, unfoliated, dark red granite (Fig. 10.5a), which consists mainly of K-feldspar, plagioclase and quartz. Biotite is the only mafic mineral and

the rock contains minor amounts of muscovite and accessory epidote. The granite is undeformed except for moderately undulating extinction in quartz.

The zircons from sample 16/5–1 are similar to those found in samples 16/3–2 and 16/4–1, albeit slightly smaller. The zircons are prismatic, 100–200 μm, with well-developed external crystal faces (Fig. 10.5b), and often contain large, rounded CL-bright cores, surrounded by thick, oscillatory-zoned rims (Fig. 10.5c). As above, we interpret the cores to be inherited from the source of the granitic magma or assimilated during ascent and/or emplacement, whereas the rims most likely represent zircon crystallised from the magma.

Twelve SIMS analyses of oscillatory-zoned rims yield a concordia age of 463.3 ± 5.5 Ma (2σ; MSWD = 2.0), interpreted to date the crystallisation age of the granitic magma (Fig. 10.5d). Seven LA–ICP–MS analyses from 7 grains yield a significantly younger concordia age of 433.4 ± 5.2 Ma (2σ; MSWD = 1.5). Clearly, there must be analytical reasons for this large discrepancy of 30 Ma. In theory, the young LA-ICP-MS dates could be influenced by both very shallow ablation depths (as low laser energies were applied), contamination from substratum ablation, or calibration biases. The latter seems improbable, as other samples from the same batch give no indications of calibration biases of significant magnitude. We therefore speculate that the not all surface affected material was removed during the surface ablation stage, and that subsequent analyses deeper in the crystals reflect a mix with surface material. We can nevertheless not completely discard the possibility of substratum contamination (even though there is no apparent correlation between the age and the amount of substratum ablation).

Six SIMS analyses of zircon cores yield $^{207}Pb/^{206}Pb$ ages ranging from 1040 to 1877 Ma (Fig. 10.5e). Two analyses with excessive common Pb (S3c and S16c) were excluded.

10.3.1.4 16/6–1 (2059.7 m), dacite

Sample 16/6–1 (2059.7 m) is a fine-grained, undeformed, grey volcanic rock with abundant phenocrysts of plagioclase. The plagioclase phenocrysts <1–2 mm and are blocky to angular prismatic, typically with albite twinning. The phenocrysts are strongly saussuritised, but many of the larger crystals contain less altered cores. The matrix consists of fine-grained plagioclase and slightly larger biotite, with small amounts of quartz. The phenocrysts are unoriented and the rock does not appear deformed (Fig. 10.6a). The sample also contains a small (ca. 4 cm) xenolith of slightly coarser grey rock.

The zircons from sample 16/6–1 are biprismatic, 75–200 μm, with well-developed, slightly rounded crystal faces (Fig. 10.6b). They are colourless to skin coloured and clear. Inclusions occur in some grains. The zircons have a well developed oscillatory zoning (Fig. 10.6c), and a few have brighter cores and/or brighter layers in the core. One crystal (no 5) has a core with an internal diffuse zoning that is truncated by the surrounding mantle.

Ten SIMS analyses of oscillatory-zoned zircons yield a concordia age of 429.8 ± 5.5 Ma (2σ; MSWD = 2.0) (Fig. 10.6d), interpreted to represent the crystallisation age of the porphyritic magma. Two zircon cores (#5 and # 8) yield $^{206}Pb/^{238}U$ ages of 491 and 1100 Ma. We interpret the oscillatory-zoned zircons to have crystallised from the porphyritic magma/lava, whereas the cores may be derived from the magma source or represent grains entrained in the magma during ascent and emplacement.

10.3.1.5 25/7–1S (3554. 3 m), metasandstone

Sample 25/7–1S (3554.3 m) is a faintly banded, grey metasandstone (Fig. 10.7a) consisting of fine-grained quartz with minor plagioclase and K-feldspar layers alternating with more feldspar-rich, very fine-grained layers. Muscovite is abundant as oriented laths, up to a few mm long. Subhedral pyrite is rather common and appears to be associated with the feldspar-rich layers. The metasandstone is criss-crossed by numerous calcareous veins.

The zircons from sample 25/7–1S are slightly to moderately abraded/rounded, with shapes ranging from imperfect biprismatic (sometimes multifaceted), via rounded (abraded) biprismatic to rounded elongate (Fig. 10.7b). The grains are colourless to faint yellowish, and commonly have fractures or contain inclusions. The zircons range in size from 90 to 200 μm and are typically oscillatory-zoned (Fig. 10.7c), in some grains combined with sector zoning (cf., Corfu et al. 2003), attesting to the magmatic origin of the zircons. The internal zoning is cut in some grains, demonstrating sedimentary transport and abrasion. Some grains contain homogeneous zones or patchy, flame-like domains, possibly due to replacements/alterations. A thin, typically 2–10 μm, CL-bright rim is present in about one half of the grains (e.g., Fig. 10.7c).

Fig. 10.7d shows a concordia diagram of common Pb-corrected data obtained by LA–ICP–MS from sample 25/7–1S. Most of the grains yield ages between 1000 and 1750 Ma and two grains yield ages around 2800 Ma. A cumulative probability plot based on 93 analyses that are <10% discordant (Fig. 10.7d inset) shows that the main age group 1000–1800 Ma is comprised of several populations at 1000–1150 Ma, c.1350 Ma and 1600–1650 Ma, with a subordinate peak at 1500 Ma. In addition there are a few data points at c. 1900 and c. 2800 Ma.

10.3.1.6 35/3–4 (4088.3 m), mica-rich quartzofeldspathic gneiss

Sample 35/3–4 (4088.3 m) is a mylonitic dark grey, quartzofeldspathic gneiss with mm- to cm-sized deformed feldspar augens and abundant biotite, subhedral epidote, and minor muscovite in the matrix (Fig. 10.8a), all minerals now recrystallised to a fine-grained

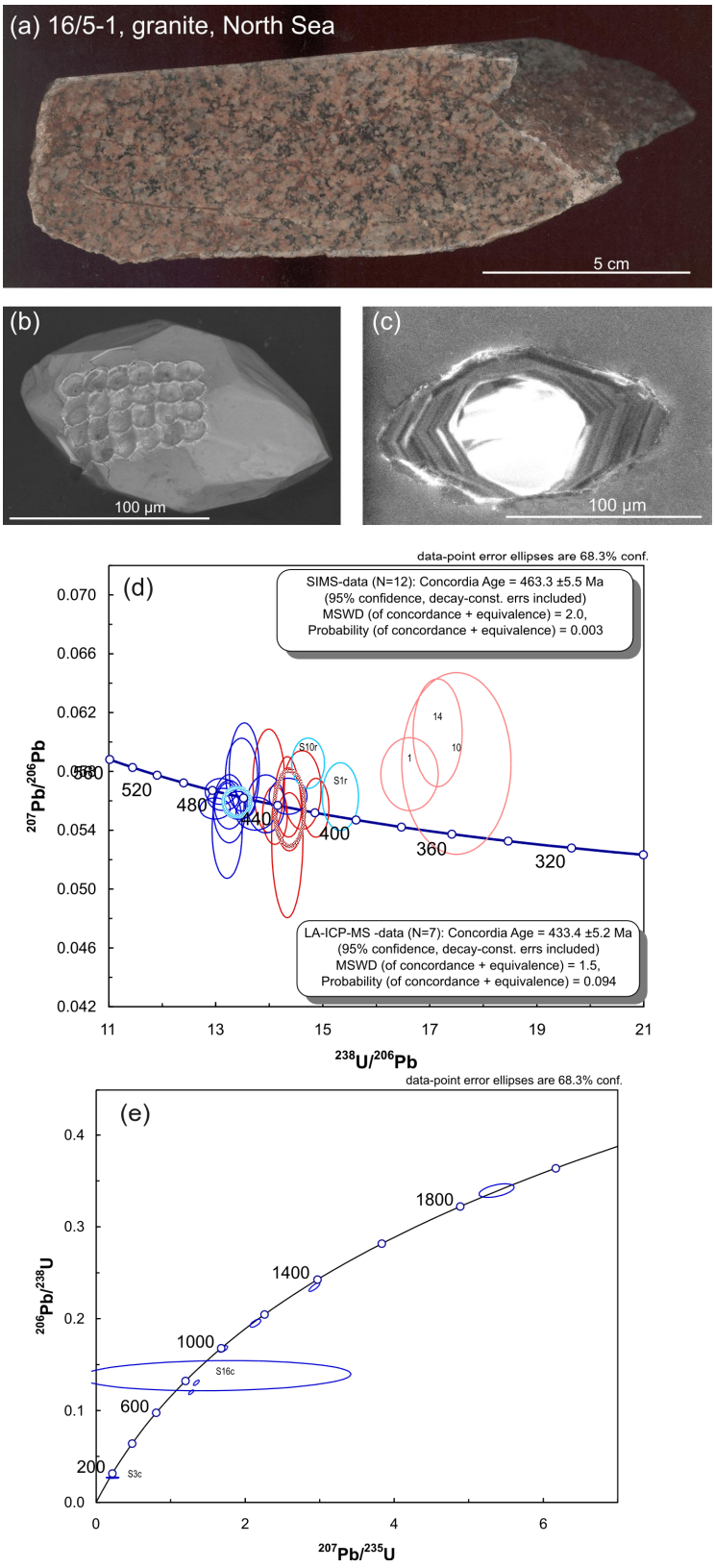

Figure 10.5. (a) Sample photo of granite from well 16/5–1 in the North Sea. (b) Backscatter image of tape mounted zircon. (c) CL image of zircon mounted in epoxy with CL-bright and rounded inherited core and oscillatory-zoned rim. (d) and (e) Terra-Wasserburg concordia diagrams showing U–Pb SIMS data from oscillatory-zoned rims and inherited cores, respectively.

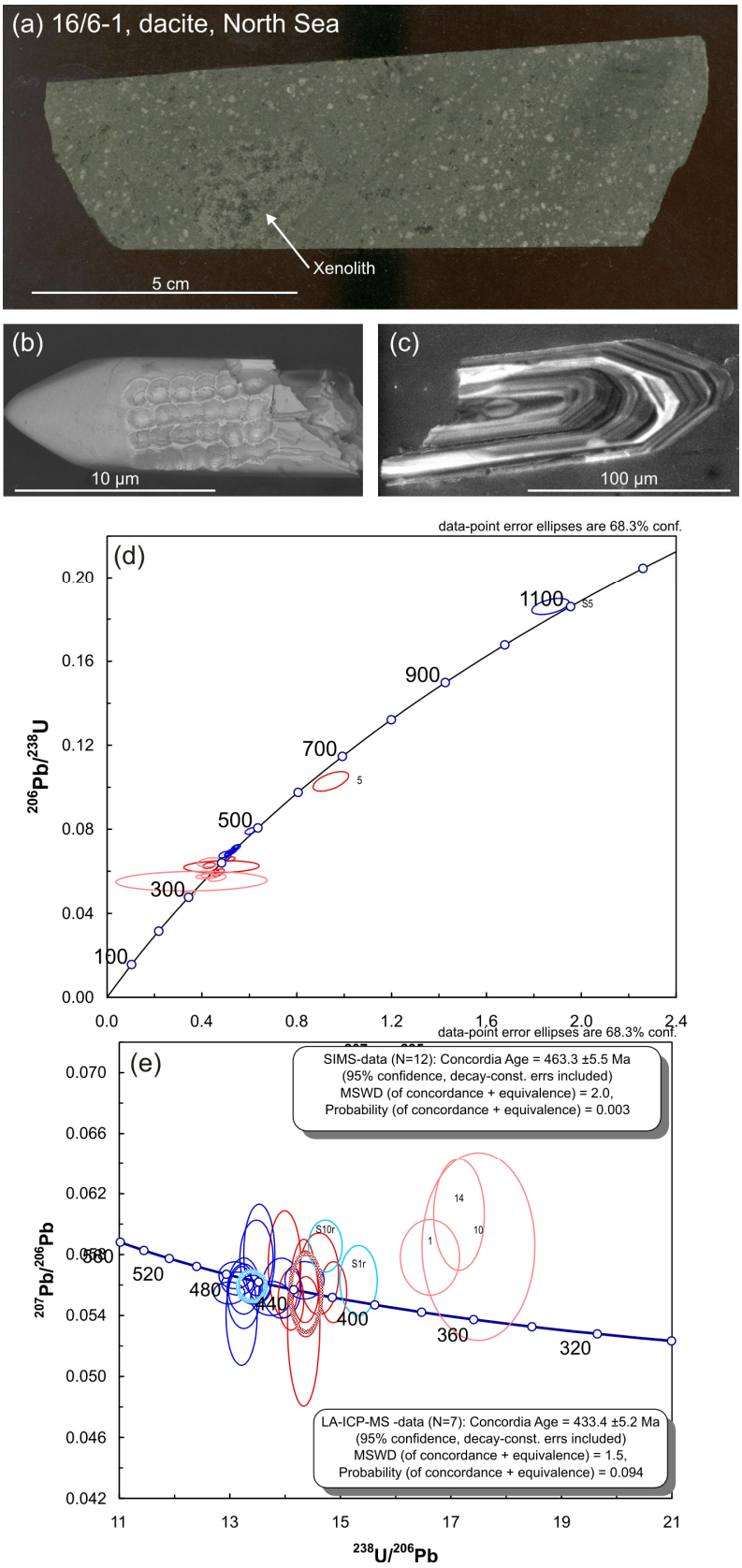

Figure 10.6. (a) Sample photo of dacite from well 16/6–1 in the North Sea. (b) Backscatter image of tape mounted zircon. (c) CL image of zircon mounted in epoxy with CL-bright and rounded inherited core and oscillatory-zoned rim. (d) Terra-Wasserburg concordia diagram showing U–Pb SIMS data from oscillatory-zoned rims and two inherited cores.

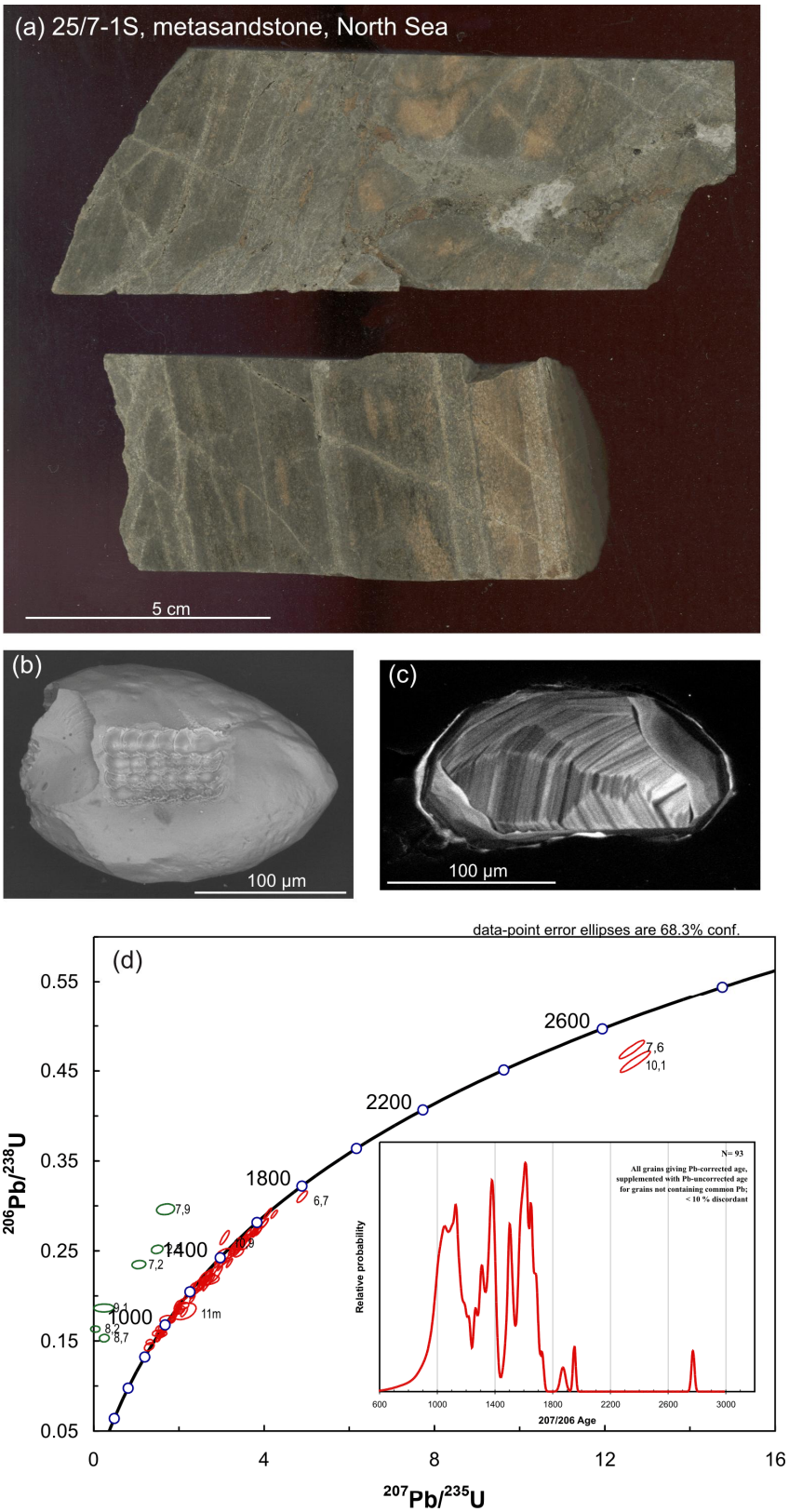

Figure 10.7. (a) Sample photo of metasandstone from well 25/7–1S in the North Sea. (b) Backscatter image of tape mounted zircon. (c) CL image of zircon mounted in epoxy. (c) concordia diagram showing U–Pb LA–ICP–MS data obtained from detrital zircons similar to that shown in (b). The inset in (c) shows a relative probability vs. age plot of the detrital zircons.

assemblage of alternating bands. The zircons from sample 35/3–4 are mostly stubby biprismatic, commonly with irregular or poorly developed crystal faces that give them a rounded, elongate appearance (Fig. 10.8b). The zircons range in size from 150 to 400 μm, and normally display oscillatory zoning, but occasionally only present as diffuse remnants. In some grains it may be partly replaced by more homogeneous, low luminescent material, often with amoeboid contacts. All examined grains also display a CL-bright rim (0–20 μm) (Fig. 10.8c), and very often also stringer and patches of the same material (as alterations/replacements). Inclusions are common, and some grains are fractured.

LA–ICP–MS U–Pb data for a total of 20 dated zircon crystals are shown in Fig. 10.8d. All epoxy-mounted grains were ablated twice in the same spot. Twelve of the grains were grains were first dated on tape mounts, including surface ablation. Surface ablation results are shown in pink. The grains provide a reasonably well-defined discordia with an upper intercept of 1613 ±11 Ma (2σ; MSWD = 3.8) (Fig. 10.8d), interpreted to represent the crystallisation age of the magmatic protolith. The discordia also gives a less well defined lower intercept of 325 ±94. The exact age is rather sensitive to the values of the common Pb-corrected surface ablation data points, and should be treated as suggestive only. Nevertheless, it hints to a probable Caledonian event, most likely responsible for the CL-bright rims and alterations / replacements in the crystals.

10.3.1.7 36/1–1 (5212.3 m), mica-rich quartzofeldspathic gneiss

Sample 36/1–1 (5212.3 m) is a medium-grained, dark grey, quartofeldspathic gneiss with abundant biotite, subhedral epidote, and minor muscovite (Fig. 10.9a), slightly coarser grained and less anisotropic than sample 35/3-4, but otherwise similar.

The zircons from sample 36/1–1 are prismatic and mostly stubby biprismatic, commonly with imperfect crystal faces and a rounded aspect (Fig. 10.9b). They range in size from 150 to 300 μm, display well-developed oscillatory zoning and are typically mantled by CL-bright rims and stringers into the crystal (Fig. 10.9c). These CL-bright alterations/replacements are, however, less extensive than in sample 35/3–4. Inclusions and fractures are common.

LA–ICP–MS U–Pb data from 20 dated zircons are shown in Fig. 10.9d. All epoxy-mounted grains were ablated twice in the same spot. Twelve of the grains were first dated on tape mounts, including surface ablation. Surface ablation results are shown in pink. The grains give a well-defined discordia with an upper intercept of 1641.1 ±5.3 Ma (2σ; MSWD = 2.3) (Fig. 10.9d), interpreted to represent the crystallisation age of the magmatic protolith. No data points are omitted from regression.

The discordia also provides a less well defined lower intercept of 274 ±96. Again, the exact age is sensitive to the values of the common-Pb-corrected surface ablation data points, and

should be treated as suggestive only. Nevertheless, it hints to a probable Caledonian event, most likely responsible for the CL-bright rims and alterations/replacements in the crystals.

10.3.2 Norwegian Sea

10.3.2.1 6306/10–1 (3158.5 + 3159.2 m), leucogabbro

Sample 6306/10–1 is a medium-grained leucogabbro (Fig. 10.10a), mainly consisting of strongly saussuritised plagioclase and amphibole, with accessory, secondary calcite in thin veins. The rock appears undeformed apart from a slight kinking observed in some plagioclase grains where albite twinning is preserved.
The zircons from sample 6306/10–1 are mostly stubby biprismatic, 100–200 μm, with well-developed crystal faces (Fig. 10.10b), and internal oscillatory or parallel zoning, often combined with sector zoning.. They are colourless to smoke coloured and clear. Inclusions may occur, while fractures are more abundant.

A total of 14 zircon crystals were dated, 12 using the LA-ICP-MS two-stage analysis protocol on tape mounts, and 8 grains using SIMS. 6 of the analyses by SIMS are doublets of the LA-ICP-MS. Th eight SIMS analyses yield a concordia-age of 446.9 ± 4.0 Ma (2σ; MSWD = 1.5), whereas the twelve LA–ICP–MS analyses yield two populations: a young group with a concordia age of 431.2 ± 3.8 Ma (2σ; MSWD = 1.4), and an old group with a concordia age of 454.5 ± 4.6 Ma (2σ; MSWD = 1.15). Combining the SIMS data with the old LA–ICP–MS group yields a combined age of 450.3 ± 3.9 Ma (2σ; MSWD = 1.6), interpreted as the crystallisation age of the leucogabbroic magma.

10.3.2.2 6407/10–3 (2972.1 m), granite

Sample 6407/10–3 is a fine-grained granite (Fig. 10.11a), consisting mainly of K-feldspar, plagioclase and quartz. Biotite is the only mafic mineral, occurring as small (<1 mm), dispersed specks. Muscovite is an accessory phase. The granite is undeformed except for moderately undulating extinction in quartz.

The zircons from sample 6407/10–3 are commonly stubby biprismatic to stubby, 100–300 μm, sometimes multifaceted and sometimes with irregular or poorly developed crystal faces that gives them a rounded appearance (Fig. 10.11b). They are clear, colourless to yellowish, often with an iron oxide stained surface. A few grains contain inclusions. The zircons are oscillatory-zoned and some of the grains have CL-bright cores or CL- brighter domains within the grains (Fig. 10.11c); however, such cores are not nearly as ubiquitous as in the granite samples from the North Sea. The cores typically display oscillatory zoning that in some case appear to be in crystallographic continuity with the surrounding oscillatory-zoned rim. The cores and rims of the zircons may be therefore represent episodic growth in a magma of fluctuating composition, or –alternatively – the cores could represent grains entrained in the magma during ascent and/or emplacement. The two cores analysed by SIMS

(S3c and S4c) yield ages indistinguishable from the darker, oscillatory-zoned margins in other grains, lending support to the first interpretation.

Six SIMS analyses of oscillatory-zoned zircon (including the two 'cores') yield a concordia age of 436.6 ± 4.4 Ma (2σ; MSWD = 1.11) (Fig. 10.11d), interpreted as the crystallisation age of the granitic magma. Besides some obvious outliers, the LA–ICP–MS data show significant scatter toward a lower age range, and were not included The reason for this deviation might be as discussed under sample 16/5-1.

10.3.2.3 6609/7–1 (1945.8 m), metasandstone/-siltstone

Laminated metasediment consisting of <1 cm, light orange layers dominated by very fine-grained quartz (sandstone/quartzite) with some muscovite, and thinner grey layers dominated by very fine-grained quartz and abundant muscovite (siltstone) (Fig. 10.12a). Weak undulatory extinction of quartz attests to some deformation. The rock is jointed with calcite-filled veins, and also contains dispersed calcite within the quartzitic matrix.

The zircons from sample 6609/7–1 are and rather small, in mounts they typically have cross-sections between 50 and 100 μm. The majority of the grains are rounded equidimensional to elongate, but sub-rounded biprismatic (sometimes multifaceted) grains also occur. In general, the zircons display oscillatory zoning, sometimes combined with sector zoning. Many grains represent abraded fragments of larger crystals, obviously reflecting sedimentary transport and abrasion. A few grains have a distinct core, but there is no evidence of metamorphic growth of zircon in the rock, in agreement with the low metamorphic grade.

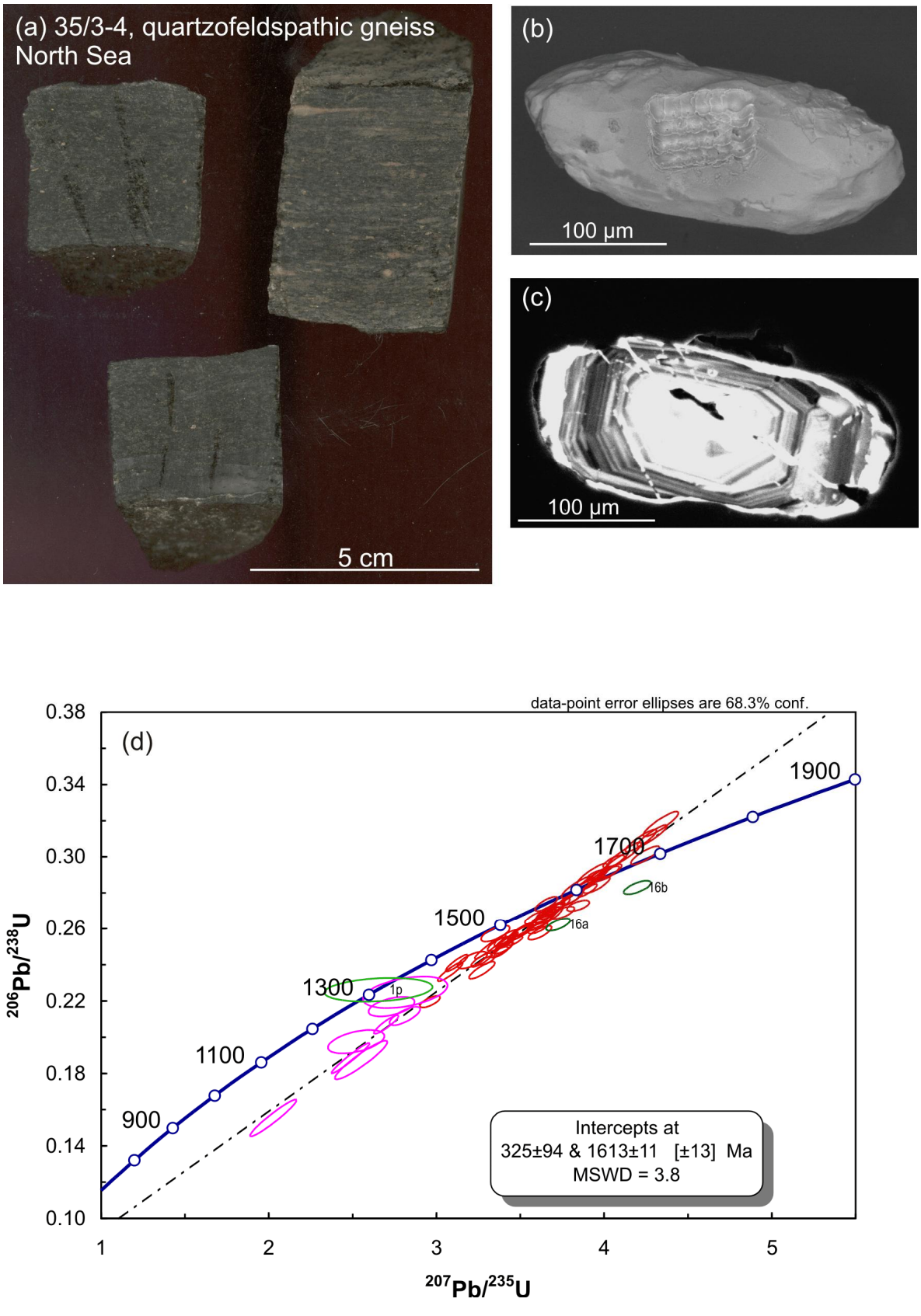

Figure 10.8. (a) Sample photo of quartofeldspathic gneiss from well 35/3–4 in the North Sea. (b) Backscatter image of tape mounted zircon. (c) CL image of zircon mounted in epoxy. (d) concordia diagram showing U–Pb LA–ICP–MS data obtained from magmatic zircons similar to those shown in (b) and (c)

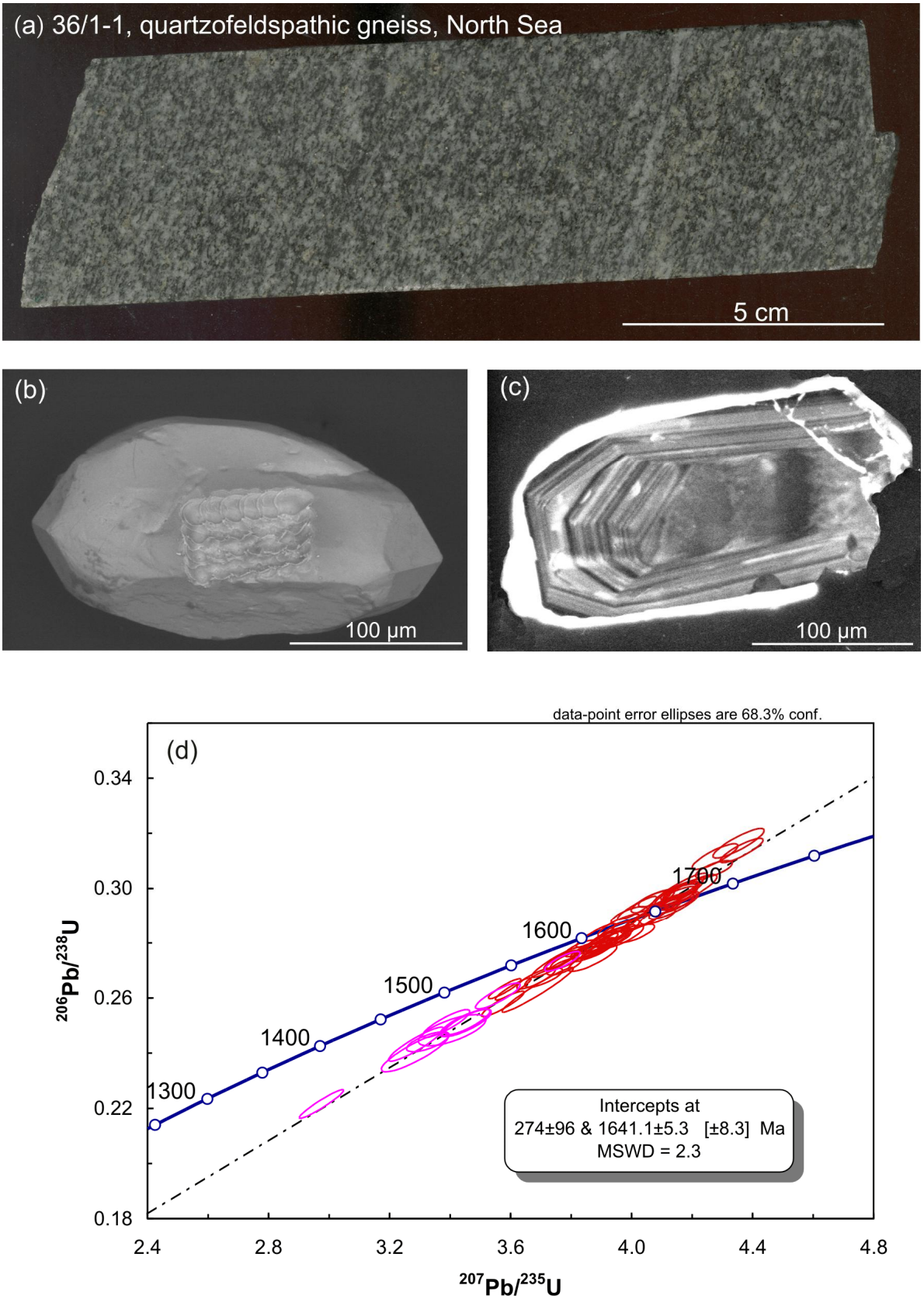

Figure 10.9. (a) Sample photo of quartofeldspathic gneiss from well 36/1–1 in the North Sea. (b) Backscatter image of tape mounted zircon. (c) CL image of zircon mounted in epoxy. (d) concordia diagram showing U–Pb LA–ICP–MS data obtained from magmatic zircons similar to those shown in (b) and (c)

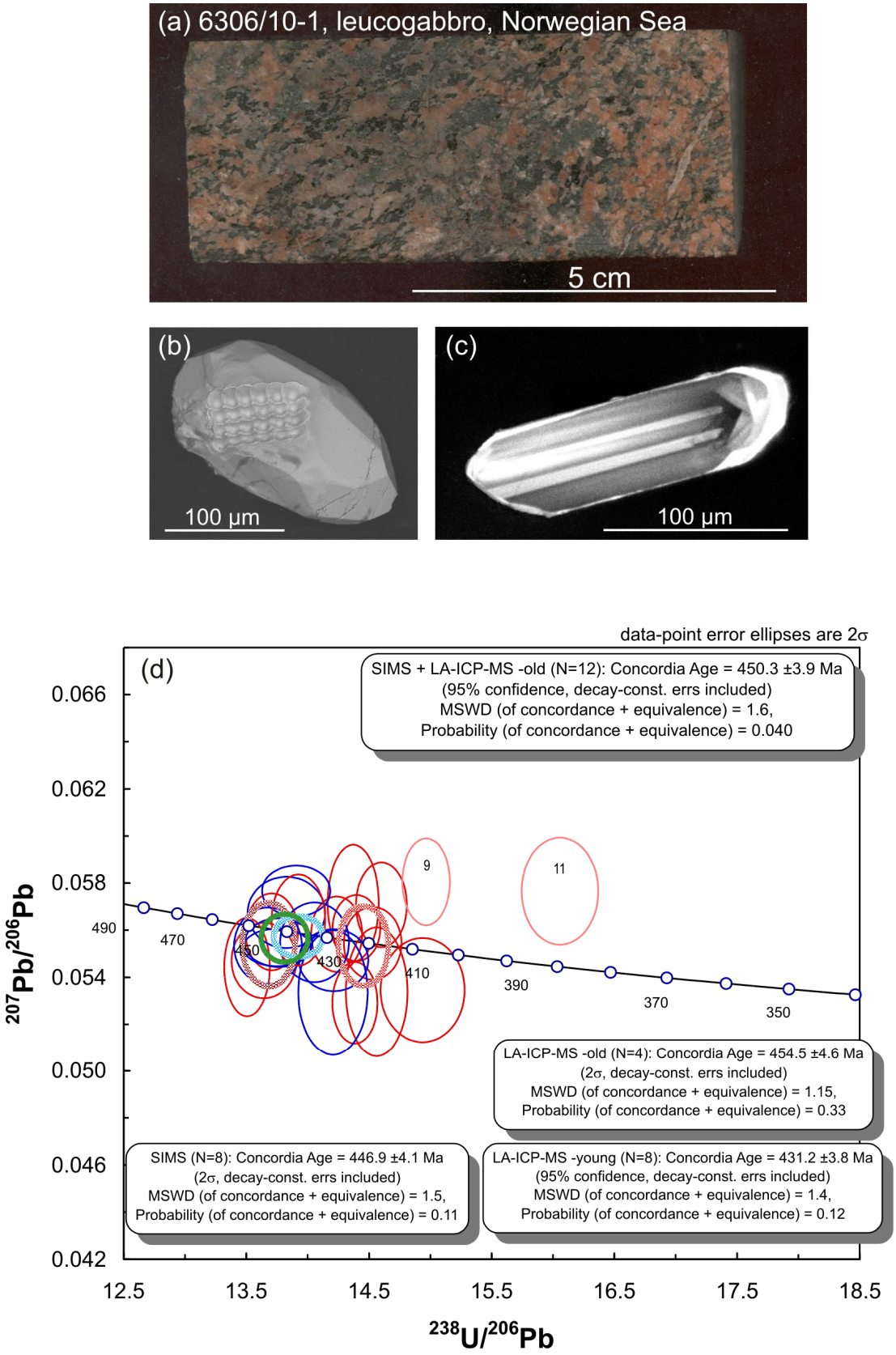

Figure 10.10. (a) Sample photo of leucogabbro from well 6306/10–1 in the Norwegian Sea. (b) Backscatter image of tape mounted zircon. (c) CL image of zircon mounted in epoxy. (d) Terra-Wasserburg concordia diagram showing U–Pb SIMS data obtained from magmatic zircons similar to those shown in (b) and (c).

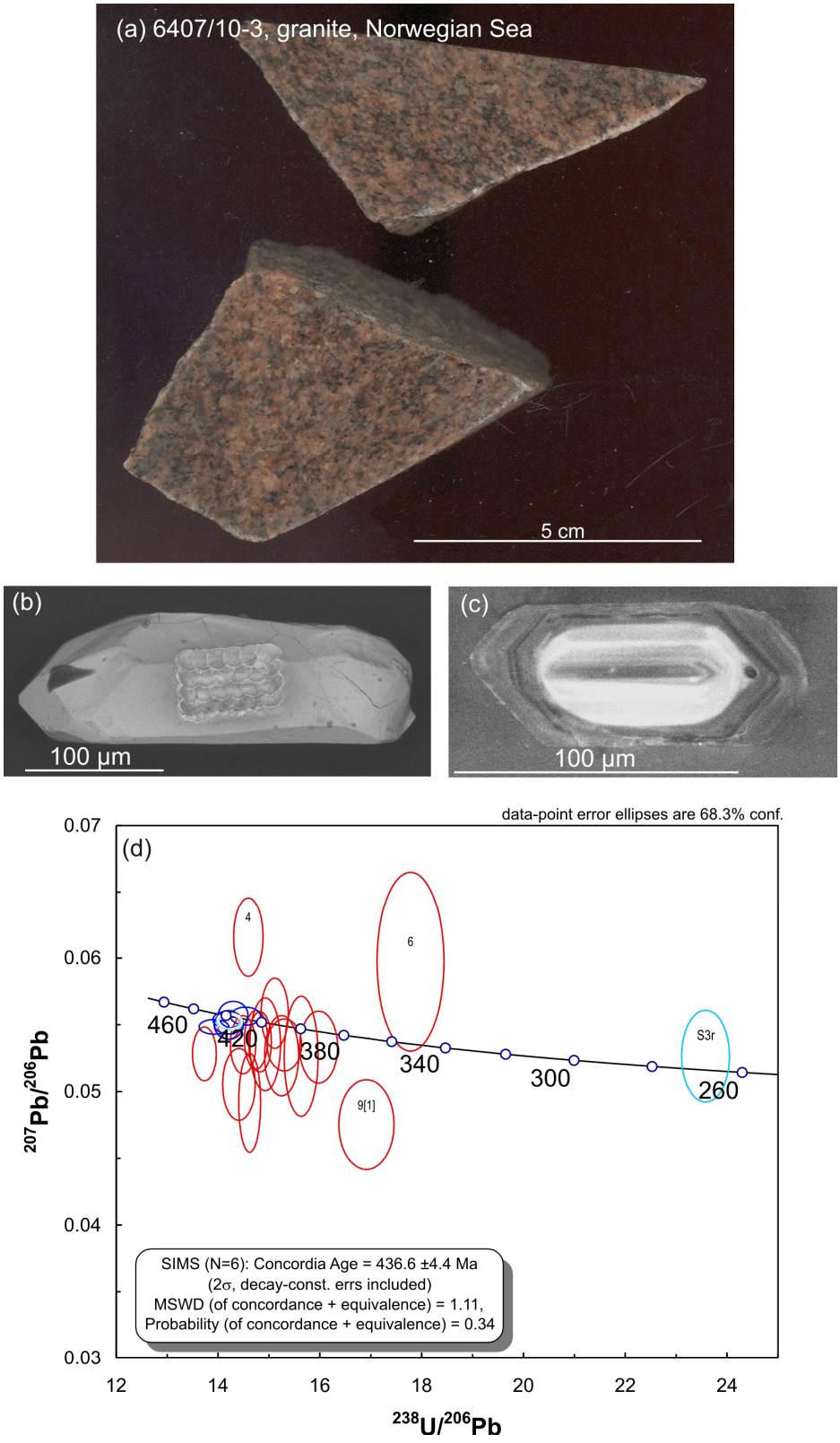

Figure 10.11. (a) Sample photo of granite from well 6407/10–3 in the Norwegian Sea. (b) Backscatter image of tape mounted zircon. (c) CL image of zircon mounted in epoxy with CL-bright and rounded inherited core and oscillatory-zoned rim. (d) Terra-Wasserburg concordia diagram showing U–Pb SIMS data obtained from magmatic zircons similar to those shown in (b) and (c).

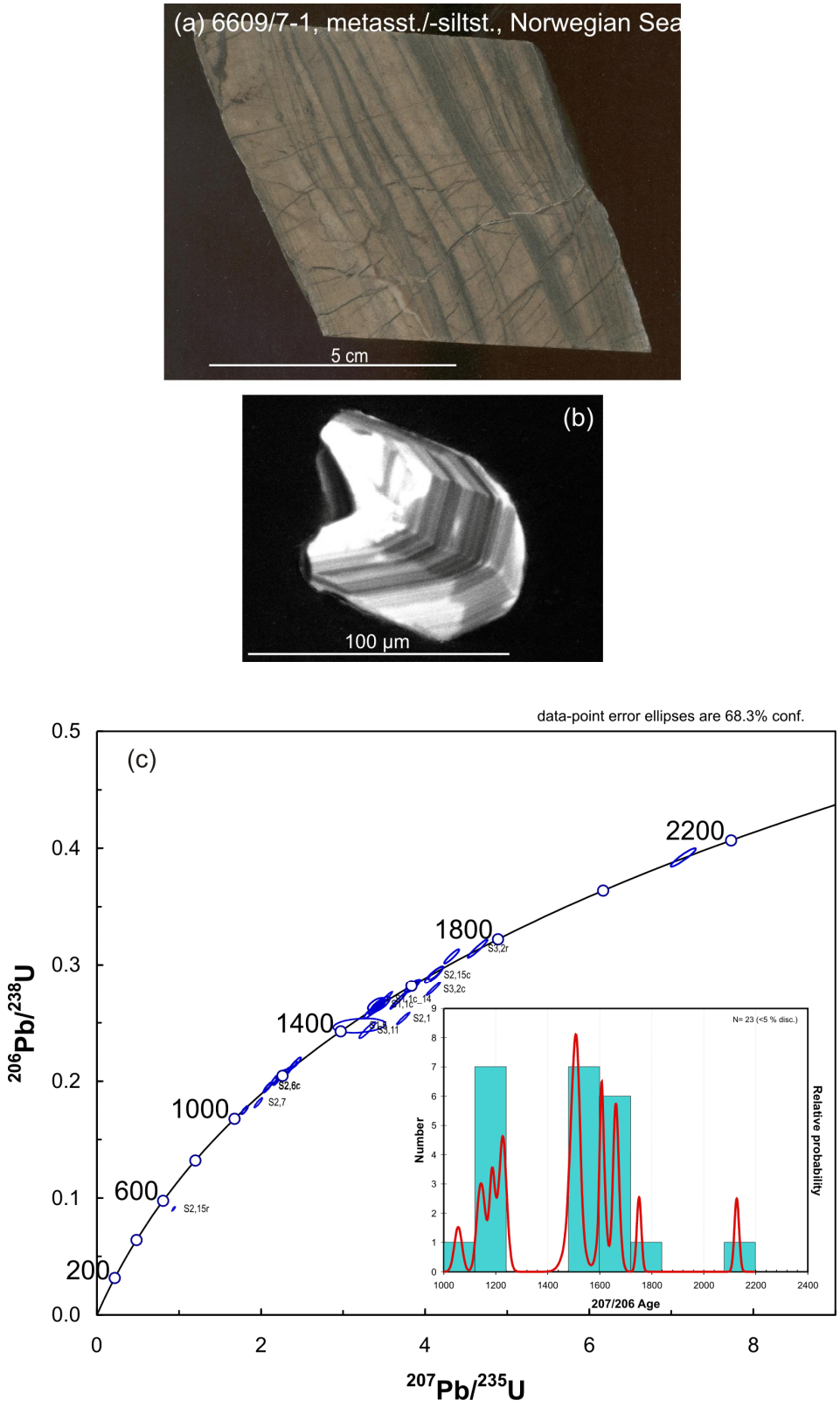

Figure 10.12. (a) Sample photo of metasediment from well 6609/7–1 in the Norwegian Sea. (b) CL image of zircon mounted in epoxy. (c) Terra-Wasserburg concordia diagram showing U–Pb SIMS data obtained from detrital zircons similar to that shown in (b). The inset in (c) shows a relative probability vs. age plot of the detrital zircons.

Twenty-seven SIMS analyses yield $^{207}Pb/^{206}Pb$ ages between 1056 and 2127 Ma (Fig. 10.12b). Fig. 12b inset shows a cumulative probability plot of 23 analyses that are <5% discordant. The dominant populations are 1600–1750 Ma, 1500 Ma and 1100–1200 Ma.

10.4 Discussion

The Scandinavian Caledonides are generally considered to consist of four more or less distinct nappe complexes, referred to as the Lower, Middle, Upper and Uppermost Allochthons, overlying Parautochthonous and Autochthonous Baltican rocks (Roberts & Gee 1985). The allochthonous units were emplaced toward the southeast, along generally NW-dipping thrusts, although locally west vergent structures are preserved (Roberts et al. 2002a, Yoshinobu et al. 2002). Thus, the samples described here from the Norwegian continental margin are likely to come from structurally high nappes, most likely representing the Upper or Uppermost Allochthon (or higher) or the Precambrian gneiss regions (e.g., Western Gneiss Region). The low sample density from the continental margin obviously makes correlation between samples futile; we therefore limit our discussion to pointing out possible onshore equivalents within the Caledonian–Appalachian orogenic belt (Fig. 10.13) and consider the implications for the continuity of this belt.

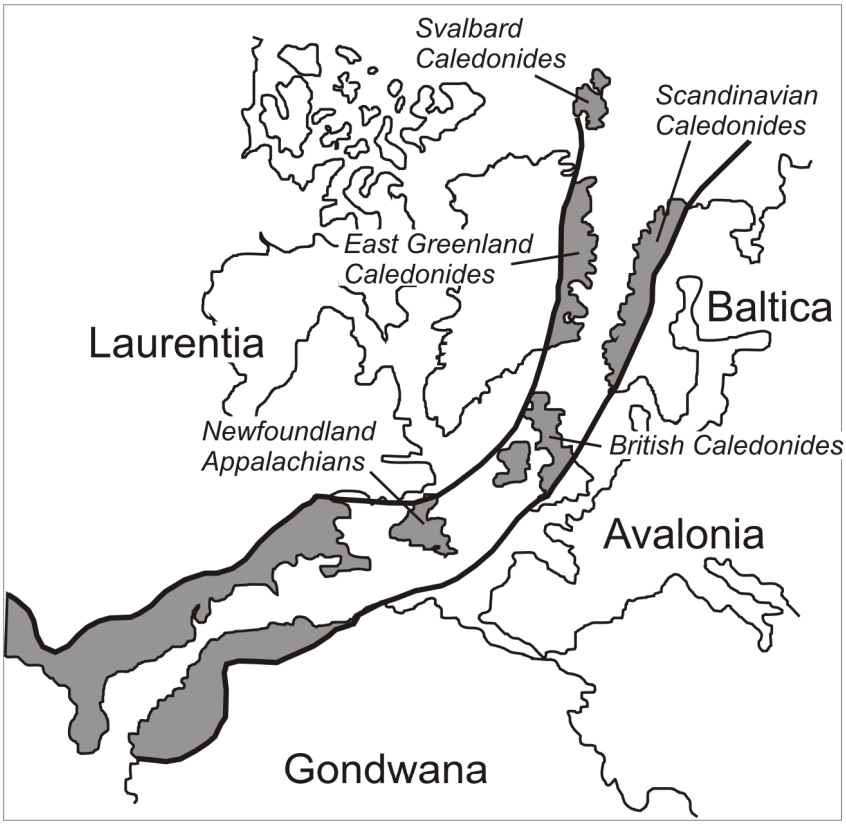

Figure 10.13. Map showing the extent of the Caledonian–Appalachian orogenic belt in the North Atlantic region. Areas within the belt that are referred to in the text are indicated.

The majority of samples are of magmatic rocks with ages ranging from 463 to 421 Ma; two samples are of metasedimentary rocks that most likely constitute part of Caledonian nappes (see below); and two samples are of Proterozoic gneisses that probably represent an offshore continuation of the Western Gneiss Region (Fig. 10.1b). Here, we discuss the two samples of Proterozoic gneiss briefly before turning to Caledonian geology for the remainder of the section.

Fig. 10.14b shows a compilation of U–Pb age data from the Western Gneiss Region taken from Skår (2000). The dated rocks include migmatitic, granitic, quartz dioritic and gabbroic orthogneisses whose protoliths crystallised between c. 1653 and 1686 Ma in the northern parts and between 1621 and 1641 Ma in the southern parts of the Western Gneiss Region; however, more data are needed to establish whether there is a systematic difference between the two areas. These ages are similar to those obtained from the Gothian orogen in southern Sweden (Åhäll & Gower 1997). Only three U–Pb ages from post-Gothian and pre-Sveconorwegian times have been published and range from 1520 to 1462 Ma. This event is likely to be related to widespread magmatism in the Sveconorwegian orogen at that time (Bingen et al. 2005; Slagstad et al., unpub. data, 2007). The gneisses from wells 36/1–1 and 35/3–4 yield ages of 1641 ± 5 and 1613 ± 11 Ma, respectively, which overlaps with those obtained from the Western Gneiss Region onshore. We interpret this result to suggest that rocks of the Western Gneiss Region extend at least 50 km west of the exposed shoreline. This result also shows that the offshore extension of the east-west trending, south dipping detachment beneath the Devonian Hornelen Basin (e.g., Osmundsen et al. 1998) is situated to the south of the two wells.

10.4.1 Correlation with 'Caledonian' magmatism in the Caledonian–Appalachian orogen

Fig. 10.14a shows a compilation of published 'Caledonian' magmatic ages from the Scandinavian Caledonides, and Fig. 15 shows relative probability vs. age plots of Caledonian magmatism in Scandinavia, East Greenland and Svalbard, Great Britain and in the Newfoundland Appalachians. The data and references are presented in Tables 10.2–10.5. Between c. 420 and 440 Ma (c. 445 in Norway), widespread magmatism related to final closing of the Iapetus ocean and initiation of continent-continent collision is recorded along the length of the orogen. Well-known examples of this event in the Scandinavian Caledonides include the Bindal Batholith in the Helgeland nappe complex in Nordland (e.g., Nordgulen et al. 1993, Yoshinobu et al. 2002) and the Smøla–Hitra Batholith in Central Norway (Roberts 1980, Nordgulen et al. 2001) (Fig. 10.1b), and numerous examples have been reported from other parts of the Caledonian–Appalachian orogen (Table 10.2–10.4). Magmatic ages reported from the Bindal and Smøla–Hitra Batholiths are similar to those obtained from the leucogabbro in well 6306/10–1 (450 ± 4 Ma) and the granite from well 6407/10–3 (437 ± 4 Ma), and we believe that the samples could represent offshore equivalents of these batholiths. This interpretation implies, not surprisingly, that continental margin in central Norway is underlain by units comparable to the Upper/Uppermost Allochthon onshore.

In West Norway, only the Middle and Upper Allochthons are exposed and most of the reported magmatic U–Pb ages are older than c. 470 Ma (Fig. 10.14, Table 10.2). There are, however, several notable exceptions that have only been dated by the Rb/Sr or Sm/Nd methods. These include the gabbroic to granitic Sunnhordaland Batholith, south of Bergen, which has been dated at 430 ± 6 Ma (Rb/Sr whole-rock isochron, Andersen & Jansen 1987); the Kattnakken volcanics (Lippard 1976) dated at 445 ± 5 Ma (Rb/Sr whole-rock isochron, Priem & Torske 1973) and cut by a dolerite dyke swarm at 435 ± 5 Ma (Ar-Ar maximum age, Lippard & Mitchell 1980); the bimodal Siggjo Group (Nordås et al. 1985) including andesitic and rhyolitic lavas dated at 468 ± 23 Ma and 464 ± 16 Ma, respectively (Rb/Sr whole-rock isochron, Furnes et al. 1983). These data suggest that the absence of rocks younger than c. 470 Ma in West Norway may be more apparent than real. The samples from the North Sea can be divided in two age groups: a young group (421–430 Ma) consisting of leucogabbro from well 16/1–4 and dacite from well 16/6–1, and an older group (457–463 Ma) consisting of granites from wells 16/3–2, 16/4–1 and 16/5–1. We believe that the leucogabbro dated at 423 ± 2 Ma and the dacite dated at 430 ± 6 (young group) may represent

Caledonian magmatism, Upper and Uppermost Allochthon

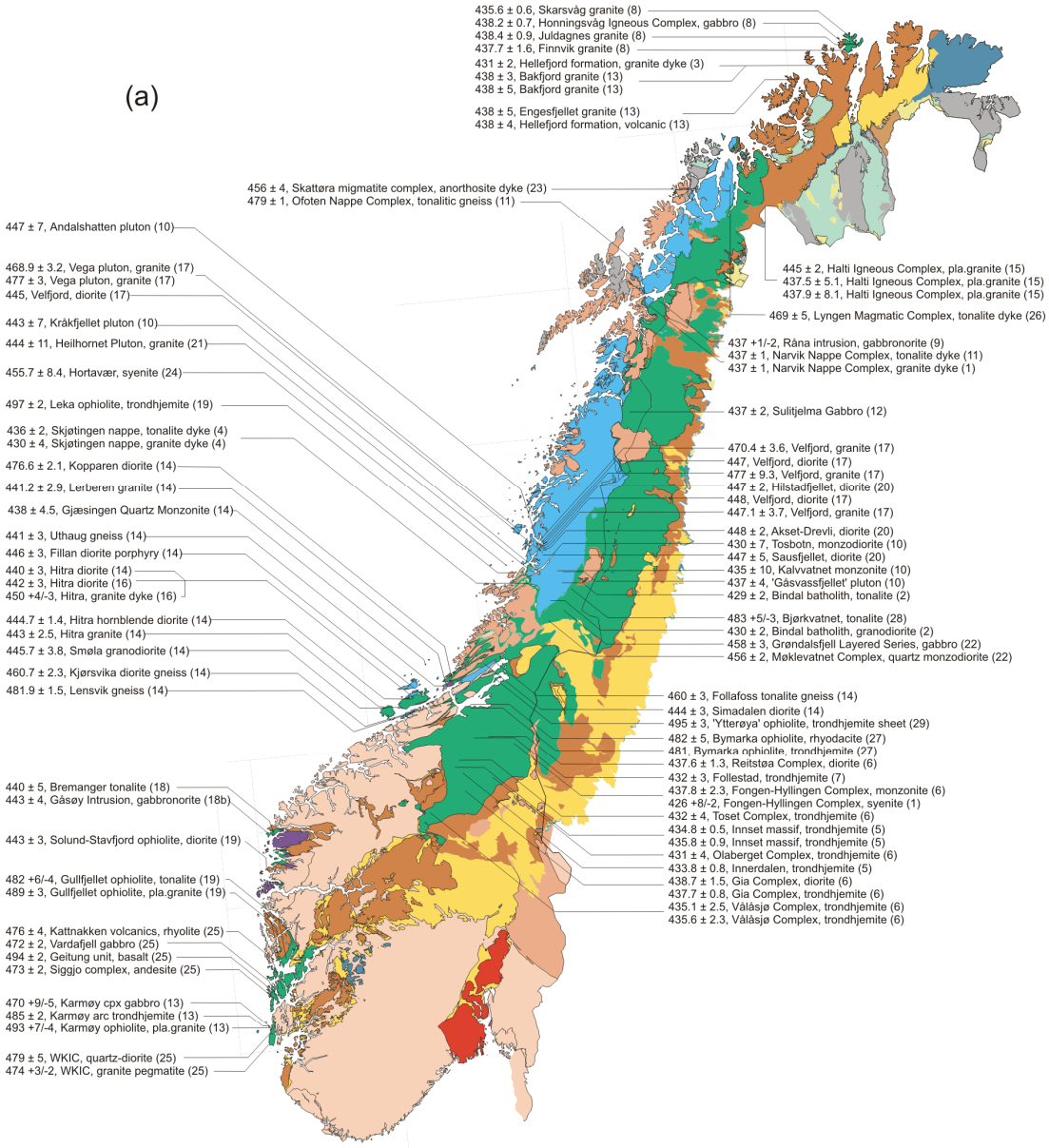

Oslo Rift
(Permian - Carboniferous)
Sediments outside the Caledonian Orogen
(Neoproterozoic - Phanerozoic)

Caledonian Orogen
Intermontane basin deposits
(Late Silurian - Devonian)
Uppermost Allochthon
(Neoproterozoic - Ordovician)
Upper Allochthon
(Mesoproterozoic - Silurian)
Middle Allochthon
(Mesoproterozoic - Cambrian)
Lower Allochthon
(Mesoproterozoic - Palaeozoic)

Proterozoic
Igneous and supracrustal rocks
(1700 - 900 Ma, Gothian and Sveconorwegian)
Transscandinavian Igneous Belt and rapakivi granite
(1800 - 1650 Ma)
Igneous and supracrustal rocks
(1960 - 1750 Ma, mainly Svecofennian)
Igneous and supracrustal rocks
(2300 - 1900 Ma, Lapland Granulite Belt)
Supracrustal rocks and layered gabbros
(2500 - 1950 Ma, Svecokarelian)

Archaean
Igneous and supracrustal rocks
(3200 - 2500 Ma)

Protolith ages, Western Gneiss Region

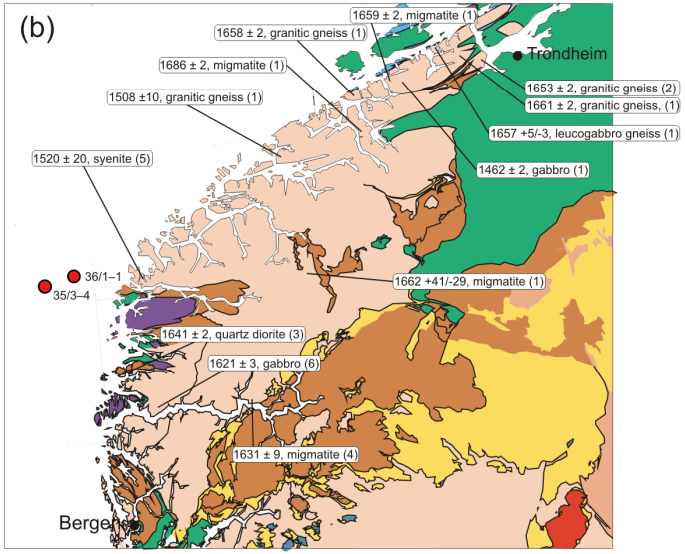

Figure 10.14. (previous page) (a) Simplified geological map of Norway (modified after Solli and Nordgulen (2006)) showing published U–Pb age data from Caledonian magmatic rocks the Norwegian Caledonides. References in parentheses are presented in Table 10.2. (b) U–Pb protolith ages from the Western Gneiss Region (from compilation by Skår, 2000). References: (1) Tucker et al. (1990b), (2) Tucker and Krogh (1988), (3) Skår et al. (1994), (4) Skår (1998), (5) Lappin et al. (1979), (6) Skår and Pedersen (2003).

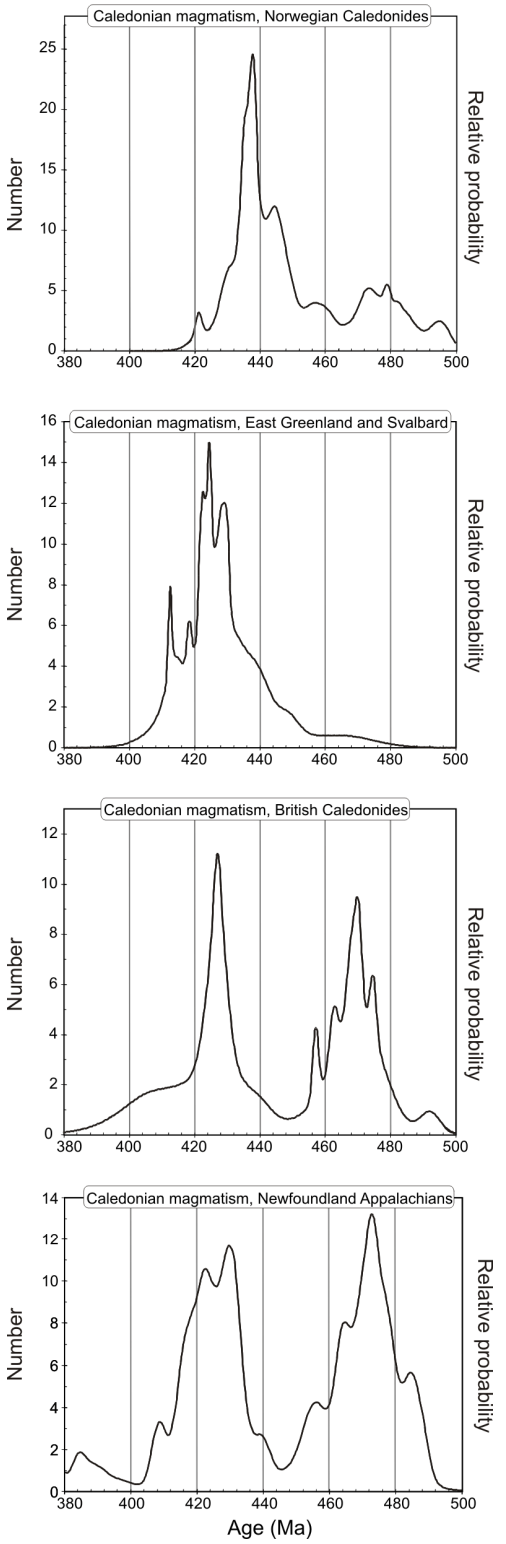

Figure 10.15. Relative probability plots vs. age showing published age data from Caledonian magmatic rocks in the Caledonides of Norway, East Greenland and Svalbard, and Great Britain and the Newfoundland Appalachians. References are presented in Tables 10.2–10.5.

the same event that formed the Sunnhordaland Batholith. Magmatic ages between 420 and 430 Ma are quite rare in the Scandinavian Caledonides but are widespread in the British and East Greenland/Svalbard Caledonides and the Newfoundland Appalachians (Fig. 10.14, Tables 10.2–10.4). However, the new data presented here, along with previously published Rb/Sr and Sm/Nd data, show that such rocks do exist also in the Scandinavian Caledonides. The older age group consists of granites dated at 459±5, 457 ± 5 and 463 ± 6 Ma. Rocks of similar age are rare in the Scandinavian Caledonides, and gabbroic to tonalitic magmatism of this age is only reported from a few locations in Central Norway (Fig. 10.14, Table 10.2). In the British Caledonides and Newfoundland Appalachians, dioritic to granitic rocks of this age are common, whereas in the Caledonides of East Greenland and Svalbard, such rocks are rare. This study shows that c. 460 Ma magmatism in the Scandinavian Caledonides is not restricted to Central Norway but is preset within a significant portion of the orogenic belt; thus, we believe that the apparent lack of such ages results more from biased sampling (i.e., many analyses of the Bindal and Smøla–Hitra Batholiths and minor trondhjemitic and associated dioritic c. 435 Ma magmatic bodies (Table 10.2)) than from the lack of such rocks. A similar lack of c. 460 Ma magmatism is observed in the East Greenland/Svalbard Caledonides. Recently, however, Rehnström (in press) suggested that magmatic rocks in the Scoresby Sund region in the central East Greenland Caledonides formed during to events at c. 450–460 and 420 Ma. This result shows that rocks older than c. 440 Ma are present in the East Greenland Caledonides, but may have gone undetected because most workers have focussed on processes related to crustal anatexis and associated magmatism, which took place at c. 435 Ma (e.g., Kalsbeek et al. 2001). We therefore conclude that major differences in magmatic activity along the Caledonian–Appalachian orogenic belt are unlikely. The data presented from the Norwegian continental margin show that the distribution of 'Caledonian' magmatic rocks is continuous from the British Caledonides and into and along the Scandinavian Caledonides. Furthermore, this work along with that of Rehnström (in press) suggest that apparent differences in magmatic activity along the Caledonian–Appalachian orogenic belt (cf., Fig. 10.15) may be due to biased sampling.

10.4.2 Correlation with sedimentary successions within the Caledonian orogenic belt

Two samples of metasedimentary rocks were obtained from wells 25/7–1S in the North Sea and 6609/7–1 in the Norwegian Sea (Fig. 10.1b). The samples display very similar age distributions characterised by dominantly Late Palaeoproterozoic and Mesoproterozoic zircons, with rare older, Palaeoproterozoic grains (Figs. 7 and 12). The age distributions observed in these two samples strongly resembles those observed in samples from the Kalak Nappe Complex in Finnmark, North Norway (Kirkland et al. 2007), the Moine Supergroup in the Scottish Caledonides (Friend et al. 2003, Cawood et al. 2004) and the Krummedal sequence in the East Greenland Caledonides (Kalsbeek et al. 2000, Watt et al. 2000). Kirkland et al. (2007) discuss the similarities between these and other sedimentary successions within the Caledonian orogenic belt in detail and will not be restated here; suffice it to say that a statistical test shows that the detrital zircon populations observed in these two

samples are not distinctly different to the aforementioned sedimentary sequences (C. Kirkland, pers. comm., 2007). These two samples therefore strengthen the impression that geological units, be they magmatic or sedimentary, within tectonostratigraphically higher nappes of the Scandinavian Caledonides, can be correlated with similar units in other parts of the Caledonian–Appalachian orogenic belt. In particular, the results obtained from these two samples as well as from the 'Caledonian' magmatic rocks, provide a direct link between the Scandinavian and Scottish Caledonides; a link that has generally been viewed as somewhat obscure.

10.5 Conclusions

The new geochronological data from basement samples from the North Sea and Norwegian Sea provide a unique glimpse into the nature of the Norwegian continental margin. The basement appears to consist of magmatic and metasedimentary rocks that can be correlated with rocks in tectonostratigraphically high (i.e., Upper and Uppermost Allochthons) nappes within the Scandinavian Caledonides. The conclusions are consistent with the results from the BAT Project based on onshore structural mapping and potential field modeling (Olesen et al. 2002, Osmundsen et al. 2002, Skilbrei et al. 2002) The data also show that distinct units within the Scottish Caledonides, forming the southward continuation of the Scandinavian Caledonides, can be identified within the latter.

Table 10.1. Geochemical data.

Well	16/1-4	16/3-2	16/4-1	16/4-1	16/5-1	16/6-1	17/3-1	17/3-1	18/11-1	25/7-1S	25/7-1S	25/11-17	35/3-4	35/9-1
Depth	1937	2017.7	2907.4	2908.6	1929.3	2059.7	2849.5	2850.7	2082.3	3548.2	3554.3	2259.5	4088.3	2313.6
Rock type	Leucogabbro	Granite	Qtzite/ siltstone	Granite	Granite	Dacite	Breccia	Breccia	Porph. volcanic rock	Brecciated siltstone	Qtz-rich sandstone	Siltstone	Qtz-rich mica schist	Breccia
SiO_2	49.05	70.15	58.20	71.46	68.66	65.83	40.23	67.94	71.52	29.34	77.66	60.64	62.59	42.89
Al_2O_3	16.01	16.05	14.17	15.01	16.71	15.86	14.66	11.49	13.70	3.80	7.40	14.54	14.20	7.57
Fe_2O_3	7.39	1.97	4.88	1.67	2.60	3.98	10.02	2.63	3.76	27.33	4.27	7.04	7.31	7.08
TiO_2	1.40	0.24	0.64	0.18	0.30	0.62	0.87	0.28	0.39	0.17	0.28	0.78	1.20	0.73
MgO	7.44	0.84	8.38	1.01	1.07	2.52	6.55	1.21	1.35	2.19	0.19	4.18	2.66	2.90
CaO	5.28	2.39	4.69	1.14	2.35	0.75	11.04	5.36	0.54	9.40	0.14	1.60	2.63	17.85
Na_2O	3.29	4.17	1.73	4.08	3.41	4.59	3.98	5.52	6.13	0.25	1.38	0.71	2.56	0.77
K_2O	3.37	2.71	4.60	3.75	3.48	2.72	0.05	0.06	0.13	0.13	3.22	5.79	3.81	1.53
MnO	0.14	0.06	0.06	0.05	0.05	0.04	0.17	0.05	0.06	9.32	0.02	0.14	0.13	0.18
P_2O_5	0.58	0.10	0.15	0.11	0.09	0.24	0.06	0.02	0.10	0.05	0.02	0.17	0.33	0.20
LOI	4.84	1.12	1.77	1.18	1.43	2.26	11.32	4.85	1.41	16.04	2.56	4.13	1.66	16.34
Total	98.81	99.80	99.26	99.64	100.16	99.40	98.97	99.41	99.08	98.01	97.14	99.72	99.08	98.05
Zr	204	164	209	114	172	175	47	103	110	109	260	164	312	114
Y	25	11	23	9	7	14	18	34	40	7	6	14	49	28
Sr	957	671	483	406	563	526	53	45	62	172	206	104	310	544
Rb	141	81	175	115	105	78	<5	<5	<5	<5	96	175	145	60
Cr	345	<10	31	<10	<10	53	150	<10	<10	11	<10	68	<10	671
V	179	20	67	14	21	93	264	61	23	104	35	153	123	180
Ba	1289	816	917	686	980	1047	37	33	20	397	13380	841	1090	660
Ga	14	11	<10	<10	14	12	<10	<10	<10	<10	<10	11	12	<10
Zn	143	42	161	61	49	69	81	23	20	79	19	117	87	69
Ni	121	<5	28	<5	<5	50	51	8	<5	28	5	36	18	86
Co	30	6	11	6	<5	13	34	9	6	87	<5	17	22	19
Nb	13.3	13.3	11.4	13.5	13.0	11.5	0.70	2.98	2.04	4.22	6.30	14.1	22.1	6.63
La	54.3	34.7	29.7	21.6	28.2	24.8	1.43	6.72	5.19	23.4	17.8	28.1	63.7	56.2
Ce	124	59.6	65.7	38.9	53.3	49.5	4.19	15.5	21.2	25.8	39.3	58.3	137	116
Pr	15.4	6.30	7.25	4.19	5.41	5.41	0.61	2.05	2.17	2.72	4.06	6.08	14.9	14.8
Nd	67.8	25.2	30.2	17.4	20.9	22.1	3.97	10.5	13.0	11.1	16.6	25.6	63.6	69.3
Sm	11.8	4.37	5.66	3.57	3.53	4.12	1.63	3.34	4.21	1.88	2.91	4.69	12.2	14.2
Eu	2.86	1.12	1.05	0.86	0.99	1.07	0.62	0.52	1.28	0.39	0.76	0.96	2.40	3.74
Gd	7.21	2.89	3.63	2.56	2.33	2.92	2.08	3.73	4.82	1.55	2.21	3.25	8.99	8.95
Tb	1.00	0.46	0.64	0.43	0.33	0.46	0.46	0.90	1.07	0.27	0.30	0.54	1.53	1.26
Dy	4.59	2.47	3.59	2.17	1.76	2.68	2.88	6.06	7.27	1.61	1.76	2.89	8.58	5.62
Ho	0.79	0.51	0.76	0.43	0.33	0.52	0.68	1.27	1.57	0.34	0.33	0.58	1.66	0.94
Er	1.95	1.38	2.22	1.00	0.86	1.47	1.82	4.23	4.72	0.97	1.03	1.68	4.35	2.28
Tm	0.26	0.23	0.31	0.16	0.14	0.23	0.31	0.69	0.74	0.13	0.16	0.27	0.65	0.32
Yb	1.50	1.36	2.01	0.95	0.93	1.34	2.10	4.58	4.56	0.80	0.97	1.78	3.73	1.60
Lu	0.21	0.19	0.31	0.16	0.15	0.20	0.33	0.76	0.80	0.12	0.19	0.29	0.58	0.23
Hf	4.08	3.86	4.89	3.50	4.41	4.23	1.50	4.71	3.67	3.76	8.53	4.41	8.56	2.96
Ta	0.57	0.77	0.74	0.78	0.92	0.73	0.03	0.28	0.11	0.26	0.58	0.89	1.51	0.33
Th	2.83	8.70	10.8	7.99	11.1	10.3	0.20	3.08	1.67	2.92	3.65	9.00	9.13	3.31
U	8.37	2.62	3.64	2.26	1.07	2.77	0.58	1.03	0.58	0.86	0.96	1.56	2.22	1.19

Table 10.1. continued.

Well	36/1-1	6305/12-2	6306/10-1	6306/10-1	6407/10-3	6609/7-1	6609/7-1	7120/1-1	7120/12-2	7120/12-2	7128/4-1	7128/4-1	7128/6-1	7226/11-1
Depth	5212.3	3158.3	3158.5	3159.2	2972.1	1944.7	1945.8	4002.2	4675.8	4678.2	2527.2	2528.1	2540.5	5198.8
Rock type	Granitic gneiss	Brecciated siltstone	Leucogabbro	Leucogabbro	Granite	Brecciated silt/ sandstone	Altern. silt-/ sandstone	Amphibolite	Qtz-rich augen gneiss§	Qtz-rich augen gneiss	Altern. silt-/ sandstone	Altern. silt-/ sandstone§	Sandstone	Biotite-rich schist/gneiss
SiO_2	69.15	49.70	53.97	59.99	72.67	87.57	75.02	38.24	71.13	70.80	65.20	67.88	75.79	63.20
Al_2O_3	14.46	15.48	17.36	17.04	14.06	4.35	11.11	11.49	15.41	15.41	18.22	16.37	4.17	14.14
Fe_2O_3	3.23	9.63	7.88	5.72	1.98	0.26	0.68	12.89	2.01	1.72	4.30	4.09	2.56	5.79
TiO_2	0.40	1.14	0.81	0.58	0.28	0.16	0.62	3.50	0.28	0.29	0.94	0.82	0.06	1.05
MgO	1.37	6.10	4.71	3.85	0.34	0.15	0.28	8.26	0.69	0.86	1.34	1.44	2.04	5.48
CaO	1.93	7.22	4.48	3.05	1.18	2.27	3.56	15.35	2.57	1.63	0.28	0.50	5.13	3.33
Na_2O	3.22	2.67	5.16	4.62	3.27	0.26	0.32	1.99	4.63	4.36	0.48	0.40	0.63	1.30
K_2O	4.68	0.87	1.55	1.93	5.31	2.00	3.33	1.12	2.04	3.49	5.04	4.43	1.77	2.93
MnO	0.08	0.16	0.13	0.10	0.02	0.02	0.03	0.19	0.03	0.02	0.02	0.02	0.42	0.06
P_2O_5	0.11	0.06	0.20	0.17	0.08	0.03	0.06	0.47	0.07	0.08	0.14	0.23	0.01	0.27
LOI	0.88	6.46	3.13	2.63	0.59	2.33	4.76	5.39	0.51	0.96	3.59	3.39	7.70	1.83
Total	99.50	99.49	99.37	99.68	99.79	99.41	99.77	98.88	99.37	99.61	99.55	99.57	100.28	99.39
Zr	112	58	71	126	208	149	314	251	130	135	374	357	39	195
Y	13	16	13	12	5	13	28	22	<5	<5	50	65	21	38
Sr	159	111	235	712	301	18	50	349	346	270	97	99	33	140
Rb	164	17	40	55	190	74	113	24	56	55	247	219	42	130
Cr	<10	436	<10	13	<10	<10	<10	519	<10	<10	14	12	<10	32
V	50	299	195	128	12	13	45	314	25	25	96	80	10	86
Ba	716	328	313	534	784	249	497	237	655	1131	895	841	382	1040
Ga	13	10	11	<10	14	<10	<10	18	15	10	20	15	<10	14
Zn	47	64	109	89	33	12	12	94	44	38	94	59	18	103
Ni	10	155	22	22	<5	<5	<5	174	<5	<5	12	7	<5	15
Co	9	53	22	17	<5	<5	5	48	6	<5	<5	6	<5	16
Nb	9.81	1.69	7.75	6.57	8.76	3.54	10.6	44.5	3.66	2.60	20.8	20.7	2.29	17.1
La	19.4	3.05	24.0	17.4	79.7	15.7	24.8	35.9	21.0	17.9	55.7	60.4	18.0	43.3
Ce	33.8	8.46	45.7	35.8	193	31.3	49.2	76.2	36.5	29.7	122	124	33.8	89.8
Pr	4.35	1.26	4.77	3.76	15.2	3.68	5.70	9.45	3.68	2.86	13.5	14.2	3.78	10.2
Nd	17.6	7.15	19.5	16.0	58.2	16.4	25.6	43.6	14.1	10.3	57.4	59.9	16.0	43.4
Sm	3.23	2.09	3.57	3.04	9.05	3.52	5.36	9.05	2.24	1.63	11.3	12.4	3.46	9.07
Eu	0.73	0.63	1.08	0.86	1.21	0.78	1.14	2.77	0.66	0.53	1.86	2.06	0.96	1.76
Gd	2.28	2.30	2.70	2.23	4.46	2.66	4.76	6.46	1.40	0.98	8.22	10.7	3.05	6.86
Tb	0.36	0.48	0.44	0.39	0.42	0.51	0.89	1.02	0.18	0.16	1.47	2.09	0.62	1.25
Dy	2.15	3.31	2.34	2.29	1.57	2.86	5.59	5.27	0.74	0.71	8.39	12.1	3.62	6.91
Ho	0.46	0.71	0.50	0.45	0.24	0.57	1.20	0.95	0.14	0.14	1.73	2.46	0.74	1.40

Er	1.46	2.21	1.33	1.20	0.51	1.65	3.47	2.38	0.36	0.32	5.11	7.01	2.14	3.93
Tm	0.22	0.33	0.20	0.19	0.07	0.26	0.54	0.32	0.04	0.04	0.82	1.11	0.33	0.61
Yb	1.62	2.20	1.17	1.08	0.42	1.54	3.49	1.80	0.35	0.28	5.06	6.46	1.82	3.95
Lu	0.25	0.35	0.19	0.19	0.09	0.26	0.57	0.25	0.03	0.05	0.81	1.03	0.29	0.57
Hf	3.81	1.49	1.75	3.23	6.53	5.55	10.7	6.48	3.71	3.86	10.8	11.1	1.38	5.35
Ta	0.69	0.08	0.60	0.44	0.38	0.25	0.79	2.95	0.09	0.10	1.74	1.48	0.14	1.03
Th	11.9	0.11	4.66	7.08	58.3	3.25	7.84	3.42	16.2	4.29	21.2	19.3	2.58	12.6
U	1.75	0.29	2.68	1.96	2.65	0.92	2.34	1.07	4.85	0.40	5.51	4.62	0.87	2.55

Table 10.2. Caledonian U–Pb magmatic ages, Norwegian Caledonides

Age (Ma)	Rock type	Geological unit and/or geographical location		Ref.
426 +8/-2	Syenite	Fongen-Hyllingen Complex	Central Norway	1
427 ± 1	Granite dykes	Jotun Nappe Complex	South-west Norway	30
429 ± 2	Tonalite	Bindal batholith	North-central Norway	2
430 ± 2	Granodiorite	Bindal batholith	North-central Norway	2
431 ± 2	Granite dyke	Hellefjord formation	North	3
430 ± 4	Granite dyke	Skjøtingen nappe	Central Norway	4
433.8 ± 0.8	Trondhjemite	Innerdalen	South-central Norway	5
431 ± 4	Trondhjemite	Olaberget Complex	South-central Norway	6
432 ± 3	Trondhjemite	Follestad	Central Norway	7
434.8 ± 0.5	Trondhjemite	Innset massif	South-central Norway	5
432 ± 4	Trondhjemite	Toset Complex	South-central Norway	6
435.6 ± 0.6	Granite	Skarsvåg granite	North Norway	8
437 +1/-2	Gabbronorite	Råna intrusion	North Norway	9
435.8 ± 0.9	Trondhjemite	Innset massif	South-central Norway	5
430 ± 7	Monzodiorite	Tosbotn	North-central Norway	10
435.1 ± 2.5	Trondhjemite	Vålåsjø Complex	South-central Norway	6
435.6 ± 2.3	Trondhjemite	Vålåsjø Complex	South-central Norway	6
436 ± 2	Tonalite dyke	Skjøtingen nappe	Central Norway	4
437 ± 1	Tonalite dyke	Narvik Nappe Complex	North Norway	11
437 ± 1	Granite dyke	Narvik Nappe Complex	North Norway	11
437.7 ± 0.8	Trondhjemite	Gia Complex	South-central Norway	6
438.2 ± 0.7	Gabbro	Honningsvåg Igneous Complex	North	8
437.6 ± 1.3	Diorite	Reitstøa Complex	Central Norway	6
437 ± 2	Gabbro	Sulitjelma Gabbro	North Norway	12
438.4 ± 0.9	Granite	Juldagnes granite	North	8
437.7 ± 1.6	Granite	Finnvik granite	North	8
437.8 ± 2.3	Monzonite	Fongen-Hyllingen Complex	Central Norway	6
438.7 ± 1.5	Diorite	Gia Complex	South-central Norway	6
438 ± 3	Granite	Bakfjord granite	North	13
437 ± 4	Granodiorite	'Gåsvassfjellet' pluton	Central Norway	10
438 ± 4	Volcaniclastic	Hellefjord formation	North	13
438 ± 4.5	Monzonite	Gjæsingen Quartz Monzonite	Central Norway	14
437.5 ± 5.1	Plagiogranite	Halti Igneous Complex	North Norway	15
438 ± 5	Granite	Bakfjord granite	North	13
438 ± 5	Granite	Engesfjellet granite	North	13
440 ± 3	Diorite	Hitra diorite	Central Norway	14
441 ± 3	Granitic gneiss	Uthaug gneiss	Central Norway	14
441.2 ± 2.9	Granite	Lerberen granite	Central Norway	14
442 ± 3	Diorite	Hitra diorite	Central Norway	16
445	Diorite	Velfjord	North-central Norway	17
440 ± 5	Tonalite	Bremanger tonalite	North-west Norway	18
435 ± 10	Monzonite	Kalvvatnet monzonite	Central Norway	10
443 ± 2.5	Granite	Hitra granite	Central Norway	14
443 ± 3	Diorite	Solund-Stavfjord ophiolite	North-west Norway	19
437.9 ± 8.1	Plagiogranite	Halti Igneous Complex	North Norway	15
444.7 ± 1.4	Hornblende diorite	Hitra diorite	Central Norway	14
443 ± 4	Gabbronorite	Gåsøy Intrusion	North-west Norway	18b
444 ± 3	Diorite	Simadalen diorite	Central Norway	14

Age (Ma)	Rock type	Geological unit and/or geographical location		Ref.
c. 447	Diorite	Velfjord	North-central Norway	17
445 ± 2	Plagiogranite	Halti Igneous Complex	North Norway	15
c. 448	Diorite	Velfjord	North-central Norway	17
450 +4/-3	Granite dyke	Hitra	Central Norway	16
446 ± 3	Diorite	Fillan diorite porphyry	Central Norway	14
447 ± 2	Diorite	Hilstadfjellet	North-central Norway	20
445.7 ± 3.8	Granodiorite	Smøla granodiorite	Central Norway	14
443 ± 7	Tonalite	Kråkfjellet pluton	North-central Norway	10
448 ± 2	Diorite	Akset-Drevli	North-central Norway	20
447.1 ± 3.7	Granite	Velfjord	North-central Norway	17
447 ± 5	Diorite	Sausfjellet	North-central Norway	20
447 ± 7	Porphyritic granite	Andalshatten pluton	North-central Norway	10
444 ± 11	Granite	Heilhornet Pluton	North-central Norway	21
456 ± 2	Quartz monzodiorite	Møklevatnet Complex	Central Norway	22
456 ± 4	Anorthosite dyke	Skattøra migmatite complex	North Norway	23
458 ± 3	Gabbro	Grøndalsfjell Layered Series	Central Norway	22
460.7 ± 2.3	Diorite gneiss	Kjørsvika diorite gneiss	Central Norway	14
460 ± 3	Tonalite gneiss	Follafoss tonalite gneiss	Central Norway	14
455.7 ± 8.4	Syenite	Hortavær igneous complex	North-central Norway	24
470 +9/-5	Cpx gabbro	Karmøy ophiolite	West Norway	19
468.9 ± 3.2	Granite	Vega pluton	North-central Norway	17
474 +3/-2	Granite-pegmatite	West Karmøy Igneous Complex	West Norway	25
472 ± 2	Gabbro	Vardafjell gabbro	West Norway	25
470.4 ± 3.6	Granite	Velfjord	North-central Norway	17
469 ± 5	Tonalite dyke	Lyngen Magmatic Complex	North Norway	26
473 ± 2	Andesite	Siggjo complex	West Norway	25
476.6 ± 2.1	Diorite	Kopparen diorite	Central Norway	14
477 ± 3	Granite	Vega pluton	North-central Norway	17
476 ± 4	Rhyolite	Kattnakken volcanics	West Norway	25
479 ± 1	Tonalite gneiss	Ofoten Nappe Complex	North Norway	11
482 +6/-4	Tonalite	Gullfjellet ophiolite	West Norway	19
c. 481	Trondhjemite	Bymarka ophiolite	Central Norway	27
483 +5/-3	Tonalite	Bjørkvatnet	Central Norway	28
481.9 ± 1.5	Felsic gneiss	Lensvik gneiss	Central Norway	14
479 ± 5	Quartz-diorite	West Karmøy Igneous Complex	West Norway	25
477 ± 9.3	Granite	Velfjord	North-central Norway	17
485 ± 2	Trondhjemite	Karmøy ophiolite	West Norway	19
482 ± 5	Rhyodacite	Bymarka ophiolite	Central Norway	27
493 +7/-4	Plagiogranite	Karmøy ophiolite	West Norway	19
489 ± 3	Plagiogranite	Gullfjellet ophiolite	West Norway	19
494 ± 2	Basalt	Geitung unit	West Norway	25
495 ± 3	Trondhjemite sheet	Ytterøya ophiolite	Central Norway	29
497 ± 2	Trondhjemite	Leka ophiolite	Central Norway	19

References: (1) Wilson et al. (1983), (2) Nissen et al. (2006), (3) Kirkland et al. (2006), (4) Nordgulen et al. (2002), (5) Nilsen et al. (2003), (6) Nilsen et al. (submitted) (7), Dunning and Grenne (2000), (8) Corfu et al. (2006), (9) Tucker et al. (1990), (10) Nordgulen et al. (1993), (11) Northrup (1997), (12) Pedersen et al. (1991), (13) Kirkland et al. (2005), (14) Tucker et al. (2004), (15) Andréasson et al. (2003), (16) Tucker (1988), (17) Yoshinobu et al. (2002), (18) Hansen et al. (2002), (18b) R.B. Pedersen, unpub. data in (18), (19) Dunning and

Pedersen (1988), (20) Pedersen et al. (1999), (21) Nordgulen and Schouenborg (1990), (22) Meyer et al. (2003), (23) Selbekk et al. (2000), (24) Barnes et al. (2003), (25) Pedersen and Dunning (1997), (26) Oliver and Krogh (1995), (27) Roberts et al. (2002), (28) Stephens et al. (1993), (29) Roberts and Tucker (1998), (30) Lundmark and Corfu (2007).

Table 10.3. Caledonian U–Pb magmatic ages, Svalbard and East Greenland

Age	Rock type	Geological unit and/or geographical location		Ref.
409 +4/-8	Granite	Intrudes Smallefjord sequence	Grandjean Fjord-Bessel Fjord (EGR)	12
412.5 ± 0.5	Granite	Rijpfjorden granite	Nordaustlandet terrane (SVA)	2
417 +18/-7	Granitoid	Djupkilsodden pluton	Nordaustlandet terrane (SVA)	3
413 ± 3	Granite	Intrudes Eleonore Bay Supergroup	Payer Land (EGR)	5
413 ± 3	Granite		Payer Land (EGR)	5
414 ± 2	Granodiorite	Nordvestfjord Granodiorite	Scoresby Sund (EGR)	16
418 +5/-18	Monzonite	Bregnepynt Monzonite	Scoresby Sund (EGR)	19
418.4 ± 0.8	Granitoid	Hornemanntoppen granitoid	North-Western terrane (SVA)	4
c. 420	Granite	Wisnesbreen granite	Nordaustlandet terrane (SVA)	2
417 ± 3	Granite		Renland (EGR)	8
422.2 ± 0.7	Diorite	Bjørnøer Diorite	Scoresby Sund (EGR)	16
422.0 ± 1.2	Granite		Bartholin Nunatak (EGR)	9
423 ± 1.5	Granitoid	Bjørnfjorden	North-Western terrane (SVA)	4
424 ± 1	Granite	Intrudes Eleonore Bay Supergroup	Forsblad Fjord (EGR)	10
423 ± 2	Monzonite	Øfjord Monzonite	Scoresby Sund (EGR)	16
c. 425	Quartz-monzonite	NE Milne Land Quartz-monzonite	Scoresby Sund (EGR)	16
424.6 ± 0.5	Leucogranite	Tindern allochthon	Forsblad Fjord (EGR)	13
423.8 ± 1.5	Granite	Caledonia Ø Granite	Forsblad Fjord (EGR)	13
c. 426	Granite		Alpefjord (EGR)	10
425.8 ± 2	Granitic mylonite		Fjord Region Detachment Zone (EGR)	15
426.6 ± 1.4	Granite		Intrudes Moskusoksefjord Inlier (EGR)	9
426 ± 3	Granite		Payer Land (EGR)	5
428.2 ± 1.0	Leucogranite	Intrudes Smallefjord Sequence	Slamsø (EGR)	14
428 ± 1.8	Granite	Intrudes Smallefjord Sequence	Langsø (EGR)	14
424 ± 6	Monzonite		Renland (EGR)	8
429 ± 1	Granite	Intrudes Eleonore Bay Supergroup	Bredefjord Granite (EGR)	14
430 ± 0.7	Granitoid	Newtontoppen Granitoid	North-Western terrane (SVA)	4
432 +9/-14	Granite	Intrudes Eleonore Bay Supergroup	Grandjean Fjord-Bessel Fjord (EGR)	12
424 ± 8	Monzonite		Renland (EGR)	8
426 ± 6	Monzonite	Øfjord Monzonite	Scoresby Sund (EGR)	18
424 ± 9	Monzonite	Bregnepynt Monzonite	Scoresby Sund (EGR)	16
427 ± 6.3	Granite	Intrudes Eleonore Bay Supergroup	Kap Klinkerfues Granite (EGR)	14
431.3 ± 2.8	Granite	Intrudes Eleonore Bay Supergroup	Knæksø Granite (EGR)	14
430 ± 6.5	Granitic veins	Junctiondal	Fjord Region Detachment Zone (EGR)	15
431 ± 7	Aplite dyke	Kvitøya	Nordaustlandet terrane (SVA)	1
434 ± 5	Granite dyke		Renland (EGR)	8
432 ± 8	Granite	Intrudes Krummedal sequence	Frænkel Land (EGR)	7
433 ± 8	Granite	Intrudes Nathorst Land Group	Stauning Alper/Nathorst Land	6

Age	Rock type	Geological unit and/or geographical location		Ref.
			(EGR)	
434 ± 8	Syenite	Nordmarka syenite	Nordaustlandet terrane (SVA)	1
432 ± 10	Granodiorite/Qtz-diorite		Scoresby Sund (EGR)	11
432 ± 10	Monzonite	Bregnepynt Monzonite	Scoresby Sund (EGR)	17
440 ± 3	Granite	Nordkapp granite	Nordaustlandet terrane (SVA)	2
438 ± 5	Gabbro	Intrudes Krummedal sequence	Frænkel Land (EGR)	7
436 ± 8	Granite	Intrudes Krummedal sequence	Frænkel Land (EGR)	7
434 ± 11	Pegmatitic granite		Payer Land (EGR)	5
440 ± 8	Tonalite	Intrudes Krummedal sequence	Frænkel Land (EGR)	7
437 ± 12	Granite	Foynøane grey granite	Nordaustlandet terrane (SVA)	1
438 ± 14	Granite	Intrudes Krummedal sequence	Frænkel Land (EGR)	7
449 ± 3	Quartz diorite	Danmark Ø Quartz diorite	Scoresby Sund (EGR)	16
456 ± 16	Granodiorite	Korridoren Granodiorite	Scoresby Sund (EGR)	16
466 ± 9	Granodiorite/Qtz-diorite		Scoresby Sund (EGR)	11
466 ± 9	Granodiorite	Korridoren Granodiorite	Scoresby Sund (EGR)	17

Abbreviations: EGR=East Greenland Caledonides; SVA=Svalbard Caledonides.

References: (1) Johansson et al. (2004), (2) Johansson et al. (2002), (3) Gee et al. (1999), (4) Myhre (2005), (5) Gilotti and McClelland (2005), (6) Watt et al. (2000), (7) Kalsbeek et al. (2001), (8) Leslie and Nutman (2003), (9) Hartz et al. (2001), (10) Andresen et al. (1998), (11) Nutman and Kalsbeek, unpub. data in Higgins et al (2004), (12) Hansen et al. (1994), (13) White et al. (2002), (14) R.A. Strachan et al. (2001), (15) Hartz et al. (2000), (16) Rehnström (in press), (17) Kalsbeek et al. (in press), (18) Leslie and Nutman (2000), (19) Hansen and Friderichsen (1987).

Table 10.4. Caledonian U–Pb magmatic ages, British Caledonides

Age (Ma)	Rock type	Geological unit and/or geographical location		Ref.
400–415	Granite	Lochnagar granite	Northern Highlands (SCO)	9
400 ± 10	Granodiorite	Laggan granite	Northern Highlands (SCO)	9
c. 405	Granodiorite	Ben Cruachan granite	Northern Highlands (SCO)	9
405 ± 11	Granite	Vagastie Bridge granite	Strath Vagastie (SCO)	9
406 ± 6	Andesite / rhyolite	Glencoe Volcanic Complex	W Highlands (SCO)	23
c. 417	Granodiorite	Cluanie granite	Northern Highlands (SCO)	9
c. 420	Granite	Helmsdale granite	Northern Highlands (SCO)	9
420 ± 6	Granite	Klibreck granite	Intrudes Moine Supergroup (SCO)	4
425 ± 3	Granodiorite	Strontian granodiorite	W Highlands (SCO)	3
425 ± 3	Diorite	Ratagain intrusion	W Highlands (SCO)	3
426 ± 2	Granite	Strath Halladale Granite	East Sutherland (SCO)	14
426 ± 3	Appinite	Arrochar complex	W Highlands (SCO)	3
427 ± 1	Appinite / monzodiorite	Ballachulish Igneous Complex	W Highlands (SCO)	23
427.8 ± 1.9	Tonalite	Clunes Tonalite	Intrudes Moine Supergroup (SCO)	2
427 ± 3	Appinite	Rubha Mór appinite pipe	W Highlands (SCO)	3
429 ± 2	Appinite	Garabal Hill/Glen Fyne complex	W Highlands (SCO)	3
424 ± 8	Granite	Vagastie Bridge granite	Intrudes Moine Supergroup (SCO)	4
430 ± 4	Alkaline granitoids	Loch Borrolan complex	Moine Thrust Zone (SCO)	7
430 ± 4	Syenite	Loch Borrolan complex	Assynt (SCO)	19
426 ± 9	Syenite	Cnoc-nan-Cuilean syenite	Loch Loyal (SCO)	21
429 ± 11	Granite	Strathnaver granite	Intrudes Moine Supergroup (SCO)	4
439 ± 4	Syenite	Loch Ailsh intrusion	Assynt (SCO)	21
435 ± 10	Tonalite	Strontian granite	Northern Highlands (SCO)	9
439 ± 8.8	Hornblendite	Kiloran Bay intrusion	Colonsay (SCO)	8
457 ± 0.9	Granite	Kennethmont granite	Grampian terrane (SCO)	5
456 ± 5	Syenite	Glen Dessary Syenite	Inverness-shire (SCO)	20
462.5 ± 1.2	Granite	Oughterard granite	Connermara (IRL)	1
463 ± 4	Quartz diorite	Connemara Complex	Connemara (IRL)	12
467 ± 2	Granite pegmatite	Connemara complex	Connemara (IRL)	13
467.9 ± 1.2	Quartz diorite gneiss	Connemara complex	Connemara (IRL)	13
c. 470	Monzonite	Morven Cabrach intrusion, part of the Newer Gabbros	Scottish Highlands (SCO)	18
470 ± 1	Granite	Aberdeen granite	Grampian terrane (SCO)	6
470.1 ± 1.4	Gabbro	Cashel–Lough Wheelaun gabbro	Connemara (IRL)	1
466 ± 6	Granite	Connemara Complex	Connemara (IRL)	12
467.1 ± 5.9	Granite	Strichen granite	Grampian terrane (SCO)	5
467 ± 6	Tonalite	Ballygawley Tonalite	Slishwood Division (IRL)	15
474.5 ± 1	Gabbro	Currywongaun gabbro	Connemara (IRL)	1
468 ± 8	Gabbro	Newer gabbros	Grampians (SCO)	10
471 ± 5	Granite	Lough Keola Granite Sheet	Slishwood Division (IRL)	15
472 ± 6	Tonalite	Giant's Rock Tonalite	Slishwood Division (IRL)	15

Age (Ma)	Rock type	Geological unit and/or geographical location		Ref.
474 ± 5	Granite	Ballygawley Granite	Slishwood Division (IRL)	15
470 ± 9	Syenogabbro	Insch gabbro, part of the Newer Gabbros	Scottish Highlands (SCO)	18
475 ± 5	Granite	Strichen granite	Northern Highlands (SCO)	9
474.6 ± 5.5	Meta-rhyolite	Delaney Dome Formation	Connemara (IRL)	16, 17
475 ± 7	Granite	Ardclach granite	Grampian Highlands (SCO)	22
492 ± 3	Plagiogranite	Shetland Island oceanic fragment	Shetland (SCO)	11

Abbreviations: SCO=Scottish Caledonides; IRL=Irish Caledonides.

References: (1) Friedrich (1999), (2) Stewart et al. (2001), (3) Rogers and Dunning (1991), (4) Kinny et al. (2003), (5) Oliver et al. (2000), (6) Kneller and Aftalion (1987), (7) Aftalion (1979), (8) Muir et al. (1997), (9) Pidgeon and Aftalion (1978), (10) G. Rogers et al. (1994), (11) Spray and Dunning (1991), (12) Cliff et al. (1993), (13) Friedrich et al. (1999), (14) Kocks et al. (2006), (15) Flowerdew et al. (2005), (16) Draut and Clift (2002), (17) Friedrich (1998), (18) Dempster et al. (2002), (19) van Breemen et al. (1979), (20) van Breemen et al. (1979), (21) Halliday et al. (1987), (22) Zaleski (1983), (23) Fraser et al. (2004).

Table 10.5. Caledonian U–Pb magmatic ages, Newfoundland.

Age (Ma),	Rock type	Geological unit and/or geographical location		Ref.
374 ± 2	Granite	St. Lawrence Granite	Avalon Zone	38
378 ± 2	Granite	Francois Granite	Gander Zone	38
384 ± 2	Granite	Strawberry Granite	Dunnage Zone	30
386 ± 3	Granite	Isle aux Morts Granite	Dunnage Zone	30
390 ± 3	Granite	Chetwynd Granite	Dunnage Zone	20
396 +6/-3	Granite	North Bay Granite Suite	Dunnage Zone	34
408 ± 2	Granodiorite	Loon Bay granodiorite	Dunnage zone	1
408 ± 2	Granodiorite	Loon Bay Batholith	Dunnage Zone	36
410 ± 2	Granite	Middle Ridge granite	Gander zone	13b
420 +8/-2	Tuff	Georges Brook Formation, La Poile Group	Dunnage Zone	22
420 +8/-2	Tuff	Georges Brook Formation, La Poile Group	Dunnage Zone	34
418 +2/-1.5	Porphyry	Hawks Nest Pond Porphyry	Dunnage Zone	20
415 ± 2	Syenite	Skull Hill syenite	Dunnage zone	15
415 ± 2	Granite		Gander zone	18
415 ± 2	Granite	Burgeo Intrusive Suite	Dunnage Zone	34
c. 418	Granite	Locker's Bay granite	Gander zone	21
417 ± 2	Granite	Cape Freels granite	Gander zone	13b
418 ± 2	Granite	Rose Blanche granite	Gander zone	12
419 ± 2	Granite	Otter Point granite	Gander zone	20
423 +3/-2	Tuff	Stony Lake Volcanics	Dunnage Zone	34
423 +3/-2	Rhyolite	Phillips Brook Rhyolite	Dunnage Zone	20
424 +7/-3	Rhyolite	Georges Brook Formation, La Poile Group	Dunnage Zone	34
424 +4/-3	Gabbro sill	unnamed, intrudes Windsor Point Group	Dunnage Zone	30
421 ± 2	Granite	Gaultois granite	Gander zone	18
421 ± 2	Granite	Gaultois Granite	Gander Zone	34
c. 424	Gabbro	Mount Peyton intrusive suite	Dunnage zone	19
422 ±2	Granite	Port Albert Peninsula dyke	Dunnage Zone	36
423 ± 2	Granite	Wild Cove Pond intrusive suite	Humber zone	14
424 ± 2	Granite	Windowglass Hill Granite	Dunnage Zone	30
429 +7/-3	Rhyolite	Bear Pond Rhyolite	Dunnage Zone	34
429 +5/-3	Granite	Burgeo intrusive suite	Gander zone	18
429 +5/-3	Granodiorite	Burgeo Intrusive Suite	Dunnage Zone	34
429 +6/-5	Rhyolite	Springdale Group	Dunnage Zone	24
427 ± 2	Granite	Wild Cove Pond intrusive suite	Humber zone	14
427 ± 3	Granodiorite, syenite, granite	Topsails intrusive suite	Dunnage zone	3
429 ± 2	Granodiorite	Western Head Granite	Gander Zone	20
429 ± 2	Tuff	Grand Bruit Gull Pond tuff, La Poile Group	Gander Zone	20
429 ± 3	Granite	Dunamagon granite	Humber zone	14
429 ± 3	Granodiorite, syenite, granite	Topsails intrusive suite	Dunnage zone	3
429 ± 4	Felsic volcanics	Springdale Group	Dunnage zone 16	
431 ± 2	Gabbro, diorite	Main Gut intrusion	Dunnage zone	18

Age (Ma),	Rock type	Geological unit and/or geographical location		Ref.
435 +6/-3	Gabbro, diorite	Boogie Lake intrusion	Dunnage zone	18
431 ± 2	Gabbro	Main Gut intrusion	Dunnage Zone	34
435 +6/-3	Monzonite	Boogie Lake complex	Dunnage Zone	34
432 ± 2	Granodiorite	Burlington granodiorite	Dunnage zone	14
432 ± 2	Granite	Coney Head Complex	Dunnage Zone	31
440 ± 2	Granodiorite	Glover Island Granodiorite	Dunnage Zone	23
438 ± 8	Gabbro, diorite	Rainy Lake complex	Dunnage zone	3
452 +28/-11	Tuff	Georges Brook Formation, La Poile Group	Dunnage Zone	25
435 ± 15	Syenite	Seal Island Bight syenite	Dunnage zone	17
453 +5/-4	Rhyolite	Windsor Point Group	Dunnage Zone	30
453 ± 3	Granite	Port-aux-Basques granite	Dunnage zone	12
458 +29/-22	Tuff	Dolman Cove formation, Bay du Nord Group	Dunnage Zone	25
459 +24/-16	Granite	Dunamagon Granite	Dunnage/Humber Zones	28
456 ± 3	Tonalite, granodiorite	Burgeo Road	Dunnage zone	4
456 ± 3	Tonalite	Southwest Brook tonalite	Dunnage Zone	22
456 ± 3	Tonalite	Southwest Brook tonalite	Dunnage Zone	35
462 +4/-2	Rhyolite	Victoria Lake Group	Dunnage Zone	33
464 +4/-3	Pegmatitic granite	Through Hill granite	Dunnage zone	9, 10
464 +4/-3	Granite	Through Hill Granite	Gander Zone	26
463.7 ± 2	Gabbro sill	Thwart Island gabbro	Dunnage Zone	20
464 ± 2	Granite	Great Burnt Lake granite	Dunnage zone	9, 10
464 ±2	Granite	Great Burnt Lake Granite	Gander Zone	26
c. 467	Granite	Coaker porphyry	Dunnage zone	1b
469 +5/-3	Rhyolite	Cutwell Group	Dunnage zone	22
466 ± 3	Tuff	Bay du Nord Group	Dunnage Zone	34
460 ± 10	Granodiorite	Hinds Lake granodiorite	Dunnage zone	3
468 ± 2	Tuff	Twillick Brook Member, Baie d'Espoir Group	Dunnage Zone	26
460 ± 10	Charnockite	Cormacks Lake complex	Humber Zone	27
469 ± 2	Tonalite	Cape Ray Igneous Complex	Dunnage Zone	30
473 +3/-2	Rhyolite	Buchans Group	Dunnage zone	22
473 +3/-2	Rhyolite	Buchans Group	Dunnage Zone	33
472 +2/-9	Gabbro sill	Wild Bight Group	Dunnage Zone, Exploits Subzone	39
474 +6/-3	Granite	Partridgeberry Hills Granite	Dunnage Zone	26
474 +6/-4	Granite	Partridgeberry Hills granite	Dunnage zone	9
471 ± 2	Tuff	Pig Island tuff, Wild Bight Broup	Dunnage Zone, Exploits Subzone	39
472 ± 2	Tonalite	Cape Ray area	Dunnage zone	5, 6
467 ± 8	Gabbro, diorite, tonalite	Hungry Mountain complex	Dunnage zone	3
c. 475	Trondhjemite	Costigan Lake pluton	Dunnage zone	13
473 ± 2	Rhyolite	Roberts Arm Group	Dunnage Zone	22
473 ± 2	Rhyolite	Roberts Arm Group	Dunnage Zone	33
471 ± 4	Gabbro sill	Wild Bight Group	Dunnage Zone, Exploits Subzone	39

Age (Ma),	Rock type	Geological unit and/or geographical location		Ref.
472 ± 3	Tuff	Locks Harbour tuff, Wild Bight Group	Dunnage Zone, Exploits Subzone	39
472 ± 3	Tuff	Duck Island tuff, Wild Bight Group	Dunnage Zone, Exploits Subzone	39
474 ± 2	Diorite, tonalite, granite	Coney Head allochthon	West coast allochthons	8
474 ± 2	Tonalite	Coney Head Complex	Dunnage Zone	31
472 ± 4	Granite	Woodford's Arm pluton	Dunnage Zone	37
477.5 +2.6/-2	Trondhjemite	Annieopsquotch Complex	Dunnage Zone	32
480 +4/-3	Tuff	Catcher's Pond Group	Dunnage Zone	42
477.6 ± 1.8	Granite	Baggs Hill Granite	Dunnage Zone	43
478 ± 2	Granite	Baggs Hill granite	Dunnage zone	11
483 +3/-2	Gabbro sill	Stog'er Tight Gabbro	Humber Zone	41
479 ± 3	Quartz-feldspar granitoid	Mansfield Cove pluton	Dunnage zone	2
479 ± 3	Plagiogranite	Mansfield Cove Complex	Dunnage Zone	33
485.7 +1.9/-1.2	Trondhjemite	Bay of Islands Complex	Humber Zone	32
484 ± 2	Tuff	Fortune Harbour Formation, Cottrells Cove Group	Dunnage Zone	29
484 ± 5	Plagioclase-rich granitoid	Bay of Islands complex	West coast allochthons	7
486 ± 3	Tonalite	South Lake Igneous Complex	Dunnage Zone, Exploits Subzone	40
486 ± 3	Tuff	Tea Arm Formation, Exploits Group	Dunnage Zone	20
488 ± 2	Granodiorite	Cape Ray area	Dunnage zone	5, 6
505 +3/-2	Gabbro, amphibolite, trondhjemite	Little Port complex	West coast allochthons	7
507 +3/-2	Quartz-plagioclase granitoid	Twillingate pluton	Dunnage zone	1
430–425	Volcanics	Cape St. John Group	Dunnage zone	14, 17

References: (1) Elliot et al. (1991), (1b) Dunning in (1), (2) Dunning et al. (1987), (3) Whalen et al. (1987), (4) Dunning et al. (1989), (5) Dubé et al. (1994), (6) Dubé et al. (1993), (7) Jenner et al. (1991), (8) Dunning (1987a), (9) Colman-Sadd (1985), (10) Colman-Sadd et al. (1992), (11) Tucker et al. (1994), (12) van Staal et al. (1994), (13) Kerr (1997), (13b) Tucker in (13), (14) Cawood and Dunning (1993), (15) Kean and Jayasinghe (1982), (16) Coyle and Strong (1987), (17) DeGrace et al. (1976), (18) Dunning et al. (1990), (19) Dickson (1993), (20) O'Brien et al. (1991), (21) Dunning (1993), (22) Dunning and Krogh (1991), (23) Cawood et al. (1996), (24) Chandler et al. (1987), (25) Chorlton and Dallmeyer (1986), (26) Colman-Sadd et al. (1992), (27) Currie et al. (1992), (28) Dallmeyer and Hibbard (1984), (29) Dec et al. (1997), (30) Dube et al. (1996), (31) Dunning (1987b), (32) Dunning and Krogh (1985), (33) Dunning et al. (1987), (34) Dunning (1990), (35) Dunning (1989), (36) Elliott et al. (1991), (37) Kerr and Dunning (2003), (38) Kerr et al. (1993), (39) MacLachlan and Dunning (1998), (40) MacLachlan and Dunning (1998), (41) Ramezani et al. (2002), (42) Ritcey et al. (1995), (43) Tucker et al. (1994).

11 3D MODELLING OF GRAVITY AND MAGNETIC DATA ON THE TRØNDELAG PLATFORM

Jörg Ebbing & Per Terje Osmundsen, NGU

11.1 Introduction

In this chapter the crustal structure of the mid-Norwegian margin with special focus on the Trøndelag Platform is presented. By 3D forward modelling of gravity and magnetic field considering a wealth of constraining information, we were able to model the crustal structure of this area and to map and characterize the basement. Herby, especially the role of the lower basement and magnetic highs observed on the Trøndelag Platform are important to identify the connection between the overlying less magnetic nappe structures and the underlying, generally high-magnetic basement.

The study is based on work performed within a variety of previous NGU projects (Ebbing et al. 2006a; Olesen et al. 2002, 2003, 2004, 2006a,b; Osmundsen et al. 2002, 2006; Skilbrei et al. 2002). While the potential field studies in these projects mainly concentrated on the outer Vøring or the Lofoten margin, the present study (Ebbing et al. 2006b) is presenting (1) a regional 3D model of the entire Møre-Vøring-Lofoten margin segments, and (2) a detailed 3D picture of the Trøndelag Platform.

For the Trøndelag Platform, we could make use of new, hitherto unpublished OBS data (Raum & Mjelde, pers. comm.) and information from Statoil about selected seismic horizons. Following tests of the 3D density and magnetic model against seismic depth-models, we have produced a series of updated maps displaying Top upper basement, Top lower basement (i.e. top high-density and high-magnetic basement), lower crustal bodies and Moho depth. The derived maps, the 3D density model, and the magnetic response are integrated in our discussion of deep and basement internal structures.

We will present the main structural elements of the mid-Norwegian margin Ch. 11.2, and the available data for our study in Ch. 11.3. In Ch. 11.4 the 3D modelling and the structural maps of the study area are presented. Ch. 11.5 gives a tectonic synthesis.

11.2 Main structural elements in the study area

The Vøring Margin has been extensively studied by the use of multi-channel seismic reflection data, seismic refraction data, commercial drilling on the continental shelf as well as scientific drilling (e.g. Planke et al. 1991, Skogseid et al. 1992, Doré et al. 1999, Brekke 2000, Mjelde et al. 2001, Raum et al. 2002, Mjelde et al. 2003a, b, c, 2005).

The Vøring margin is located between 64° and 68° N, off Norway, and comprises three main geological provinces: the Trøndelag Platform, the Vøring Basin and the Vøring Marginal High (Figs. 11.1 & 11.2). These segments are further separated by NE-SW striking faults systems, developed since late Caledonian time. Northward the Vøring Margin is bounded by the Bivrost Lineament, representing the transition to the Lofoten Margin, while the East Jan Mayen Fracture Zone and the Jan Mayen lineament represent the southern boundary and represents the transition to the Møre Margin.

Investigating the transitional areas between the different margin segments (Møre, Vøring, and Lofoten) helps to understand the role and presence of the supposed tectonic lineaments. The definition of the lineaments is supposed to be guided primarily by changes in the structure and composition in the basement and lower crust (Mjelde et al. 2005). In this sense the lineaments can represent crustal scale shear zones or detachments.

Early Tertiary continental break-up and initial seafloor spreading between Eurasia and Greenland was characterized by massive emplacement of magmatic rocks (e.g. Eldholm and Grue 1994). On the Vøring Margin these rocks were partially extruded on the surface as flood basalts and partially intruded as sills into the sedimentary rocks in the Vøring Basin and presumably into continental crust (Mjelde et al. 2001). On the Vøring margin a lower crustal body with P-velocities and densities can be found (e.g. Mjelde et al. 2005).

We refer to this layer as lower crustal body (LCB). The LCB is not evenly distributed along the margin and is often referred to as magmatic underplating (e.g. Skogseid et al. 1992; van Wijk et al. 2004; Mjelde et al. 2005). However, while the high velocity/high density of the LCB may be considered as an objective observation, its origin as a layer of underplated material is an interpretation that dates back to work by e.g. White et al. (1987). Currently there is a renewed discussion about the interpretation of the LCB (e.g. Gernigon et al. 2003; Mjelde et al. 2005, Ebbing et al. 2006a). Determining the nature of the LCB is clearly relevant for the thermal history of volcanic margins, and arguably also for the entire concept of the development of such margins.

The Trøndelag Platform forms the innermost, landward part of the Vøring margin system (Fig. 11.1). The Trøndelag Platform has been a relatively stable area since the Jurassic and it is covered by relatively flatlying and mostly parallel-bedded strata which usually dip gently northeastwards (Blystad et al. 1995). Within the area of the Trøndelag Platform several sub-units can be found like the Nordland Ridge, Helgeland Basin, Frøya High and Froan Basin.

The Halten Terrace is separated from the Trøndelag Platform to the east by the Bremstein Fault Complex, and from the Frøya High to the southeast by the Vingleia Fault Complex. The

Halten Terrace was separated from the Trøndelag Platform during the Neocomian, after the deep erosion of the uplifted western margin of the early platform (Frøya High, and Sklinna and Nordland Ridges).

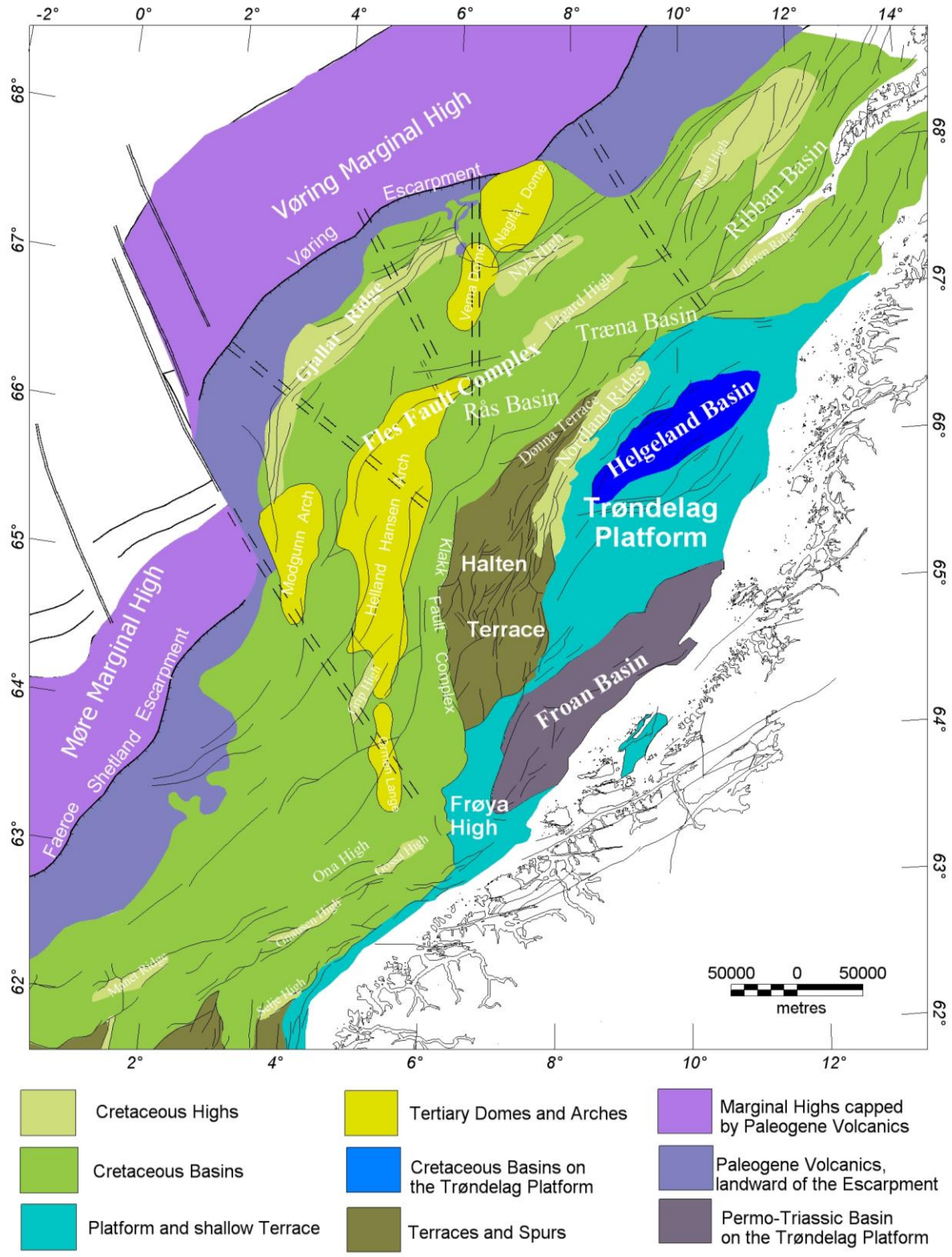

Figure 11.1 Tectonic setting of the mid-Norwegian margin (after Blystad et al. 1995).

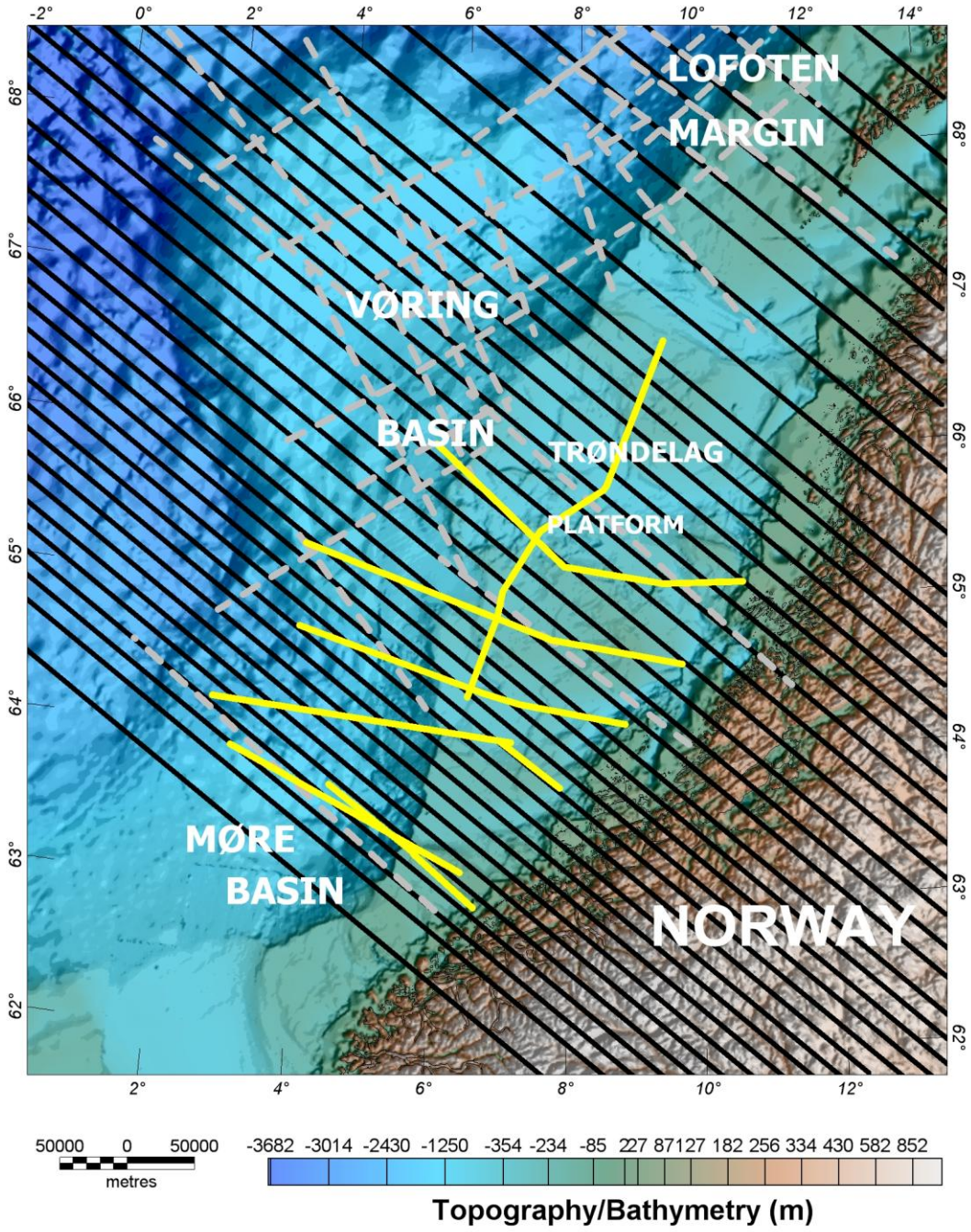

Figure 11.2 Bathymetry of the mid-Norwegian margin. The bathymetric data are from a compilation by Dehls et al. (2000), which is based on satellite altimeter data released by Smith & Sandwell (1997) for the deep-water part of the study are, and data provided by the Norwegian Mapping Authority, Marine Department Stavanger for the shallow water areas. The grey dotted lines in (a) mark the location of the OBS profiles (see Mjelde et al. 2005 for more details), while the thin black lines indicate the cross-sections of the 3D density model. Yellow lines show the long-offset profiles after Osmundsen et al. (2006).

11.3 Data sets

11.3.1 Gravity data

Gravity data were compiled by Skilbrei et al. (2000) from gravity stations on mainland Norway in addition to marine gravity data from the Geological Survey of Norway, the Norwegian Mapping Authority, the Norwegian Petroleum Directorate and Norwegian and foreign universities and commercial companies. The compiled grid was merged with gravity data from satellite altimetry in the deep-water areas (Andersen & Knudsen 1998). The compiled free-air dataset has been interpolated to a square grid of 2 km x 2 km using the minimum curvature method (Geosoft 2005). The simple Bouguer correction at sea (Mathisen 1976) was carried out using the bathymetry data in Fig. 11.2 and a density of 2200 kg/m^3. The International Standardization Net 1971 (I.G.S.N. 71) and the Gravity Formula 1980 for normal gravity have been used to level the surveys. Figs. 11.3 and 11.4 show the gravity anomaly and the Bouguer anomaly, while the location of the gravity stations and the marine profiles are shown in Fig. 9.3.

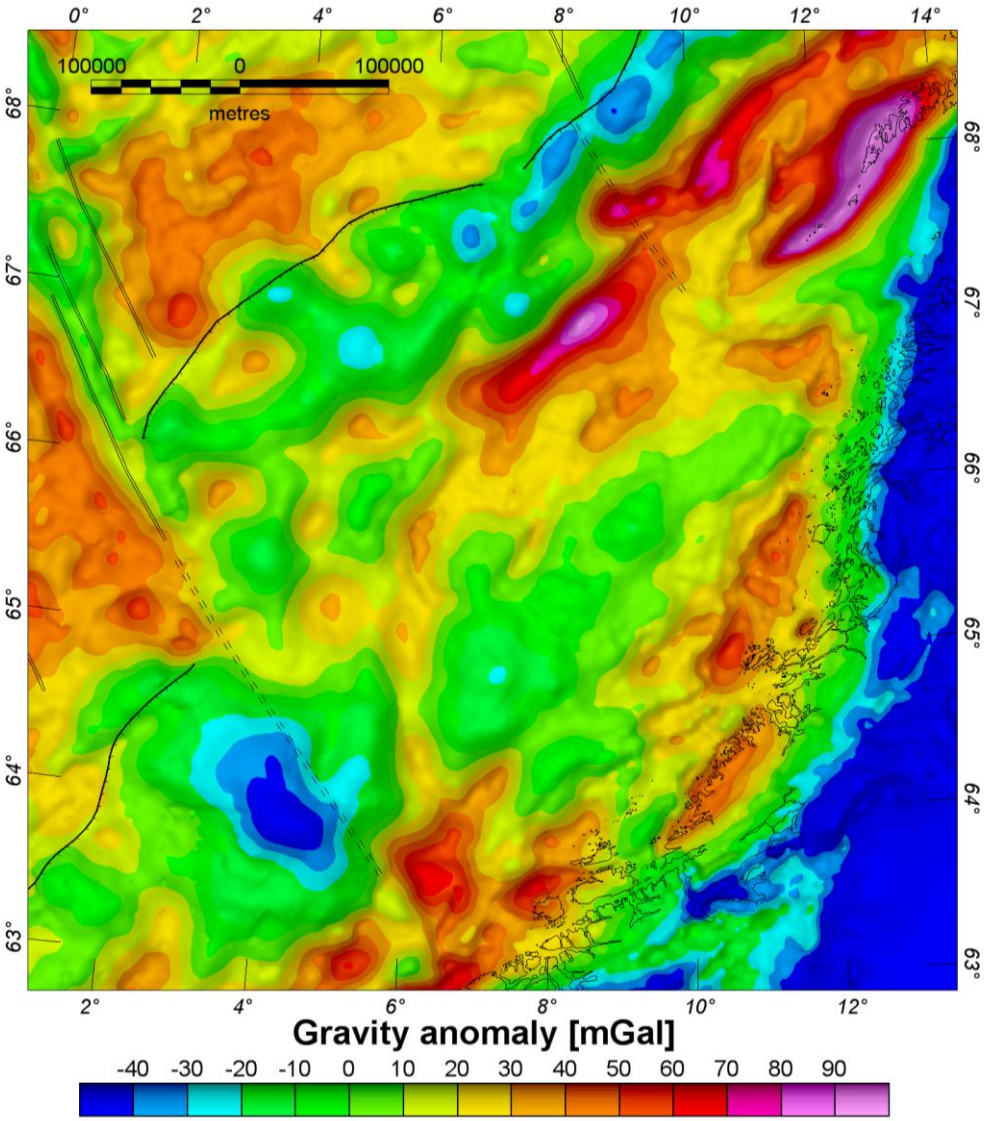

Figure 11.3. The gravity anomaly map is a combination of the free-air anomaly offshore and the Bouguer anomaly onshore (modified from Skilbrei et al. 2000). Offshore measurements of approximately 59,000 km of marine gravity profiles have been acquired by the Norwegian Petroleum Directorate, oil companies, and the Norwegian Mapping Authorities. In addition gravity data from satellite altimetry in the deep-water areas have been used (Andersen & Knudsen 1998). The surveys have been levelled using the International Standardization Net 1971 (I.G.S.N. 71) and the Gravity Formula 1980 for normal gravity.

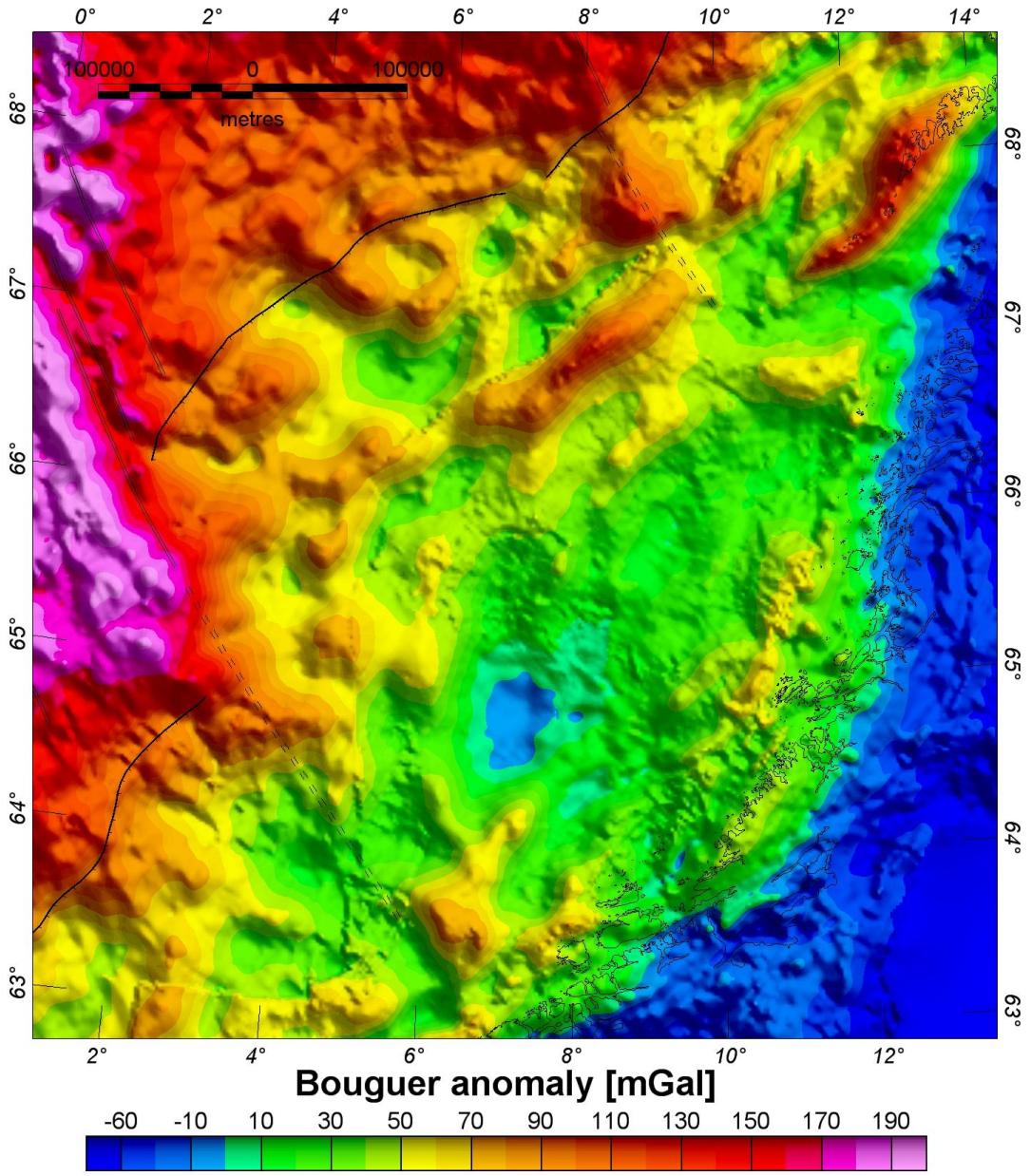

Figure 11.4. The Bouguer anomaly is calculated using the bathymetry data in Fig. 11.2 and an offshore reduction density of 2200 kg/m3.

11.3.2 Aeromagnetic data

The magnetic anomaly map (Fig. 11.5) is based on a NGU compilation of different onshore and offshore surveys (Olesen et al. 2006a). Aeromagnetic data from Norway and the adjacent continental margin have been compiled earlier (Skilbrei et al. 1991a; Olesen et al. 1997). The pre-1996 surveys were reprocessed during the periods of 1999-2001 and 2003-2004 using the median levelling and loop closure methods (Mauring et al. 2002, 2003) and these new versions of the NGU-73, Hunting-86, SPA-88, LAS-89, Viking-93 and NAS-94, have been included in the present. Statoil financed parts of this reprocessing within the Dragon database project (DiRect Access to Geophysics On the Net) in 1999/2000. Reprocessed data from the mid-Norwegian continental margin have been published by Olesen et al. (2002, 2004) and Skilbrei et al. (2002) and Skilbrei & Olesen (2005), but the North Sea and Barents Sea datasets remain unpublished. The more recent surveys VGVB-94, MBAM-97, VAS-97, VBE-AM-00 and RAS-03 are also included in the new data compilation.

Table 11.1. Offshore aeromagnetic surveys compiled for the present study (Fig. 11.5). NOO - Naval Oceanographic Office; NGU – Geological Survey of Norway; NPD – Norwegian Petroleum Directorate.

Year	Area	Operator	Survey name	Sensor elevation m	Line spacing km	Length km
1973	Vøring Basin	NGU	NGU-73	500	5	6.000
1986	Trøndelag Platform	Hunting	Hunting-86	200	2	57.000
1987	Vøring Plateau	NOO	NOO-87	230	5	16.900
1989	Lofoten	NGU	LAS-89	250	2	24.000
1993	Hel Graben- Nyk High	World Geo-science	SPT-93	80	0.75	19.000
1994	Nordland Ridge-Helgeland Basin	NGU	NAS-94	150	2	28.000
1994	Vøring Basin	Amarok	VGVB-94	140	1-3	31.800
1997	Møre Basin	Amarok/TGS-Nopec	MBAM-97	220	1-2	46.600
1998	Vestfjorden	NGU	VAS-98	150	2	6.000
2000	Southern Gjallar Ridge	TGS-Nopec	VBE-AM-00	130	1-4	17.000
2003	Røst Basin	NGU	RAS-03	230	2	28.000
2005	Jan Mayen FZ	NGU	JAS-05	230	5	32.600

The offshore aeromagnetic surveys have been gridded to 500 x 500 m cells and added to the regional mainland data compilation. Specifications for these surveys are shown in Table 11.1 The mainland of Norway grid has previously been digitised into a 500x500 m matrix from manually drawn contour maps and the Definite Geomagnetic Reference Field (DGRF) has been subtracted (Nor. geol. unders. 1992). The mainland area was flown at different flight altitudes and line spacing dependent on the topography (Table 11.2). The grids were trimmed to c. 10 km overlap and merged using a minimum curvature algorithm, GRIDKNIT, developed by Geosoft (2005).

Table 11.2. Mainland aeromagnetic surveys compiled for the present interpretation.

Year	Area	Operator	Navigation	Sensor elevation	Line spacing km	Recording
1964	Andøya	NGU	Visual	150 m above ground	1	Analogue
1965	Vesterålen area	NGU	Visual	300 m above ground	2	"
1971-73	Nordland-Troms	NGU	Decca	1000 m above sea level	2	"
1971-1972	Namdalen	NGU	Visual and Decca	300 m above ground	1	"
1959-1969	Central Norway	NGU	Visual	150 m above ground	0.5	"

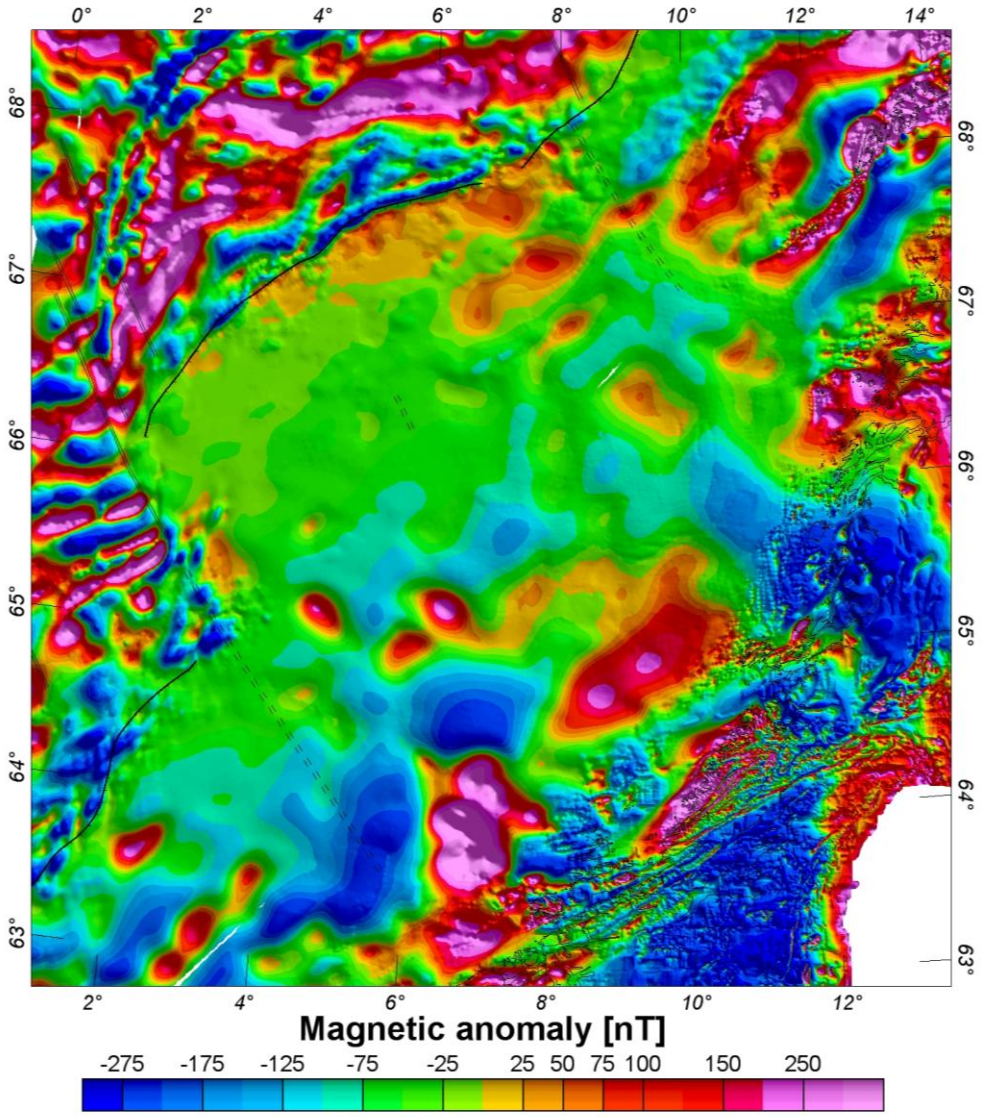

Figure 11.5. The total magnetic field anomaly is referred to DGRF on the mid-Norwegian continental margin. A total of 12 offshore aeromagnetic surveys have been processed and merged to produce the displayed map (Mauring et al. 2003, Olesen 2002, 2004, 2006a).

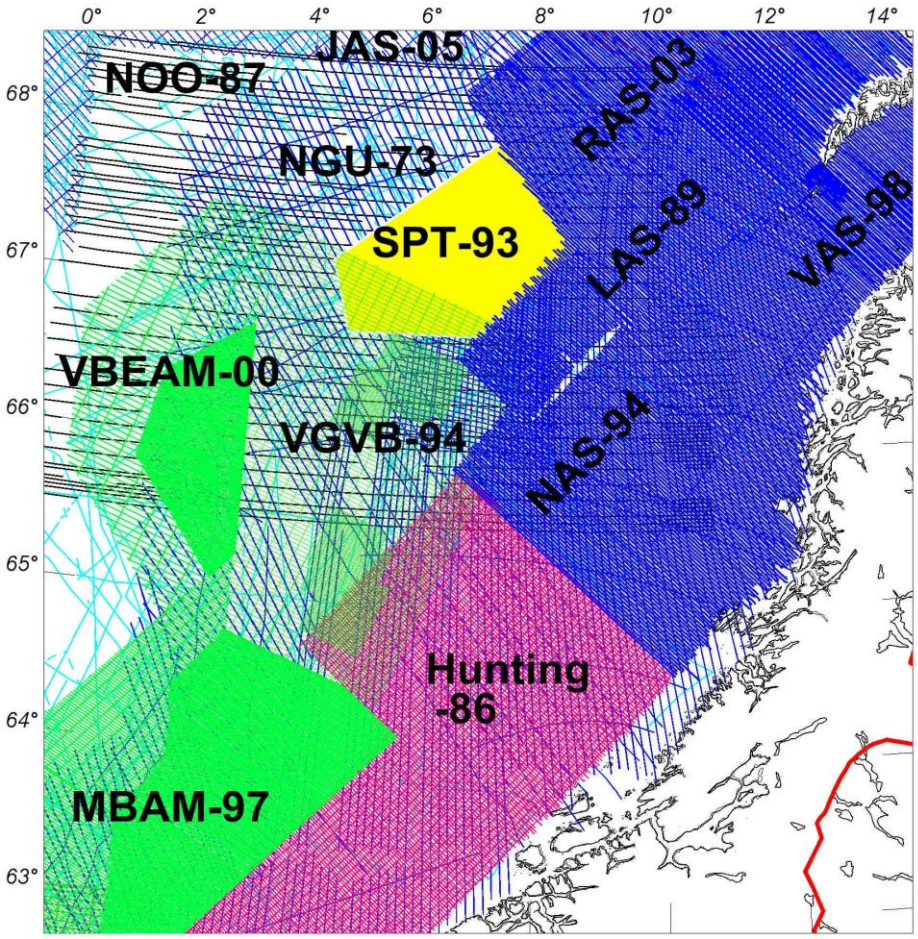

Figure 11.6. Compilation of magnetic surveys in the Norwegian Sea area. The sub-grids from the aeromagnetic surveys listed in Table 11.1 are produced from original profile data.

A first comparison of the gravity and magnetic anomalies reveals different structures, probably reflecting sources at different crustal levels. The amplitudes of the magnetic anomalies in the Vøring Basin are very low (around -50±50 nT) and the complex shape of the magnetic anomalies result possibly from changes in bathymetry (distance to near-surface sources), intra-basement variations of magnetic attributes, as well as intrusives (e.g. sills) located at shallower depths within the sediments. Towards the Trøndelag Platform the amplitudes and wavelength of the magnetic anomaly increase, pointing to additional sources in the basement.

11.3.3 Geometric constraints from seismic data and other sources

Previously, investigations of the mid-Norwegian continental margin have largely been based on interpretation of multi-channel reflection seismic data, refraction seismic data, commercial and scientific drilling, and analysis of potential field data (e.g. Skogseid et al. 1992, Doré et al. 1999, Brekke 2000, Mjelde et al. 2001, Raum et al. 2002, Mjelde et al. 2003a,b, Gomez et al. 2004, Fernàndez et al. 2004, 2005, van Wijk et al. 2004). The geometries of the deeper crust and the upper mantle on the mid-Norwegian margin are reasonably well defined by

OBS data (see Fig. 11.2 for location). Interpretations of OBS arrays are available from the studies by Mjelde et al. (1992, 1993, 1997, 1998, 2001, 2002, 2003a, 2003b, 2005) and Raum et al. (2002). In addition, the research group of Rolf Mjelde at UiB provided us with information about the velocity structure along three yet-unpublished OBS transects. These three profiles are especially helpful for our interpretation as two of them cross the Trøndelag Platform and extend onshore, and the third one is located on the Møre margin, where few other regional profiles are available (Fig. 11.2). In addition, the Moho compilation by Kinck et al. (1993) and its modifications by Olesen et al. (2002) have been used to constrain the model in the onshore area.

Our estimate of the offshore basement depth was based on the seismic results mentioned above, plus additional studies by Olesen et al. (1997), Doré et al. (1999), Brekke (2000), Olesen et al. (2002), Osmundsen et al. (2002), and Skilbrei et al. (2002) and Olesen et al. (2004). We have also incorporated the interpretation to depths of magnetic sources (e.g. Skilbrei et al. 2002; Olesen et al. 2004; Skilbrei & Olesen 2005).

We also made use of selected seismic cross-sections that were combined into a series of depth-converted, crustal-scale transects that cross main domain boundaries in the southeastern mid-Norway rift (Fig. 11.2). These transects were compared to the 3D model to constrain the interpretation of the deep basement geometry.

11.3.4 Information from Statoil

Statoil provided gridded data for the area of the Trøndelag Platform:

- Seabed
- Top Paleocene
- Base Tertiary
- Base Cretaceous
- Top Salt
- Top Perm (Fig 11.8)

These grids have a cell size of 500m x 500 m and are based on the interpretation of Statoil internal seismic database. The interpreted horizons were evaluated against the regional seismic lines and used to refine the 3D model of the Trøndelag Platform. An agreement of the 3D modelling and the seismic horizons could be achieved with the exception of the southern Trøndelag Platform (see discussion in Ch. 11.4).

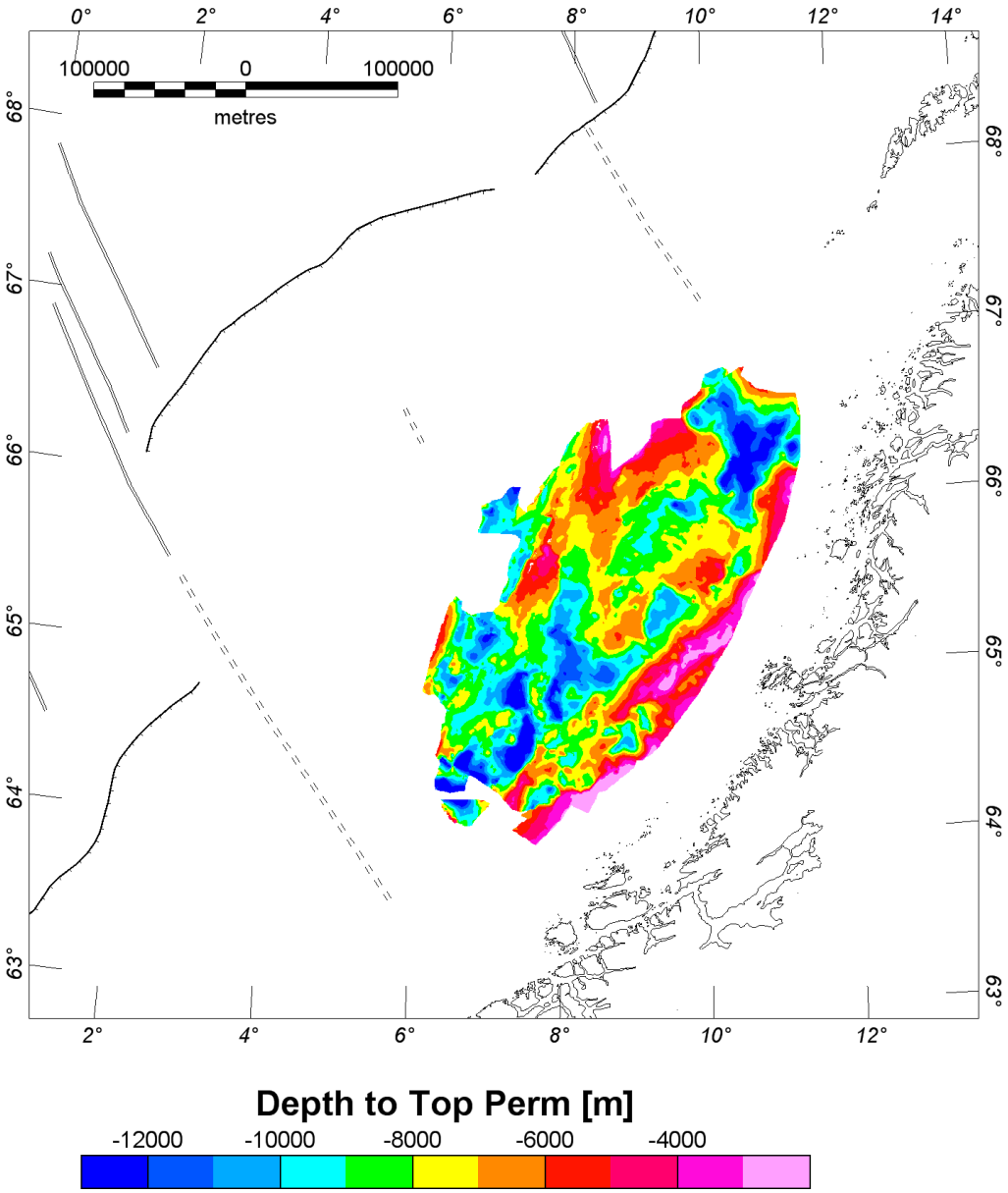

Figure 11.7. The depth to the top of the Permian as compiled by Statoil. The figure shows also the extent of the provided grid data.

11.3.5 Petrophysical information

The two parameters most important for constructing the 3D density and magnetic model are the geometry and the density of the structures. The densities used in the model process are based on published values (Raum et al. 2002, Mjelde et al. 1998, 2001, Olesen et al. 2002, Olesen and Smethurst 1995) and are based on different sources as velocity-density relationships (e.g. Ludwig et al. 1970) or density logs of exploration wells on the Nordland Ridge and Utgard High (e.g. Olesen et al. 2002). The density model values used are shown in Table 11.3. The errors from the velocity-density relations on the applied densities are in the order of ±0.05 Mg/m^3 and ±0.1 Mg/m^3 for the upper basement and deep crustal layers, respectively (Ebbing et al. 2006a).

Table 11.3. Densities of geological structures in the Norwegian Sea. Density values in Mg/m^3. LCB: lower crustal body.

	Raum et al. 2002	**Mjelde et al. 2001**	**Mjelde et al. 1998**	**Olesen et al. 2002**	**Fernàndez et al. 2004**	**this study**
Water	1.03	1.03	1.03	1.03	1.03	**1.03**
Tertiary	1.95-2.25	1.9-2.15	1.95-2.2	2.2	2.2	**2.05-2.1**
Cretaceous Sediments	2.4-2.65		2.45-2.67	2.35-2.5	2.4-2.65	**2.3-2.6**
Upper Cretaceous	265			2.35	2.4	**2.3-2.4**
Lower Cretaceous				2.5	2.58	**2.45-2.55**
Pre Cretaceous	2.68-2.76	2.7-2.81	2.83		<2.6	**2.65-2.7**
Lower Volcanics /Sills		2.62-2.8				
Upper Volcanics		2.7-2.77			2.5	
Cont. Crust	2.82-2.84	2.82-2.9	2.7-2.95	2.75-2.95	2.65-2.95	
Upper Basement						**2.65-2.7**
Lower Basement						**2.75-2.85**
Lower Crust						**2.95-3.0**
LCB	3.0-3.12	3.11-3.22	3.1-3.23	3.1	3.0	**3.1**
Mantle	3.3-3.34	3.33-3.36	3.33	3.25	3.2	**3.3**

In general, magnetic anomalies are modelled by applying magnetic parameters to the density modelling. Here, modelling of the magnetic anomalies has been performed, rather on a regional basis for the entire mid-Norwegian margin and more detailed within the Trøndelag Platform. The magnetic parameters we applied to the 3D model are listed in Table 11.4. These parameters are consistent with previous modelling studies in the area (Fichler et al. 1999) and petrophysical measurements (Olesen et al. 1991; Skilbrei et al. 1991b; Mørk et al. 2002).

Table 11.4. Magnetic parameters applied in the 3D model. The inclination and declination of all remanent fields is set to 77.0º and 0.5º, approximately parallel to the present magnetic field. For more details see text.

	susceptibility in SI	Q-ratio
Water	0	0
Tertiary Sediments	0.0001	0.4
Other Sediments	0.0002-0.003	0.4
Upper Basement	0.005-0.01	0.5-1.0
Lower Basement	0.02-0.035	0.4-1.1
Lower Crust	0.005	0.5
LCB	0.005-0.0075	0.5
Mantle	0.0025	0.5

Most magnetic material is expected to reside within basement rocks (e.g. Fichler et al. 1999), the overlaying sedimentary rocks making only a small magnetic contribution. Susceptibilities of the basement can range between 0.005 and 0.035 SI (with Königsberg ratios between 0.4-1.1) while susceptibilities of the overlying sedimentary rocks are in the order of 0.0003 SI (see also Table 11.4), some two orders of magnitude lower. The upper basement is considered to be less magnetic than the lower basement. (As will be shown later, high-magnetic-intensity basement rocks at shallow crustal levels are related to prominent gravity and magnetic anomalies, especially below the Trøndelag Platform). The main magnetic signature is caused by the changing geometry between the low- and the high-magnetic basement.

Magnetic data will only provide information for the part of the model that presently resides below the Curie temperature. Rocks at higher temperatures will not generate a discernible magnetic signal. Magnetite is regarded to be the dominant magnetic mineral in the region and has a Curie temperature of 580 ºC (cf. Hunt et al. 1995). The depth to the Curie temperature and between magnetic and non-magnetic material runs generally through the lower continental and oceanic crust. Therefore, the upper mantle and the LCB have only a minor contribution to the observed magnetic anomaly.

In previous studies a very shallow depth to Curie temperature has been assumed for the outer Vøring margin (e.g. 12.5 km at the COB, deepening landwards to 22.5 km below the coastline; Fichler et al. 1999, Olesen et al. 2004). This would imply that only the uppermost basement has a contribution to the magnetic field. Recent studies cast some doubts about this assumption (Gernigon et al. 2006a; Olesen et al. 2006a) and therefore the Curie depth is here assumed to be located below the crust. This allows testing the influence of deep-seated sources to the magnetic field.

The geometry of the model is based on the studies described above. The model geometry was derived from the seismic studies described above. These studies constrained the internal geometries of the sedimentary succession, which reduced the uncertainties in the density modelling. Our new interpretation places additional focus on the presence of the basement

internal structures (e.g. rotated fault blocks) and their correlation with the gravity and magnetic signal.

11.4 3D modelling

For 3D modelling we utilized the Interactive Gravity and Magnetic Application System (IGMAS; http://www.gravity.uni-kiel.de/igmas). This method calculates the potential field effect of the model by triangulation between modelling planes (Götze & Lahmeyer 1988). The 3D model of the entire mid-Norwegian margin consists of ~40 cross-sections with a spacing of 10-25 km and 26 of these profiles cross the Trøndelag Platform (Fig. 11.2). The varying distance between the cross-sections was chosen to provide good coverage of the main geological features and a good overlay with the OBS and seismic reflection profiles.

The geometry of the models is based on the studies as described above. These studies constrained the internal geometries of the sedimentary succession, which reduced the uncertainties in the density modelling. Our new interpretation focuses further on the presence of basement structures (e.g. rotated fault blocks) and their correlation with gravity and magnetic signal.

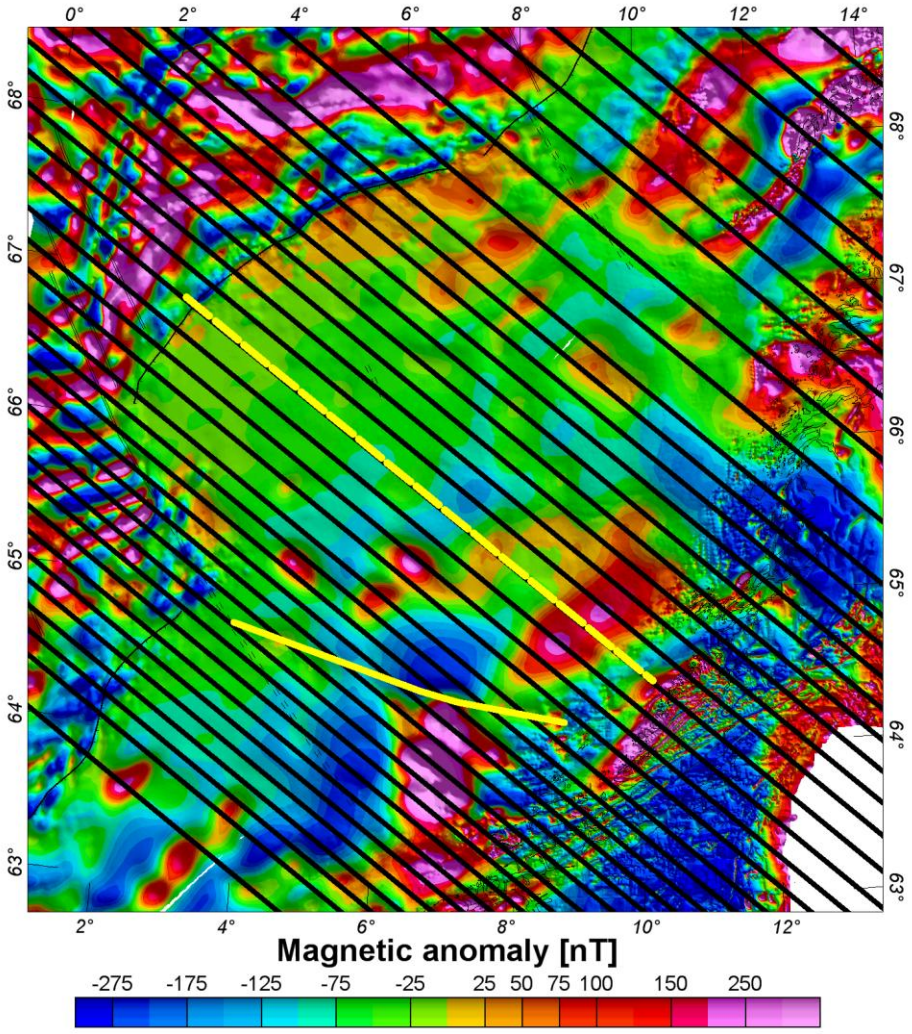

Figure 11.8. Location of the transects presented in Figs. 11.9 (stippled yellow line) and 11.11 (solid yellow line) on top of the magnetic anomaly map.

Fig. 11.8 shows the location of two regional transects crossing the Trøndelag Platform. Figs. 11.9 and 11.10 show two cross-sections through the 3D model to demonstrate the geometry of the model. From the 3D model we can extract maps of a variety of surfaces, which again allow a discussion of some structural elements on the mid-Norwegian margin. We will first present depth maps of the key horizons of the model before we discuss maps of crustal/basement thickness.

11.4.1 Gravity and magnetic response along transects crossing the Trøndelag Platform

The first transect is crossing the central part of the Trøndelag Platform and running from the outer Vøring margin through the Rås Basin and Halten Terrace into the Trøndelag Platform (Fig. 11.9). This transect shows all the characteristics of the crustal structure of the mid-Norwegian margin: very thick sedimentary sequences divided by major domain boundary faults; a thin upper basement underlain by a thick high-magnetic basement, locally cutting through the upper basement; low magnetic anomalies on the outer Vøring margin, but high magnetic anomalies on the Trøndelag Platform; core complexes associated with high magnetic anomalies; a thick high-density lower crustal body on the outer Vøring margin; a flat Moho geometry, rapidly deepening landwards below the Trøndelag Platform. Most of the structures are associated with large density contrasts. A small density contrast (50-100 kg/m^3) occurs between the upper and lower basement only, but a high magnetic contrast exists (Fig. 11.9a,b). The boundary can also be seen on OBS profiles and partly on long-offset seismic profiles. Modelling of the magnetic anomalies reveals further the importance of the remanent magnetisation for the upper basement. Only induced magnetisation within reasonable magnetic parameters is not sufficient to create the observed magnetic highs. Only with the remanent magnetisation component the magnetic anomalies can be adjusted. The direction of the remanent magnetisation is here modelled to be parallel to the present magnetic field, as observed for high-grade rocks in Lofoten (Olesen et al. 1991) and on the Fosen Peninsula (Skilbrei et al. 1991b).

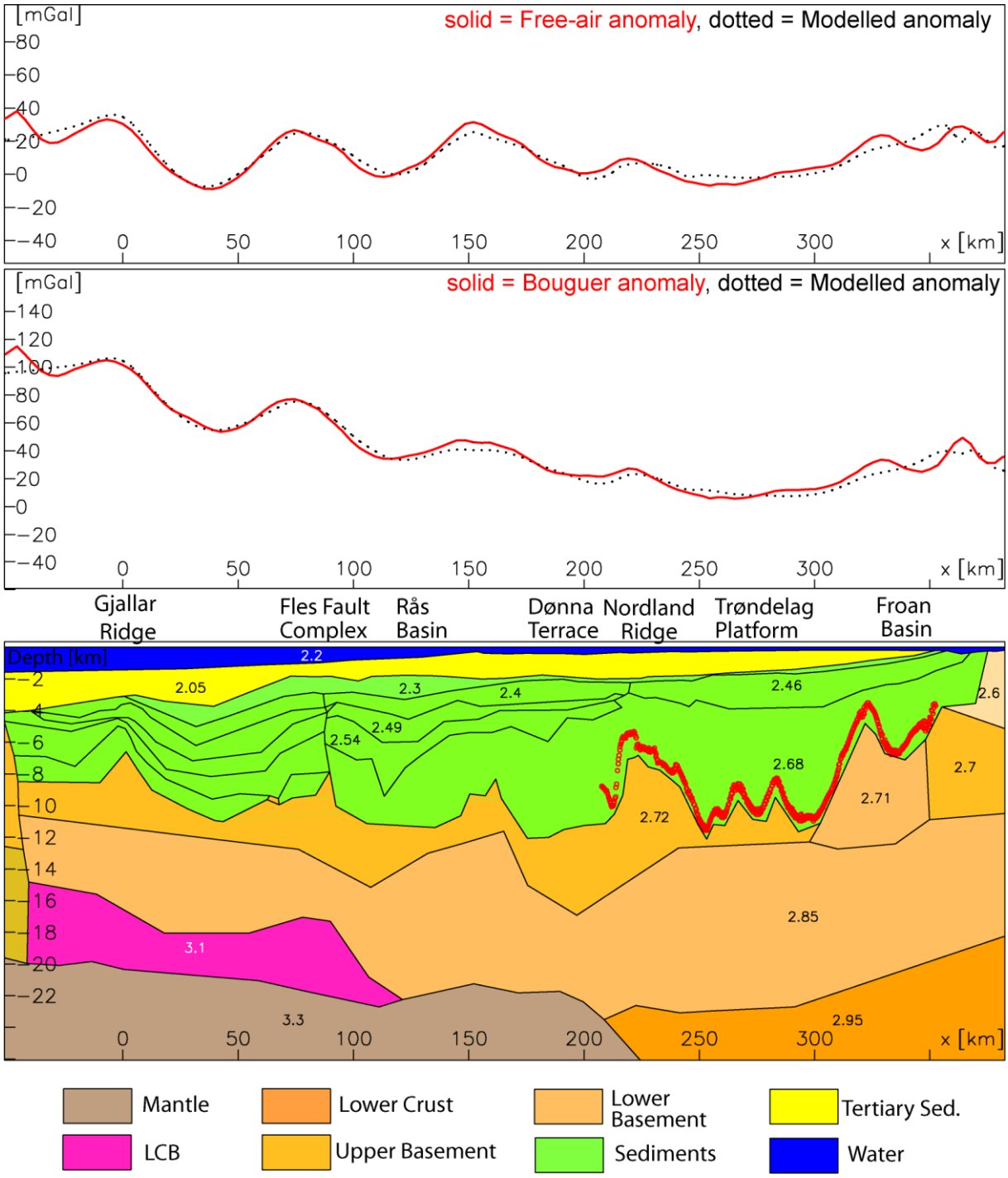

Figure 11.9a. The central transect along the mid-Norwegian margin. The upper panel shows the free air anomaly, the middle panel the Bouguer anomaly. The lower panel shows the modelled density cross-section. Black numbers are density values in Mg/m^3. The free-air anomaly has been modelled with a water density of 1.03 Mg/m^3. Red line shows the depth to Top Permian from the Statoil compilation. LCB: lower crustal body. See Fig. 11.8 for exact location of the section and text for further details.

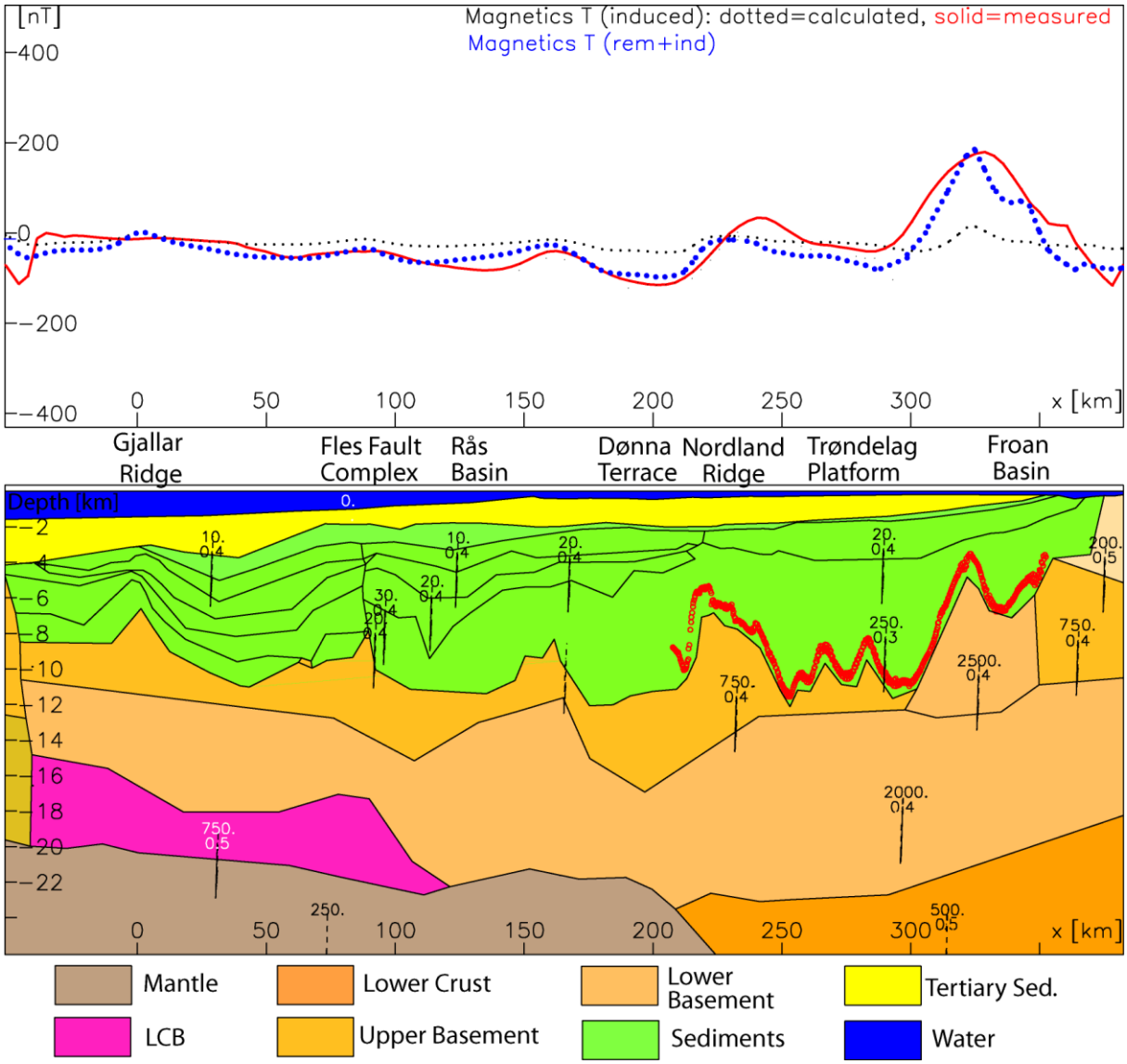

Figure 11.9b. The upper panel shows the induced and remanent magnetic anomalies. The lower panel shows the modelled magnetic properties. Numbers denote magnetic susceptibility in 10^{-5} SI and Q-ratios.

The second transect is located on the southernmost part of the Vøring Margin, crossing from the Modgunn Arch over the Helland Hansen Arch and Klakk Fault Complex into the Halten Terrace and Froan Basin, along the seismic lines GMNR94-104 and MNT88-08. The free-air gravity anomaly along the profile is varying between +/- 20 mGal and is showing no prominent anomalies. Thus, the signal merely reflects the sediment thickness and the geometry of the Moho. The deepening of the Moho to the east is somewhat compensated by thickening of the lower crust (and thinning of the sediments). The geometry of the western extension of the lower crust can be associated with a fault block. This line location takes also advantage of a thin or absent LCB. Therefore, the line was taken for preliminary thermal modelling and as we can directly study the influence of the basement architecture on the thermal structure and do not have to consider mechanisms for the evolution of the LCB.

Again, below the Trøndelag Platform the lower basement can be observed at a shallow depth, cross-cutting the normal upper basement.

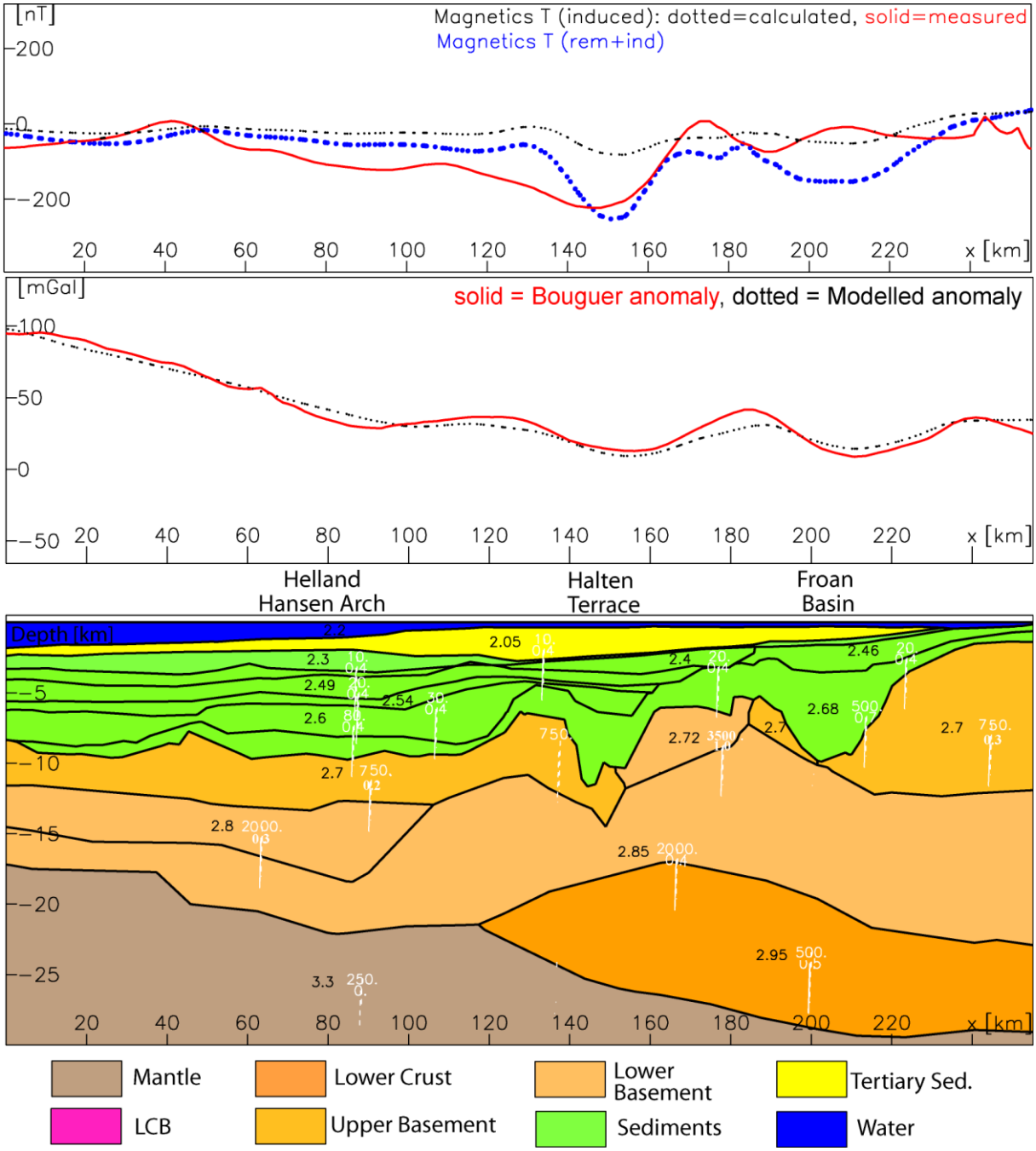

Figure 11.10. A transect along the profile seismic lines GMNR94-104 and MNT88-08 through the 3D model on the Vøring margin). The upper panel shows the magnetic anomaly, the middle panel the Bouguer anomaly. The lower panel shows the modelled density cross-section. Black numbers are density values in Mg/m3 and white numbers magnetic susceptibility in 10-5 SI and Q-ratios.

The results of the modelling enable us to construct new depth maps of the basement, high-magnetic basement, lower crustal body and Moho for the mid-Norwegian Continental Shelf (Figs. 11.11-10.14).

11.4.2 Upper and lower basement

11.4.2.1 Upper basement

The map of the top basement (Fig. 11.11) reveals a deepening from the coastal area towards the continental margin. The Trøndelag Platform features shallow depths (<9 km), while top basement in the Vøring Basin generally is encountered between 11 and 15 km. The top basement map shows a variety of local features, such as basement highs correlating with the Nyk and Utgard Highs. These structural highs reveal positive gravity anomalies. The depth to the crystalline basement is affected by the basin depth and sediment thickness and the Tertiary domes, especially in the northern Vøring Basin (e.g. Naglfar Dome and Vema Dome). In the southern Vøring Basin the depth to the top basement is similar, but this area lacks prominent basement highs.

The Møre margin to the south also reveals a deep top basement (12-15 km) but the top basement map shows less local features. The East Jan Mayen Fracture Zone marks an approximately 100 km lateral step in the margin. However, the Jan Mayen Lineament is not a well-expressed tectonic feature. Structurally, the transition between the Vøring and Lofoten margins is much more pronounced. Northeast of the Bivrost Lineament the top of the basement is located at a depth less than 10 km, and obviously reaches the surface on the Lofoten Ridge and at the northern terminations of the Vestfjorden and Ribban Basins. The Bivrost Lineament is a major tectonic boundary marked by both a vertical and apparent horizontal offset. The Utgard and Nyk Highs are suggested to be the southern continuations of the Lofoten Ridge and Røst High, respectively.

On the Trøndelag Platform the depth of the top basement is interpreted with hindsight to the structural interpretation provided by Statoil. The deepest seismic horizon was the Top Perm (Fig. 11.8), which locally exceeded 12 km in depth. At such a depth the density of the sedimentary rocks is not distinguishable from the underlying basement due to compaction (e.g. Ebbing et al. 2006a). Therefore, the depth to the basement was chosen to be deeper than the Permian horizon (except over the Frøya High, as explained below), but a depth estimate of the Permian succession from the density field model has a large degree of uncertainty.

The upper basement can be correlated with the Caledonian nappes as it is less magnetic than the underlying high-magnetic Precambrian basement. Simultaneous modelling of the magnetic and gravity field helps to improve the estimates of the depth to basement, but mainly related to the geometry of the underlying high-magnetic basement.

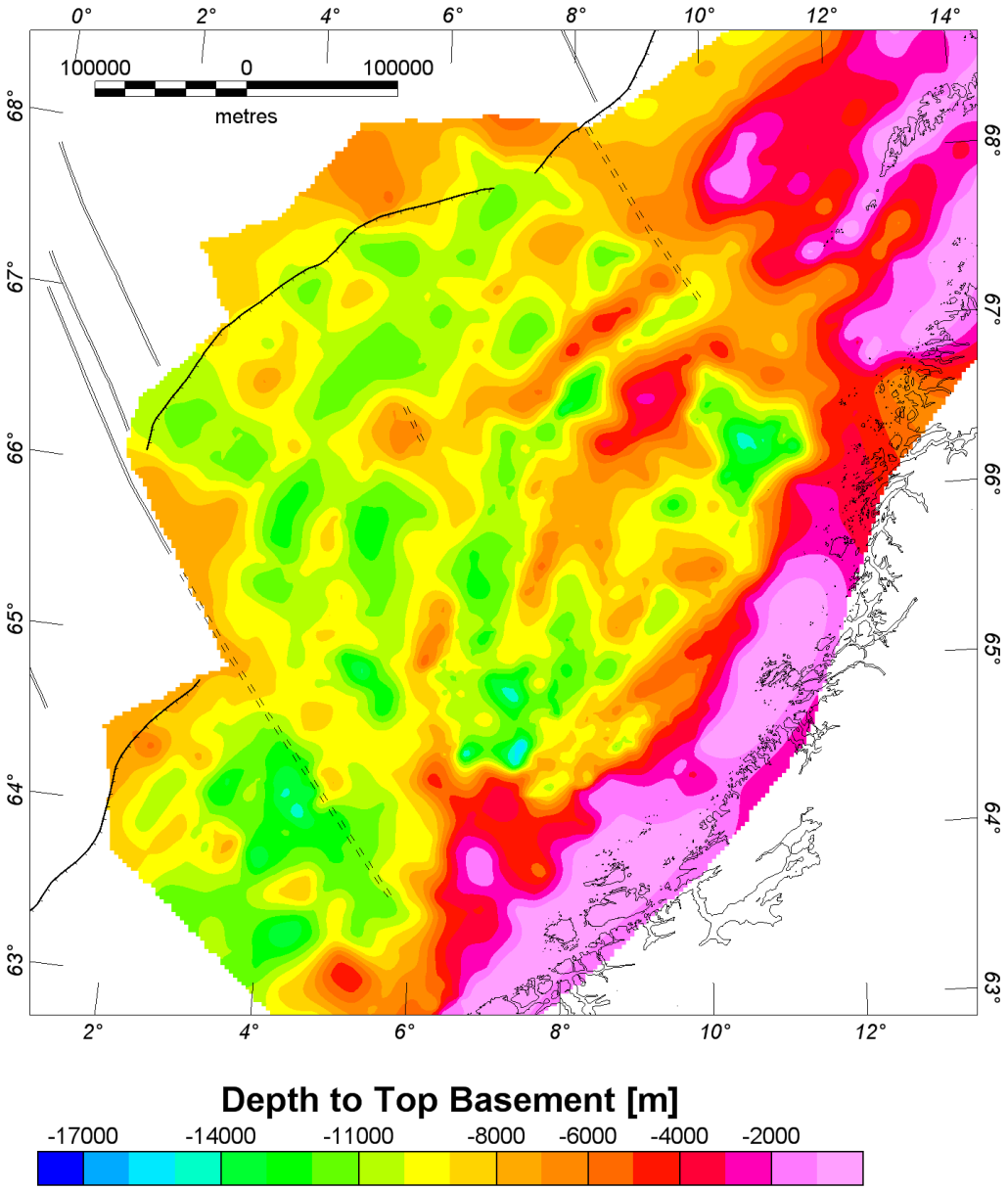

Figure 11.11. Depth to upper basement. The depth to top basement is associated with the depth to the top of the Caledonian nappes with densities around 2.7 Mg/m^3 and relatively low susceptibilities compared to the underlying Precambrian basement (Tables 11.3 and 11.4).

11.4.2.2 Lower, high-magnetic basement

The combined seismic and potential field analysis (see below) shows that the lower basement is a key element in the potential field signals on the mid-Norwegian margin, and especially on the Trøndelag Platform. The lower basement (Fig. 11.12) is defined to have densities >2.75 Mg/m^3 and higher magnetic properties (susceptibility of 0.02-0.035 (SI) and Q-ratios up to 1) than the uppermost basement.

The two-division of the basement is also consistent with the velocity structure provided from OBS interpretation (Mjelde et al. 2005, pers. comm.) and the interpretation of the regional

seismic lines. On the two transects (Figs. 11.9 & 11.10) a crustal dome (core complex) can be clearly observed which is also correlating with highs (Frøya High). On the magnetic anomaly map (Fig. 11.5) the magnetic high of the Frøya High is clearly extending towards the southern Halten Terrace. This is in disagreement with the horizons provided by Statoil and our 3D model.

The observed core complex is interpreted to be shallower than the interpretation of the Top Perm. However, the Top Perm grid is not complete in this region and the differences are located at the edge of the available data. The possibility that the core complex is located deeper in the crust is highly unlikely, as the modelling of the core complex already requires high magnetic susceptibility (0.035 SI) and Q-ratio (1.0) for the upper part to adjust the magnetic field. If the core complex would be located deeper, even higher magnetic properties would be required and it would be complicated to model the wavelength of the observed magnetic anomaly. Therefore, the current model appears to be the most reasonable, especially with regard to the potential field signal.

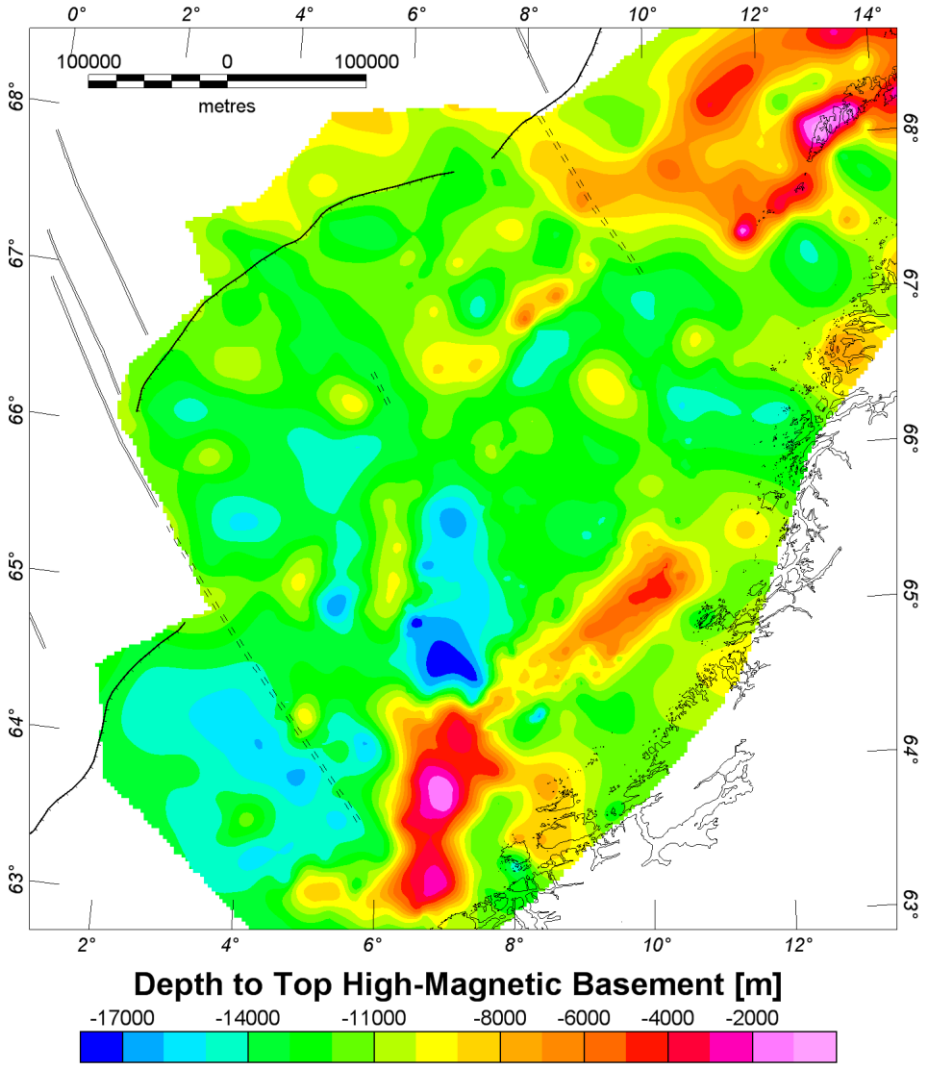

Figure 11.12. Depth to the lower basement. The lower (Precambrian) basement is defined to have higher densities and magnetic properties compared to the upper (Caledonian) basement.

11.4.3 Moho depth and LCB

In addition to the top of the basement the 3D model allows also to model the base of the crust (Moho) and the continental lower crust (CLC) and the lower crustal body (LCB). The interpretation of these horizons is mainly based on the seismic constraints and the density modelling, as the deep part of the crust has only a minor influence on the magnetic field due to the large distance to the source.

11.4.3.1 Depth to Moho

The depth to the Moho (Fig. 11.13) varies generally between 18 and 28 km. On the Møre margin the depth to the Moho deepens regularly from the coast to the margin, while the Moho depth of the Vøring and Lofoten margins varies more due to local structural features. Overall the central Vøring margin is characterized by a pronounced deep Moho, although the Utgard High is underlain by a shallow Moho, correlating to the shallow Moho below the Lofoten Ridge. Because the Lofoten margin is narrower than the Vøring and Møre margins the shallowing of the Moho is more abrupt.

Below the Trøndelag Platform the Moho is located at a depth of 25 to 30 km. The decrease from the west to east is relatively regular, with the exception of the area between the Froan and Helgeland basins, where the Moho is slightly shallower.

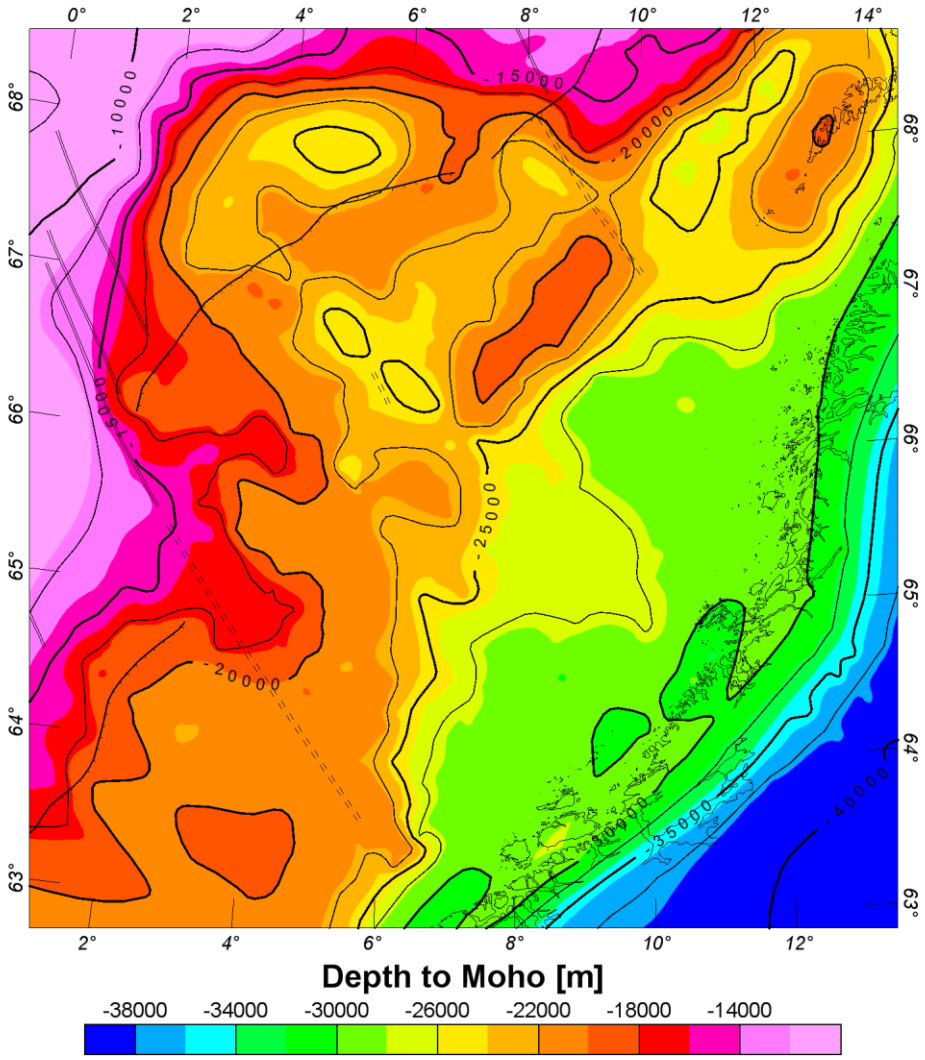

Figure 11.13. The depth to Moho map clearly shows that the Moho is deepening from a depth of around 20 km to 30 km below the Trøndelag Platform, correlating with the extent of the platform.

11.4.3.2 Continental Lower Crust (CLC) and Lower Crustal Body (LCB)

On the innermost part of the mid-Norwegian margin the lowermost crust has increased P-velocities (6.5 km/s) and a density of 2.95-3.0 Mg/m^3. These values are slightly increased from the basement and normal for continental crust. The CLC is located below the Trøndelag Platform and the entire Lofoten margin and is continuing from the margin and eastwards beneath the Scandes (Fig. 4.7), where it is observed in seismic and isostatic studies (Ebbing 2007, Pascal et al. 2007). However, the CLC is not present on the outer margin areas of the Vøring and Møre margin, where the lower crustal body (LCB) can be observed (Figs. 11.14 & 11.15).

The high-density and high-velocity body is located at the base of the crust below large portions of the outer parts of the Mid-Norwegian margin (Fig. 11.15). This lower crustal

body (LCB) has a density of around 3100 kg/m^3 and velocities of > 7 km/s. The extension and thickness of the LCB have been mapped in a series of studies (e.g. Mjelde et al. 2005; Ebbing et al. 2006a). While the origin of the LCB remains disputed, its presence is unarguably. For a thorough discussion see Ebbing et al. (2006a). We consider the LCB to have in general different petrophysical properties than the lower basement.

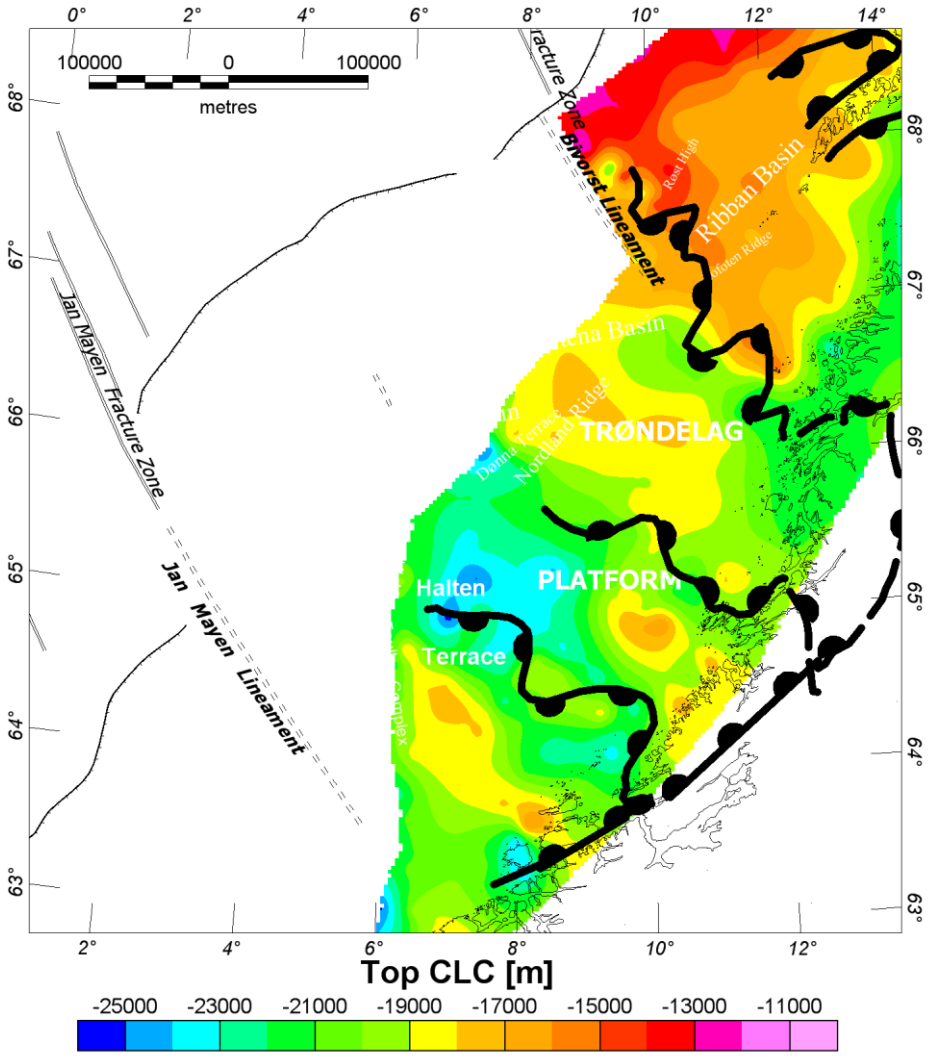

Figure 11.14. Depth to top of continental lower crust (CLC). The LCB has a density of 2.95-3.0 Mg/m3 and P-velocities of 6.5-6.9 km/s.

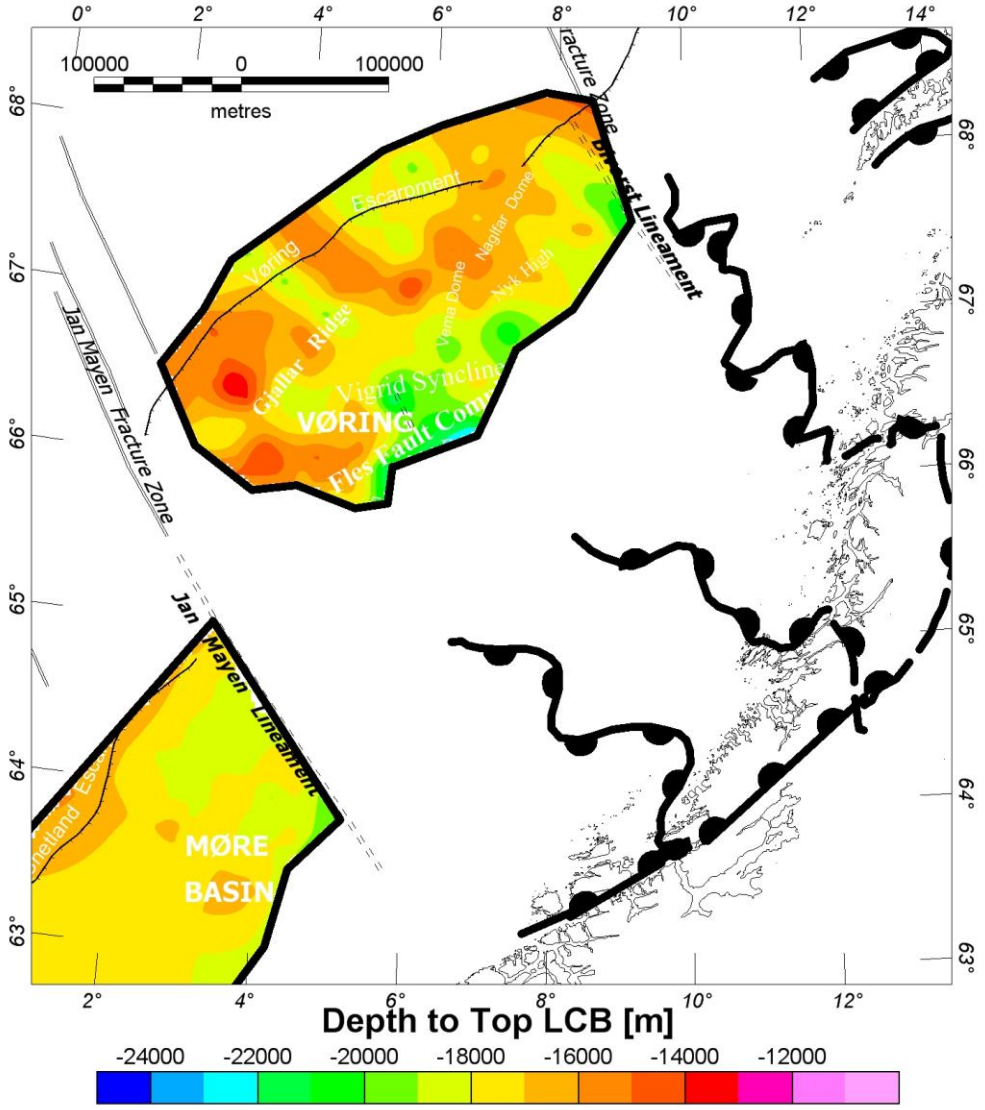

Figure 11.15. Depth to top of lower crustal body (LCB). The LCB has a density of 3.1 Mg/m^3 and P-velocities >7 km/s.

11.4.4 Basement thickness

Mapping of the different crustal horizons allows us further to estimate the basement and crustal thickness. Fig. 11.16 shows the thickness of the entire crust from the top basement to the Moho.

As mentioned above, the high magnetic basement can be interpreted due to its petrophysical properties to correspond to Precambrian granulite facies whereas the upper, low magnetic basement can be associated to Caledonian nappes and amphibolite facies Precambrian basement.

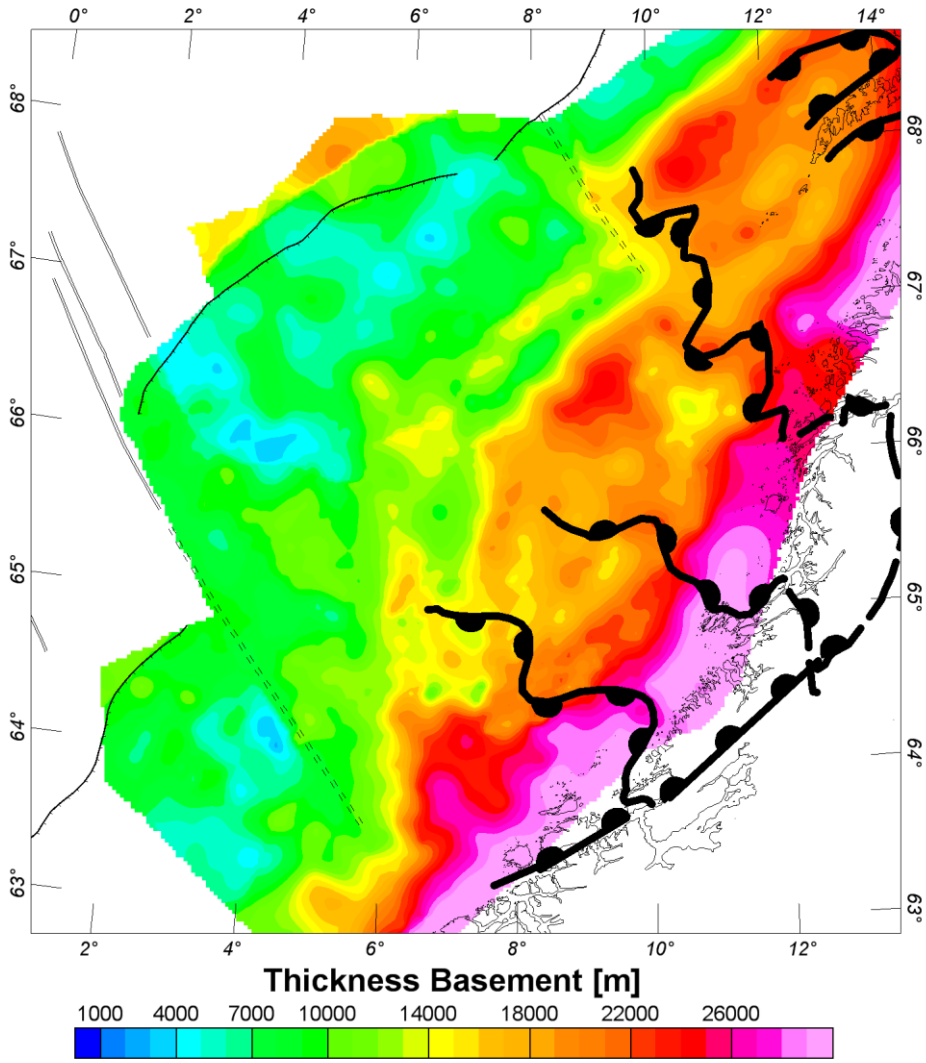

Figure 11.16. The basement thickness is the entire crustal thickness from the top of the upper basement (Fig. 11.11) to the depth of the Moho (Fig. 11.13). The lateral extend of the lower basement is given by the extent of the 3D density model.

11.4.4.1 Thickness upper basement

The upper basement can be associated from its petrophysical properties to be correlating to the Caledonian basement. The thickness map (Fig. 11.17) shows that the Caledonian basement is thickening towards the coastline, but has generally a thickness of 1-3 km on the outer Vøring margin. On the Lofoten margin the upper basement is generally thicker, but has zero thickness on the Lofoten Ridge, where the underlying lower basement is penetrating it. On the Trøndelag Platform the Caledonian basement is also thinning out in the areas of the core complexes.

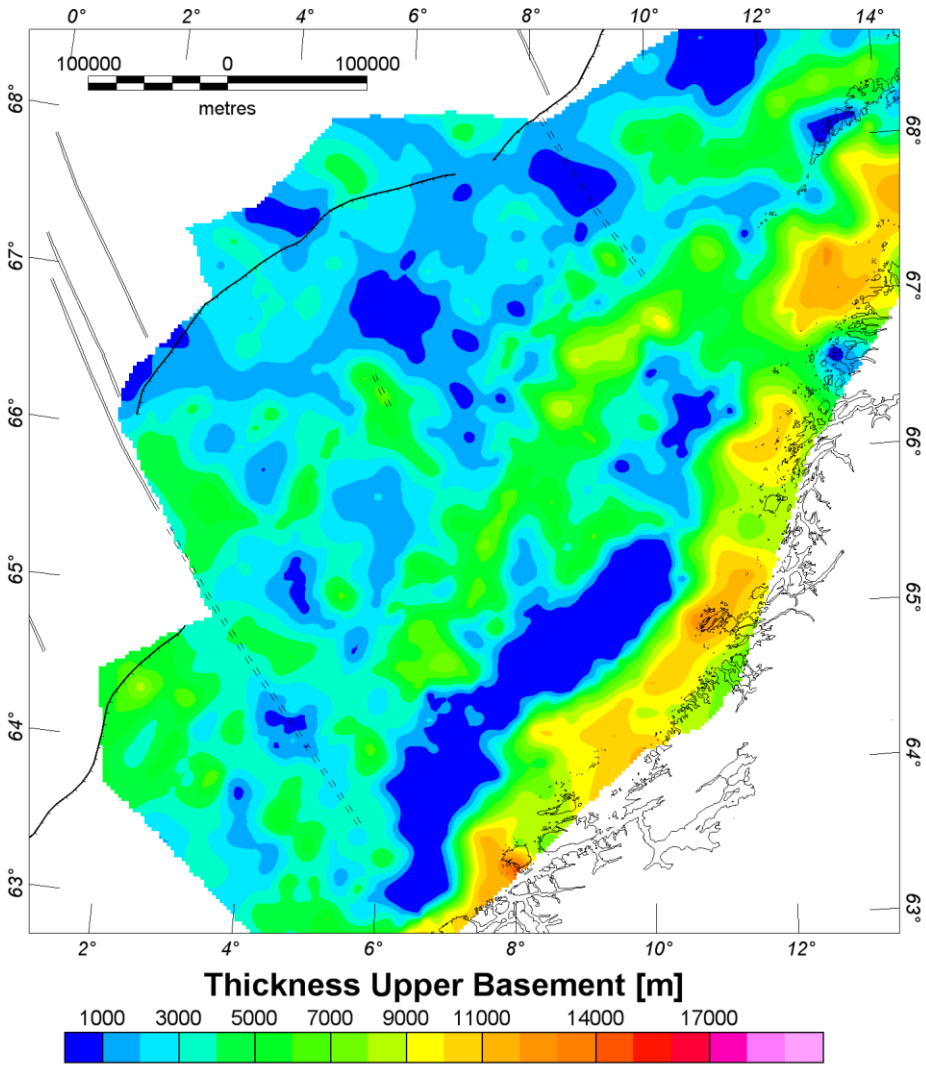

Figure 11.17. The thickness of the upper basement can be associated with the thickness of the Caledonian basement and is calculated from the top of the upper basement (Fig. 11.11) to the top of the high-magnetic lower basement (Fig. 11.12). The lateral extend of the lower basement is given by the extent of the 3D density model.

11.4.4.2 Thickness of lower basement

The thickness of the lower basement is calculated from the top of the lower basement to the Moho. The thickness of the lower basement is roughly correlating with the extent of the Trøndelag Platform (compare Figs. 11.18 and 11.1). However, the isopach map includes the Precambrian portion of the basement, the continental lower crust and the LCB. The thickness of the high-magnetic basement is furthermore correlating surprisingly well with the shape of the magnetic anomalies.

The CLB and the LCB have different petrophysical properties than the Precambrian basement (Tables 11.3 & 11.4). Therefore, we have to remove the portion of the CLB and LCB

(Fig.10.19) from the thickness of the lower basement (Fig. 11.18) to calculate the correct thickness of the Precambrian, high-magnetic basement (Fig. 11.13). The resulting thickness of the Precambrian basement is correlating less well with the extension of the Trøndelag Platform, but shows a thinning towards the outer margin from 7-12 km below the Trøndelag Platform to less than 6 km on the outer Vøring margin. The thickness of the high-magnetic basement is again correlating with the magnetic anomalies that are especially visible in the areas of the core complexes below the Trøndelag Platform.

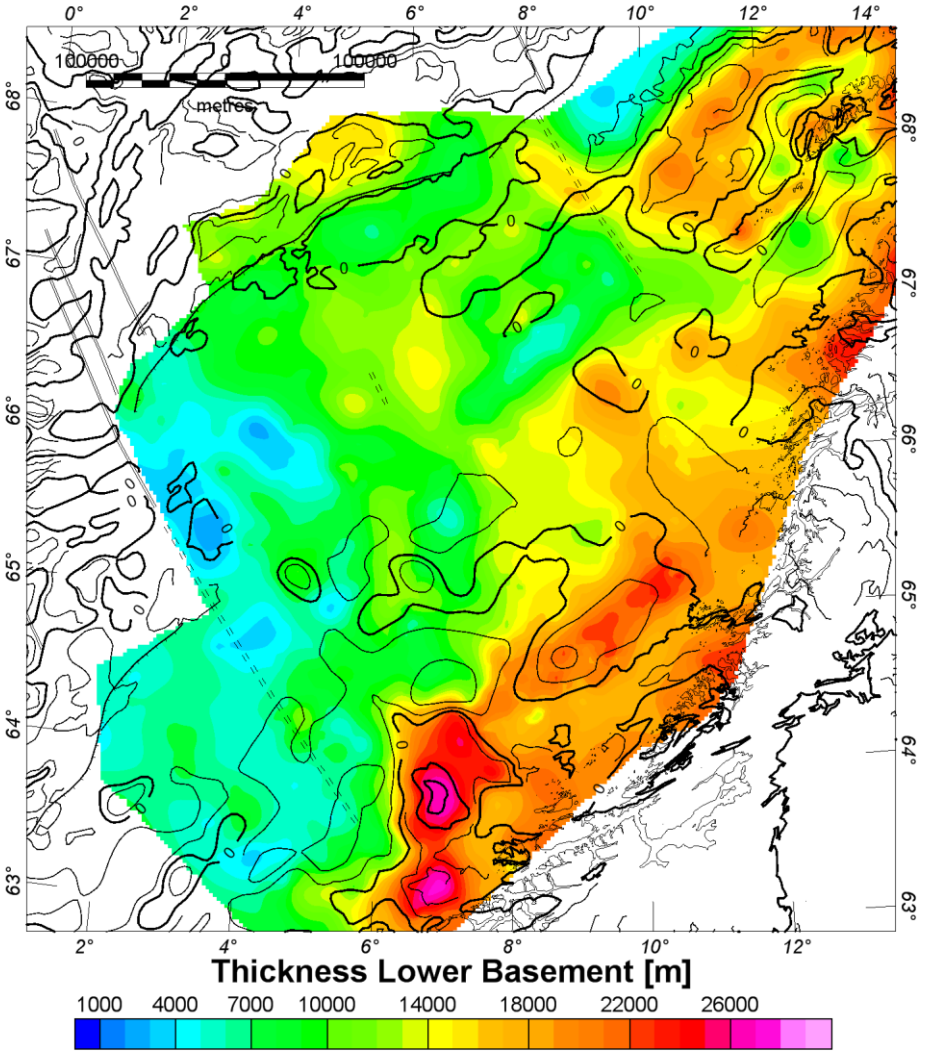

Figure 11.18. The thickness of the lower basement is calculated from the top of the upper basement (Fig. 11.11) to the Moho (Fig. 11.13) and includes the Precambrian basement and the LCB. The contour lines show the total magnetic field anomaly from Fig. 11.5 (contour distance 100 nT). The lateral extend of the lower basement is given by the extent of the 3D density model.

The thickness maps indicate that the geometry and thickness of the lower, Precambrian basement is the main element controlling the magnetic anomaly on the mid-Norwegian

margin. The Frøya High is an effect of very shallow lower high-magnetic basement and the general presence of a thick magnetic basement. The thickness on the outer Vøring margin is significantly reduced and the magnetic anomaly field is relatively quiet. Consequently, our analysis allows arguing that the relatively low-amplitude magnetic anomalies on the outer Vøring margin are mainly related to the thinning and deepening of high-magnetic material in the basement.

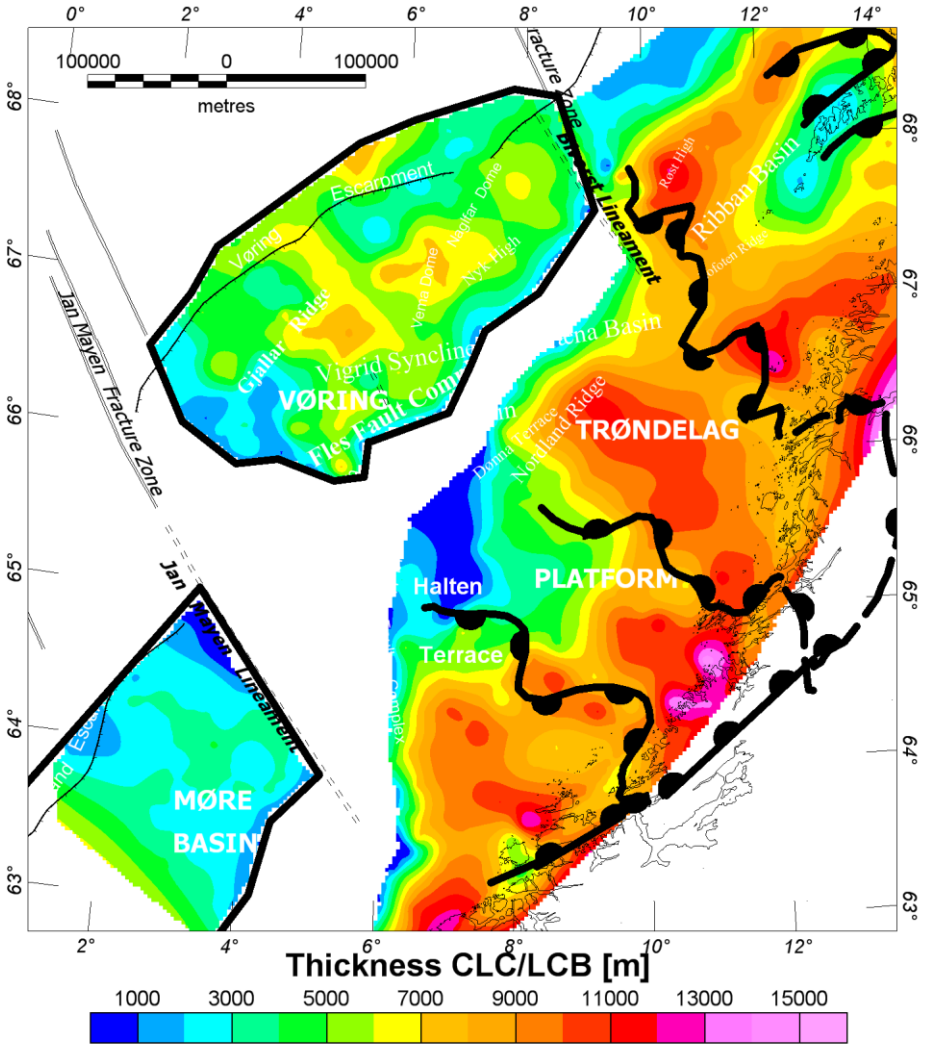

Figure 11.19. The thickness of the continental lower crust (CLC) and lower crustal body (LCB) is calculated from the top of the CLC and LCB (Figs. 11.14 & 11.15) to the Moho (Fig.10.13). The lateral extend of the lower basement is given by the extent of the 3D density model.

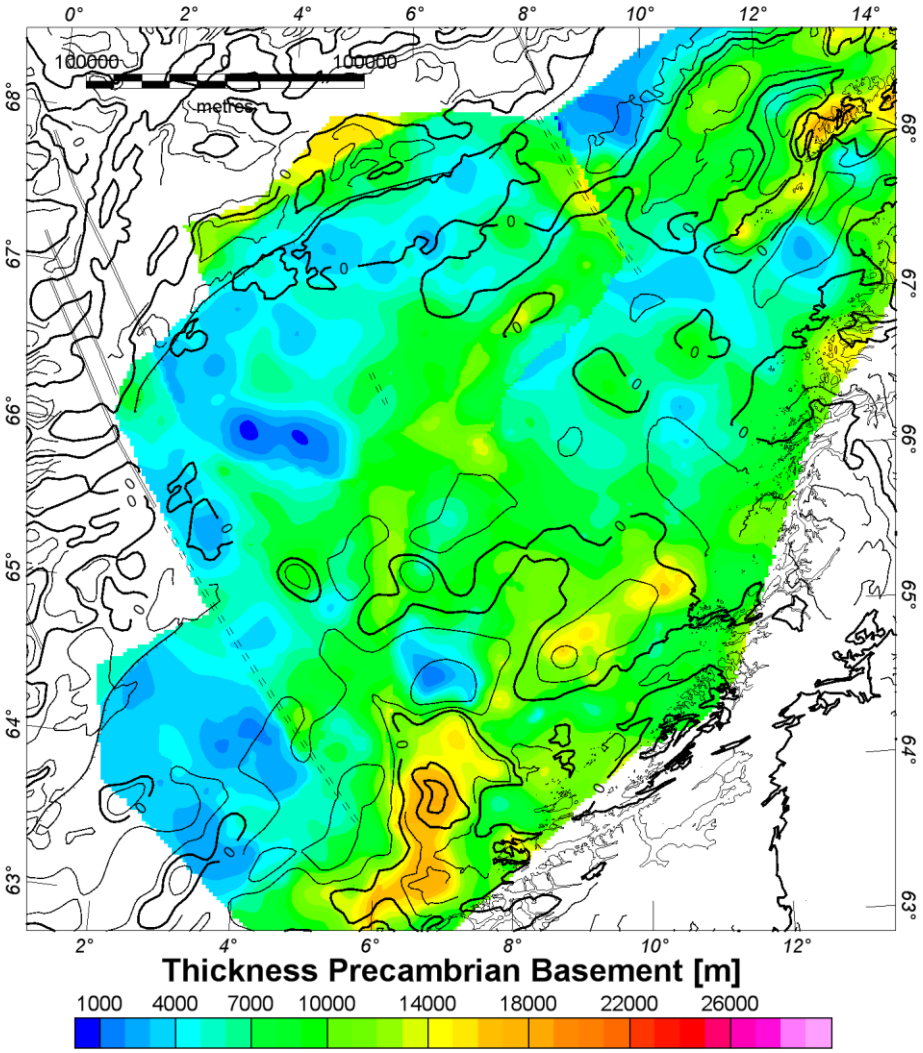

Figure 11.20. The thickness of the lower, high-magnetic basement is calculated from the top of the upper basement (Fig. 11.11) to the CLC/LCB or Moho (Fig. 11.13, 11.14 & 11.15) and includes only the portion of the basement, which can be associated with Precambrian basement. The contour lines show the total magnetic field anomaly from Fig. 11.5 (contour distance 100 nT). The lateral extend of the lower basement is given by the extent of the 3D density model.

11.5 Tectonic synthesis/interpretation

11.5.1 Basement

The basement can be subdivided in the upper and lower basement, which are different with regard to their petrophysical properties. The term crystalline basement is avoided in the study, as there exist different meanings of this term. Some studies associate the basement with the crystalline basement (e.g. Christiansson et al. 2000), while others associate it only with the lower basement (e.g. Raum et al. 2002). To avoid confusion with the applied terminology, we use the terms upper and lower basement.

The upper basement has generally lower densities and magnetic properties than the lower basement (Tables 11.3 & 11.4). Comparison to petrophysical sampling onshore Norway allows associating the upper basement with Caledonian nappes and the lower basement with Precambrian basement (e.g. Olesen et al. 1991). However, the division between the upper and lower basement is not everywhere associated with a clear contrast in density and velocity. But modelling of the magnetic field anomalies makes a regional mapping of these structures possible. The confidence in the top lower basement estimates is however less than for the upper basement. This is partly due to the large variability of magnetic properties. Petrophysical measurements show large variations in susceptibility and Q-ratio. Further, the direction of the remanent magnetisation is modelled to be parallel to the present magnetic field, but is dependent on the polarity of the magnetic field when the remanent magnetisation was formed.

Our interpretation is constrained by the seismic profiles and we applied magnetic properties that make it reasonable to connect horizons between the seismic profiles. However, the lower basement may feature more complexity in its internal structure than we are able to resolve. Any further interpretation using the depth to high-magnetic basement (Fig. 11.12) and/or the thickness of the lower basement (Figs. 11.18 & 11.20) must consider these uncertainties.

11.5.2 Correlation with onshore structural data

In the Trøndelag Platform area, comparison between seismic and potential field data lend support to previous interpretations of the relationship between positive magnetic anomalies and the offshore continuation of onshore detachment zones. The role of Palaeozoic detachment zones in the denudation of deep, magnetic levels of the crust postulated by previous authors is substantiated by our work. The role of the detachments is especially clear in the thickness and distribution of the continental lower crust (CLC) and the distribution of core complexes.

11.5.3 The Trøndelag Platform: correlation between seismic and potential field data

The distribution and thickness of high-density (>2.75 Mg/m^3) lower crust shows good correlation with the pattern of positive magnetic anomalies in the Trøndelag Platform area. One particularly strong, positive magnetic anomaly in the Central Trøndelag Platform area can be correlated with a doming of the lower crust, interpreted from long-offset seismic reflection data and consistent with our 3D density model. The dome has an amplitude in the order of kilometres and appears associated with crustal thinning along Palaeozoic extensional detachment faults. A deep, NNE-plunging structural culmination underneath the ramp-flat segment of the Bremstein Fault Complex can be traced from the southernmost Halten Terrace into the Frøya High. This correlates well with the strong positive magnetic anomaly that characterises the high, and that crosses the boundary to the Halten Terrace. In the Frøya High, relatively dense basement rocks subcrop sedimentary rocks, consistent with an interpretation of the basement rocks of the Frøya High as originally having belonged to the Caledonian

lower crust. Thus, Caledonian lower crust was exhumed in the Frøya High through a combination of post-Caledonian extension and extension related to Mesozoic rifting.

11.5.4 The domain boundary faults and the deep basin areas

Low- to moderate-angle domain boundary faults that separate platform, terrace and subbasin areas from the deep Møre and Vøring basins display geometries consistent with large magnitudes of horizontal separation (10-30 km) and denudation of high-density lower crust in dome-shaped culminations that reside in the footwalls. Osmundsen et al. (2006) interpret the domain boundary faults as main agents in the production of the areas of strongly thinned crust that evolved into deep basins.

11.5.5 Lower Crustal body

The LCB in the outer part of the mid-Norwegian margin is one of its most prominent features and it is still under discussion (e.g. Gernigon et al. 2003; Mjelde et al. 2005; Ebbing et al. 2006a). Different interpretations exist for this structure and the strong crustal reflectors often associated with it (e.g. Gernigon et al. 2003, Osmundsen et al. 2006). This study is not attempting to address details about the LCB, and we refer to the above-mentioned studies for further details. However, the distribution of the CLC and the LCB allows to question whether the LCB is not generically linked to the CLC. The density and velocity of the LCB is higher than for the CLC, but the spatial distribution allows to argue that the LCB is only a part of the high-grade rocks in the lower crust from the original Caledonian orogeny more affected by extensional and thinning processes of the margin and maybe by some percentage of additional magmatic intrusions.

The origin of the LCB is in any case certainly linked to the palaeo-temperatures on the mid-Norwegian margins. Geodynamic modelling and reconstructions of the Vøring margin must therefore ideally include the LCB (i.e. that the LCB represents magmatically underplated material) since the addition of such material affects the area isostatically (e.g. van Wijk et al 2002). Disregarding the addition of material to the base of the crust leads to underestimation of stretching factors. While dense, the underplated material is lighter than the mantle it replaces and therefore causes uplift. A similar statement can be made for the CLC.

What is generally observed from 2D forward and reverse modelling of profiles is that the mid-Norwegian margin has subsided considerably more than what can be predicted from seismically observable extension (e.g. Roberts et al. 1997). This phenomenon, known as depth dependent stretching, has since become a common observation along passive margins worldwide (Davis and Kusznir 2004). Notably, even if underplating is included or excluded in such modelling, there appears to be a mismatch between subsidence-based stretching factor estimates, those derived from observable faulting, and from whole crustal thinning (Davis & Kusznir 2004).

11.5.6 Curie depth vs. high-magnetic basement

Our analysis allows arguing that the relatively magnetic quietness on the outer Vøring margin is mainly related to the thinning and deepening of high-magnetic basement material. Earlier studies explained the relative magnetic quietness on the outer Vøring margin by a shallow depth to the Curie temperature (e.g. Fichler et al. 1999). Gernigon et al. (2006a) showed that thermal modelling along regional transects leads to temperatures for the lower crust below the Curie temperature of magnetite. They found the 580°C to be located in the uppermost mantle. The comparison shows that a contribution from mantle material to the magnetic signal can be largely excluded.

Strong evidence for the connection of the magnetic anomalies and the lower basement is given by seismic data on the Lofoten margin and the Trøndelag Platform. In both areas the geometry of the high-magnetic basement is clearly related to the high magnetic anomalies and seismic evidence exists for its geometry (e.g. Olesen et al. 2002, Osmundsen et al. 2006).

12 3D MODELLING: THE SCANDINAVIAN MOUNTAINS AND THE OSLO RIFT

Jörg Ebbing, Christophe Pascal, Odleiv Olesen & Jan Reidar Skilbrei, NGU

12.1 From structural modelling to temperature modelling

One of the goals in the Kontiki Project was to perform thermal modelling in addition to potential field modelling in order to validate basement and crustal configurations and in order to estimate the influence on basement structures on the observed heat flow. In the following we will describe the density, magnetic and thermal models from two areas: (1) the Scandinavian mountains, and especially the Central Scandinavia Profile and (2) the Oslo Rift.

Section 12.2.1 will present a general description of the isostatic state of the Scandinavian mountains and considerations about the crustal structure of the Fennoscandian Shield. In Sections 12.2.2 and 12.2.3 two alternatives 2 ½D model across the central Scandinavian mountains are presented after Skilbrei *et al.* (2002) and modifications. The thermal model and a synthesis of the thermal and density modelling are presented in Section 12.2.4.

The Oslo Rift is well studied and the wealth of geophysical and geological data makes the area the perfect case example for thermal modelling. The 3D crustal model of the area is described in detail by Ebbing et al. (2007a) and is summarized here (Section 12.2). Thermal modelling is made along one of the central profiles and presented in Section 12.4.2.

Originally, it was also planned to provide a structural model for the northern Viking Graben. However, in the course of the project it was agreed not to carry out the modelling and to concentrate on the three areas introduced above.

12.1.1 Modelling methods

The 3D density and magnetic modelling of the Oslo Graben and Mid-Norwegian margin was done using the interactive forward modelling software IGMAS (Götze & Lahmeyer 1988). The 3D model is based on parallel vertical planes with a polygonal structure. Between the planes a 3D model structure is described by triangulation. For the inverse and forward modeling of the Scandinavian mountains the software package GMSYS-2D and GMSYS-3D haven been used. In GMSYS-3D a 3D structure is described by calculating and adding the gravity effect of layers using the Parker algorithm (Parker 1972).

We used the commercial Finite-Element package Ansys for the thermal modeling of the three areas. The models involve 2D steady-state (i.e. purely conductive) thermal computations. Boundary conditions are setup as constant temperatures at the surface (i.e. 0°C) and constant heat flow at the base of the models. Model geometries are imported from potential field models and heat productions are affected to the different basement units in agreement with

values deduced from geochemical analyses. We used 6-noded triangular elements, numerical models contain ~10 000 to ~20 000 elements allowing for accurate and fast computations.

12.2 The Scandinavian mountains and the Central Scandinavia Profile

In this chapter we present the density, magnetic and thermal model along the Central Scandinavia Profile. However, we will first present a general description of the Scandinavian mountains (Section 12.2.1), before the density and magnetic model along the Central Scandinavia Profile is summarized after Skilbrei *et al.* (2002*)* in Section 12.2.3. In Section 12.2.4 we present an alternative model based on the results and in Section 12.2.5 thermal modelling is performed to evaluate the alternative models.

12.2.1 Isostatic state of the Scandinavian mountains

The Scandinavian mountain range is located at the western edge of the Fennoscandian Shield and includes two dome-like areas of high mountains and plateaus, the northern and southern Scandinavian mountains (Fig. 12.1). The Scandinavian mountains extend over more than 1400 km and are not one continuous mountain range, but can be divided into distinct segments according to their topographic shape and gravity signal. Tectonically the Scandinavian landmass has an intracratonic position in close relation to the passive continental margin along the northeast Atlantic. As part of the Fennoscandian Shield the Scandinavian mountains were largely affected by its tectonic evolution. Presently, Fennoscandia is affected by high uplift rates. The rates of present uplift in Fennoscandia range from close to zero along the Norwegian coast to more than 8 mm/yr in central parts of the Gulf of Bothnia. The main cause of the present uplift is related to post-glacial rebound (e.g. Niskanen 1939, Lambeck *et al.* 1998, Milne *et al.* 2001, 2004). But in the

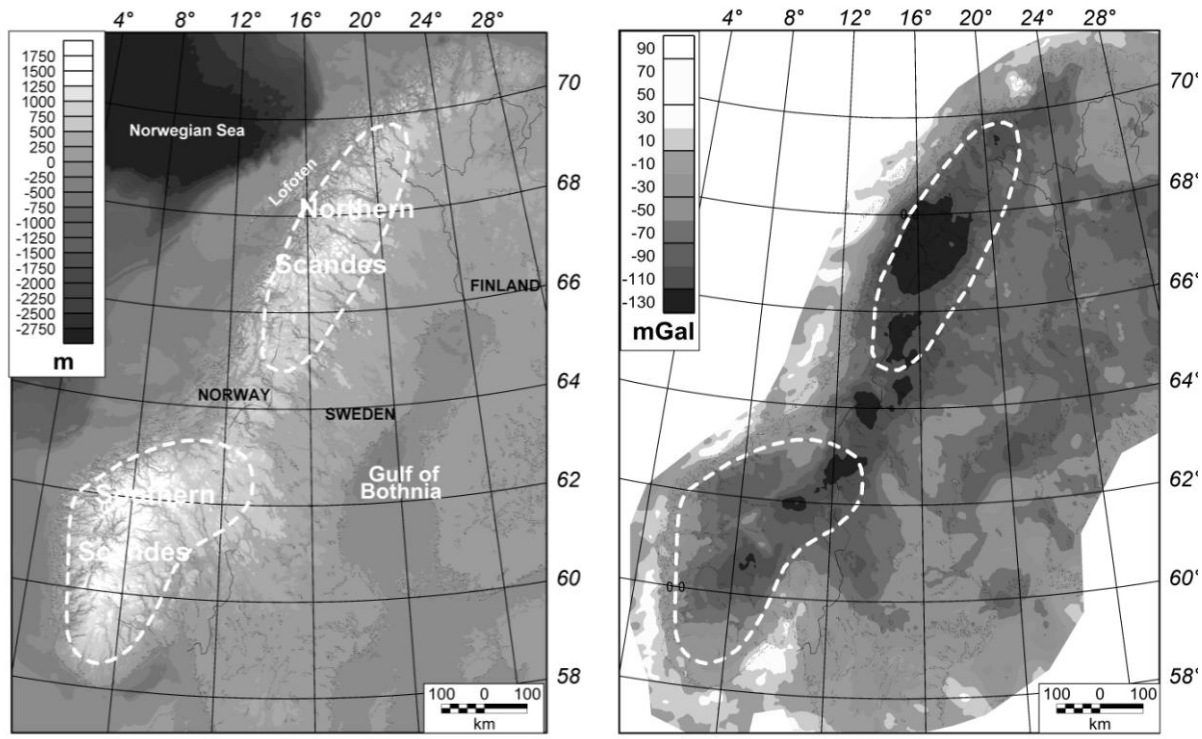

Figure 12.1. (left) Topography/bathymetry of Fennoscandia (after Dehls et al., 2000). Dotted lines depict the northern and southern Scandinavian mountains and correspond roughly to 500 m above sea level. (right) Bouguer anomaly. See text for details.

Northern and Southern Scandes two (Cenozoic?) uplift centres have been resolved, mainly by thermochronologic data (e.g. Redfield *et al.* 2005 and references therein). The gravity field provides a means to study the structural differences within the Scandinavian mountains and the mechanism of exhumation of the mountain range. The load imposed by the Scandinavian mountains must be isostatically supported at depth by substantial volumes of low-density material within the crust or the mantle. Thus, the crust-mantle and lithosphere-asthenosphere interfaces are important boundaries with regard to isostatic processes. This study presents an isostatically balanced density model for the Fennoscandian Shield with emphasis on the Scandinavian mountains. First, the data sets are introduced before a description of the 3D density model and the isostatic state of the Scandinavian mountains is given.

12.2.1.1 Gravity

Fig. 12.1 shows the complete Bouguer anomaly of the Scandinavian mountains and adjacent regions from the compilations by Skilbrei *et al.* (2000) and Korhonen (2002a). The Bouguer anomaly shows a gravity low correlating with the topography of the Scandinavian mountains. In the southern Scandinavian mountains local features can be identified in the Bouguer anomaly and in the northern Scandinavian mountains the maximum axis of the gravity low is slightly shifted with respect to the topography (compare Fig. 12.1 right and left). The correlation between topography and Bouguer gravity anomaly points to the presence of a

crustal root. However, in the reminder we will show that such a root cannot be imaged by seismic studies. For the isostatic gravity modelling a lowpass-filtered gravity anomaly is used with a cut-off wavelength of 100 km. The filter removes short-wavelength features that are not a subject of the present study. We will concentrate on the general lithospheric structure.

12.2.1.2 The seismic image of the Scandinavian mountains

To investigate the crustal structure of the Scandinavian mountain range a variety of reflection and refraction seismic profiles have been carried out in the past (e.g. Kanestrøm & Haugland 1971, Hirschleber *et al.* 1975, Cassell *et al.* 1983, Schmidt 2000). Interpretations combining seismic and gravity data, have enabled compilations of the Moho geometry Kinck *et al.* 1993, Korsman *et al.* 1999, Olesen *et al.* 2002, Mjelde *et al.* 2005). These compilations indicate that the Scandinavian mountains, despite their topographic expression, have no pronounced crustal root (Fig. 12.2). However, the topography has to be isostatically compensated. Candidates might be low-density bodies within the crust or the mantle, or the flexural forces within the elastic lithosphere. We can calculate the gravity effect related to the density contrast at the seismic Moho to study the residual sources in the gravity field and the isostatic loading. The gravity effect of the Moho is calculated using a density contrast at the seismic Moho of 350 kg/m^3. This value is in agreement with densities converted from seismic velocities from regional studies (Kanestrøm & Haugland 1971, Schmidt 2000), which indicate a density contrast between 300 and 400 kg/m^3. Indications of a high-velocity lower crust below the central Fennoscandian Shield can also be found in seismic observations (P-velocities > 7km/s; Korsman *et al.* 1999, Perez-Gussinye *et al.* 2004), providing support for a minor density contrast (200 kg/m^3) between crust and mantle. The insufficient distribution of seismic lines prevents us from clearly defining this structure. Especially, its westwards extension below the Scandinavian mountains is obscure. Mapping the high-density lower crust is, however, an important element when computing the lithospheric loading.

12.2.1.3 Base of the lithosphere

In addition to the Moho image, a model of the lithosphere-asthenosphere boundary below the Fennoscandian Shield is also available (Calcagnile 1982). The model shows a deepening of the lithospheric base from 110 km below the southern Scandinavian mountains to 170 km below the Bothnian Sea without revealing local patterns below the Northern and southern Scandinavian mountains (Fig. 12.2). The geometry of the lithospheric thickness has to be taken into account to calculate the effect on the gravity (and geoid) from the density distribution at the lithosphere-asthenosphere boundary. The geometry of the lithosphere-asthenosphere boundary has, due to its long-wavelength, a substantial influence on geoid undulations but is less visible in the gravity signal. The gravity effect was calculated with an asthenospheric density contrast of -30 kg/m^3 compared to the lithospheric mantle density. This contrast was previously applied to isostatically balance a lithospheric profile running

from the Norwegian shelf to the central Fennoscandian Shield (Bielik *et al.* 1996), and is in agreement with global reference models (e.g. PREM: Dziewonski & Anderson 1981).

12.2.1.4 Forward modelling

The 3D forward modelling was carried out with the software package GMSYS-3D. The density modelling is relative to a reference lithosphere: upper crust 0-12 km depth: 2670 kg/m^3, middle crust 12-20 km depth: 2800 kg/m^3, lower crust 20-30 km depth: 2900 kg/m^3, lithospheric mantle 30-120 km depth: 3250 kg/m^3; asthenospheric mantle: 120-220 km depth: 3220 kg/m^3. The density of the asthenospheric mantle can only be

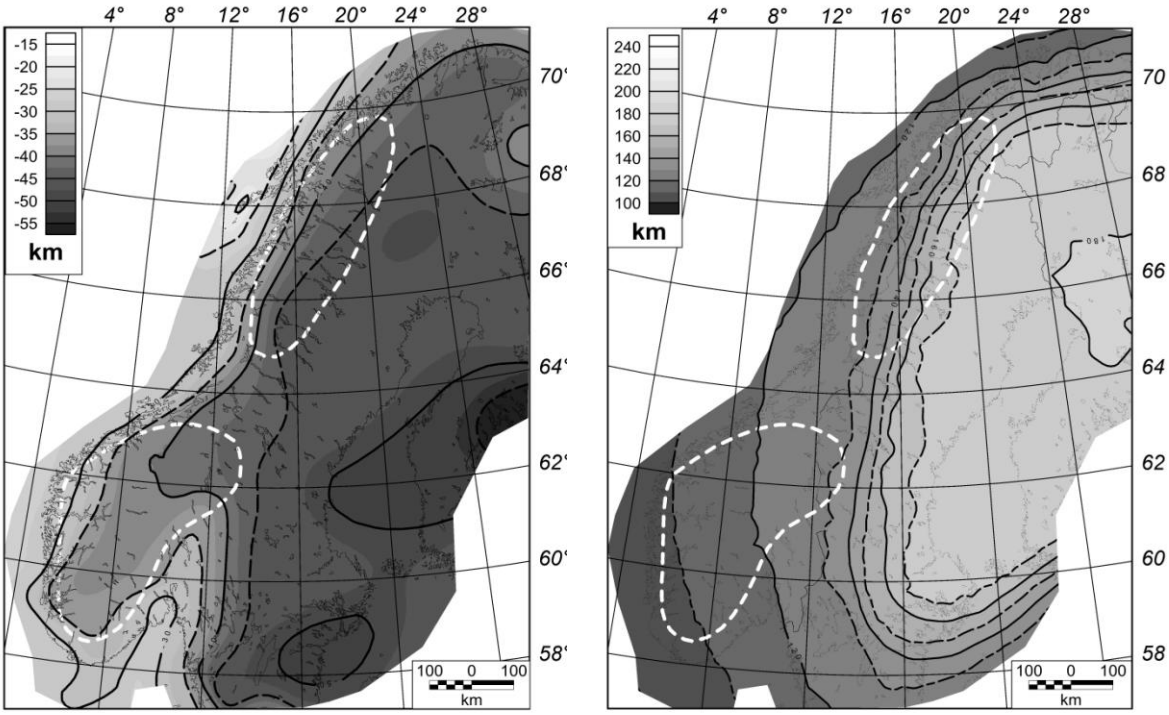

Figure 11.2. (left) Depth to Moho and (right) lithospheric thickness as compiled by seismic/-tomographic studies. The depth to Moho was compiled by a combined analysis of refraction seismic data and gravity studies (see text). The lithosphere-asthenosphere boundary was derived from an analysis of Rayleigh-wave dispersion data (Calcagnile 1982).

regarded as a relative density and is chosen to reflect the small density contrast at the base lithosphere as described above. Using a reference model allows us to model the level of the gravity field and not only the shape of the anomaly.

The 3D lithospheric model features a three-layered crust as described above, a crustal base according to the Moho model and the lithospheric base as shown in Fig. 12.2. The simple model provides already a good correlation between the modelled and observed gravity at the Norwegian coastline, but increasingly large negative differences towards the central Fennoscandian Shield. Consequently, high-density material in the lithosphere has to be added

and the first candidate is the high-density lower crust as observed in seismic studies. We have to map its distribution by isostatic considerations, because the seismic coverage and resolution is insufficient.

12.2.1.5 Isostatically balanced gravity model

We calculate the isostatically balanced loading of the lithospheric model described above with:

$$\rho_{Topo}D_{Topo} + \sum_{i=1}^{3}\rho_{ci}D_{ci} + \rho_{mantle}D_{mantle} + \rho_{asth}D_{asth} - \sum_{i=1}^{5}\rho_{refi}D_{refi} = \Delta Load / g$$

with densities ρ and height/thickness D for topography, crust, lithospheric and asthenospheric mantle and reference model as described above. g is the normal gravity field and $\Delta Load$ is giving indication of mass surplus and deficiency. The calculation shows that high-density material is missing especially below the central Fennoscandian Shield. As we know from the seismic studies that such a layer is observed, we convert $\Delta Load$ in a high-density Lower Crustal Body (LCB) with density 3100 kg/m^3 and the isostatic balanced equation becomes:

$$\rho_{Topo}D_{Topo} + \sum_{i=1}^{3}\rho_{ci}(D_{ci}) + \rho_{LCB}D_{LCB} + \rho_{mantle}D_{mantle} + \rho_{asth}D_{asth} = \sum_{i=1}^{5}\rho_{refi}D_{refi}$$

Hereby, we consider mass surplus as not related to the LCB and balance only for the missing masses, as there are no indication for low-density lower crust below the Fennoscandian Shield. This approach results in a LCB (Fig. 12.3) with a thickness up to 25 km in the central Fennoscandian Shield, which is in agreement with estimates from seismic studies (Korsman *et al.* 1999). The next step is to include the LCB into the density model and to calculate the gravity effect. The resulting gravity effect of the isostatic model features a north-south trending band of negative residual from the northern Scandinavian mountains to east of the Oslo Rift. This more than 100 km wide anomaly is coinciding with the Transcandinavian-Igneous-Belt (TIB) with low densities (~2640 kg/m^3) and high heat production, which is also reflected in the heat flow of Fennoscandia (e.g. Olesen *et al.* 2005). Forward modelling in the northern and central Scandinavian mountains indicated that these granites can have a depth-extension up to 20 km (Olesen *et al.* 2002, Skilbrei *et al.* 2002). We introduce a low-density band in the upper crust (2640 kg/m^3) according to the TIB and calculate the gravity effect of the lithospheric model. The residual between the observed and the calculated gravity field is now within 25+/-25 mGal, except in two regions: The southern and northern Scandinavian mountains, where the residual shows two gravity minima (Fig. 12.3).

12.2.2 Discussion and conclusions

The results of the present study show that a crustal root corresponding to the topographic load of the Scandinavian mountains exists. But the crustal root is coinciding with the distribution of high-density lower crust in the central Fennoscandian Shield, which is compensating the deep Moho.

Below the Scandinavian mountains the high-density lower crust thins out (Fig. 12.3). A second structure overprinting the root of the Scandinavian mountains is the TIB. Isostatic analysis show that the observed root of the Scandinavian mountains cannot explains the gravity low (Ebbing & Olesen 2005). Introduction of low-density granites into the upper crust does, however, explain the gravity low and these granites can be observed at the surface and correlated with magnetic anomalies (Skilbrei *et al.* 2002). The two regions that are not explained by the present model are the areas of Neogene tectonic uplift and the negative gravity residual point to low-density material in the crust or mantle. There is no or only minor evidence from seismic experiments for low-density structures in the middle and lower crust (e.g. Kinck *et al.*1993). Therefore, the presence of light material in the mantle seems more likely. To refine our results subsurface loading, both in the crust and upper mantle, has to be introduced. The information about the depth to the Moho is however ambiguous, due to the quality and resolution of the seismic experiments. (Kinck *et al.* 1993, Korsman *et al.* 1999, Ottemöller & Midzi 2003). A careful review of seismic and seismological investigations shows that new, detailed studies of the deep crust and upper mantle are needed to provide such information (Ebbing & Olesen 2005). If the low-density structure in the upper mantle exists, it is the most likely cause for Cenozoic uplift of the northern and southern Scandinavian mountains. This would imply that models of dynamic topography or related processes in the upper mantle are more valid than recent models suggested by combining AFT analysis and comparison with flexural modelling (Redfield *et al.* 2005).

The general shift between the levels of the presented lithospheric model and the reference model can be explained by a low-velocity/low-density zone in the asthenosphere related to the glacial rebound of Fennoscandia (e.g. Lambeck *et al.* 1998). The results for the base of the lithosphere from Calcagnile (1982) are consistent with a more recent study of the thermal lithospheric thickness by Artemieva & Mooney (2001), but for asthenospheric structures no detailed model is yet available. From theoretical calculations there is also some evidence for an increase in mantle densities from the Norwegian coast towards the central Fennoscandian Shield. However, incorporation of such a density distribution goes beyond the scope of the present study.

12.2.3 Gravity model across the central Scandinavian mountains - Model A

A detailed 2 1/2 D gravity and density model along the central part of the Scandinavian mountains has been presented by Skilbrei *et al.* (2002). We will repeat here the main description of the profile. The modelled profile is located in the central part of the Scandinavian mountain chain and is crossing the Bouguer anomaly low (Fig. 12.4), which is approximately aligned along the axis of the highest elevation of the Scandinavian mountains. Towards the west, the Bouguer gravity is dominated by a pronounced positive coastal gradient, with increasing values towards the shelf. On the residual gravity map (Fig. 12.5), more local gravity lows occur directly correlating to the (Precambrian) basement windows

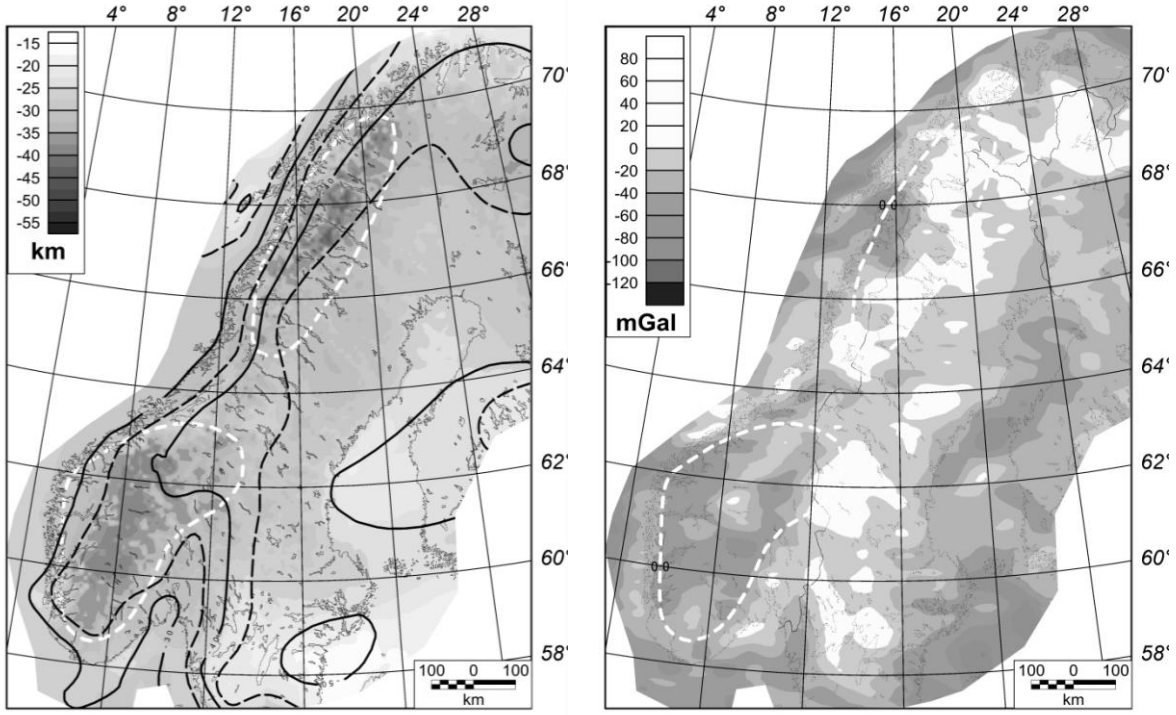

*Figure 11.3. (**left**) Depth to top of the high-density lower crust from the isostatic balanced gravity model. (**right**) Residual gravity anomaly: Note the large negative residuals below the Northern and Southern Scandes.*

within the Caledonides (e.g. Wolff 1979, Dyrelius 1985). The residual gravity highs correlate to the basic rock units within the different thrust-sheets belonging to the Central Norwegian Caledonides. Quantitative gravity interpretations constrained by density measurements of representative rock units have given nappe thicknesses of about 1 km to 4 km in Sweden (Elming 1980, 1988) and of about 8 km to 10 km as a maximum in Central Norway (Wolff 1984, Skilbrei & Sindre 1991). In eastern Trøndelag (Meråker-Storlien) gravity models demonstrate that the nappes form a half-graben indicating post-Caledonian extensional faulting (Skilbrei & Sindre 1991). A discussion of the gravity field and its relation to the mapped geology in different areas within Central Norway, and to the Moho depth, can be found in Wolff (1984), Dyrelius (1985), and Skilbrei & Sindre (1991). These results were used to constrain the upper part of the model across the central Scandinavian mountains.

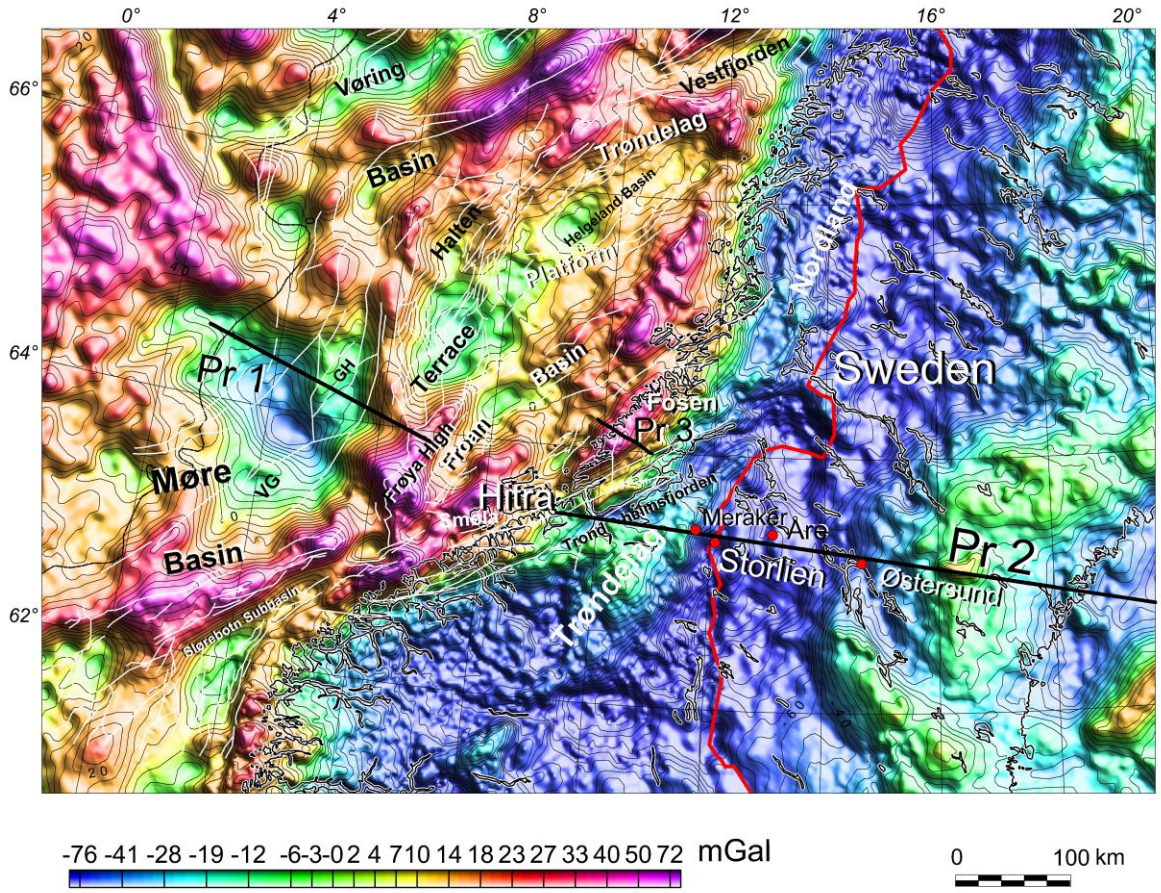

Figure 12.4. Gravity map (Bouguer on land, Free-air at sea). Pr2 shows the location of the modelled profile (Skilbrei et al. 2002).

The model calculations were performed using 2½ D bodies, i.e. bodies of polygonal cross-section with perpendicular end surfaces at variable distance from the profile. The deep interfaces (mantle and lower crust) were extended far away from both ends of the profile in order to avoid edge effects. The location and strike extents of the upper layers were taken from the seismic data and the geological maps (Elming 1988, Juhojuntti et al. 2001, Koistinen et al. 2001, Wolff 1984). The depth to the Moho and the upper crustal layers were adapted from seismic data interpretations (Juhojuntti et al. 2001).

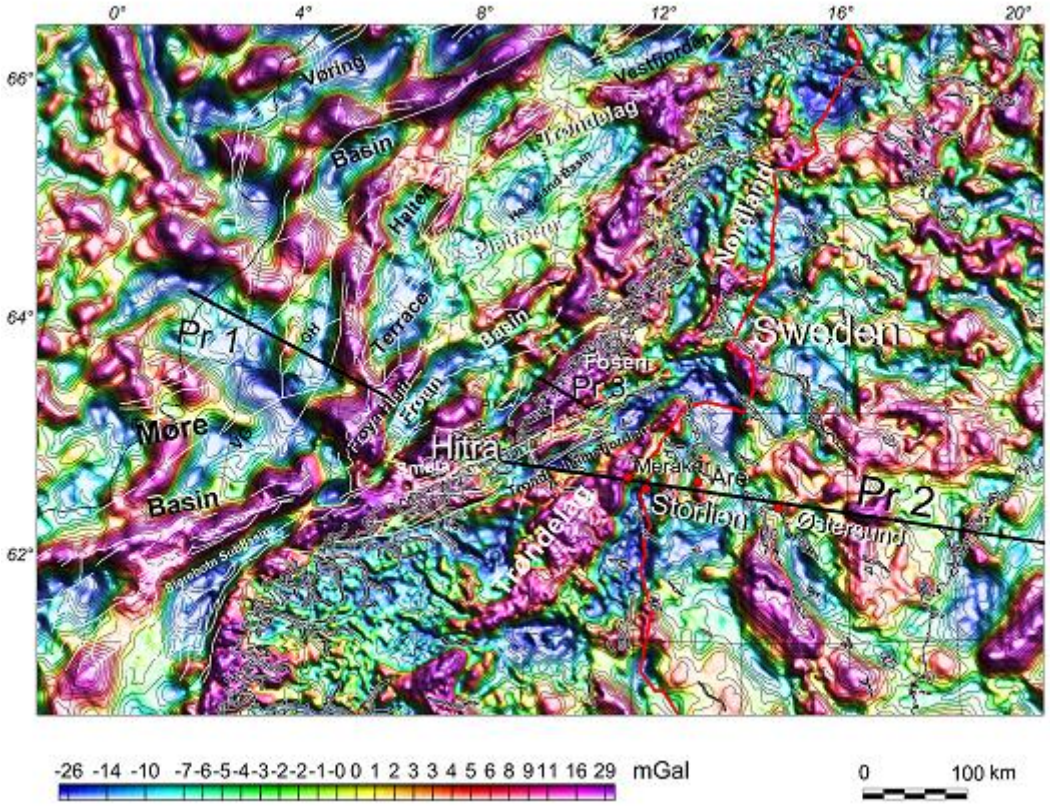

Figure 12.5. Residual, high-pass filtered, gravity map. VG=Vigra High, GH= Grip High. Structural elements in white solid lines. Black solid lines show location of model lines.

Table 12.1. Densities applied to the Central Scandinavia Profile (Figs. 12.6 and 12.7)

Formation	Density (kg/m^3)
Caledonian Nappe Sequence (primarily metasedimentary rocks, weighted mean)	2760
Caledonian Nappe Sequence (primarily metavolcanics, weighted mean)	2840
Seve-Køli	2850
Basement windows (Tømmerås-Grong-Olden)	2650
TIB, granite (Rætan)	2690
Gabbros, dolerite, some granite (Basic rocks in profile)	2850
Jotnian sediments	2610
Rapakivi granite	2640
Lower Crust	2900
Mantle	3250

One of the goals of the modelling was to check whether or not the topography of the Moho surface seen in the depth-converted seismic line of Juhojuntti et al. (2001) could be in

agreement with the gravity data. In order to improve the model and avoid edge effects along the seismic lines, the profile extends to the coast of Norway (near Hitra) in the west and to Vasa near the coast of Finland in the east. To the east of Østersund, and to the west of Trondheim, the model was kept as simple as possible, using Moho depths close to that of the Moho depth map of (Kinck et al. 1993)). In the model by Skilbrei et al. (2002, Fig. 12.6a) the shape of the Moho surface mirrors the depth-converted published seismic line of Juhojuntti et al. (2001). However, the depths are 2-3 km shallower, because we think that the velocity used in the depth conversion (6.2 km/h) lies on the low side for middle-lower continental crust values. Refraction seismic data along the same transect (Vogel & Lund 1971), and farther to the north (Lund 1979) support this conclusion and Vogel & Lund (1971) applied seismic velocities of 6.2, 6.6 and 7.1 (km/s) for the upper-, middle- and lower crust, respectively. The seismic line from Trondheimsfjorden to Storlien (Hurich et al. 1989) did not image the Moho properly. The short wavelength variations of the gravity field correlate with the allochthonous units as explained by Elming (1980), Dyrelius (1985), Wolff (1984) and Skilbrei & Sindre (1991). The main part of the negative gravity and the positive magnetic high is modelled as granitoid units within the Transcandinavian Igneous Belt (TIB). The magnetic modelling indicates that these magnetic batholiths extend to at least 20 km depth, similar to the results of Juhojuntti et al. (2001) and Dyrelius (1985).

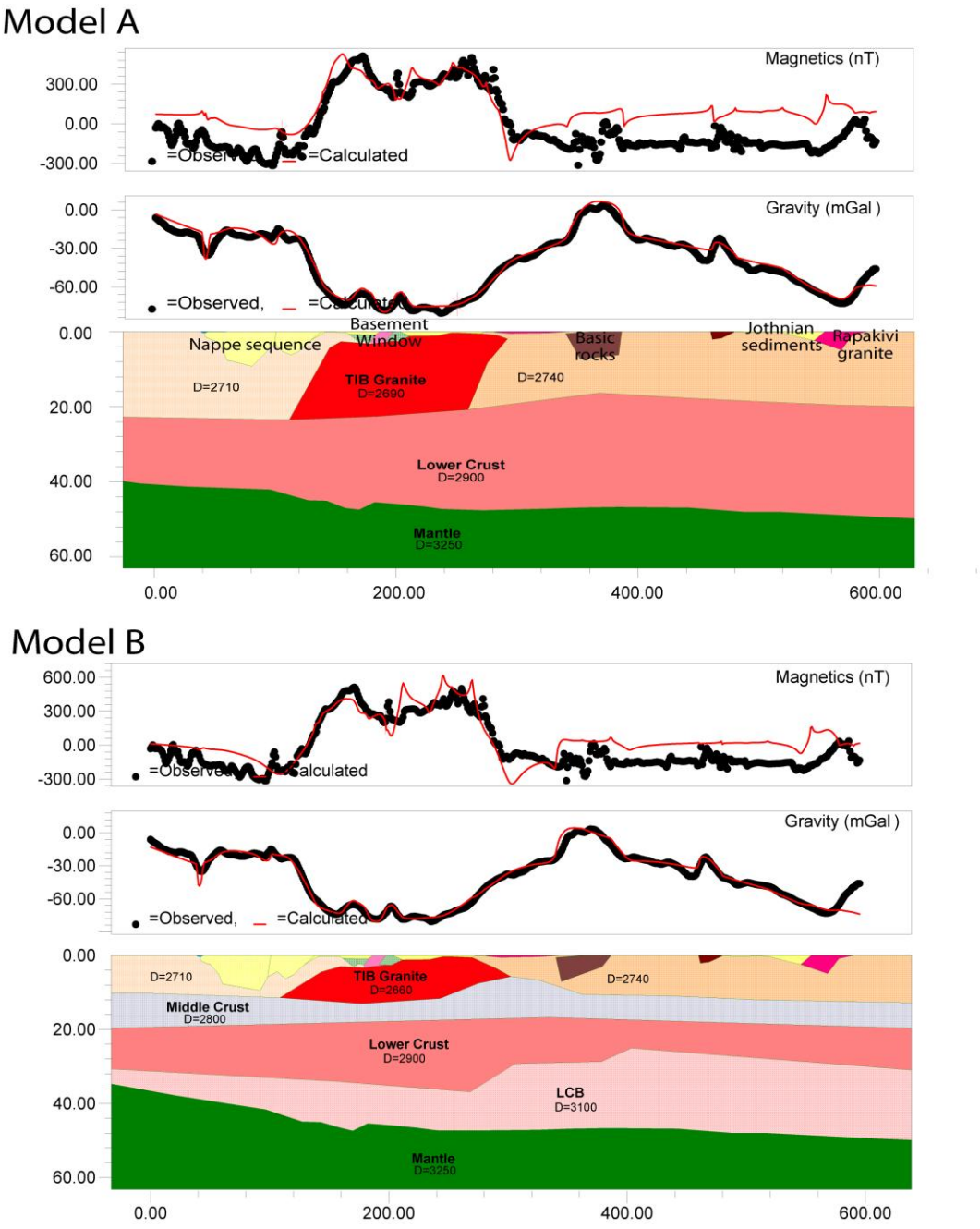

Figure 12.6. Two alternative models of the density and magnetic structure for the central Scandinavian mountains – Model A: Density structure after Skilbrei et al. (2002). Model B: Density structure with consideration of a high density lower crust. In both model calculations, the asthenosphere-mantle boundary is included at a depth of 120 (west) to 160 km (east) (not shown). Applied near-surface densities and magnetic parameters are shown in Table 12.1. Location of the profile (Pr 2) on Fig. 12.5.

The density modelling along the deep reflection seismic lines (Fig. 12.6) demonstrates that the paired, high, positive to negative Bouguer gravity anomalies that run parallel to the coast and the mountains are mainly a complex bulk effect of the following: (1) Moho topography

due to extensional events, (2) the extension which has brought lower crustal rocks (relatively high grade and high density) up to, or closer to, the present surface along the coastal zone, (3) the local lows (Bouguer minima) associated with basement culminations and caused by granitoids/batholiths of the Transscandinavian Igneous Belt and an increased Moho depth. The latter is demonstrated by the regional, negative gravity anomaly. The variation of the Bouguer pattern is then partly related to undulations in the 'Moho-surface' both along and across Scandinavia. This may represent the main components of the local Airy isostatic compensation, as discussed also by Olesen *et al.* (2002) based on isostatic corrections. The effect of the present topography (surface uplift minus erosion) and the local geology, is obvious The Caledonian-, Svecofennian- and Sveconorwegian domains represent regional bulk differences in density and thickness of the crust (Pratt compensation +/- regional compensation). Thus, the density model suggests that isostatic balancing of the topographic masses is of combined Airy- and Pratt types.

12.2.4 An alternative model for the Central Scandinavia Profile - Model B

Here, we present an alternative density model for the Central Scandinavia Profile based on the description given in Section. 12.2.2 and the isostatic considerations in Section 12.2.1. The general lithospheric density structure is given by: upper crust 0-12 km depth: 2670 kg/m^3, middle crust 12-20 km depth: 2800 kg/m^3, lower crust 20-30 km depth: 2900 kg/m^3, lithospheric mantle 30-120 km depth: 3250 kg/m^3 and asthenospheric mantle: 120-220 km depth: 3220 kg/m^3. The geometry of the near-surface structures and the Moho geometry are identical to Skilbrei *et al.* (2002). The TIB, however, is modelled with a thickness of 12 km, similar to the isostatic considerations in Section 12.2.1. To isostatically balance the section we have to introduce a high-density lower crust (3100 kg/m^3). The high-density lower crust (LCB) has a thickness of up to 20 km, but is only up to 12 km thick below the TIB granite. The presence of the LCB is constrained by a wide-angle seismic velocity model that shows high-velocities (~6.8-7.2 km/s) at the base of the crust (Schmidt 2000). But, the distribution of areas with high-velocities is not directly correlating to the isostatic gravity model. The resolution of the seismic velocity model makes a clear correlation difficult, as the velocities in the deep crust have a relatively high uncertainty range and biased by the assumed depth to Moho (Schmidt 2000).

12.2.5 Thermal modelling of the Central Scandinavia Profile

For the thermal modelling we considered the two geometries obtained from potential field modelling (i.e. models A and B). Because our current knowledge on surface heat flow values along the Central Scandinavia Profile is relatively poor, we preferred to keep the models simple. Consequently we kept similar conductivities and radioactive heat generations for each unit as well as basal heat flow (i.e. 25 mW/m^2) in the two models (Fig. 12.8).

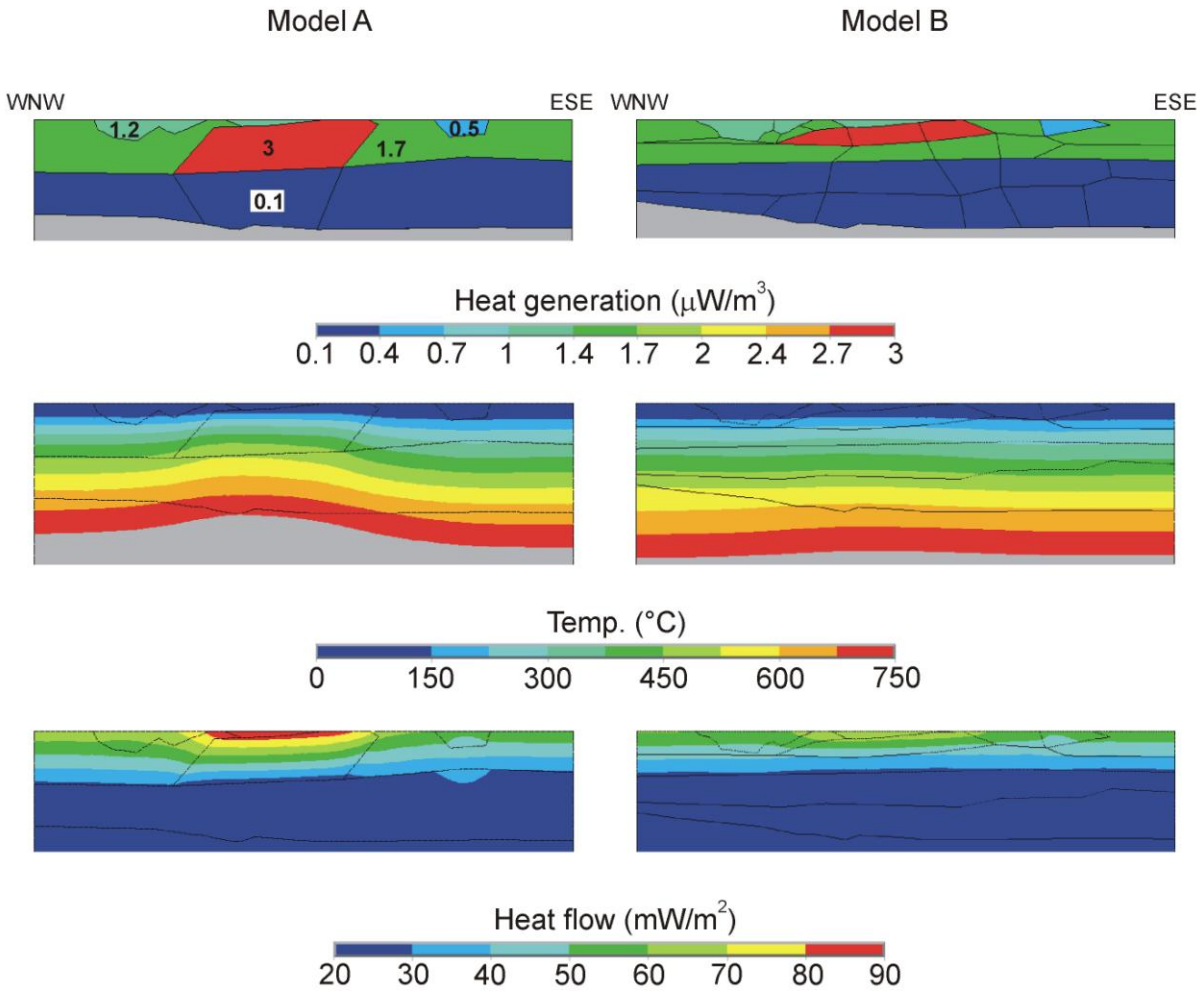

Figure 12.7. Input heat generation values and computed temperature and heat flow values for the Central Scandinavia Profile models A (left) and B (right) (Pascal et al. 2007). Used heat generations for each crustal unit are indicated on Model A. Conductivities are 2.5 and 3.5 W/m/K for the crust and the mantle respectively. Boundary conditions are T=0°C at the top and a basal heat flow of 25 mW/m^2 (VE:x2).

Computed geotherms and heat flow values for both model A and model B are presented in Fig. 12.7. In the case of model A, we note that the modelled thick granite results in a significant increase of the temperature in the lower crust below it. Moho temperatures below the granite are predicted to reach up to ~750°C, exceeding by 100°C Moho temperatures of the surrounding areas (Fig. 12.7) and close to melting temperatures associated to most crustal materials. Modelled surface heat flow values above the granite reach ~90 mW/m^2, which, if confirmed, would be an anomalously high value for a Precambrian shield.

Computed isotherms for model B (Fig. 12.7 right) show a much more moderate rise below the modelled granite that is thinner than in model A. Moho temperatures remain close to

600°C along the profile decreasing by 100°C west of the Caledonian nappes. Interestingly, predicted surface heat flow values are in the range between 50 to 70 mW/m^2, reaching their maximum above the high heat-producing TIB granite. These computed surface heat flow values appear to be in better agreement with commonly measured values in Proterozoic shields (Artemieva & Mooney 2001).

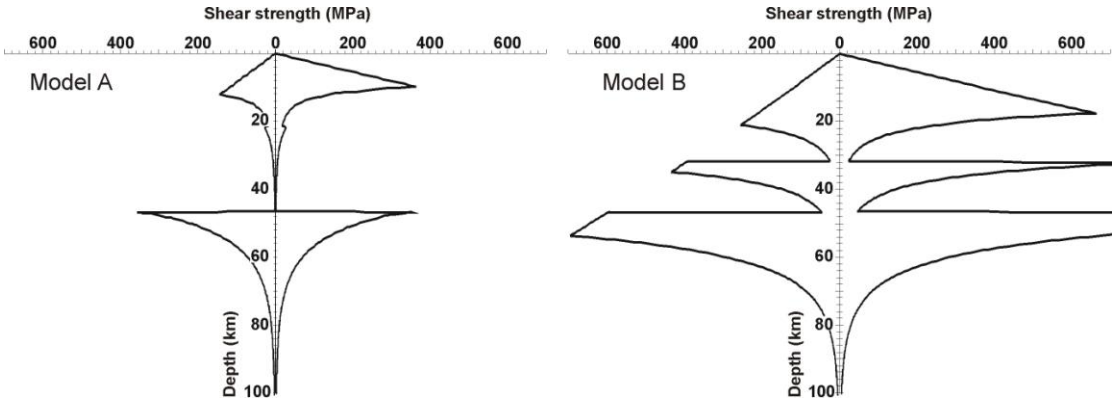

Figure 12.8. Lithosphere strength envelopes calculated on the basis of thermal Models A and B at the location of the TIB body. Applied rheological parameters are given in Table 12.2.

12.2.6 Implications for the thermal and rheological structure of the lithosphere

From our thermal models it is possible to calculate the depth to the thermal base of the lithosphere taken as the 1300 °C isotherm. Model A predicts a base lithosphere plunging from 130 km depth in the west to 136 km in the east, whereas Model B predicts deeper but less variable depths in the order of 140 km. Although the depth difference in between the two models remains well inside the error bars of results from most available methods used to determine the thickness of the lithosphere, base lithosphere depth values as computed for Model B remain in better agreement with values obtained from surface wave studies (140 to 150 km, Calcagnile 1982) and thermal modelling (~150 km, Artemieva 2003). However, much care has to be taken when discussing these previous determinations, because (1) there is no a systematic correlation between seismic and thermal lithosphere and (2) the two studies were conducted at the regional scale providing a crude resolution along the CSP. In particular, short-wavelength variations in the depth to the base of the lithosphere are at the present stage beyond the resolution of the existing data sets.

Table 12.2. Rheological parameters used for lithosphere strength computations. A strain rate of 10-15 was applied to build the strength envelopes. Creep parameters after Carter & Tsenn (1987).

Brittle deformation	Friction	Pore pressure ratio	
	0.6	0.35	
Power-law creep	Strain-rate coef. (Pa^{-n}/s)	Stress exponent	Activation energy (J/mol)
TIB: dry granite	$3.16\ 10^{-26}$	3.3	187000
Lower and middle crust: felsic granulite	$2.01\ 10^{-21}$	3.1	243000
LCB: mafic granulite	$8.83\ 10^{-22}$	4.2	445000
Lithospheric mantle: dry dunite	$7.94\ 10^{-18}$	3.6	535000

The thermal state of the lithosphere exerts a strong control on its integrated strength (e.g. Ranalli 1995). We tentatively determined the strength envelopes for the central parts (i.e. at the location of the TIB granitoid) of Models A and B (Fig. 12.8). The parameters used for the construction of the envelopes are listed in Table 12.2. The strength envelopes give a first-order idea of the relative strength of the lithosphere, noteworthy the strength of the lithosphere can be drastically reduced by, for example, the pre-existence of weak fault zones (e.g. Bos and Spiers 2002) or water-saturated rocks (e.g. Ranalli 1995). At the location of the TIB batholith, Model A results in a very weak lithosphere with a brittle-ductile transition at ~10 km depth in the crust and a large viscous channel above the Moho. For Model B, the brittle-ductile transition is predicted to occur at ~20 km depth and the lower crust viscous channel is much less developed.

The Fennoscandian lithosphere is submitted present-day to relatively high tectonic stresses (Stephansson 1989, Pascal et al. 2005). Therefore, the extremely weak lithosphere predicted by Model A would reasonably be expected to show signs of high strain-rates. In contrast, the region under interest here (i.e. the region underlain by the TIB granitoid) is practically void of earthquakes (Dehls et al. 2000). Moreover, the reconstructed uplift patterns do not show any significant deviation at that location (Dehls et al. 2000). These independent observations argue again against a very thick TIB granitoid below the Central Scandinavian mountains.

12.2.7 Discussion and conclusion

12.2.7.1 About homogeneous heat production through depth

The thermal modelling suggests that an extremely (i.e. ~20 km) thick TIB batholith below the Central Scandinavian mountains is not likely. Our conclusion is mainly based on the impact of the thickness of the batholith on surface heat flow Moho temperatures and lithosphere strength, assuming a homogeneous heat production inside the body. This later hypothesis has been questioned since the 60s and an exponentially decaying with depth of radioactive heat

producing elements is very often adopted (Lachenbruch 1968). It is worth noting that until now none of the two hypotheses has been validated from natural data. Furthermore, recent work on the Sierra Nevada Batholith in California (Brady *et al.* 2006) suggests a much more complex depth-distribution for heat production than previously anticipated, where heat production globally decreases with depth but also significantly increases for some depth intervals. In other words, we strongly suspect that the Sierra Nevada Batholith does not represent a particular case but that similar erratic patterns for the heat production also characterise other plutons including the studied TIB granitoid. In summary, in absence of other firm constraints we preferred to keep the thermal models as simple as possible and concentrate on variations in crustal geometry.

12.2.7.2 Crustal structure and topography of the Central Scandinavian mountains

The two alternative models for the Central Scandinavian mountains show clearly that the interplay between the TIB and the Scandinavian mountains is influencing the gravity and magnetic field as well as the isostatic state of the lithosphere. The TIB shows a prominent signal in the magnetic anomalies and finds also an expression in the Bouguer gravity. However, estimates of the depth extension of the TIB are dependent on the deep crustal configuration.

In any case, our study shows that the TIB coincides with the main topography and Bouguer gravity low in the northern and central Scandinavian mountains. While the magnetic signal can be associated directly with the TIB granitoids, the Bouguer gravity low is caused by a superposition of the TIB and the deep crustal geometry. Therefore, the Bouguer gravity low can be interpreted to be largely related to the low-density granitoids of the TIB. The low-density rocks of the TIB have to be especially considered to explain the gravity field of the Scandinavian mountains. The distribution near the surface causes a strong signal in the gravity field, even with relatively small density contrast to the surrounding rocks. However, the effect on the isostatic balance of the Scandinavian mountains is less pronounced compared to the influence of deep-seated masses.

12.2.8 Conclusion

From the potential field modelling both presented models are possible for the central Scandinavian mountains. However, isostatic considerations and especially the thermal and rheological modelling make Model B more likely. The key to unveil the structure along the CSP is to do more focussed seismic studies. The results of a new receiver function study along the profile will be available in the near future and combined processing with the wide-angle data will hopefully allow more insights in the deep structure along the transects, that in turn will provide a better background to model the shallow structure of the central Scandinavian mountains.

12.3 3D density and magnetic model of The Oslo Rift

The 3D model of the Oslo Rift is presented by excerpts of Ebbing et al. (2007). Here, we present merely the summary and give a short presentation of their Profile 3, which is here used for the thermal modelling.

12.3.1 Summary

We present a new interpretation of the crustal structure of the Oslo Graben and the northern Skagerrak Graben. Integrated interpretation of seismic, gravity and magnetic field data constrained by petrophysical data and surface geology reveals the location of magmatic intrusions below the Oslo Graben. Source depth estimates by Euler deconvolution of the magnetic field measured at a shallow and a high-altitude flight level show mainly two sets of solutions around <4 km and between 12-16 km depth. 3D modelling of the gravity and magnetic fields gives a depth extent of 1.5-4 km for the exposed magmatic rocks. These are only the cap of a mushroom shaped intrusion that has a depth extent of up to 15 km. Within this structure the magnetization and density are increasing with depth. This leads to a small density contrast to the surrounding, and therefore only magnetic field modelling is able to resolve this deep structure. In addition, the 3D density modelling shows that the gravity high above the Oslo Rift is caused by a combination of crustal thinning and the presence of a high density structure in the upper crust, which is related to the Bamble and Kongsberg Gneiss Complexes. The lower crust below the area shows no significant petrophysical contrast to the surrounding areas; hence no large-volume magmatic underplating is interpreted.The 3D model of the Oslo Graben provides a new volume estimate of the magmatic material in the Oslo Graben system. Our estimate of 63.000 km^3 is only 2/3 of the values estimated in previous studies (>95.000 km^3) as we disregard high-volume magmatic underplating. Thus, our estimate overcomes the discrepancy between the observed extension by upper crustal faulting and magma emplacement. Correlation with structural data and the surface geology as with deep lithospheric features show that differences in the volume of extrusive magmatism within the Oslo Rift can be related to the timing and onset of rifting in the Oslo and Skagerrak Graben.

12.3.2 3D modelling of the Oslo Rift

An integrated interpretation of seismic, petrophysical and gravity and magnetic field data provides the possibility to construct a 3D crustal model of the rift and a more thorough insight into the location of the source for the Permian volcanism in the Oslo Graben. However, in contrast to the well-defined potential field and petrophysical data sets, the knowledge about the structure of the Oslo Graben from seismic experiments is rather sparse. Therefore, we integrate all the different data sets (two aeromagnetic fields flown at two different altitudes, the gravimetric field, as well as petrophysical data), into one model that fulfils all observed data sets. In total, the 3D model is constructed by 28 vertical sections in the study area (Fig. 12.9). The spacing between the planes varies from 15 km outside the Oslo Graben, to 3-7.5 km within the Oslo Graben depending on the surface geology. Special

emphasis was given to the resolution of the volcanic and plutonic structures of the Oslo Graben in the construction of the model.

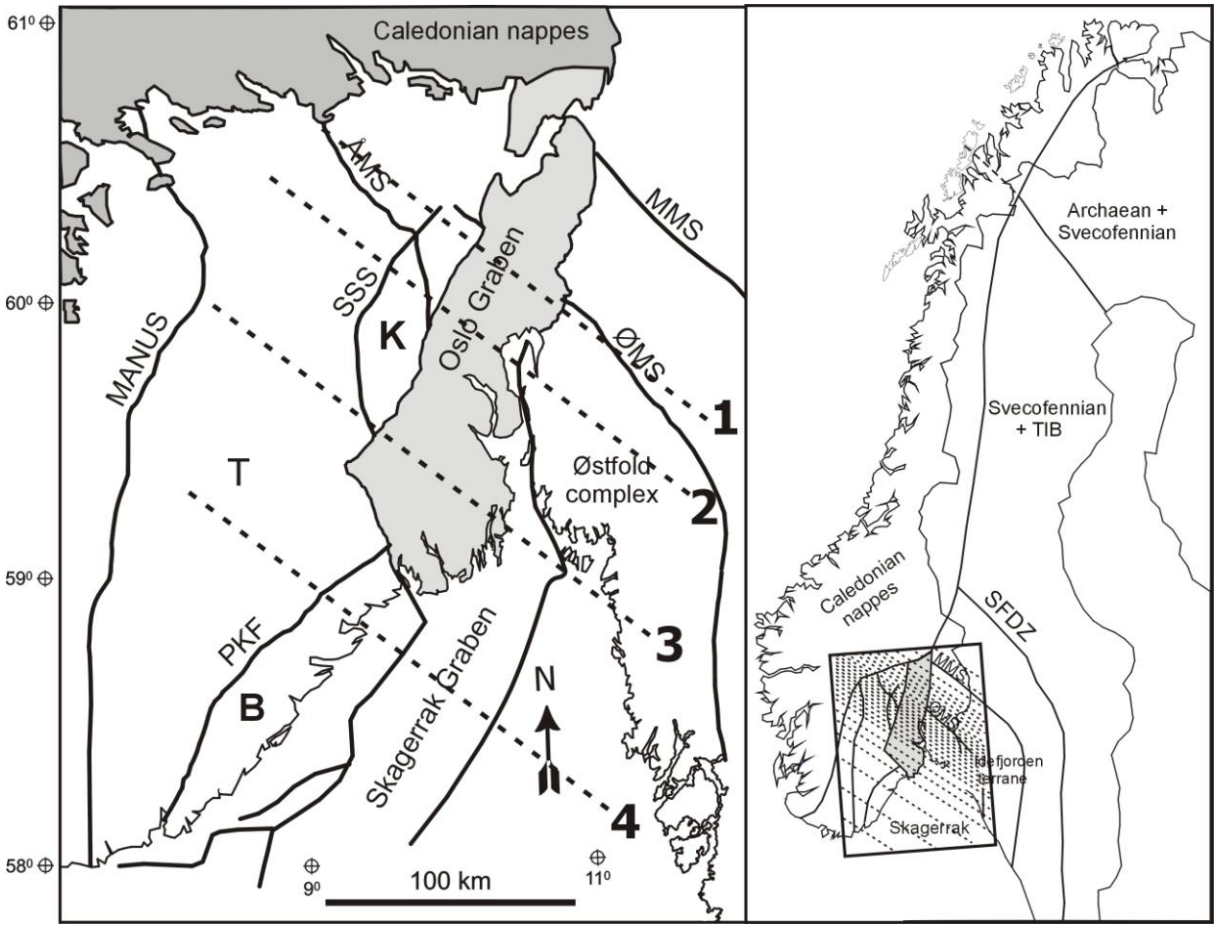

Figure 12.9. Structural map of the Oslo Rift and surrounding areas. The black dotted lines show the location of the profiles through the 3D density model. The map to the left shows the locations of the profiles presented in Ebbing et al. (2007) and in Fig 12.11. The overview figure to the right shows all 28 profiles of the 3D model. T: Telemark sector; K: Kongsberg sector; B: Bamble sector; SFDZ: Sveconorwegian frontal deformation zone, SSS: Saggrenda-Sokna shear zone, MMS: Mjøsa-Magnor mylonite zone, ØMS: Ørje mylonite zone, ÅMS: Åmot-Vardefjell shear zone; PKF: Porsgrunn-Kristiansand shear zone; MANUS: Mandal-Ustaoset Fault, TIB: Transcandinavian Igneous Belt.

The interpretation of potential field data is ambiguous and only good constraints minimize the possibilities for the source geometry. The combination of the gravity field and magnetic field (Fig. 12.10) at different flight altitudes helps to constrain the interpretation. The 3D model is presented by a profile crossing the Oslo Rift in the Vestfold Graben (Fig. 12.11). First, the available information on surface geology, petrophysical measurements and seismics was used in order to constrain a density model of the Oslo Rift. The 3D density model of the Oslo Rift explains the regional shape of the Bouguer anomaly as a combined effect of crustal thinning and the presence of a transcrustal ramp related to a mid-crustal layer

that reaches the surface in the Kongsberg and Bamble Complexes (Ebbing et al. 2005a). This is in agreement with the observed high-densities in the over-thrusted high-grade and high-density Kongsberg and Bamble Complexes and the asymmetric shape of the gravity high (Ebbing et al. 2005a, 2007). Comparison of the Bouguer anomaly and the crustal thickness reveals an inverse correlation between the crustal thickness and the gravity lows outside the rift area: thinner crust in the west, but a higher level of gravity signal in the east. This feature is associated to the density distribution and the internal geometry of the crust. Seismic and density data constrain the changes in upper surface densities from west to east in the Oslo Rift region, hereby reflecting the regional bedrock geology of southeastern Norway (Berthelsen et al. 1996; Dons & Jorde 1978; Koistinen et al. 2001). Based on the seismic velocities (c. 7-7.1 km/s), the lower crust in the model has been assigned a density of 3000 kg/m^3. This value is similar to the values used for the lower crust below the Oslo Graben in the studies of Ramberg (1976), Olsen et al. (1987), Wessel & Husebye (1987). The high-density lower crust is not limited to the Oslo Graben but extends through the whole 3D model. The seismic velocities of the middle crustal layer range between 6.5-6.8 km/s and we have assigned it a density of 2830 kg/m^3, consistent with the interpretations of Tryti & Sellevoll (1977) and Sindre (1993). This layer is here interpreted to be upthrusted to the Bamble and Kongsberg Complexes along the western boundary of the Oslo Graben (transcrustal ramp after Lie & Husebye 1993).

The steep gravity gradient to the west of the Oslo Rift can best be explained by a shallow to intermediate crustal source. Our model connects the Bamble Complex with the Kongsberg Complex below the steep gravity gradient along the western margin of the Oslo Rift (Fig. 12.10). However, the 3D density structure alone does not yet give an indication of the source of the Permian volcanism in the Oslo Graben and to identify these, the simultaneous modelling of the magnetic field at two different levels was performed.

The construction of the 3D magnetic model is based on the structure of the density model. Magnetic field anomalies are generally more strongly affected by near surface rocks due to faster decay with the distance to the source rock, and the disappearance of magnetization with temperatures higher than the Curie temperature. Rocks at higher temperatures will not show the ferromagnetic behaviour necessary to generate the discernible magnetic signal. The dominant material is regarded to be magnetite, which has a Curie temperature of 580 ºC (cf. Hunt *et al.* 1995). With typical Moho temperatures in between 500 to 600ºC within continental crust (McKenzie *et al.* 2005), the importance of the crustal geometry in magnetic modelling is obvious. In addition to the magnetic structure, the magnetic anomalies are also affected by the normal magnetic field. During modelling we applied the values as presented in Table 11.2.

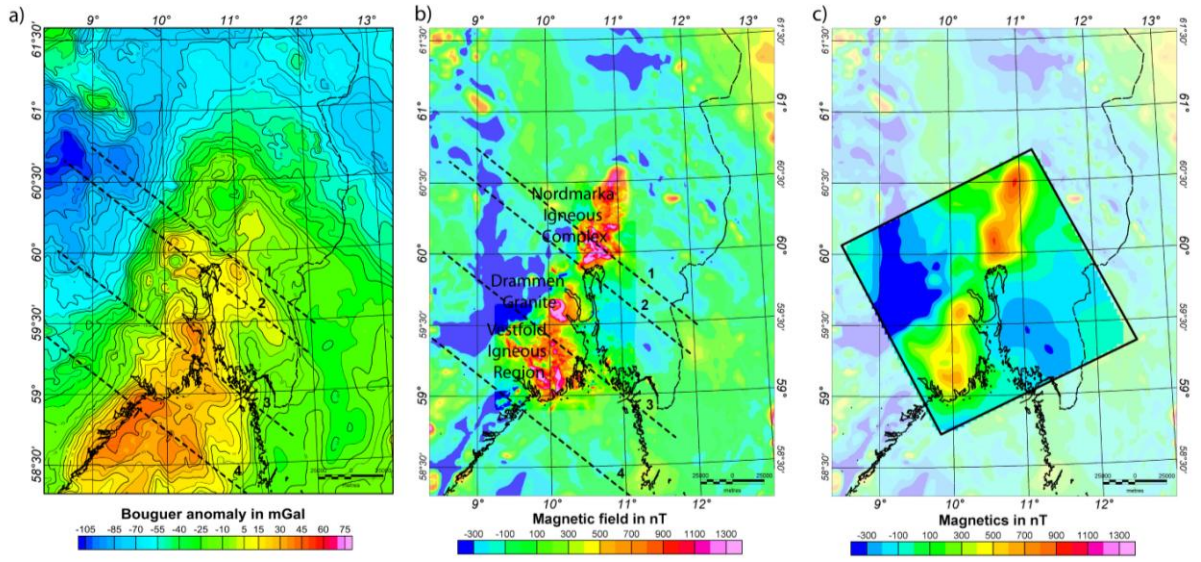

Figure 12.10. Gravity and magnetic fields of the Oslo Rift Region. a) Bouguer anomaly map. The data compilation is based on data sets collected by NGU, SGU, the Norwegian Petroleum Directorate, ExxonMobil, Statoil and the Norwegian Mapping Authority (Skilbrei et al 2000). b) High-resolution aeromagnetic survey (REF) merged with adjacent low-altitude, draped aeromagnetic survey flown in 1973 (Olesen et al. 1997a, Korhonen et al. 2002b). c) The square indicates the data of the high altitude aeromagnetic survey (3000 m flight altitude) as part of the Norwegian Geotraverse project (Aalstad et al. 1977, Heier 1977). Surrounding low-altitude data are shown in transparent colours.

The two major magnetic anomalies in the Oslo Graben are located above the Nordmarka Igneous Complex and the Vestfold Igneous Region. The rocks at the surface are heterogeneous and feature a variety of igneous rocks (e.g. syenite, granite, basalt), which have to be included with their magnetic properties in the model.

The Vestfold Igneous Region in the south Oslo Graben is less well sampled by petrophysical measurements than the northern region, but the available data show a distinction between the susceptibilities measured in the lava flows of Vestfold and the larvikites around Larvik. Most of the susceptibility measurements of the lava flows show values less then 0.001 SI, while the larvikites have susceptibilities from 0.025 SI to 0.075 SI with an average around 0.045 SI. Hence, in the south an indication for high magnetic material at the surface is given, while in the northern part the lava flows have a susceptibility that is only slightly higher than the surrounding rocks. The amplitude of the magnetic anomaly and the average power spectrum analysis give indication of a maximum source depth of more than 17 km (Aalstad *et al.* 1977). But as the surface expression of the mafic rocks and the associated susceptibilities are also larger than in the Nordmarka Region, the most reasonable model represents a broad intrusion with a maximum depth of 14 km (Fig. 12.11). Hereby, the surface rocks are underlain by a broad area of slightly higher susceptibilities (0.055) and Q-rations (1.0) than measured at the surface.

Table 12.2 Petrophysical parameters and volume of Permo-Carbonifereous magmatic rocks in the Oslo Graben as estimated from the 3D model. a) estimated from the density model by Ramberg (1976).

	Mean measured Susceptibility (min/max) [SI]	Model Susceptibility SI	Mean measured densities (min/max) [kg/m^3]	Model densities [kg/m^3]	Volume (km^3) this study	Volume (km^3) Neumann *et al.* 1994
Extrusive rocks						
Basaltic lavas	0.05 (0.0005-0.11)	0.035	2950 (2700-3100)	2900	300	300
RP lavas	0.011 (0.0001-0.058)	0.01	2680 (2480-2770)	2700	1250	~1200
Rhyolitic lavas	0.001 0.001-0.002	0.002-0.02	2645 2620-2670	2550	100	50 [a)]
Intrusive rocks						
Gabbroic rocks	0.058 (0.0009-0.165)	0.001-0.08	3040 (2760-3300)	3000	50	~5 [a)]
Larvikites	0.032 (0.0001-0.109)	0.025-0.04	2700 (2550-3090)	2650	2.000	10.000
Syenites, granites, etc.	0.016 (0.0001-0.136)	0.015-0.035	2610 (2490-2980)	2600	7.600	14.045 [a)]
Exposed magmatic rocks, total					**10.500**	**25.600**
Dense, subsurface bodies						
Vestfold		0.045-0.065		2750	25.000	4.610[a)]
Nordmarka		0.020-0.055		2800	17.500	
Magmatic rocks in the deep crust/upper mantle		<0.0001	2950-3100[a)]	3000	<9.000	65.000
TOTAL					**~63.000**	**> 95.200**

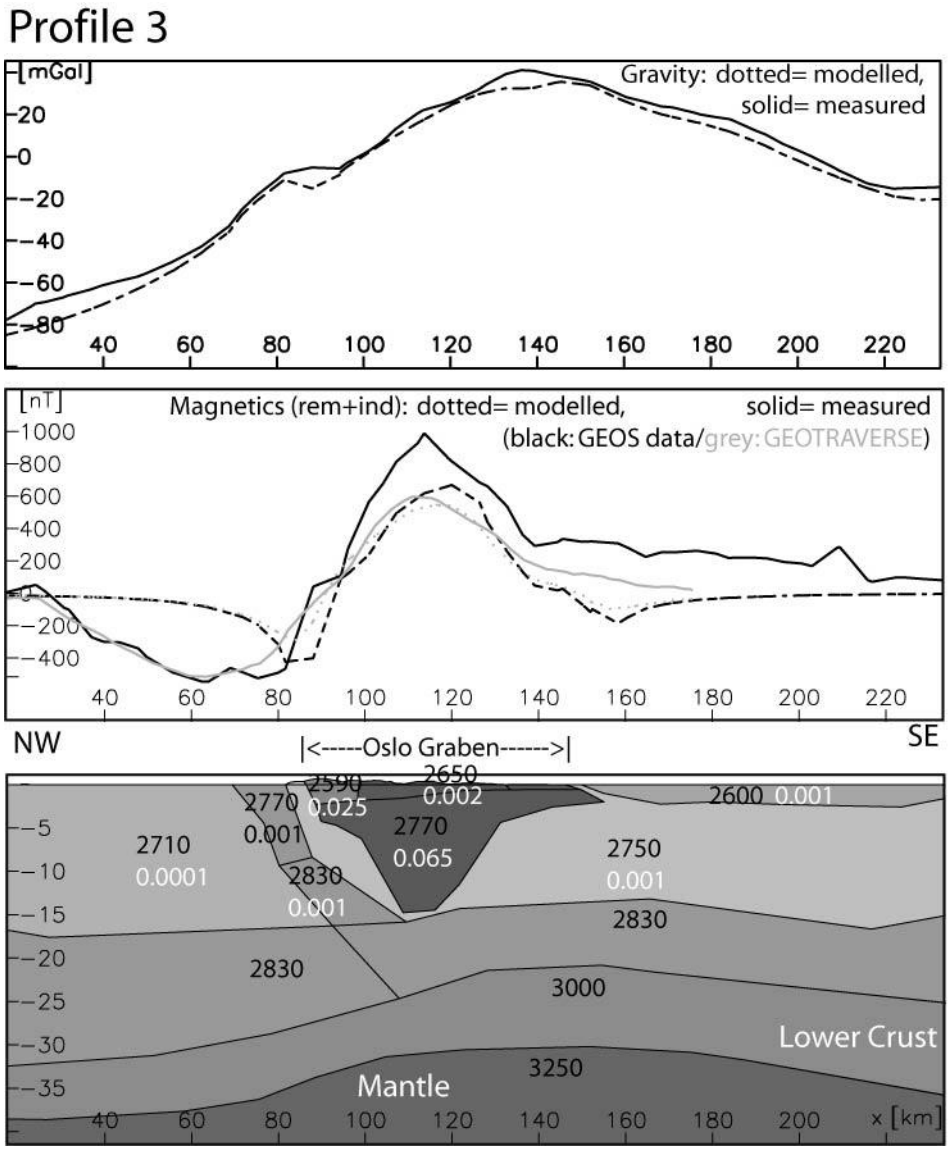

Figure 12.11. Profile 3: Cross-section through the southern Oslo Graben (Vestfold Graben). The upper panel shows observed and modeled Bouguer gravity, in the middle the observed and modeled magnetic anomaly for the GEOS (50 m a. ground) and Geotraverse (3400 m a.s.l.) data are shown. The lower panel shows the crustal density (black numbers in kg/m^3) and magnetic structure (white numbers: susceptibility in SI). The high-magnetic bodies are interpreted to show the magmatic intrusion. For profile location see Fig. 12.9.

12.3.3 Thermal model

Using the geometry given in Profile 3 and heat generation data from NGU's litho database we built and ran a thermal model (Fig. 12.12). Input for each unit is given in Fig. 12.12. In contrast with the Central Scandinavia Profile model (see Section 12.2.4) we fixed the temperature at the base of the model representing the base of the lithosphere (i.e. 1300°C isotherm). In agreement with results from surface-wave studies (Calcagnile 1982), the base of the lithosphere was modelled at ~120 km depth below the Oslo Graben. Two configurations

were modelled: firstly, we assumed that the inferred intrusive material below the Oslo Graben produced as much heat as the country rock (Fig. 12.12, Model 1) and secondly, we assumed that this intrusive body was associated with relatively high heat generation.

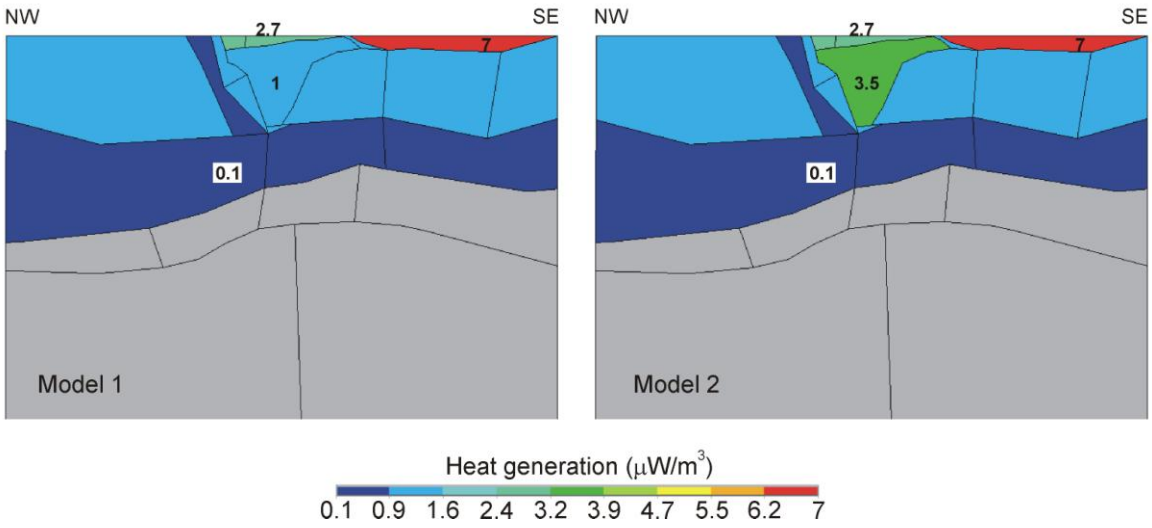

Figure 12.12. Heat generation values used for thermal Model 1 and thermal Model 2 of the Oslo Graben Profile 3. Used heat generations for each crustal unit are indicated. Conductivities are 2.5 and 3.5 W/m/K for the crust and the mantle respectively. Boundary conditions are T=0°C at the top and T=1300°C at 120 km depth (VE:x3).

Computed isotherms and heat flow values are given in Fig. 12.13. Moho temperatures are predicted to remain in between 450°C and 550°C for both models 1 and 2. Below the Oslo Graben, a slight increase in Moho temperatures occurs for Model 2 with respect to Model 1. Isotherms are almost flat and variations in Moho temperatures are controlled here mostly by variations in crustal thickness. In particular, minimum Moho temperatures are predicted where the Moho has been previously "arched" during Permian rifting. Noteworthy, the very high heat-producing Iddefjord granite does not affect significantly the shape of the isotherms at deeper crustal levels below it. This is because the granite appears not to show deep roots in the crust. Modelled Moho heat flow in both models is ~30mW/m^2. This value is slightly higher than those commonly inferred for Proterozoic terrains (i.e. ~25 mW/m^2) but can be the result of the last thermo-tectonic event having affected the region (i.e. Permian rifting). It is interesting to note that for Model 1 surface heat flow values scatter along a relatively narrow range of values (i.e. in between ~50 to 60 mW/m^2) and are consistent with values commonly measured in the Oslo region and in Proterozoic terrains. In the case of Model 2 a relatively high heat flow but still in between reasonable bounds (i.e. ~70mW/m^2) is predicted at the location of the graben. This relatively high heat flow at the surface associated with a pronounced rise of the isotherms at mid-crustal levels below the Oslo Graben. Finally, it is worth noting that the modelled moderate and short-wavelength variations in surface heat flow for both models are the result of the uneven distribution of the different lithological units at relatively shallow

depths.

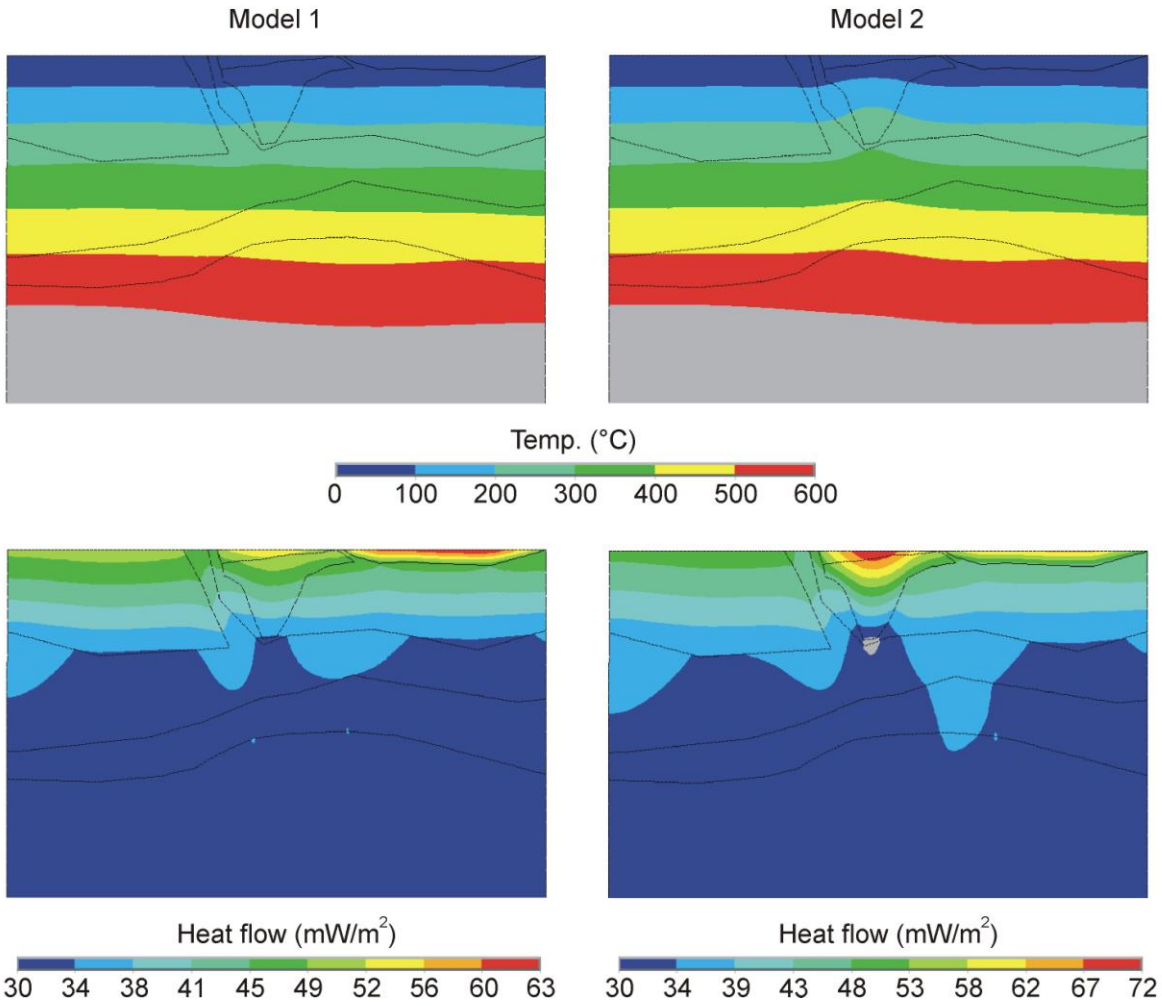

Figure 12.13. Computed temperature and heat flow values for the Oslo Profile 3, models 1 and 2. VE:x3.

12.4 Discussion and conclusion

The presented 2D models for the central Scandinavian mountainsand Oslo Graben show clearly the influence of crustal geometry on the present thermal structure and observed heat flow. For all the areas 3D thermal modelling is beneficial for future studies. However, the feasibility of constrained 3D thermal modelling is not only dependent on the geophysical constraints, but also on surface measurement on heat flow (Slagstad 2005) and radiogenic heat production (Slagstad, Chapter 2 in present report).

For the Central Scandinavia thermal modelling is indicating that the granitoids of the TIB are only present in the upper crust or are less heat-productive with increasing depth. However, the TIB is clearly influencing the isostatic state of the Scandinavian mountains, especially for the northern and central part, and might be related to the Neogene uplift of the Scandinavian mountains. It is important to complete the heat flow database of the Norwegian mainland for correlations with topography and uplift data.

For the Oslo Graben the modelled moderate and short-wavelength variations in surface heat flow are mainly the result of the uneven distribution of the different lithological units at relatively shallow depths. Here, the heat-productive rocks are not buried below thick sedimentary rocks and therefore the near-surface structures control the observed heat flow. The influence of deep crustal intrusives is less important.

13 AN ATTEMPT TO ESTIMATE THE DEPTH TO THE CURIE TEMPERATURE FROM AEROMAGNETIC DATA

Laurent Gernigon & Claudia Haase, NGU

13.1 Introduction

Tempearture estimation in depth can be considered as a major issue in Earth Science and petroleum exploration. However it remains one of the most difficult and challenging tasks. This chapter investigate the possibility to get informations about crustal temperature using magnetic data.

Estimation of source depths from analysis of crustal magnetic anomalies has always been a tricky problem with ambiguous solutions. The deepest boundary of the Earth's magnetic crust may have two alternate interpretations. It may suggest a crustal interface; generally characteristic of areas with normal or low heat flow. The second possibility may be that at such depths rocks loose their ferromagnetic properties, as in young crust and geothermal regimes where heat flow is large. In the second case, the interface could be interpreted as the Curie isotherm depth. However, the interpretation of the computed depth of the interface as Curie isotherm needs careful data analysis and logical inference from other considerations such as heat flow and history of the concerned area. In this study, we rather refer to the depth of the deepest magnetic source (DDMS) to avoid any controversies.

Several techniques have been used in the past to estimate Curie temperature depth from aeromagnetic survey. One commonly used technique is to estimate the average source depth as half the decay rate of logarithmic power spectrum from gridded data (Bhattacharyya 1964, Spector & Grant 1970, Connard et al. 1983, Blakely 1996, Naidu and Mathew 1998, Ross et al. 2006). Surprisingly, nobody in the scientific literature has tested this method offshore Norway. In this chapter, we applied different spectral methods along the mid-Norwegian margin and adjacent areas in order to test the validity of this technique.

13.2 Curie temperature and crustal nature

The Curie temperature is a term in physics and material science named after the French Pierre Curie (1859-1906), and refers to a characteristic property of a ferromagnetic material. The Curie temperature of a ferromagnetic material is the temperature where the material looses its characteristic ferromagnetic ability: the ability to possess a net and spontaneous magnetization in the presence of an external magnetic field.

In a geological setting, major sources of magnetic anomalies are often basaltic, mafic or ultramafic igneous rocks. Minerals like titanomagnetite are usually the most common magnetic minerals in mafic igneous rocks. The Curie temperature for this mineral is about 580° C (Shuey *et al.* 1977, Blakely 1996). Byerly & Stold (1977) suggest also that Curie

temperatures could be less for felsic plutonic rocks and could range form 400°C to 550°C. The level between the 400 and 600°C isotherms could accordingly represent the Curie windows for most of the crustal rocks

13.3 Power spectrum and magnetic sources: general theory

The general topic of the frequency (or wave-number) domain theory for magnetic field data was initiated by Bhattacharyya (1964, 1966) and developed later in detail by Allan Spector in his Doctoral thesis submitted to the University of Toronto titled "Spectral Analysis of Aeromagnetic Data" (Spector & Grant 1970). Much of the formal theories developed afterwards in later publications are taken and/or modified somewhat directly from his text. Spectral methods to estimate the depth extent of magnetic sources have been used in the last 30 years and have showed both encouraging but as also controversial results. Various papers (Connard *et al.* 1983, Shuey *et al.* 1977, Naidu & Mathew 1998, Ross et al. 2006) illustrate geological implication of the spectral methods to define the Curie temperature. They have all used the shape of the magnetic radially averaged power energy spectrum to estimate the depth extent of magnetic sources.

For the purpose of analysing aeromagnetic maps, the ground is assumed to consist of a number of independent anomalies, characterised by a joint frequency distribution in depth width, length and direction cosines of magnetisation. The aim of the spectral methods is to separate the effects of each ensemble in the aeromagnetic map. No attempt will be made here to present rigorously the equations presented. In fact, we have tried to present a simple synopsis of the theory and workflow used during his study. For more details about the physical and mathematical expressions of the power spectrum analysis we rather refer to (Bhattacharyya 1964, Spector & Grant 1970, Blakely 1996, Naidu & Mathew 1998).

The relationship between the power energy spectrum and the depth distribution of magnetic sources was demonstrated for a simple magnetic prism by Battacharrya (1966). Battacharrya (1966) showed that the power energy sprectrum of the magnetic total field produced by a syntetic prism (Φ_{prism}) can be approximated as a function depending on depths of the top (z_{top}) and base of the prism (z_{base}) (Fig. x). At medium to high wavenumbers (=long wavelengths):

$$\boldsymbol{\Phi_{prim}(k) \approx e^{-k.z_{top}} - e^{-k.z_{base}}}$$

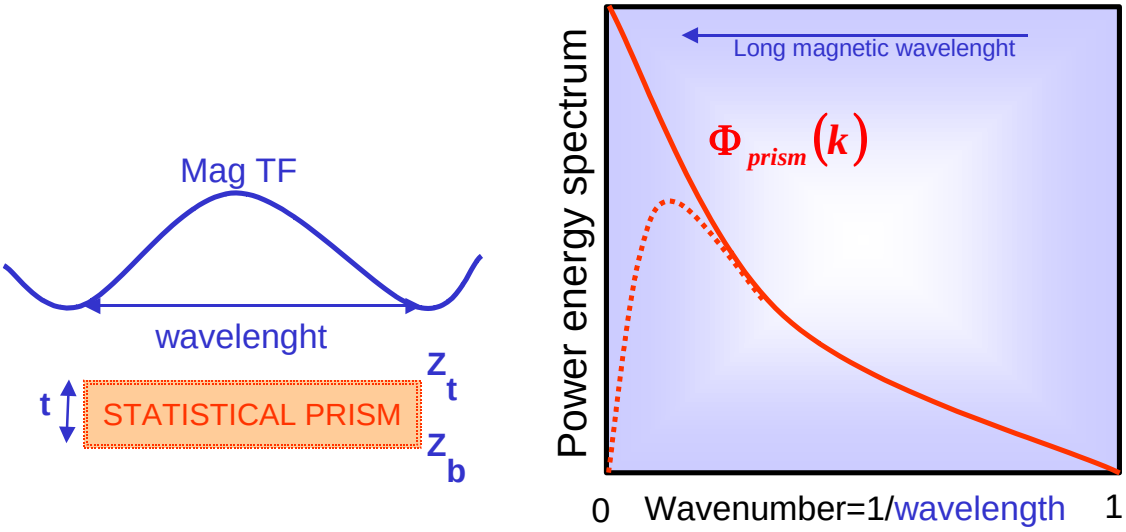

$$\Phi_{prism}(k) \approx e^{-k \cdot z_{top}} - e^{-k \cdot z_{base}}$$

At medium to high wavenumber !

Figure 13.1. Magnetic totat field produced by a simple prim (left) and power energy spectrum of this magnetic Total field as function of the wavenumbers (k).

Sensitivity studies shows that the shaped of the power energy spectrum can provide rough informations about the depths and/or the thickness of the magnetic source in depths. As suggested by Fig. 13.2a, the spectrum of a deep prism does not exceed the amplitude of the same prism at less depth and only the peak of the spectrum is shifted to low wavenumbers. If the top of the prism is fixed (Fig. 13.2b), the peak of the spectrum is usually shifted when the thickeness of the prim is increasing

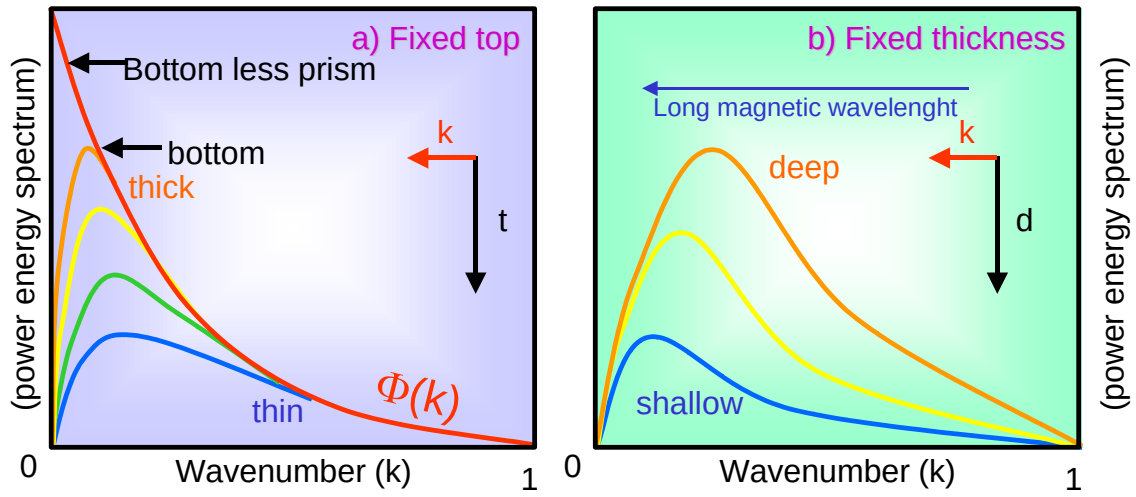

Figure 13.2. Examples of power energy spectrum for a simple magnetic prism. Parameter d and t represent the depth and thiknesss of the prism.

The previous spectrums are applicable to magnetic field produced by only one simple prism. Howver, in complex geological domains, the magnetic anomalies usually represent a large collection of magnetic sources with different shapes, depth and thickness. In their approach, Spector & Grant (1970) suggest that a set of different an independent scattered magnetic source can be approximate by a simple statistical prism. The base of this prism should coincide with the base of the shallowest magnetic bodies averaged by this statistic prism.

Using a magnetic grid, we can also explain the power density spectrum of the magnetic total field as a function of its 2D Fourier transform $F(k_x, k_y)$ and its magnetisation $\Phi(k_x, k_y)$:

$$\Phi(k_x, k_y) = \Phi_{Mag}(k_x, k_y) \times F(k_x, k_y)$$

Fourier theory states that any signal, in our case the magnetic signature, can be expressed as a sum of a series of sinusoids. In the case of the magnetic, these are sinusoidal variations in total field across the sampled grid. This sinusoidal magnetic pattern can be captured in a single Fourier term that encodes: 1) the spatial frequency, 2) the magnitude (positive or negative), and 3) the phase. These three values capture all of the information of the magnetic grid. The spatial frequency is the frequency across space (latitude, longitude in our case) with which the amplitude modulates.

The fourrier transform can also be expressed (Blakely, 1995) as:

$$\Phi(k_x, k_y) = \Phi_{Mag}(k_x, k_y) \times S^2_{(a,b)} \times (4\pi^2 . C_m{}^2 . M_d{}^2 . G_d{}^2) \times (e^{-2k.z_{top}} (1 - e^{-k(z_{base} - z_{top})})^2$$

where

$S^2_{(a,b)}$ is the shape factor which is function of the lateral shape of the statistical prism
M_d is the factor for magnetisation direction
G_d is the geomagnetic field direction

If we consider the average Power density spectrum, this function can be simplified and approximated as:

$$\Phi_{average}(k) = Cste.e^{-2.kz_{top}} \times (e^{-2k.z_{top}} (1 - e^{-k(z_{base} - z_{top})})^2$$

This expression is somhow relatively similar to the simple prim expression proposed by Battacharrya (1966). However, this approximation requires some assumption (Blakely, 1995). First, we consider that the prism extends to infiny and if we considered that the magnetisation is random, it does not have any fourrier transform and consequently

$\Phi_{Mag}(k_x, k_y)$ is assume to be constant. If we consider the average Power density spectrum then the radial average of M_d and G_d are also constant.

As it turns out, we can learn something about the contribution of the long and shorth wavelengths in the spectrum itself. At medium to high wavenumbers, the logarithm of $\Phi_{average}(k)$ on both sides suggests a linear relation between $Ln\Phi_{average}(k)$ and $-2\,.kz_{top}$ since:

$$Ln\Phi_{average}(k) \cong B - 2k.ztop + 2\ln(1 - e^{-k(z_{base} - z_{top})})$$

or if the second term is ignored

$$Ln\Phi_{average}(k) \approx B - 2k.ztop$$

Therefore, the slope of $Ln\Phi_{average}(k)$ can easily be used to estimate the depth to the top of a statistical prim (Figs. 13.3, 13.4).

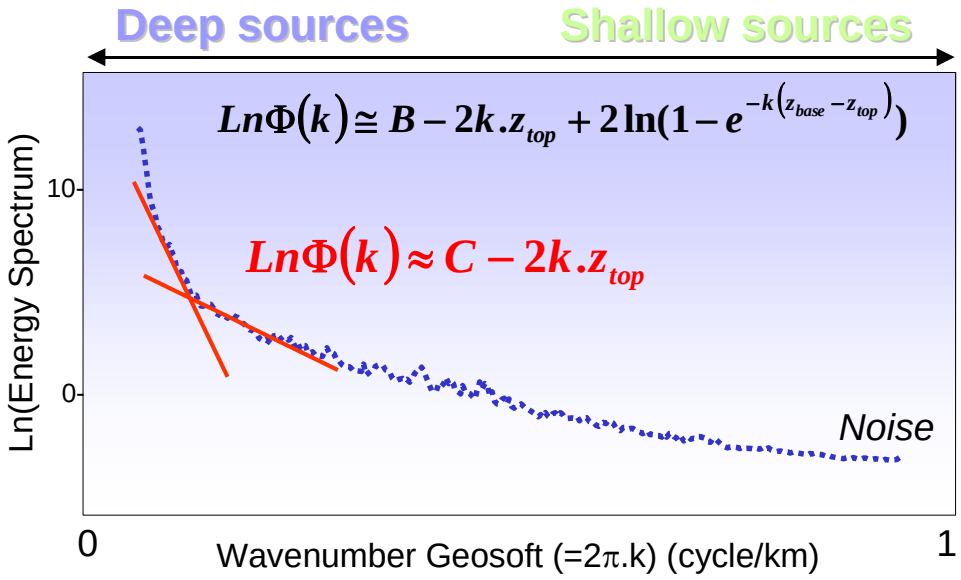

Figure 13.3. Example of power Energy spectrum. At medium to high wavenumbers, a linear relation between $Ln\Phi_{average}(k)$ *and* $-2\,.kz_{top}$ *can be suggested.*

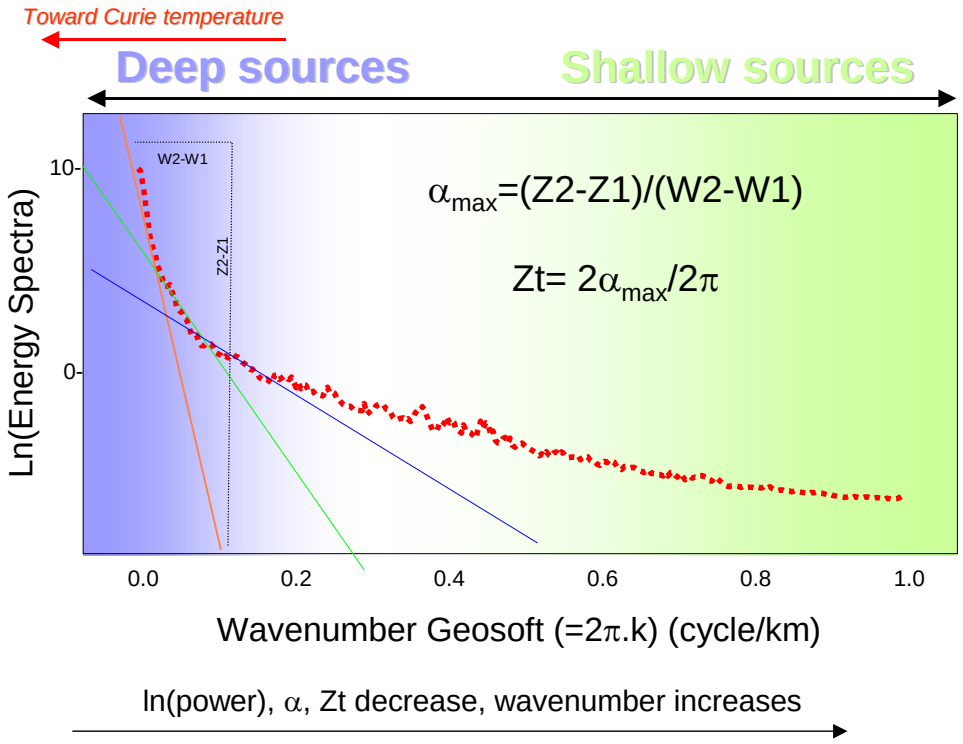

Figure 13.4. Example of power Energy spectrum. The depth of the top prism is obtained by fitting a straight line through the low wave number portion of the data. The slope provided the depth of the prism highlighted by the linear segment of the power spectrum

This fundemental approach proposed by Spector and Grants (1970) provides infomation about the depth of a magnetic source sources. In their theory, the anomaly is assumed to be produced by a large number of blocks but the parameters describing any one block are assumed to obey probabilities common to an entire set of differents sources. The slope of each linear segments provides information about the deep of a magnetic discontinuity and magnetic interfaces. The DDMS is espected to be close to the Curie temperature, if we consider that the top and the base of the statistical prims are close enough for the long wavelenghts.

13.4 Database

The spectral methods have been applied to the more recent grid compilation undertaken by NGU (Olesen et al. 2006b). The more recent surveys SAS-96, VGVB-94, MBAM-97, VAS-97, VBE-AM-00, RAS-03 and JAS-95 are also included in the new data compilation. Specifications for these surveys are shown in Table 9.1. The grid onshore Norway has previously been digitised into a 500x500 m matrix from manually drawn contour maps and the Definite Geomagnetic Reference Field (DGRF) has been subtracted. The mainland area

was flown at different flight altitudes and line spacing dependent on the topography. The 5 x 5 km grids were regridded to 500 x 500 m cells before the final merge with the regional compilation, using the minimum curvature GRIDKNIT software from Geosoft (2005).

13.5 Calculation of the power spectrum and estimation of the deepest depth of the magnetic source (DDMS)

The first thing that one should do to evaluate the DDMSs is to calculate the power spectrum of a sampled magnetic grid. The following filtering sequences have been led using the Oasis Montaj Magmap filtering toolbox (Geosoft 2005).

The processing sequence includes:

Step 1: The sampling of sub-magnetic grid extracted from the main magnetic compilation. Most of the time, we considered square windows as complex shapes introduced filtering artefacts during the processing.

Step 2: The preparation of the initial grid. Before transforming the grid to the wave-number domain by forward fast Fourier transform (FFT), the grid must be prepared in order to be perfectly square, without dummies and to have the right dimensions acceptable for the FFT (Fig. 13.5). During this preparation, the first order trends from the grid are removed in order to avoid the introduction of large step function and ringing problem during the Fourier domain transformation.

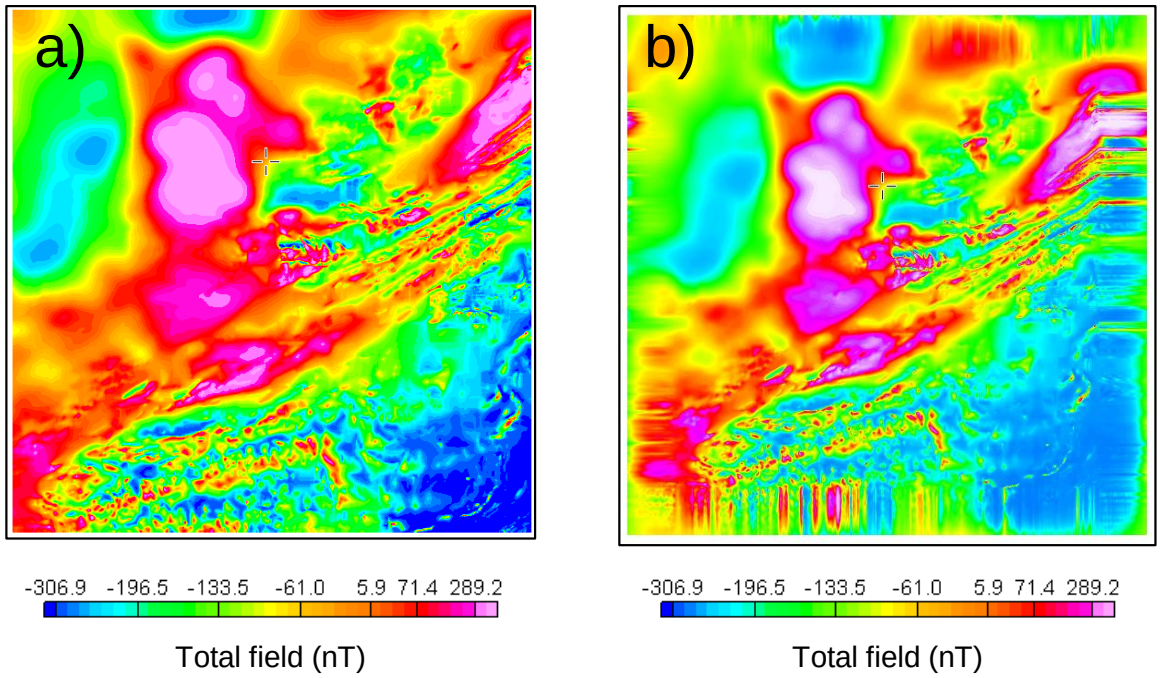

Figure 13.5. a) An example of an initial sampled grid around Trondheim, Norway and b) the same dataset after grid preparation

Step 3: The wave-number domain processing to get the frequency domain representation of the magnetic signal.
The initial grid in space domain is transformed to a wavenumber domain by the use of a fast Fourier transform (FFT) algorithm. A Fourier transform encodes not just a single sinusoid, but a whole series of sinusoids through a range of spatial frequencies from zero (i.e. no modulation, i.e. the average amplitude of the whole grid) all the way up to the "Nyquist frequency", i.e. the highest spatial frequency that can be encoded in the magnetic grid, which is related to the resolution, or size of the pixels [(2xcell size)$^{-1}$].

The significant point is that the Fourier image encodes exactly the same information as the initial grid, except expressed in terms of amplitude as a function of spatial frequency, rather than magnetic amplitude as a function of spatial displacement. An inverse Fourier transform of the Fourier image produces an exact replica of the original grid.

Step 4: The calculation of the radially averaged power energy spectrum using a 2D function of the energy relative to wavenumber and direction. The radially averaged energy spectrum is then computed by averaging the power energy (=the square of the Fourier amplitude spectrum) at all direction for the same wavenumber. As it turns out, we can learn something about the contribution of the long and short wavelengths in the spectrum by studying the spectrum itself as previously described in section 12.3

Once the processing is completed, thee power spectrum is usually presented in one of two forms, a radially averaged plot in log-linear space for presentation in graph form or as a grid displayed either as a contour plot or an image. Fig. 13.6a displays the power spectrum as an image and Fig. 13.6b displays the power spectrum as a graph.

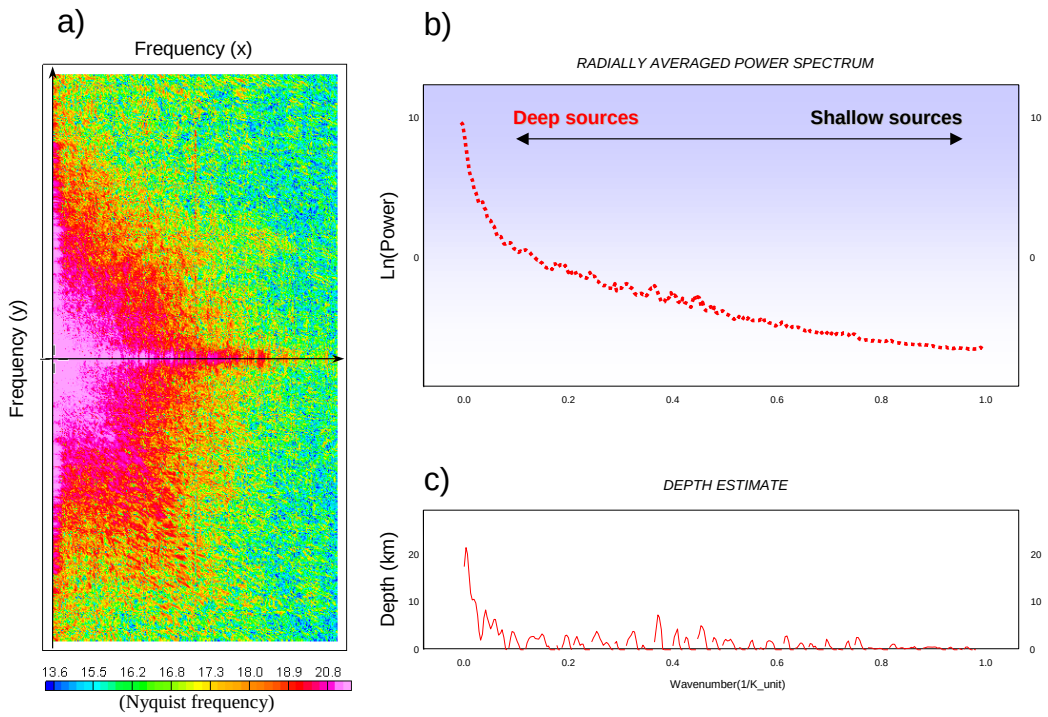

Figure 13.6. (a)Two-dimensional display of the radially power spectrum for the sampled data. (b) Power spectrum with characteristic slopes. Steeper slopes increasing to the left of the plot, coincides with the deep-seated contribution. (c) The depth estimate plot is an automatic 4-5 points slope and depth calculation, derived from the spectrum file.

When considering a grid that is large enough to provide many magnetic sources, the spectrum of this data can be easily interpreted to determine the statistical depth to the tops of the sources using the relationship:

$$\text{Log } E(r)=4\pi hr$$

If we examine the shape of a spectrum caused by bottomless bodies (pole sources) at some depth we will see in Fig. 13.7 that the shape is a straight line with a negative slope defining the depth to the top of the bodies. In the real world the bodies are, of course, not all at the same depth so the line defining the spectrum of the deep bodies will represent the average for a considered window.

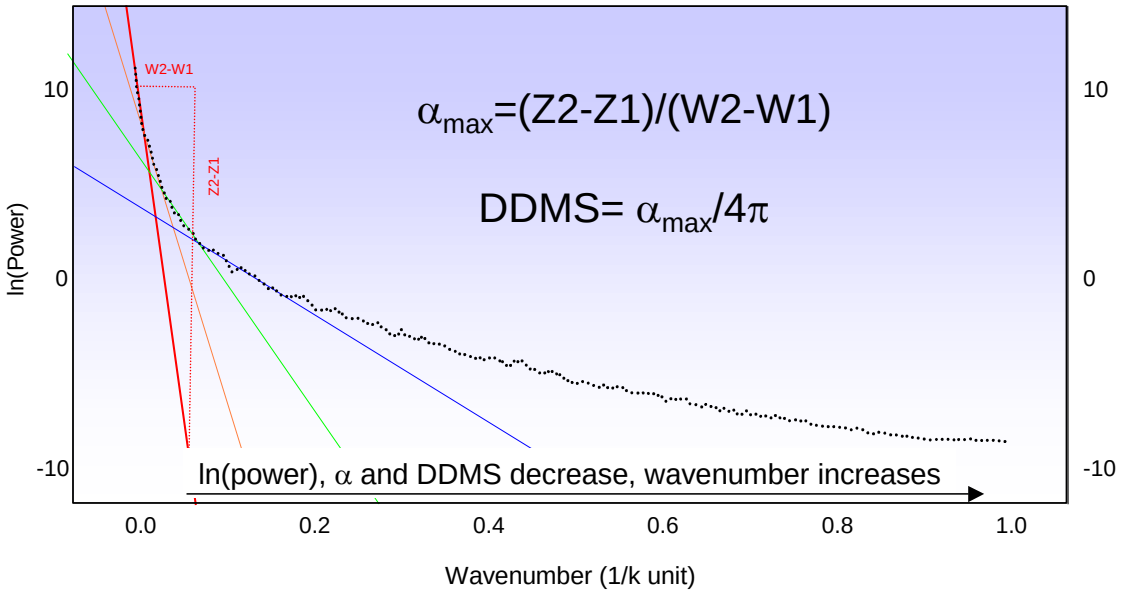

Figure 13.7. Power spectrum analysis of an aeromagnetic map. The steepest slope observed along the spectrum curve, at low wavenumber can be related to the depth of the deepest magnetic source (DDMS).

The statistical average depth for an ensemble of sources can be easily determinated using the value of the slope α along the steepest straight segment observed along the radial spectrum divided by 4π (Fig. 13.7). The steepest slope imaged at low wavenumbers is expected to represent the location of the DDMS (Spector & Grant 1970). From previous papers, the DDMS could represent the depth of the Curie temperature.

Oasis Montaj can calculate automatic slopes using a gradient routine along few adjacent points (Fig. 13.6c). Unfortunately, some artefacts at low wavenumbers persist in and sometimes wrongly affect the 4 to 5 points automatic estimation. It should be noted that it is easier and more reasonable to measure the slopes on a printout, as the spectrum is more stretched out. The graphical technique is time-consuming but it makes it easier to identify and valid straight-line segments. Due to graphical uncertainties we estimate an uncertainties of ± 2km, in average for each depth calculation. All the values presented in this chapter have been manually deduced.

Once a DDMS has been calculated over one window, the same processes are made for new windows. After completion of the depth picking for all windows covering the data grid, we edit the individual data points to make the depth estimation over the grid more consistent internally and with external constraints. It is also recommended to check the regional consistency of the DDMSs and to check with other adjacent windows if one result appears suspicious. Then, it could be useful to recalculate the spectrum and reevaluate the depth if large discrepancies exist.

13.6 Windows size, peaks in the spectra and resolution of the data

Using the signal processing approach, the size of the sampled windows is relatively important. As a matter of fact, minimum dimension are required in order to solve the depth extends of the average magnetic depths. As a consequence, small windows cannot sometime solve deeper magnetic sources. Connard *et al.* (1983) used the shape of the radially averaged spectra to estimate the maximum depth extend to the bottom of the magnetic layer. In particular, the position of the kmax, characterized by a peak in the spectrum, is expected to better constrain the steeper slope along the graph (Fig. 13.8).

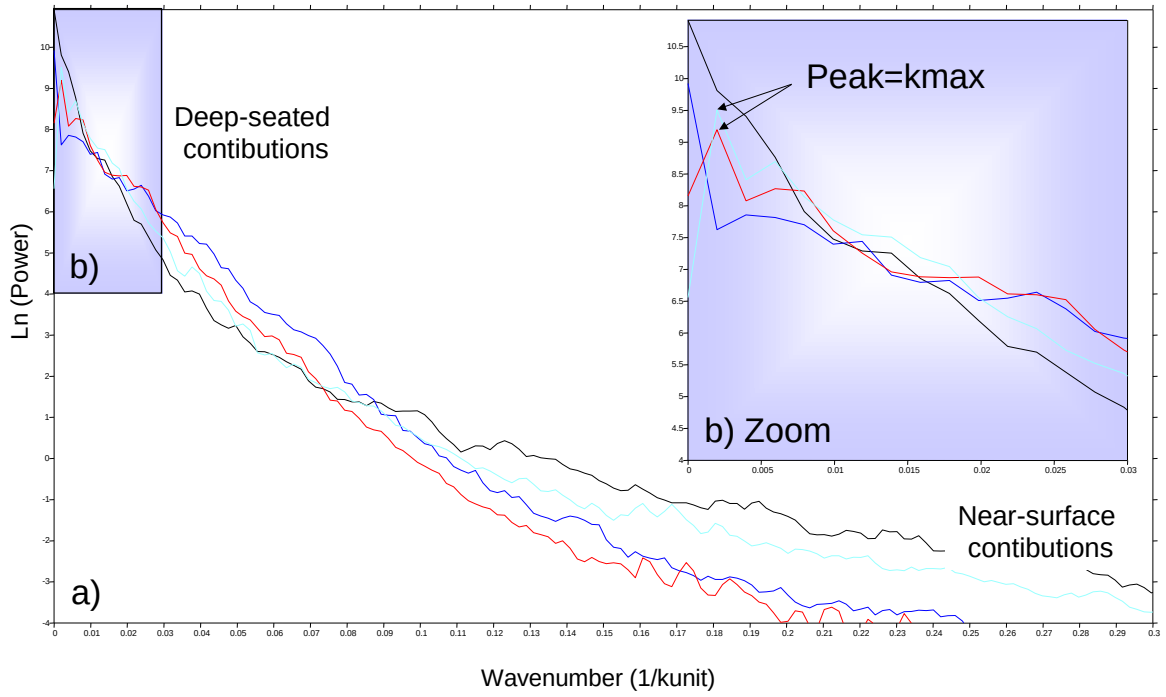

Figure 13.8. a) Power spectrum analysis for different sampled aeromagnetic grids. The graph on Fig. 13.4b illustrates the peaks and the location of the kmax locally observed for small wavenumbers.

At low wavenumbers, a peak or a deep null can mean that only the top of a thick magnetic layer is observed (Naidu & Mathew 1998) and the related spectrum can not characterise the bottom of this layer due to inappropriate window size. In such case, we selected a larger window to get a refined spectral representation for the deeper interface.

This part of the spectrum is, however, susceptible to noise from various sources, particularity from poorly known fields that may be unrelated to the real bottom sources of concern (Blakely 1996). The peak is not detected easily in most of the cases, but we can assume that the steepest slope of the spectrum represents a depth close to this value or a mean depth for the deepest sources (Spector & Grant 1970).

A significant problem linked with the window sizes is the precise location of the DDMSs inside the selected windows themselves. Small windows define relatively small semi-regional areas and the DDMSs results can easily represent an average for specific structural segments along the margin. However, if we are looking for deep sources, the sampled windows and the statistical analysis cover larger areas. Consequently, the location of the estimated DDMS is imprecise compared to smaller windows. The smaller the window is, the better the x,y geographic location of the DDMS point would be (Fig. 13.9). Consequently, if a large window covers several distinct crustal segments, the geodynamic meaning of such a single point could be unreliable and ambiguous.

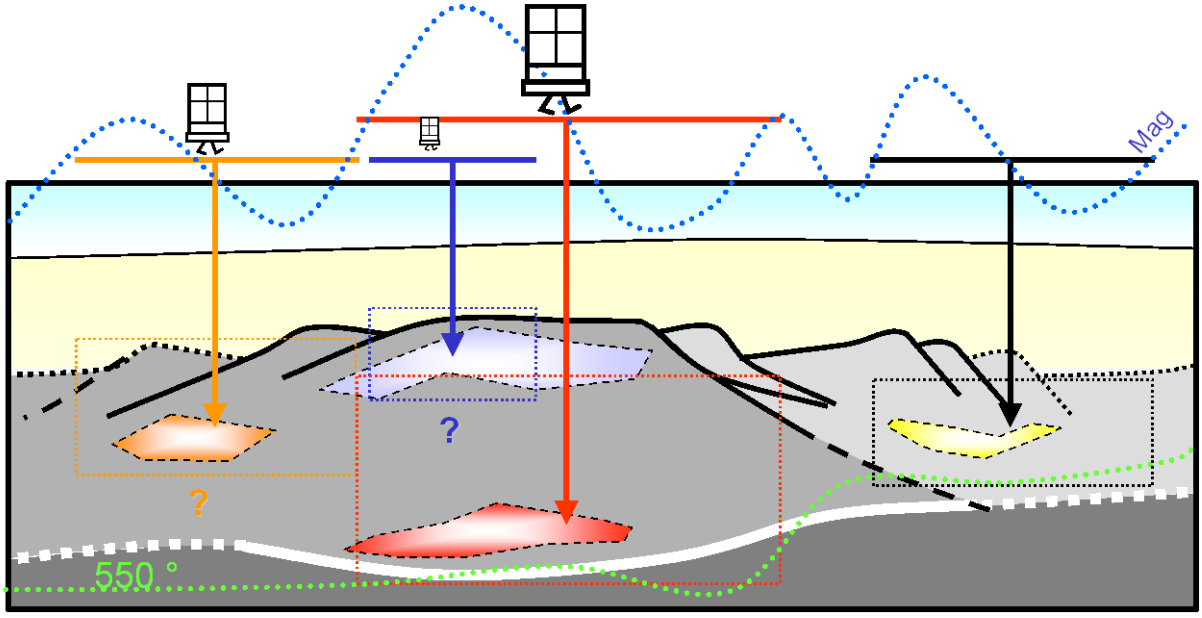

Figure 13.9. Effects of the window size in estimating deep sources. Some windows do not allow to image deep magnetic sources if their sizes are not large enough. However the bigger the window is, the less accurate the geographic location of the DDMS will be.

Another problem deals with the quality of the dataset used for the spectral analasys. As a matter of fact, the shape of the power spectrum and consrquently the estimation of the magnetic source is mostly function of both resolution and quality of the magnetic grid. To illustrate this importance, the Fig. 13.10 displays two power spectrums which compare the power spectrums of an old and a recent magnetic surevy computed along the same windows. You can see that the shape can change significntyly and can seriously influence the depth estimation of the magnetic sources.

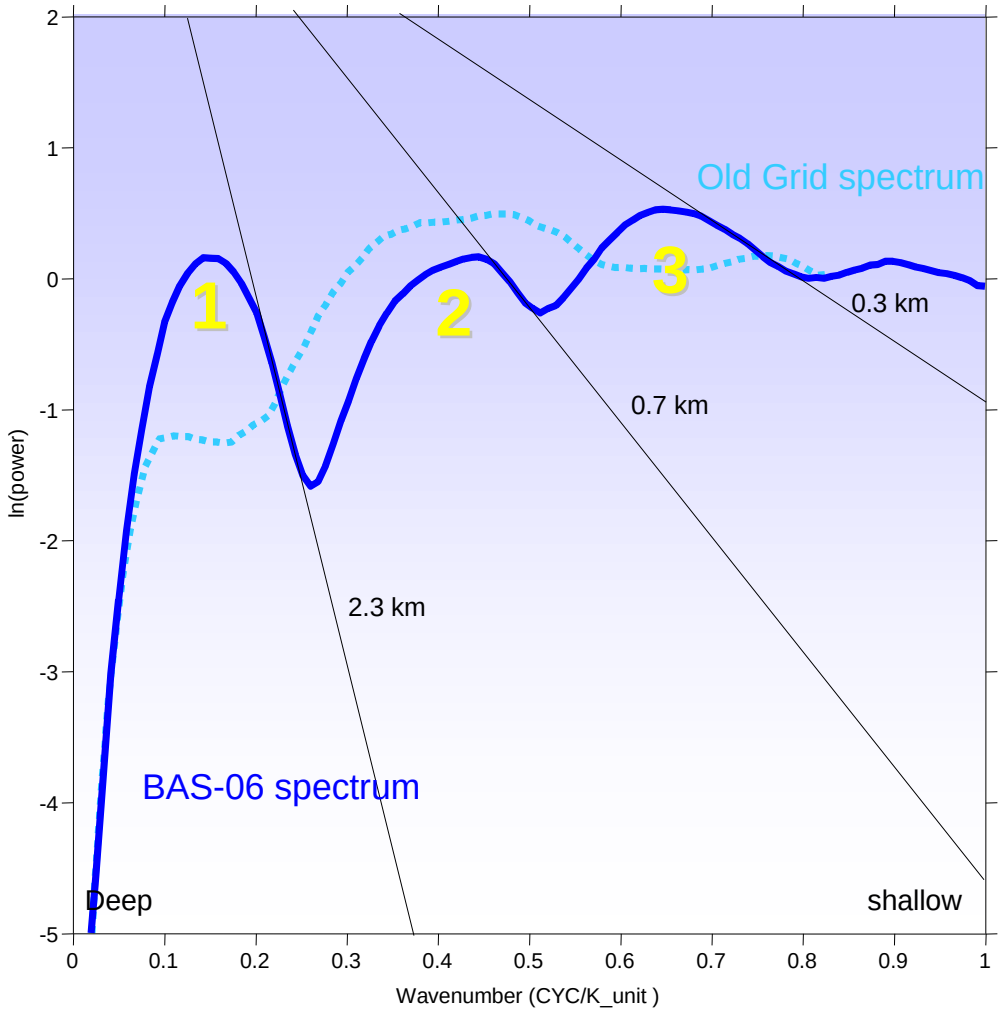

Figure 13.10 Comparison between two spectrum calculated along the same windows along the recent BAS-06 survey in the Barents Sea (Gernigon et al. 2007). The curves illustrate the spectral response of the magnetic total field along the same area but of two different grids (the old compilation and the recent BAS-06 aeromagnetic surevy). With moderen aermagnetic data, the shape and estimation of the source can change significantly. There is higher energy power in the BAS-06 at medium to low wavelengths (~high wavenumbers). At low wavenumbers, the peak or the deep null can mean that only the top of a thick magnetic layer is observed (Naidu and Mathew 1998) and the related spectrum cannot characterise the bottom of this layer due to small window size.

13.7 Application along different segments of the Norwegian shelf

We tested and applied the method in several sampled windows across the main features of the Mid-Norwegian margin and adjacent oceanic domain (Figs. 13.11, 13.12, 13.13, 13.14, 13.15, 13.16). Some windows have been selected along the main segments and structural features of the Mid-Norwegian margin and adjacent oceanic basins (Figs. 13.11, 13.15, 13.16). During the sampling, both large and small windows have been tested.

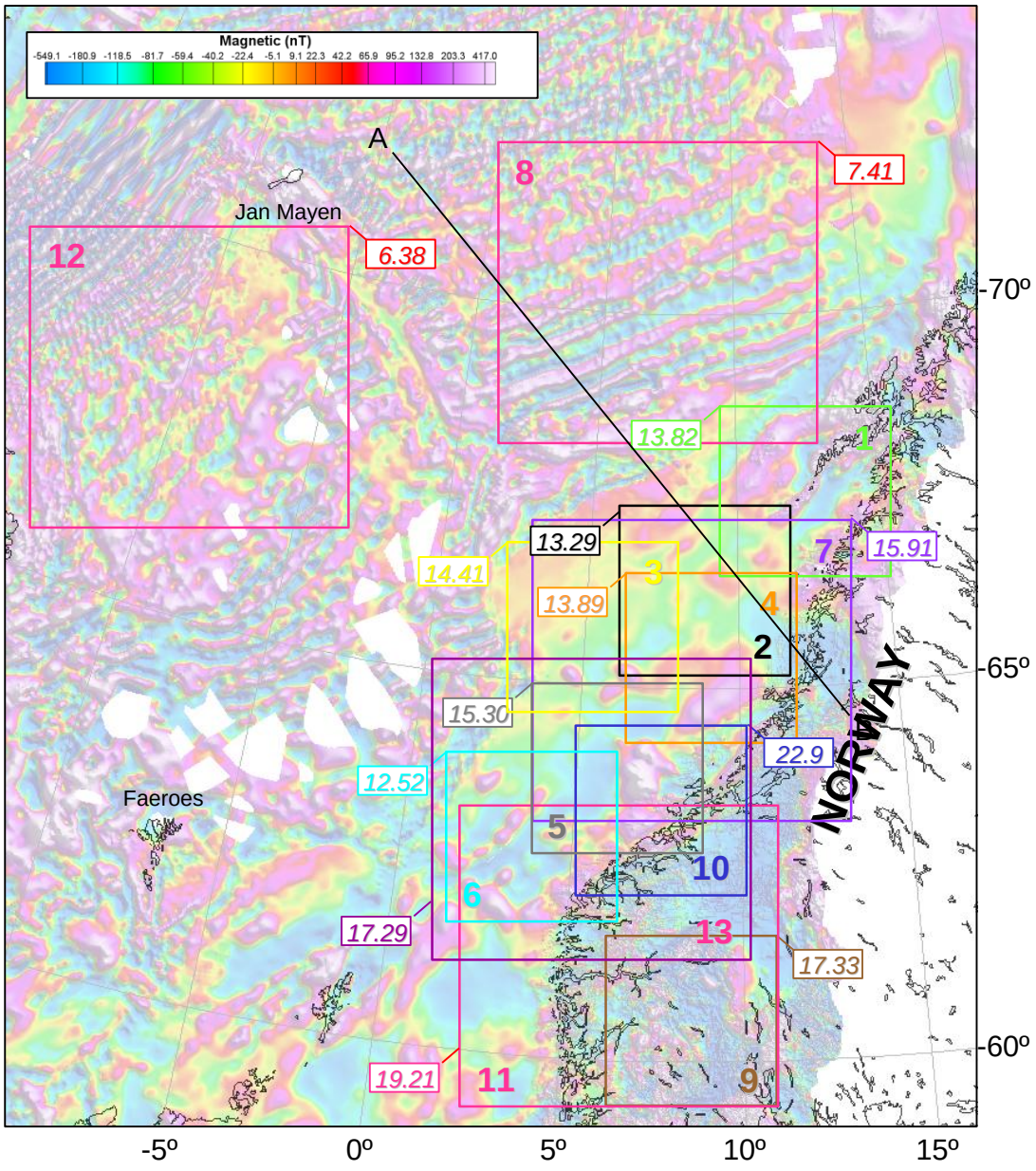

Figure 13.11. Selected windows along the main segments and structural features of the Mid-Norwegian margin and adjacent oceanic basins. Small windows are ~250x250 km wide. Large windows are 475x475 km wide. Numbers indicate the values of the different DDMSs.

Small windows have been selected first across the followings areas:

- Lofoten area (window 1)
- The Nyk-Utgard High area (window 2)
- The Fles-Gjallar area (window 3)
- The Nordland area (window 4)
- The Ormen Lange area (window 5)
- The Møre Basin (window 6)
- The central southern Norway (window 9)
- The Froan Basin-Frøya High (window 10)

Large windows have been tested along:

- The Vøring Basin area (window 7)
- The Lofoten Basin area (window 8)
- The South Norway-Viking Graben area (window 11)
- The Jan Mayen Ridge area (window 12)

Large windows overlap some of the small windows to test the reliability of the measurements estimates.

Using small windows in the continental domain (Fig. 13.11), the DDMSs estimations vary from 22.9 km (deeper values) near Frøya Basin to 12.52 in the central part of the Møre Basin (shallower value) (Figs. 13.12, 13.12, 13.14). In the Vøring Basin and along the Lofoten margin, the DDMS values ranges from 13.3 km to 14.4 km.

Using large windows the DDMSs vary between 19.25 km in the south Norway-Viking Graben area to 17.29 km in the Møre Basin and 15.91 km in the Vøring Basin area. Intermediate values suggested also deep magnetic material at around 12.4 km in south Norway (windows 11), 4.54 km in the Møre Basin and 8.48 km in the Vøring Basin. The DDMS values along the Møre and Vøring Basin (windows 7 and 13) appeared to be slightly higher than the DDMS indicated by smaller windows sampled along the same areas (windows 2, 3, 4, 5) (Figs. 13.11, 13.12, 13.13). Deeper values are, however, indicated using small windows near the Frøya High (window 10)

In the oceanic domain, windows provide shallower DDMSs (Figs. 13.11 and 13.14). DDMS for the Lofoten Basin is 7.41 km and a value of 6.38 km has been obtained along the Jan Mayen Ridge. Intermediate depths around 3 km are also deduced for the two windows. We point out that any good estimation of the DDMS could not be estimated in the Norway Basin due to poor magnetic coverage and significant gaps in this area.

The DDMS values, in the oceanic domain, appear to be systematically lower that the continental values and clearly reflect the contrast of the magnetic anomalies also observed between the two distinct geophysical and geodynamic domains.

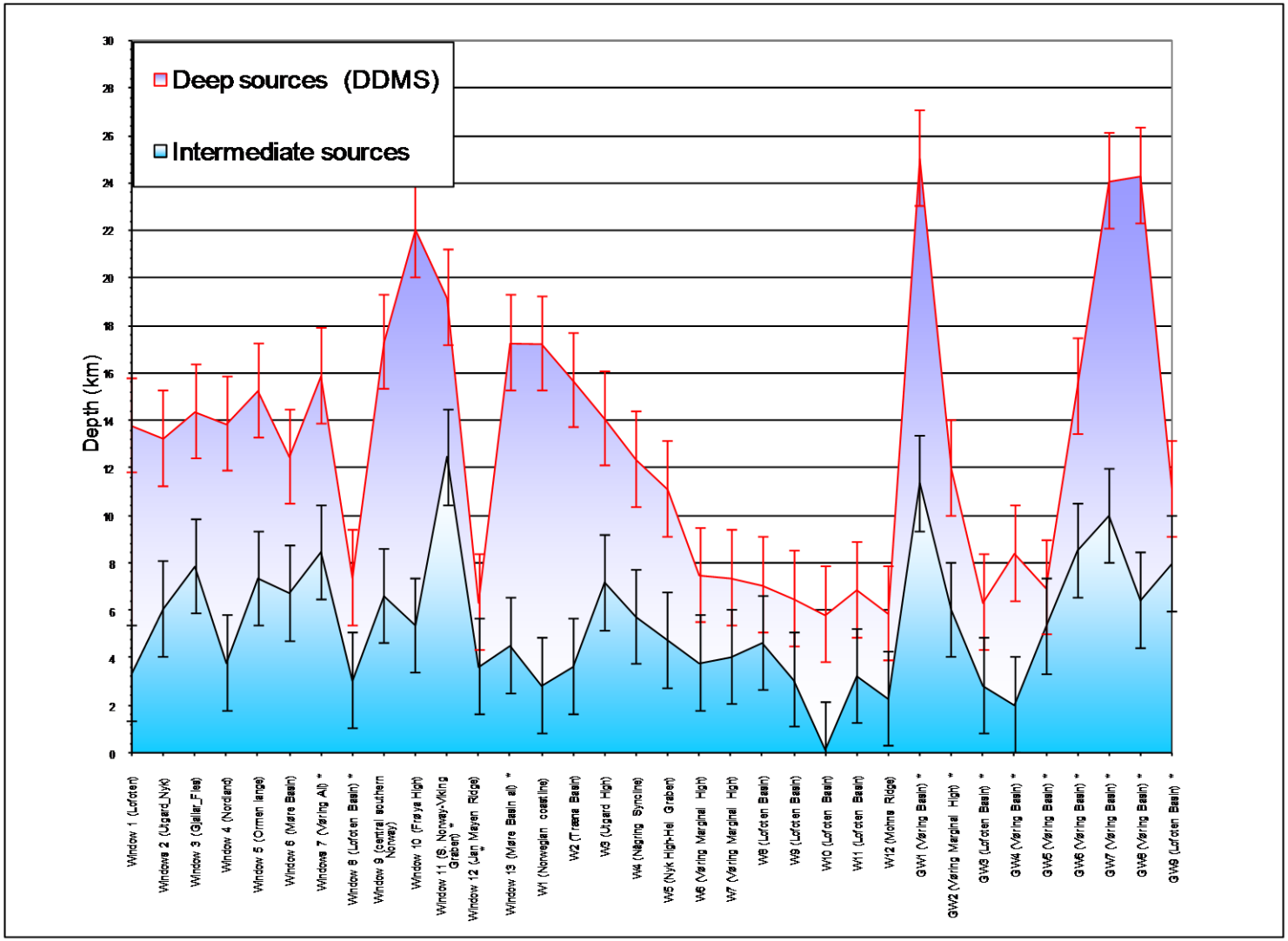

*Figure 13.12. Summary of the deep and intermediate magnetic sources measurements obtained from spectrum analysis at different location. * Indicates large windows.*

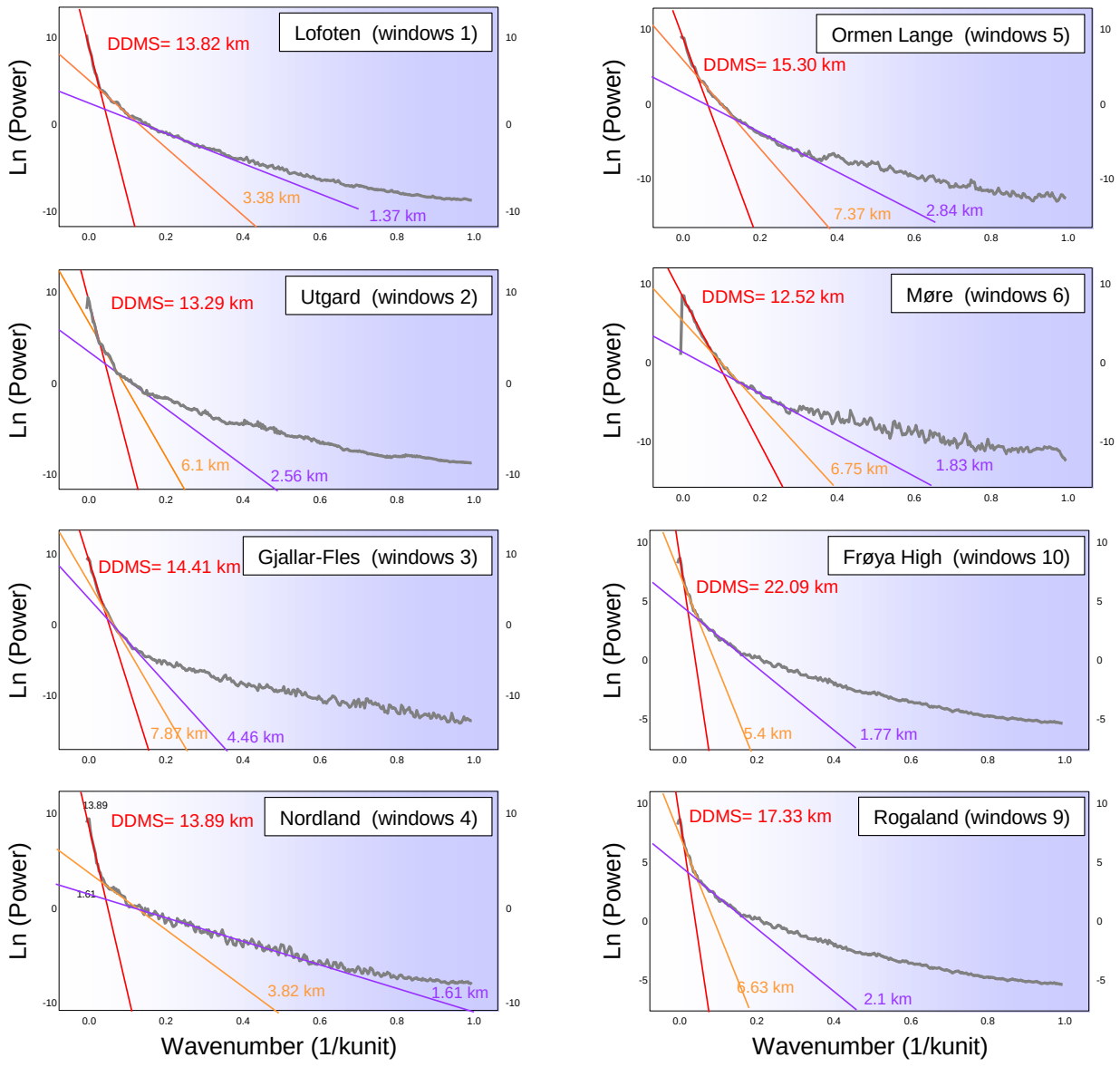

Figure 13.13. Examples of power spectrum analysis along different structural element of the Norwegian shelf and mainland. Location of the windows on Fig. 13.11.

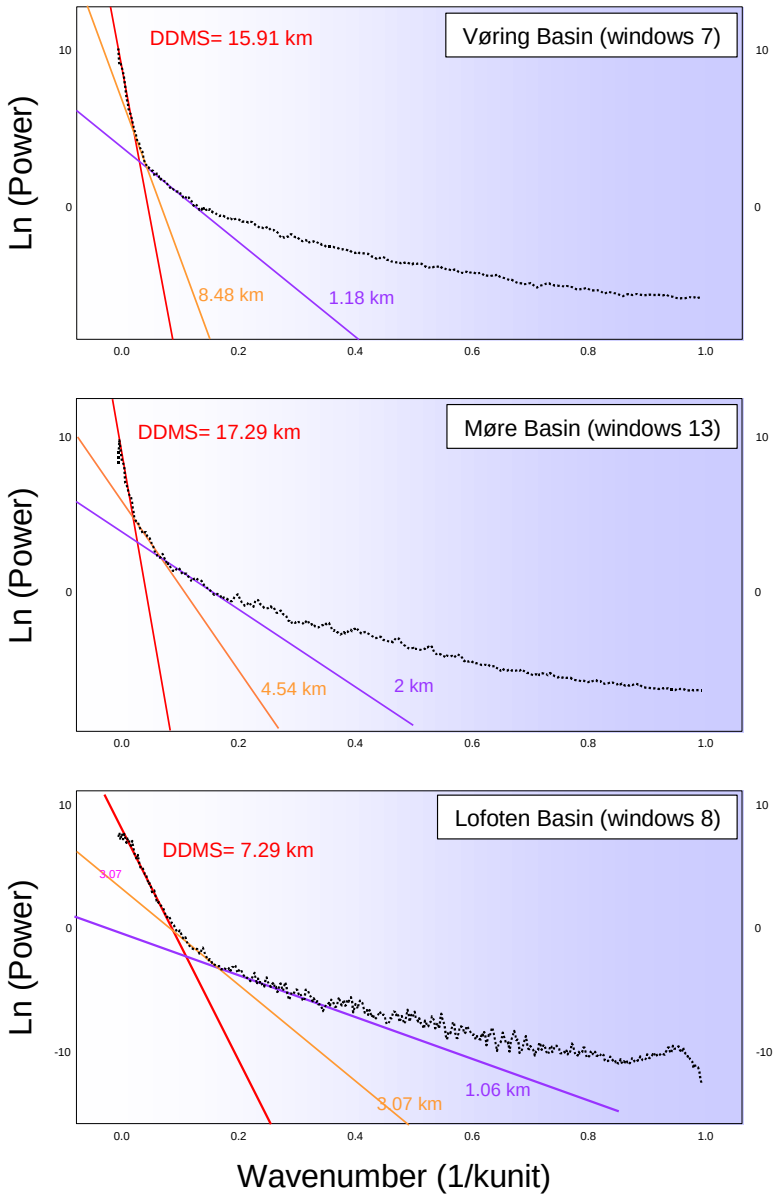

Figure 13.14. Power spectrum analysis of large windows, offshore Norway. The location of the windows are shown in Fig. 13.11

13.8 Application along a NW-SE corridor from the Mid-Norwegian margin to the oceanic spreading ridge.

In a second phase, we sampled some windows along a corridor from the Norwegian mainland to the oceanic spreading axis to the west in order to test the lateral evolution of these values (Fig. 13.15). The main idea was to check the relationships between the depth of Curie temperature and the geodynamic setting of the main magnetic units.

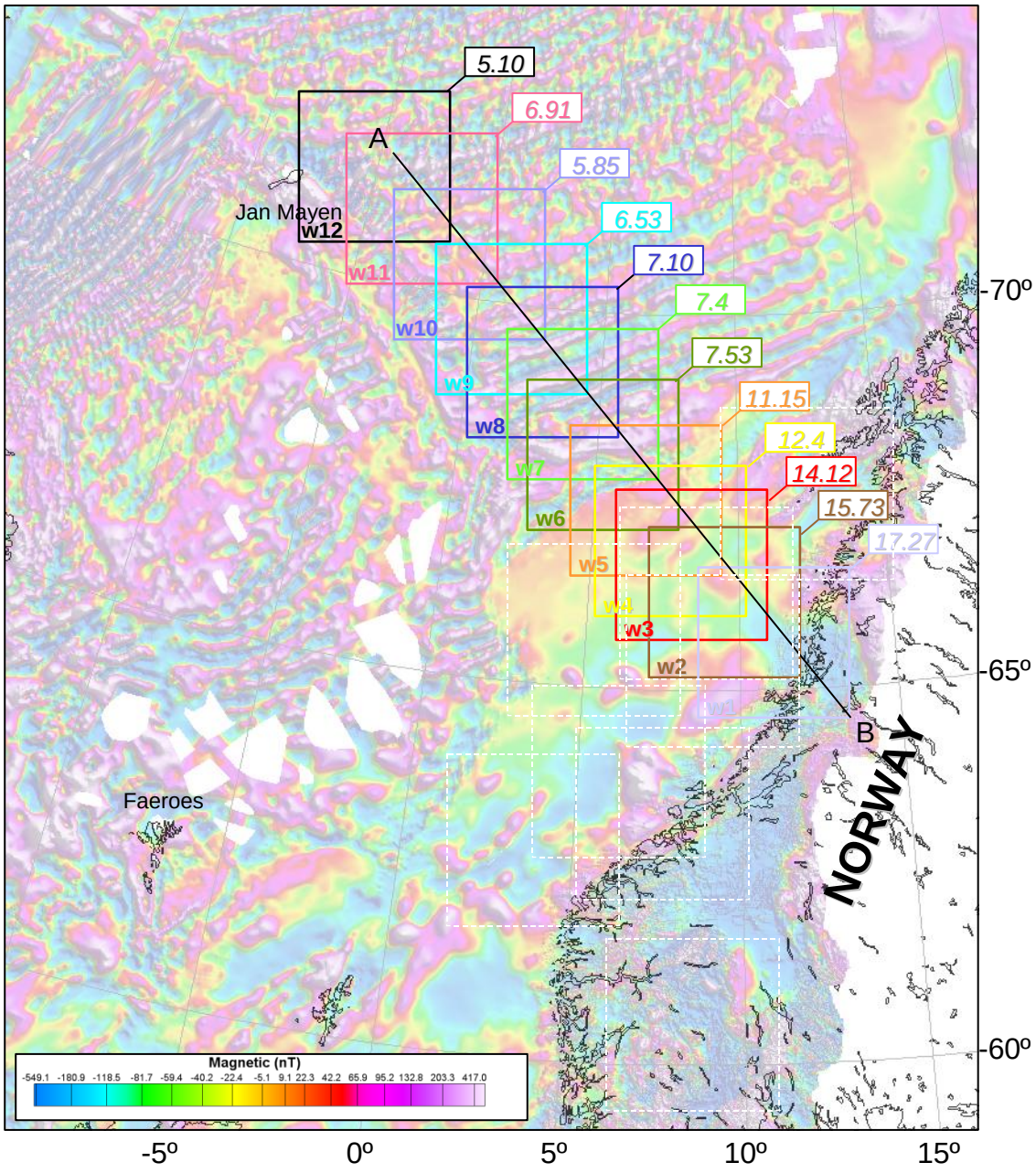

Figure 13.15. Selected windows along a NW-SE corridor from the Norwegian mainland to oceanic spreading axis. Transect AB is illustrated by Fig. 13.18. White dashed lines represent the small windows previously described in Fig. 13.11.

Results for DDMS computation of the main areas are summarised in Tables 13.1- 13.3 (annexes) and a comparison with the previous DDMS estimations is still possible using Fig. 13.18.

Along the selected corridor, we test different window sizes to test the effect of these parameters (Figs. 13.15 and 13.16).

Across the Vøring Basin the DDMSs progressively decrease from East to West from 15.73 km to 11.15 km along the outer Vøring Basin. A sudden fall of the DDMS is recorded near the Vøring marginal High from 11.15 to 7.5 km (Fig. 13.18). The drop coincides with the continental-oceanic transition zone near the Vøring Marginal High.

West of the Vøring Marginal High (windows W7 to W10), a progressive swallowing of the DDMS is observed from the continental crust toward the oceanic. Along the Lofoten Basin (oceanic domain) the DDMSs do not vary so much and evolve from 7.5 to 5.1 km, close to the Mohns Ridge and Jan Mayen area.

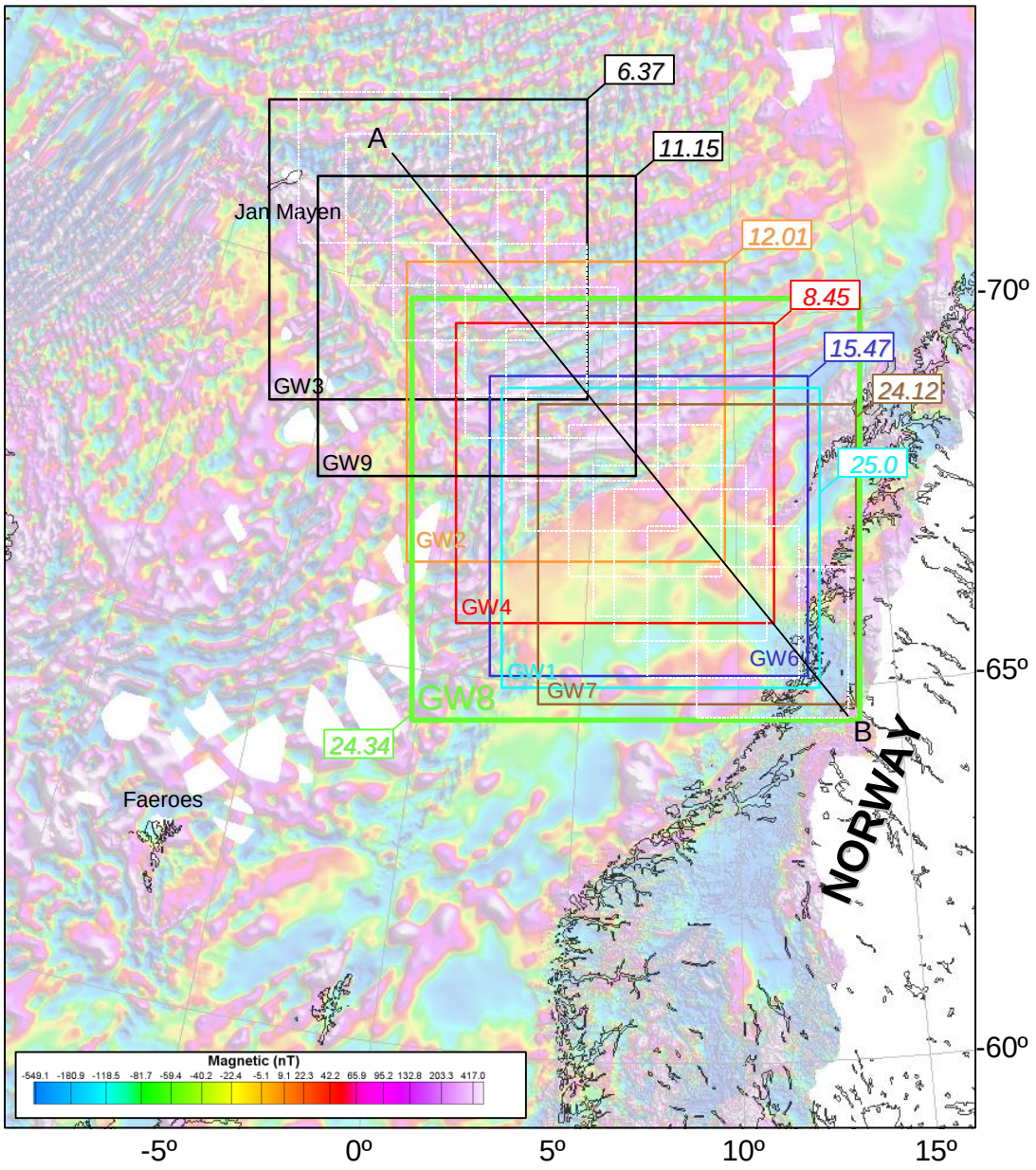

Figure 13.16. Selected large windows along a NW-SE corridor from the Norwegian mainland to oceanic spreading axis.

In the continental domain, the DDMS results obtained using larger windows (~475x475 km), do not vary so much across the Lofoten Basin. The spectrum analysis suggests DDMS values between 6.3 and 12.01 km in the Lofoten Basin (windows GW3 and GW9). Near the coastline and across the Vøring Basin, some windows suggest, however, deeper values of the DDMS (Fig. 13.16). The DDMSs reach 24 to 25 km in windows GW1, GW7, GW8. Compared to the small windows (Figs 13.15 and 13.16) the DDMSs are 5 to 7 km deeper if we use larger windows.

Additional intermediate magnetic material are also indicated at the depth s of 11.37 km (GW1), 5 km (GW5), 8.54 km (GW6), 10 km (GW7), 6.44 km (GW8) but are shallower that the DDMS values obtained with small windows along the corridor.

In the oceanic domain, the large window GW3 provides a DDMS of 6.37 km, which is close to the values obtained by the small adjacent windows 10, 11 and 12 (Figs. 13.15 and 13.16). However, large windows GW2 and GW9 provide deeper DDMS values of 11.15 and 12.01 km. These deep DDMSs are also different from the 7.41 km result obtained using the same window size previously described across the Lofoten Basin (cf. window 8, Fig. 13.11). The discrepancies could be explained as a misinterpretation of the spectrum, bad quality of the initial magnetic dataset or by the fact that GW2 and GW9 partly cover the Vøring Spur and the Jan Mayen Fracture Zone. We know from NGU report 2006.018 (Olesen *et al.* 2006b) that this area represents an atypical thick oceanic domain that significantly influences the magnetic signal in the area. The deepening of the DDMS could be linked with this lateral variation of the oceanic crust thickness and may reflect the presence of deep gabbroic units in this area. We note also that intermediate magnetic depth values obtained for GW2 (6.04 km) and GW9 (7.99 km) are quite similar to the values obtained using small windows, from windows W8 to W12 (Fig.10.11).

13.9 Does the DDMS represent the Curie temperature?

At this stage of the spectrum approach, a link between the Curie temperature and the values of the DDMS is unfortunately not so obvious and the estimation of source depths from analysis of crustal magnetic sources remains a tricky problem with ambiguous solutions. The DDMS may have two alternate interpretations. It may suggest a lithological interface generally characteristic of areas with normal or low heat flow. The second possibility may be that at such depths, rocks really loose their ferromagnetic properties.

In the oceanic domain, our DDMS values are most of the time shallower than values expected from theoretical models (Fig. 13.17). From the continental-ocean transition zone, the Curie temperature is expected between 30 near the continental ocean transition zone to 5 km near the Mohns ridge assuming the plate model of Parsons & Sclater (1977). Unfortunately, our DDMS values are most of the time shallower that the values expected (Fig. 13.18). Small windows analysis suggests depths from 7.53 km near the COT to 5.10 km near the Mohns Ridge. Even with large windows the depth of the DDMS are still shallower to represent the one of the Curie isotherm. The only exceptions are from the DDMS value estimated near the current spreading ridge. Here, the DDMS, located at around 6-5km may likely represent the Curie windows. For other DDMS values, the geological meaning of these values rather suggests an interval located between the Moho and the top of the oceanic gabbros.

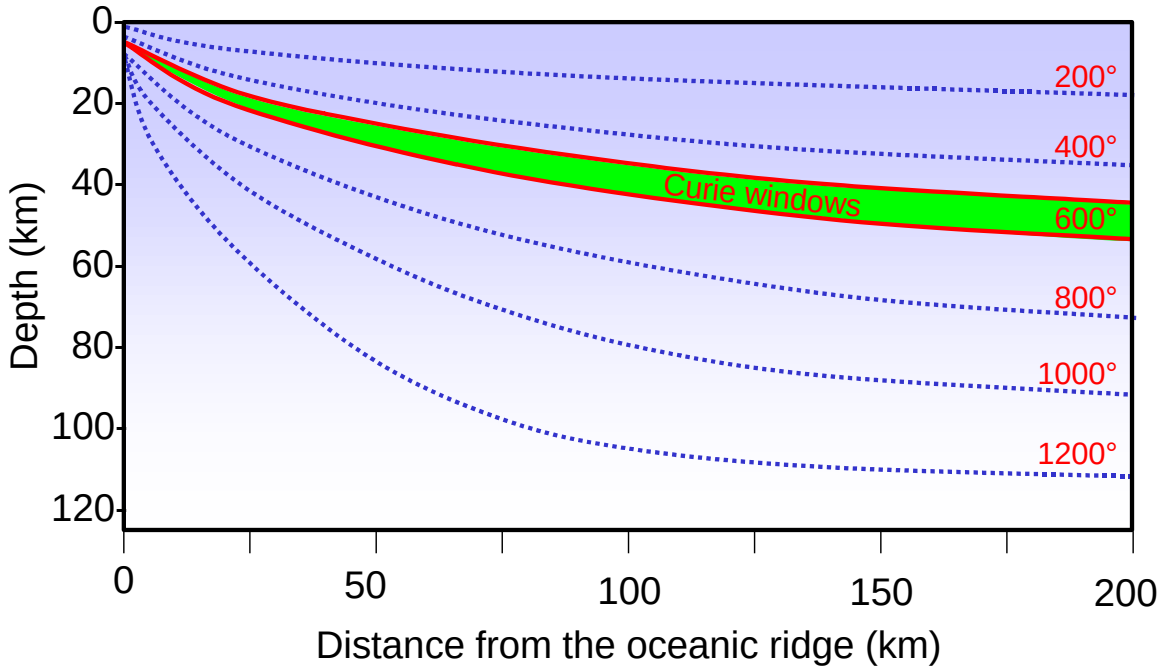

Figure 13.17. Isotherm and Curie temperature evolution along an oceanic spreading system. The graph illustrates the progressive cooling of the oceanic lithospheric plate as a distance (=age) function from the current oceanic ridge. Model from Parsons and Sclater (1977).

In the continental domain, it is even more difficult to estimate and judge the location of the Curie isotherm versus the DDMSs. As a matter of fact, the Curie isotherm does not necessarily represent any strong seismic contrast (like the top basement for example) and/or is locally to deep to be detected with conventional 2D seismic lines. Therefore, it is really difficult to compare our DDMS results with other reliable datasets.

To test the validity of the DDMS, we refer to a recent thermal modelling (Gernigon *et al.* 2006) located near the transect AB described in this chapter (Figs. 13.18, 13.19). This model provides the more recent evaluation of the Curie isotherms expected from the Norwegian mainland to the oceanic crust.

Comparing the thermo-kinematical model and the spectral solution, we find that some of the DMMS values between 25 km and 15.47 km (windows GW1, GW7 and GW8) are close to the Curie temperature suggested by this thermal model. Unfortunately, shallower DDMSs between 15 km to 11 km are certainly too shallow to likely represent the actual Curie isotherms. They may represent, at best, crustal features from Moho to top crystalline basement described by wide-angle seismic data (Mjelde *et al.* 2005).

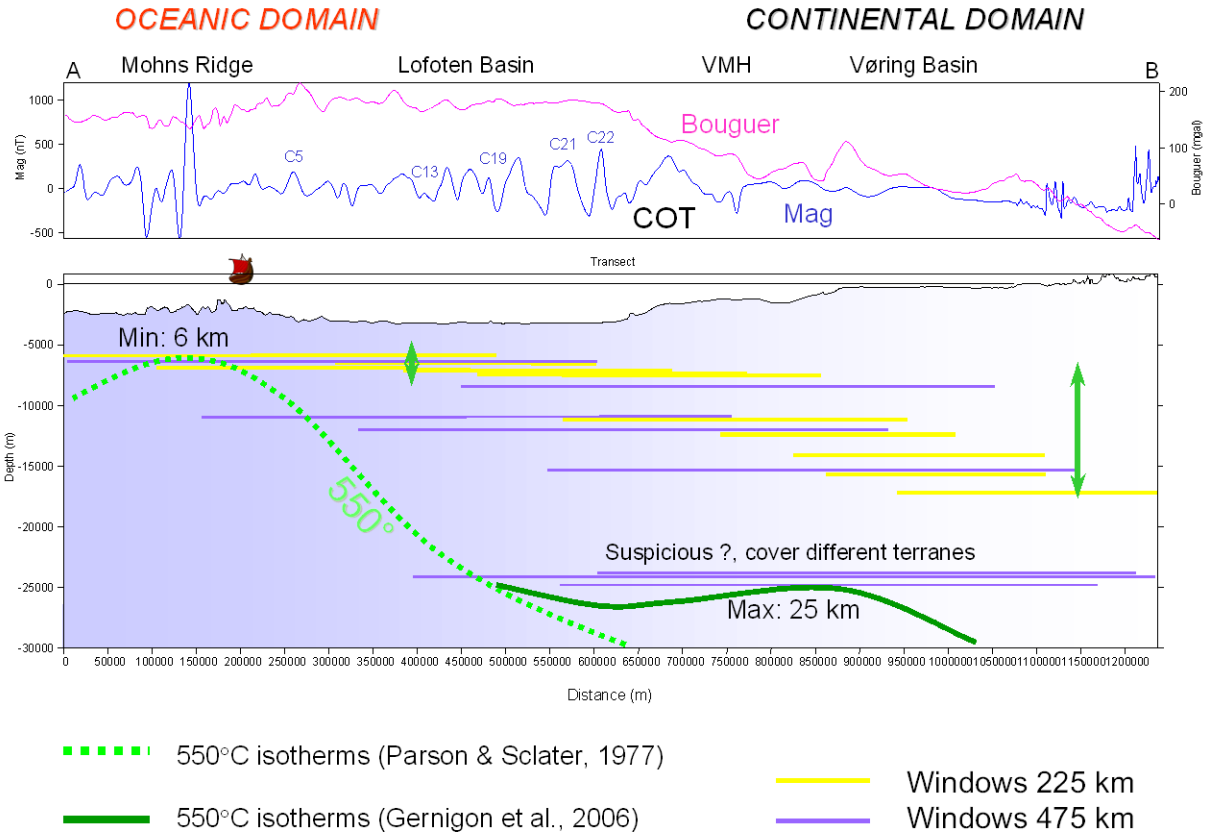

Figure 13.18. Bathymetric transects across the sampled windows. Horizontal bars represent the projection of the sampled windows at the depth of the DDMS obtained by spectral analysis for each of these windows. The red lines represent the projection of the small windows located on Fig. 13.15, the blue lines represent the large windows, described in Fig. 13.16. The green dashed lines represent the 550℃ isotherms calculated assuming the analytic model of Parson & Sclater (1977). Location of the profiles is shown in Fig. 13.15.

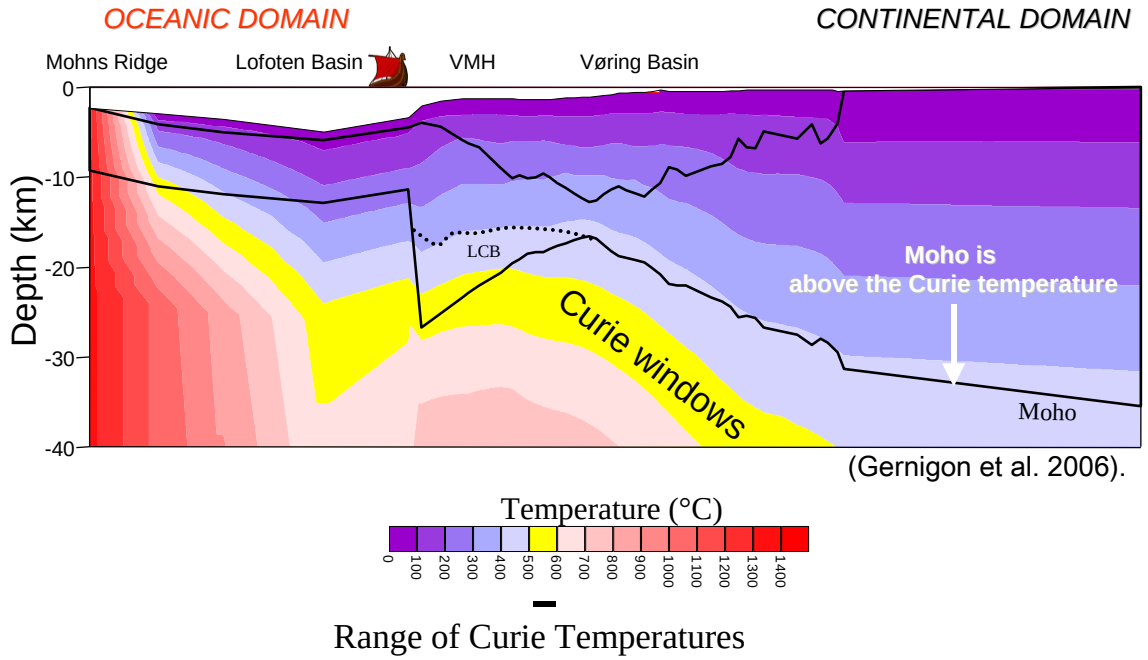

Figure 13.19. Thermal modelling across the Norwegian mainland to the Mohns oceanic spreading ridge, cross-cutting the Vøring Basin (Gernigon et al. 2006). This model provides an independent estimation of the actual Curie isotherm, offshore Norway.

13.10 Okubo´s technique applied to mid-Norway and Barents Sea

Previous chapter shows that the simple approach of Spector and Grant (1970) is probably mot efficient to reach to Curie temperature along the mid-Norwegian margin. There are two main problems with this classic approach:

1) The windows size must be wide enough to detect the deepest magnetic source and this does not allow a precise location of this source
2) Even if Spector and Grant (1970) suggest that at long wavelengts, the prism should be very thin with a negigeable distance between the top and the base of the statistical prism, the theory still suggests that only the top of the magnetic sources is detectable.

An alternative to these problems has been proposed by Okubo et al (1985) and Tanaka et al. (1999). Okubo et al. (1985) approach the estimation of bottom depths in two steps: first, find the centroid depth $z_{centroid}$; and second, determine the depth to the top $z_{centroid}$. The depth to the bottom (inferred Curie point depth) is calculated from these values: $z_{base} = 2.z_{centroid} - zt_{op}$ (Fig. 13.20).

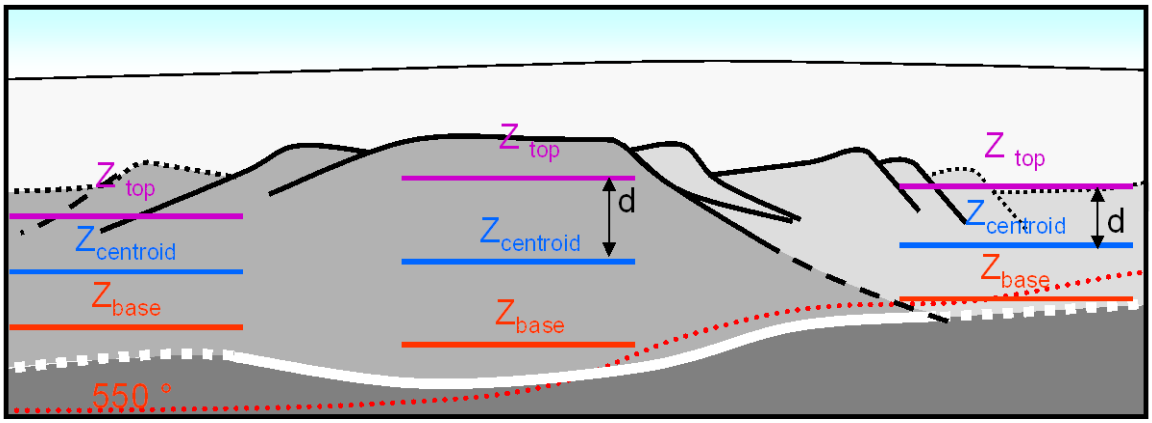

Figure 13.20. The Okubo´s technique. Using spectral analysis to obtain the top and the centroid part of the synthetic prism, we can deduce the base of the magnetic source without involving wider sampled windows

This method recognizes that there is no wavelength range in which the exponential signal from the bottom dominates the one from the top and that a direct calculation of depth to the bottom requires a simultaneous computation of the depth to the top – a much more complex problem. The terms involving z_{base} and z_{top} can be recast into a hyperbolic sine function of z_{base} and z_{top} plus the centroid term $z_{centroid}$. At very long wavelengths (compared to the body dimensions), the hyperbolic sine tends to unity, leaving a single term containing $z_{centroid}$, the centroid.

Okubo et al (1985) estimate z_{top} using the Spector and Grant (1970) expression as reviously used:

$$Ln\Phi_{average}(k)^{1/2} \approx C1 - k.z_{top}$$

Okubo et al. (1985) consider that the DDMS as defined of Spector and Grant (1970) most likely represent the top of the source and not the real deepest magnetic source. Similarly $z_{centroid}$ and z_{base} can be obtained using a modified version of the average spectrum divided by the wavenumbers:

$$Ln\left[\Phi_{average}(k)^{1/2}/k\right] \approx C2 - k.z_{centroid}$$

Using the slope of each spectrum, $z_{base} = 2.z_{centroid} - zt_{op}$ can be easily deduced, without involving wider moving windows. Consequently, the geographical location of the base to the DDMS could be more precise. The technique has been apllied along the regional transect and allows to detect

depper magnetic source compares to the previouss DDMS approach. Using a moving window of 225x225 km the bases of the magnetic sources ranges from 18 km to 7km near the Mohns Ridge. However thes values still reflect mid-crustal or oceanic Moho levels. Using a moving window at 475x475, deeper values are obtain and depth up to 30 km can be obtain in the continental domain. These values are more compatible with the thermo-kinematical estimation but still the large windows size does not allowed a precise location of the sources.

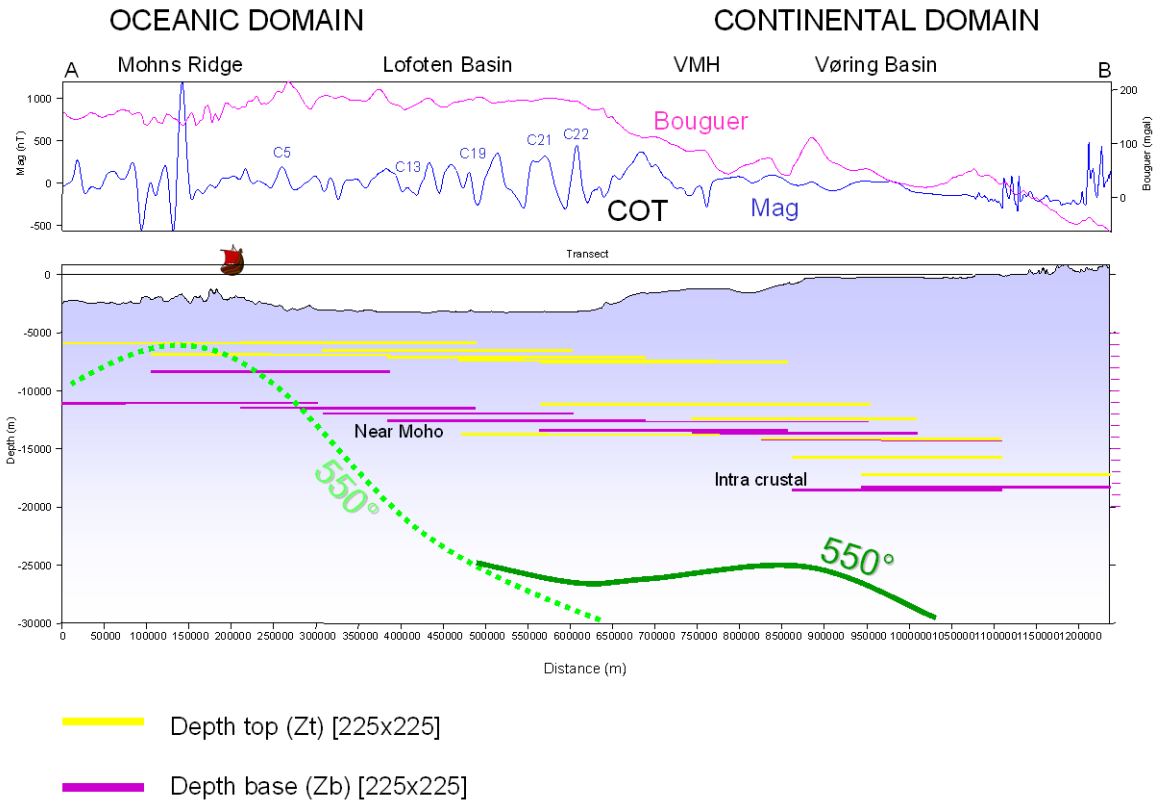

Figure 13.21. The Okubo´s technique used along the regional transect using a windows size of 225x225 km

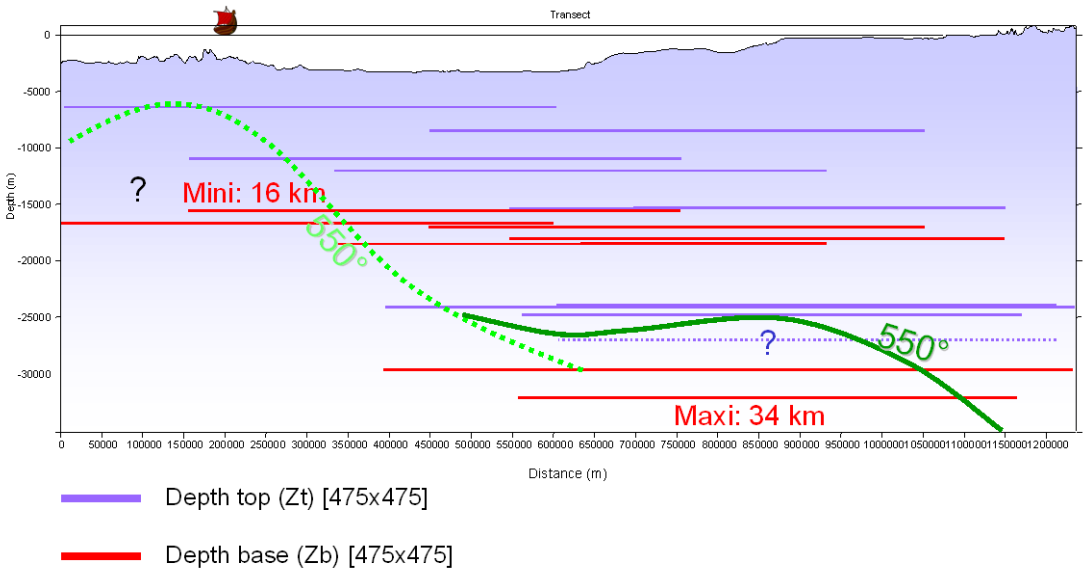

Figure 13.22. The Okubo´s technique used along the regional transect using a windows size of 475x475 km

The spectral technique has been also tested in the Barents Sea and compared with the 3D crustal compilation (Barents 50) of Ritzmann et al. (in press). At that stage some of the interpreation mostly rely on this compilation.

First, we used a 100x100km moving windows size applied along a regional E-W transect running from Novaya-Zemlya to the Senja Ridge (Fig. 13.23, 13.24). Suprisningly, most of the z_{top} results fit the top basement deduced from previous modelling and compilation (Fig. 13.24). This observation suggest that in such a case, the spectral technique could be used an interesting tool to estimate the depth to top basement. Once again, with such a small windows size a Curie temperature at less that 15 km could appear suspicious.

Using wider moving windows (200x200 km), some z_{top} values do move change significantly and might suggest real deep magnetic sources at around 20 km in the Loppa High and 22 km in the South Barents Sea. From the Norsel High to the West Fendisky Bench, deeper values have been observed (Fig. 13.25).

Results with a windows size of 400x400 km provided the deepest top of magnetic sources. Arround the Loppa High, depths did not really changed and still agree with magntic units at around 20-22 km depth. To the east, z_{top} estimation locally with with the top of a high velocity lower crust (Vp>7km/s). This unit, probably mafic could explain the long wavelengths in the east Barents Sea area. Using the Okubo technique the base of the magnetic sources are estimated

between 25-26 km in the western Barents Sea and reach 29-31 km in the eastern Barents Sea. This could eventually fit a Curie temnpearture estimation but this assumption should be confirmed and/or compared with other and independant crustal temperature estimation.

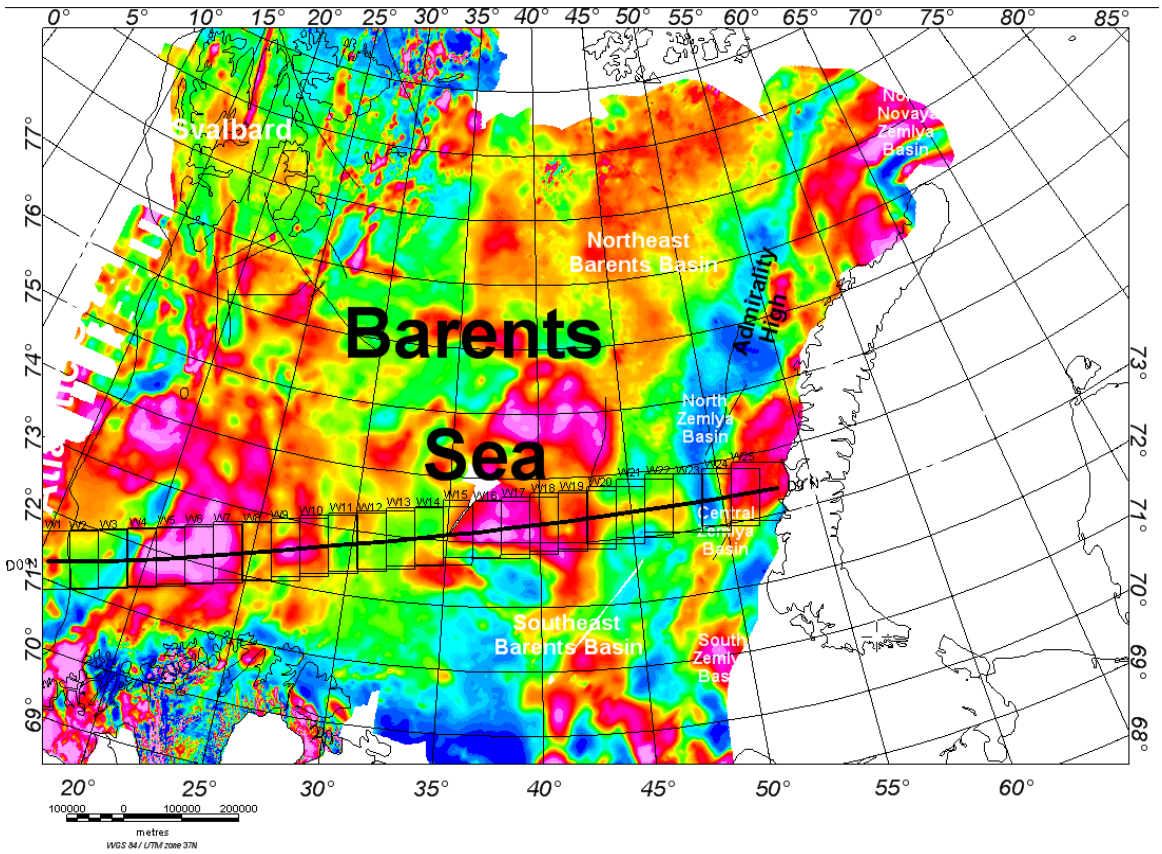

Figure 13.23. Selected transect acoss the Barents Sea.

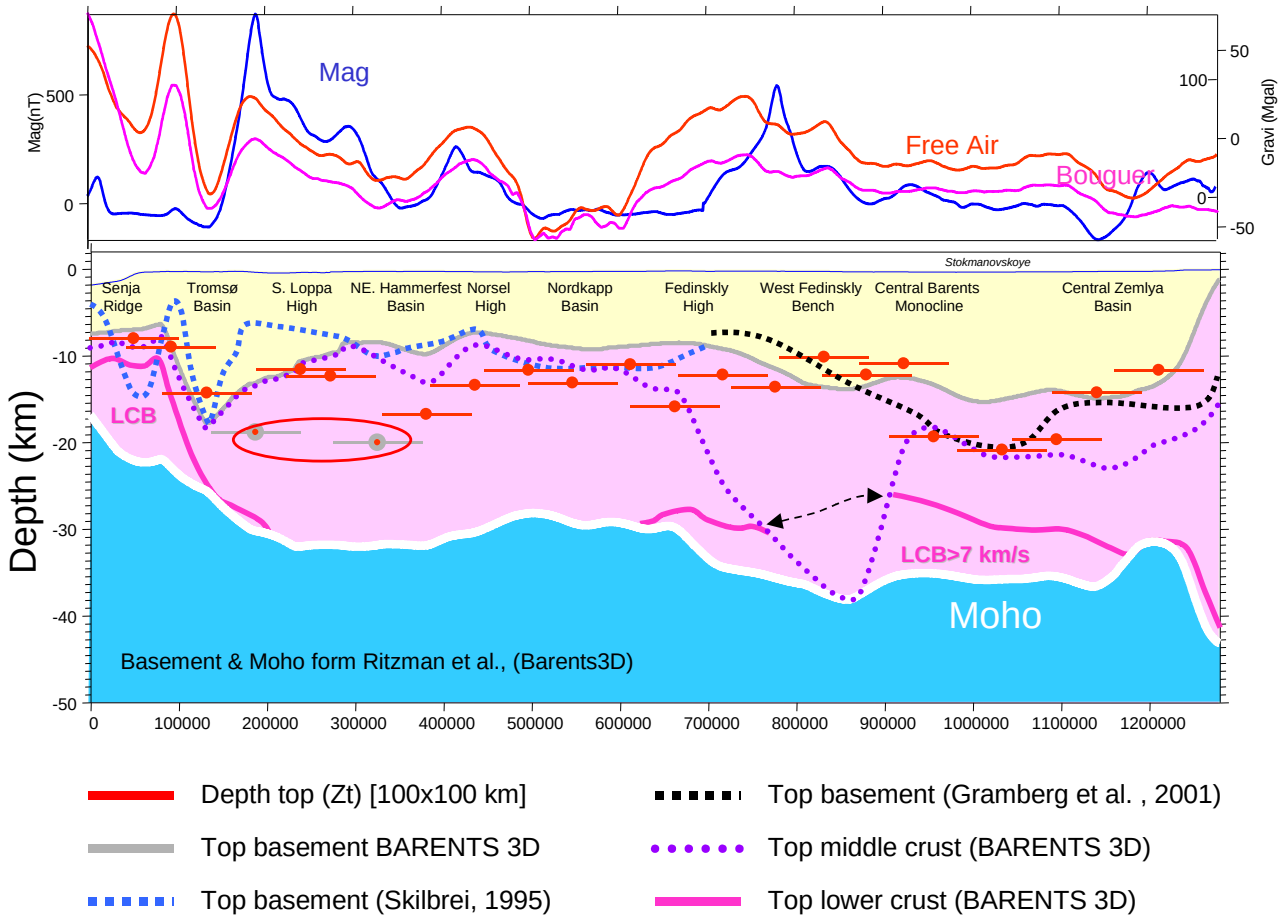

Figure 13.24. Spectral methods along the regional transect across the Braents Sea using a windows size of 100x100 km. The results are compared with the previous estimation of the top basement. Some correlation with the previous top basement estimations (Skilbrei 1995, Gramberg et al. 2001 and the 3D BARENTS 50 km model from University of Oslo) and the values obatined using a small windows size has been obtained and could suggest that the spectral technique could be also used to invsetigate the position of the top basement.

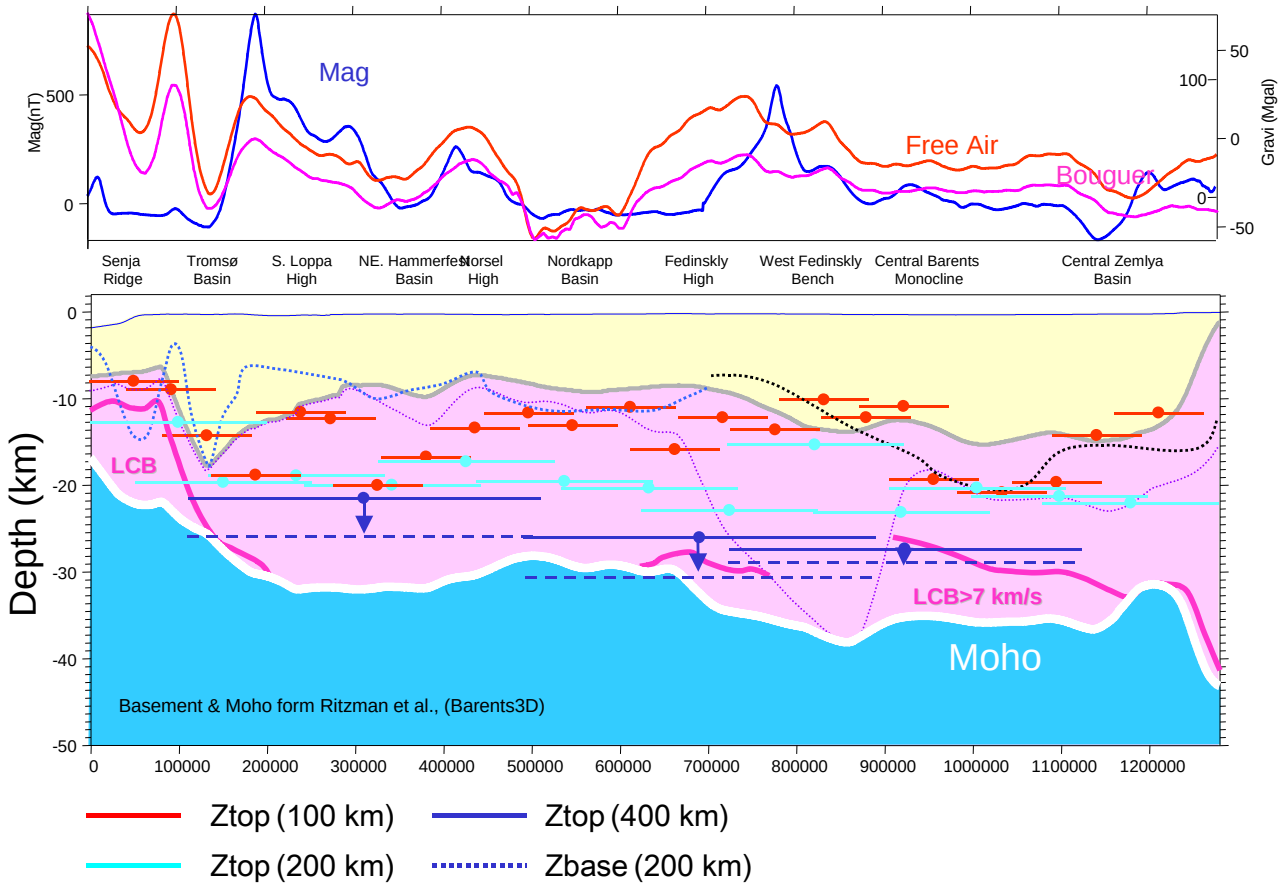

Figure 13.25. Spectral methods along the regional transect across the Braents Sea using different windows sizes (100x100 km; 200x200km; 400x400km). The results are compared with the main crustal units from different compilation. Note that locally some magnetic sources estimation fit with the location of high velocity lower crust in the East Barents Sea.

13.11 Conclusions

- In this chapter we estimated depths of the deepest magnetic sources (DDMSs) along the Mid-Norwegian margin and adjacent areas using spectral analysis of aeromagnetic sub-grids. We applied the technique along a wide area and the main magnetic grid was based on a regional compilation of different magnetic datasets with different processing, line spacing and quality. The DDMSs have been deduced from the steepest slopes observed within several grid windows.
- This analysis suggests that the size of the windows is a significant parameter, which limits the depth penetration of the spectrum analysis. Estimation of deep values requires large

windows. Therefore, the x, y location of the calculated value remains geographically imprecise.

- At this stage, we cannot conclude that the DDMSs represents represent the depth to Curie temperatures. The DDMSs values are too scattered to firmly affirm that they represent real Curie depths.
- Even if the spectral methods do not appear successful along the Mid-Norwegian margin, the distribution of the DDMS, suggest however interesting and coherent lateral variations from the oceanic domain to the continental crust even with varying windows sizes. Lateral variation is also suggested in the continental domain. This could be useful to determine any structural segmentation along the sedimentary basins even if the real geological meaning of the iso-DDMSs values reminds a complex problem. The DDMSs represent, by definition, statistical values along a certain window and should be considered as an average and rough values of "concrete" magnetic sources existing within the windows. Another problem is probably related to the quality and the non-uniformity of the data.
- Using the Okubo´s technique, we tried to find a solution to get the depths of the base of the deeper magnetic sources, assumed to be closer to the Curie temperature. However, we still obtained depths along the Mid-Norwegian transect which do not agree with any Curie temperatures estimation. Deeper values in the Barents Sea may eventually fit a Curie isotherm but at that stage this interpretation reamains highly speculative, especially due to fact that the magnetic grid in the Barenst Sea is far from being so reliable everywhere.
- If both the techniques of Spector & Grants (1970) and Okubo et al. (1985) do not appear to be so efficient to obtain an estimation of the Curie temperature. These techniques could indicate at least that some magnetic sources are still present at certain levels (z_{top} and $z_{centroid}$). Therefore, we can assume that at such levels the temperature could eventually be lower than the Curie temperature.
- From a practical point of view, we believe that the spectral methods could be better applied to provide information about the depth to top basement, using small windows or intra-crustal magnetic units, using bigger windows. The interpretation of computed values needs careful data analysis and additional geological and geophysical information should be used to constrain the interpretation of magnetic anomalies. In the future, it seems to be judicious to compare and calibrate the DDMS estimation (and the windows size) with seismic data (not available for this study) to constrain the top basement in order to get the best fit between seismic reflections and the windows size. Without seismic marker calibration, such technique could appear useless. The technique could also be applied to the gravity dataset and could be compared with other magnetic methods (e.g. Werner, Euler and deconvolution) or thermo-kinematical models.

Table 13.1. Source depths from spectral analysis of aeromagnetic anomalies along different areas of the Norwegian shelf and mainland.

	ln(power)	wavenumber	slope	depth estimate
Windows 1	**Lofoten**			
deep	9.73	0.056	173.75	**13.82658568**
intermediate	5.11	0.12	42.58333333	3.388673997
shallow	2.42	0.14	17.28571429	1.375553437
Windows 2	**Utgard_Nyk**			
deep	9.52	0.057	167.0175439	**13.29083384**
intermediate	6.9	0.09	76.66666667	6.100939485
shallow	3.55	0.11	32.27272727	2.568182036
Windows 3	**Gjallar Fles**			
deep	9.78	0.054	181.1111111	**14.41236429**
intermediate	7.52	0.076	98.94736842	7.873981395
shallow	3.92	0.09	43.55555556	3.466040983
Windows 4	**Nordland**			
deep	9.43	0.054	174.6296296	**13.89658438**
intermediate	5.86	0.122	48.03278689	3.822327732
shallow	2.3	0.113	20.3539823	1.619718447
Windows 5	**Ormen Lange**			
deep	10	0.052	192.3076923	**15.30335991**
intermediate	6.86	0.074	92.7027027	7.377046687
shallow	2.29	0.064	35.78125	2.847381404
Windows 6	**Møre**			
deep	9.44	0.06	157.3333333	**12.52018886**
intermediate	7.05	0.083	84.93975904	6.759291258
shallow	2.54	0.11	23.09090909	1.837516161
Windows 7	**Vøring Basin all**			
deep	10	0.05	200	**15.91549431**
intermediate	7.78	0.073	106.5753425	8.480996283
shallow	2.05	0.138	14.85507246	1.182129106
Windows 8	**Lofoten Basin**			
deep	8.578	0.092	93.23913043	**7.419734249**
intermediate	3.474	0.09	38.6	3.071690402
shallow	0.94	0.07	13.42857143	1.068611761
Windows 9	**Rogaland**			
deep	10	0.0459	217.8649237	**17.33713977**
intermediate	7.67	0.092	83.36956522	6.634339204
shallow	4.71	0.178	26.46067416	2.105673545
Windows 10	**Frøya High**			
deep	10.55	0.038	277.6315789	**22.09321907**
intermediate	6.45	0.095	67.89473684	5.402891489

shallow	3.16	0.142	22.25352113	1.770878944
Windows 11	***South Norway-Viking Graben***			
deep	9.9	0.041	241.4634146	**19.21504801**
intermediate	8	0.051	156.8627451	12.48274063
shallow	5.05	0.158	31.96202532	2.54345716
Windows 12	***Jan Mayen Ridge***			
deep	8.42	0.105	80.19047619	**6.381355337**
intermediate	5.189	0.113	45.92035398	3.654225662
shallow	2.79	0.111	25.13513514	2.000190501
Windows 13	***Møre Basin all***			
deep	10	0.046	217.3913043	**17.29945034**
intermediate	6.23	0.109	57.1559633	4.548327043
shallow	4.04	0.16	25.25	2.009331157

Table 13.2. Source depths from spectral analysis of aeromagnetic anomalies along a NW-SE transect between the Norwegian mainland and the Mohns Ridge.

	ln(power)	wavenumber	slope	depth estimate
Windows W1				
deep	9.77	0.045	217.1111111	**17.27715327**
intermediate	5.12	0.142	36.05633803	2.869272213
Windows W2				
deep	9.49	0.048	197.7083333	**15.73312927**
intermediate	5.53	0.12	46.08333333	3.667195147
Windows W3				
deep	9.94	0.056	177.5	**14.1250012**
intermediate	6.16	0.068	90.58823529	7.208782717
Windows W4				
deep	9.35	0.06	155.8333333	**12.40082265**
intermediate	7.23	0.1	72.3	5.753451193
Windows W5				
deep	9.25	0.066	140.1515152	**11.15290321**
intermediate	6.01	0.1	60.1	4.78260604
Windows W6				
deep	8.52	0.09	94.66666667	**7.533333973**
intermediate	5.27	0.11	47.90909091	3.812484319
Windows W7				
deep	8.47	0.091	93.07692308	**7.406826198**
intermediate	4.6	0.09	51.11111111	4.06729299
Windows W8				
deep	8.48	0.095	89.26315789	**7.103336407**
intermediate	5.28	0.09	58.66666667	4.668544997
Windows W9				
deep	8.21	0.1	82.1	**6.533310414**
intermediate	3.16	0.081	39.01234568	3.104503828
Windows W10				
deep	8.09	0.11	73.54545455	**5.852561316**
intermediate	1.72	0.74	2.324324324	0.184963853
Windows W11				
deep	8.69	0.1	86.9	**6.915282277**
intermediate	4.53	0.11	41.18181818	3.277144965
Windows W12				
deep	8.17	0.11	74.27272727	**5.910435841**
intermediate	2.33	0.08	29.125	2.317693859

Table 13.3. Source depths from spectral analysis of aeromagnetic anomalies along a NW-SE transect between the Norwegian mainland and the Mohns Ridge.

	ln(power)	wavenumber	slope	depth estimate
Windows GW1				
deep	10.4	0.033	315.1515152	**25.07896073**
intermediate	9.15	0.064	142.96875	11.37709164
shallow	6.68	0.06	111.3333333	8.859625165
shallow	3.7	0.13	28.46153846	2.264897267
Windows GW2				
deep	9.06	0.06	151	**12.0161982**
intermediate	7.6	0.1	76	6.047887837
shallow	3.14	0.08	39.25	3.123415758
shallow	0.98	0.038	25.78947368	2.052261108
Windows GW3				
deep	8.01	0.1	80.1	**6.374155471**
intermediate	3.53	0.098	36.02040816	2.866413006
Windows GW4				
intermediate	8.92	0.084	106.1904762	**8.450369597**
shallow	1.55	0.06	25.83333333	2.055751348
Windows GW5				
intermediate	8.26	0.094	87.87234043	**6.99265867**
shallow	7.38	0.11	67.09090909	5.338924909
Windows GW6				
deep	9.53	0.049	194.4897959	**15.4770062**
intermediate	8.8	0.082	107.3170732	8.540021337
shallow	6.02	0.083	72.53012048	5.771763599
Windows GW7				
deep	9.7	0.032	303.125	**24.12192106**
intermediate	8.8	0.07	125.7142857	10.00402499
shallow	7.73	0.09	85.88888889	6.834820612
Windows GW8				
deep	10.4	0.034	305.8823529	**24.34134424**
intermediate	7.7	0.095	81.05263158	6.449963483
shallow	6.78	0.11	61.63636364	4.904865973
Windows GW9				
deep	9.11	0.065	140.1538462	**11.1530887**
intermediate	9.04	0.09	100.4444444	7.99311492
shallow	7.87	0.1	78.7	6.262747011

14 A DISCUSSION OF STRUCTURAL AND THERMAL CONTROL OF MAGNETIC ANOMALIES ON THE MID-NORWEGIAN MARGIN

Jörg Ebbing, Laurent Gernigon, Christophe Pascal & Per Terje Osmundsen, NGU

In this chapter, we discuss the correlation between the crustal structures on the mid-Norwegian margin (Chapter 11), the depth extent of magnetic sources and the Curie temperature depth (Chapter 13). The thermal state of the crust is usually mostly constrained by surface heat flow data. In absence of good constraints on the structure of the crust and on its associated thermal parameters (i.e. thermal conductivities and distribution of radioactive heat sources), extrapolation of these (near) surface data to deeper levels into the crust can lead to large uncertainties, increasing with depth. An additional thermal boundary condition in the subsurface would, ideally, allow for better constraining the thermal structure of the crust. Estimates of the depth to the base of the lithosphere (assumed to be the ~1300°C isotherm) from independent geophysical methods or the study of mantle xenoliths can eventually furnish this missing boundary condition (e.g. Kukkonen & Peltonen 1999, Artemieva & Mooney 2001). However, the occurrence of mantle xenoliths is very rare and geophysical methods have not enough resolution yet.

The geophysical data set that is most dependent on temperature, other than heat-flow itself, is the magnetic field. Rocks loose effectively their magnetic properties with temperatures higher than the Curie temperature and the magnetic field reflects this temperature dependency (e.g. Fowler 2005). If it would be possible to identify the depth to the Curie temperature from magnetic data, it would be possible to give an independent constraint for the present-day thermal state. One commonly used technique to estimate maximum source depth of magnetic data is by calculating the half decay rate of a logarithmic power spectrum from gridded data (see Chapter 12). However, the question arises, if these conventional spectral techniques can give reliable depth estimates and if these estimates represent the Curie isotherms or a structural boundary.

We discuss in this chapter the thermal versus structural control on the depth to the magnetic sources for the mid-Norwegian margin. The magnetic field over the Vøring margin shows a clear distinction between low-amplitude anomalies over the Vøring Basin and high-amplitude anomalies over the Trøndelag platform (Fig. 11.5). Fichler et al. (1999) presented a model where the observed discrepancy between the gravity and magnetic patterns was explained by a high thermal gradient, based on the assumption that thermal gradients of 30ºC=km and 50ºC=km are typical for the continental shelf and oceanic crust, respectively, which place the Curie isotherms at depths of around 20 km and 11 km (Kappelmeyer & Hänel 1974). In the resulting model only the uppermost basement has a contribution to the magnetic field (Fichler et al. 1999). Gernigon et al. (2006) on the other hand modelled the thermal structure along the Vøring margin and obtained a lower thermal gradient, which places the Curie isotherms in the lower crust or upper mantle.

Here we present a model where we assume that the Curie isotherms are below the crust, which allows us to test the influence of deep-seated sources to the magnetic field. Thermal modelling will be presented afterwards to evaluate the thermal gradient in more detail.

14.1 Comparison of crustal transect and thermal modelling

Fig. 14.1 shows a cross-section through the 3D model (as presented in Chapter 11), crossing the central part of the margin from the outer Vøring Basin through the Rås Basin and Halten Terrace into the Trøndelag Platform. The profile shows that the influence of the high-magnetic lower basement on the magnetic signal of the outer Vøring margin is relatively small due to the flat-lying boundary between the upper and lower basement and its large depth. The division of the basement in the upper low magnetic basement, and the lower high magnetic basement sufficiently explains the different characteristics of the magnetic anomalies on the mid-Norwegian margin without the need to introduce the Curie temperature depth at shallow crustal depths or with a high gradient.

The lower (Precambrian) basement is a key element in the potential field signals on the mid-Norwegian margin and can be directly associated with potential field anomalies on the Trøndelag Platform (Figs. 11.4, 11.5, 11.12 & 11.18). The lower basement is defined to have densities >2.75 Mg/m^3 and higher magnetic properties than the uppermost basement (see Table 11.3). The top lower basement is generally located at depths >12 km and on the Trøndelag Platform it defines extended structural highs at depths <3 km. These highs are aligned and can appear to be a continuous high from the Frøya High along the western border of the Froan Basin. The comparison with the magnetic field anomaly shows that the top of the lower basement correlates directly with the magnetic anomalies for the Frøya High and the shape of the main magnetic lows. The area of the low magnetic anomalies on the outer Vøring margin is in general associated with depth to the top lower basement of more than 12 km.

The resulting thickness of the lower basement is also showing a thinning towards the outer margin from 7-12 km below the Trøndelag Platform to less than 6 km below the outer Vøring margin. The lower basement thickness is also correlating surprisingly well with the shape of the magnetic anomaly. The magnetic high associated with the Frøya High is an effect of very shallow and thick lower high-magnetic basement. The thickness of the lower basement below the Vøring Basin is significantly reduced and the magnetic anomaly field is relatively low-amplitude. Consequently, our analysis allows us to argue that the relatively low-amplitude magnetic anomalies on the outer Vøring Basin could be mainly related to the thinning and deepening of high-magnetic material in the lower basement. These results indicate a strong relation between thickness and depth of the lower basement and the magnetic signal of the mid-Norwegian margin.

In the next step, we model the thermal structure along a profile to evaluate the possibility of shallow Curie isotherms in more detail.

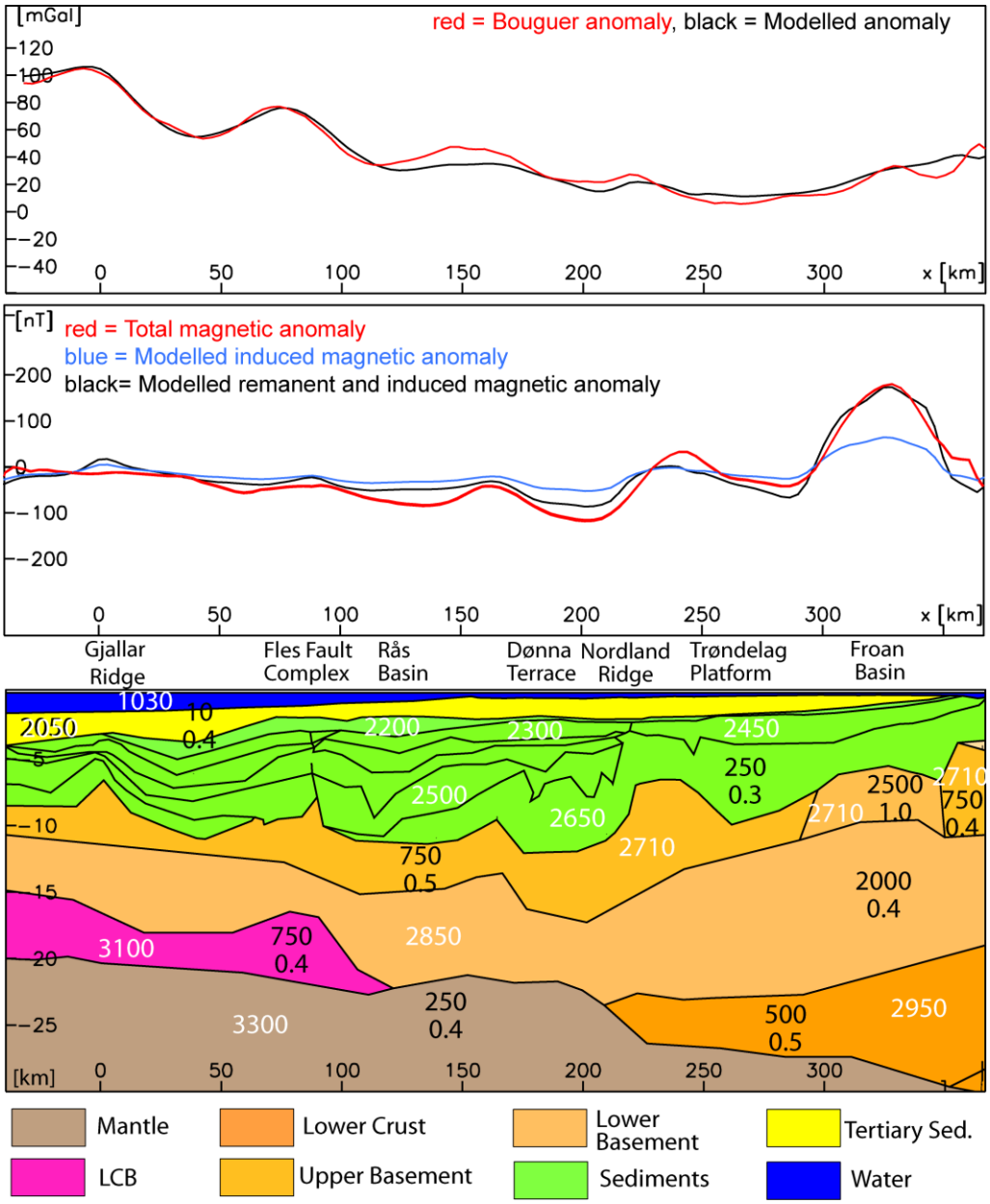

Figure 14.1 Profile through the 3D model (see Figure 1 or 3 for location). The upper panel shows the magnetic anomaly, the middle panel the gravity anomaly. The lower panel shows the modelled cross-section. White numbers are density values in kg/m3; black numbers show magnetic susceptibility (10-5 SI) and Q-ratio. LCB: lower crustal body. The profile represents a typical transects through the mid-Norwegian margin and clearly illustrates the changes in gravity and magnetic anomalies as well as in crustal structure from the outer Vøring margin landwards towards the Trøndelag Platform.

14.2 Thermal modelling

We carried out 2D thermal modelling, by means of finite element methods, in order to test the reliability of the Curie depths as deduced from the spectral analysis of the magnetic field (Fig. 13.22). Selected parameters and the adopted geometry for the modelled profile are given in Table 14.1 and in Figure 14.2 respectively. Heat generation values were attributed assuming that the low magnetic basement corresponds to Caledonian nappes whereas the high magnetic basement is the Precambrian substratum as suggested by onshore petrophysical measurements. Typical thermal conductivity values are inferred for the different layers of the model (Table 14.1). Noteworthy the results presented below are not sensitive to the uncertainties commonly attached to thermal conductivity values. Temperatures and horizontal heat flow are set equal to zero at the surface and the lateral edges of the model respectively.

Table 14.1. Parameters used in the thermal modelling.

Layer	k (W/m/K)	A_0 ($\mu W/m^3$)
Cenozoic sed.	1.5	0.5
Other sediments	2.0	0.5
Upper basement	2.5	1.5
Lower basement	2.5	0.1
Lower crust and LCB	3	0.1
Mantle	3.5	0

We made different modelling tests by varying basal heat flow values. Relevant modelling results for the present discussion are shown in Fig. 14.6 together with the upper and lower boundaries for Curie temperatures as determined from the spectral analysis. For the first modelling case (Fig. 14.2), basal heat flow is set constant to 45 mW/m^2 in agreement with recent estimates (see Chapter 15). Near the eastern boundary of the model (i.e. close to the Norwegian coastline) we found a reasonable fit between the range of depths to the Curie temperatures estimated from the spectral analysis and the modelled depths for the 400 and 600°C isotherms. However, from the central part of the model to its western boundary (i.e. ocean-continent transition), predicted temperatures drop quickly well below 400°C for the specific Curie depth range suggested by the spectral analysis. Increasing the basal heat flow to 60 mW/m^2 (Figure 14.2b) does not improve notably the fit at the western edge of the model and this latter value appears to be somehow excessive at its eastern edge. Alternatively, basal heat flow can be assumed to increase gradually from the coastline to the ocean-continent transition. Figure 6c presents predicted isotherms for a

basal heat flow increasing westwards from 45 to 80 mW/m^2. The thermal pattern mimics what is very often assumed in the literature (e.g. Fichler et al. 1999) and reasonably fits our previously estimated Curie depths, except at the OCT where the 400°C isotherm hardly meets their lowermost boundary. This last result calls for a further increase of the applied basal heat flow below the OCT (i.e. more than 80 mW/m^2) in order to get modelled temperatures in the range of 400 to 600°C at the depths predicted for the Curie temperatures by the spectral analysis. An alternative could be to increase modelled heat generation values in the lower crust. However, even an increase of heat generation rates to 0.5 μW/m^3, would result in a negligible upwelling of the isotherms. Such a value is extremely high for lower crustal rocks, especially if there are considered as mafic, as suggested by the high seismic P-velocities values (e.g. Mjelde et al. 2005).

Finally, we compared our modelled surface heat flow values with published data (Figure 14.3). Although much care has to be taken here, especially with marine heat flow data (see discussion in Ritter et al. 2004), surface heat flow seems to increase oceanwards from the middle of the study area. Heat flow values predicted by model A are in reasonable agreement with data in the eastern to the central part of the margin but seem to underestimate measured values near the OCT. Nevertheless, the main and clear result from this modelling exercise is that model B, the most satisfactory one in terms of fitting Curie temperature depths as determined from spectral analysis, clearly overestimates by 15 to more than 20 mW/m^2 measured heat flow values. In brief, near the coastline Curie depths estimated by spectral analysis can be reasonably correlated to crustal temperatures ranging from 400 to 600°C, but at the OCT, the modelling and the data at hand demonstrate that the determined depth estimates from the spectral method do not reflect the thermal state of the crust.

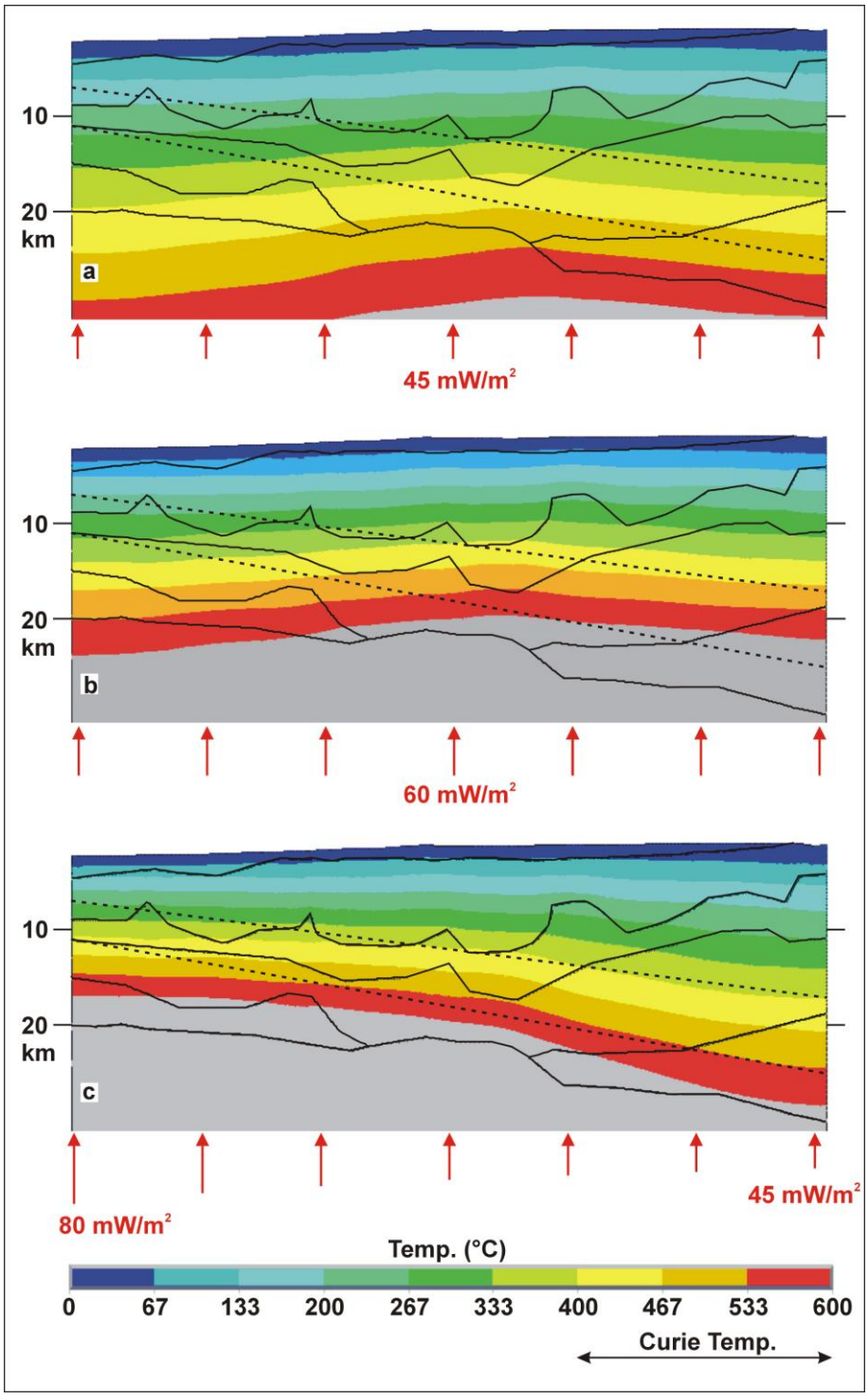

Figure 14.2. Modelled isotherms in function of basal heat flow. Dashed lines represent the uppermost and lowermost estimates for Curie depths as derived from the spectral analysis (Figure 3). Model parameters are given in Table14. 2.

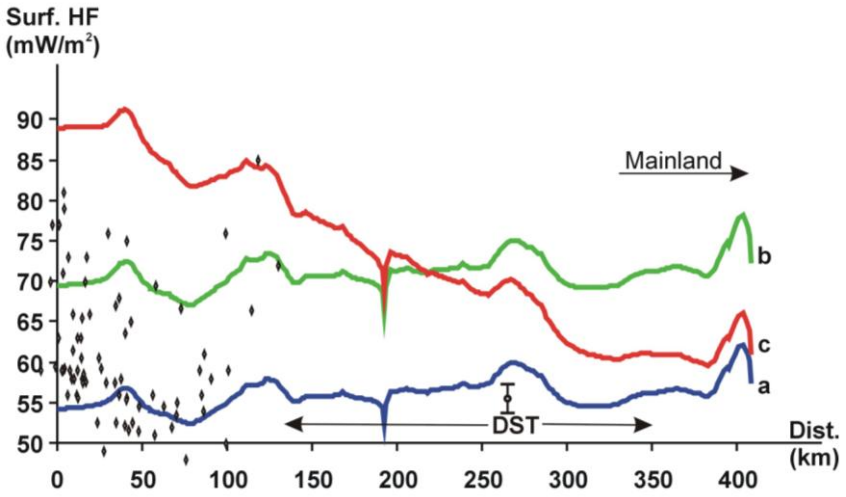

Figure 14.3. Modelled surface heat flow. a, b, and c correspond to model cases depicted in Figure 6. Diamonds represent marine heat flow measurements from Haenel (1974), Sundvor et al. (1989) and Ritter et al. (2004) projected on the modelled line. Mean heat flow and its associated standard deviation from borehole temperature data (DST) are from Ritter et al. (2004), the arrows show the approximate spatial coverage of the wells.

14.3 Discussion

The thermal model in Figure 14.2 show along a transect the geometry of the 3 D model and the spectral estimates for the deepest magnetic source. For the transect the depth estimates for the bottom of the magnetic sources are around 10 km in the oceanic domain and 18 km depth in the continental domain. These depth estimates are located in the lower crust and show an apparent correlation with the border between the lower (Precambrian) basement and the underlying lower crust below the Trøndelag Platform and between upper and lower basement on the outer Vøring margin. A correlation between estimated Curie depth and modelled isotherms appears near the Norwegian coastline but this good fit is difficult to obtain at the ocean-continent transition as previously suggested by Gernigon et al. (2006). On the oceanic domain the depth solution are not modelled in any detail but should be around 40 km depth according the classic half plate cooling model of Parsons and Sclater (1977).

In our interpretation, the main magnetic signature of the mid-Norwegian margin is related to the changing geometry of the basement. Consequently, the bottom of the magnetic sources is controlled by the structure of the margin and not everywhere its thermal state. We therefore suggest that that the Curie temperature depths cannot be easily derived from magnetic data. Clearly, in areas with a large sedimentary overburden, larger windows must be used to estimate the bottom of magnetic sources, which is increasing the uncertainty of the results. Using only depth estimates from the power spectrum method, it is further difficult to distinguish between a thermal and structural control of the deepest magnetic sources.

Another important point is the implication of our study for the thermal state of the mid-Norwegian margin. Fichler et al. (1999) explained the observed discrepancy between the gravity and magnetic patterns by a high thermal gradient. They state that if a shelf-type isotherm is assumed, the magnetic data covering the Vøring Basin would be expected to show the topography of the basement and intra-crustal inhomogeneities within the upper crust, placing the lower boundary of the magnetic crust, i.e. the Curie isotherm, at a depth of approximately 20 km beneath the Halten Terrace and at a depth of 13 km in the western Vøring Plateau (Fichler et al. 1999). This restricts the magnetic sources to the uppermost part of the basement as the depths to the top of the basement are close to the depths of the Curie isotherm. Consequently, this would explain the low magnetic amplitudes. However, the high thermal gradient they used is only valid for the uppermost sediments, related to their relatively low thermal conductivity and cannot be reasonably extrapolated downwards, as previously suggested by Gernigon et al. (2004, 2006). Fichler et al. (1999) did, however, also open for an explanation where the basement rocks have very low magnetic attributes, and that a normal shelf-type thermal gradient could be applicable.

Applying a "normal" thermal gradient, and thus a depth to the Curie isotherms in the lower crust or upper mantle, a model featuring a distinct boundary between the upper and lower basement can easily explain the observed potential field signatures. In our interpretation, the lower high-magnetic basement is looses its influence on the magnetic field solely by the increased depth and the flat-lying contrast to the upper basement, due to the high dependency of the magnetic field to the source distance. This interpretation appears to be reasonable, even if the confidence in the depth estimates of the boundary is less than for the upper basement due to the large variability of magnetic properties and the small density contrast at the boundary.

With increasing depth, the influence of the lower (Precambrian) basement on the magnetic anomalies decreases. Furthermore, the contact between the upper and lower basement becomes flat on the outer Vøring margin, but can be traced below the Trøndelag platform where it culminates in the core complexes. These core complexes cause the most prominent anomalies on the mid-Norwegian margin and their distribution is controlled by the late-Caledonian bounding detachments, which can be linked from onshore Norway (Olesen et al. 2002, Ebbing et al. 2006).

Along the platform boundaries, the normal configuration of the lower basement can be observed, with the superposition of Mesozoic structures on the late-Caledonian configuration (Osmundsen & Ebbing, 2007).

The ambiguity in potential field modelling leaves the possibility of a change in Curie temperature depth along the margin. However, our thermal modeling showed that a high thermal gradient would be expressed by a larger surface heat-flow than measured. However, heat-flow measurements on the mid-Norwegian margin are concentrated on the Vøring Basin and show large variations (Sundvor, Myhre and Eldholm 1989; Ritter et al. 2004). Comparison between structural and thermal modelling confirms our interpretation that the observed magnetic field on the mid-Norwegian margin does not reflect the Curie temperature depth as previously assumed, but the geometry of the basement and lower crust. Further evidence against a high-thermal gradient comes from thermal modelling based on structural models of the margin.

14.4 Conclusion

Depth estimates by spectral methods indicate a shallowing of deepest magnetic sources from the Norwegian coast towards the outer Vøring margin. Thermal modelling assuming a high thermal gradient, under the assumption that spectral estimates represent the Curie isotherms, leads to unreasonable surface heat-flow values on the outer Vøring margin. The combined interpretation of gravity and magnetic allows to identify the crustal structure on the Norwegian passive margin. In combination with seismic data potential field models can be used to identify the top of the basement, even at large depths, as well as the deep crustal configuration. The integrated interpretation of all the different methods presented in this study, makes us conclude that the relatively magnetic quietness on the outer Vøring margin is mainly related to the deep and thin, high-magnetic lower 'Precambrian' basement. The 3D model shows that the lower basement is a key source for the potential field signals on the mid-Norwegian margin, and especially on the Trøndelag Platform. The changes in the magnetic anomaly pattern from the Trøndelag Platform to the Vøring Basins and the discrepancy between gravity and magnetic anomaly patterns on the outer Vøring margin are likely to have a structural, and not a thermal, explanation.

15 3D THERMAL MODELLING OF THE HELGELAND BASIN AREA

Christophe Pascal & Jörg Ebbing, NGU

15.1 Introduction

The final objective of the KONTIKI Project is to use all the thermal data collected onshore together with basement models derived from potential field studies in order to achieve 3D thermal modelling of the mid Norwegian Margin. In this chapter we present the results of such a modelling attempt in the Helgeland Basin area (Fig. 14.1). The main objective of the present investigation is to quantify the amount of heat flowing from the basement to the sedimentary basins and its spatial distribution in 3D.

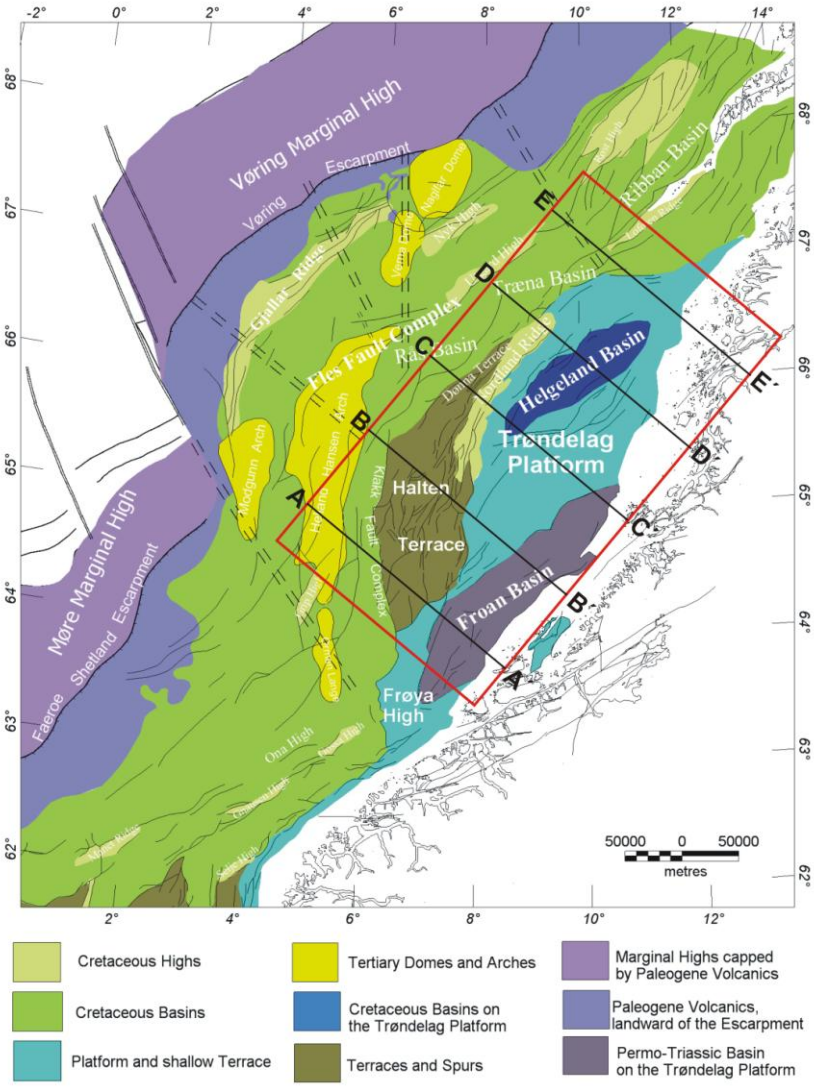

Figure 15.1. Main structural elements of the mid-Norwegian Margin (after Blystad et al. 1995). The red frame indicates the modelled area. Black lines represent model sections.

15.2 Modelling strategy

3D thermal modelling was carried out using finite-element methods. The 3D approach adopted here is fully justified by the structural complexity of the Norwegian Margin and, in particular, its dramatic along-strike variations.

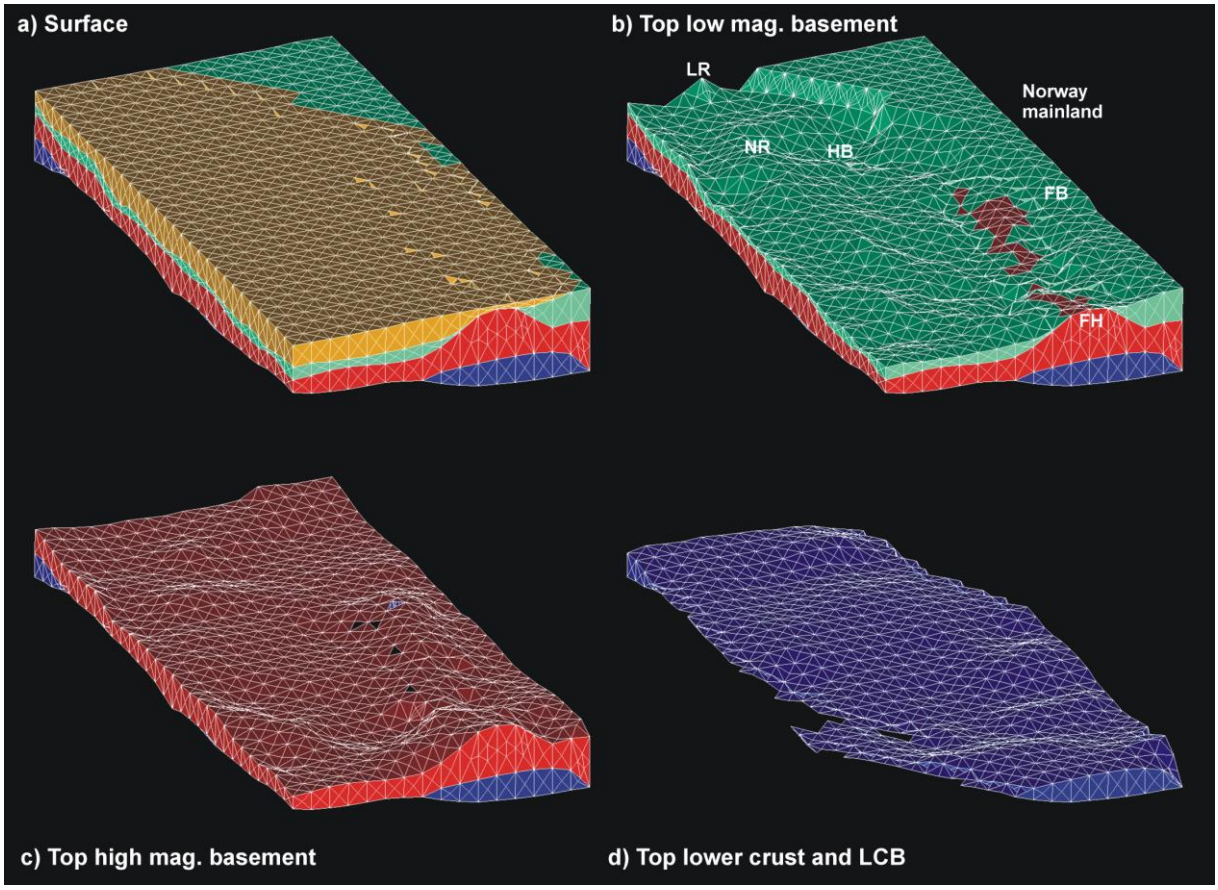

Figure 15.2. Geometry of the four layers involved in the 3D numerical model: (1) sedimentary rocks (orange), (2) low-magnetic basement (green), (3) high-magnetic basement (red) and (4) the high-density lower crust and LCB (blue). Horizontal dimensions are 230 x 430 km and maximum Moho depth is ~30 km. LR, Lofoten Ridge, HB, Helgeland Basin, NR, Nordland Ridge, FB, Froan Basin, FH, Frøya High. View due to the NNE.

The geometry of the model was constrained by 3D potential field modelling of the Norwegian Margin that, in turn, was calibrated by seismic experiments (Ebbing et al., Chapter 11 in the present report). The geometry of the modelled 3D block (Figs. 15.1 & 15.2) has been simplified in order to keep the main features influencing the medium to long-wavelength (i.e. ~10 to ~100 km) thermal field. These main features, which are also the best resolved by potential field data

are from top to bottom: (1) the sedimentary rocks (2) the low-magnetic basement (Caledonian mainly), (3) the high-magnetic basement (Precambrian) and (4) the high-density lower crust including the LCB. Typical horizontal dimensions of the model are 230 x 430 km and maximum Moho depth is ~30 km. The used finite-element mesh involves ~100 000 10-noded tetrahedral thermal elements with horizontal and vertical lengths by ~10 km and from ~100 m to ~1 km respectively. Thermal calculations were done using the full 3D development of the steady-state Fourier's law and including variations in heat generation and thermal conductivity between the four modelled layers. Boundary conditions are T = 0°C at the surface of the model, no heat escape from its lateral boundaries and fixed heat flow at its base. The modelling approach adopted here is similar to the one presented in Pascal et al. (2007).

15.3 Data and constrains

As explained above, the physics involved in the modelling are relatively simple and only two sets of parameters, representing material properties, are needed: thermal conductivities and heat generations. Thermal conductivities for the basement units, including the lower crust and the LCB, were fixed to standard values (Table 15.1). Those values remain in agreement with the results from thermal conductivity measurements carried out on basement samples form Norway (Midttømme et al., Chapter 6 in the present report) but, more important, those values are deemed to represent an average thermal behaviour of the basement units considered in the present study. Sediment conductivity was set to a relatively low value (i.e. 1.5 W/m/K, Table 15.1). This value is of course not representative of all the sedimentary layers but, again, aims to represent an average value for the whole sedimentary pile and also accounts for the unconsolidated and very low conductive Plio-Pleistocene wedges.

Table 15.1. Parameters used in the thermal modelling.

Layer	k (W/m/K)	A_0 ($\mu W/m^3$)
Sediments	1.5	0.5
Low mag. basement	2.5	1.7
High mag. basement	2.5	1.2
Lower crust and LCB	3.5	0.1

Heat generation values for the low and high magnetic basement were adapted from the geochemical analyses on numerous basement samples of Norway carried out during the Lito and Kontiki projects (Slagstad et al., Chapter 2 in the present report). These suggest higher heat production in Caledonian rocks (i.e. mainly low magnetic) than in Precambrian ones (i.e. mainly high magnetic). In agreement with previous studies heat generation in the lower crust is low (e.g. Heier and Adams 1965). Heat generation for the sedimentary rocks was also set to relatively low values (Rybach 1986).

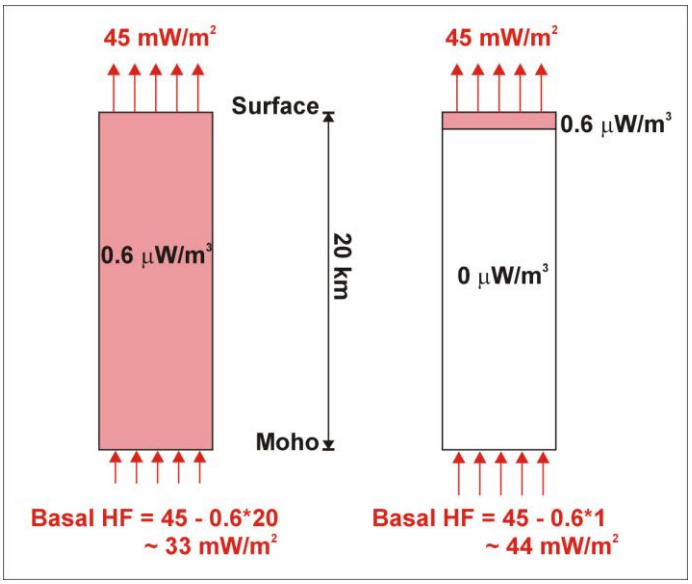

Figure 15.3. Two end-member models for estimating basal heat flow at the location of the Leknes drillhole: heat-generating elements are distributed uniformly in the crust or concentrated at very shallow levels (see text).

The applied basal heat flow value has a strong impact on modelling results. Heat flow determinations carried out in the framework of the KONTIKI Project show that corrected onshore heat flow values range from 45 to 66 mW/m^2 at sites located close to the Mid-Norwegian Margin (i.e. Aure and Løkken, Slagstad et al., Chapter 7 in the present report, and Leknes, Drag and Sulitjelma, Pascal et al., Chapter 8 in the present report), if the relatively high and uncertain value found for Bleikvassli is excluded. Those heat flow values are the result of two components, one being stable at wavelengths in the order of 100 km (the basal or Moho heat flow) the second one being dependent on the local crustal structure are explaining the observed variability. Among our heat flow sites, the Leknes site offers a unique and previously unexpected chance to get decent estimates on the basal heat flow value to be applied in the modelling. This is because: (1) the measured heat flow in the well was found remarkably stable (Pascal et al., Chapter 8 in the present report), (2) measured heat generation in the Lofoten AMCG complex is very low (i.e. ~0.6 μW/m^3 Slagstad et al., Chapter 2 in the present report) and is reasonably expected to further decrease at depth and (3) the crust of the Lofoten Islands is anomalously thin (i.e. ~20 km, Olesen et al. 2002), further reducing the error in estimating Moho heat flow. The reasoning is the following (Fig. 15.3). Assuming that the average heat production value found for the Lofoten AMCG complex is representative of the whole crust from the surface down to the Moho, the lowermost bound for the basal heat flow would be ~33 mW/m^2. Conversely, assuming that heat production decays very fast through depth and reaches zero below ~800 m depth (i.e. below the deepest level reached by the Leknes drillhole where the corresponding gamma log shows almost

constant radioactivity from top to bottom, Elvebakk and Rønning, this report), the uppermost bound for the basal heat flow would be ~44 mW/m^2. This latter value is of course largely overestimated. In the modelling we tested 30 and 40 mW/m^2 as basal heat flow values.

15.4 Modelling results

The main objective of the modelling was to quantify the amount of heat flowing from the basement into the sedimentary basins and its 3D distribution in the modelled area. The results obtained using a basal heat flow of 30 mW/m^2 and the parameters listed in Table 15.1 are shown in Fig. 15.4.

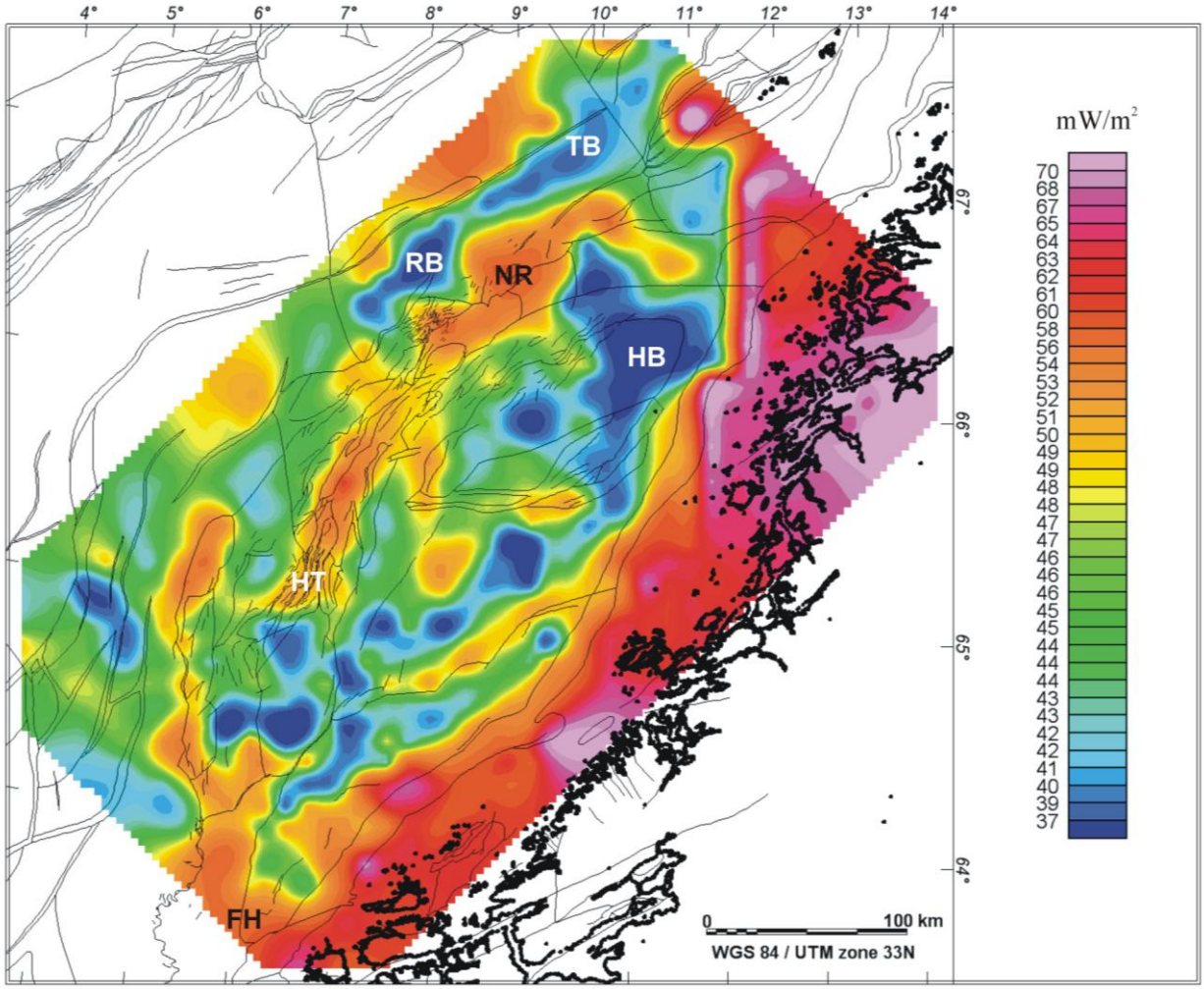

Figure 15.4. Modelled heat flow distribution at top basement depths. Basal heat flow is 30 mW/m^2 other parameters are given in Table 15.1. Structural outline from NPD (Blystad et al. 1995). TB, Træna Basin, RB, Rås Basin, HB, Helgeland Basin, NR, Nordland Ridge, HT, Halten Terrace, FH, Frøya High. Note that heat flow in mainland Norway is overestimated (see text).

The most interesting result consists in the simulated heat flow variations. We see that basement highs are associated with high heat flow (e.g. Nordland Ridge) whereas very thick basins are characterised by low heat flow (e.g. Helgeland Basin). This significant contrast (i.e. locally more than 20 mW/m^2, Fig. 15.4) is due to low heat production in the sedimentary rocks with respect to basement, in conjunction with extreme attenuation of the basement below the deep basins. This result is also in agreement with marine heat flow measurements farther to the west in the Vøring Basin, where Ritter et al. (2004) remarked that the lowest values were mainly found above the deep sedimentary basins.

Simulated heat flow values at top basement levels range here in between ~35 to more than 70 mW/m^2. Note that the simulated heat flow pattern remains basically unchanged if we apply a value of 40 mW/m^2 for the basal heat flow, the absolute heat flow values being simply increased by 10 mW/m^2. Modelled values for mainland Norway appear to be overestimated, in particular at the northeastern corner of the modelled area (Fig. 15.4). This is because our crustal model is poorly constrained there and that the high magnetic basement was assumed to reach Moho depths. As an implication the whole crust has, in the model, a heat generation value equal or higher than 1.2 $\mu W/m^3$ (instead of dropping to ~0.1 $\mu W/m^3$ at great depths) that results in too high heat flow values at the surface. This model artefact has no significant impact on the results obtained in the offshore. There, modelled heat flow values at the location of the basement highs seem to be in reasonable agreement with previous heat flow measurements (Ritter et al. 2004). In contrast, our modelled heat flow values for the sedimentary basins and, in particular, for the Helgeland Basin, are lower by 20 mW/m^2 than previously proposed values (Ritter et al. 2004). It is however worth noting that the wells used by Ritter et al. (2004) are not located in the Helgeland Basin itself but on basement highs and projected on their modelled section.

Modelled thermal gradients for five representative sections across the 3D model and for the two basal heat flow values are shown in Fig. 15.5. Before further commenting the results of the modelling, we need to emphasise its limitations when simulating geothermal gradients. A major one comes from the assumption of a constant conductivity value for the whole sedimentary pile, where it is expected to increase at great depths at least because of porosity loss and eventually because metamorphic phase changes near the bottom of the deepest basins.

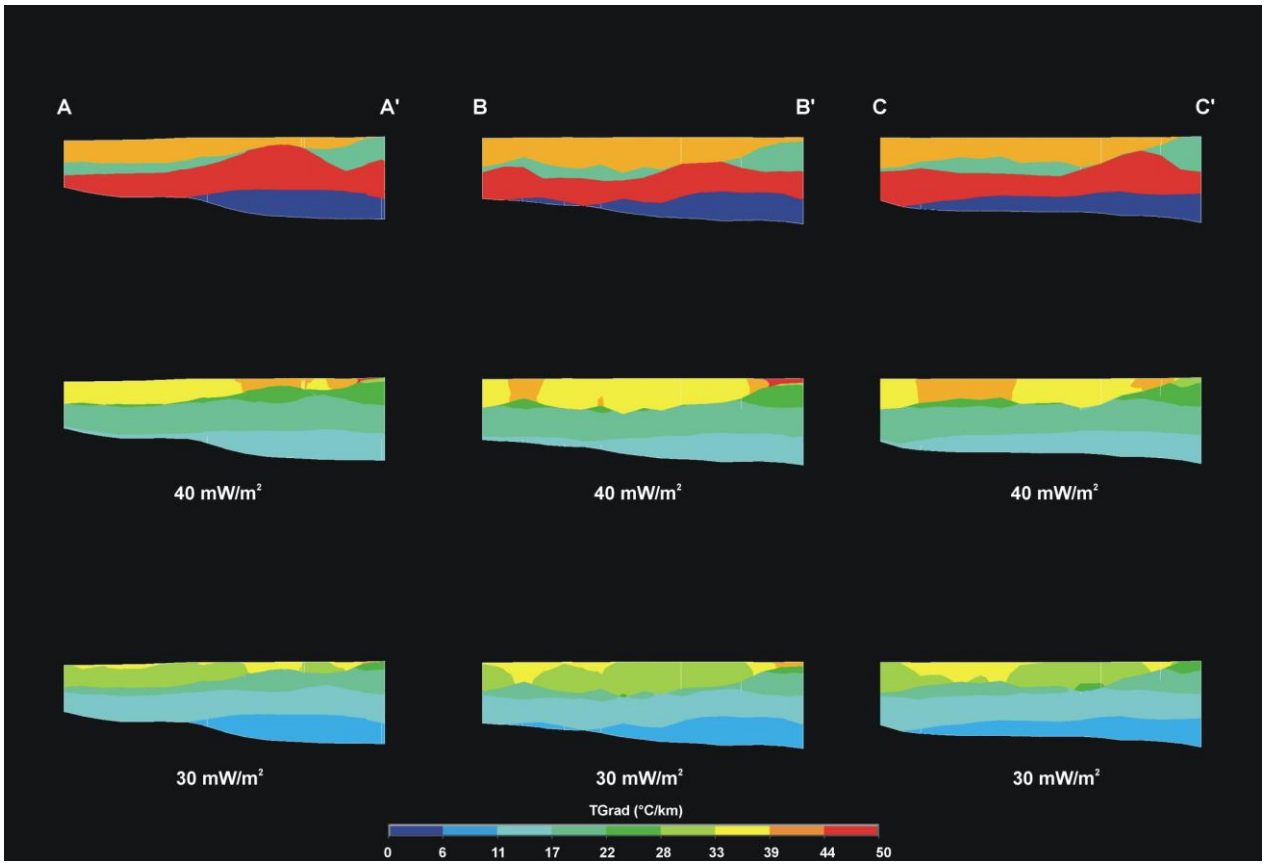

Figure 15.5. Modelled thermal gradients along five sections of the 3D model (see Fig. 15.1 for locations). Upper panel: crustal structure, color codes are similar to Fig. 15.2. Middle and lower panels depict thermal gradients calculated for basal heat flows equal to 40 mW/m^2 and 30 mW/m^2 respectively.

Bearing this in mind, the modelled gradients shown in Fig. 15.5 are obviously overestimated for the deepest levels of the deepest basins and should only be used as primary estimates at relatively shallow depths (i.e. down to 3-4 km depth), which are the focus here. The modelled sediment conductivity value (i.e. 1.5 W/m/K) was indeed meant to represent a gross average value in between the unconsolidated Plio-Pleistocene deposits (with characteristic conductivity values down to ~1 W/m/K) and the immediately underlying Mesozoic and Tertiary sedimentary rocks (with typical values up to ~2 W/m/K, Midttømme 1997). Nevertheless the modelling results emphasise the role played by the nature and structure of the basement on the thermal state of the sedimentary basins. Thermal gradients are, as normally expected, higher in sedimentary rocks than in the basement, the lowest ones being found in the lower crust/LCB. This is an effect of the decrease in thermal conductivity from the base to the top of the crust but also of the increase in heat flow when travelling upwards, radiogenic heat sources in the basement adding their input to the applied heat flow at the Moho. The clear feature that emerges from Fig. 15.5 is that

temperature gradients, like heat flow values (Fig. 15.4), are systematically increased above basement highs. Conversely, the lowest gradients in the sedimentary basins are found where the basement has been drastically attenuated by rifting (e.g. sections BB' and DD', Fig. 15.5).

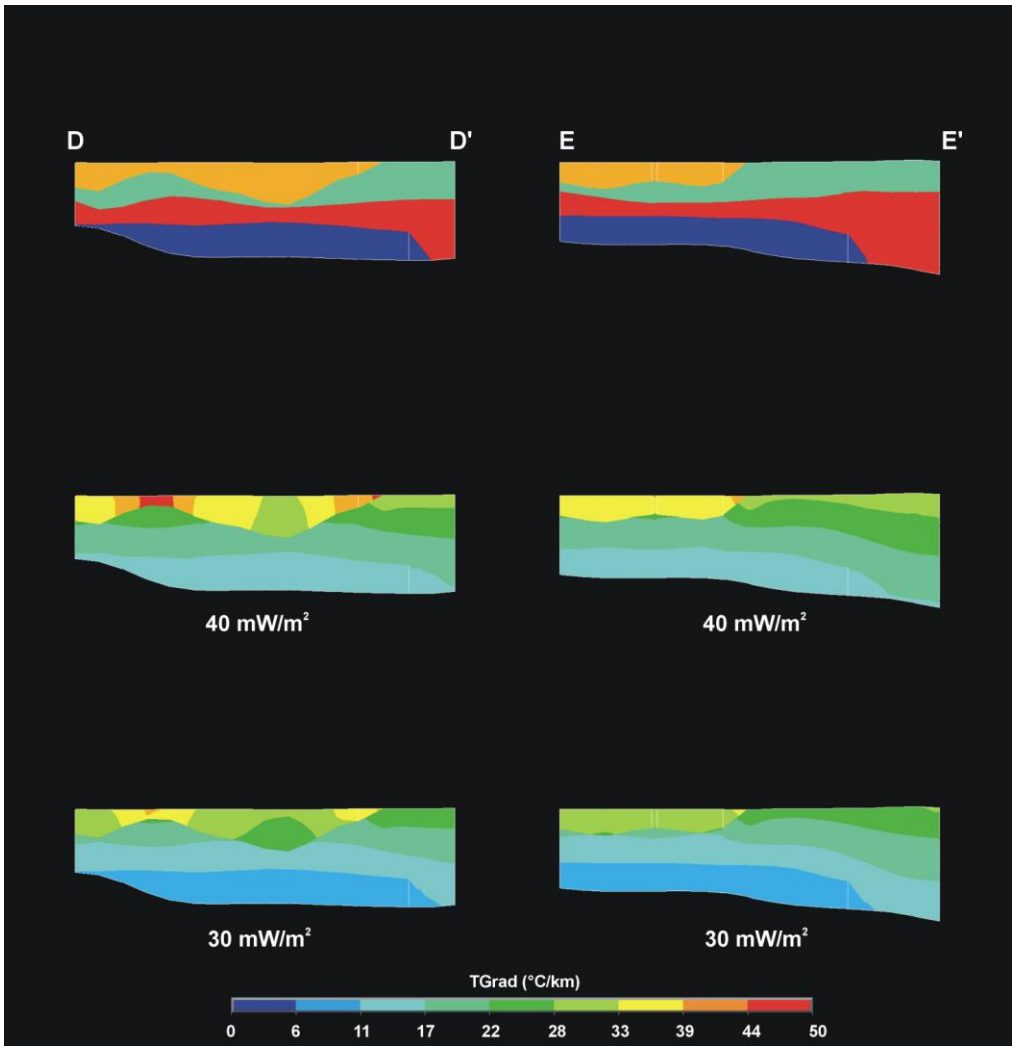

Figure 15.5. Continued.

In detail, modelled temperature gradients in the sedimentary rocks and at shallow depths range from ~31 to ~47°C/km and ~28 to ~40°C/km for applied basal heat flow values equal to 40 mW/m^2 and 30 mW/m^2 respectively. A tentative comparison between our results and measured actual gradients (Fig. 15.6) is problematic. There are at least two main reasons that renders the comparison difficult: (1) the used database is by nature geographically biased towards basement highs and (2) the measured gradients show very short-wavelength variations that are probably caused by very local effects (e.g. fluid circulations, abrupt changes in thermal conductivities, etc) and/or related to perturbations caused by the drilling activities (e.g. cooling by drilling mud,

forced water convection by logging operations, etc.). It is, however, interesting to note that most measured gradients on the basement highs fall in the range between 32 to 40 °C/km in reasonable agreement with the modelling results obtained using 30 mW/m^2 as basal heat flow value.

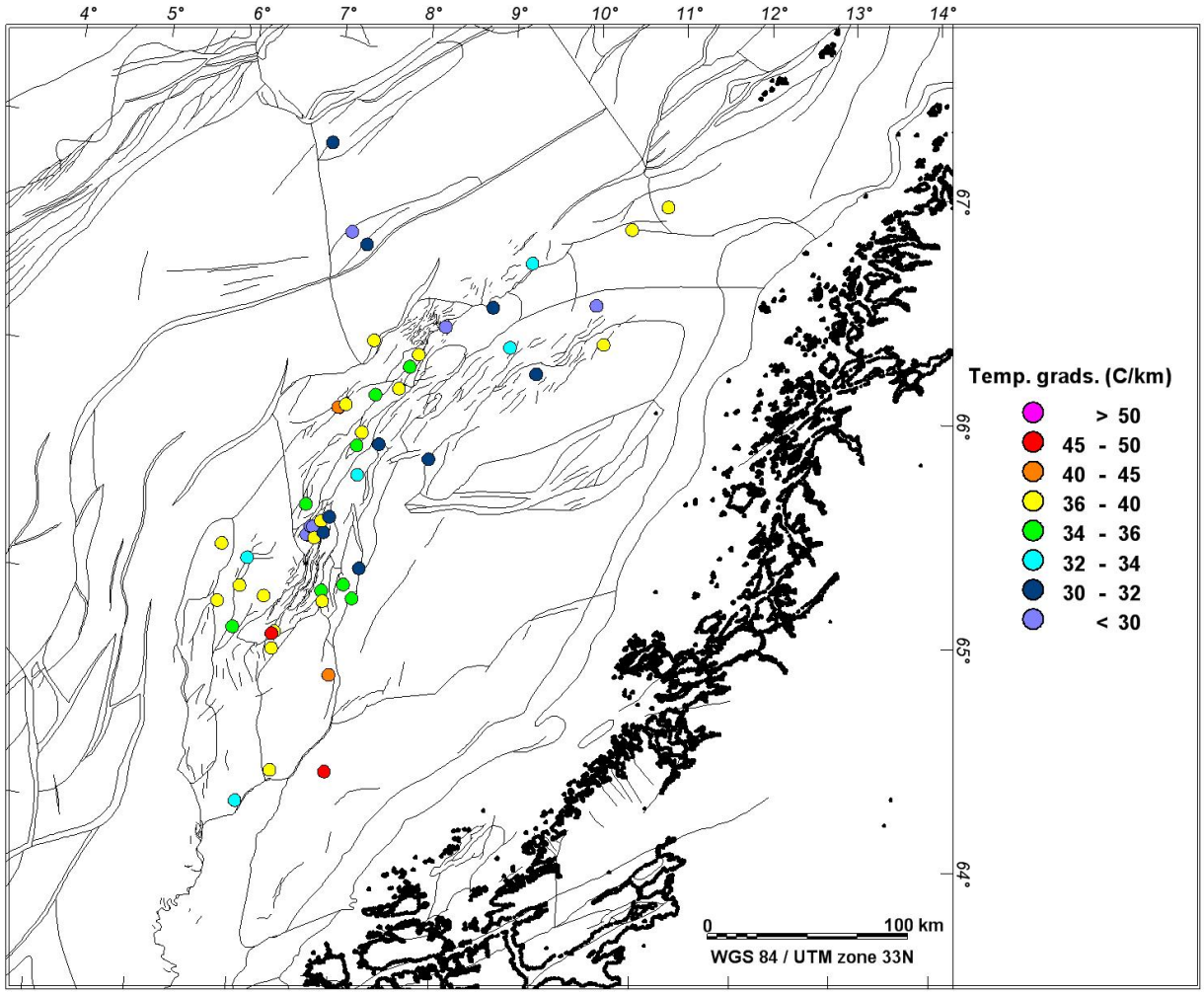

Figure 15.6. Measured thermal gradients in exploration drillholes (StatoilHydro in-house database).

15.5 Conclusions and recommendations

Our 3D modelling suggests that drastic heat flow variations occur at the base of the sedimentary basins in the inner parts of the mid-Norwegian Margin. We showed that the structure and nature of the basement underlying these basins are the most likely factors influencing heat flow variations at typical wavelengths of 10s to 100s of km. One of the major outcomes of the modelling and the heat flow and heat production data collected on land, is that the Moho heat flow should range in between 30 to 40 mW/m^2, a value close to the lowermost bound being our preferred one.

Calibration of the model using available temperature data from the wells offshore is difficult. One of the reasons for that is the lack of thermal conductivity data from the wells that would eventually provide estimates on actual heat flow values that could, in turn, be compared to our modelled values. Nevertheless, the main lesson to be learnt from the present study is that, in order to provide more realistic results, basin models need to take into account the heat flow variability that arises from the structure of the basement.

16 HEAT FLOW MAP OF NORWAY

Kontiki working group

The heat flow map of Norway (Fig. 16.1) was built on the basis of the measurements made in the course of the Kontiki project. In this map we gave more priority to the quality of the data rather than to their quantity and therefore excluded previously acquired heat flow measurements. After careful checking we retained 11 heat flow sites (Table 16.1), excluding Arnestad, Bleikvassli and Lærdal where heat flow determinations were of poor quality (Chapters 7 & 8 in the present report). We also added three reliable heat flow measurements from Sweden but close to the Norwegian territory (Parasnis 1975, 1982). Finally, in order to extend the map to the Norwegian margin, we attached to the spreading anomaly 24 a heat flow value of 65 mW/m^2, in agreement with values measured on oceanic crusts of similar age (Stein & Abbot 1991). The compiled data were interpolated using a kriging technique with an exponential model and a typical grid size of 100 km.

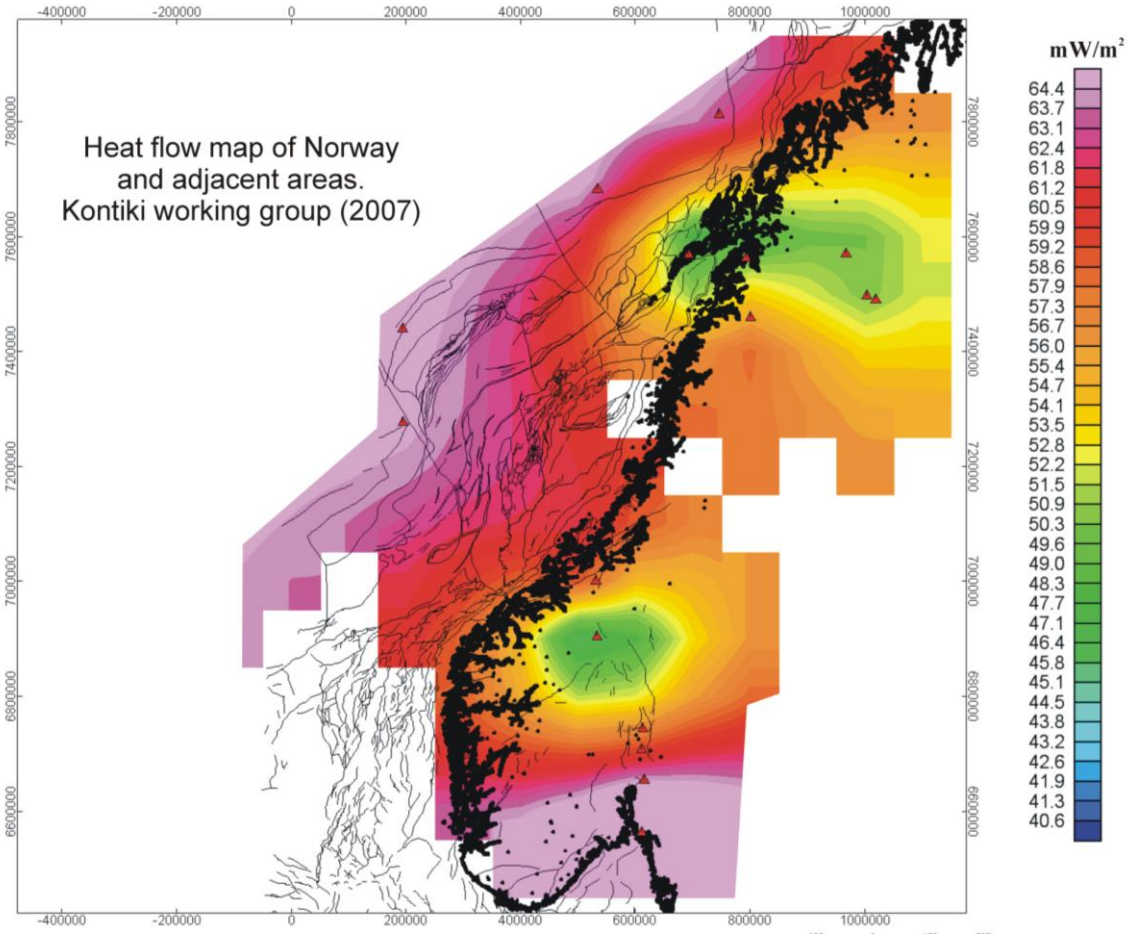

Figure 16.1. Heat flow map of Norway and adjacent areas. Data used (red triangles for location) are given in Table 16.1. Structural outline is from NPD.

The new heat flow map shows that heat flow values in Norway are much higher than proposed on previous releases (Fig. 16.2). The two most robust features on the map are the relatively high and low heat flows in the Oslo Region and Nordland respectively. For both regions the number of available determinations strengthens the reliability of the simulated pattern. Noteworthy, low heat flow values in central southern Norway depend on only one determination (i.e. at Hjerkinn). The heat flow pattern becomes far more uncertain in southwestern Norway where there are no data points. A moderate increase in heat flow values from the coastline to the ocean-continent transition is suggested for the Vøring Margin (i.e. ~5 mW/m^2). The increase is sharper for the Lofoten Margin (i.e. ~20 mW/m^2), where heat flow values are definitively low onland and the margin is thin. The present map is expected to be improved when the results from the HeatBar Project will be made available.

Table 16.1 Data used to construct the heat flow map.

Site	UTM32N (WGS84)	Heat flow (mW/m^2)
Berger	615271 6654660	49
Løkken	530797 7001453	57
Hjerkinn	532846 6904727	42
Aure	486454 7031460	66
Hamar	612540 6744160	58
Hurdal	610379 6707593	73
Fredrikstad	610104 6563857	73
Sulitjelma	800563 7459972	59
Drag	792580 7563653	47
Leknes	692574 7568570	45
Aitik [1]	1018777 7490911	50
Malmberget [2]	1002768 7497388	51
Kiruna [2]	966672 7570269	49
Anomaly 24 [3]		65

[1] Parasnis (1975), [2] Parasnis (1982), [3] inferred from Stein and Abbot (1991).

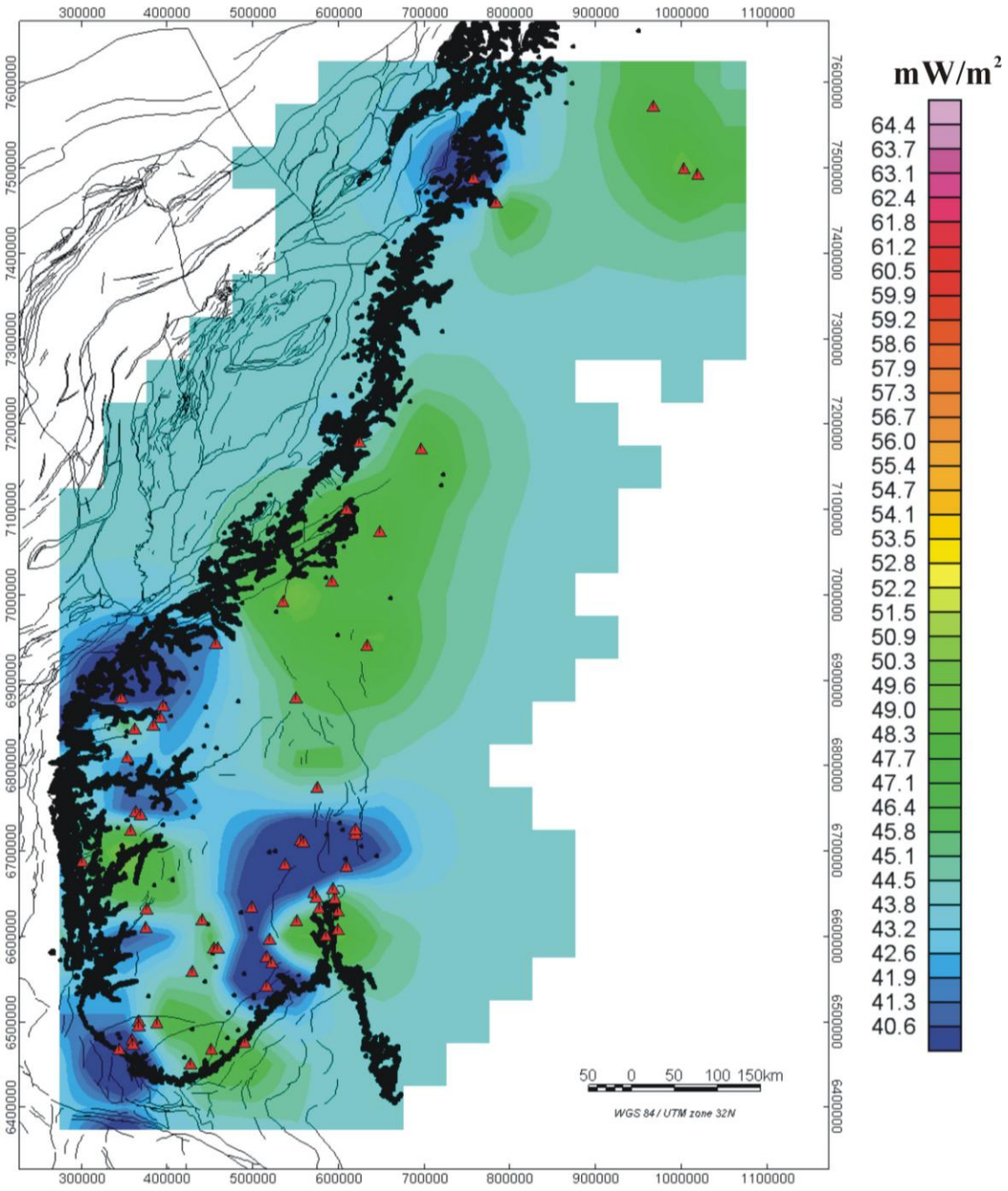

Figure 16.2. Heat flow map of Norway and adjacent areas based on pre-Kontiki data. Data used (red triangles for location) are from Hänel et al. (1974), Swanberg et al. (1974), Parasnis (1975, 1982), Grønlie et al. (1977) and Hänel et al. (1979). The procedure to build the map is similar to the one used for Fig.16.1 except that the grid size is here 50 km. Structural outline is from NPD.

17 CONCLUSIONS

1. A compilation of c. 4000 new and old geochemical data is used to produce the first map of radiogenic heat production in bedrock, covering large tracts of Norway. In general, granitic rocks have higher heat production than intermediate and mafic rocks. Sedimentary rocks display variation in heat production that can be ascribed to sedimentary processes. Age and metamorphic grade do not appear to affect heat production significantly, whereas tectonic setting appears to impart some effect in that extensional or within-plate rocks have higher heat production than similar rocks formed along constructive plate margins.

2. A total of 11 deep wells (c. 350-1000 m) have been established for temperature logging and heat flow calculations in mainland Norway. Calculated palaeoclimatic corrections range from +2 to +9 mW/m² (i.e. 5-20% of original heat flow values).

3. A new heat flow map of Norway shows that heat flow values are much higher than proposed on previous overview maps. The two most robust features on the map are the relatively high and low heat flows in the Oslo Region and Nordland, respectively.

4. New geochronological data from basement samples from the North Sea and Norwegian Sea show that the upper basement to a large degree consists of magmatic and metasedimentary rocks that can be correlated with rocks in tectonostratigraphically high (i.e. the Upper and Uppermost Allochthons) nappes within the Scandinavian Caledonides.

5. The first compilations of depth to crystalline basement maps for the entire Norwegian continental shelf and depth to Precambrian basement maps for all of mainland Norway have been produced. The data have been used in the present thermal modelling and will also constitute important constraints in future modelling projects. The maximum depths to crystalline basement (> 12 km) occur along the outer continental margin (i.e. the Møre, Vøring and Sørvestsnaget basins).

6. The combined interpretation of gravity and magnetic data allows us to identify the crustal structure on the Mid-Norwegian passive margin. In combination with seismic data, potential field models can be used to identify the deep crustal configuration. A 3D crustal model could consequently be produced from the Mid-Norwegain continental margin.

7. A 3D thermal modelling based on the 3D crustal model and heat production data from mainland Norway has been carried out for the Mid-Norwegian continental margin. Our 3D modelling suggests that substantial heat flow variations between 35 and 65 mW/m² occur at the base of the sedimentary basins in the inner parts of the mid-Norwegian Margin. The map of the modelled heat flow shows that the structure and nature of the basement underlying these basins are the most likely factors influencing heat flow variations at typical wavelengths of 10s to 100s of km.

8. Depth estimates by spectral methods indicate a shallowing of deepest magnetic sources from the Norwegian coast towards the outer Vøring margin. Thermal modelling assuming a high thermal gradient, under the assumption that spectral estimates represent the Curie isotherms, leads to unreasonable surface heat-flow values on the outer Vøring margin.

9. The integrated interpretation makes us conclude that the relatively magnetic quietness on the outer Vøring margin is mainly related to the deep and thin, high-magnetic lower 'Precambrian' basement. The changes in the magnetic anomaly pattern from the Trøndelag Platform to the Vøring Basins and the discrepancy between gravity and magnetic anomaly patterns on the outer Vøring margin are likely to have a structural, and not a thermal, explanation.

10. The modelling and the heat flow and heat production data collected on land indicate that the Moho heat flow ranges in between 30 to 40 mW/m^2 in the Nordland area, a value close to the lowermost bound being our preferred one.

11. The temperature of the outer Mid-Norwegian margin is lower than previously assumed and the petroleum potential of the area should be reconsidered.

12. The Central Scandinavia thermal modelling is indicating that the granitoids of the TIB are only present in the upper crust or are less heat-productive with increasing burial depth. However, the TIB is clearly influencing the isostatic state of the Scandinavian mountains, especially for the northern and central part, and might be related to the Neogene uplift of the Scandinavian mountains.

13. The modelled moderate and short-wavelength variations in surface heat flow within the Oslo Rift are mainly the result of the different lithological units at relatively shallow depths. The heat-productive rocks are not buried below thick sedimentary rocks and therefore the near-surface structures control the observed heat flow. The influence of deep crustal intrusive rocks is less important.

18 OUTLOOK AND RECOMMENDATION FOR FURTHER WORK

There is a need to extend the mapping of heat flow in Norway, both offshore and onshore. Onshore data can be acquired by temperature logging of other existing deep bore holes (e.g. at Ullandhaug in Stavanger and at Evje in the southernmost Norway). In other areas new bore holes have to be established. A new bore hole is for instance planned in the Kautokeino-Karasjok area in Finnmark within the frame of the HeatBar Petromaks Project. Several new bore holes are also drilled in Norway at the moment because of the high metal prices leading to substantial exploration for new mineral deposits. NGU should make sure that deep bore holes are utilised for heat flow measurements.

The reliability of the oceanic heat flow values is still uncertain. We could, however, produce good estimates of the mantle heat flow by acquiring new heat flow data on oceanic crust in the Lofoten Basin. The heat production in the oceanic crust is close to zero.

The KONTIKI Project has shown that thermal modelling of 3D crustal models can provide estimates of the heat flow into sedimentary basins. Such data-sets are important when evaluating the petroleum potential in frontier exploration areas. Similar work is now carried out in the Barents Sea Region within the Petromaks HeatBar Project. There is also a need for similar datasets in frontier areas in the North Sea such as the Egersund, Stord and Farsund basins. The petroleum potential in these areas is not well constrained at the moment.

Acknowledgement

This study was funded by StatoilHydro ASA. Øyvind Steen has carefully followed up the Kontiki Project on behalf of the sponsor. Arne Bjørlykke, NGU and Per Arne Bjørkum, StatoilHydro initiated the project. We are also thankful to Jan Ove Hansen, Kjell Olaf Hartvigsen, Tormod Henningsen, Oddbjørn Kløvjan, Hallstein Lie, Peter Midbøe & Jan Erik Skeie (all at StatoilHydro) for their support and the helpful discussions. The NGU laboratory provided a large number of high-quality analysis to the KONTIKI Project. We are especially grateful to Ilmo Kukkonen at the Geological Survey of Finland (GTK) for providing assistance with the calibration of the thermal conductivity measurements and the temperature logging and to Rolf Mjelde at the University of Bergen (UiB), who provided results of the OBS modelling before publication.

19 REFERENCES

Åhäll, K.-I. & Larson, S.Å. 2000: Growth-related 1.85-1.55 Ga magmatism in the Baltic Shield; a review addressing the tectonic characteristics of Svecofennian, TIB 1-related and Gothian events. Geologiska Föreningen i Stockholm Förhandlingar, 122: 193-206.

Åhäll, K.-I. & Gower, C. F. 1997: The Gothian and Labradorian orogens: Variations in accretionary tectonism along a late Paleoproterozoic Laurentia-Baltica margin. *Geologiska Föreningen i Stockholm Förhandlingar 119*, 181-191.

Aalstad, I., Åm, K., Håbrekke, H. & Kihle, O. 1977: Aeromagnetic investigations along the Norwegian Geotraverse. In: K.S. Heier (ed.): *The Norwegian Geotraverse Project: A Norwegian contribution to the international upper mantle project and the international geodynamics project.* Geological Survey of Norway (NGU), 77-98.

Abramovitz, T. & Thybo, H. 2000: Seismic images of Caledonian, lithosphere-scale collision structures in the southeastern North Sea along Mona Lisa Profile 2. *Tectonophysics 317*, 27-54.

Afonso, J. C. & Ranalli, G. 2004: Crustal and mantle strengths in continental lithosphere: Is the jelly sandwich model obsolete? *Tectonophysics 394*, 221-232.

Aftalion, M., van Breemen, O. & Johnson, M. R. W. 1979: Age of the Loch Borrolan complex, Assynt, and late movements along the Moine Thrust Zone. *Journal of the Geological Society of London 136*, 489-495.

Andersen, T. B. & Jansen, Ø. J. 1987: The Sunnhordaland Batholith, W. Norway: Regional setting and internal structure, with emphasis on the granitoid plutons. *Norsk Geologisk Tidsskrift 67*, 159-183.

Andersen, T., Andresen, A. & Sylvester, A.G. 2001: Nature and distribution of deep crustal reservoirs in the southwestern part of the Baltic Shield: Evidence from Nd, Sr and Pb isotope data on late Sveconorwegian granites. *Journal of the Geological Society of London 158*, 253-267.

Andersen, B. G. & Borns Jr, H. W. 1994: *The Ice Age World*, Oslo, Scandinavian University Press (Universitetsforlaget AS), 208 pp.

Andersen, B.G. 2000: *Istider i Norge. Landskap formet av istidens breer*, Oslo, Universitetsforlaget, 216 pp.

Andersen, O.B. & Knudsen, P. 1998: *Gravity anomalies derived from the ERS-1 satellite altimetry*. Kort og Matrikelstyrelsen, Copenhagen (**www.kms.dk**).

Anderson, E. M. 1934: Earth contraction and mountain building. *Beitrage zur Geophysik 42*, 133-159.

Andersson, U.B. 1991: Granitoid episodes and mafic-felsic magma interaction in the Svecofennian of the Fennoscandian shield, with main emphasis on the ca. 1.8 Ga plutonics. *Precambrian Research 51*, 127-149.

Anderson, J.L. & Morrison, J. 2005: Ilmenite, magnetite, and peraluminous Mesoproterozoic anorogenic granites of Laurentia and Baltica. *Lithos 80*, 45-60.

Andersson, A., Dahlman, D., Gee, D.G. & Snäll, S. 1985: The Scandinavian alum shales. *Sveriges Geologiska Undersökning Ca 56,* 1-50.

Andreoli, M.A.G., Hart, R.J., Ashwal, L.D. & Coetzee, H. 2006: Correlations between U, Th Content and Metamorphic Grade in the Western Namaqualand Belt, South Africa, with Implications for Radioactive Heating of the Crust. *Journal of Petrology 47,* 1095-1118.

Andréasson, P. G., Gee, D. G., Whitehouse, M. J. & Schöberg, H. 2003: Subduction-flip during Iapetus Ocean closure and Baltica–Laurentia collision, Scandinavian Caledonides. *Terra Nova 15*, 362-369.

Andresen, A., Walker, N. & Hartz, E. H. 1998: U-Pb and $^{40}Ar/^{39}Ar$ isotopic constraints on Caledonian and Grenvillian orogenesis in the Kong Oscar Fjord region. *Rapport Grønlands Geologiske Undersøgelse 46*, 33-34.

Archie, G.E. 1942: The electrical resistivity log as an aid in determining some reservoir characteristics. *Petroleum Technology 5*, 1422 – 1430.

Artemieva I.M. 2003: Lithospheric structure, composition, and thermal regime of the East European craton: Implications for the subsidence of the Russian Platform. *Earth and Planetary Science Letters 213,* 429-444

Artemieva, I.M. & Mooney, W.D. 2001: Thermal thickness and evolution of Precambrian lithosphere: A global study. *Journal of Geophysical Research 106,* 16387-16414.

Ashwal, L.D., Morgan, P., Kelley, S.A. & Percival, J.A. 1987: Heat production in an Archean crustal profile and implications for heat flow and mobilization of heat-producing elements. *Earth and Planetary Science Letters 85*, 439-450.

Assael, M. J., Gialou, K., Kakosimos, K. & Metaxa, I. 2004: Thermal Conductivity of Reference Solid Materials. *International Journal of Thermophysics 25*, 397-408.

Balling, N. 1995: Heat flow and thermal structure of the lithosphere across the Baltic Shield and northern Tornquist Zone. *Tectonophysics 244,* 13-50.

Balling, N.P. & Falkum, T. 1975: A combined geophysical and structural-geological investigation of the Precambrian intrusive Homme granite in south-western Norway. *Geol. Fören. Stockh. Förh. 97,* 338-356.

Balling, N., Kristiansen, J.I., Breiner, N., Poulsen, K.D., Rasmussen, R. & Saxov, S. 1981: Geothermal Measurements and Subsurface Temperature Modelling in Denmark. GeoSkrifter 16, University of Aarhus. 172 pp.

Barnes, C. G., Prestvik, T., Barnes, M. A. W., Anthony, E. Y. & Allen, C. M. 2003: Geology of a magma transfer zone: the Hortavær Igneous Complex, north-central Norway. *Norwegian Journal of Geology 83*, 187-208.

Barrére, C., Ebbing, J., Skilbrei, J. R. & Zeyen, H. 2007: Lithospheric characterisation by joint interpretation of potential fields and thermal modelling - southwestern Barents Sea, Norway, *In* EGM 2007 International Workshop Innovation in EM, Grav and Mag Methods: a new Perspective for Exploration, Capri, Italy.

Bea, F. 1996: Residence of REE, Y, Th, and U in granites and crustal protoliths: Implications for the chemistry of crustal melts. *Journal of Petrology 37,* 521-552.

Beardsmore, G.R. & Cull, J.P. 2001: *Crustal Heat Flow, a guide to measurement and modelling*, Cambridge University Press, 324 pp.

Beck, A.E. & Balling, N. 1988: Determination of virgin rock temperatures. *In* Haenel, R., Rybach, L., and Stegena, L. (eds.), *Handbook of terrestrial heat-flow density determination.* 59-85. Kluwer Academic Publ., 486 pp.

Benfield, A. E. 1939: Terrestrial heat flow in Great Britain. *Procedings of the Royal Society of London, Series A 173*, 474-502.

Bernard-Griffiths, J., Peucat, J.J., Postaire, B., Vidal, P., Convert, J. & Moreau, B. 1984: Isotopic data (U-Pb, Rb-Sr, Pb-Pb, Sm-Nd) on mafic granulites from Finnish Lapland. *Precambrian Research 23,* 325-348.

Berthelsen, A., Olerud, S. & Sigmond, E.M.O. 1996: Geologisk kart over Norge, berggrunnskart OSLO 1:250.000. Geological Survey of Norway (NGU), Trondheim.

Bhattacharyya B. 1964: Magnetic anomalies due to prism-shaped bodies with arbitrary polarization: *Geophysics 29*, 517-530.

Bielik, M., Dyrelius, D. & Lillie, R.J. 1996: Caledonian lithosphere - gravity structure and comparison with Carpathian lithosphere. *Contributions of the Geophysical Institute of the Slovak Academy of Sciences 26*, 72-84.

Bingen, B. & van Breemen, O. 1996: U-Pb titanite geochronology in Rogaland -Vest Agder (SW Norway): Regional temperature at the time of intrusion of the Rogaland anorthosites. *In* D. Demaiffe (ed.) *Petrology and geochemistry of magmatic suites of rocks in the continental and oceanic crusts. Université Libre de Bruxelles. Royal Museum for Central Africa (Tervuren)*, 145-160.

Bingen, B., Davis, W.J. & Austrheim, H. 2001: Zircon U-Pb geochronology in the Bergen arc eclogites and their Proterozoic protoliths, and implications for the pre-Scandian evolution of the Caledonides in western Norway. *Geological Society of America Bulletin 113*, 640-649.

Bingen, B., Mansfeld, J., Sigmond, E.M.O. & Stein, H.J. 2002: Baltica-Laurentia link during the Mesoproterozoic: 1.27 Ga development of continental basins in the Sveconorwegian Orogen, southern Norway. *Canadian Journal of Earth Sciences 39,* 1425-1440.

Bingen, B., Skår, Ø., Marker, M., Sigmond, E. M. O., Nordgulen, Ø., Ragnhildstveit, J., Mansfeld, J., Tucker, R. D. & Liégeois, J.-P. 2005: Timing of continental building in the Sveconorwegian orogen, SW Scandinavia. *Norwegian Journal of Geology 85*, 87-116.

Bingen, B., Stein, H. J., Bogaerts, M., Bolle, O. & Mansfeld, J. 2006: Molybdenite Re–Os dating constrains gravitational collapse of the Sveconorwegian orogen, SW Scandinavia. *Lithos 87*, 328-346.

Bjørkum, P. A. & Nadeau, P. H. 1998: Temperature controlled porosity/permeability reduction, fluid migration, and petroleum exploration in sedimentary basins. *Australian Petroleum Production and Exploration Journal 38*, 453-464.

Bjørkum, P.A., Oelkers, E.H., Nadeau, P.H., Walderhaug, O. & Murphy, W.M. 1998: Porosity prediction in quartzose sandstones as a function of time, temperature, depth, stylolite frequency, and hydrocarbon saturation. AAPG Bulletin – American Association of Petroleum Geologists 82, 637-648.

Bjørlykke, K. 1974: Depositional history and composition of Lower Palaeozoic epicontinental sediments from the Oslo Region. *Norges geologiske undersøkelse 305*, 1-81.

Blackwell, D. D., Steele, J. L. & Brott, C. A. 1980: The terrain effect on terrestrial heat flow. *Journal of Geophysical Research 85*, 4757-4772.

Blakely R. 1996: *Potential Theory in Gravity and Magnetic Applications*. Cambridge University Press, 461p.

Blystad, P., Brekke, H., Færseth, R.B., Larsen, B.T., Skogseid, J. & Tørudbakken, B. 1995: Structural elements of the Norwegian continental shelf, Part II. The Norwegian Sea Region. *Norwegian Petroleum Directorate Bulletin 8*, 45 pp.

Bolle, O., Demaiffe, D. & Duchesne, J.-C. 2003: Petrogenesis of jotunitic and acidic members of an AMC suite (Rogaland anorthosite province, SW Norway): A Sr and Nd isotopic assessment. *Precambrian Research 124*, 185-214.

Bos, B. & Spiers, C.J. 2002: Frictional-viscous flow of phyllosilicate-bearing fault rock: Microphysical model and implications for crustal strength profiles. *Journal of Geophysical Researc*h *107*, doi:10.1029/2001JB000301.

Braathen, A. & Davidsen, B. 2000: Structure and stratigraphy of the Palaeoproterozoic Karasjok Greenstone Belt, north Norway - regional implications. Norsk Geologisk Tidsskrift, 80: 33-50.

Braathen, A., Nordgulen, Ø., Osmundsen, P.T., Andersen, T.B., Solli, A. & Roberts, D. 2000: Orogen-parallel, opposed extension in the Central Norwegian Caledonides. *Geology 28*, 615-618.

Brady, R.J., Ducea, M.N., Kidder, S.B., & Saleeby, J.B. 2006: The distribution of radiogenic heat production as a function of depth in the Sierra Nevada Batholith, California. *Lithos 86*, 229-244.

Breivik, A.B., Verhoef, J. & Faleide, J.I. 1999: Effects of thermal contrasts on gravity modeling at passive margins: results from the western Barents Sea. *Journal of Geophysical Research 104*, 15293-15311.

Brekke, H. 2000: The tectonic evolution of the Norwegian Sea continental margin with emphasis on the Vøring and Møre basins. *In* Nøttvedt, A. (ed.) *Dynamics of the Norwegian Margin.* Geological Society of London, Special Publication, 167, 327-378.

Brewer, T.S., Åhäll, K.-I., Menuge, J.F., Storey, C.D. and Parrish, R.R., 2004. Mesoproterozoic bimodal volcanism in SW Norway, evidence for recurring pre-Sveconorwegian continental margin tectonism. Precambrian Research, 134: 249-273.

Bryhni, I. & Andréasson, P.-G. 1985: Metamorphism in the Scandinavian Caledonides. *In* D.G. Gee and B.A. Sturt (eds.). *The Caledonide Orogen - Scandinavia and Related Areas.* John Wiley & Sons Ltd, 763-781.

Bullard, E.C. 1939: Heat slow in South Africa, *Proceedings of the Royal Society of London A 173*, 474-503.

Bullard, E.C. 1947: The time necessary for a borehole to attain temperature equilibrium. *Mon. Not. R. Astr. Soc., Geophys. Suppl. 5.* 125-130.

Byerly P. & Stolt R. 1977: An attempt to define the Curie point iostherm in northern and central Arizona. *Geophysics 42,* 1394-1400.

Calcagnile, G. 1982: The lithosphere-asthenosphere system in Fennoscandia. *Tectonophysics 90*, 19-35.

Carslaw, H. S. & Jaeger, J. C. 1959: *Conduction of heat in solids*, London, Oxford University Press, 386 pp.

Carter, N.L. & Tsenn, M.C. 1987: Flow properties of continental lithosphere. *Tectonophysics 136*, 27-33.

Cassell, B.R., Mykkeltveit, S., Kanestrøm, R. & Husebye, E.S. 1983: A North Sea southern Norway seismic crustal profile. *Geophysical Journal of the Royal Astronomical Society 72,* 733-753

Cawood, P. A. & Dunning, G. R. 1993: Silurian age for movement on the Baie Verte Line: Implictions for accretionary tectonics in the northern Appalachians. *Geological Society of America Abstracts with Programs 25*, A422.

Cawood, P. A., van Gool, J. A. M. & Dunning, G. R. 1996: Geological development of eastern Humber and western Dunnage zones: Corner Brook - Glover Island region, Newfoundland. *Canadian Journal of Earth Sciences 33*, 182-198.

Cawood, P. A., Nemchin, A. A., Strachan, R. A., Kinny, P. D. & Loewy, S. 2004: Laurentian provenance and an intracratonic tectonic setting for the Moine Supergroup, Scotland, constrained by detrital zircons from the Loch Eil and Glen Urquhart successions. *Journal of the Geological Society of London 161*, 861-874.

Cermák, V., Balling, N., Kukkonen, I. T. & Zui, V. I. 1993: Heat flow in the Baltic Shield-results of the lithospheric geothermal modelling. *Precambrian Research 64*, 53-65.

Chandler, F. W., Sullivan, R. W. & Currie, K. L. 1987: The age of the Springdale Group, western Newfoundland, and correlative rocks - evidence for a Llandovery overlap assemblage in the Canadian Appalachians. *Transactions of the Royal Society of Edinburgh: Earth Sciences 78*, 41-49.

Christiansson, P., Faleide, J.I. & Berge, A.M. 2000: Crustal structure in the northern North Sea: an integrated geophysical study. *In:* Nøttvedt, A. (ed.) *Dynamics of the Norwegian Margin*, Geological Society of London Special Publications 167, 15-40.

Christoffel, C.A., Connelly, J.N. Åhäll, K.-I. 1999: Timing and characterization of recurrent pre-Sveconorwegian metamorphism and deformation in the Varberg-Halmstad region of SW Sweden. *Precambrian Research 98*, 173-195.

Chorlton, L. B. & Dallmeyer, R. D. 1986: Geochronology of early to middle Paleozoic tectonic development in the southwest Newfoundland Gander Zone. *Journal of Geology 94*, 670-890.

Cliff, R. A., Yardley, B. W. D. & Bussy, F. 1993: U-Pb and Rb-Sr geochronology of magmatism and metamorphism in the Dalradian of Connemara, W. Ireland. *Journal of the Geological Society of London 153*, 109-120.

Colman-Sadd, S. P. 1985: Geology of the Burnt Hill map area (2D/5) Newfoundland, Report 85-3.

Colman-Sadd, S. P., Dunning, G. R. & Dec, T. 1992: Dunnage-Gander relationships and Ordovician Orogeny in Central Newfoundland: A sediment provenance and U-Pb age study. *American Journal of Science 292*, 317-355.

Connard G., Couch R. & Gemperle, M. 1983: Analysis of aeromagnetic measurements from the Cascade Range in central Oregon. *Geophysics 48,* 376-390.

Corfu, F. & Emmet, T. 1992: U-Pb age of the Leirungsmyran gabbroic complex, Jotun Nappe, southern Norway. *Norsk Geologisk Tidsskrift 72*, 369-374.

Corfu, F., Hanchar, J. M., Hoskin, P. W. O. & Kinny, P. D. 2003: Atlas of zircon textures. *In* Hanchar, J. M. & P. W. O. Hoskin (eds.). *Zircon*. Reviews in Mineralogy & Geochemistry 53, 469-500.

Corfu, F. 2004a: U-Pb age, setting and tectonic significance of the anorthosite-mangerite-charnockite suite, Lofoten-Vesterålen, Norway. *Journal of Petrology 45*: 1799-1819.

Corfu, F. 2004b: U–Pb geochronology of the Leknes Group: an exotic Early Caledonian metasedimentary assemblage stranded on Lofoten basement, northern Norway. *Journal of the Geological Society of London 161,* 619-627.

Corfu, F., Armitage, P.E.B., Kullerud, K. & Bergh, S.G. 2003: Preliminary U-Pb geochronology in the West Troms Basement Complex, North Norway: Archaean and Palaeoproterozoic events and younger overprints. *Norges geologiske undersøkelse Bulletin 441,* 61-72.

Corfu, F., Torsvik, T. H., Andersen, T. B., Ashwal, L. D., Ramsay, D. M. & Roberts, R. J. 2006: Early Silurian mafic-ultramafic and granitic plutonism in contemporaneous flysch, Magerøy, northern Norway: U-Pb ages and regional significance. *Journal of the Geological Society of London 163,* 291-301.

Currie, K. L., van Breemen, O., Hunt, P. A. & van Berkel, J. T. 1992: Age of high-grade gneisses south of Grand Lake, Newfoundland. *Atlantic Geology 28,* 153-161.

Dallmeyer, R. D. & Hibbard, J. 1984: Geochronology of the Baie Verte Peninsula, Newfoundland: implications for the tectonic evolution of the Humber and Dunnage Zones of the Appalachian orogen. *Journal of Geology 92*, 489-512.

Davis, M. & Kusznir, N.J. 2004: Depth-dependent lithospheric stretching at rifted continental margins. *In* Karner, G.D. (ed.) *Proceedings of NSF Rifted Margins Theoretical Institute*, Columbia University Press, New York, 92-136

Dec, T., Swinden, H. S. & Dunning, G. R. 1997: Lithostratigraphy and geochemistry of hte Cottrells Cove Group, Buchans - Roberts Arm volcanic belt: new constraints for the paleotectonic setting of the Notre Dame Subzone, Newfoundland Appalachians. *Canadian Journal of Earth Sciences 34*, 86-103.

DeGrace, J. R., Kean, B. F., Hsu, E. & Green, T. 1976: Geology of the Nippers Harbour map area, Newfoundland, Report 76-3.

Dehls, J.F., Olesen, O., Bungum, H., Hicks, E., Lindholm, C.D. & Riis, F. 2000: Neotectonic map, Norway and adjacent areas 1:3 mill. Norges geologiske undersøkelse, Trondheim, Norway.

Dempster, T. J., Rogers, G., Tanner, P. W. G., Bluck, B. J., Muir, R. J., Redwood, S. D., Ireland, T. R. & Paterson, B. A. 2002: Timing of deposition, orogenesis and glaciation within the Dalradian rocks of Scotland: Constraints from U-Pb zircon ages. *Journal of the Geological Society of London 159*, 83-94.

Dickson, W. L. 1993: Geology of the Mount Peyton map area (2D/14), Central Newfoundland. *In* C. P. G. Pereira, D. G. Walsh & R. F. Blackwood (eds.) *Current Research: Newfoundland Department of Mines and Energy, Geological Survey Branch*. Report 93-1, 1-12.

Dons, J. & Jorde, K. 1978: *Geologisk kart over Norge, bergrunnskart SKIEN 1:250.000*. Geological Survey of Norway (NGU), Trondheim.

Doré, A. G., Lundin, E., Fichler, C. & Olesen, O. 1997: Patterns of basement structure and reactivation along the NE Atlantic margin. *Journal of the Geological Society of London 154*, 85-92.

Doré, A.G., Lundin, E.R., Jensen, L.N., Birkeland, Ø., Eliassen, P.E. & Fichler, C. 1999: Principal tectonic events in the evolution of the northwest European Atlantic margin. *In:* Fleet, A.J. and Boldy, S.A.R. (eds.) *Petroleum Geology of Northwest Europe: Proceedings of the 5th conference*, 41-61. Geological Society, London.

Draut, A. E. & Clift, P. D. 2002: The origin and significance of the Delaney Dome Formation, Connemara, Ireland. *Journal of the Geological Society of London 159*, 95-103.

Dube, B., Dunning, G. R., Lauziere, K. & Roddick, J. C. 1996: New insights into the Appalachian Orogen from geology and geochronology along the Cape Ray fault zone, southwest Newfoundland. *Geological Society of America Bulletin 108*, 101-116.

Dubé, B., Dunning, G. R., Lauziere, K. & Roddick, C. 1993: The Gondwanan-Laurentian suture: Timing of deformation on the Cape Ray fault, Newfoundland Appalachians. *Geological Society of America Abstracts with Programs 25*, A421.

Dubé, B., Dunning, G. R., Lauziere, K. & Roddick, C., 1994, Deformational events and their timing along the Cape Ray Fault, Newfoundland Appalachians. *In* New perspectives in the Appalachian-Caledonian Orogen (NUNA) Conference, Grand Falls, Newfoundland, p. 13.

Dunning, G.R. 1987: U-Pb geochronology of the Coney Head Complex, Newfoundland. *Canadian Journal of Earth Sciences 24*, 1072-1075.

Dunning, G.R. & Krogh, T.E. 1985: Geochronology of ophiolites of the Newfoundland Appalachians. *Canadian Journal of Earth Sciences 22*, 1659-1670.

Dunning, G. & Pedersen, R.-B. 1988: U/Pb ages of ophiolites and arc-related plutons of the Norwegian Caledonides: Implications for the development of Iapetus. *Contributions to Mineralogy and Petrology 98*, 13-23.

Dunning, G. R. & Krogh, T. E. 1991: Stratigraphic correlation of the Appalachian Ordovician using advanced U-Pb zircon geochronology techniques. *Geological Survey of Canada, Paper 90-9*, 5-25.

Dunning, G. & Grenne, T. 2000: U-Pb age dating and palaeotectonic significance of trondhjemite from the type locality in the central Norwegian Caledonides. *Norges geologiske undersøkelse Bulletin 437*, 57-65.

Dunning, G. R., Kean, B. F., Thurlow, J. G. & Swinden, H. S. 1987: Geochronology of the Buchans, Roberts Arm and Victoria Lake Groups, and the Mansfield Cove Complex, Newfoundland. *Canadian Journal of Earth Sciences 24*, 1175-184.

Dunning, G. R., Wilton, D.H.C. & Herd, R. K. 1989: Geology, geochemistry and geochronology of a Taconic calc-alkaline batholith in southwest Newfoundland. *Royal Society of Edinburgh Transactions, Earth Sciences 80*, 159-168.

Dunning, G. R., O'Brien, S. J., O'Brien, B. H., Holdsworth, R. E. & Tucker, R. D. 1993: Chronology of Pan-African, Penobscot and Salinic shear zones on the Gondwanan margin, northern Appalachians. *Geological Society of America Abstracts with Programs 25*, A421.

Dunning, G. R., O'Brien, S. J., Colman-Sadd, S. P., Blackwood, R. F., Dickson, W. L., O'Neill, P. & Krogh, T. E. 1990a: Silurian orogeny in the Newfoundland Appalachians. *Journal of Geology 98*, 895-913.

Dunning, G. R., O'Brien, S. J., Colman-Sadd, S. P., Blackwood, R. F., Dickson, W. L., O'Neill, P. P. & Krogh, T. E. 1990b: Silurian orogeny in the Newfoundland Appalachians. *Journal of Geology 98*, 895-913.

Dyrelius, D. 1985: A geophysical perspective of the Scandinavian Caledonides. *In* Gee, D.G. & Sturt, B. (eds.) *The Caledonide Orogen – Scandinavia and related areas*, John Wiley and Sons, Chichester, 185-194.

Dziewonski, A.M. & Anderson, D.L. 1981: Preliminary reference earth model. *Phys. Earth. Plan. Int. 25*, 297-356.

Ebbing, J. 2007. Isostatic density modelling explains the missing root of the Scandes. *Norwegian Journal of Geology 87,* 13-20.

Ebbing, J. & Lundin, E. 2005: 3D modelling and the Mid-Norwegian Atlantic margin. *In:* Olesen, O. et al. *Kontiki Annual Report 2004, Continental crust and heat generation in 3D.* NGU Report 2005.008, 30-49.

Ebbing, J. & Olesen, O. 2005: The Northern and Southern Scandes - Structural differences revealed by an analysis of gravity anomalies, the geoid and regional isostasy. *Tectonophysics 411,* 73-87.

Ebbing, J., Afework, Y., Olesen, O. & Nordgulen, Ø. 2005a: Is there evidence for magmatic underplating beneath the Oslo Rift? *Terra Nova 17,* 129–134.

Ebbing, J., Braitenberg, C. & Skilbrei, J.R. 2005b: Basement characterisation by regional isostatic methods in the Barents Sea. *NGU Report 2005.074,* 78 pp. *Confidential Industry Report.*

Ebbing, J., Lundin, E., Olesen, O. & Hansen, E.K 2006a: The mid-Norwegian margin: A discussion of crustal lineaments, mafic intrusions, and remnants of the Caledonian root by 3D density modelling and structural interpretation. *Journal of the Geological Society, London 163,* 47-60.

Ebbing, J., Osmundsen, P.T. & Pascal, C. 2006b: 3D modeling of gravity and magnetic data in the Trøndelag Platform. *NGU Report 2006.082,* 50 pp.

Ebbing, J., Pascal, C., Olesen, O. & Skilbrei, J.R. 2006c: 3D modeling: The Mid-Norwegian margin, the Scandinavian mountains and the Oslo Rift. *In:* Olesen, O. et al. *Kontiki Annual Report 2005-2006, Continental crust and heat generation in 3D.* NGU Report 2006.059, 67-108.

Ebbing, J., Skilbrei, J.R. & Olesen, O. 2007a: Insights into the magmatic architecture of the Oslo Graben by petrophysically constrained analysis of the gravity and magnetic field. *Journal of Geophysical Research 112,* B04404, doi:10.1029/2006JB004694.

Eldholm, O. & Grue, K. 1994: North Atlantic volcanic margins; dimensions and production rates. *Journal of Geophysical Research B99,* 2955-2968.

Eliasson, T. 1992: Magma genesis and emplacement characteristics of the peraluminous Sveconorwegian Bohus granite, SW Sweden. *Geologiska Föreningen i Stockhom Förhandlingar 114,* 452-455.

Eliasson, T. & Schöberg, H. 1991: U-Pb dating of the post-kinematic Sveconorwegian (Grenvillian) Bohus granite, SW Sweden: Evidence of restitic zircon. *Precambrian Research 51,* 337-350.

Elliot, C. G., Dunning, G. R. & Williams, P. F. 1991: New U-Pb zircon age constraints on the timing of deformation in north-central Newfoundland, and implications for early Paleozoic Appalachian orogenesis. *Geological Society of America Bulletin 103,* 125-135.

Elliott, C. G., Dunning, G. R. & Williams, P. F. 1991: New U/Pb zircon age constraints on the timing of deformation in north-central Newfoundland and implications for early Paleozoic Appalachian orogenesis. *Geological Society of America Bulletin 103*, 125-135.

Elming, S.Å. 1980: Density and magnetic properties of rocks in the Caledonides of Jamtland, Sweden. *Geologiska Föreningens i Stockholm Förhandlingar 102*, 439-453.

Elming, S.Å. 1988: Geological modelling based on gravity data from the central parts of the Swedish Caledonides. *Geologiska Föreningens i Stockholm Förhandlingar 108*, 280-283.

Fernàndez, M., Torne, M., Garcia-Castellanos, D., Vergés, J., Wheeler, W. & Karpuz, R. 2004: Deep structure of the Vøring margin: the transition from a continental shield to a young oceanic lithosphere. *Earth and Planetary Science Letters 221*, 131-144.

Fernàndez, M., Ayala, C., Torne, M., Vergés, J., Gómez, M. & Karpuz, R., 2005: Lithospheric structure of the Mid-Norwegian Margin: comparsion between the Møre and Vøring margins. *Journal of the Geological Society of London 162*, 1005-1012.

Fichler C. & Hospers J. 1990a: Gravity modelling in the Viking Graben area. *In* D.J. Blundell & A.D. Gibbs (eds.) *Tectonic evolution of the North Sea rifts*, 71-81.

Fichler C. & Hospers J. 1990b: Deep crustal structure of the northern North Sea Viking Graben: results from deep reflection seismic and gravity data. *Tectonophysics 178*, 241-254.

Fichler, C., Rundhovde, E., Olesen, O., Sæther, B.M., Rueslåtten, H., Lundin, E. & Doré, A.G. 1999: Regional tectonic interpretation of image enhanced gravity and magnetic data covering the Mid-Norwegian shelf and adjacent mainland. *Tectonophysics 306*, 183-197.

Flowerdew, M. J., Daly, J. S. & Whitehouse, M. J. 2005: 470 Ma granitoid magmatism associated with the Grampian Orogeny in the Slishwood Division, NW Ireland. *Journal of the Geological Society of London 162*, 563-575.

Flowers, R.M., Mahan, K.H., Bowring, S.A., Williams, M.L., Pringle, M.S. & Hodges, K.V. 2006: Multistage exhumation and juxtaposition of lower continental crust in the western Canadian Shield: Linking high-resolution U-Pb and $^{40}Ar/^{39}Ar$ thermochronometry with pressure-temperature-deformation paths. *Tectonics 25*, doi:10.1029/2005TC001912.

Folldal Verk 1985: Logg for borehullet ved Gåvålivatnet, Hjerkinn. Diamond drill hole 2000D. 73 pp.

Fountain, D.M. 1986: Is there a relationship between seismic velocity and heat production for crustal rocks? *Earth and Planetary Science Letters 79*, 145-150.

Fowler, C.M.R. 2005: *The solid Earth – an introduction to global geophysics (2nd edition).* Cambridge University Press.

Fraser, G. L., Pattison, D. R. M. & Heaman, L. M. 2004: Age of the Ballachulish and Glencoe Igneous Complexes (Scottish Highlands), and paragenesis of zircon, monazite and baddeleyitye in the Ballachulish Aureole. *Journal of the Geological Society of London 161*, 447-462.

Friedrich, A. M. 1998: $^{40}Ar/^{39}Ar$ and U-Pb geochronological constraints on the thermal and tectonic evolution of the Connemara Caledonides, Western Ireland [PhD thesis], Massachusetts Institute of Technology.

Friedrich, A. M., Bowring, S. A., Martin, M. W. & Hodges, K. V. 1999a: Short-lived continental magmatic arc at Connemara, western Irish Caledonides: Implications for the age of the Grampian orogeny. *Geology 27,* 27-30.

Friedrich, A. M., Hodges, K. V., Bowring, S. A. & Martin, M. W. 1999b: Geochronological constraints on the magmatic, metamorphic and thermal evolution of the Connemara Caledonides, western Ireland. *Journal of the Geological Society of London 156,* 1217-1230.

Friend, C. R. L., Strachan, R. A., Kinny, P. D. & Watt, G. R. 2003: Provenance of the Moine Supergroup of NW Scotland: Evidence from geochronology of detrital and inherited zircons from (meta)sedimentary rocks, granites and migmatites. *Journal of the Geological Society of London 160*, 247-257.

Frost, B.R. & Frost, C.D. 1987: CO_2, melts and granulite metamorphism. *Nature 327,* 503-506.

Frost, R. T. C., Fitch, F. J. & Miller, J. A. 1981: The age and nature of the crystalline basement of the North Sea Basin. *In* Illing, L. V. & G. D. Hobson (eds.) *Petroleum Geology of the Continental Shelf of North-West Europe*. London, Heyden and Son Ltd, 43-57.

Frost, C.D., Frost, B.R., Chamberlain, K.R. & Edwards, B.R. 1999: Petrogenesis of the 1.43 Ga Sherman batholith, SE Wyoming, USA: A reduced, rapakivi-type anorogenic granite. *Journal of Petrology 40,* 1771-1802.

Furnes, H., Austrheim, H., Amaliksen, K. G. & Nordås, J. 1983: Evidence for an incipient early Caledonian (Cambrian) orogenic phase in southwestern Norway. *Geological Magazine 120*, 607-612.

Gaál, G. & Gorbatschev, R. 1987: An outline of the Precambrian evolution of the Baltic Shield. *Precambrian Research 35*, 15-52.

Gautneb, H. & Roberts, D. 1989: Geology and petrochemistry of the Smøla-Hitra Batholith, Central Norway. Norges geologiske undersøkelse Bulletin, 416: 1-24.

Gee, D.G. 1987: The Scandinavian alum shales - Mid Cambrian to Tremadoc deposition in response to early Caledonian subduction. Norsk *Geologisk Tidsskrift 67,* 233-235.

Gee, D. G., Johansson, Å., Larionov, A. N. & Tebenkov, A. M. 1999: A Caledonian granitoid pluton at Djupkilsodden, central Nordaustlandet, Svalbard: Age, magnetic signature and tectonic significance. *Polarforschung 66*, 19-32.

Geosoft 2005: Montaj GridKnit, Grid extension for OASIS Montaj v6.1, Tutorial and user guide, *Geosoft Incorporated*, 27 pp.

Gernigon, L., Ringenbach, J.C., Planke, S., Le Gall, B. & Jonquet-Kolstø, H. 2003: Extension, crustal structure and magmatism at the outer Vøring Basin, Norwegian margin. *Journal of the Geological Society, London 160,* 197-208.

Gernigon, L., Ringenbach, J.-C., Planke, S. & Le Gall, B. 2004: Deep structure and breakup along volcanic rifted margins: insights from integrated studies along the outer Vøring Basin (Norway). *Marine and Petroleum Geology 21*, 363–372.

Gernigon, L., Lucazeau, F., Brigaud, F., Ringenbach, J.C., S., P. & Le Gall, B. 2006a: A moderate melting model for the Vøring margin (Norway) based on structural observations and a thermo-kinematical modeling: Implication for the meaning of the lower crustal bodies. *Tectonophysics 412*, 255-278.

Gernigon, L., Olesen, O., Ebbing, J., Mogaard, J.O., Pascal, C., Wienecke, S., Mondt, J., Norvik, O., Sand, M. & Stehen, Ø. 2006b: Structure of the Jan Mayen Fracture Zone, Norwegian-Greenland Sea - Insights from the New Aeromagnetic Survey JAS-05. EAGE/EAGO/SEG Conference, Saint Petersburg.

Gernigon, L., Marello, L., Mogaard, J.O., Werner, S.C. & Skilbrei, J.R. 2007: Barents Sea Aeromagnetic Survey BAS-06 - Acquisition - processing report and preliminary interpretation. Geological Survey of Norway. *NGU Report no. 2007.035*, 144 pp.

Geosoft 2005: Montaj GridKnit, Grid extension for OASIS Montaj v6.1, Tutorial and user guide, *Geosoft Incorporated*, 27 pp.

Gilotti, J. A. & McClelland, W. C. 2005: Leucogranites and the time of extension in the East Greenland Caledonides. *Journal of Geology 113*, 399-417.

Goldschmidt, V.M. 1911: Die Kontaktmetamorphose im Kristiania-gebiet. Skr. Vidensk. Selsk. I. Mat. Naturv. Kl. 1, 483 pp.

Gomez, M., Verges, J., Fernandez, M., Torne, M., Ayala, C., Wheeler, W. & Karpuz, R. 2004: extensional geometry of the Mid Norwegian margin before early Tertiary continental breakup. *Marine and Petroleum Geology 21*, 177-194.

Grenne, T. 1989: Magmatic evolution of the Løkken SSZ Ophiolite, Norwegian Caledonides: Relationship between anomalous lavas and high-level intrusions. *Geological Journal 24*, 251-274.

Grenne, T. & Roberts, D. 1998: The Hølonda Porphyrites, Norwegian Caledonides: Geochemistry and tectonic setting of Early-Mid-Ordovician shoshonitic volcanism. *Journal of the Geological Society of London 155*, 131-142.

Grønlie, G., Heier, K.S. & Swanberg, C.A. 1977: Terrestrial heat flow determinations from Norway. *Norsk Geologisk Tidsskrift 57*. 153-162.

Götze, H.-J. & Lahmeyer, B. 1988: Application of three-dimensional interactive modeling in gravity and magnetics. *Geophysics 53*, 1096-1108.

Griffin, W.L., Austrheim, H., Brastad, K., Bryhni, I., Krill, A.G., Krogh, E.J., Mørk, M.B.E., Quale, H. & Tørudbakken, B. 1985: High-pressure metamorphism in the Scandinavian Caledonides. *In* D.G. Gee and B.A. Sturt (eds.), *The Caledonide Orogen: Scandinavia and Related Areas*. Wiley, 783-801.

Griffin, W.L., Taylor, P.N., Hakkinen, J.W., Heier, K.S., Iden, I.K., Krogh, E.J., Malm, O., Olsen, K.I., Ormaasen, D.E. & Tveten, E. 1978: Archaean and Proterozoic crustal

evolution in Lofoten-Vesterålen, N. Norway. *Journal of the Geological Society of London 135,* 629-647.

Halliday, A. N., Aftalion, M., Parsons, I., Dickin, A. P. & Johnson, M. R. W. 1987: Syn-orogenic alkaline magmatism and its relationship to the Moine Thrust Zone and the thermal state of the lithosphere in NW Scotland. *Journal of the Geological Society of London 144,* 611-617.

Hänel R. 1974; Heat flow measurements in the Norwegian Sea. *Meteor-Forschungsergebnisse Reihe C: Geologie und Geophysik 17,* 74-78.

Hänel, R. 1979: A critical review of heat flow measurements in sea and lake bottom sediments. *In* V. Cermak and L. Rybach (eds.), *Terrestrial heat flow in Europe,* p. 49-73, Springer-Verlag, Berlin.

Hänel, R. Grønlie, G. & Heier, K.S. 1979: Terrestrial heat-flow determination in Norway and an attempted interpretation. *In* V. Cermak and L. Rybach (eds.), *Terrestrial heat flow in Europe,* p. 232-240, Springer-Verlag, Berlin.

Hänel, R. Grønlie, G. & Heier, K.S. 1979: Terrestrial heat-flow determinations from lakes in southern Norway. *Norsk Geologisk Tidsskrift 54,* 423-428.

Hansen, B. T. & Friderichsen, J. D. 1987: Isotopic age dating in Liverpool Land, East Greenland. *Geological Survey of Greenland Report 134,* 25-37.

Hansen, B. T., Henriksen, N. & Kalsbeek, F. 1994: Age and origin of Caledonian granites in the Grandjean Fjord - Bessel Fjord region (75°-76°N), North-East Greenland. *Rapport Grønlands Geologiske Undersøgelse 162,* 139-151.

Hansen, J., Skjerlie, K. P., Pedersen, R.-B. & De La Rosa, J. 2002: Crustal melting in the lower parts of island arcs: An example from the Bremanger Granitoid Complex, west Norwegian Caledonides. *Contributions to Mineralogy and Petrology 143,* 316-335.

Hartmann, D. L. 1994: *Global Physical Climatology,* Academic Press, 411 pp.

Hartz, E. H., Andresen, A., Martin, M. W. & Hodges, K. V. 2000: U-Pb and $^{40}Ar/^{39}Ar$ constraintson the Fjord Region Detachment Zone: A long-lived extensional fault in the central East Greenland Caledonides. *Journal of the Geological Society of London 157,* 795-809.

Hartz, E. H., Andresen, A., Hodges, K. V. & Martin, M. W. 2001: Syncontractional extension and exhumation of deep crustal rocks in the east Greenland Caledonides. *Tectonics 20,* 58-77.

Hartz, E.H., Eide, E.A., Andresen, A., Midbøe, P., Hodges, K.V. & Kristiansen, S.N. 2002: $^{40}Ar/^{39}Ar$ geochronology and structural analysis: Basin evolution and detrital feedback mechanisms, Hold With Hope region, East Greenland. *Norwegian Journal of Geology 82,* 341-358.

Heier, K.S. 1960: Petrology and chemistry of high-grade metamorphic and igneous rocks on Langøy, Northern Norway. *Norges geologiske undersøkelse 207,* 1-246.

Heier, K.S. 1965: Metamorphism and the chemical differentiation of the crust. *Geologiska Föreningen i Stockhom Förhandlingar 87,* 249-256.

Heier, K.S. 1977: *The Norwegian Geotraverse Project: A Norwegian contribution to the international upper mantle project and the international geodynamics project.* Geological Survey of Norway (NGU), Trondheim.

Heier, K.S. & Adams, J.A.S. 1965: Concentration of radioactive elements in deep crustal material. *Geochimica et Cosmochimica Acta 29*, 53-61.

Heiskanen, W.A. & Moritz, H. 1967: Physical Geodesy. *W.H. Freeman, San Fransisco.* 364 pp.

Henkel, H. 1991: Magnetic crustal structures in Northern Fennoscandia. *In* Wasilewski, P. & Hood, P. (eds.) Magnetic anomalies - land and sea. *Tectonophysics 192*, 57-79.

Higgins, A. K., Elvevold, S., Escher, J. C., Frederiksen, K. S., Gilotti, J. A., Henriksen, N., Jepsen, H. F., Jones, K. A., Kalsbeek, F., Kinny, P. D., Leslie, A. G., Smith, M. P., Thrane, K. & Watt, G. R. 2004: The foreland-propagating thrust architecture of the East Greenland Caledonides 72°-75°N. *Journal of the Geological Society of London 161,* 1009-1026.

Hirschleber, H.B., Lund, C., Meissner, R., Vogel, A. & Weinrebe, W. 1975: Seismic investigations along the Blue Road traverse. *J. Geophys. 41*, 135-148.

Hospers, J. & Rathore, J.S. 1984: Interpretation of aeromagnetic data from the Norwegian sector of the North Sea. G*eophysical Prospecting 32*, 929-942.

Hospers, J. & Ediriweera, K.K. 1991: Depth and configuration of the crystalline basement in the Viking Graben area, Northern North Sea. *Journal of the Geological Society, London 148,* 261-265.

Hospers, J., Rathore, J.S., Jianhua, F. & Finnstrøm, E.G. 1986: Thickness of pre-Zechstein-salt Palaeozoic sediments in the southern part of the Norwegian sector of the North Sea. *Norsk Geologisk Tidsskrift 66,* 295-304.

Hossack, J.R. 1984: The geometry of listric normal faults in the Devonian basins of Sunnfjord, Western Norway. *Journal of the Geological Society of London 141,* 629-637.

Hunt, C., Moskowitz, B.M. & Banerje, S.K. 1995: Magnetic properties of rocks and minerals. In: Rock Physics and Phase Relations. A Handbook of Physical Constraints. *AGU Reference Shelf 3,* 189-204.

Hurich, C.A., Palm, H., Dyrelius, D. & Kristoffersen, Y. 1989: Deformation of the Baltic continental crust during Caledonide intracontinental subduction: Views from seismic reflection data. *Geology 17,* 423-425.

Iversen, T. 2000: Støy, kaos og sirkulasjonsregimer. *Cicerone 3*, 24-28.

Jaupart, C. & Mareschal, J.-C. 2003: Constraints on crustal heat production from heat flow data. *In* Rudnick, R. L. (ed.) *The Crust*. Treatise on Geochemistry 3, Oxford, Elsevier-Pergamon, 65-84.

Jenner, G. A., Dunning, G. R., Malpas, J., Brown, M. & Brace, T. 1991: Bay of Islands and Little Port complexes, revisited: Age, geochemical and isotopic evidence confirm suprasubduction-zone origin. *Canadian Journal of Earth Sciences 28,* 1635-1652.

Jessop, A. M. 1971: The distribution of glacial perturbation of heat flow in Canada. *Canadian Journal of Earth Sciences 8*, 162-166.

Jessop, A. M. 1990: *Thermal geophysics*, Developments in Solid Earth Geophysics 17. Amsterdam, Elsevier Science Publishers B.V., 306 pp.

Johansson, Å., Larionov, A. N., Tebenkov, A. M., Ohta, Y. & Gee, D. G. 2002: Caledonian granites of western and central Nordaustlandet, northeast Svalbard. *Geologiska Föreningen i Stockholm Förhandlingar 124*, 135-148.

Johansson, Å., Larionov, A. N., Gee, D. G., Ohta, Y., Tebenkov, A. M. & Sandelin, S. 2004: Grenvillian and Caledonian tectono-magmatic activity in northeasternmost Svalbard. In: Gee, D. G. & V. Pease eds. *The Neoproterozoic Timanide Orogen of Eastern Baltica*. Geological Society, London, Memoirs 30, 207-232.

Jorde, K., Sigmond, E.M.O. & Thorsnes, T. 1995: STAVANGER. Berggrunnsgeologisk kart 1:250 000. *Norges geologiske undersøkelse, Trondheim.*

Juhojuntti, N., Juhlin, C. & Dyrelius, D. 2001: Crustal reflectivity underneath the Central Scandinavian Caledonides. *Tectonophysics 334*, 191-210.

Jung, W.Y. & Vogt, P. 1997: A gravity and magnetic anomaly study of the extinct Aegir Ridge, Norwegian Sea. *Journal of Geophysical Research 12*, 5065-5089.

Kalsbeek, F., Jepsen, H. F. & Nutman, A. P. 2001: From source migmatites to plutons: Tracking the origin of ca. 435 Ma S-type granites in the East Greenland Caledonian orogen. *Lithos 57*, 1-21.

Kalsbeek, F., Thrane, K., Nutman, A. P. & Jepsen, H. F. 2000: Late Mesoproterozoic to early Neoproterozoic history of the East Greenland Caledonides: Evidence for Grenvillian orogenesis? *Journal of the Geological Society of London 157*, 1215-1225.

Kalsbeek, F., Higgins, A. K., Jepsen, H. F., Frei, R. & Nutman, A. P. in press: Granites and granites in the East Greenland Caledonides.

Kanestrøm, R. & Haugland, K. 1971: Crustal structure in Southeastern Norway from Seismic Refraction measurements. *Scientific Report No. 5, Seismological Observatory, University of Bergen, Norway,* 72 pp.

Kappelmeyer, O. & Hänel, R. 1974: *Geothermics with Special Reference to Application*. Borntraeger, Berlin.

Kean, B. F. & Jayasinghe, N. 1982: Geology of the Badger map area, Newfoundland. Report 81-2.

Kerr, A. 1997: Space-time composition relationships among Appalachian-cycle plutonic suites in Newfoundland. *In* Sinha, A. K., J. B. Whalen & J. P. Hogan (eds.) *The Nature of Magmatism in the Appalachian Orogen*. Geological Society of America Memoir 191, Boulder, Colorado, 193-220.

Kerr, A. & Dunning, G. R. 2003: A note on the U-Pb zircon age of the Woodford's Arm Granite, and its relationship to the Roberts Arm Group, central Newfoundland (NTS 2E/12).

Current Research (2003), Newfoundland Department of Mines and Energy, Geological Survey, Report 03-1 0, 47-50.

Kerr, A., Dunning, G. R. & Tucker, R. D. 1993: The youngest Paleozoic plutonism of the Newfoundland Appalachains: U-Pb ages from the St. Lawrence and Francois granites. *Canadian Journal of Earth Sciences 30*, 2328-2333.

Killeen, P.G. & Heier, K.S. 1975: Radioelement distribution and heat production in Precambrian granitic rocks, southern Norway. *Det Norske Videskaps-Akademi, I. Mat.-Naturv. Klasse. Skrifter, Ny Serie 35*, 1-32.

Kinck, J.J., Husebye, E.S. & Larsson, F.R. 1993: The Moho depth distribution in Fennoscandia and the regional tectonic evolution from Archean to Permian times. *Precambrian Research 64*, 23-51.

Kirkland, C. L., Daly, J. S. & Whitehouse, M. J. 2005: Early Silurian magmatism and the Scandian evolution of the Kalak Nappe Complex, Finnmark, Arctic Norway. *Journal of the Geological Society of London 162*, 985-1003.

Kirkland, C. L., Daly, J. S., Eide, E.A. & Whitehouse, M. J. 2006a: The structure and timing of lateral escape during the Scandian Orogeny: A combined strain and geochronological investigation in Finnmark, Arctic Norwegian Caledonides. *Tectonophysics 425*, 159-189.

Kirkland, C.L., Daly, J.S. & Whitehouse, M.J. 2006b: Granitic magmatism of Grenvillian and late Neoproterozoic age in Finnmark, Arctic Norway - Constraining pre-Scandian deformation in the Kalak Nappe Complex. *Precambrian Research 145*, 24-52.

Kirkland, C. L., Daly, J. S. & Whitehouse, M. J. 2007: Provenance and terrane evolution of the Kalak Nappe Complex, Norwegian Caledonides: Implications for Neoproterozoic Paleogeography and tectonics. *Journal of Geology 115*, 21-41.

Kinny, P. D., Strachan, R. A., Friend, C. R. L., Kocks, H., Rogers, G. & Paterson, B. A. 2003: U–Pb geochronology of deformed metagranites in central Sutherland, Scotland: Evidence for widespread late Silurian metamorphism and ductile deformation of the Moine Supergroup during the Caledonian orogeny. *Journal of the Geological Society of London 160*, 259-269.

Kneller, B. & Aftalion, M. 1987: The isotopic and structural age of the Aberdeen Granite. *Journal of the Geological Society of London 144*, 717-722.

Kocks, H., Strachan, R. A. & Evans, J. A. 2006: Heterogeneous reworking of Grampian metamorphic complexes during Scandian thrusting in the Scottish Caledonides: Insights from the structural setting and U-Pb geochronology of the Strath Halladale Granite. *Journal of the Geological Society of London 163*, 525-538.

Koistinen, T., Stephens, M.B., Bogatchev, V., Nordgulen, Ø., Wennerstrøm, M. & Korhonen, J. 2001: *Geological map of the Fennoscandian Shield, scale 1:2 million.* Geological Surveys of Finland, Norway and Sweden and the Northwest Department of Natural Resources of Russia.

Korhonen, J.,V., Aaro, S., All, T., Elo, S., Haller, L.Å., Kääriäinen, J., Kulinich, A., Skilbrei, J.R., Solheim, D., Säävuori, H., Vaher, R., Zhdanova, L. & Koistinen, T. 2002a: *Bouguer anomaly map of the Fennoscandian shield 1: 2 000 000.* Geological Surveys of Finland, Norway and Sweden and Ministry of Natural Resources of Russian Federation.

Korhonen, J.,V., Aaro, S., All, T., Nevanlinna, H., Skilbrei, J.R., Säävuori, H., Vaher, R., Zhadanova, L. & Koistinen, T. 2002b: *Magnetic anomaly map of the Fennoscandian shield 1: 2 000 000.* Geological Surveys of Finland, Norway and Sweden and Ministry of Natural Resources of Russian Federation.

Korsman, K., Korja, T., Pajunen, M., Virransalo, P. & GGT/SVEKA Working Group 1999: The GGT/SVEKA Transect: Structure and evolution of the continental crust in the Paleoproterozoic Svecofennian Orogen in Finland. *International Geology Review 41*, 287-333.

Krill, A.G., Bergh, S., Lindahl, I., Mearns, E.W., Often, M., Olerud, S., Olesen, O., Sandstad, J.S., Siedlecka, A. & Solli, A. 1985: Rb-Sr, U-Pb and Sm-Nd isotopic dates from Precambrian rocks of Finnmark. *Norges geologiske undersøkelse Bulletin 403*, 37-54.

Krill, A.G. & Zwaan, B.K. 1987: Reinterpretation of Finnmarkian deformation on western Sørøy, northern Norway. *Norsk Geologisk Tidsskrift 67*, 15-24.

Kukkonen, I.T. & Peltonen, P. 1999: Xenolith-controlled geotherms for the central Fennoscandian Shield: implications for lithosphere-asthenosphere relations. *Tectonophysics 304*, 301-315.

Kukkonen, I. T. & Lahtinen, R. 2001: Variation of radiogenic heat production rate in 2.8-1.8 Ga old rocks in the central Fennoscandian shield. *Physics of the Earth and Planetary Interiors 126*, 279-294.

Kullerud, L., Tørudbakken, B.O. & Ilebekk, S. 1986: A compilation of radiometric age determinations from Western Gneiss Region, South Norway. *Norges geologiske undersøkelse Bulletin 406*, 17-42.

Lachenbruch, A.H. 1968: Preliminary geothermal model of the Sierra Nevada. *Journal of Geophysical Research 73,* 6977-6989.

Lambeck, K., Smither, C. & Johnston, P. 1998: Sea-level change, glacial rebound and mantle viscosity for northern Europe. *Geophysical Journal International 134,* 102-144.

Lappin, M. A., Pidgeon, R. T. & van Breemen, O. 1979: Geochronology of basal gneisses and mangeritie syenites of Stadtlandet, west Norway. *Norsk Geologisk Tidsskrift 59*, 161-181.

Laxon, S. & McAdoo, D. 1994: Arctic Ocean gravity field derived from ERS-1 satellite altimetry. *Science 256,* 621-624.

Leslie, A. G. & Nutman, A. P. 2000: Episodic tectono-thermal activity in the southern part of the East Greenland Caledonides. *Geological Survey of Greenland Bulletin 186*, 42-49.

Leslie, A. G. & Nutman, A. P. 2003: Evidence for Neoproterozoic orogenesis and early high temperature Scandian deformation events in the southern East Greenland Caledonides. *Geological Magazine 140*, 309-333.

Levchenkov, O.A., Levsky, L.K., Nordgulen, Ø., Dobrzhintskaya, L.F., Vetrin, V.R., Cobbing, J., Nilsson, L.P. & Sturt, B.A. 1993: U-Pb zircon ages from Sørvaranger, Norway, and the western part of the Kola Peninsula, Russia. *Norges geologiske undersøkelse Special Publication 7:* 29-47.

Lie, J.E. 1995: Deep seismic reflection mapping of crustal and upper mantle structures beneath the Skagerrak Sea, SW Scandinavia. PhD Thesis, University of Oslo, 138 pp.

Lie, J.E. & Husebye, E.S. 1993: Seismic imaging of upper crustal basement faults in the Skagerrak Sea. *Tectonophysics 219,* 119-128.

Lindahl, I., Sørdal, T. & Ekremseter, J. 1996: Naturlig radioaktivitet fra berggrunnen, Norge. M. 1:2 000 000, GeologicalSurvy of Norway.

Lindroos, H. & Henkel, H. 1978: Regional geological and geophysical interpretation of Precambrian structures in Northeastern Sweden. *Sver. geol. unders. C751,* 19 pp.

Lippard, S. J. 1976: Preliminary investigations of some Ordovician volcanics from Stord, West Norway. *Norges geologiske undersøkelse 327*, 41-66.

Lippard, S. J. & Mitchell, J. G. 1980: Late Caledonian dolerites from the Kattnakken area, Stord, SW Norway, their age and tectonic significance. *Norges geologiske undersøkelse 358*, 47-62.

Ludwig, K. R. 2003: Isoplot 3.00, A Geochronological Toolkit for Microsoft Excel. *Berkley Geochronology Center, Special Publication 4*, 1-74.

Ludwig, J.W., Nafe, J.E. & Drake, C.L. 1970: Seismic refraction. *In* Maxwell., A. (ed.) *The sea, Vol. 4*, Wiley, New York.

Lund, C. 1979: Crustal structure along the Blue Road Profile in northern Scandinavia. *Geologiska Föreningens i Stockholm Förhandlingar 101,* 191-204.

Lundmark, A. M. & Corfu, F. 2007: Age and origin of the Årdal dike complex, SW Norway: False isochrons, incomplete mixing, and the origin of Caledonian granites in basement nappes. *Tectonics 26*, TC2007, doi:10.1029/2005TC001844.

Lutro, O. & Tveten, E. 1996: Geologisk kart over Norge, berggrunnskart ÅRDAL M 1:250.000. *Norges geologiske undersøkelse, Trondheim.*

Lyngsie, S. B., Thybo, H. & Rasmussen, B. L. 2006: Regional geological and tectonic structures of the North Sea area from potential field modelling. *Tectonophysics 413*, 147-170.

MacLachlan, K. & Dunning, G. R. 1998a: U-Pb ages and tectono-magmatic evolution of Middle Ordovician volcanic rocks of the Wild Bight Group, Newfoundland Appalachians. *Canadian Journal of Earth Sciences 35*, 998-1017.

MacLachlan, K. & Dunning, G. R. 1998b: U-Pb ages and tectonomagmatic relationships of early Ordovician low-Ti tholeiites, boninites and related plutonic rocks in central Newfoundland, Canada. *Contributions to Mineralogy and Petrology 133*, 235-258.

Marker, M. 1985: Early Proterozoic (c, 2000-1900 Ma) crustal structure of the northeastern Baltic Shield: Tectonic division and tectogenesis. *Norges geologiske undersøkelse Bulletin 403,* 55-74.

Markl, G., Frost, B.R. & Bucher, K. 1998: The origin of anorthosites and related rocks from the Lofoten Islands, Northern Norway: I. Field relations and estimation of intrinsic variables. *Journal of Petrology 39*, 1425-1452.

Markl, G. & Höhndorf, A. 2003: Isotopic constraints on the origin of AMCG-suite rocks on the Lofoten Islands, N Norway. *Mineralogy and Petrology 78*, 149-171.

Mathisen, O. 1976: A method for Bouguer reduction with rapid calculation of terrain corrections. *Geographical Survey of Norway geodetic publications 18*, 40 pp.

Mauring, E., Beard, L.P., Kihle, O. & Smethurst, M.A. 2002: A comparison of aeromagnetic levelling techniques with an introduction to median levelling. *Geophysical Prospecting 50*, 43-54.

Mauring, E., Mogaard, J.O. & Olesen, O. 2003: Røst Basin Aeromagnetic Survey 2003 (RAS-03). Ra 3 aeromagnetic compilation. Data acquisition and processing report. *NGU Report 2003.070*, 20 pp.

McKenzie, D.P., Jackson, J. & Priestley, K. 2005: Thermal structure of oceanic and continental lithosphere. *Earth and Planetary Science Letters 233*, 337– 349.

Mekonnen, A.Y. 2004: A geophysical study of the Central Norwegian Caledonides. *Unpublished Master of Science Thesis*. NTNU, Trondheim, 80 pp.

Meyer, G. B., Grenne, G. & Pedersen, R. B. 2003: Age and tectonic setting of the Nesåa Batholith: Implications for Ordovician arc development in the Caledonides of Central Norway. *Geological Magazine 140*, 573-594.

Middleton, M. 1993: A transient method of measuring the thermal properties of rocks. *Geophysics 58*, 357-365

Midttømme, K. 1997: *Thermal conductivity of sedimentary rocks – selected methodological mineralogical and textural studies*. Dr.ing. thesis, NTNU 1997:142.

Midttømme, K., Skarphagen, H., Nordgulen, Ø. & Longva, O. 2000a: Utredning om grunnvarme til planlagte sykehus i Akershus. Feltundersøkelser. *NGU Rapport 2000.073*.

Midttømme, K., Hilmo, B.O., Skarphagen, H. & Nissen, A. 2000b: Kartlegging av energipotensialet i berggrunn på kartblad Bekkestua, Bærum kommune: Varmeledningsevne til bergarter *NGU Report 2000.036*, 105 pp.

Midttømme, K., Ramstad, R.K., Solli, A., Sørdal, T. & Elvebakk, H. 2004: Grunnvarmekartlegging i Asker og Bærum. *NGU Report 2004.013*, 44 pp.

Midtun, R.D. 1988: Karasjok-grønnsteinsbeltet, Regional geofysisk og geologisk tolkning. *NGU Skrifter 88*, 19 pp.

Milne, G.A., Davis, J.L., Mitrovica, J.X., Scherneck, H.-G., Johansson, J.M., Vermeer, M. & Koivula, H. 2001: Space-geodetic constraints on glacial isostatic adjustment in Fennoscandia. *Science 291*, 2381-2385.

Milne, G.A., Mitrovica, J.X., Scherneck, H.-G., Davis, J.L., Johansson, J.M., Koivula, H., & Vermeer, M. 2004: Continuous GPS measurements of postglacial adjustment in

Fennoscandia - 2. Modeling results. *Journal of Geophysical Research 109*, B02412, doi:10.1029/2003JB002619.

Milnes, A.G., Wennberg, O.P., Skår, Ø. & Koestler, A.G. 1997: Contraction, extension and timing in the South Norwegian Caledonides: The Sognefjord transect. *In* J.-P. Burg & M. Ford (eds.), *Orogeny Through Time*. Geological Society Special Publication 121, 123-148.

Mjelde, R., Sellevoll, M.A., Shimamura, H., Iwasaki, T. & Kanazawa, T. 1992: A crustal study off Lofoten, N. Norway, by use of 3D-component Ocean Bottom Seismographs. *Tectonophysics 212*, 269-288.

Mjelde, R., Sellevoll, M.A., Shimamura, H., Iwasaki, T. & Kanazawa, T. 1993: Crustal structure beneath Lofoten, N. Norway, from vertical incidence and wide-angle seismic data. *Geophysical Journal International 114*, 116-126.

Mjelde, R., Kodaira, S., Shimamura, H., Kanazawa, T., Shiobara, H., Berg, E.W. & Riise, O. 1997: Crustal structure of the central part of the Vøring Basin, mid-Norway margin, from ocean bottom seismographs. *Tectonophysics 277*, 235-257.

Mjelde, R., Digranes, P., Shimamura, H., Shiobara, H., Kodaira, S., Brekke, H., Egebjerg, T., Sørenes, N. & Thorbjørnsen, S. 1998: Crustal structure of the northern part of the Vøring Basin, mid-Norway margin, from wide-angle seismic and gravity data. *Tectonophysics 293*, 175-205.

Mjelde, R., Digranes, P., van Schaack, M., Shimamura, H., Shiobara, H., Kodaira, S. & Næss O. 2001: Crustal structue of the outer Vøring Plateau, offshore Norway, from ocean bottom seismic and gravity data. *Journal of Geophysical Research 106*, 6769-6791.

Mjelde, R., Kasahara, J., Shimamura, H., Kamimura, A., Kanazawa, T., Kodaira, S., Raum, T. & Shiobara, H. 2002: Lower crustal seismic velocity-anomalies; magmatic underplating or serpentinized peridotite? Evidence from the Vøring Margin, NE Atlantic. *Marine Geophysical Research 23*, 169-183.

Mjelde, R., Raum, T., Digranes, P., Shimamura, H., Shiobara, H. & Kodaira, S. 2003a: V_p/V_s ratio along the Vøring Margin, NE Atlantic, derived from OBS data: implications on lithology and stress field. *Tectonophysics 369*, 175-197.

Mjelde, R., Shimamura, H., Kanazawa, T., Kodaira, S., Raum T. & Shiobara, H. 2003b: Crustal lineaments, distribution of lower crustal intrusives and structural evolution of the Vøring Margin, NE Atlantic; new insight from wide-angle seismic models. *Tectonophysics 369*, 199-218.

Mjelde, R., Iwasaki, T., Shimamura, H., Kanazawa, T., Kodaira, S., Raum, T. & Shiobara, H. 2003c: Spatial relationship between recent compressional structures and older high-velocity crustal structures; examples from the Vøring Margin, NE Atlantic, and Northern Honshu, Japan. Journal: *Journal of Geodynamics 36-4*, 537-562.

Mjelde, R., Raum, T., Breivik, A., Shimamura, H., Mural, Y., Takanami, T. & Faleide, J.I. 2005: Crustal structure of the Vøring margin, NE Atlantic: a review of geological implications

based on recent OBS data. In: Doré, A.G., Vining, B.A. (Eds.), *Petroleum Geology: North-West Europe and Global Perspectives - Proceedings of the 6th Petroleum Geology Conference.* Geological Society of London, Special Publication, 803– 813.

Möller, C., Andersson, J., Lundqvist, I. & Hellström, G. 2007: Linking deformation, migmatite formation and zircon U–Pb geochronology in polymetamorphic orthogneisses, Sveconorwegian Province, Sweden. *Journal of Metamorphic Geology 25,* 727-750.

Morgan, P. & Sass, J.H. 1984: Thermal regime of the continental lithosphere. *Journal of Geodynamics 1,* 143-166.

Muir, R. J., Ireland, T. R., Bentley, M. R., Fitches, W. R. & Maltman, A. J. 1997: A Caledonian age for the Kiloran Bay appinite intrusion on Colonsay, Inner Hebrides. *Scottish Journal of Geology 33,* 75-83.

Myhre, P. I. 2005: The tectonomagmatic evolution of Svalbards North-Western Terrane. U/Pb-ages for Proterozoic crust and Caledonian magmatic evolution in Spitsbergen, University of Oslo, 99 p.

Mørk, M.B.E., McEnroe, S.A. & Olesen, O. 2002: Magnetic susceptibility of Mesozoic and Cenozoic sediments off Mid Norway and the role of siderite: implications for interpretation of high-resolution aeromagnetic anomalies. *Marine and Petroleum Geology 19,* 1115-1126.

Nadeau, P.H., Bjørkum, P.A. & Walderhaug, O. 2005: Petroleum system analysis: Impact of shale diagenesis on reservoir fl uid pressure, hydrocarbon migration and biodegradation risks. *In* Doré, A. G. & Vining, B. (eds.) *Petroleum Geology: North-West Europe and Global Perspectives - Proceedings of the 6th Petroleum Geology Conference,* 1267-1274. Geological Society, London.

Naidu P. S. & Mathew M. P. 1998: Correlation filtering: a terrain correction method for aeromagnetic maps with application. *Journal of Applied Geophysics 32,* 269-277.

Neumann, E.-R. 1994: The Oslo Rift: P-T relations and lithospheric structure. *Tectonophysics 240,* 159-172.

Neumann, E.-R., Wilson, M., Heeremans, M., Spencer, E.A., Obst, K., Timmermann, M.J. & Kirstein, L. 2004: Carboniferous-Permian rifting and magmatism in southern Scandinavia, the North Sea and northern Germany: A review. In: M. Wilson, E.-R. Neumann, G.R. Davies, M.J. Timmermann, M. Heeremans and B.T. Larsen (Editors), Permo-Carboniferous Magmatism and Rifting in Europe. Geological Society of London, Special Publications Vol. 223, pp. 11-40.

NGU laboratorium rapport 0297-2005: Varmeledningsevne for prøver fra borehull Lærdal 2, Lærdalstunnelen.

NGU laboratorium rapport 0311-2005: Varmeledningsevne for prøver fra borehull Lærdal 1, Lærdalstunnelen.

NGU laboratorium rapport 0311-2005: Varmeledningsevne for prøver fra Gåvålivatnet Hjerkinn og Løkken.

Nilsen, O. & Wolff, F.C. 1989: Geologisk kart over Norge, berggrunnskart RØROS & SVEG - M 1:250.000. *Norges geologiske undersøkelse, Trondheim*.

Nilsen, O., Sundvoll, B., Roberts, D. & Corfu, F. 2003: U-Pb geochronology and geochemistry of trondhjemites and a norite pluton from the SW Trondheim Region, Central Norwegian Caledonides. *Norges geologiske undersøkelse Bulletin 441*, 5-16.

Nilsen, O., Sundvoll, B., Roberts, D. & Corfu, F. 2003: U-Pb geochronology and geochemistry of trondhjemites and a norite pluton from the SW Trondheim Region, Central Norwegian Caledonides. *Norges geologiske undersøkelse Bulletin 441*, 5-16.

Nilsen, O., Corfu, F. & Roberts, D. 2007: Silurian gabbro-diorite-trondhjemite plutons in the Trondheim Nappe Complex, Caledonides, Norway: petrology and U-Pb geochronology. *Norwegian Journal of Geology 87*, 329-342.

Niskanen, E. 1939: On the upheavel of land in Fennoscandia. *Ann. Acad. Sci. Fenn., Ser. A 53*, 1-30.

Nissen, A. L., Roberts, D. & Gromet, L. P. 2006: U-Pb zircon ages of a tonalite and a granodiorite dyke from the southeastern part of the Bindal Batholith, central Norwegian Caledonides. *Norges geologiske undersøkelse Bulletin 446*, 5-9.

Nordås, J., Amaliksen, K. G., Brekke, R., Furnes, H., Sturt, B. A. & Robins, B. 1985: Lithostratigraphy and petrochemistry of Caledonian rocks on Bømlo, SW Norway. *In* Gee, D.G. & B.A. Sturt (eds.) *The Caledonide Orogen - Scandinavia and Related Areas*. Chichester, Wiley.

Nordgulen, Ø. & Schouenborg, B. 1990: The Caledonian Heilhornet Pluton, north-central Norway: Geological setting, radiometric age and implications for the Scandinavian Caledonides. *Journal of the Geological Society of London 147*, 439-450.

Nordgulen, Ø., Braathen, A., Corfu, F., Osmundsen, P. T. & Husmo, T. 2002: Polyphase kinematics and geochronology of the late-Caledonian Kollstraumen detachment, north-central Norway. *Norwegian Journal of Geology 82*, 299-316.

Nordgulen, Ø. 1999: Geologisk kart over Norge, berggrunnskart Hamar, 1:250,000, Norges geologiske undersøkelse, Trondheim.

Nordgulen, Ø., Bickford, M.E., Nissen, A.L. & Wortman, G.L. 1993: U-Pb zircon ages from the Bindal batholith, and the tectonic history of the Helgeland Nappe Complex, Scandinavian Caledonides. *Journal of the Geological Society of London 150*, 771-783.

Nordgulen, Ø., Tucker, R.D., Sundvoll, B., Solli, A., Nissen, A.L., Zwaan, K.B., Birkeland, A. & Sigmond, E.M.O. 1997: Paleo- to Mesoproterozoic intrusive rocks in the area between Numedal and Mjøsa, SE Norway. *In* Ø. Nordgulen, P. Padget, P. Robinson & S.A. McEnroe (eds.), *COPENA conference at NGU, August 18-22.*

Nordgulen, Ø., Lindstrøm, M., Solli, A., Barnes, C.G. & Sundvoll, B. 2001: The Caledonian Smøla-Hitra Batholith, Central Norway. *GSA Northeastern Section - 36th Annual Meeting.*

Norges geologiske undersøkelse 1992: Aeromagnetisk anomalikart, Norge M 1:1 mill, Norges geologiske undersøkelse, Trondheim.

Northrup, C. J. 1997: Timing of structural assembly, metamorphism, and cooling of Caledonian Nappes in the Ofoten-Efjorden Area, North Norway: Tectonic insights from U-Pb and $^{40}Ar/^{39}Ar$ geochronology. *Journal of Geology 105*, 565-582.

Norton, M.G. 1986: Late Caledonian extension in Norway; a response to extreme crustal thickening. *Tectonics 5,* 195-204.

Nystuen, J.P., 1981: The Late Precambrian "Sparagmites" of Southern Norway: A major Caledonian allochton – The Osen-Roa nappe Complex. *American Journal of Science 281,* 69-94.

O'Brien, B. H., O'Brien, S. J. & Dunning, G. R. 1991: Silurian cover, Late Precambrian-Early Ordovician basement, and the chronology of Silurian orogenesis in the Hermitage Flexure (Newfoundland Appalachians). *American Journal of Science 291*, 760-799.

Okubo, Y, Graft, R. J., Hansen, R.O., Ogawas, K. & Tsu, H. 1985: Curie point depths of the Island of Kyushu and surrounding areas, Japan. *Geophysics 53,* 481-494.

Olesen, O. 1988: Petrofysiske undersøkelser, Finnmark. *NGU Report 88.222,* 154 pp.

Olesen, O. 2005: Crystalline basement in the Norwegian sector of the North Sea. *In* Olesen, O. et al. *Kontiki Annual Report 2004, Continental crust and heat generation in 3D.* NGU Report 2005.008, 50-55.

Olesen, O. & Sandstad, J.S. 1993: Interpretation of the Proterozoic Kautokeino Greenstone Belt, Finnmark, Norway from combined geophysical and geological data. *Nor. geol. unders. Bull. 425,* 41-62.

Olesen, O. & Smethurst, M.A. 1995: NAS-94 interpretation Report, Part III: Combined interpretation of aeromagnetic and gravity data. *NGU Report 95.040,* 50 pp.

Olesen, O., Roberts, D., Henkel, H., Lile, O.B. & Torsvik, T.H. 1990: Aeromagnetic and gravimetric interpretation of regional structural features in the Caledonides of West Finnmark and North Troms, northern Norway. *Norges geologiske undersøkelse Bulletin 419,* 1-24.

Olesen, O., Henkel, H., Kaada, K. & Tveten, E. 1991: Petrophysical properties of a prograde amphibolite - granulite facies transition zone at Sigerfjord, Vesterålen, Northern Norway. *Tectonophysics 192,* 33-39.

Olesen, O., Gellein J., Håbrekke H., Kihle O., Skilbrei J. R., & Smethurst M. 1997a: *Magnetic anomaly map Norway and adjacent ocean areas, scale 1:3 million* Geological Survey of Norway (NGU), Trondheim.

Olesen, O., Torsvik, T.H., Tveten, E., Zwaan, K.B., Løseth H. & Henningsen, T. 1997b: Basement structure of the continental margin in the Lofoten-Lopphavet area, northern Norway: constraints from potential field data, on-land structural mapping and palaeomagnetic data. *Norsk Geologisk Tidsskrift 77,* 15-33.

Olesen, O., Lundin, E., Nordgulen, Ø., Osmundsen, P.T., Skilbrei, J.R., Smethurst, M.A., Solli, A., Bugge, T. & Fichler, C. 2002: Bridging the gap between the onshore and offshore geology in Nordland, northern Norway. *Norwegian Journal of Geology 82*, 243-262.

Olesen, O., Ebbing, J., Skilbrei, J.R. and Lundin, E. 2003: Interpretation of potential field data along the Lofoten margin, Part 1. *NGU Report 2003.089,* 68pp.

Olesen, O., Smethurst, M.A., Torsvik, T.H. & Bidstrup, T. 2004a: Sveconorwegian igneous complexes beneath the Norwegian–Danish Basin. *Tectonophysics 387,* 105-130.

Olesen, O., Ebbing, J., Lundin, E., Skilbrei, J.R., Smethurst, M.A. & Torsvik, T.H. 2004b: Interpretation of the Ra 3 potential field data along the Lofoten-Vøring continental margin, Part 2. *NGU Report 2004.027,* 56 pp.

Olesen, O., Ebbing, J., Elvebakk, H., Koziel, J., Lundin, E., Midttømme, K., Nordgulen, Ø., Rønning, J.S., Skilbrei, J.R., Slagstad, T., Wissing, B. & Cramer, J. 2005: Kontiki Annual Report 2004, Continental Crust and Heat Generation in 3D. *NGU Report 2005.008,* 70 pp.

Olesen, O., Balling, N., Bárrere, C., Breiner, N., Davidsen, B., Ebbing, J., Elvebakk, H., Gernigon, L., Koziel, J., Midttømme, K., Nordgulen, Ø., Olsen, L., Pascal, C., Ramstad, R. K., Rendall, H. O., Rønning, J. S., Skilbrei, J. R., Slagstad, T. & Wissing, B. 2006a: KONTIKI Report 2005-2006, Continental Crust and Heat Generation in 3D. *NGU Report 2006.059*, 185 pp.

Olesen O., Gernigon, L., Ebbing J., Mogaard J., Pascal C. & Wienecke S. 2006b: Interpretation of aeromagnetic data along the Jan Mayen Fracture Zone, JAS-05: Geological Survey of Norway. *NGU Report 2006.018,* 161 pp.

Oliver, G. H. J. & Krogh, T. E. 1995: U-Pb zircon age of 469±5 Ma for a metatonalite from the Kjosen Unit of the Lyngen Magmatic Complex, northern Norway. *Norges geologiske undersøkelse Bulletin 428*, 27-32.

Oliver, G. H. J., Chen, Y. D., Buchwaldt, R. & Hegner, E. 2000: Fast tectonometamorphism and exhumation in the type area of the Barrovian and Buchan zones. *Geology 28*, 459-462.

Olsen, L., 2006, Fennoscandia M-L Weichselian glacial variations - much more than just local ice-margin fluctuations, *in* The 27th Nordic Geological Wintermeeting, Oulu, Finland, p. 118.

Olsen, K.H., Baldridge, W.S., Larsen, B.T., Neumann, E.-R. & Ramberg, I.B. 1987: A lithospheric transect across the Oslo palaeorift. *EOS, Trans. Am. Geophys. Union 68*, 1480.

Orkla Industrier, Grubeseksjonen: Orkla Vest, hull nr 1, 18 pp.

Ormaasen, D.E. 1976: Geochemistry and petrology of the mangeritic rocks in Lofoten–Vesterålen Cand. real./M.Sc. thesis, University of Oslo.

Osmundsen, P. T., Andersen, T. B., Markussen, S. & Svendby, A. K. 1998: Tectonics and sedimentation in the hangingwall of a major extensional detachment: The Devonian Kvamshesten Basin, western Norway. *Basin Research 10*, 213-234.

Osmundsen, P.T., Sommaruga, A., Skilbrei, J.R. & Olesen, O. 2002: Deep structure of the Mid Norway rifted margin. *Norwegian Journal of Geology 82*, 205-224.

Osmundsen, P.T. & Andersen, T.B. 2001: The middle Devonian basins of western Norway: Sedimentary response to large-scale transtensional tectonics? *Tectonophysics 332*, 51-68.

Osmundsen, P.T. & Ebbing, J. 2007: Styles of extension offshore Mid Norway and implications for mechanisms of Late Jurassic-Early Cretaceous rifting. Submitted to Tectonics.

Osmundsen, P.T., Bøe, R., Davidsen, B., Ebbing, J., Eide, E.A., Hendriks, B.W.H., T.F. & Smelror, M. 2006: The recycling of an orogen: provenance and routing of detritus from Norway to the Mid-Norwegian margin. *NGU Report 2006.022*.

Ottemöller, L. & Midzi, V. 2003: The crustal structure of Norway from inversion of teleseismic receiver functions. *Journal of Seismology* 7, 35-48.

Parasnis, D.S., 1975. Temperature phenomena and heat flow estimates in two Precambrian ore-bearing areas North Sweden. *Geophysical Journal of the Royal Astronomical Society 43*, 631-654.

Parasnis, D.S. 1982: Geothermal flow and phenomena in two Swedish localities north of the Arctic circle. *Geophysical Journal of the Royal Astronomical Society 71*, 545-554.

Parker, R.L. 1972: The rapid calculation of potential anomalies, *Geophys. J. Royal Astr. Society 31*, 447-455.

Parsons B. & Sclater J. 1977: An analysis of the variation of ocean floor bathymetry and heat flow with age. *Journal of Geophysical Research 82*, 803-827.

Pascal, C. Roberts, D. & Gabrielsen, R.H. 2005: Quantification of neotectonic stress orientations and magnitudes from field observations in Finnmark, northern Norway. *Journal of Structural Geology 27*, 859-870.

Pascal, C., Ebbing, J. & Skilbrei, J.R. 2007: Interplay between the Scandes and the Transscandinavian Igneous Belt: integrated thermal and potential field modelling of the Central Scandes profile. *Norwegian Journal of Geology 87*, 3-12.

Pearce, J.A. & Cann, J.R. 1973: Tectonic setting of basic volcanic rocks determined using trace element analyses. *Earth and Planetary Science Letters 19*, 290-300.

Pedersen, S. & Maaloe, S. 1990: The Iddefjord granite: Geology and age. *Norges geologiske undersøkelse Bulletin 417*, 55-64.

Pedersen, R.-B., Furnes, H. & Dunning, G. 1991: A U/Pb age for the Sulitjelma Gabbro, North Norway: further evidence for the development of a Caledonian marginal basin in Ashgill-Llandovery time. *Geological Magazine 128*, 141-153.

Pedersen, R.-B. & Dunning, G. 1997: Evolution of arc crust and relations between contrasting sources: U-Pb (age), Nd and Sr isotope systematics of the ophiolitic terrain of SW Norway. *Contributions to Mineralogy and Petrology 128*, 1-15.

Pedersen, R. B., Nordgulen, Ø., Barnes, C. G., Prestvik, T. & Barnes, M. A. 1999: U-Pb dates from dioritic and granitic rocks in Velfjord, north-central Norway. Norsk Geologisk Forenings 16. landsmøte, Stavanger. *Geonytt*, p. 81.

Perez-Gussinye, M., Lowry, A.R., Watts, A.B. & Velicogna, I. 2004: On the recovery of effective elastic thickness using spectral methods: Examples from synthetic data and from the Fennoscandian shield. *Journal of Geophysical Research 109*, B10409, doi: 10.1029/2003JB002788.

Pidgeon, R. T. & Aftalion, M. 1978: Cogenetic and inherited zircon U-Pb systems in granites: Palaeozoic granites of Scotland and England. *In* Bowes, D. R. & B. E. Leake (eds.) *Crustal Evolution in Northwestern Britain and Adjacent Areas, Geological Journal Special Issue*. 10, 183-220.

Planke, S., Skogseid, J. & Edholm, O. 1991: Crustal structure of Norway, 62° to 70° North. *Tectonophysics 189*, 91-107.

Poldervaart, A. 1956: Zircons is rocks 2: Igneous rocks. *American Journal of Science 254*, 521-554.

Powell, W.G., Chapman, D.S., Balling, N. & Beck, A. E. 1988: Continental heat flow density. *In* R. Hänel, L. Rybach & L. Stegena (eds.). *Handbook of Terrestrial Heat-Flow Density Determinations*, 167-222. Dordrecht, Kluwer Academic Publishers, 486 pp.

Priem, H. N. A. & Torske, T. 1973: Rb/Sr isochron age of Caledonian acid volcanism from Stord, Western Norway. *Norges geologiske undersøkelse 300*, 83-85.

Raade, G. 1973: *Distribution of radioactive elements in the plutonic rocks of the Oslo region.* M.Sc. Thesis, University of Oslo, 162 pp.

Ragnhildstveit, J. & Helliksen, D. 1997: Geologisk kart over Norge, berggrunnskart Bergen – M 1:250.000. *Norges geologiske undersøkelse, Trondheim.*

Ragnhildstveit, J., Naterstad, J., Jorde, K., & Egeland, B. 1998: Geologisk kart over Norge; Berggrunnskart Haugesund – M 1:250.000. *Norges geologiske undersøkelse, Trondheim*.

Ramberg, I.B. 1976: Gravimetry interpretation of the Oslo Graben and associated igneous rocks. *Nor. geol. unders. 325*, 194 pp.

Ramezani, J., Dunning, G. R. & Wilson, M. R. 2002: Geologic setting, geochrmistry of alteration, and U-Pb age of hydrothermal zircon from the Silurian Stog'er Tight gold prospect, Newfoundland Appalachians, Canada. *Exploration And Mining Geology 9*, 171-188.

Ranalli, G. 1995: *Rheology of the Earth*, Chapman and Hall, New-York, 413 pp.

Raum, T., Mjelde, R., Digranes, P., Shimamura, H., Shiobara, H., Kodaira, S., Haatvedt, G., Sørenes, N. & Thorbjørnsen, T. 2002: Crustal structure of the southern part of the Vøring Basin, mid-Norway, from wide-angle seismic and gravity data. *Tectonophysics 355*, 99-126.

Redfield, T. F., Osmundsen, P. T. & Hendriks, B. W. H. 2005: The role of fault reactivation and growth in the uplift of western Fennoscandia. *Journal of the Geological Society of London 162*, 1013-1030.

Rehnström, E. F. in press: Two generations of Palaeozoic calc-alkaline magmatism in the central E Greenland Caledonides: Constraints from U-Pb ages and Hf isotopes.

Ritcey, D. H., Wilson, M. R. & Dunning, G. R. 1995: Gold mineralization in the Paleozoic Appalachian orogen: constraints from geologic, U/Pb, and stable isotope studies of the Hammer Down prospect, Newfoundland. *Economic Geology 90*, 1955-1965.

Ritter, U., Zielinski, G.R., Weiss, H.M., Zielinski, R.L.B., and Sættem, J. 2004: Heat flow in the Vøring Basin, Mid-Norwegian Shelf. *Petroleum Geoscience 10*, 353-365.

Roberts, A. Lundin, E.R. & Kusznir, N.J. 1997: Subsidence of the Vøring Basin and the influence of the Atlantic continental margin. *Journal of the Geological Society of London 154*, 551-557.

Roberts, D. 1980: Petrochemistry and Palaeogeographic Setting of the Ordovician Volcanic Rocks of Smøla, Central Norway. *Norges geologiske undersøkelse 359*, 43-60.

Roberts, D. 1985: The Caledonian fold belt in Finnmark: A synopsis. *Norges geologiske undersøkelse 403*, 161-177.

Roberts, D. & Gee, D. G. 1985: An introduction to the structure of the Scandinavian Caledonides. In: Gee, D. G. & B. A. Sturt eds. *The Caledonide Orogen - Scandinavia and Related Areas*. Chichester, Wiley, 55-68.

Roberts, D. & Tucker, R. D. 1998: Late Cambrian U-Pb zircon age of a meta-trondhjemite from Ytterøya, Trondheimsfjorden, central Norwegian Caledonides. *Norsk Geologisk Tidsskrift 78*, 253-258.

Roberts, D., Melezhik, V. A. & Heldal, T. 2002a: Carbonate formations and early NW-directed thrusting in the highest allochthons of the Norwegian Caledonides: Evidence of a Laurentian ancestry. *Journal of the Geological Society of London 159*, 117-120.

Roberts, D., Walker, N., Slagstad, T., Solli, A. & Krill, A. 2002b: U-Pb zircon ages from the Bymarka ophiolite, near Trondheim, central Norwegian Caledonides, and regional implications. *Norsk Geologisk Tidsskrift 82*, 19-30.

Roberts, R.J., Corfu, F., Torsvik, T.H., Ashwal, L.D. & Ramsay, D.M. 2006: Short-lived mafic magmatism at 560-570 Ma in the northern Norwegian Caledonides: U-Pb zircon ages from the Seiland Igneous Province. *Geological Magazine.*

Robins, B. & Often, M. 1996: The Seiland Igneous Province, North Norway. Field Trip Guidebook, IGCP project 336. *NGU Report 96.127*.

Rogers, G. & Dunning, G. R. 1991: Geochronology of appinitic and related granitic magmatism in the W Highlands of Scotland: Constraints on the timing of transcurrent fault movement. *Journal of the Geological Society of London 148*, 17-27.

Rogers, G., Paterson, B. A., Dempster, T. J. & Redwood, S. D., 1994, U-Pb geocrhonology of the Newer gabbros, NE Grampians. *In* Caledonian Terrane Relationships in Britain. Programme with Abstracts, British Geological Survey, Keyworth, p. 8.

Ross, H.E., Blakely, R.J. & Zoback, M.D. 2006: Testing the use of aeromagnetic data for thedetermination of Curie depth in California, *Geophysics 71*, P.L51-L59.

Rudnick, R. L., McDonough, W. F. & O'Connell, R. J. 1998: Thermal structure, thickness and composition of continental lithosphere. *Chemical Geology 145*, 395-411.

Rudnick, R. L. & Gao, S. 2003: The composition of the continental crust. *In* Rudnick, R. L. (ed.) *The Crust*. Treatise on Geochemistry 3, Oxford, Elsevier-Pergamon, 1-64.

Rybach, L., 1986. Amount and significance of radioactive heat sources in sediments. *In* J. Burrus (ed.), *Thermal modeling in sedimentary basins*, Editions Technip, Paris, 311-322.

Rybach, L. 1988: Determination of heat production rate. *In* R., Hänel, L. Rybach & L. Stegena (eds.) *Handbook of Terrestrial Heat-Flow Determination*. Dordrecht, Kluwer Academic Publishers, 125-142.

Samuelsson, J. & Middleton, M.F. 1998: The Caledonian foreland basin in Scandinavia: Constrained by the thermal maturation of the Alum Shale. *Geologiska Föreningen i Stockhom Förhandlingar 120,* 307-314.

Sandiford, M. & McLaren, S. 2002: Tectonic feedback and the ordering of heat producing elements within the continental lithosphere. *Earth and Planetary Science Letters 204*, 133-150.

Sandiford, M., McLaren, S. & Neumann, N. 2002: Long-term thermal consequences of the redistribution of heat-producing elements associated with large-scale granitic complexes. *Journal of Metamorphic Geology 20*, 87-98.

Schärer, U. 1980: U-Pb and Rb-Sr dating of a polymetamorphic nappe terrain: The Caledonian Jotun Nappe, southern Norway. Earth *and Planetary Science Letters 49*, 205-218.

Schärer, U., Wilmart, E. & Duchesne, J.-C. 1996: The short duration and anorogenic character of anorthosite magmatism: U-Pb dating of the Rogaland complex, Norway. Earth and *Planetary Science Letters 139*, 335-350.

Schiellerup, H., Lambert, D.D., Prestvik, T., Robins, B., McBride, J.S. & Larsen, R.B. 2000: Re-Os isotopic evidence for a lower crustal origin of massif-type anorthosites. *Nature 405*, 781-784.

Schmidt, J. 2000: Deep seismic studies in the western part of the Baltic shield. Uppsala Dissertations from the Faculty of Science and Technology 24.

Schmidt-Aursch, M.C. & Jokat, W. 2005a: The crustal structure of central east Greenland - I: From the Caledonian orogen to the Tertiary igneous province. Geophys. J. Int., 160, 736-752.

Schmidt-Aursch, M.C. & Jokat, W. 2005b: The crustal structure of central east Greenland - II: From the Precambrian shield to the recent mid-oceanic ridges. Geophys. J. Int., 160, 753-760.

Selbekk, R. S., Skjerlie, K. P. & Pedersen, R. B. 2000: Generation of anorthositic magmas by H_2O-fluxed anatexis of silica-undersaturated gabbro: An example from the north Norwegian Caledonides. *Geological Magazine 137*, 609-621.

Shuey R., Schlechinger D., Tripp A. & Alley L. 1977: Curie depth determination from aeromagnetic spectra. *Geophys. J. R. Astron. Soc. 50,* 75-102.

Siedlecka, A., Iversen, E., Krill, A.G., Lieungh, B., Often, M., Sandstad, J.S. & Solli, A. 1985: Lithostratigraphy and correlation of the Archean and Early Proterozoic rocks of

Finnmarksvidda and the Sørvaranger district. *Norges geologiske undersøkelse Bulletin, 403*: 7-36.

Siedlecka, A., Nystuen, J.P., Englund, J.O., Hossack, J. 1987: Lillehammer, Berggrunnsgeologisk kart 1:250 000. *Norges geologiske undersøkelse, Trondheim*.

Sigmond, E.M.O. 1998: Geologisk kart over Norge. Berggrunnsgeologisk kart ODDA, M 1: 250 000. *Norges geologiske undersøkelse, Trondheim*.

Sigmond, E.M.O. 2002: Geological Map, Land and Sea Areas of Northern Europe, Scale 1:4 million, *Geological Survey of Norway, Trondheim.*

Sigmond, E.M.O., Gustavson, M. & Roberts, D. 1984: Bedrock map of Norway, 1:1 million. *Norges geologiske undersøkelse, Trondheim*.

Simpson, R.W., Jachens, R.C., & Blakely, R.J. 1983: AIRYROOT: A Fortran program for calculating the gravitational attraction of an Airy isostatic root out to 166.7 km. *United States Department of the Interior, Geological Survey, Open-File Report 83-883*, 24 pp.

Sindre, A. 1993: *Regional tolkning av geofysiske data, kartblad Arendal*. NGU Report 92.213, 30 pp.

Size, W.B., 1985. Origin of trondhjemite in relation to Appalachian-Caledonide palaeotectonic settings. In: D.G.a.S. Gee, B. A. (Editor), The Caledonide Orogen-Scandinavia and Related Areas Vol. John Wiley and Sons Ltd, pp. 735-744.

Skår, Ø. 1998: *The Proterozoic and Early Paleozoic evolution of the southern parts of the Western Gneiss Complex, Norway* [Ph.D. thesis], University of Bergen.

Skår, Ø. 2000: Field relations and geochemical evolution of the Gothian rocks in the Kvamsøy area, southern Western Gneiss Complex, Norway. *Norges geologiske undersøkelse Bulletin 437*, 5-23.

Skår, Ø. 2002. U-Pb geochronology and geochemistry of early Proterozoic rocks of the tectonic basement windows in central Nordland, Caledonides of north-central Norway. Precambrian Research, 116: 265-283.

Skår, Ø. & Pedersen, R. B. 2003: Relations between granitoid magmatism and migmatization: U-Pb geochronological evidence from the Western Gneiss Complex, Norway. *Journal of the Geological Society of London 160*, 935-946.

Skår, Ø., Furnes, H. & Claesson, S. 1994: Middle Proterozoic magmatism within the Western Gneiss Region, Sunnfjord, Norway. *Norsk Geologisk Tidsskrift 74*, 114-126.

Skilbrei, J.R. 1988: Geophysical interpretation of the Fosen-Namsos Western Gneiss Region and northern part of the Trondheim Region Caledonides, central Norway. *Norges geologiske undersøkelse Special Publication 3*, 70-79.

Skilbrei, J.R. 1989: Petrofysiske undersøkelser, Midt-Norge., NGU Rapport 89.164.

Skilbrei, J.R. 1991: Interpretation of depth to the magnetic basement in the northern Barents Sea (south of Svalbard). *Tectonophysics 200*, 127-141.

Skilbrei, J.R. 1992: Preliminary interpretation of aeromagnetic data from Spitsbergen, Svalbard Archipelago (76^0-79^0 N): Implications for structure of the basement. *Marine Geol*. *106*, 53-68.

Skilbrei, J.R. 1993: An evaluation of magnetic basement depth determinations from the southwestern Barents Sea. (Chapter eight). *Doktor ingeniøravhandling 1993:68*. Norges tekniske høgskole, Trondheim.

Skilbrei, J.R. 2005: Basement depth map from the Barents Sea and Svalbard. *In:* Olesen, O. et al. *Kontiki Annual Report 2004, Continental crust and heat generation in 3D.* NGU Report 2005.008, 56-61.

Skilbrei, J.R. & Sindre, A. 1991: Tolkning av gravimetri langs ILP-profilet, Hemne-Storlien. *NGU Report 91.171*, 27 pp.

Skilbrei, J. R**.** & Kihle, O. 1998: Gravity modelling and petrophysical data from western Norway. *NGU Report 98.008*, 36 pp.

Skilbrei, J.R. & Olesen, O. 2005: Deep structure of the Mid-Norwegian shelf and onshore-offshore correlations: Insight from potential field data. In: B.T.G. Wandås, E.A. Eide, F. Gradstein, & J.P. Nystuen (Eds), *Onshore-Offshore relationships on the North Atlantic Margin.* Norwegian Petroleum Society (NPF), Special Publication 12. Elsevier, Amsterdam, 43-68.

Skilbrei, J.R., Faleide, J.I. & Myklebust, R. 1990: Magnetic anomalies and regional geology of the Barents Sea. Paper presented in Tromsø, Norway, 15-17 August 1990: International conference on Arctic Geology and Petroleum Potential. *Abstracts Volume*, p. 18.

Skilbrei, J.R., Håbrekke, H., Olesen, O., Kihle, O., Macnab, R. 1991a: Shaded relief aeromagnetic colour map of Norway and the Norwegian-Greenland and Barents seas: Data compilation and examples of interpretation. *NGU Report 91.269,* 15 pp.

Skilbrei, J.R., Skyseth, T. & Olesen, O. 1991b: Petrophysical data and opaque mineralogy of high grade and retrogressed lithologies: Implications for the interpretation of aeromagnetic anomalies in northern Vestranden, Western Gneiss Region, Central Norway. *Tectonophysics 192,* 21-31.

Skilbrei, J.R., Kihle, O., Olesen, O., Gellein, J., Sindre, A., Solheim, D. & Nyland, B. 2000: Gravity anomaly map Norway and adjacent ocean areas, scale 1:3 Million. Geological Survey of Norway, Trondheim.

Skilbrei, J.R., Olesen, O., Osmundsen, P.T., Kihle, O., Aaro, S. & Fjellanger, E. 2002: A study of basement structures and onshore-offshore correlations in Central Norway. *Norwegian Journal of Geology 82*, 263-279.

Skogseid, J., Pedersen, T., Eldholm, O. & Larsen, B.T. 1992: Tectonism and magmatism during NE Atlantic continental break-up: the Vøring margin. *In* B.C. Story, T. Alabaster and R.J. Plankhurst (eds.). *Magmatism and the Causes of Continental Break-up.* Geological Society of London Special Publications 68, 305-320.

Slagstad, T. 2005: Heat flow. *In* Olesen, O. et al. *Kontiki Annual Report 2004, Continental crust and heat generation in 3D.* NGU Report 2005.008, 21-24.

Slagstad, T. 2006: Did hot, high heat-producing granites determine the location of the Oslo Rift? *Tectonophysics 412,* 105-119.

Slagstad, T., Culshaw, N.G., Jamieson, R.A. & Ketchum, J.W.F. 2004: Early Mesoproterozoic tectonic history of the southwestern Grenville Province, Ontario: Constraints from geochemistry and geochronology of high-grade gneisses. *In* R.P. Tollo, L. Corriveau, J. McLelland and M.J. Bartholomew (eds.), Proterozoic tectonic evolution of the Grenville orogen in North America. *Geological Society of America, Memoir 197,* 209-241.

Slagstad, T., Jamieson, R.A. & Culshaw, N.G., 2005. Formation, crystallisation, and migration of melt in the mid-orogenic crust: Muskoka domain migmatites, Grenville Province, Ontario. *Journal of Petrology 46,* 893-919.

Slagstad, T., Melezhik, V.A., Kirkland, C.L., Zwaan, K.B., Roberts, D., Gorokhov, I.M. & Fallick, A.E. 2006: Carbonate isotope chemostratigraphy suggests revisions to the geological history of the West Finnmark Caledonides, North Norway. *Journal of the Geological Society of London 163,* 277-289.

Smethurst, M.A. 2000: Land-offshore tectonic links in western Norway and the northern north Sea. *Journal of the Geological Society, London 157,* 769-781.

Smith, W. H. F. & Sandwell, D. T. 1997: Global seafloor topography from satellite altimetry and ship depth soundings. *Science 277,* 1957-1962.

Smithson, S.B. 1963: Granite studies: I. A gravity investigation of two Precambrian granites in South Norway. *Nor. geol. unders. 214B,* 53-140.

Smithson, S.B. & Barth, T.F.W. 1967: The Precambrian Holum ganite, South Norway. *Nor. Geol. Tidsskr. 47,* 21-56.

Smithson, S.B.& Ramberg, I.B. 1979: Gravity interpretation of the Egersund anorthosite complex, Norway: Its petrological and geothermal significance. *Geol. Soc. Am. Bull. 90,* 199-204.

Söderlund, U., Möller, C., Andersson, J., Johansson, L. & Whitehouse, M. 2002: Zircon geochronology in polymetamorphic gneisses in the Sveconorwegian orogen, SW Sweden: Ion microprobe evidence for 1.46-1.42 and 0.98-0.96 Ga reworking. *Precambrian Research 113,* 193-225.

Spray, J. G. & Dunning, G. R. 1991: A U/Pb age for the Shetland Islands oceanic fragment, Scottish Caledonides: Evidence from anatectic plagiogranites in 'layer 3' shear zones. *Geological Magazine 128,* 667-671.

Spector, A. & Grant, F. 1970: Application of high sensitivity aeromagnetic surveying to offshore petroleum exploration. *Geophysical Prospecting 18,* 474-475.

Stacey, J. S. & Kramers, J. D. 1975: Approximation of terrestrial lead isotope evolution by a two-stage model. *Earth and Planetary Science Letters 26,* 207-221.

Stein, C.A. & Abbott, D.H. 1991: Heat flow constraints on the South Pacific Superswell. *Journal of Geophysical Research 96,* 16083-16099.

Steltenpohl, M.G., Hames, W.E. & Andresen, A. 2004: The Silurian to Permian history of a metamorphic core complex in Lofoten, northern Scandinavian Caledonides. *Tectonics 23*, TC1002, doi: 10.1029/2003TC001522.

Stephansson, O. 1989: Stress measurements and modelling of crustal rock mechanics in Fennoscandia. *In* Gregersen, S. & Basham, P.W. (eds.), *Earthquakes at North-Atlantic passive margins: neotectonics and postglacial rebound*, Kluwer Academic Publishers, Dordrecht, The Netherlands, 213-229.

Stephens, M. B., Kullerud, K. & Claesson, S. 1993: Early Caledonian tectonothermal evolution in outbpard terranes, central Scandinavian Caledonides: New constraints from U-Pb zircon dates. *Journal of the Geological Society of London 150*, 51-56.

Stewart, M., Strachan, R. A., Martin, M. W. & Holdsworth, R. E. 2001: Constraints on early sinistral displacements along the Great Glen Fault Zone, Scotland: Structural setting, U-Pb geochronology and emplacement of the syn-tectonic Clunes tonalite. *Journal of the Geological Society of London 158*, 821-830.

Strachan, R. A., Martin, M. W. & Friderichsen, J. D. 2001: Evidence for contamperaneous yet contrasting styles of granite magmatism during extensional collapse of the northeast Greenland Caledonides. *Tectonics 20*, 458-473.

Sundvor, E., Myhre, A. M. & Eldholm, O. 1989: Heat flow measurements on the Norwegian continental margin during the FLUNORGE project. *Seismo-Series 27*, Seismological Observatory, University of Bergen.

Swanberg, C. A., Chessman, M. D., Simmons, G., Smithson, S. B., Grønlie, G. & Heier, K. S. 1974: Heat-flow - heat-generation studies in Norway. *Tectonophysics 23*, 31-48.

Tanaka, A., Okubo, Y. & Matsubayashi, O. 1999: Curie point depth based on spectrum analysis of the magnetic anomaly data in East and Southeast Asia. *Tectonophysics 306*, 461-470.

Terry, M. P., Robinson, P. & Ravna, E. J. K. 2000: Kyanite eclogite thermobarometry and evidence for thrusting of UHP over HP metamorphic rocks, Nordøyane, Western Gneiss Region, Norway. *American Mineralogist 85*, 1637-1650.

Thunhead, H. & Olsson, O. 2004: Borehole corrections for a thick resistivity probe. *JEEG 9*, 217-224.

Torsvik, T. H. & Olesen, O. 1988: Petrophysics and palaeomagnetism initial report of the Norwegian Geological Survey Laboratory. *NGU Report 88.171*, 108 pp.

Tryti, J. & Sellevoll, M.A. 1977: Seismic crustal study of the Oslo Rift. *Pure and Applied Geophysics 115*, 1061-1085.

Tucker, R. D. 1988: Contrasting crustal segments in the Norwegian Caledonides: Evidence from U-Pb dating of accessory minerals. *In* GAC-MAC Program with abstracts, St. Johns.

Tucker, R. D. & Krogh, T. E. 1988: Geochronological investigations of the Ingdal Granite Gneiss and discordant pegmatites from the Western Gneiss Region, Norway. *Norsk Geologisk Tidsskrift 68*, 201-210.

Tucker, R. D., Boyd, R. & Barnes, S.-J. 1990a: A U-Pb zircon age for the Råna intrusion, N. Norway: New evidence of basic magmatism in the Scandinavian Caledonides in Early Silurian time. *Norsk Geologisk Tidsskrift 70*, 229-239.

Tucker, R. D., Krogh, T. E. & Råheim, A. 1990b: Proterozoic evolution and age-province boundaries in the central part of the Western Gneiss Region, Norway: Results of U-Pb dating of accessory minerals from Trondheimsfjord to Geiranger. *In* Gower, C. F., T. Rivers & A. B. Ryan (eds.) *Mid-Proterozoic Laurentia-Baltica*. Geological Association of Canada, Special Paper 38, 149-173.

Tucker, R. D., O'Brien, S. J. & O'Brien, B. H. 1994a: Age and implications of Early Ordovician (Arenig) plutonism in the type area of the Bay du Nord Group, Dunnage zone, southern Newfoundland Appalachians. *Canadian Journal of Earth Sciences 31*, 351-357.

Tucker, R. D., OBrien, S. J. & OBrien, B. H. 1994b: Age and implications of Early Ordovician (Arenig) plutonism in the type area of the Bay du Nord Group, Dunnage Zone, southern Newfoundland Appalachians. *Canadian Journal of Earth Sciences 31*, 351-357.

Tucker, R. D., Robinson, P., Solli, A., Gee, D. G., Thorsnes, T., Krogh, T. E., Nordgulen, Ø. & Bickford, M. E. 2004: Thrusting and extension in the Scandian hinterland, Norway: New U-Pb ages and tectonostratigraphic evidence. *American Journal of Science 304*, 477-532.

van Breemen, O., Aftalion, M. & Johnson, M. R. W. 1979a: Age of the Loch Borrolan complex, Assynt, and late movements along the Moine Thrust Zone. *Journal of the Geological Society of London 136*, 489-495.

van Breemen, O., Aftalion, M., Pankhurst, R. J. & Richardson, S. W. 1979b: Age of the Glen Dessary Syenite, Inverness-shire: Diachronous Palaeozoic metamorphism across the Great Glen. *Scottish Journal of Geology 15*, 49-62.

van Staal, C. R., Dunning, G. R., Valverde, P., Burgess, J. & Brown, M. 1994: Arenig and younger evolution of the Gander Margin: A comparison of the New Brunswick and Newfoundland segments. *In* New perspectives in the Appalachian-Caledonian Orogen (NUNA) Conference, Grand Falls, Newfoundland, p. 28.

van Wijk, J.W., van der Meer, R. & Cloetingh, S.A.P.L. 2004: Crustal thickening in an extensional regime: application to the mid-Norwegian Vøring margin. *Tectonophysics 387*, 217-228.

Vander Auwera, J., Bogaerts, M., Liégeois, J.-P., Demaiffe, D., Wilmart, E., Bolle, O. & Duchesne, J.-C. 2003: Derivation of the 1.0.0.9 Ga ferro-potassic A-type granitoids of southern Norway by extreme differentiation from basic magmas. Precambrian Research, 124: 107-148.

Verschure, R.H., Andriessen, P.A.M., Boelrijk, N.A.I.M., Hebeda, E.H., Maijer, C., Priem, H.N.A. & Verdurmen, E.A.T. 1980: On the thermal stability of Rb-Sr and K-Ar biotite systems: Evidence from co-existing Sveconorwegian (ca. 870 Ma) and Caledonian (ca. 400 Ma) biotites in SW Norway. *Contributions to Mineralogy and Petrology 74*, 245-252.

Vogel A. & Lund, C.-E. 1971: Profile Section 2-3. *In* Vogel, A. (ed.), *Deep seismic sounding in northern Europe*, 62-75. University of Uppsala, Swedish Natural Science Research Council, Stockholm.

Vogt, P.R., Taylor, P., Kovacs, L.C. & Johnson, G.L. 1979: Detailed aeromagnetic investigations of the Artic Basin. *Journal of Geophysical Research 84*, 1071-1079.

Vogt, P.R., Johnson, G.L. & Kristjansson, L. 1980: Morphology and magnetic anomalies north of Iceland. *Journal of Geophysics 47*, 67-80.

Wade, S.J.R. 1985: Radiogenic isotope studies of crust-forming processes in the Lofoten-Vesterålen Province of North Norway. PhD Thesis, University of Oxford.

Watt, G. R., Kinny, P. D. & Friedrichsen, J. D. 2000: U-Pb geochronology of Neoproterozoic and Caledonian tectonothermal events in the East Greenland Caledonides. *Journal of the Geological Society of London 157*, 1031-1048.

Wessel, P. & Husebye, E.S. 1987: The Oslo Graben gravity high and taphrogenesis. *Tectonophysics 142*, 15-26.

Whalen, J. B., Currie, K. L. & van Breemen, O. 1987: Episodic Ordovician-Silurian plutonism in the Topsails Igneous Terrane, western Newfoundland. *Royal Society of Edinburgh Transactions, Earth Sciences 78*, 17-28.

White, A.P., Hodges, K.V., Martin, M.W. & Andresen, A. 2002: Geologic constraints on middle-crustal behavior during broadly synorogenic extension in the central East Greenland Caledonides. *International Journal of Earth Sciences (Geologische Rundschau) 91*, 187-208.

White, R.S., Spence, G.D., Fowler, S.R., McKenzie, D.P., Westbrook, G.K. & Bowen, N. 1987: Magmatism at rifted continental margins. *Nature 330*, 439-444.

Whitehouse, M., Claesson, S., Sunde, T. & Vestin, J. 1997: Ion microprobe U-Pb zircon geochronology and correlation of Archaean gneisses from the Lewisian complex of Gruinard Bay, northwestern Scotland. *Geochimica et Cosmochimica Acta 61*, 4429-4438.

Whitehouse, M. J., Kamber, B. S. & Moorbath, S. 1999: Age significance of U-Th-Pb zircon data from early Archaean rocks of west Greenland - a reassessment based on combined ion-microprobe and imaging studies. *Chemical Geology 160*, 201-224.

Wiedenbeck, M., Allé, P., Corfu, F., Griffin, W. L., Meier, M., Oberli, F., Von Quadt, A., Roddick, J. C. & Spiegel, W. 1995: Three natural zircon standards for U-Th-Pb.Lu-Hf, trace element and REE analyses. *Geostandards Newsletter 19*, 1-23.

Wilson, J. R., Hansen, B. T. & Pedersen, S. 1983: Zircon U-Pb evidence for the age of the Fongen-Hyllingen complex, Trondheim region, Norway. *Geologiska Föreningen i Stockholm Förhandlingar 105*, 68-70.

Wilson, M.R. 1980: Granite types in Sweden. *Geologiska Föreningen i Stockholm Förhandlingar 102*, 167-176.

Wolff, F.C. 1979: Beskrivelse til de bergrunngeologiske kart Trondheim og Østersund 1:250,000. *Norges geologiske undersøkelse 353*, 76 pp.

Wolff, F.C. 1984: Regional geophysics in the Central Norwegian Caledonides. *Norges geologiske undersøkelse Bulletin 397*, 1-27.

Yoshinobu, A. S., Barnes, C. G., Nordgulen, Ø., Prestvik, T., Fanning, M. & Pedersen, R.-B. 2002: Ordovician magmatism, deformation, and exhumation in the Caledonides of central Norway: An orphan of the Taconic orogeny? *Geology 30*, 883-886.

Zaleski, E. 1983: The geology of Strathspey and Lower Findhorn granitoids - a study involving field relations, petrography, mineralogy, geochemistry and geochronology [MSc thesis], University of St. Andrews.

Zwaan, K.B. 1995: Geology of the West Troms Basement Complex, northern Norway, with emphasis on the Senja Shear belt: A preliminary account. *Norges geologiske undersøkelse Bulletin 427*, 33-36.

20 APPENDIX A - ZIRCON U–PB ANALYSES BY LA–ICP–MS AT NGU

Børre Davidsen & Trond Slagstad, NGU

Methodology

The U–Pb age measurements on zircons were performed at the Geological Survey of Norway (NGU), using laser ablation inductively coupled plasma mass spectrometry (LA–ICP–MS), and at the NORDSIM facility in Stockholm, Sweden, using secondary ion microprobe spectrometry (SIMS).

Mineral separates were prepared at NGU, using standard techniques of crushing, followed by Frantz magnetic field separator and heavy liquids. Because of the small size of the samples, the Wilfley table was not used. Zircons selected for analysis were handpicked from the least magnetic fractions of heavy minerals, taking into consideration that the LA–ICP–MS technique used requires zircons to be larger than c. 90x70 μm. A total of 11 samples have been dated, 10 with LA–ICP–MS and 8 using both LA–ICP–MS and SIMS.

LA–ICP–MS set-up at NGU

The instrumentation used at NGU consists of a Finnigan MAT Element 1 single collector high-resolution sector ICP-MS, in this case alimented by a Finnigan MAT 266 nm (Nd:YAG) UV-laser. During analysis the laser is operated in Q-mode, at a frequency of 10 Hz. Depending on the sample, the energy used on samples typically varies from about 0.01 mJ to 1.0 mJ, tuned to give the optimum counting statistics (with ~ 3 kcps ^{207}Pb as the lower limit, and 4000 kcps ^{238}U as the higher limit). To minimize elemental fractionation, the zircon crystals are ablated in a raster area mode, typically 80x60 μm. However, some grains have been analysed using a reduced raster area, c. 50x40 μm. Also, it is important to limit the ablation energy used, as high energies will lead to relatively deep ablation craters, with increased Pb/U mass fractionation as a consequence.

The sample aerosol is transported from the sample chamber in He gas, and introduced in the ICP-MS instrument as a mixture of He and Ar gas. The data are acquired in a time-resolved counting scanning mode for 60 sec. Masses ^{202}Hg, ^{204}(Hg+Pb), ^{206}Pb, ^{207}Pb, ^{208}Pb, ^{232}Th and ^{238}U are measured. Monitoring ^{202}Hg and assuming a ^{202}Hg/^{204}Hg ratio of 4.36 corrects the interference of ^{204}Hg on ^{204}Pb. A 60 sec delay is performed after each zircon analysis, and a 60 sec gas blanks acquired at regular intervals. Each analytical session typically takes 10–15 hours.

The measured isotope ratios are corrected for element- and mass-bias effects using the Geostandard 91500 reference zircon (Wiedenbeck et al. 1995), normally based on 15 to 30

analyses during one analytical session. The data reduction is performed using MS Excel spreadsheets with Visual Basic macros developed in-house (Mansfeld 2001a,b,c). Common lead correction is conducted if necessary, estimated from the Stacey & Kramers (1975) Pb-evolution model. Diagrams and age calculations are generated with the ISOPLOT program (version 3.00, Ludwig 2003). From routine analyses of reference samples with known isotopic composition, the accuracy of the U–Pb ages of this method has shown to be better than 1-2 % and the precision normally better than 1-2 % (1 σ-level, though prone to reduced precision when subject to common lead correction, due to error propagation) (cf., Bingen et al. 2005). Unless otherwise stated, errors given are given on 1 σ-level.

Common lead correction, when applied, is for simplicity normally conducted using present day Pb isotopic compositions. This is considered justified as the LA–ICP–MS analyses are more exposed to contamination by young Pb compositions, compared to other techniques such as TIMS (with less rigorous cleaning and crystal selection procedures, e.g. larger numbers and no abrasion of altered/metamict parts). In addition, the surface ablation is likely to involve rather young ages. However, for the age spans and compositions involved, the choice of recent versus older Pb compositions is in practice without importance, as the results will not differ.

We observe that some of the analyses give $^{202}Hg/(^{204}Hg + ^{204}Pb)$ higher than the natural ratio of 4.36 for $^{202}Hg/^{204}Hg$, which should not be possible. For the analyses concerned, this causes the data reduction involving common lead correction to collapse, producing either no result or overcorrected, erroneous data points. This problem will commonly affect otherwise good and near-concordant analyses, with no or little common lead. In some cases we will therefore use values not corrected for common Pb for these samples (as they do not contain detectable ^{204}Pb), in combination with the common Pb corrected data set for the remaining samples. For age calculations and statistical analyses such combined data sets should be used with caution, as lower error figures for the Pb uncorrected samples gives them higher statistical weight. The reason for the 202/204 > 4.36 is not understood, but the possibility of an artefact from the data reduction cannot be excluded.

Normally, only isotope ratios are reported. A quantitative determination of selected elements (i.e., Pb, U, Th) requires control on the ablated volume of mass, through additional measurements of isotopes appropriate as internal standards (i.e., zirconium or silicon). However, a semi quantitative determination of Pb, U and Th is possible, using a specific analytical protocol and processing sequence based on laser energy matching against analysed NIST-standard(s) and/or zircon standards; in this work we calibrate against NIST 610. Compared to results for control samples of known composition, the expected accuracy is normally within ±50 % when laser energies > c. 0.3 mJ are applied. Below this energy limit, inaccuracy increases rapidly and calculated values might be overestimated by an order of magnitude (presumably due to enhanced

ablation yields at low energies on rough sample surfaces compared to the smoother standards). Spurious results may, however, occur. For data points with measured ratios 202/204 > 4.36, in addition to some analyses with high ^{238}U, the data reduction collapse and produce erroneous concentrations of Pb_{tot}, as well as Pb_{init}. Otherwise, the accuracy and quality of values given for Pb_{init} are unknown.

To monitor the accuracy of the dating results, control samples were analysed during the analytical sessions: Multiple zircon grains from granite ØS-99-14 with an age of 1797 ±3 Ma (Skår 2002), and fragments of gem-zircon GJ-1 with an age of 608.5 ±1.5 Ma (Jackson et al. 2004). Ideally, these samples should be treated as unknowns during analysis and data processing (but see below).

The age determinations using LA–ICP–MS have been performed on two types of zircon mounts, in a total of four analytical sessions:

1) Zircon crystals mounted on double sided tape on transparent polycarbon slices (for LA–ICP–MS), and
2) Zircon crystals embedded in epoxy (Struers Epofix) and polished down to the centre of the grains (for LA–ICP–MS + SIMS).

The first type of mount enables rim-analysis of the zircon crystals, and have been used for 10 of the 11 samples. In our experience, surface ablation of whole, tape-mounted zircon crystals will often provide a lower intercept on the concordia that may be valuable for interpreting the geological history of the rock. In the analytical protocol tape-mounted zircons are ablated twice; first with as low laser energy (and hence shallow ablation depth) as possible, then a subsequent ablation with as high energy as possible (se below). In favourable situations the first ablation provides information about the rim composition, if present. In many cases, however, a secondary rim will not be present, or is thin and U-poor and will thereby provide an analytical signature that is lost in the combined signal arising from ablation through the rim and into the inner parts of the zircon crystal. In addition, there are numerous situations where complex overgrowths and lead-loss histories, and/or contamination during sample processing and/or instrument-dependent artefacts (i.e., laser-induced mass-biases), creates disturbances or results that have no geological meaning. Therefore, rim-results obtained applying this analytical protocol must be interpreted and used with caution.

The second ablation will normally provide good quality results from the inner part of the zircon, though depending on the quality and complexity of the zircon itself. In fact, with the laser used at NGU, tape mounts will often be less prone to laser-induced mass biases than ablation of polished crystals embedded in epoxy. The reasons are not completely understood, but different energy-dependent ablation behaviour on polished versus non-polished surfaces (where polished

surfaces requires higher laser energies that hence creates deeper ablation craters), is a major factor.

Table A1 shows the gas blanks obtained during the four analytical sessions (all but ^{232}Th and ^{238}U normally decreases to near constant values during an analytical session).

Table A1. Gas blanks obtained during the four analytical sessions.

Session / Mount: *Sample(s)* / *Isotope*	**061120** Tape # 6 *16/1-4, 16/3-2, 16/4-1b, 16/5-1, 16/6-1, 25/7-1S*	**061124** Tape # 6 *35/3-4, 36/1-1, 6306/10-1, 6407/10-1*	**061214** Epoxy # 4 *25/7-1S*	**070129** Epoxy # 4 *35/3-4, 36/1-1*
^{202}Hg	3000-2400	1800-1500	3000-2800	3500-2500
^{204}Hg+^{204}Pb	750-590	450-390	700-690	850-600
^{206}Pb	~60	80-60	130-110	150-110
^{207}Pb	~60	65-50	120-90	150-90
^{208}Pb	80-70	100-75	250-200	300-200
^{232}Th	40-45	40-50	20-40	50-100
^{238}U	~40	35-40	20-25	30-40

The values observed are not only a function of the contamination / blank level, but will also vary with tuning and instrumental sensitivity at each analytical session.

Zircon selection and mounting

As described above, zircons were selected from the least magnetic fractions, with a size requirement of minimum 90x70 μm for LA–ICP–MS analyses. Preferably, clear crystals with few inclusions and cracks were chosen. For the sedimentary sample 25/7-1Sb zircon grains were selected on basis of shape and size to be representative for the population as a whole (but again limited to the size constraints of the LA–ICP–MS technique).

Of the 11 samples, 10 were first mounted on double coated tape. For each sample, c. 20 crystals (6 for sample 16/6-1) were mounted in a row, of which 12 crystals for each (6 for 16/6-1) were analysed by the combined surface ablation / core ablation protocol.

After analysis, zircons were detached from the tape and embedded in epoxy for supplementary analysis, either by LA-IC-MS or by SIMS. Upon remounting each analysed zircon were turned

90º so that the ablation crater in the zircon (hopefully) would show up in the polished cross-section of the epoxy mount. For some samples additional crystals were mounted.

The numbering system used in reporting is based on the position of the individual grain in the tape mount (row.pos), expanded where crystals were added to the epoxy mounts. Each individual zircon crystal thereby keeps the same numerical identification on all reported analyses. Surface ablation points are denoted by the suffix "p", while ablation of mounted zircons previously analysed on tape are denoted by the suffix "m". In some cases, reanalyses produces two analyses in the same point, in which the first is denoted by the suffix [1].

Possible contamination from epoxy ablation

As the ablation area is relatively large, it is difficult to completely avoid undesired ablation into the mounting medium of the zircons. In particular, this was the case for the sedimentary sample 25/7-1S, where 88 out of 114 analyses touch the surrounding epoxy. Therefore the question arises to what extent, if any, this affects the results obtained?

One data set is available from ablation of the possible contaminator, in this case epoxy covered by tape, Fig. A1. The pre-ablation stage, comprising two subsequent ablations applying energies of 0.005 and 0.01 mJ, does not provide any signal that survives data processing. With the energies deployed, it is likely that the pre-ablation, mostly or entirely, only sampled the tape covering the epoxy. For the ablation stage, two subsequent ablations using energies of 0.1 and 1.0 mJ provides data points that contain information, cf., Fig. A1. Their compositions are such that they could (in particular for spot "Bom") create discordant data points when contributing to a composite signal from ablated zircons. The semi quantitative determination yields the following data set for the epoxy:

Table A2. Composition of epoxy.

Abl. energy / Element	**U** (ppm)	**Th** (ppm)	$\mathbf{Pb}_{tot}$ (ppm)	$\mathbf{Pb}_{init}$ (ppm)	202Hg rel. counts	204Pb rel. counts	206Pb rel. counts	207Pb rel. counts	208Pb rel. counts
0.1 mJ	1.51 ±0.41	0.65 ±0.34	0.93 ±?	0.57 ±?	0.022	0.0094	0.062	0.0007	0.00011
1.0 mJ	1.06 ±0.17	0.25 ±0.10	7.76 ±2.25	7.52 ±2.25	0.106	0.0336	0.093	0.0031	0.00055

As the matrix of the epoxy is widely different from the NIST-glass, this determination is likely to be sluggish, providing only the orders of magnitude (with highly inaccurate error figures). However, for this purpose it is irrelevant, as it is the ablated *amount* of the interfering elements (expressed as *detected* concentration), not the concentration, that matters when evaluating the contamination potential on the zircon analyses.

The content of Pb in epoxy (with relative amounts possibly between 5 and 10 ppm, referred to appropriate ablation energy levels) is at a magnitude that potentially could create significant contamination. Still, it is not quite clear how much weight that can be put on these figures. For example, it is known that the epoxy contains elevated contents of Hg (as evidenced by elevated blanks when the epoxy mount is slightly heated in the sample chamber under the illuminating device), and the 1.0 mJ ablation gives 5 times as high ^{202}Hg (expressed in relative counts) compared to the 0.1 mJ ablation. This will certainly affect the results through data reduction involving correction of ^{204}Hg on ^{204}Pb. For example, ^{204}Pb shows a 3-fold increase from 0.1 mJ to 1 mJ laser energy, while ^{206}Pb only increases 50%. This non-consistency suggests that artefacts are present in the calculated concentrations. The data points otherwise disappears when a common Pb-correction is applied.

When ablating sample 25/7 1S for provenance study, various types of epoxy interaction took place, ranging from no observed epoxy melting, via slight epoxy melting due to laser light refracted by the zircon crystal, to direct hits of the surrounding epoxy. The ablation results for 25/7-1Sb have been subdivided into six categories, based on various degrees of epoxy interaction (Fig. A2). As can be seen from the figure, there is no obvious correlation between epoxy involvement and degree of discordance of the plotted data points. Neither do the same data set corrected for common Pb hint to differences related to the degree of epoxy contribution (Fig A3).

However, the calculated Pb concentrations in the zircons are highly variable, ranging from 4 to 159 ppm (mean 29 ppm ±25). It would be expected that analyses yielding low Pb concentrations are more prone to be affected by eventual contaminating effects from the epoxy, than those high in Pb. This implies that the potential contamination sensitivity of a data point will be proportional to the ablated volume of epoxy, and inversely proportional to the Pb concentration; i.e.:

Epoxy sensitivity factor = 100 x Epoxy coeff / conc. Pb

If the ablation into the epoxy is responsible for (some of) the discordance of the data points, the discordance then should show a positive correlation with the epoxy sensitivity factor. As is observed in Fig. A4. The correlation is statistically significant, but with a considerable scatter that gives a regression factor of 35 %. Subsets comprised of each epoxy factor (not shown) give the same results, a part from subset 0 (without any epoxy ablation) and subsets 4+5 (with too few data points). Similar correlations are seen on subsets dived in Pb concentration intervals, up to 50 ppm Pb. Discordance values obtained by regression range from 5% to 20%, with an error mean square ranging from 1.2 to 5.

However, the variation in discordance in subset 0 alone ranges from 2.3 % to 16.9 % (mean 9.1 % ±3.7), in which case epoxy contamination can be ruled out as a source for the observed variation. Also, if epoxy contamination statistically affects the results, it is puzzling that the five data points associated with the largest volumes of ablated epoxy (3m, 4.7, 9.6, 9.7, 10.3) do not show this correlation, despite low Pb concentrations in the range 13-30 ppm, and with discordances as low as 5.8 (mean 11.6 %). Therefore, epoxy contamination, if present, cannot be an explanation alone.

In conclusion, the arguments in favour of a contamination effect from ablated epoxy are very ambiguous. We might or might not have such an effect, in which case it is anyway confined to Pb concentrations below 50 ppm, and with a limited effect. Other causes for discordant behaviour must be of larger importance, including zircon compositions, instrumental artefacts (mainly ablation effects) and processing artefacts. In cases where ablation of the zircon rim takes place – either at the surface or at depth – this may of course also contribute to a composite signal that deviates from the ablated (otherwise concordant?) core.

Detailed treatment of U–Pb zircon data from 25/7–1S

The dating results for all 110 analysed grains mounted in epoxy are shown in (Fig. A5) as a Concordia plot without common Pb correction. The main group have ages between 1000 and 1800 Ma, but there are also two data points giving ages around 2800 Ma. The majority of the data points are discordant, with a mean discordance around 9 %. The data set clearly benefits from a common lead correction (Fig. **A**6), reducing the mean discordance to c. 7 %. However, 14 (mostly good) data points are lost in the data reduction when the common Pb correction is applied.

A cumulative probability plot based on 82 analyses from the same data set filtered to <10% discordance (Fig. A7) shows that the main age group 1000–1800 Ma is comprised of several subgroups, respectively, centred around 1000–1150 Ma, c.1350 Ma and 1600–1650 Ma, with a subordinate peak at 1500 Ma. In addition there are a few outliers at c. 1900 and c. 2800 Ma. An alternative plot supplemented with 11 data points (< 10 % discordant) without common lead correction for those samples not surviving data reduction with common lead correction, is shown in Fig. A8. Figs. A7 and A8 are virtually identical, as is the case with other plots incorporating all samples regardless of discordance (not shown).

As 12 grains from the sample has been subject to surface ablation in tape mounts, as well as epoxy mounts, this provides additional information on the sample. Fig. A9 shows a plot of combined data for the two analytical methods, for the same 12 grains. Many of the data points are highly discordant, but with those representing surface ablation situated at the younger ages of the span. A common Pb corrected data set reduces the spread considerably, and is used to extract

regression data for each individual grain (with 3 data points for each) (Fig. A10). The lower intercept ages thereby obtained range from 377 to 784 Ma, but with a large uncertainty. An average calculation will be strongly affected by three of these data sets (6, 11 and 12) that have narrows error limits and are slightly out of line with the others. If these are treated as outliers, the remaining data points provide a mean lower intercept of 462 ±180 Ma (Fig. A11). This result should be treated with caution, mainly because small errors in the common Pb correction will have a considerable impact on the calculated regression lines. Nevertheless, it seems clear that the sample have experienced a pre-recent thermal event causing lead loss or most likely overgrowths (cf., bright CL rims on the grains). This could well have been an event of Caledonian age.

Mount details

Tape mount # 6 (Kontiki):

Mounted: 17.11.2006
Photos: 19.11.2006
Analysed: 20.+24.11.2006 (contract 2006.0480)

1. 16/1-4 (1937 m): 20 grains (transferred to epoxy mount # 5)
2. 16/3-2 (2017,7 m): 20 grains (transferred to epoxy mount # 5)
3. 16/4-1b (2908,6 m): 20 grains (transferred to epoxy mount # 5)
4. 16/5-1 (1929,3 m): 22 grains (transferred to epoxy mount # 5)
5. 16/6-1 (2059,7 m): 6 grains (transferred to epoxy mount # 5)
6. 25/7-1Sb (3554,3 m): 20 grains (transferred to epoxy mount # 4)
7. 35/3-4 (4088,3 m): 20 grains (transferred to epoxy mount # 4)
8. 36/1-1 (5212,3 m): 20 grains (transferred to epoxy mount # 4)
9. 6306/10-1 3158,5-3159,2 m): 20 grains (transferred to epoxy mount # 4)
10. 6407/10-1 (2972,1 m): 20 grains (transferred to epoxy mount # 4)
11. MM 0133 (added later): 19 grains (turned out to be apatite!)

Control samples / Standards

12a. Ringvassøy: 5x2 grains (5 grains transferred to epoxy mount # 4, 5 grains to epoxy mount # 5)
12b. OS9914: 5x4 grains (10 grains transferred to epoxy mount # 4)
12c. 91500: 2 grains
12d. GJ-1: 3 grains (grain 3 transferred to epoxy mount # 4)

Epoxy mount # 4 (Kontiki for ICP-MS-analyses):

Mounted: 04.12.2006
Lappet sår: 05.12.2006 (tape glue around zircons washed off with acetone and scars filled in with new epoxy)
Polished: 8.+11. December 2006 (Trond Slagstad)
SEM images: 12. December 2006 (Trond Slagstad)
Analysed: 14. December 2006 (contract 2007.0104) + 29. January 2007 (contract 2007.0105)

1. 25/7-1s: 20 grains from tape # 6 (rotated) in one row + 9 rows of 10 new grains in each.
2. 35/3-4: 20 grains from tape # 6 (rotated) in one row
3. 36/1-1: 20 grains from tape # 6 (rotated) in one row
4. 6306/10-1: 20 grains from tape # 6 (rotated) in one row
5. 6407/10-1: 20 grains from tape # 6 (rotated) in one row

Control samples / Standards

6a. GJ1: 1 fragment (grain 3) from tape # 6
6b. ØS9914: 10 grains from tape # 6
6c. Ringvassøy: 5 grains (No. 1-5) from tape # 6
6d. Seiland: 1 grain from batch "oct. 2006" (to be checked with SIMS)
7. 91500: 2 grains (from UiTø)

Epoxy mount # 5 (Kontiki for SIMS analyses):

Mounted: 04.12.2006
Epoxy repair: 05.12.2006 (tape glue around zircons washed off with acetone and scars filled in with new epoxy; two zircons detached and remounted, one lost)
Polished: 8. december 2006
Analysed: 17.-20. january 2007

<u>Control samples</u>

1a. Seiland: 1 fragment from batch "oct. 2006"
1b. Ringvassøy: 5 grains (No. 6-10) from tape # 6 + 5 new grains

<u>Samples</u>

2. 16/1-4: 20 grains from tape # 6 (rotated) in one row

3. 16/3-2: 20 grains from tape # 6 (rotated) in one row
4. 16/4-1b: 21 grains from tape # 6 (rotated) in one row
5. 16/5-1: 20 grains from tape # 6 (rotated) in one row
6. 16/6-1: 6 grains from tape # 6 (rotated) + 14 new grains in one row (No. 6 + 20 lost)
7. 6609/7-1: 3x20 new grains, in 3 row (uncertain if all are zircons) (1 lost, No. 2,19 remounted)
8. 6306/10-1: 20 new grains in one row
9. 6407/10-1: 20 new grains in one row (No. 7 lost, No. 20 remounted)
10. LOF-09: 10 new grains in one row (to be tested as supplementary control sample for LA–ICP–MS)

Standard

91500: 3 fragments from UiTø

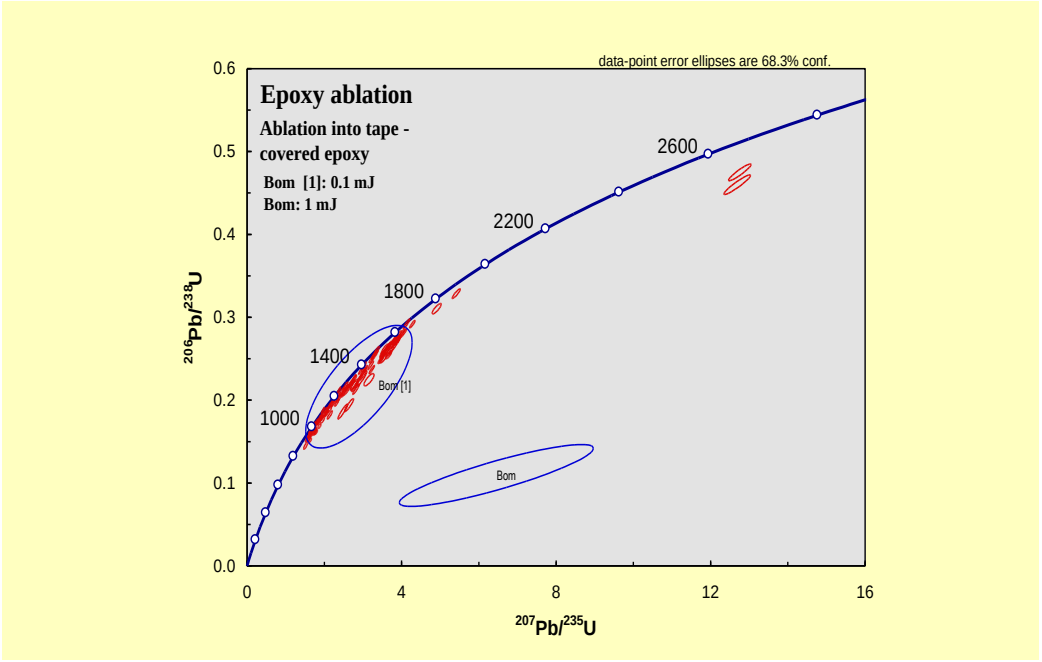

Figure A1. Ablation into epoxy covered with double coated tape. Data points for ablation with 0.1 mJ (Bom [1]) and 1 mJ laser energy are shown plotted with data points for sample 25/7-1S (without common Pb correction). The epoxy composition is potentially a contaminator for ablated zircons.

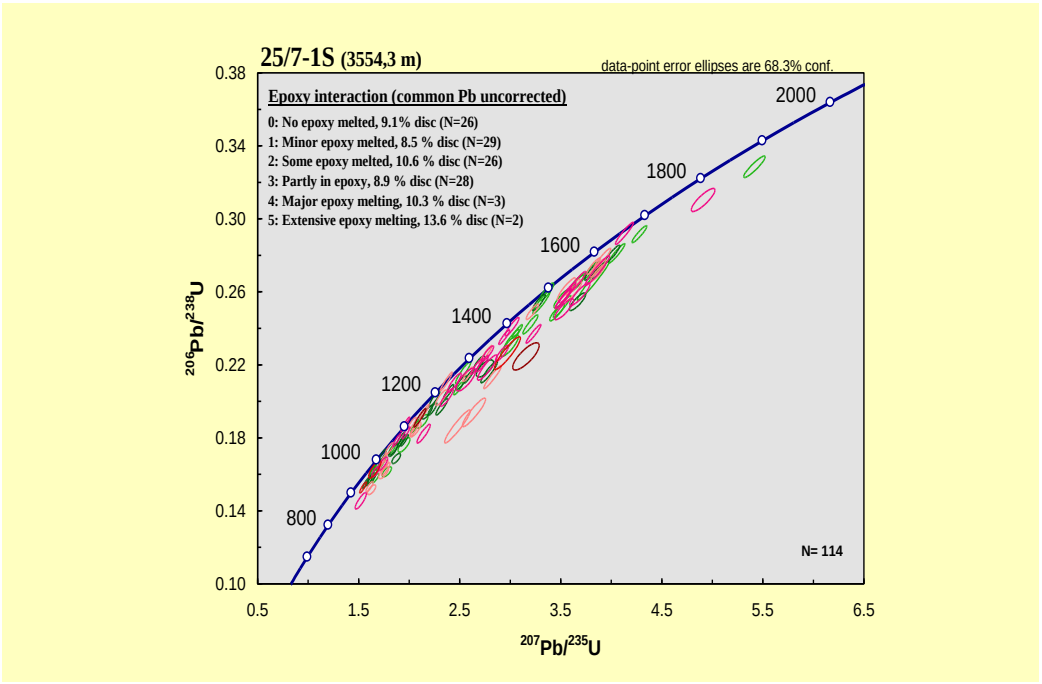

Figure A2. Data points of epoxy mounted Sample 25/7-1S subdivided according to the extent of epoxy melting during ablation. Data points without common Pb correction. No obvious visual correlation seems to occur.

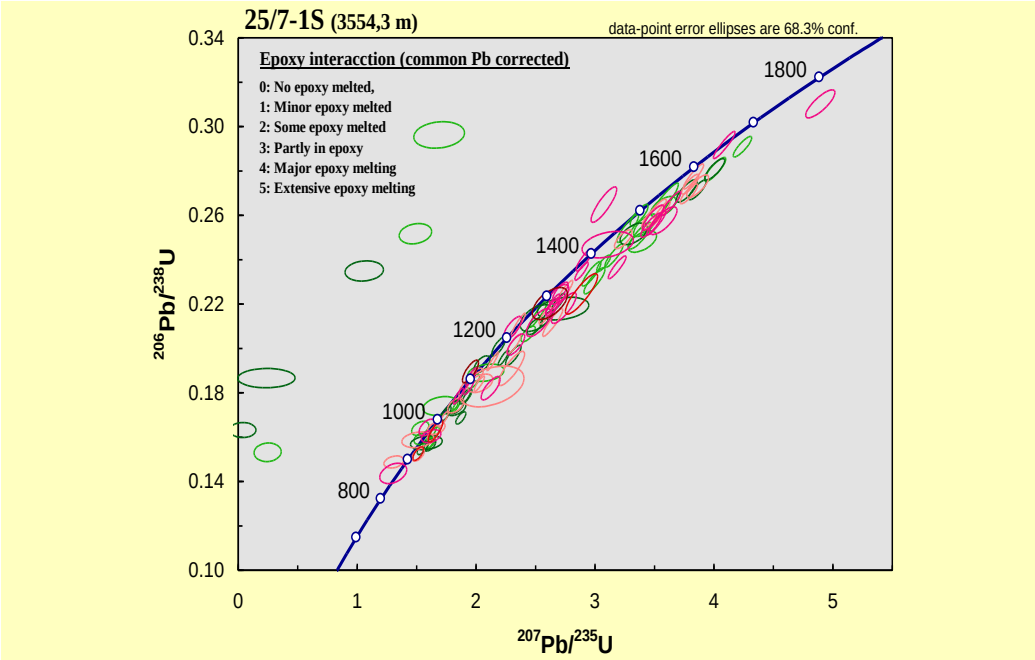

Figure A3. Data points of epoxy mounted Sample 25/7-1S subdivided according to the extent of epoxy melting during ablation. Data points with common Pb correction. No obvious visual correlation seems to occur.

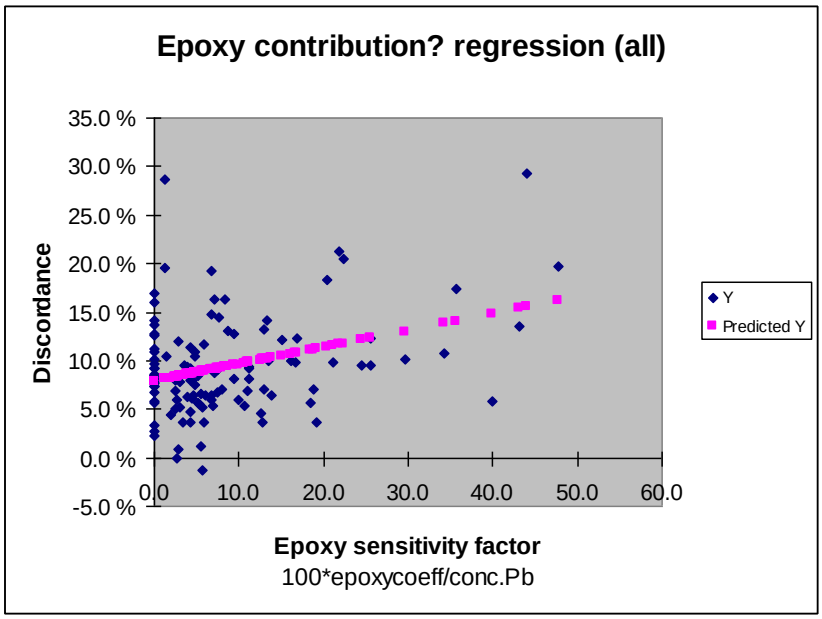

Figure A4. Statistical test for discordance of data points of epoxy mounted Sample 25/7-1S, plotted versus "Epoxy sensitivity factor". Epoxy sensitivity factor = 100 x Epoxy coeff / conc. Pb. A statistically significant positive correlation suggests that contamination from ablation into the epoxy may be responsible for some of the discordance observed. However, the correlation is weak, with a regression factor of 35 %.

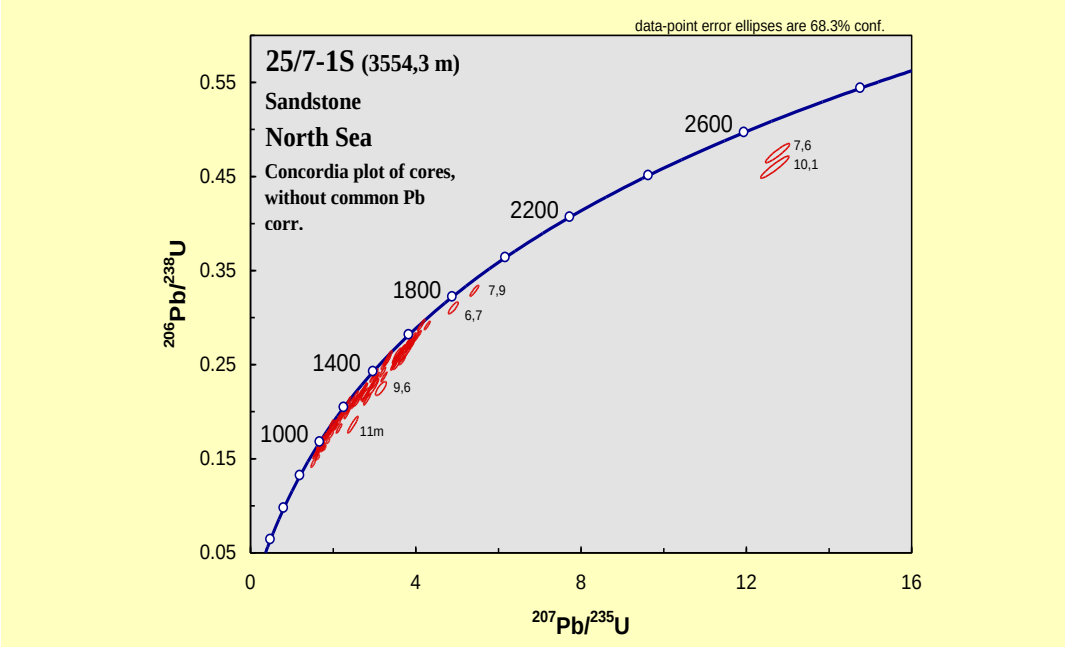

Figure A5. Concordia plot of sample 25/7-1S, epoxy-mounted grains without common Pb correction of the data points. Mean discordance c. 9 %.

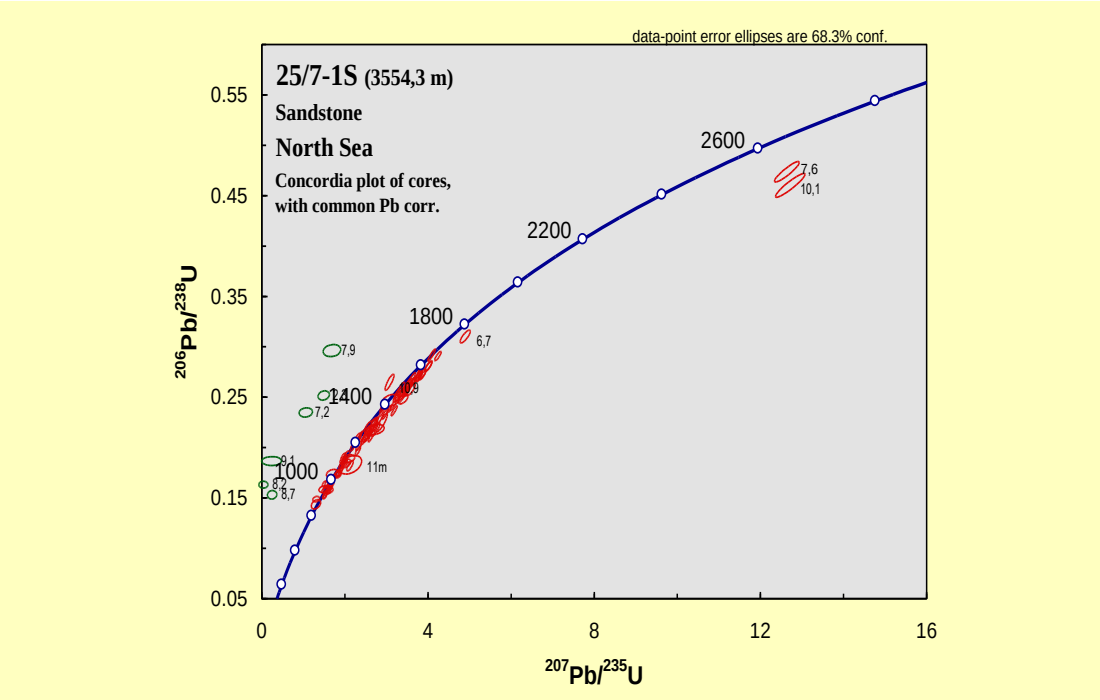

Figure A6. Concordia plot of sample 25/7-1S, epoxy-mounted grains with common Pb correction of the data points. Improved concordance compared to the data set not corrected for common Pb, with a mean discordance of c. 7 %. Some data points become over-corrected.

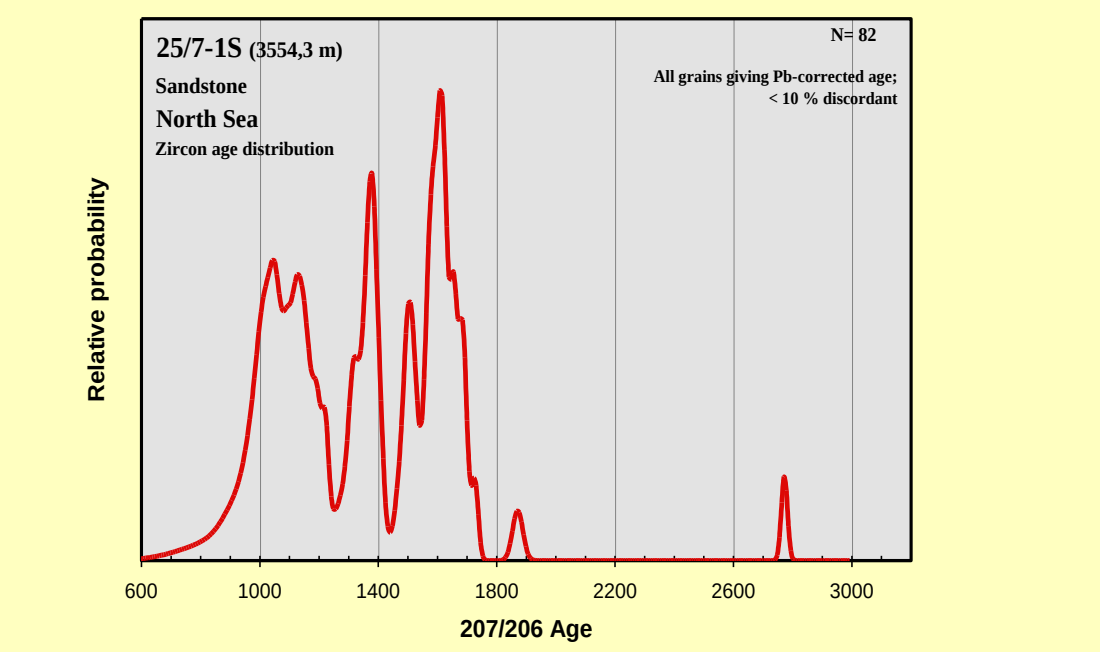

Figure A7. Cumulative probability plot for sandstone, sample 25/7-1S (3554.3 m). The plot is based on < 10 % discordant data points, after applying common Pb correction.

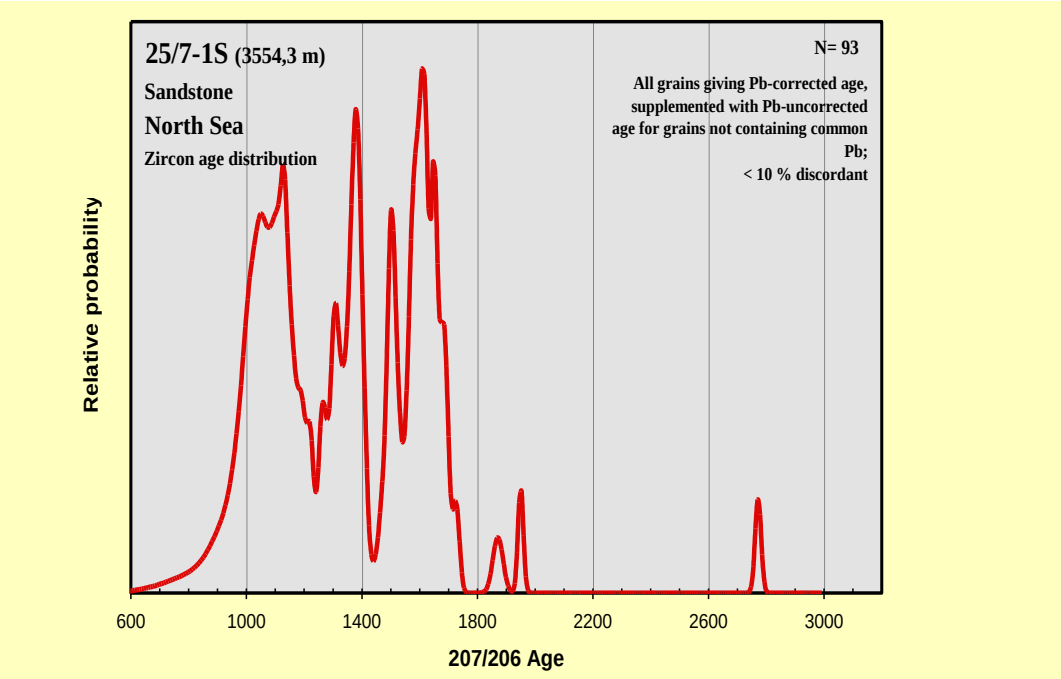

Figure A8. Cumulative probability plot for sandstone, sample 25/7-1S (3554.3 m). The plot is based on < 10 % discordant data points, after applying common Pb correction, supplemented with non-Pb corrected data points for those samples not giving any results with common Pb correction.

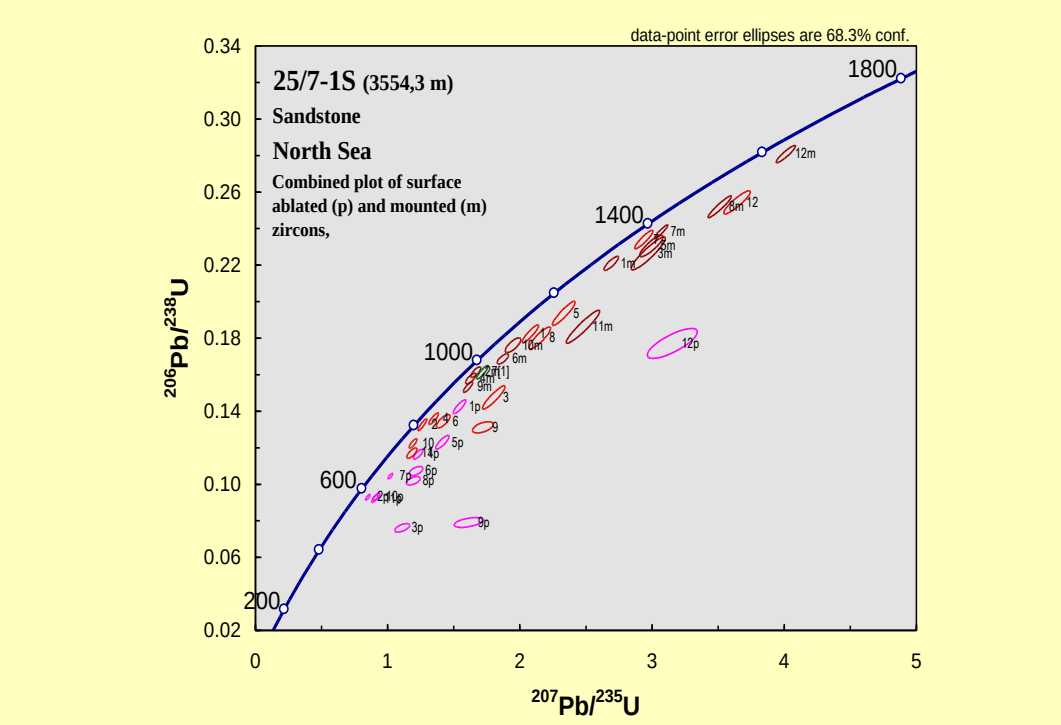

Figure A9. Combined Concordia plot for samples analysed both on tape mounts and on epoxy mounts. Common Pb correction is not applied, and many data points are highly discordant.

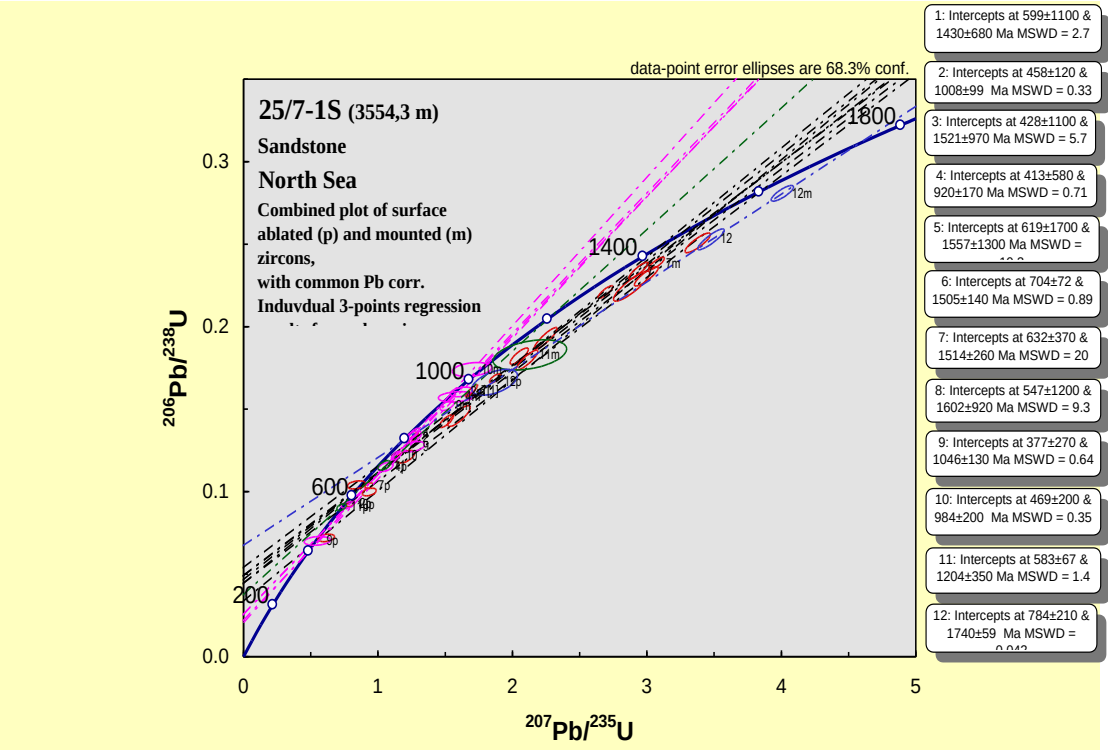

Figure A10. Regression analysis through common Pb corrected data points of individual zircon grains, based on combined data from tape mounts and epoxy mounts.

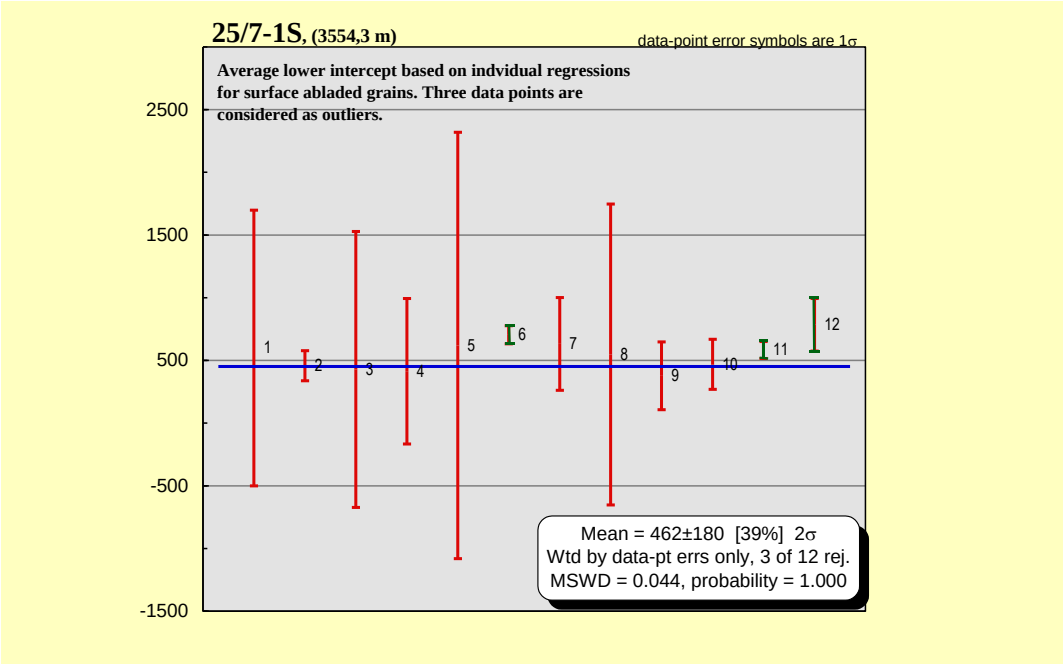

Figure A11. Average composition regression on lower intercept data from Fig. 10. Three data sets (6, 11 and 12) are treated as outliers.

20.1 References

Bingen, B., Skår, Ø., Marker, M., Sigmond, E. M. O., Nordgulen, Ø., Ragnhildstveit, J., Mansfeld, J., Tucker, R. D. & Liégeois, J.-P. 2005: Timing of continental building in the Sveconorwegian orogen, SW Scandinavia. *Norwegian Journal of Geology 85*, 87-116.

Jackson, S. E., Pearson, N. J., Griffin, W. L. & Belousova, E. A. 2004: The application of laser ablation-inductively coupled plasma-mass spectrometry to in situ U-Pb zircon geochronology. *Chemical Geology 211*, 47-69.

Ludwig, K. R. 2003: Isoplot 3.00, A Geochronological Toolkit for Microsoft Excel. *Berkley Geochronology Center, Special Publication 4*, 1-74.

Mansfeld, J. 2001a: Development of a method for U–Th–Pb age determination of minerals (zircon) with laser ablation ICP-MS. Unpublished Internal report, NGU-Lab, Geological Survey of Norway, 29 pp.

Mansfeld, J. 2001b: Guide to the determination of U–Th–Pb ages, ratios, and concentrations in Evaluation for zircon. Theory, formulas and practical handling. Unpublished Internal report, NGU-Lab, Geological Survey of Norway, 26 pp.

Mansfeld, J. 2001c: Guide to the use of ICPMS_Support and accompanying macros and workbooks. Unpublished Internal report, NGU-Lab, Geological Survey of Norway, 35 pp.

Skår, Ø. 2002: U-Pb geochronology and geochemistry of early Proterozoic rocks of the tectonic basement windows in central Nordland, Caledonides of north-central Norway. *Precambrian Research 116*, 265-283.

Stacey, J. S. & Kramers, J. D. 1975: Approximation of terrestrial lead isotope evolution by a two-stage model. *Earth and Planetary Science Letters 26*, 207-221.

Wiedenbeck, M., Allé, P., Corfu, F., Griffin, W. L., Meier, M., Oberli, F., Von Quadt, A., Roddick, J. C. & Spiegel, W. 1995: Three natural zircon standards for U-Th-Pb.Lu-Hf, trace element and REE analyses. *Geostandards Newsletter 19*, 1-23.

21 APPENDIX B - PHOTOGRAPHS OF NPD AND STATOILHYDRO CORES

Trond Slagstad and Cécile Barrère, NGU

NPD core samples

16/1-4, 1937m Utsira High, North Sea

Medium- to coarse-grained, undeformed gabbro (leucogabbro). The gabbro is strongly altered and saussuritised. A few small, calcite-filled veins and vugs.

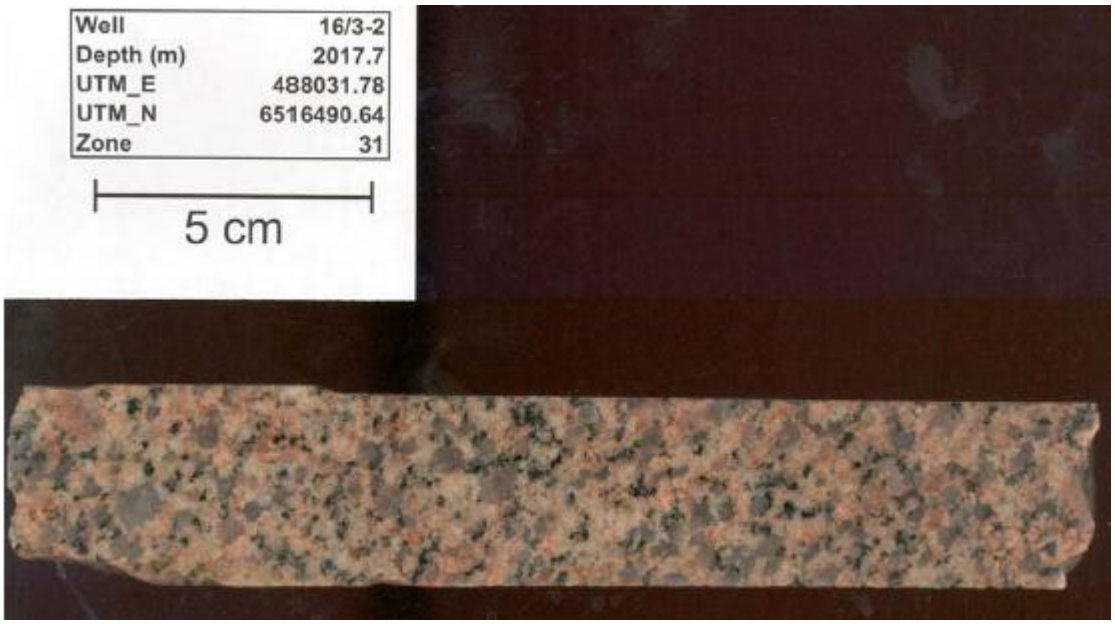

16/3-2, 2017.7m North Sea

Medium-grained, red granite consisting of fine-grained, whitish-red to red feldspar and coarser (< 1 cm) irregular, but generally rounded, grains of quartz. The granite is unfoliated and spotted with 1–4 mm black, unoriented specks of hornblende, homogeneously distributed in the rock.

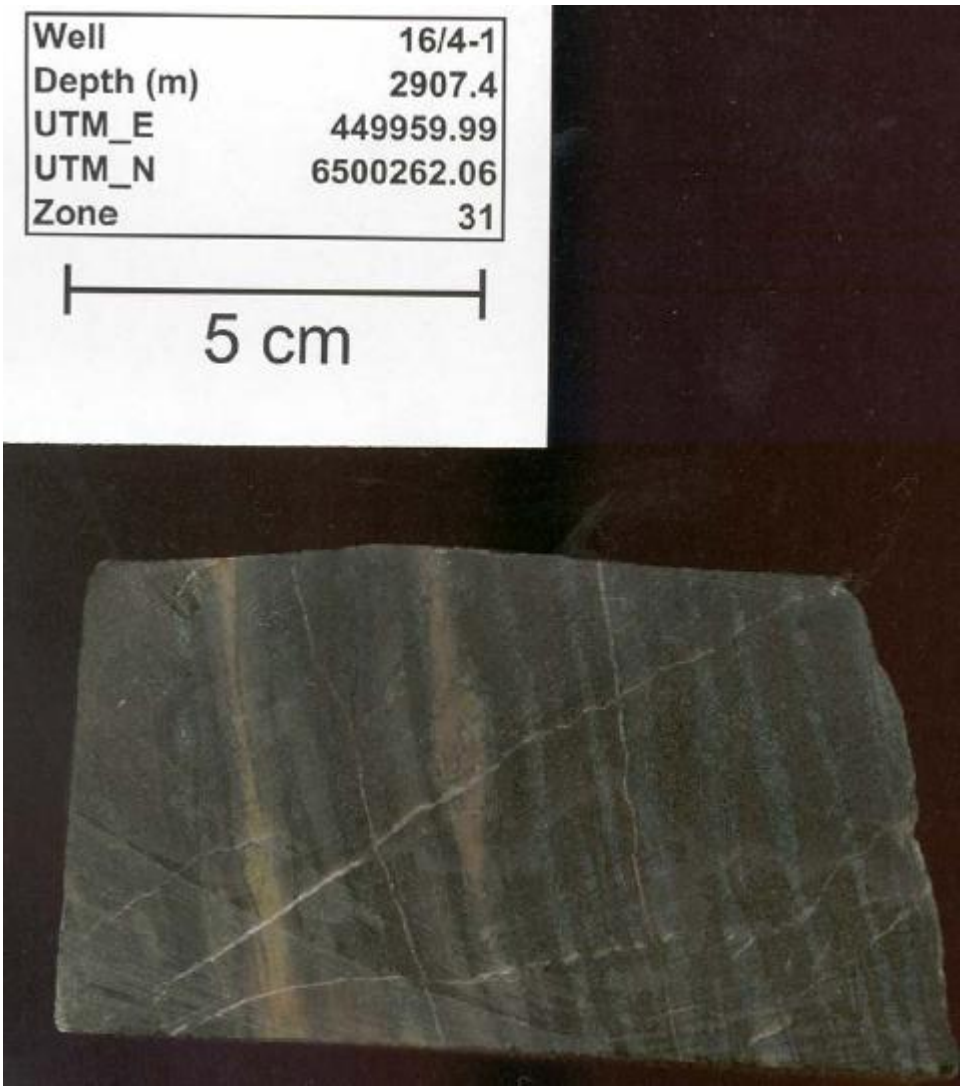

16/4-1, 2907.4m Utsira High, North Sea

Compositely layered fine-grained, light grey quartzite and dark grey siltstone. Layer thickness varies from ca. 1 mm up to several cm. The rock is criss-crossed by thin, calcite-filled vein, dominantly subvertical although subhorizontal veins are also found. The subvertical veins appear to form en echelon patterns, and some of the veins are only developed in the quartzite but are not visible in the siltstone. This effect is most likely caused by differences in rheology of the two rock types. Some cm-thick, green to orange layers, slightly oblique to the layering in the rock appear to consist of epidote and albite (?) and are most likely metasomatic.

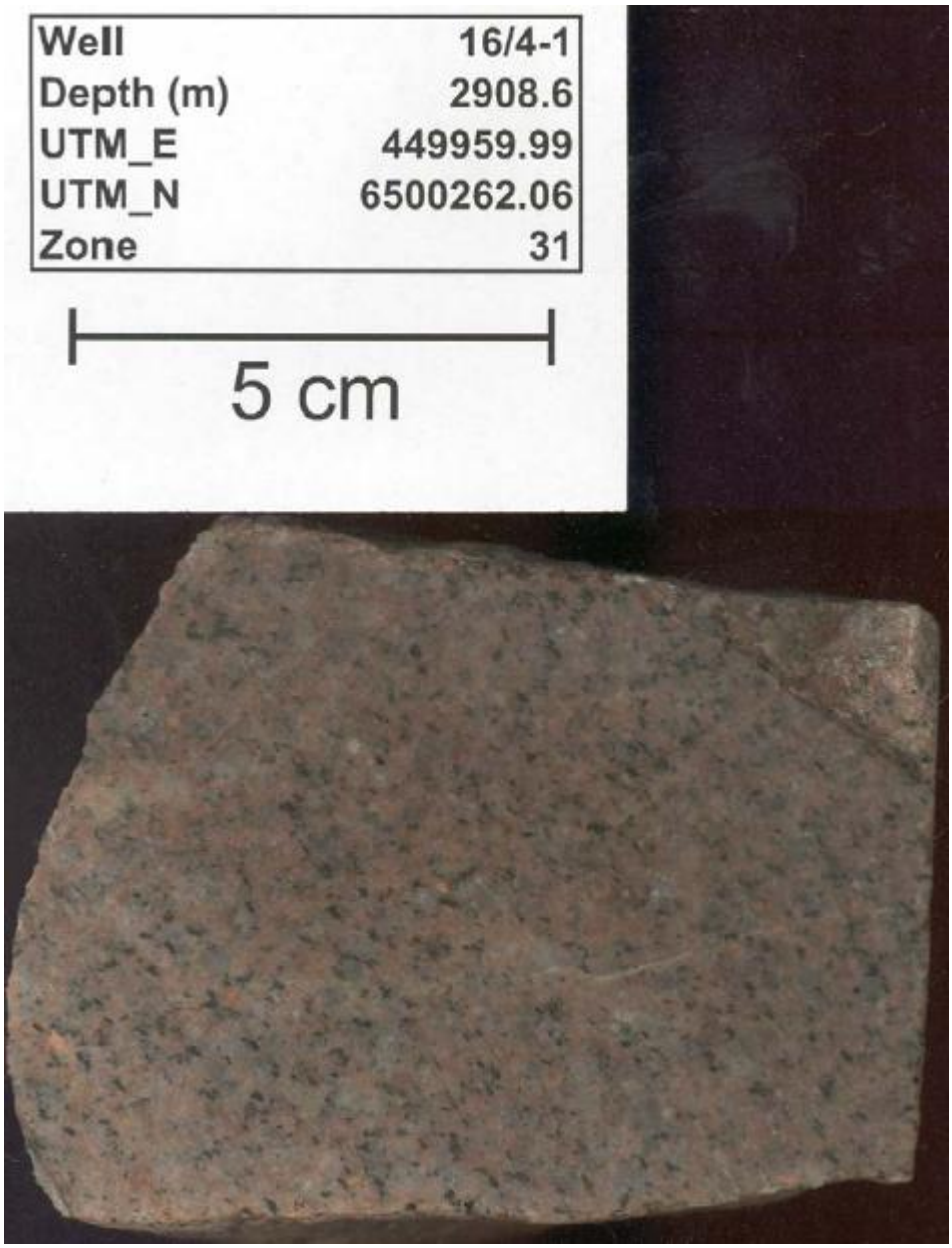

16/4-1, 2908.6m Utsira High, North Sea

Fine-grained granite, grey with a reddish hue. The granite is unfoliated and spotted with 1–3 mm black, unoriented specks of hornblende, homogeneously distributed in the rock.

16/5-1, 1929.3m Utsira High, North Sea

Fine-grained, unfoliated, dark red granite with intergrown, irregular (i.e., in matrix) hornblende. There are some cracks in the sample with discontinuous, thin, bleached margins, indicating some alteration.

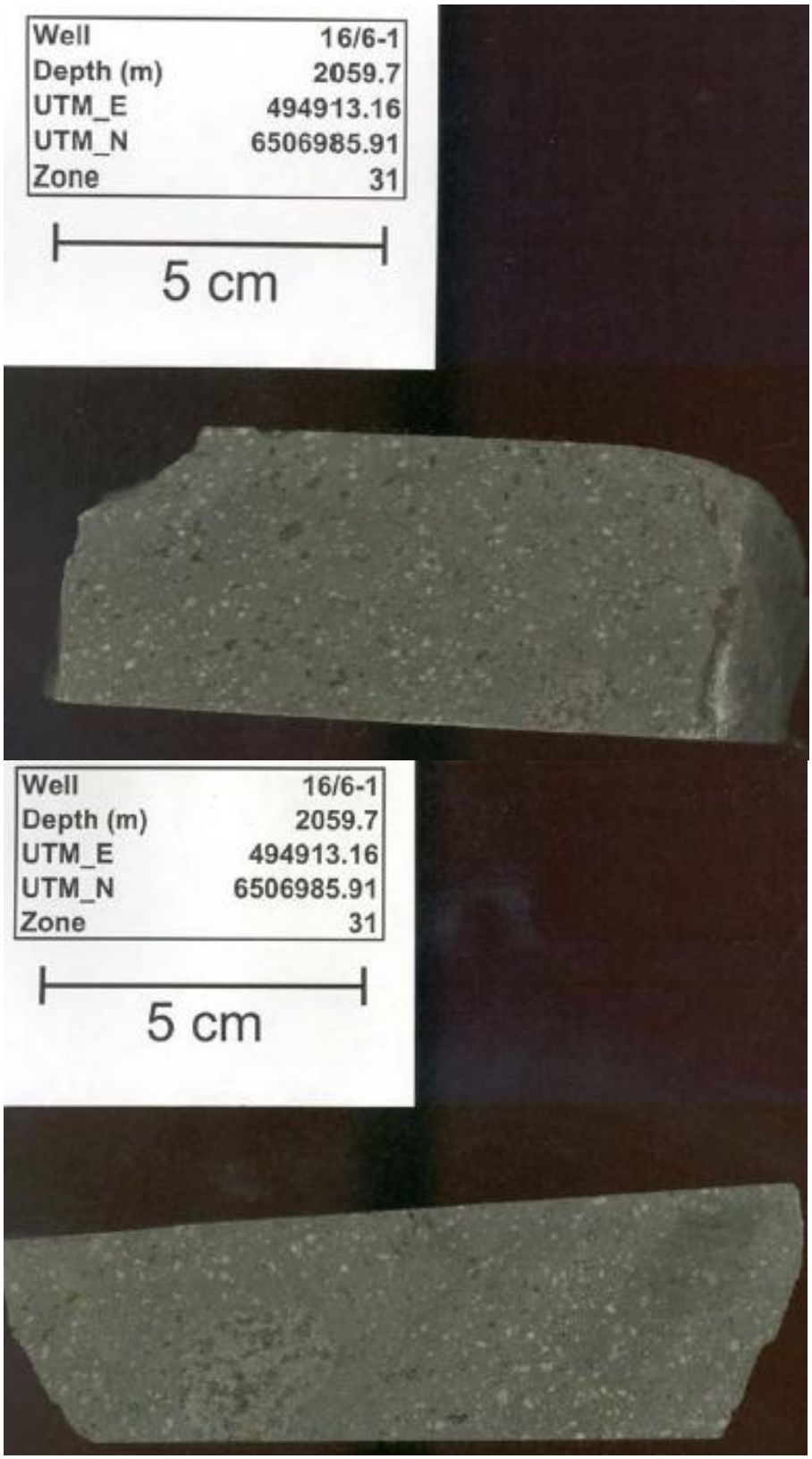

16/6-1, 2059.7m Utsira High, North Sea

Fine-grained, undeformed, grey volcanic rock with abundant small (<2 mm) phenocrysts of plagioclase and more rarely quartz, and specks of hornblende(?), set in a fine-grained, feldspar-rich (+some quartz) groundmass. The rock also contains a small (ca. 4 cm) inclusion of slightly coarser grey rock, probably a xenolith.

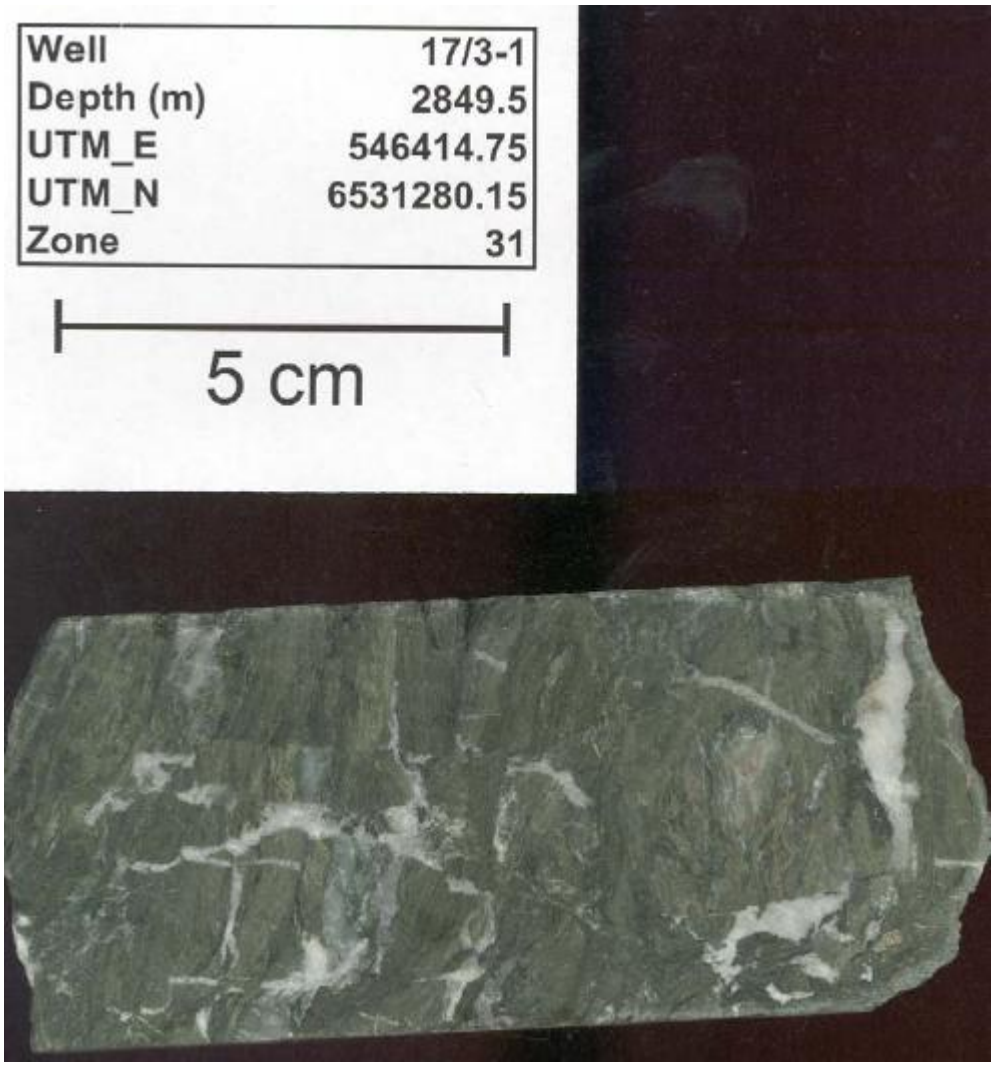

17/3-1, 2849.5m Stord Basin, North Sea

Dark green fault breccia with abundant calcite-filled veins and vugs. The rock appears to contain quite abundant chlorite and possibly epidote, but little quartzofeldspathic material, making it distinct from the other sample from this core (at 2850.7m).

From NPD's Fact-page: "…drilled […] in metamorphic basement rock, dated 410 My".

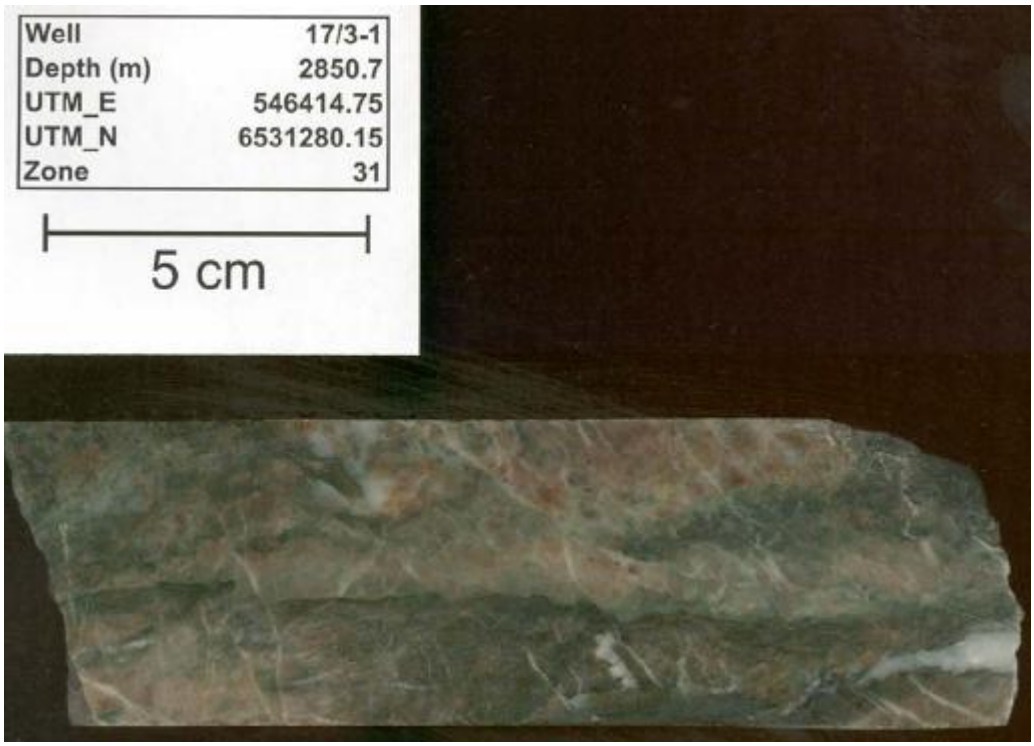

17/3-1, 2850.7m Stord Basin, North Sea

Fault breccia consisting predominantly of medium-grained feldspar, altered feldspar and epidote, as well as layers/inclusions of mafic material. The breccia is cross-cut by numerous calcite-filled veins, some of which offset the breccia, and microveins.

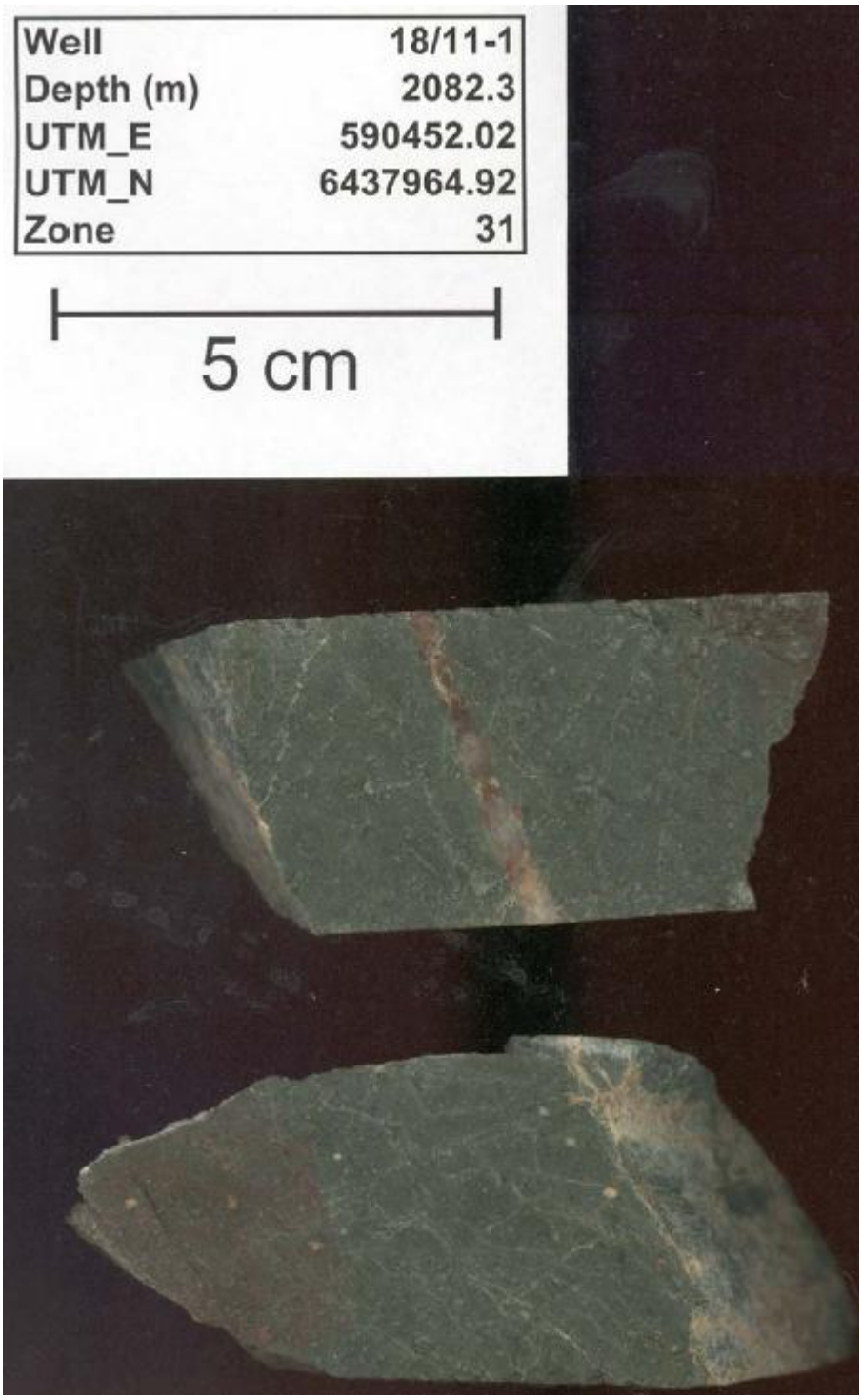

18/11-1, 2082.3m Stavanger Platform, North Sea

Dark green, volcanic rock with plagioclase phenocrysts, typically 1–2 mm across, set in a fine-grained, feldspar-rich (+ some quartz) groundmass. The rock is criss-crossed by numerous, white, hairline veins that locally are calcite-filled.

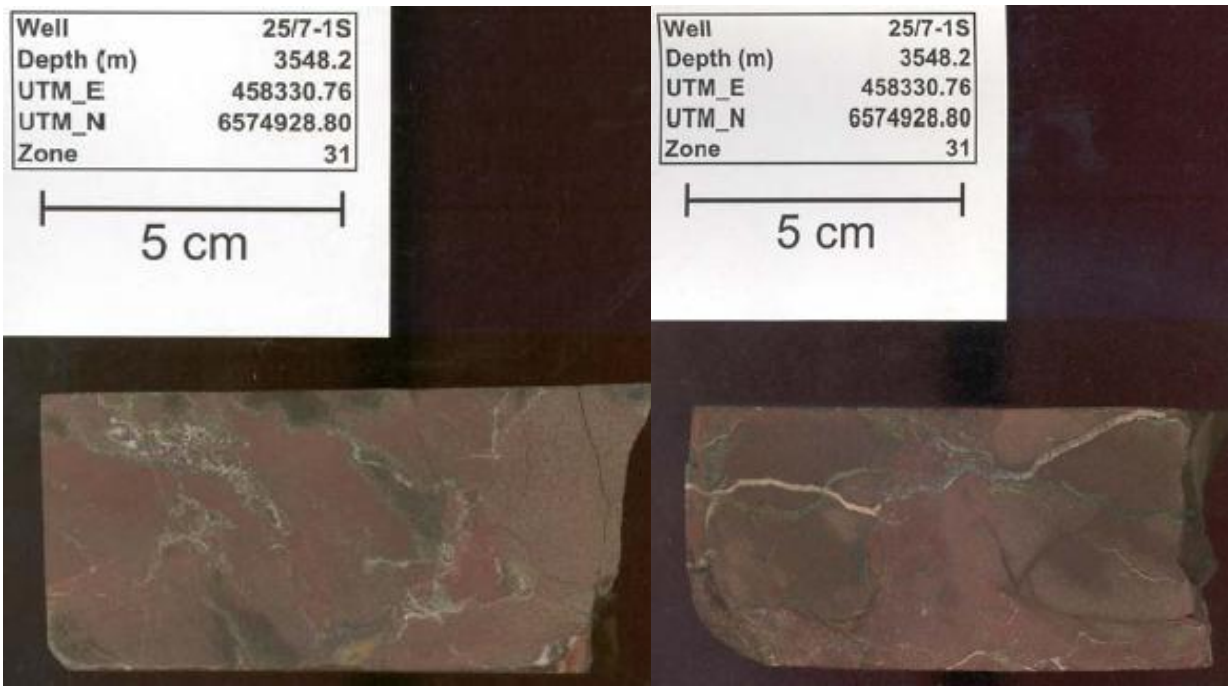

25/7-1S, 3548.2m North Sea

Breccia with irregular fragments typically ca. 5 cm long of dark red, microcrystalline calcareous siltstone(?). The fragments have slightly rounded edges. The groundmass consists of some microcrystalline, calcareous, dark green rock, and several irregular patches of microcrystalline, calcareous, dark red rock that appear to transect calcite-filled veins which in turn cut the siltstone fragments. The dark red siltstone and microcrystalline patches are difficult to distinguish, but in general the former appears slightly coarser grained.

25/7-1S, 3554.3m North Sea

Faintly banded, fine-grained, grey qtz-rich sandstone. The sandstone is criss-crossed by numerous thin veins, with dark green, white or brown infilling. The brown infilling is calcareous.

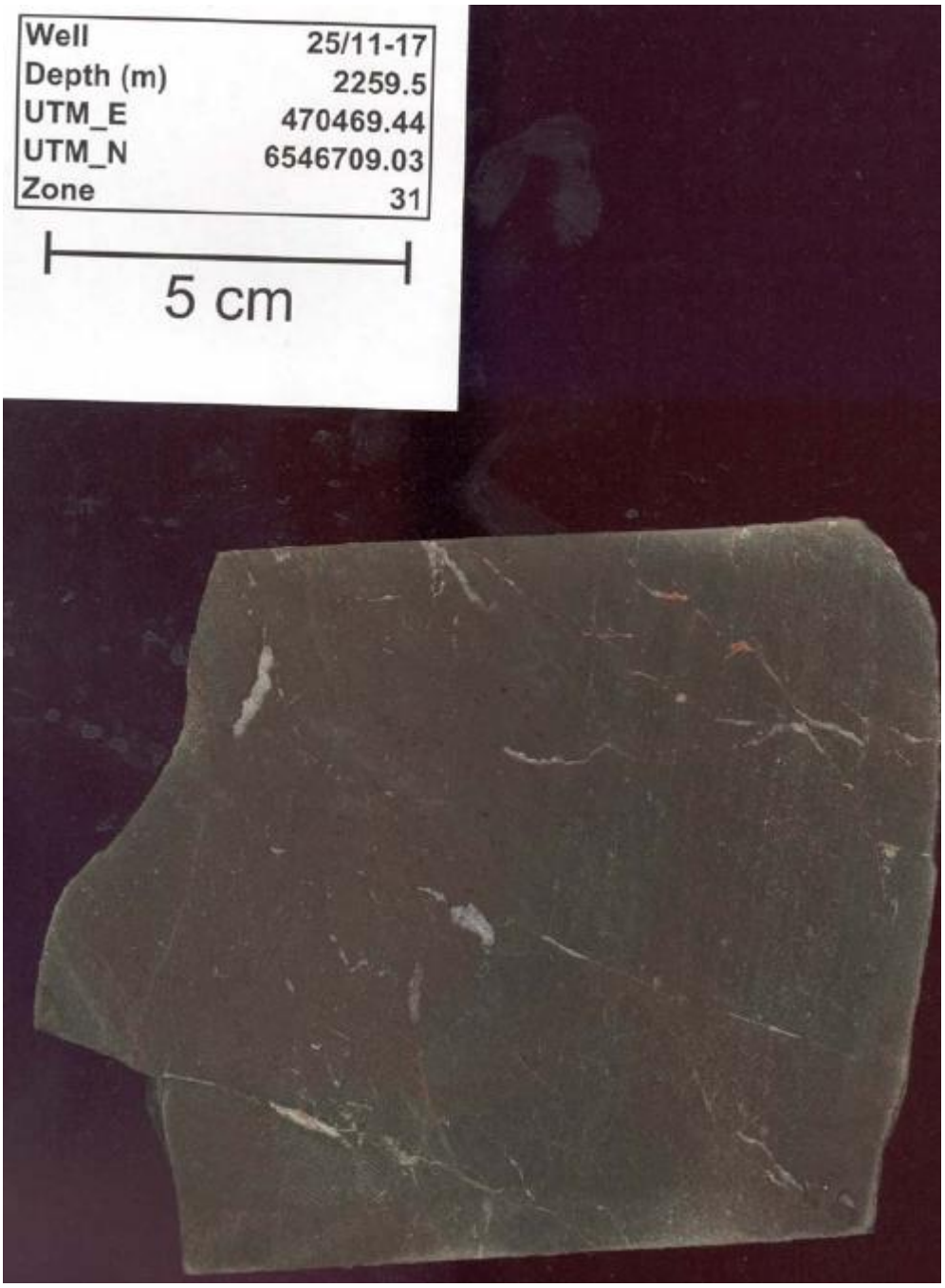

25/11-17, 2259.5m Balder/Grane area, North Sea

Microcrystalline to fine-grained, dark brown to grey siltstone with numerous short (<2 cm), irregular veins and vugs filled with white and more rarely red material, identified as calcite and possibly some zeolite.

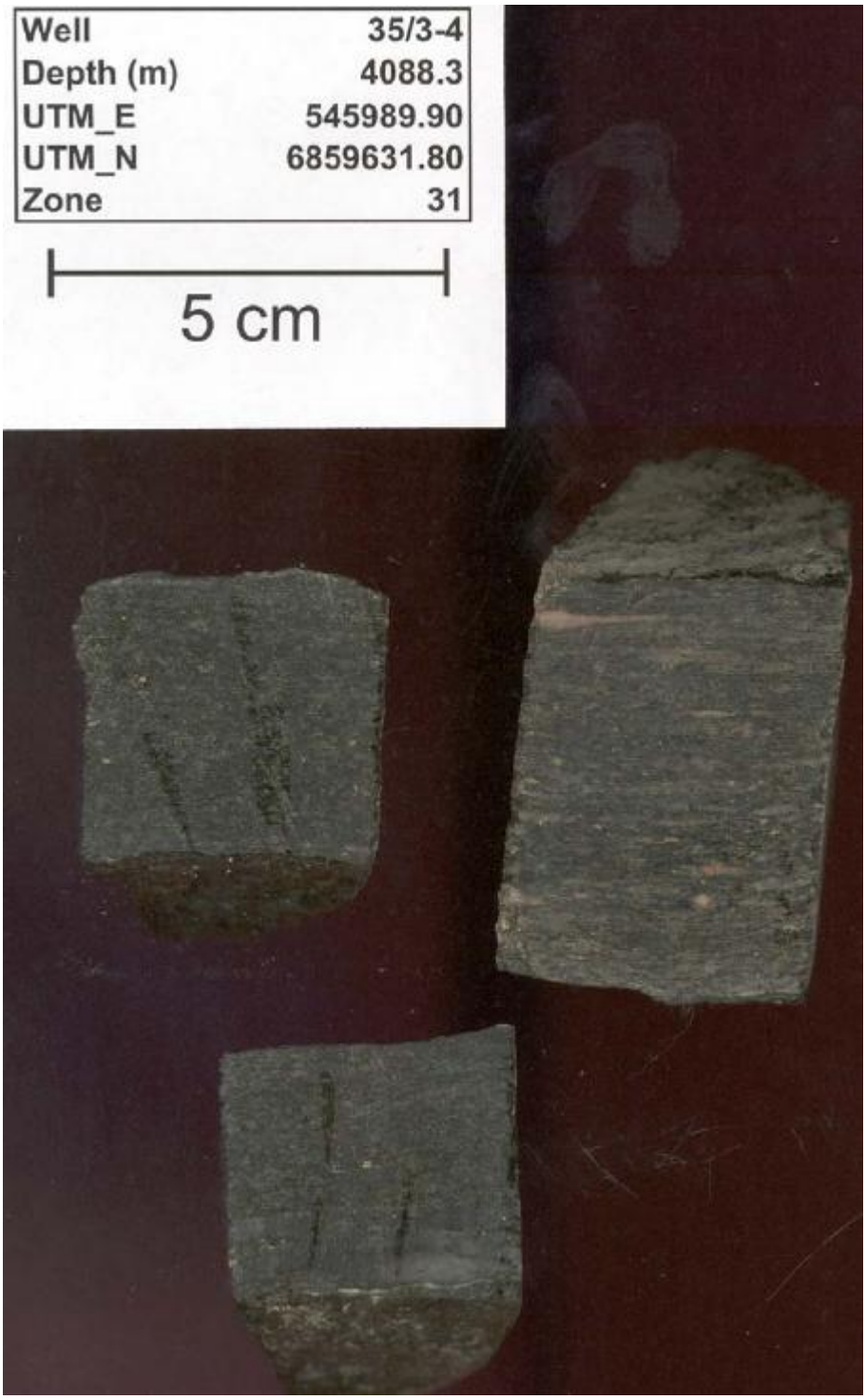

35/3-4, 4088.3m North Sea

Fine-grained, dark grey qtz-rich mica schist with several, concordant mm-sized patches and veins of granitic(?) material. The rock contains a fair amount of pyrite, some with well-developed crystal faces, typically 1–2 mm across but locally up to 5 mm.

From NPD's Fact-page: "…before reaching basement rocks of Caledonian age".

35/9-1, 2313.6m North Sea

Fine-grained, dark green breccia. Colour varies from light grey, green, dark green to dark grey, giving the rock a speckled appearance. The light grey and green material is calcareous. The breccia contains some mm-thick, calcite-filled veins. No larger clasts can be observed.

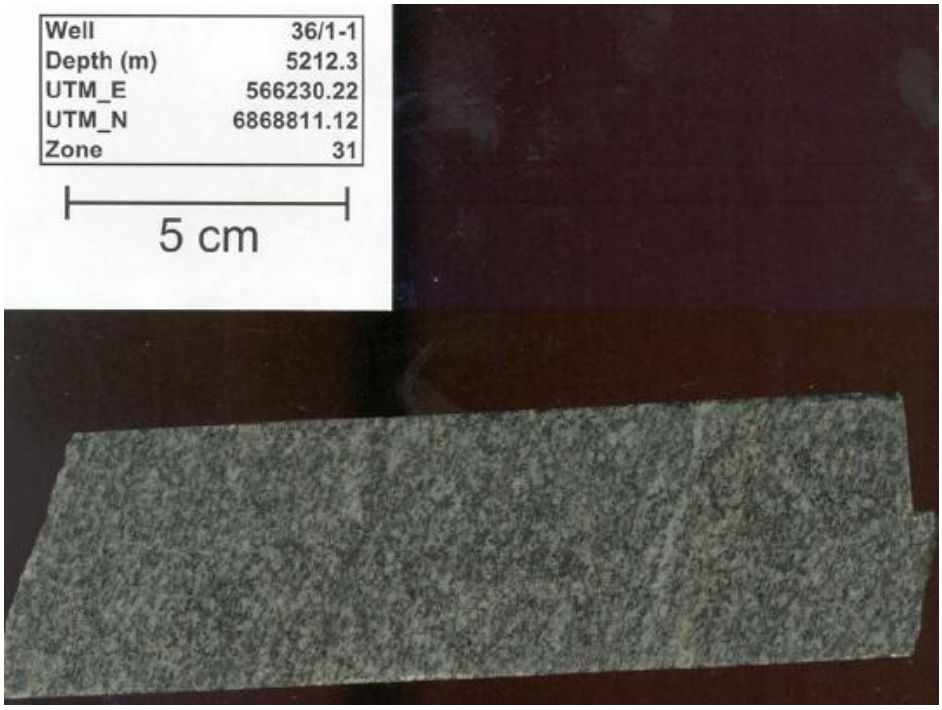

36/1-1, 5212.3m, North Sea

Fine-grained, grey, biotite-epidote-bearing granitic gneiss. Abundant biotite laths impart the gneiss with a strong foliation.

6305/12-2, 3158.3m Norwegian Sea

Grey fault(?) breccia consisting dominantly of angular fragments of siltstone, separated by thin "veins" of dark material. Some fragments of quartz and some calcite that appears to pre-date brecciation. Numerous calcite-filled veins and vugs. The breccia appears to contain abundant chlorite.

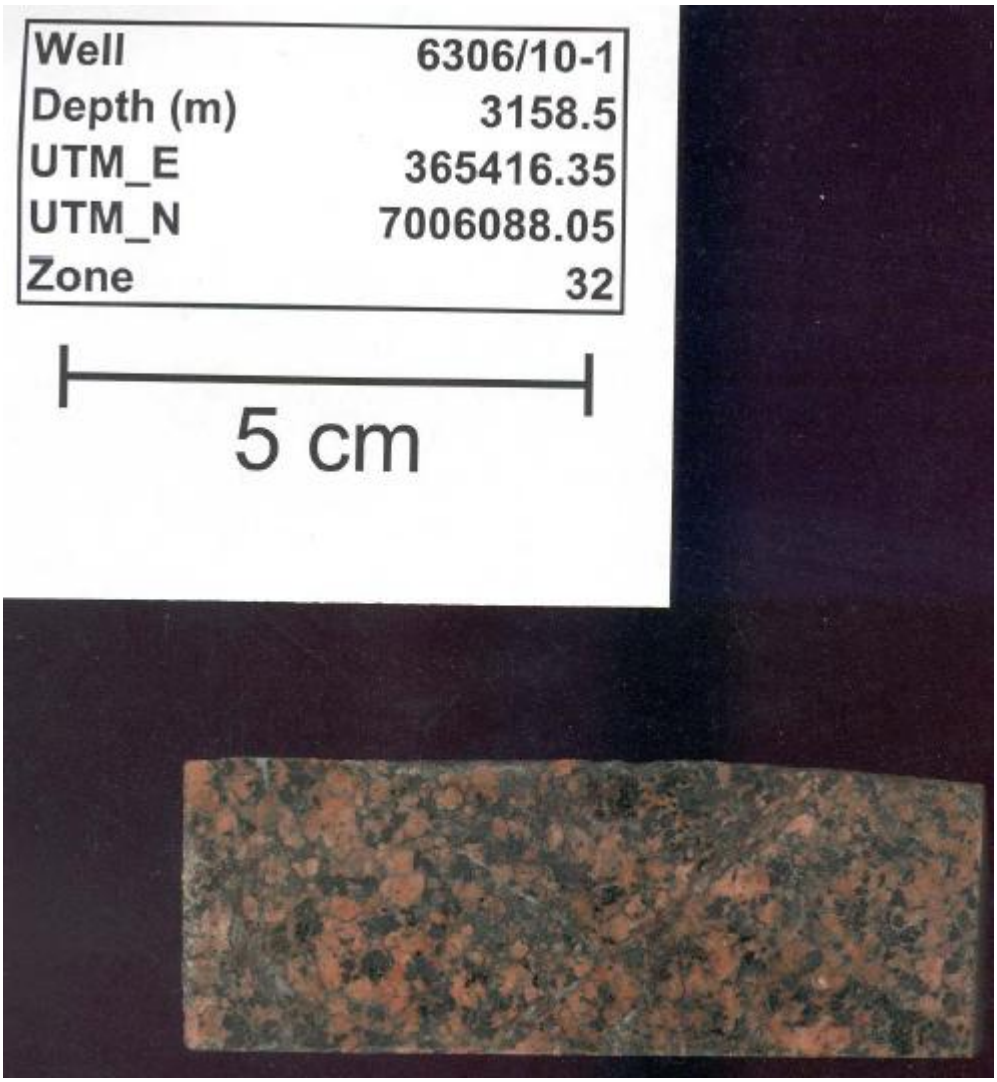

6306/10-1, 3158.5m Frøya High, Norwegian Sea

Fine- to medium-grained, unfoliated leucogabbro with a few calcite-filled cracks. The gabbro is strongly altered and saussuritised.

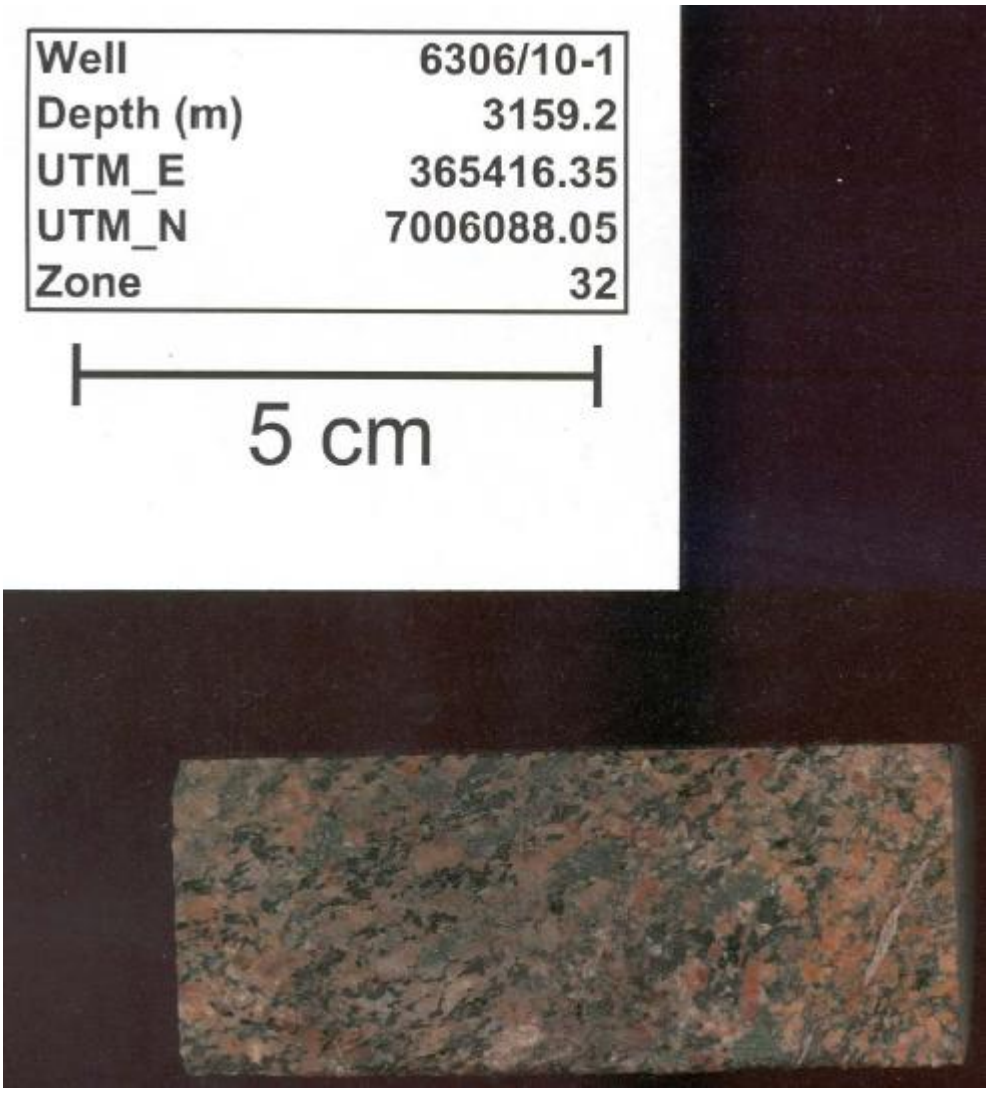

6306/10-1, 3159.2m Frøya High, Norwegian Sea

Fine- to medium-grained, unfoliated leucogabbro with a few calcite-filled cracks. The gabbro is strongly altered and saussuritised.

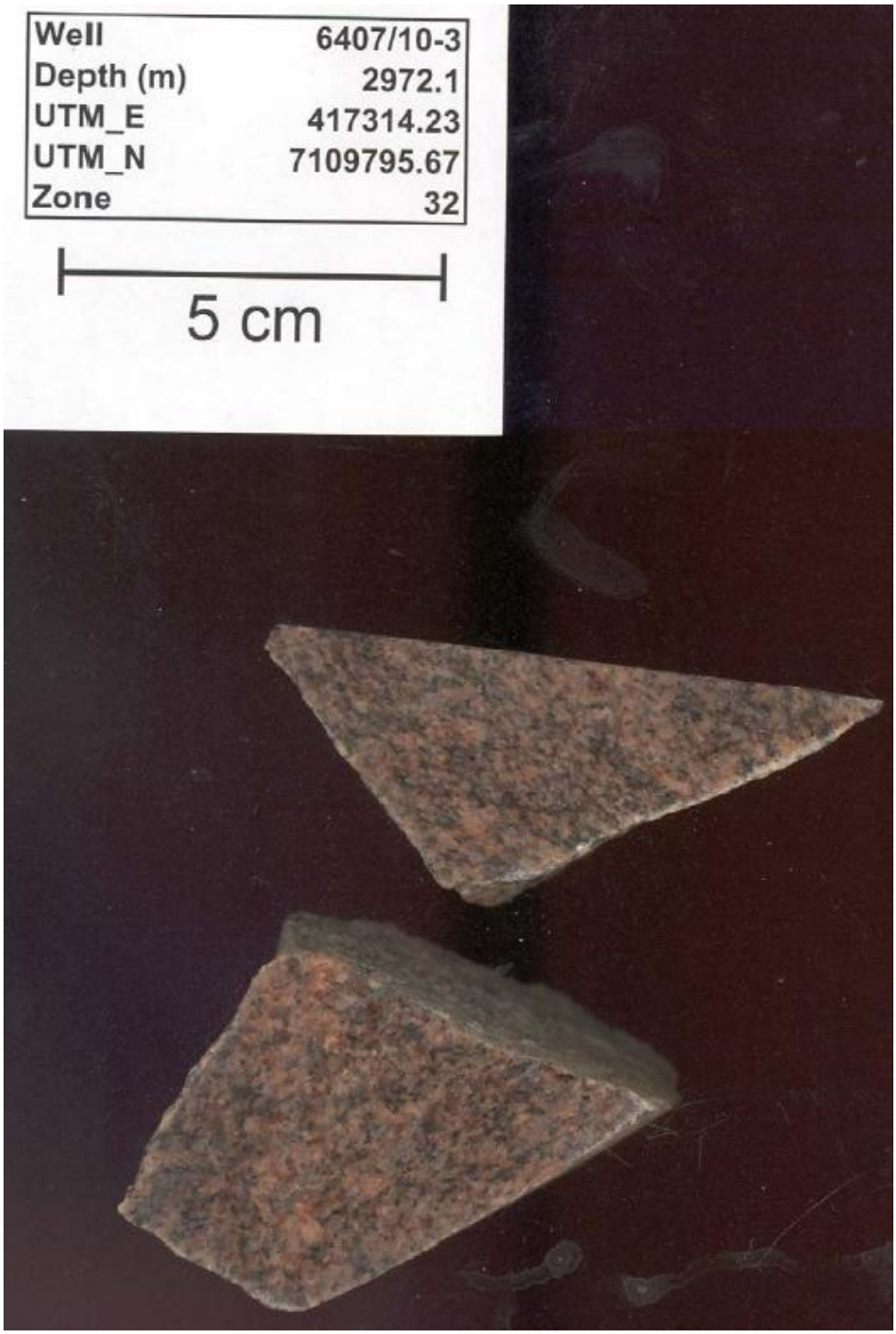

6407/10-3, 2972.1m Norwegian Sea
Fine-grained, unfoliated, dark red granite with small specks (<1 mm) of hornblende.

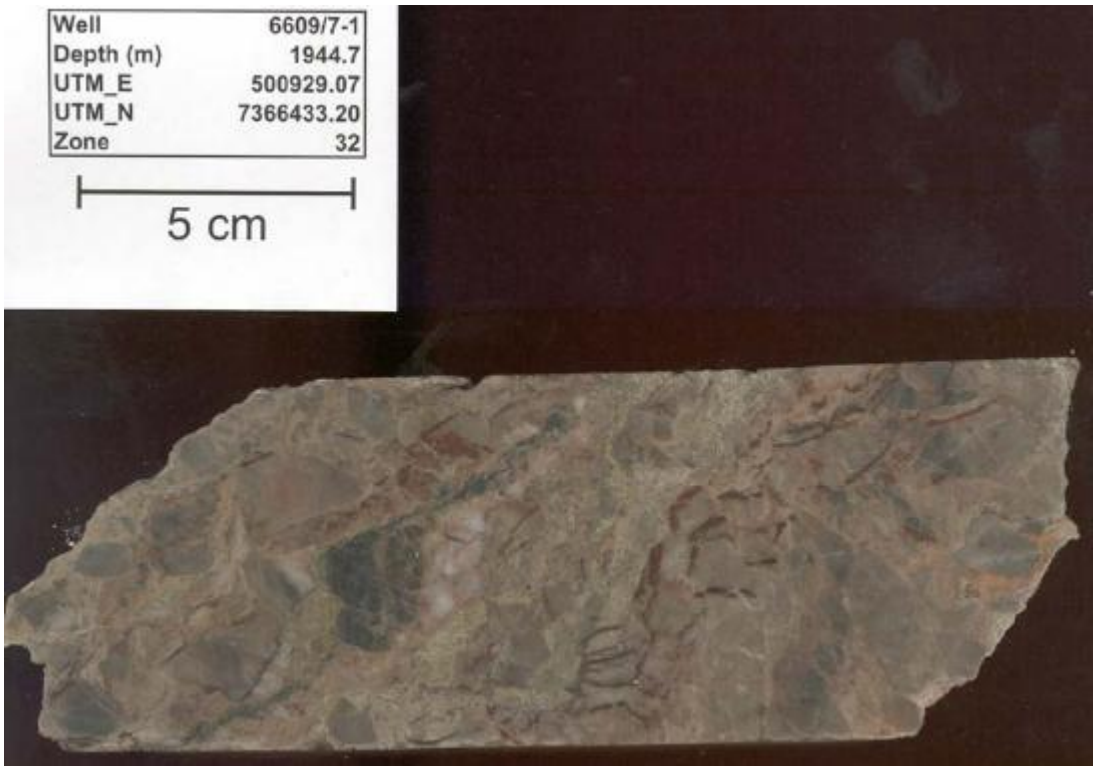

6609/7-1, 1944.7m Norwegian Sea

Breccia with angular fragments of fine-grained, qzt-rich sandstone and siltstone. The quartzite is grey with a reddish hue, and the fragments range in size from a few mm up to several cm. The matrix consists of crumbly, microcrystalline, green material, and minor amounts of red to brown calcareous material.

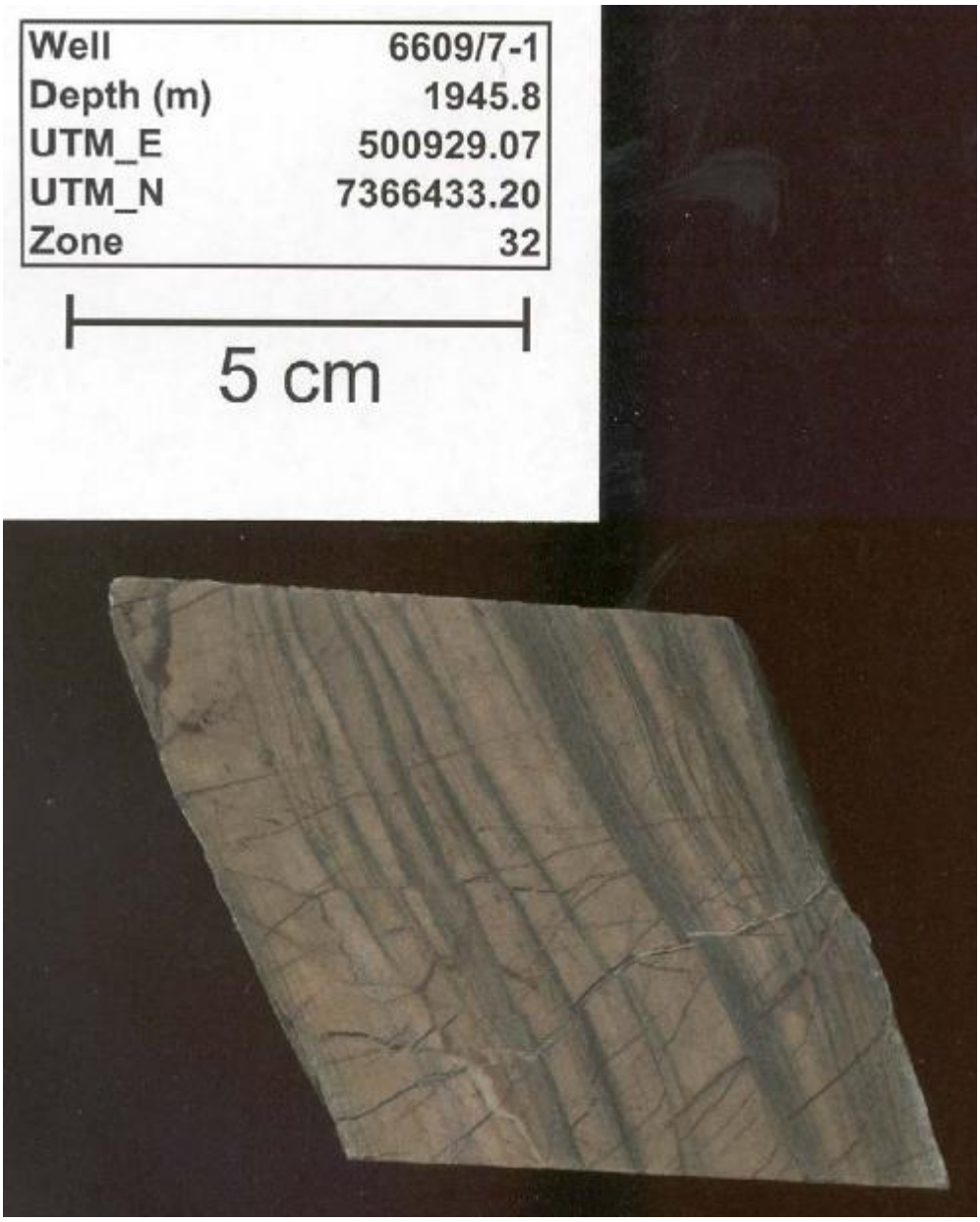

6609/7-1, 1945.8m Norwegian Sea

Laminated metasediment consisting of layers, typically < 1 cm thick, of microcrystalline sandstone/quartzite(?) with a orange hue, and thinner layers of grey, microcrystalline siltstone(?). The rock is extensively cracked with calcite-filled veins. Possible that the sandstone/siltstone is calcareous, but the large number of small calcite-filled veins makes it difficult to discern which part of the rock fizzes when exposed to HCl.

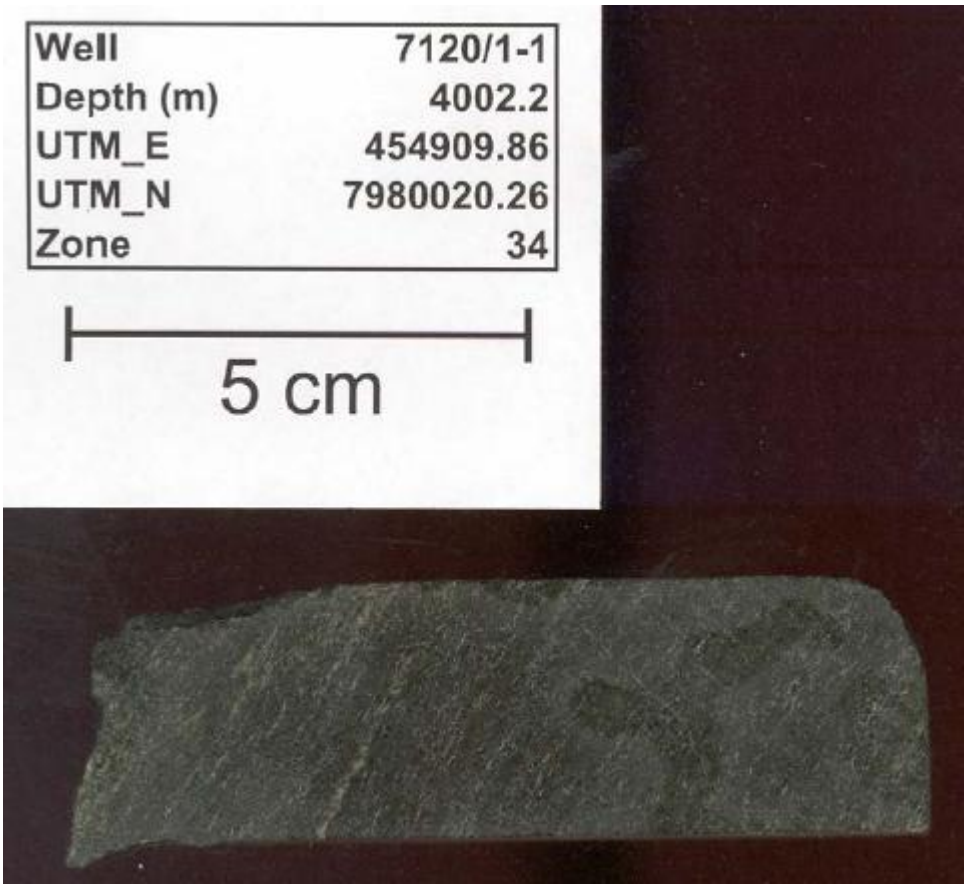

7120/1-1, 4002.2m Loppa High, Barents Sea
Fine-grained, foliated, amphibolite.

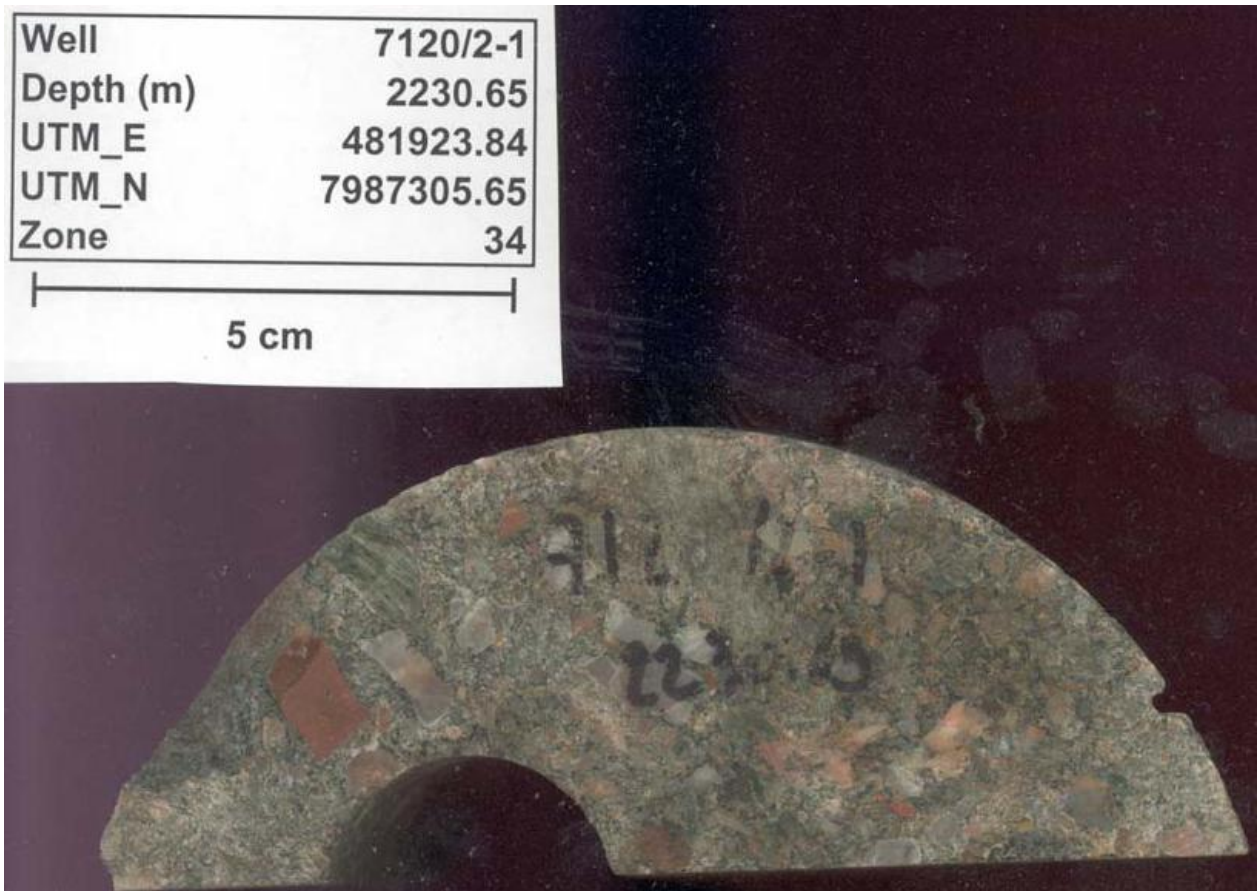

7120/2-1, 2230.65m Loppa High, Barents Sea
Polymict conglomerate.

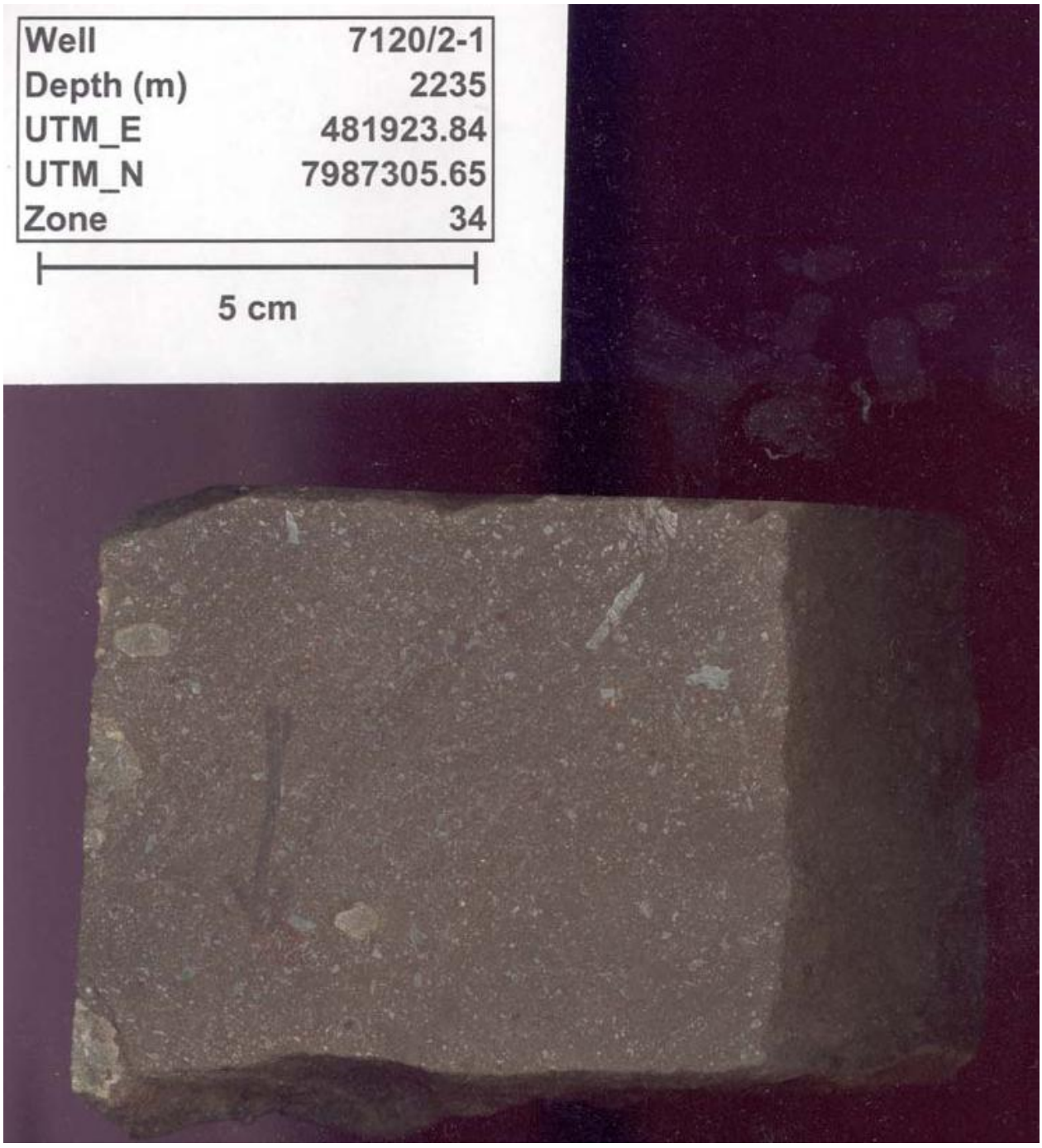

7120/2-1, 2235.0m Loppa High, Barents Sea

Reddish brown, fine-grained conglomerate or ignimbrite???

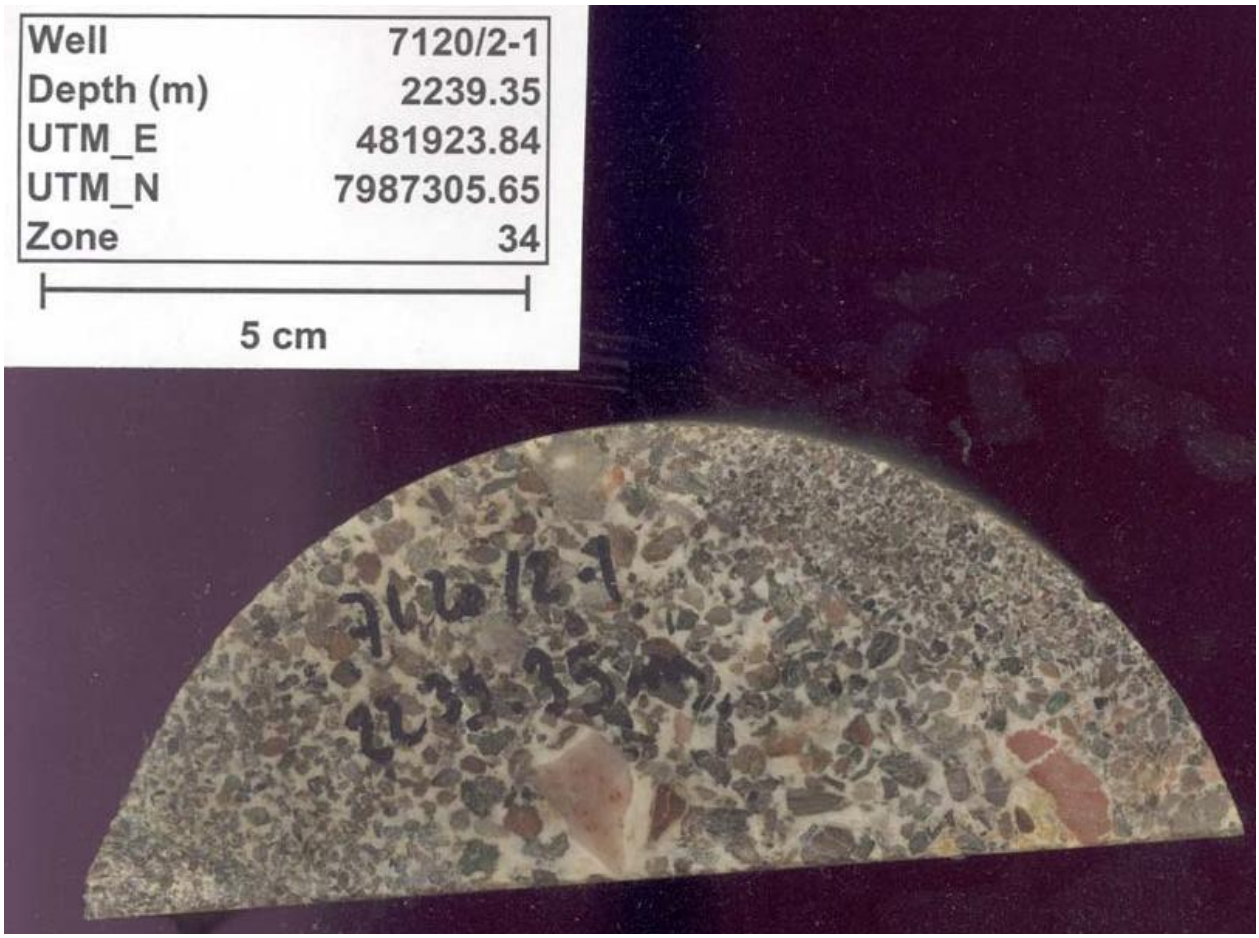

7120/2-1, 2239.35m Loppa High, Barents Sea
Polymict conglomerate.

7120/2-1, 2242.35m Loppa High, Barents Sea
Polymict conglomerate.

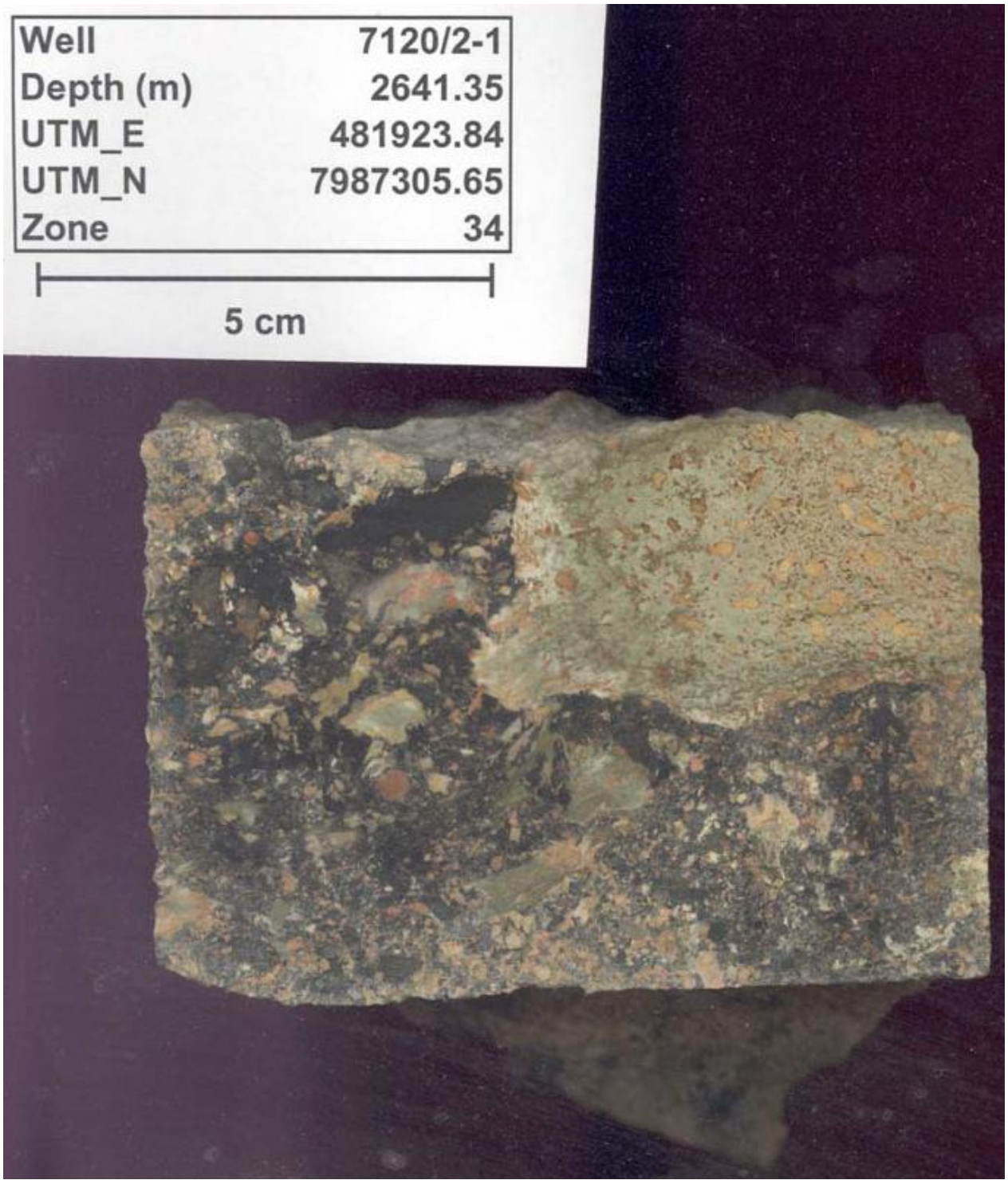

7120/2-1, 2641.35m Loppa High, Barents Sea

Breccia.

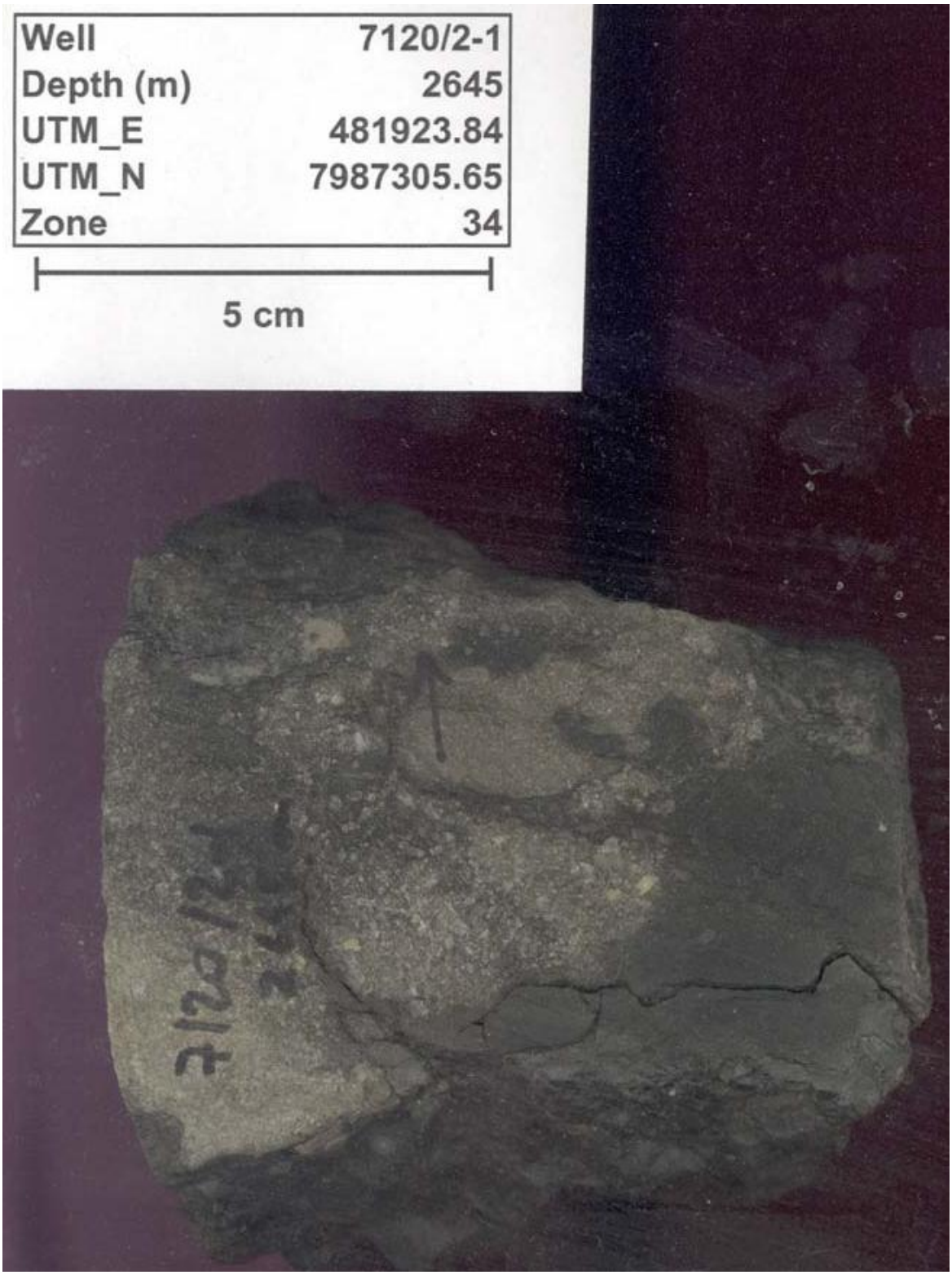

7120/2-1, 2645.0m Loppa High, Barents Sea
Conglomerate, silty and sandy matrix.

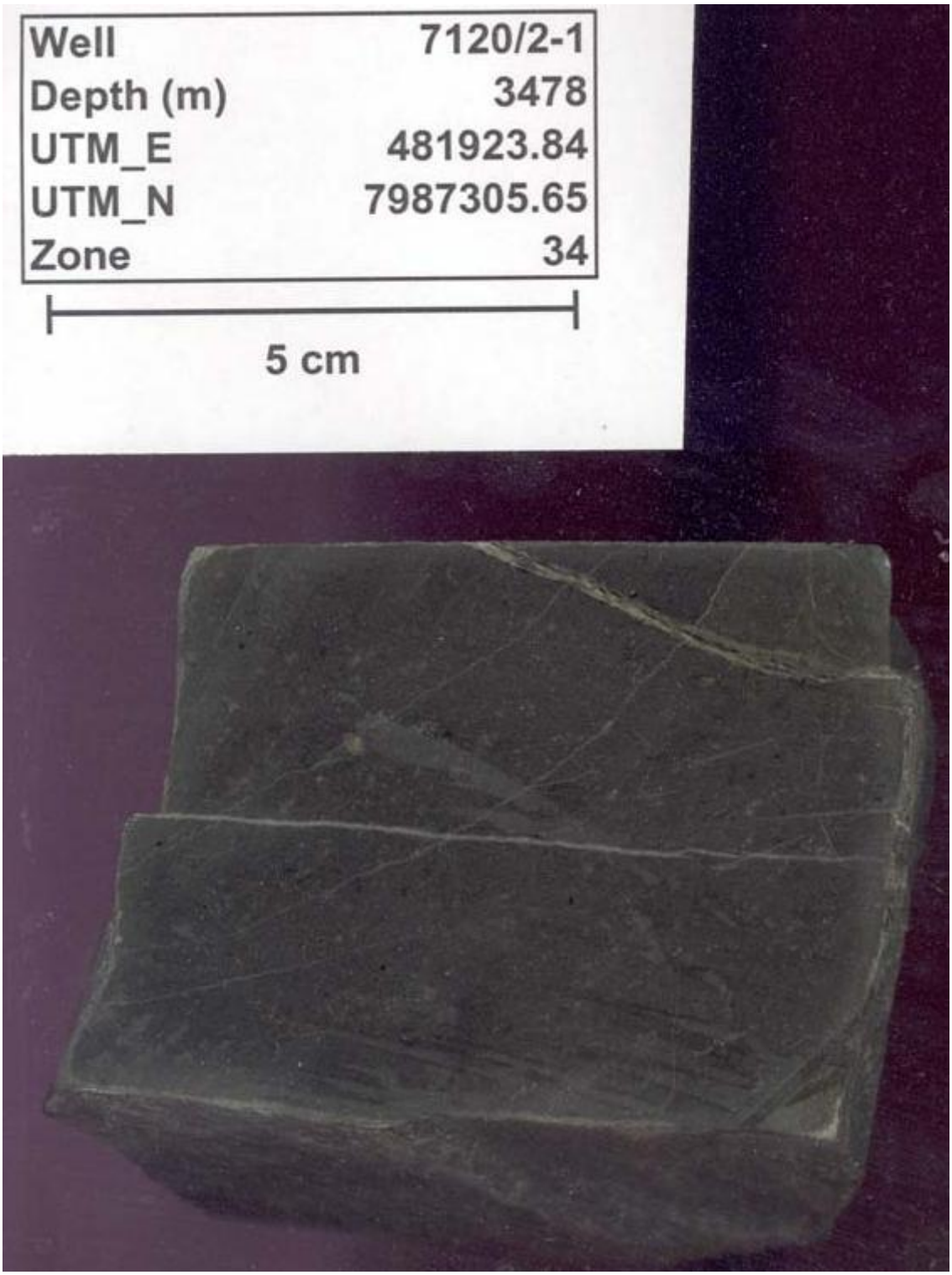

7120/2-1, 3478.0m Loppa High, Barents Sea
Diabase.

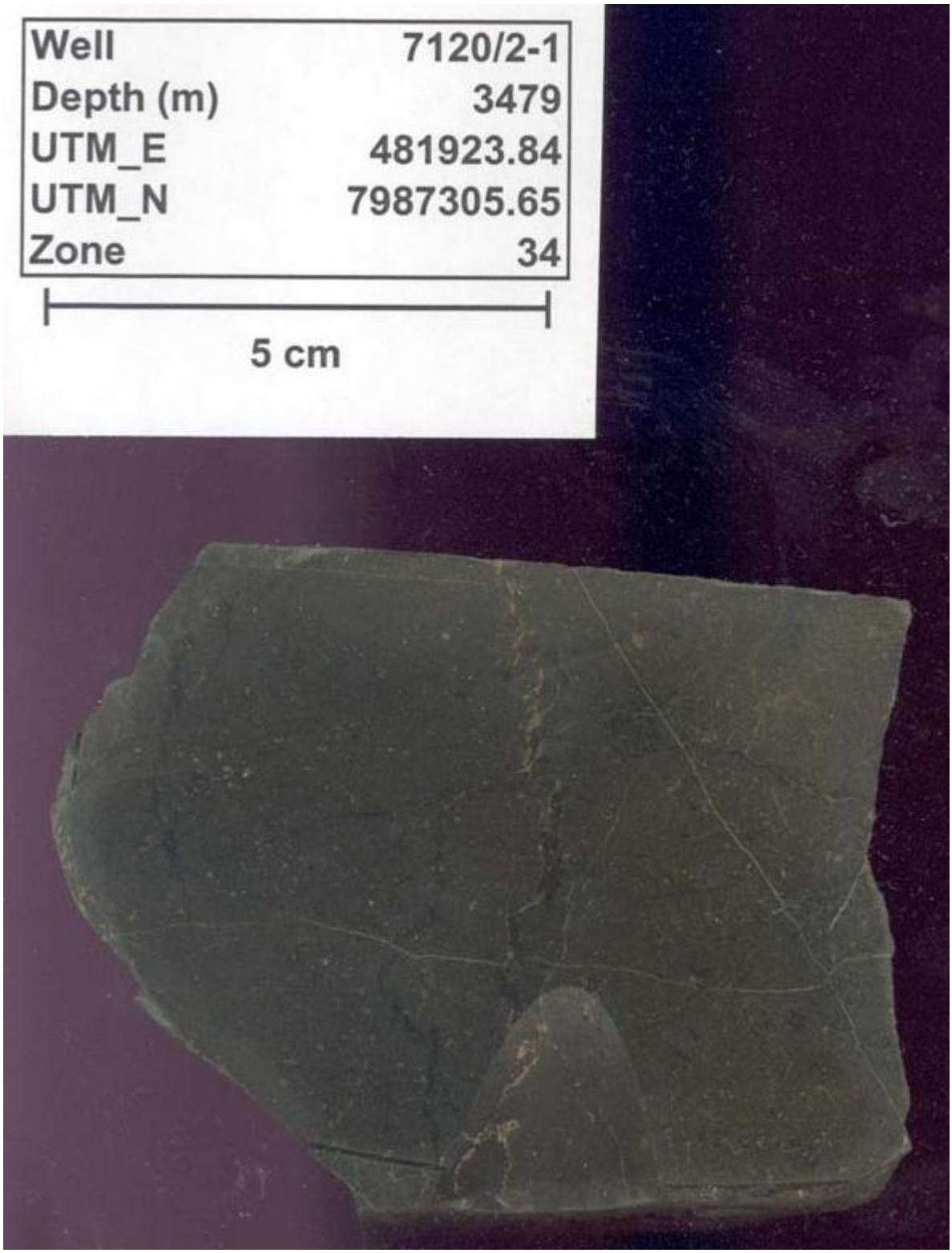

7120/2-1, 3479.0m Loppa High, Barents Sea
Diabase.

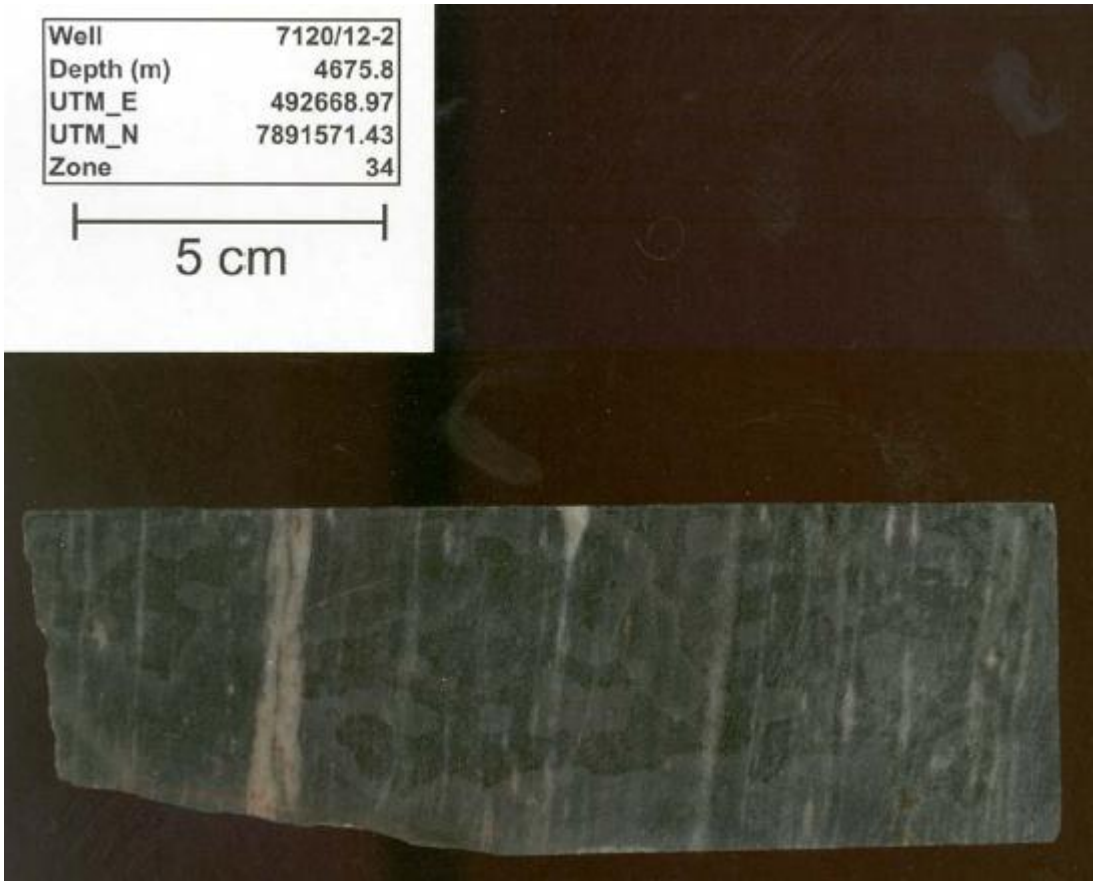

7120/12-2, 4675.8m Barents Sea

Dark grey mylonite, with numerous thin (<1 mm) and some thicker (<1 cm) leucocratic veins, concordant with the foliation in the rock.

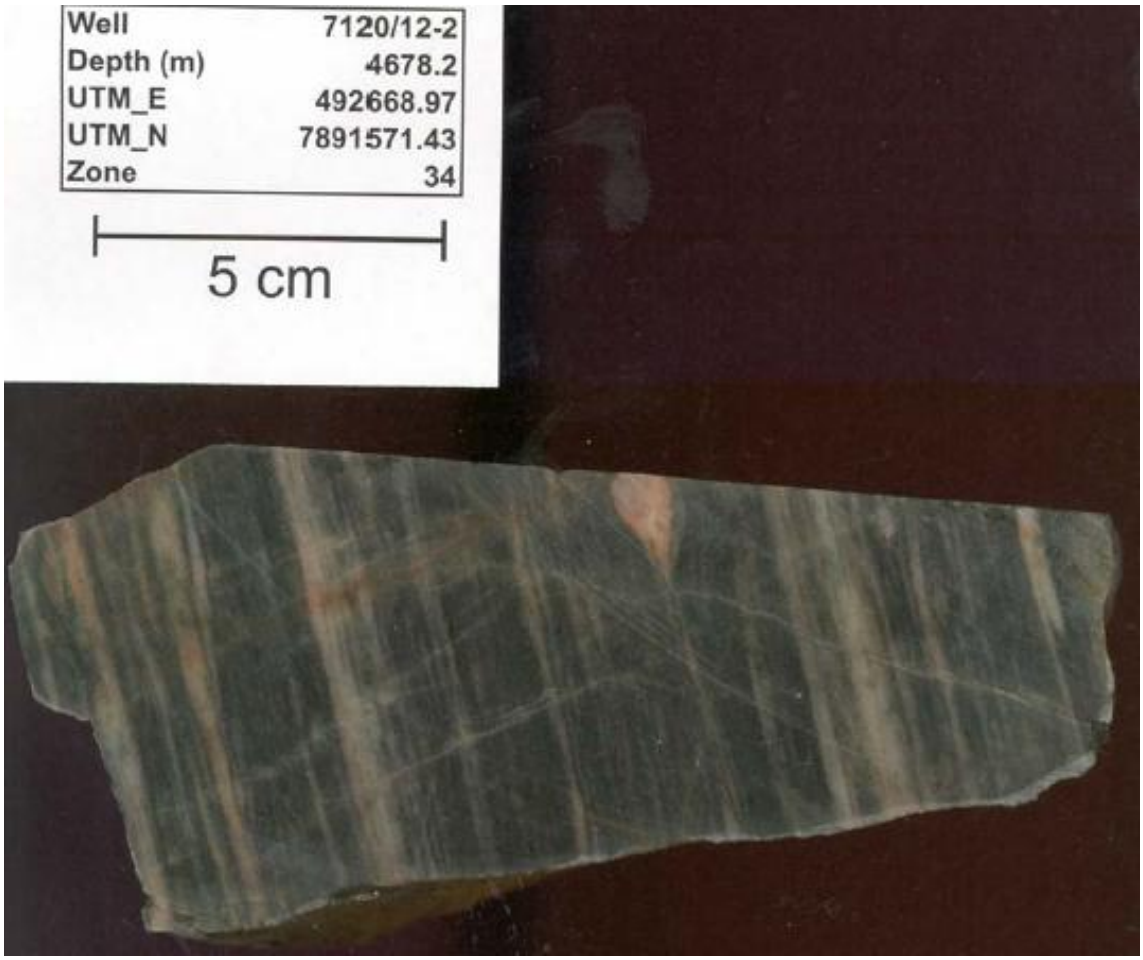

7120/12-2, 4678.2m Barents Sea

Dark grey mylonite/qtz-rich augen gneiss, with numerous thin (<1 mm) and some thicker (<1 cm) leucocratic veins, concordant with the foliation in the rock. It is conceivable that some of the leucocratic bands represent stretched out porphyroclasts.

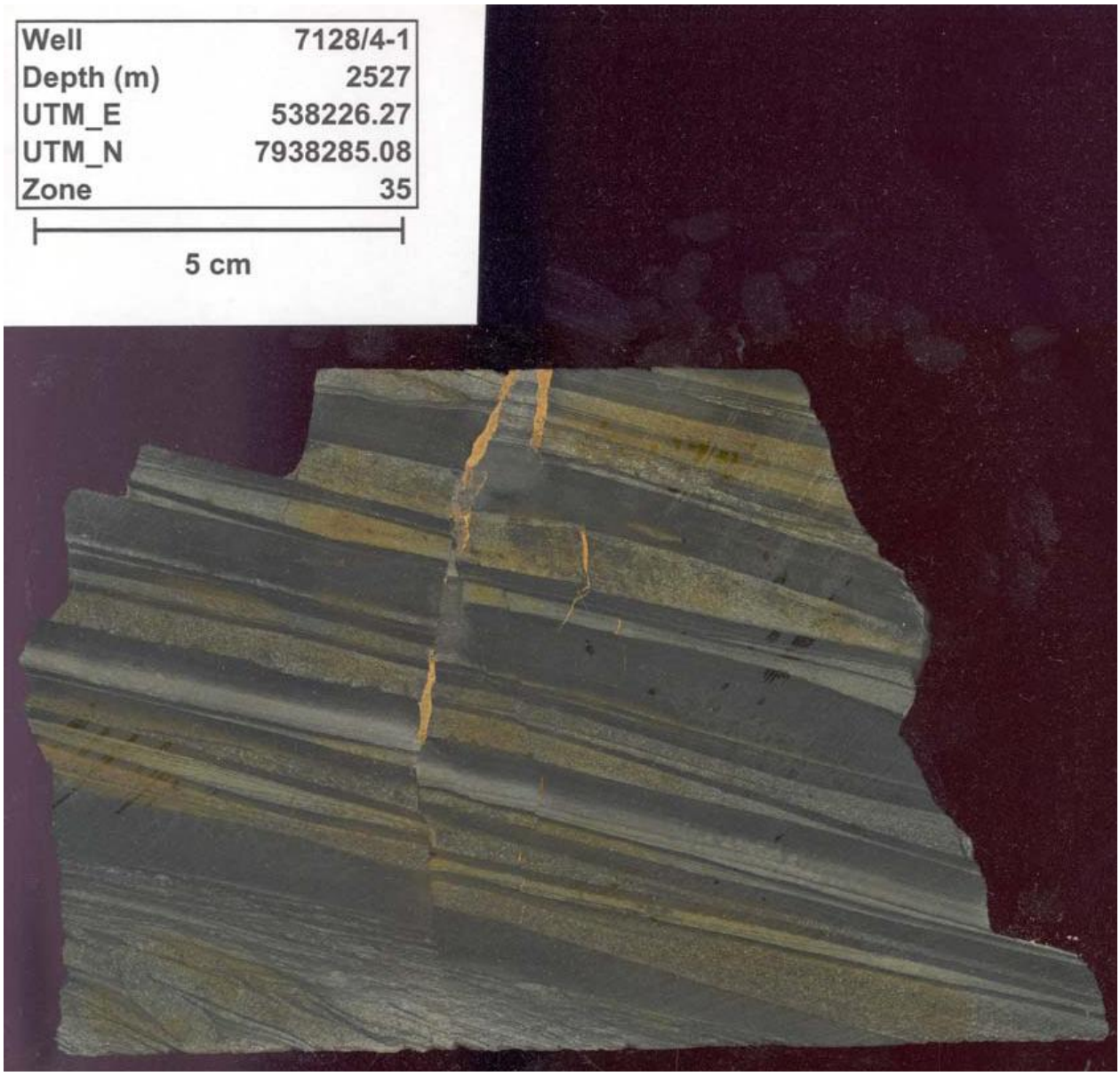

7128/4-1, 2527.0m Finnmark Øst area, Barents Sea

Laminated shaly sandstone, with apparent upward-fining layers of fine-grained sandstone (at base) through siltstone to shale (at top).

7128/4-1, 2527.2m Finnmark Øst area, Barents Sea

Laminated shaly sandstone, with apparent upward-fining layers of fine-grained sandstone (at base) through siltstone to shale (at top). Locally the sandstone layers appear to have erosional bases, indicated by what appears to be scour marks filled with relatively coarse sandstone.

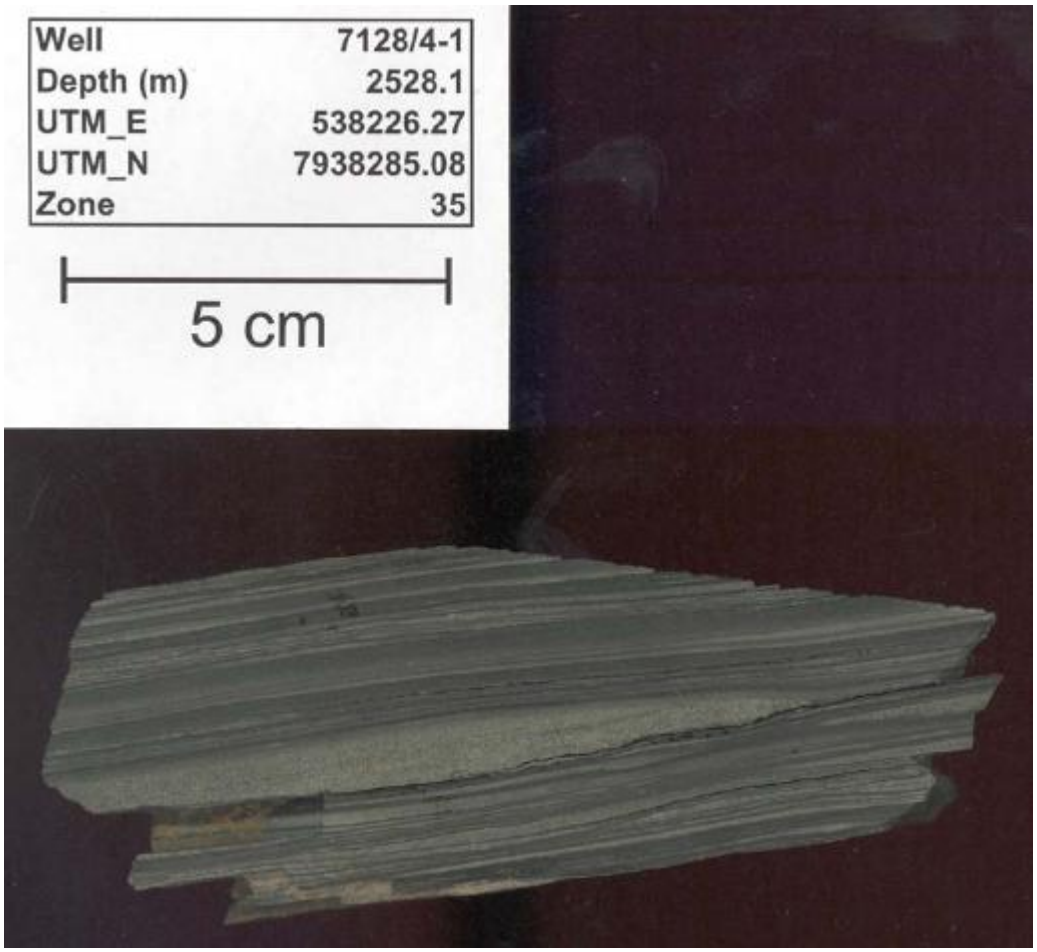

7128/4-1, 2528.1m Finnmark East area, Barents Sea

Laminated fine-grained sandstone and shale, quite similar to *7128/4-1, 2527.2m*, but without the apparent sedimentary features.

7128/6-1, 2540.5m Finnmark East area, Finnmark Platform, Norwegian Sea

Fine- to medium-grained, layered sandstone, with alternating layers of rusty brown sandstone (0.5–1.5 cm thick) and grey sandstone (0.5–1 cm thick). The rock contains a fair amount of feldspar, indicating its is relatively immature. No differences in grain size or mineralogy between the layers can be observed in hand-sample. The interfaces between the layers are typically sharp but irregular, although locally the contacts appear gradational.

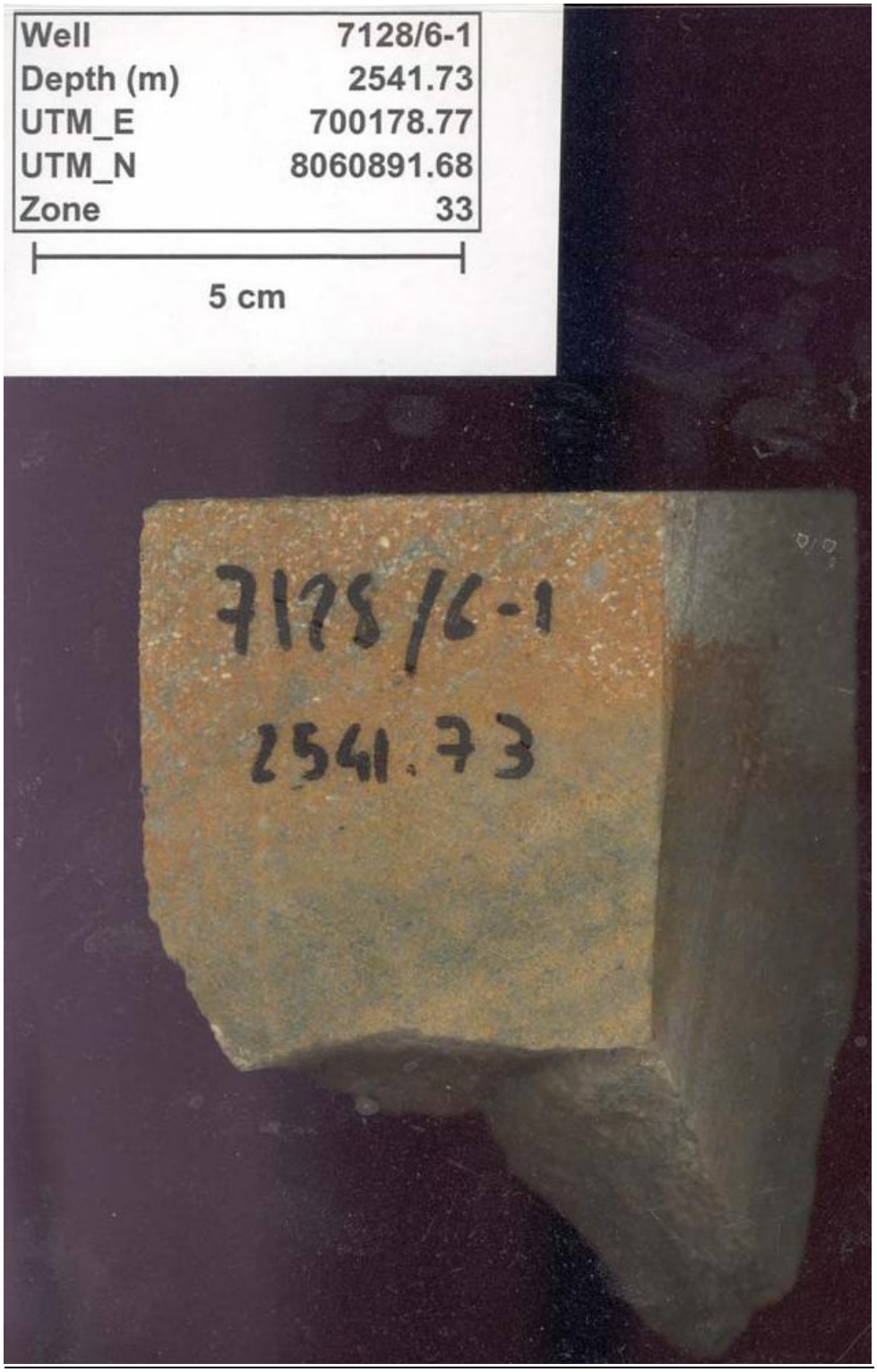

7128/6-1, 2541.73m Finnmark Øst area, Finnmark Platform, Norwegian Sea

Fine- to medium-grained, layered sandstone, with alternating layers of rusty brown sandstone (0.5–1.5 cm thick) and grey sandstone (0.5–1 cm thick).

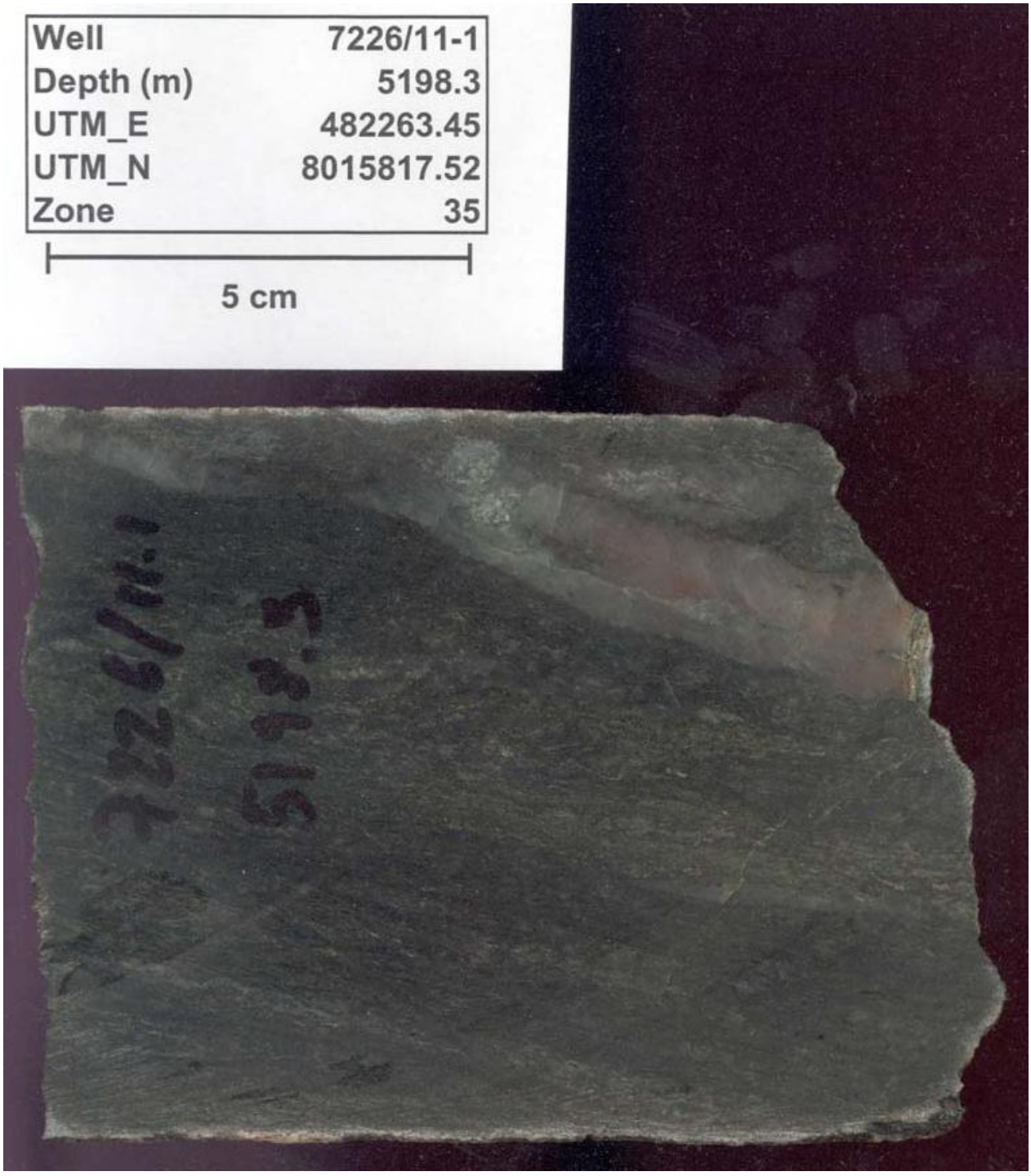

7226/11-1, 5198.3m Norsel High, Bjarmeland Platform, Barents Sea

Strongly foliated, medium-grained, biotite-rich schist (amphibolite?) with pods and layers of quartz.

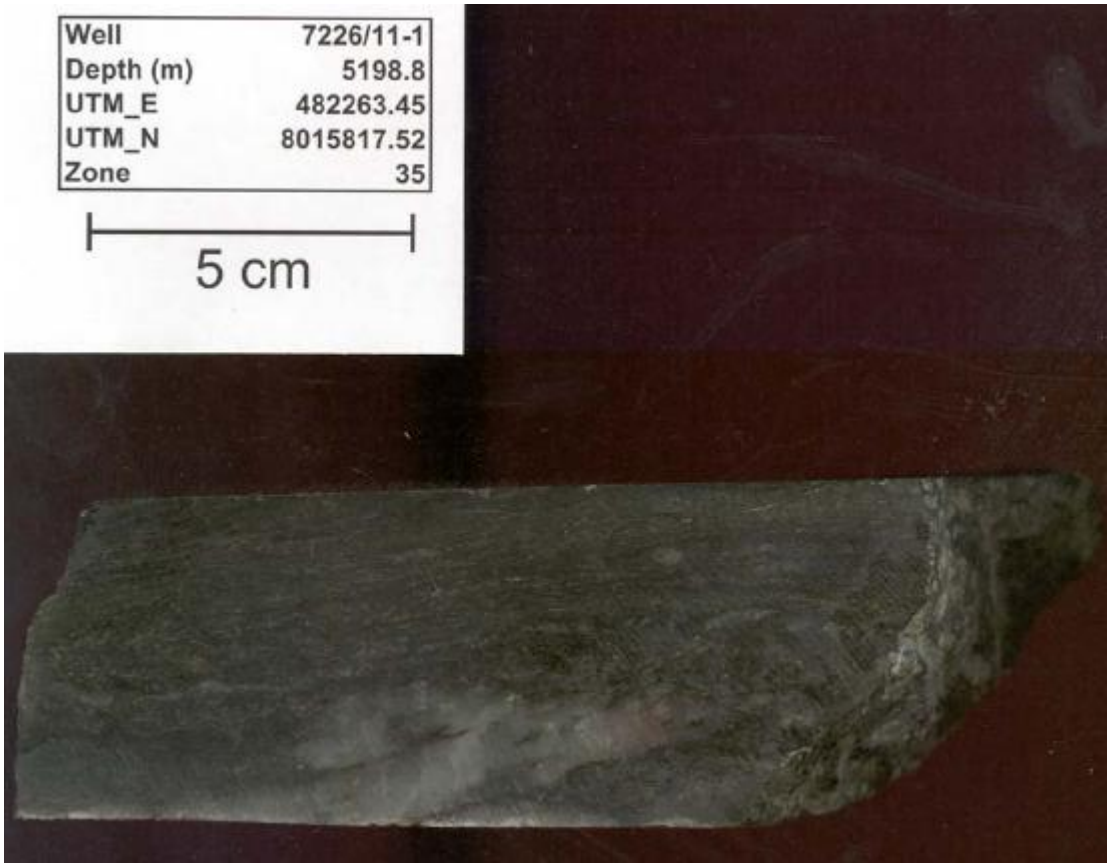

7226/11-1, 5198.8m Norsel High, Bjarmeland Platform, Barents Sea
Strongly foliated, medium-grained, biotite-rich schist (amphibolite?) with pods and layers of quartz. The rock also contains sulphides, most likely pyrite, aligned with the foliation.